Computational Approaches to Problems in Energy and Sustainability

Thesis by
Charles Bruce Musgrave III

In Partial Fulfillment of the Requirements of the
Degree of
Doctor of Philosophy

CALIFORNIA INSTITUTE OF TECHNOLOGY
Pasadena, California

2025
(Defended June 17th, 2024)

"Have lots of ideas and throw away the bad ones."
– Linus Pauling

This thesis is dedicated to my grandpa, Charles Bruce Musgrave I

© 2024
Charles Bruce Musgrave III
ORCID: 000-002-3432-0817
All rights reserved

ACKNOWLEDGMENTS

There is an endless list of people I should acknowledge for support during my time at Caltech. I've done my best to note every person who's had a profound influence on me over these past several years, regardless of the manner in which we interacted.

I will start by acknowledging some in the Goddard group; thank you Soonho for mentoring me. Thanks Vignesh for teaching me tennis and for your friendship. Thanks Max for your encouragement and for your friendship. Thanks Yuyin for putting up with my constant badgering when trying to submit the DAC paper, and for your friendship.

Thanks all the friends I made while at Caltech, including: Nick, Robert, Brian, Madeline, Frank, Phil, Ben, Jared, Dan, Ethan, Beebee, and many more. Thanks to my friends around the world, including: Quinn, Patrick, Sam, Dylan, Chris, Abdul, EJ, Tooley, James, Mat, Josh, Kev, Lukie, Mikk, Millie, and again, many more. I want to especially thank my friend and former teacher, Prof. Janet deGrazia; I am grateful for your support and kindness, although I will admit that your heat transfer course was very difficult!

Thanks to all my collaborators (in order of when our papers were published): Xiaofan, Weihao, Nathan, Shunyan, Ana, Chris, Marc, Ke, Chang, Ellen, Mo, Faisal, Marjia, Thomas, Kaeleigh, Gavin, Andong, and many more. Moreover, thank you to the

advisors of these fine scientists that I had the chance to interact with: Brent, Sen, Amy, Cliff, Theo, Jonas, and Yayuan.

I must thank my family for their unwavering support. Thanks to my family in San Jose: Grandma and Grandpa, Auntie Adriana and Uncle Long (and their numerous pets). Thanks to those in San Diego: Kafu and Auntie Jen, Auntie Gabriella and Uncle Aaron, Jack and Mila. Thanks to Uncle Richard, Mao, and Raquel in Taiwan. Thank you to those in LA: Ah Ku Joe and Auntie Gladys, Kevin and Ru, Alysha and John (and Logan), Auntie Florence and Greg. Thank you to my pets for the useful scientific discussion: Pogo, Bug, Balto, and Summit. Thank you to my siblings: Valerie, Grant, and Andrew. I am excited to see where your successes lead you; you will always have my support.

Mom, you encouraged me to come to Caltech and work for Bill. Dad, your passion for science is what encouraged me to stay at Caltech and pursue research. Thanks Mom and Dad – I would have achieved little without your love and support.

Bill, you are one of my greatest friends. I've cherished the time I've spent exploring science with you. Your love for science has truly been an inspiration to me, and I hope I can someday be just a fraction of the scientist and person that you are. Thank you for taking a chance on me – I owe my success to you. I look forward to your 100^{th} birthday symposium.

ABSTRACT

The rapid development of modern society has been met by a fierce and overwhelming increase in fossil fuel utilization and the mass production of non-renewable/recyclable materials. The escalating usage of fossil fuels results in rising greenhouse gas (GHG) emissions, while mass production of non-recyclable materials has led to unimaginable amounts of waste, which ultimately ends up in landfills or in the ocean. If we seek a sustainable future, it is imperative that we develop methods that can harness "green" electrons to generate power, particularly synthetic routes that selectively generate renewable materials via these electrons.

In this thesis, we leverage theoretical methods to investigate several platforms for the conversion of GHGs to value-added products such as methanol, ethylene, methylacetic acid, styrene, etc. To generate these products, we use heterogeneous and homogeneous catalysts, with and without the assistance of an applied potential. The overarching goal of these methods is to remediate carbon and nitrogen cycles, such that generation of harmful carbon and nitrogen-based products is immediately followed by conversion of said products back to useful reactant species.

In summation, this thesis provides several catalytic platforms for the selective and efficient production of useful fuels and feedstocks from harmful GHGs.

PUBLISHED CONTENT

1. Musgrave III, C.B., Zhu, W., Coutard, N., Ellena, J.F., Dickie, D.A., Gunnoe, T.B., Goddard III, W.A., Mechanistic Studies of Styrene Production from Benzene and Ethylene Using $[(\eta^2\text{-}C_2H_4)_2Rh(\mu\text{-}OAc)]_2$ as Catalyst Precursor: Identification of a Bis-Rh^{I} Mono-Cu^{II} Complex As the Catalyst, *ACS Catalysis.* **2021**, *11*, 9, 5688-5702. https://doi.org/10.1021/acscatal.1c01203.

2. Coutard, N., Musgrave III, C.B., Moon, J., Liebov, N., Nielsen, R.J., Goldberg, J., Li, M., Jia, X., Schinski, W., Wu, Z., Groves, J.T., Goddard III, W.A., Gunnoe, T.B., Manganese Catalyzed Partial Oxidation of Light Alkanes, *ACS Catalysis,* **2022**, *12,* 9, *5356-5370.* https://doi.org/10.1021/acscatal.2c00982.

3. Musgrave III, C.B., Bennett, M., Zhu, W., Dickie, D.A., Gunnoe, T.B., Goddard III, W.A., The Reaction Mechanism Underlying Pd(II) Catalyzed Oxidative Coupling of Ethylene and Benzene to Form Styrene: Identification of a Mono-Pd(II) Bis-Cu(II) Complex as the Active Catalyst, *Organometallics,* **2022**, *41,* 15, *1988-2000.* https://doi.org/10.1021/acs.organomet.2c00183.

4. Musgrave III, C.B., Prokofjevs, A., Goddard III, W.A., Phosphine Modulation for Enhanced CO2 Capture: Quantum Mechanics Predictions of New Materials, Journal of Physical Chemistry Letters, 2022, 13, 11183-11190. https://doi.org/10.1021/acs.jpclett.2c03145.

5. Musgrave III, C.B., Olsen, K., Liebov, N., Groves, J.T., Goddard III, W.A., Gunnoe, T.B., Partial Oxidation of Methane Enabled by Decatungstate Photocatalysis Coupled to Free Radical Chemistry, *ACS Catalysis,* **2023**, *13*, 9, 6382-6395. https://doi.org/10.1021/acscatal.3c00750.

6. Su, J., Musgrave III, C.B., Song, Y., Huang, L., Liu, Y., Li, G., Xin, Y., Xiong, P., Li, M.M., Chen, H., Tang, B.Z. Robert, M., Goddard III, W.A., Ye, R., Strain Enhances the Activity of Molecular Electrocatalysts via Carbon Nanotube Supports, *Nature Catalysis,* **2024**, *6, 818 – 828.* https://doi.org/10.1038/s41929-023-01005-3.

7. Musgrave III, C.B., Li, Y., Luo, Z., Goddard III, W.A., Dual Atom Catalyst for Rapid Electrochemical Reduction of CO to Ethylene*, Nano Energy,* **2023,** *118, 108966.* https://doi.org/10.1016/j.nanoen.2023.108966**.**

8. Goddard III, W.A., Musgrave III C.B., Electrochemical Nitrate Reduction Catalyzed by 2D MBenes, **2024**, *ACS Journal of Physical Chemistry Letters,* **2024**, *15, 7, 1899 – 1907.* https://doi.org/10.1021/acs.jpclett.4c00054,

9. Musgrave III, C.B., Su, J., Song, Y., Huang, L., Liu, L., Xin, Y., Xiong, P., Li, M.M., Chen, H., Tang, B.Z. Goddard III, W.A., Ye, R., Molecular Strain Accelerates Electron Transfer for Enhanced Oxygen Reduction [Submitted]

In all the above publications, C.B.M. participated in the conception of the project, conducted calculations, analyzed data, and participated in the writing of the manuscript.

TABLE OF CONTENTS

List of Illustrations and Tables

Chapter 1

INTRODUCTION

1.1 Summary of (some) Caltech Works

While at Caltech, I had the opportunity to work on numerous projects, collaborating with many fantastic scientists inside and outside of the Caltech community. I would like to now summarize the (fruitful) projects that I was able to contribute to during my time at Caltech, most of which will be discussed in detail throughout the remainder of this thesis.

I began by working with Prof. Brent Gunnoe and his experimental graduate students at the University of Virginia on Rh and Pd-catalyzed coupling of olefins to arenes, namely benzene to ethylene towards styrene.[1–5] This initial work began to expand in terms of collaborators and in terms of catalytic platforms. I began working also with Prof. Sen Zhang (also UVa) and Prof. John Groves at Princeton. We expanded our Rh and Pd catalysis towards functionalized arenes and olefins for the purpose of regioselective arene alkenylation. The Rh catalysis expanded towards methane partial oxidation, in which we used novel "capping arene" ligands to prohibit Rh's oxidation.[6] For methane partial oxidation we also explored Mn and decatungstate ($W_{10}O_{32}^{4-}$) systems,[7,8] the latter involving a photocatalytic process; these topics are covered in Chapters 5 and 6 of this

thesis. With these fine professors and many of their top-tier students (Weihao, Xiaofan, Marc, Kaeleigh, Ke, Chris W, Chris R, Chang, Ana, Shunyan, Zoe, Hannah), we also explored Ir, Cu, and Co catalysts for electrocatalytic water oxidation.[9–11]

In August of 2021, I was introduced to Prof. Ruquan Ye at City University of Hong Kong. Ruquan and his students were studying CO_2RR towards CO and methanol using CoPc immobilized on CNT supports. CoPc/MWCNT was previously determined to catalyze the reaction, albeit with virtually zero selectivity towards the desired methanol product. However, Ruquan and students were finding much improved results using SWCNTs. This prompted us to investigate the reaction mechanism for CO_2RR to CO (and then hopefully to methanol) for CoPc supported on MWCNTs and SWCNTs.[12] This work with Ruquan is thoroughly described in Chapter 2. The headliner for this work is that strain engineering induces molecular distortion in the CoPc molecule, which in turn enables the dramatic shift in selectivity (from CO and H_2 to methanol).

The terrific results found for CoPc on SWCNTs inspired us to also investigate NiPc for hydrogen evolution and FePc for oxygen reduction. Chapter 3 of this thesis revolves around the latter: FePc on SWCNTs accelerates the oxygen reduction reaction (ORR). The results here are somewhat analogous to the results for CoPc, in that the molecular distortion of FePc tremendously accelerated O_2 to 2 H_2O conversion. Said conversion was optimized, resulting in ORR kinetics that surpass that of commercial Pt/C materials.

These works involving molecular catalysts anchored to carbon nanotubes also led to a collaboration with Marija and Thomas (advised by Profs. Amy Cordones-Hahn and Cliff Kubiak, respectively) where we characterized a Re molecular catalyst on MWCNTs, finding that the strong electronic interaction between the two facilitated improved CO_2 reduction.[13]

Some brief work with Faisal Rehman from HKUST introduced me to the topic of dual atom catalysts (DACs), which in essence are 2-center analogs to single atom catalysts (SACs).[14,15] There are several DAC platforms, one being the extended phthalocyanine (Pc_{Ex}) structure. In addition to the Pc_{Ex} DAC having two catalyst centers, it is also intrinsically strained, which we previously claimed improves CO_2RR. With these notions in mind, we investigated 20 Pc_{Ex} DACs for the conversion of CO to ethylene. Of 20 elements screened, we found Fe, Ru, Co, and Ir to exhibit the best CO binding and CO dimerization energies. After calculating the 9-step CO-to-ethylene mechanism for these 4 DACs, we found (perhaps unsurprisingly) that the $CoPc_{Ex}$ catalyst was most promising for converting CO to ethylene. With Ir being the second best, we also investigated the bimetallic $IrCoPc_{Ex}$, and found this heteronuclear catalyst to outperform the parent $CoPc_{Ex}$ DAC. This work comprises Chapter 4 of this thesis.

1.2 Why Theory?

The catalytic systems involved herein are not easily probed with modern experimental techniques. Identifying dynamic surface coverages for heterogeneous systems and isolating active molecular catalysts for homogeneous systems is extraordinarily difficult. In addition, many of these intermediate states are often ephemeral, such that experimental time resolution on the order of picoseconds is necessary. This is currently impossible. Fear not, dear reader! Theory will illuminate the path. Specifically, we leverage the awesome power of Density Functional Theory (DFT) and Force Field (FF) Molecular Dynamics (MD) to elucidate the physical phenomena of our atomistic platforms.

1.3 Density Functional Theory Overview

Before diving into the calculations performed throughout this thesis, it is worth explaining the mechanics behind some of these methods. We begin with Density Functional Theory. The inception of DFT is described by Bill as the dream of Walter Kohn, in which the $3N$ electronic degrees of freedom needed for an N-electron wavefunction, are reduced to just 3 degrees of freedom for the electron density. In 1964, Hohenberg and Kohn published their first work (PRB 76, 6062, 1964) which shows the existence of some density functional, $G[\rho]$, that yields a system's exact energy.[16] $G[\rho]$ can be decomposed further into the kinetic energy, $T_S[\rho]$, and the exchange and correlation

energy, $E_{XC}[\rho]$. The form of this functional was not exactly known, but the development of DFT since 1964 has provided numerous approximations, with these approximations improving in accuracy over time.

$$E = \int v(r)\rho(r)dr + \frac{1}{2}\iint \frac{\rho(r)\rho(r')}{\lfloor r-r' \rfloor} drdr' + G[\rho] \quad \text{(Equation 1.1)}$$

In 1965, Kohn and Sham developed a practical method for calculating a DFT (Kohn-Sham) wavefunction based on the previous HK theorem.[17] The procedure is essentially the Hartree-Fock method but with a correction for correlation effects, in which a nonlocal effective potential operator has been introduced. That is, exchange and correlation portions of the chemical potential are treated as effective potentials.

$$E = \sum_{1}^{N} \epsilon_i - \frac{1}{2}\iint \frac{\rho(r)\rho(r')}{\lfloor r-r' \rfloor} drdr'$$
$$+\frac{1}{2}\iint \frac{\rho_1(r,r')\rho_1(r',r)}{\lfloor r-r' \rfloor} drdr'$$
$$+\int \rho(r)[\epsilon_0(\rho(r)) - \mu_0(\rho(r))]dr \quad \text{(Equation 1.2)}$$

With equation 1.2, we can self-consistently solve for the stationary state of the wavefunction using the variational principle; ϵ_i denotes the per-particle correlation energy

and $\mu_0$is the derivative of $n\epsilon_0$ wrt n. Kohn and Sham note that equation 1.2 is exact for slowly varying density and high-density regions of an electron gas. Unfortunately, most realistic systems deviate from these regions, such that additional corrections and approximations are necessary. The Local Density Approximation (LDA) was perhaps the first widely adopted DFT method. As you may have guessed, LDA assumes density varies slowly with distance, such that a local approximation is considered sufficient. This works well for uniform metals and semiconductors but fails for molecular complexes and exotic materials with dramatically varying electron densities. Generalized Gradient Approximation (GGA) improves upon LDA by scaling the Hamiltonian, such that the exchange integral includes a $|\nabla\rho|$ term.[18] Until now, we have considered our system to be fictitious, in that the electron gas is non-interacting; realistically, an ensemble of electrons is at least partially interacting. Inclusion of the Adiabatic Connection Formalism allows us to include some exact exchange in our functional (Equation 1.3), which in turn dramatically improves DFT's description of covalent bonding.

$$E_{XC}[\rho] = \int_{\lambda=0}^{\lambda=1} U_{XC,\lambda}[\rho]\, d\lambda \quad \text{(Equation 1.3)}$$

This method of including some percentage of exact exchange is commonly known as hybrid GGA. Becke's 3-parameter functional (B3LYP) is perhaps the most well-known hybrid

functional.[19] Modern improvements beyond hybrid GGA typically incorporate components such as spin kinetic energy density and its derivative(s), usually referred to as meta-GGA. For our purposes, we typically stick to hybrid GGA and meta-GGA for calculations with gaussian basis sets. For periodic calculations in which plane wave basis sets are much easier to work with, we are practically limited to GGA. I personally am an advocate for the SCAN meta-GGA functional,[20] although some (Bill) consider it to be a scam, and thus refer to it as SCAM. Hopefully Perdew and coworkers never read this.

In addition to the density functional, we must also consider relatively long-range interactions, namely London Dispersion forces. Because DFT does not guarantee the $-1/r^6$ behavior as $r \to \infty$, it is prudent to include a post correction. Grimme's D3 empirical correction for dispersion forces has virtually 0 cost relative to DFT SCF, such that it is always included when parameterized for a given functional.[21]

1.4 Force Field Overview

DFT is useful for up to hundreds of atoms and for time scales up to hundreds of picoseconds. Often times, we seek to understand physics that scale beyond the limitations of DFT. This leads us to force field (FF) methods, which operate via classical mechanics and thus evade any nasty wavefunctions or expensive QM matrices.

The fundamentals of classical FF methods boil down to the deconvolution of energy into short-range valence and long-range nonbond energies. Valence consists of bond, angle, dihedral, and inversion terms (plus cross terms), while nonbond is comprised of Van der Waals (VDW) and electrostatics. This simple decomposition allows once to fit each term to either experimental or QM barriers/force constants. The bonding term often follows a harmonic or morse potential, the latter being for reactive methods in which the bond can break/form. Angles are usually described with harmonic cosine potentials, dihedrals are often described by cosine Fourier expansions, and inversions are usually handled by an Umbrella inversion potential. A commonly invoked FF is the Universal Force Field (UFF) developed in 1992.[22] The expressions for UFF's valence terms are provided in Equations 1.4a-d.

$$E_{bond} = \frac{1}{2} k_{ij}(r - r_{ij})^2 \qquad \text{(Equation 1.4a)}$$

$$E_{\theta} = K_{IJK} \sum_{n=0}^{m} C_n \cos n\theta \qquad \text{(Equation 1.4b)}$$

$$E_{\varphi} = K_{IJKL} \sum_{n=0}^{m} C_n \cos n\varphi_{IJKL} \qquad \text{(Equation 1.4c)}$$

$$E_{\omega} = K_{IJKL}(C_0 + C_1 \cos \omega_{IJKL} + C_2 \cos 2\omega_{IJKL} \qquad \text{(Equation 1.4d)}$$

For the nonbond terms, VDW interactions are famously described by the Lennard-Jones 6-12 potential, while electrostatics are simply implemented via Coloumb's Law. The

Lennard-Jones 6-12 potential can be easily improved to more accurate potentials, such as the Universal Nonbond (UNB) developed in our group by Dr. Saber Naserifar.[23] UNB relies on a universal 2-body potential that can be easily extended to the entire periodic table through 3 atom-specific parameters. We first introduce a $E_{PR\text{-}LD}$ potential which follows a Pauli Repulsion (PR) curve at the inner wall and a London dispersion (LD) curve going from the VDW minima outward, all of which is scaled by a 7th-order taper function. We average the $E_{PR\text{-}LD}$ curves for the noble gases at fit the averaged curve to an extended Rydberg, which in turn can be converted to real space to yield the final UNB curve (Equation 1.5).

$$E_{UNB}(r_{ij}) = -D_e \exp\left[-\beta\left(\frac{(r_{ij}-R_e)}{L}\right)\right] Tap(r_{ij}) \sum_{n=0}^{5} s_n \left(\frac{(r_{ij}-R_e)}{L}\right)^n \quad \text{(Equation 1.5)}$$

For electrostatics, the functional form of the Coulomb potential is sufficient. However, the description of atomic charges that enter into the Coulomb potential requires some thought. Many general force fields assume fixed point charges for atoms. This is acceptable for some cases, but we aim to improve beyond this oversimplification. The Goddard group's first iteration of improving charges was the Charge Equilibrium (QEq) method which distributes the non-fixed charges over the volume of an atom via a gaussian.[24] More recently, polarization was embedded into the charge scheme (PQEq), in

which the atomic charge is the sum of a core gaussian and shell gaussian, which are connected via a spring.[25] The core shell remains frozen on the atom center, but the shell is permitted to polarize away; this yields an excellent description of atomic charges and dipoles. When possible, we try to incorporate the UNB and PQEq methods into our FF calculations. UNB tends to behave as intended, but for PQEq, highly-polarizable systems occasionally result in shell gaussians being displaced beyond 0.25 Å, which we consider unphysical. The simplest solution is to include a quartic term in the energy expression such that the core-shell interaction mimics a quartic oscillator as opposed to a quadratic spring.

I had the privilege of applying all these aforementioned techniques to various problems in chemistry and materials science. DFT methods were typically utilized for the exploration of reaction mechanisms. Molecular catalysts were always described with *at least* hybrid GGA, while materials calculations were limited to GGA or meta-GGA. FF methods were usually applied to simulations of local microenvironments.

1.5 References

(1) Musgrave, C. B.; Zhu, W.; Coutard, N.; Ellena, J. F.; Dickie, D. A.; Gunnoe, T. B.; Goddard, W. A. Mechanistic Studies of Styrene Production from Benzene and Ethylene Using [(H2-C2H4)2Rh(μ-OAc)]2as Catalyst Precursor: Identification of a Bis-RhIMono-CuIIComplex As the Catalyst. *ACS Catal.* **2021**. https://doi.org/10.1021/acscatal.1c01203.

(2) Musgrave, C. B.; Bennett, M. T.; Ellena, J. F.; Dickie, D. A.; Gunnoe, T. B.; Goddard, W. A. Reaction Mechanism Underlying Pd(II)-Catalyzed Oxidative Coupling of Ethylene and Benzene to Form Styrene: Identification of a Cyclic Mono-PdIIBis-CuIIComplex as the Active Catalyst. *Organometallics* **2022**. https://doi.org/10.1021/acs.organomet.2c00183.

(3) Bennett, M. T.; Reid, C. W.; Musgrave, C. B.; Goddard, W. A.; Gunnoe, T. B. Rhodium-Catalyzed Alkenylation of Arenes with Multi-Substituted Olefins: Comparison of Selectivity and Reaction Rate as a Function of Olefin Identity. *Organometallics* **2023**. https://doi.org/10.1021/acs.organomet.3c00073.

(4) Zhang, K.; Musgrave, C. B.; Dickie, D. A.; Goddard, W. A.; Gunnoe, T. B. Capping Arene Ligated Rhodium-Catalyzed Olefin Hydrogenation: A Model Study of the Ligand Influence on a Catalytic Process That Incorporates Oxidative Addition and Reductive Elimination. *Organometallics* **2022**. https://doi.org/10.1021/acs.organomet.2c00317.

(5) Bennett, M. T.; Jia, X.; Musgrave, C. B.; Zhu, W.; Goddard, W. A.; Gunnoe, T. B. Pd(II) and Rh(I) Catalytic Precursors for Arene Alkenylation: Comparative Evaluation of Reactivity and Mechanism Based on Experimental and Computational Studies. *J. Am. Chem. Soc.* **2023**. https://doi.org/10.1021/jacs.3c04295.

(6) Gu, S.; Chen, J.; Musgrave, C. B.; Gehman, Z. M.; Habgood, L. G.; Jia, X.; Dickie, D. A.; Goddard, W. A.; Gunnoe, T. B. Functionalization of RhIII-Me Bonds: Use of "Capping Arene" Ligands to Facilitate Me-X Reductive Elimination. *Organometallics* **2021**. https://doi.org/10.1021/acs.organomet.1c00223.

(7) Coutard, N.; Musgrave, C. B.; Moon, J.; Liebov, N. S.; Nielsen, R. M.; Goldberg, J. M.; Li, M.; Jia, X.; Lee, S.; Dickie, D. A.; Schinski, W. L.; Wu, Z.; Groves, J. T.; Goddard, W. A.; Gunnoe, T. B. Manganese Catalyzed Partial Oxidation of Light Alkanes. *ACS Catal.* **2022**. https://doi.org/10.1021/acscatal.2c00982.

(8) Musgrave, C. B.; Olsen, K.; Liebov, N. S.; Groves, J. T.; Goddard, W. A.; Gunnoe, T. B. Partial Oxidation of Methane Enabled by Decatungstate Photocatalysis Coupled to Free Radical Chemistry. *ACS Catal.* **2023**. https://doi.org/10.1021/acscatal.3c00750.

(9) Geer, A. M.; Liu, C.; Musgrave, C. B.; Webber, C.; Johnson, G.; Zhou, H.; Sun, C.-J.; Dickie, D. A.; Goddard, W. A.; Zhang, S.; Gunnoe, T. B. Noncovalent Immobilization of Pentamethylcyclopentadienyl Iridium Complexes on Ordered Mesoporous Carbon for Electrocatalytic Water Oxidation. *Small Sci.* **2021**. https://doi.org/10.1002/smsc.202100037.

(10) Geer, A. M.; Musgrave, C.; Webber, C.; Nielsen, R. J.; McKeown, B. A.; Liu, C.; Schleker, P. P. M.; Jakes, P.; Jia, X.; Dickie, D. A.; Granwehr, J.; Zhang, S.;

Machan, C. W.; Goddard, W. A.; Gunnoe, T. B. Electrocatalytic Water Oxidation by a Trinuclear Copper(II) Complex. *ACS Catal.* **2021**. https://doi.org/10.1021/acscatal.1c01395.

(11) Liu, C.; Geer, A. M.; Webber, C.; Musgrave, C. B.; Gu, S.; Johnson, G.; Dickie, D. A.; Chabbra, S.; Schnegg, A.; Zhou, H.; Sun, C. J.; Hwang, S.; Goddard, W. A.; Zhang, S.; Gunnoe, T. B. Immobilization of "Capping Arene" Cobalt(II) Complexes on Ordered Mesoporous Carbon for Electrocatalytic Water Oxidation. *ACS Catal.* **2021**. https://doi.org/10.1021/acscatal.1c04617.

(12) Su, J.; Iii, C. B. M.; Song, Y.; Huang, L.; Liu, Y.; Li, G.; Xin, Y.; Xiong, P.; Li, M. M.-J.; Chen, H. M.; Tang, B. Z.; Robert, M.; Iii, W. A. G.; Ye, R. Improving Molecular Catalyst Activity Using Strain-Inducing Carbon Nanotube Supports. *ChemRxiv* **2022**. https://doi.org/0.26434/chemrxiv-2022-r9r22.

(13) Zoric, M. R.; Chan, T.; Musgrave, C. B.; Goddard, W. A.; Kubiak, C. P.; Cordones, A. A. In Situ X-Ray Absorption Investigations of a Heterogenized Molecular Catalyst and Its Interaction with a Carbon Nanotube Support. *J. Chem. Phys.* **2023**. https://doi.org/10.1063/5.0129724.

(14) Rehman, F.; Kwon, S.; Musgrave, C. B.; Tamtaji, M.; Goddard, W. A.; Luo, Z. High-Throughput Screening to Predict Highly Active Dual-Atom Catalysts for Electrocatalytic Reduction of Nitrate to Ammonia. *Nano Energy* **2022**, *103b*,

107866. https://doi.org/10.1016/j.nanoen.2022.107866.

(15) Rehman, F.; Kwon, S.; Hossain, M. D.; Musgrave, C. B.; Goddard, W. A.; Luo, Z. Reaction Mechanism and Kinetics for N2 Reduction to Ammonia on the Fe-Ru Based Dual-Atom Catalyst. *J. Mater. Chem. A* **2022**, *10*, 23323–23331. https://doi.org/10.1039/d2ta06826e.

(16) Hohenberg, P.; Kohn, W. Inhomogeneous Electron Gas. *Phys. Rev.* **1964**, *136* (3B), B864. https://doi.org/10.1103/PhysRev.136.B864.

(17) Kohn, W.; Sham, L. J. Self-Consistent Equations Including Exchange and Correlation Effects. *Phys. Rev.* **1965**, *140* (4A), A1133. https://doi.org/10.1103/PhysRev.140.A1133.

(18) Perdew, J. P.; Burke, K.; Ernzerhof, M. Generalized Gradient Approximation Made Simple. *Phys. Rev. Lett.* **1996**, *77* (18), 3865–3868. https://doi.org/10.1103/PhysRevLett.77.3865.

(19) Becke, A. D. Density-Functional Thermochemistry. III. The Role of Exact Exchange. *J. Chem. Phys.* **1993**, *98* (7), 5648–5652. https://doi.org/10.1063/1.464913.

(20) Sun, J.; Ruzsinszky, A.; Perdew, J. Strongly Constrained and Appropriately Normed Semilocal Density Functional. *Phys. Rev. Lett.* **2015**. https://doi.org/10.1103/PhysRevLett.115.036402.

(21) Grimme, S.; Antony, J.; Ehrlich, S.; Krieg, H. A Consistent and Accurate Ab Initio Parametrization of Density Functional Dispersion Correction (DFT-D) for the 94 Elements H-Pu. *J. Chem. Phys.* **2010**, *132* (15), 154104. https://doi.org/10.1063/1.3382344.

(22) Rappé, A. K.; Casewit, C. J.; Colwell, K. S.; Goddard, W. A.; Skiff, W. M. UFF, a Full Periodic Table Force Field for Molecular Mechanics and Molecular Dynamics Simulations. *J. Am. Chem. Soc.* **1992**, *11425* (10024–10035). https://doi.org/10.1021/ja00051a040.

(23) Naserifar, S.; Oppenheim, J. J.; Yang, H.; Zhou, T.; Zybin, S.; Rizk, M.; Goddard, W. A. Accurate Non-Bonded Potentials Based on Periodic Quantum Mechanics Calculations for Use in Molecular Simulations of Materials and Systems. *J. Chem. Phys.* **2019**, *151* (15). https://doi.org/10.1063/1.5113811.

(24) Rappé, A. K.; Goddard, W. A. Charge Equilibration for Molecular Dynamics Simulations. *J. Phys. Chem.* **1991**. https://doi.org/10.1021/j100161a070.

(25) Naserifar, S.; Brooks, D. J.; Goddard, W. A.; Cvicek, V. Polarizable Charge Equilibration Model for Predicting Accurate Electrostatic Interactions in Molecules and Solids. *J. Chem. Phys.* **2017**. https://doi.org/10.1063/1.4978891.

Part I:
Strain Engineering for Enhanced Catalysis

Chapter 2

Improving Cobalt Phthalocyanine Catalyst Activity using Strain-Inducing Carbon Nanotube Supports

Reproduced with permission from:

Jianjun Su, Yun Song, Libei Huang, Yong Liu, Geng Li, Yinger Xin, Pei Xiong, Molly Meng-Jung Li, Haoran Wu, Minghui Zhu, Hao Ming Chen, Jianyu Zhang, Ben Zhong Tang, Marc Robert, William A. Goddard III, Ruquan Ye. *Strain enhances the activity of molecular electrocatalysts via carbon nanotube supports.*

Nat. Catal., **2023**, *6, 818 – 828 (Open Access).*

2.1 Abstract

Support-induced strain engineering is a powerful strategy to modulate the electronic structure of two-dimensional materials. However, controlling strain of planar molecules such as metallophthalocyanines and metalloporphyrins is technically challenging due to their sub–2 nm lateral size. In addition, the effect of strain on molecular properties remains poorly understood. Starting with cobalt phthalocyanine (CoPc), a model CO_2 reduction reaction (CO_2RR) catalyst, we show that carbon nanotubes (CNTs) are ideal substrates for inducing optimum properties through molecular curvature. Using a tandem-flow electrolyzer with monodispersed CoPc on single-walled CNTs (CoPc/SWCNT) as the

catalyst, we achieve a methanol partial current density of >90 mA cm^{-2} with a selectivity of >60%. CoPc on wide multi-walled CNTs (MWCNTs) leads to only 16.6% selectivity. We report vibronic and X-ray spectroscopic characterizations to unravel the distinct local coordinations and electronic structures induced by the strong molecule-support interactions. These results agree with our Grand Canonical Density Functional Theory that calculates the energetics as a function of applied potential. We find that SWCNTs induce curvature in CoPc, which improves *CO binding to enable subsequent formation of methanol, while wide MWCNTs favor CO desorption. Thus, we demonstrate that the SWCNT-induced molecular strain increases methanol formation. Our results show the important role of SWCNTs for designing improved molecular interfaces beyond catalyst dispersion and electron conduction.

2.2 Introduction

The use of curved supports for inducing local strain is well established for generating exotic properties from conventional layered materials[1]. An excellent example is graphene, which already exhibits remarkable properties in its planar configuration. Straining graphene can modify its electronic structure to create polarized carrier puddles, induce pseudomagnetic fields, and alter surface properties[2]. In MoS_2, modifying the supporting glass sphere diameter induces curvature in the MoS_2, which permits precise bandgap tuning of MoS_2 in a continuous range as large as 360 meV[3]. Curved MoS_2 conformally coated on Au nanocone arrays is a promising catalyst for the hydrogen evolution reaction

(HER). The improved HER activity is attributed to sulfur-vacancies and reduction of the bandgap under strain[4]. Graphene and MoS_2 are good candidates for strain engineering because they are relatively large (mm) in size. However, strain induction for sub–2 nm materials is challenging due to the mismatch of lateral size with supports and difficulties in material transfer.

Molecular complexes such as metalloporphyrins and metallophthalocyanines are efficient CO_2 reduction reaction (CO_2RR) catalysts because of their electronic structures and the tunable ligand environments surrounding the active sites[5]. However, these molecules along with most other molecular catalysts primarily reduce CO_2 to CO; catalysts that selectively reduce CO_2 beyond CO are scarcely reported[6,7]. An early study of cobalt phthalocyanine (CoPc) in 1984[8] showed a methanol (MeOH) Faradaic efficiency (FE) of $<5\%$. This work did not receive much attention until recently when the Wang[9] and Robert[10] groups separately reported improved FE_{MeOH} with CoPc deposited on multiwalled carbon nanotubes (MWCNTs). In the paper from the Robert group, it was emphasized that only small amount of methanol could be obtained from CO_2RR, while larger amount could be generated from CO reduction reaction (CORR). In stark contrast, the Wang group claimed that a FE_{MeOH} as high as 44% could be obtained with CoPc deposited on MWCNT. However, most CoPc-based catalysts have been unable to convert CO_2 to methanol with significant FE and current densities, instead finding CO to be the prevailing product[11,12,13,14,15]. Numerous discrepancies in reaction selectivity and kinetics amongst CoPc studies make it difficult to determine the ability of CoPc to catalyze

CO_2RR beyond the prominent CO product.

CNTs are exceptional support materials for heterogeneous catalysis. Their large specific surface areas readily disperse nanoparticles to avoid agglomeration, and their high electronic conductivities make them promising for electrochemical applications. Herein, we present new insights into the role of CNTs in heterogeneous catalysis. Thanks to recent advancements in synthesis and purification, the diameters of CNTs can be controlled from 2 nm to >50 nm, making them ideal supports for inducing strain in sub–2 nm planar molecules. Depending on the local interactions between curved CNTs and the overlayer, molecules may undergo controllable distortion to alleviate strain (Figure 2.1a). Assuming the overlayer is fully elastic and the interlayer distance is 0.3 nm, the bending angle can range from ~96^{o} (1 nm-diameter CNT) to ~1.5^{o} (100 nm-diameter CNT) (See Supplementary Methods 1 for estimates). We report X-ray spectroscopic studies and other spectra to assess the structure of molecular CoPc before and after monodispersion on various CNTs. We observe significant molecular distortion and strong molecule-CNT interactions for SWCNTs. This is supported by our DFT calculations which find that increased molecular curvature strengthens *CO absorption, which enables further reduction towards MeOH, while flat CoPc favors CO desorption, thus forming CO as the main product. As a result, the distorted CoPc/SWCNT exhibits a 385% improvement in FE_{MeOH} compared to CoPc/MWCNT. We also extend these findings to ORR and CO_2RR studies on SWCNTs, which also exhibit strain-dependent catalytic activity.

2.3 Results

2.3.1 Materials Synthesis and Characterization

Metallophthalocyanines deposited on different CNTs are denoted as MPc/X, where M is the metal and X refers to SWCNTs or the average diameter (in nm) of the MWCNTs (Appendix Figure A1 and A2). Scanning TEM energy-dispersive X-ray spectroscopy (STEM-EDS) mapping shows a uniform distribution of N and Co along the SWCNT surface (Figure 2.1b-e). In aberration-corrected HAADF-STEM (Figure 2.1f), the bright spots marked with red circles further verify the uniformly dispersed Co sites.

We sought to elucidate how interactions of CoPc with CNTs might affect catalysis. Early studies suggested that deformed phthalocyanines will have varied vibronic and electronic structures[16,17]. We first characterized the Raman spectra for CoPc and various bare and CoPc-decorated CNTs (Appendix Figure A3 and 4)[18]. In comparison, CoPc/SWCNT shows a prominent peak at 250-290 cm^{-1}, assigned to the Co-N out-of-plane deformation and ring boating[19]. This enhanced out-of-plane signal has been frequently observed on strained/curved 2D materials[3,20]. Interaction with the CNT involving π-π stacking and through-space orbital coupling, could lead to additional charge transfer processes[21]. This is validated by the UV-vis spectra of the catalysts, showing a red shift at the Q band of the CoPc molecules after deposition on CNTs (Appendix Figure A5)[22,23]. X-ray photoelectron spectroscopy (XPS) for both the Co $2p_{1/2}$ and Co $2p_{3/2}$ of CoPc/CNTs shift to higher binding energies (Figure 2.2a), reaching a maximum difference of 1.2 eV for

CoPc/SWCNT. The signal evolution is even more prominent for the N 1s peak (Figure 2.2b). Previous reports studied the interactions of MPc with various substrates such as TiO_2, Au, and other semiconductors[24,25]. It was thought that the strong molecule-substrate interaction would induce a peak splitting, while a weak interaction would cause only a peak shift. Indeed, we observe a new peak at >400 eV for all the CoPc/CNT samples. CoPc/SWCNT shows the most intense new peak at ~400.5 eV, implying strong CoPc-SWCNT interactions. The peak splitting of CoPc/SWCNT is ~1.3 eV, attributed to the shifted N 1s energies according to theoretical calculations discussed below. The $E_{1/2}(Co^{I}/Co^{II})$ redox potential also shifts from 0.162 V for CoPc/50 to 0.119 V for CoPc/SWCNT (Appendix Figure A6), which is similar to the deformed ZnPc attributed to the destabilization of the highest occupied molecular orbital[17]. The above experimental data suggest the distinct molecular structures on different CNT supports.

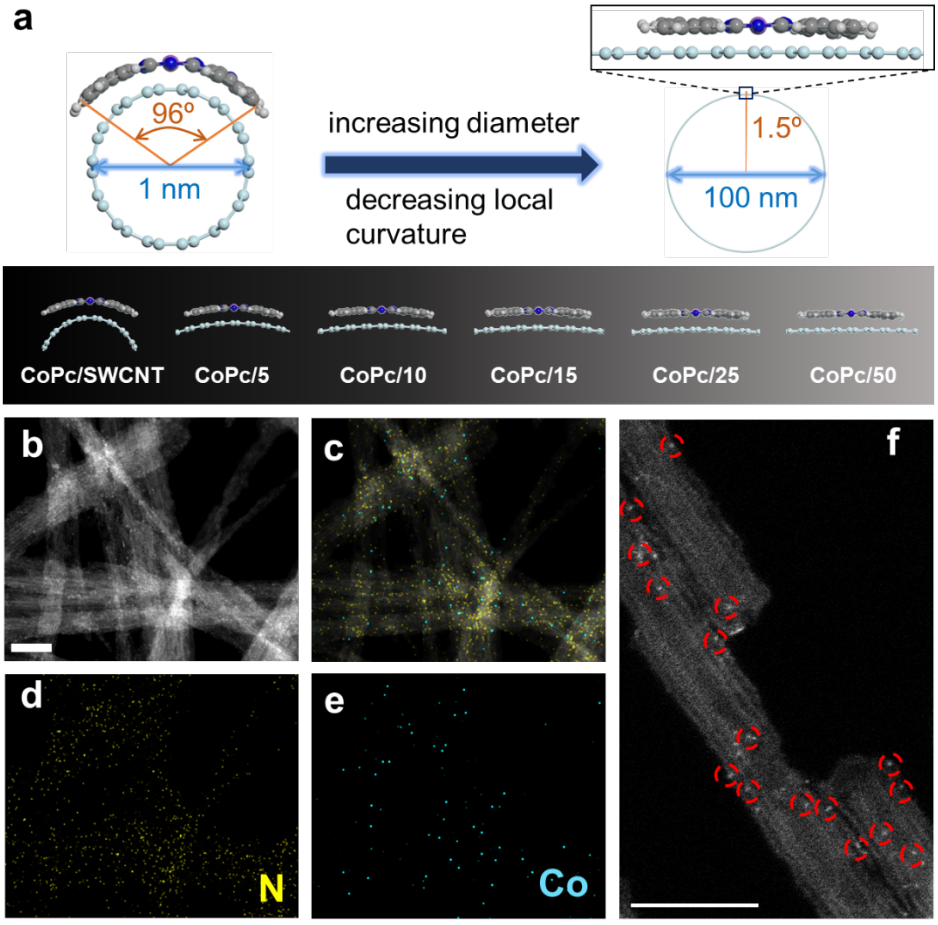

Figure 2.1: (**a**) Illustration of structural distortion of CoPc on different diameter CNTs, assuming CoPc is fully elastic. (**b**) HAADF-STEM and (**c-e**) EDS elemental mapping of CoPc/SWCNT. (**f**) Aberration-corrected HAADF-STEM of CoPc/SWCNT showing the isolated Co atoms on the SWCNT surface. The isolated Co atoms are marked with red circles. Scale bar: 20 nm in (**b**) and 5 nm in (**f**).

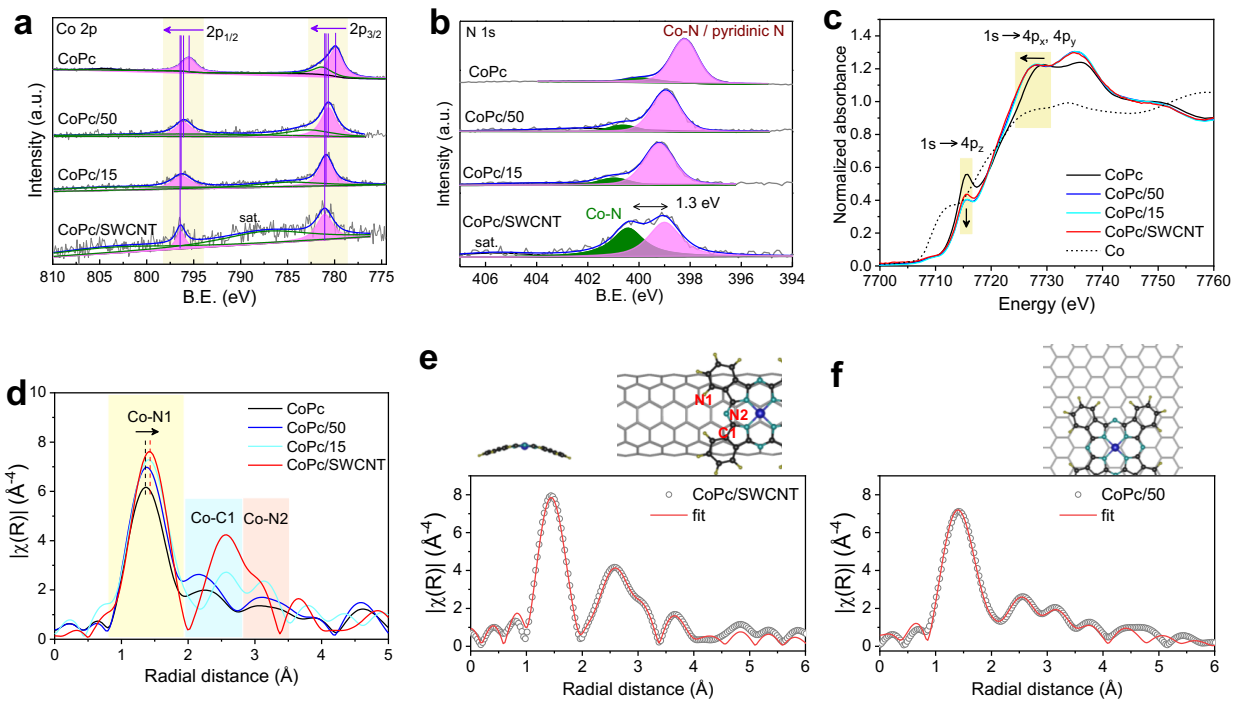

Figure 2.2: X-ray spectroscopic characterizations of CoPc/SWCNT, CoPc/15, CoPc/50 and CoPc. XPS of (**a**) Co 2p and (b) N 1s. (**c**) XANES Co K-edge spectrum and (**d**) FT-EXAFS. Simulated structures and EXAFS fitting in R space for (**e**) curved CoPc/SWCNT and (**f**) flat CoPc/50. The N atoms in the first and second coordination spheres are marked with N1 and N2.

To understand the CoPc/CNTs' local structures, we performed X-ray absorption near-edge structure (XANES) and extended X-ray absorption fine structure (EXAFS) analyses of Co. As shown in Figure 2.2c, the Co K-edge XANES spectra exhibits an obvious peak at 7715 eV; this $1s \rightarrow 4p_z$ transition is indicative of the Co-N_4 structure[26]. A decline in the $1s \rightarrow 4p_z$ transition is observed when CNTs are introduced, likely due to the decreased symmetry (D_{4h} to C_{4v}). The peaks near 7725 eV result from the $1s \rightarrow 4p_{x,y}$ transition, with the exact peak position dependent on Co's valency[27]. The peak position of CoPc/CNT shifts slightly to lower energy compared to CoPc, indicating charge transfer between CoPc and the CNT. The Fourier transform (FT) of the EXAFS spectra shows the coordination

environment around Co sites (Figure 2.2d and Appendix Figure A7). The signal can be cataloged into three groups: [CoPc, CoPc/50], [CoPc/25, CoPc/15], and [CoPc/5; CoPc/SWCNT]. As the CNT diameter decreases, both the Co-N1 (first coordination sphere) and Co-C1 (second coordination sphere) distances increase. The Co-N1 and Co-C1 peak deviations indicate distortion of the CoPc molecule[28]. In addition, the peak intensities increase with smaller-diameter CNTs; this increased Co coordination number is a result of stronger interaction of CoPc with the CNT, as inferred from signal fitting. The fitted EXAFS signals (Figure 2.2e-f and Appendix Figure A8,9, and Appendix Table A1) imply molecular bending around the CNT. The high degree of molecular bending for CoPc/SWCNT leads to elongated Co-N1 and Co-C1 distances (Appendix Table A1). In addition, the intensity of the Co-C1 peak increases due to strong Co-C_{SWCNT} interactions. For CoPc/50, the local CNT curvature is negligible, such that CoPc remains planar. Consequently, the CoPc/50 coordination environment is similar to pristine CoPc molecule. Since the EXAFS only tells the coordination environment around the Co center, an expanded flat CoPc with longer Co-N1 and Co-C1 bond will also be possible structure. However, our molecular dynamics (MD) calculations, discussed in the computation part later, suggest such configuration is unfavorable. In addition, the flat configuration cannot explain the experimental data of Raman, $E_{1/2}(Co^{I}/Co^{II})$, XPS and electrochemical performance.

2.3.2 Electrochemical CO_2 Reduction Performance of CoPc/SWCNT

Electrochemical CO_2RR was carried out in a custom glass H-cell with 0.5 M $KHCO_3$. The number of electrochemical active Co sites are similar among different sample indicated by the anodic Co^{I}/Co^{II} peak areas (Appendix Figure A6). Appendix Figure A10 shows the cyclic voltammograms (CVs) for CoPc/SWCNT, CoPc/15, and CoPc/50 catalysts in CO_2-saturated solution. The currents are very pronounced relative to the bare SWCNT, MWCNT/15, and MWCNT/50 supports. The CO_2RR selectivities of CoPc/SWCNT, CoPc/15, and CoPc/50 were further evaluated at various potentials via chronoamperometry tests (Appendix Figure A11). Nuclear magnetic resonance (NMR) and gas chromatography (GC) measurements were made to analyze the liquid and gas products, respectively. As shown in Figure 2.3a, FE_{MeOH} exhibits the typical volcano-like dependence on applied potential from -0.78 to -1.03 V vs. RHE. At -0.93 V, a maximum FE_{MeOH} of 53.4% is achieved for CoPc/SWCNT, which is significantly higher than that of CoPc/15 (17.1% at -0.93 V) and CoPc/50 (13.9% at -0.93 V). A maximum MeOH partial current density (j_{MeOH}) of 8.8 mA cm^{-2} is achieved at -0.93 V for CoPc/SWCNT (Appendix Figure A12) compared to the 1.9 mA cm^{-2} for CoPc/15 and 1.5 mA cm^{-2} for CoPc/50. To confirm that MeOH is derived from CO_2 rather than other impurities, isotopic-labelling experiments were conducted in $^{13}CO_2$-saturated 0.5 M $KH^{13}CO_3$ while under continuous $^{13}CO_2$ flow. The peak splitting of ^{1}H NMR at 3.32 ppm and the obvious ^{13}C NMR peak at 49.11 ppm verifies that the produced MeOH originates from the CO_2 input[10,29] (Appendix Figure A13). The bare CoPc, SWCNT, and MWCNT/15 samples

show negligible electrocatalytic CO_2RR activity with little CO produced throughout the potential window (Appendix Figure A14). In the durability test, the CoPc/SWCNT maintained ~30% FE_{MeOH} for 10 h at an operating total current density of 16 mA cm^{-2} (Appendix Figure A15). Appendix Figure A16 shows the relation of FE_{MeOH} with CoPc loading on SWCNT. Increasing the CoPc:SWCNT ratio from 1:50 to 1:3 and 1:1 did not increase FE_{MeOH}. This could be explained by CoPc-CoPc stacking at high loadings that weakens the support effect. High CoPc loading also leads to catalyst leaching during chronoamperometry.

We next explored how FE_{MeOH} varies with CNT diameter at -0.93 V (Appendix Figure A17). The FE_{MeOH} decreases from 53.2% for CoPc/SWCNT to 13.9 % for CoPc/50. The conversion of CO_2 to MeOH involves six electron transfers, so that high charge transfer resistance will negatively affect FE_{MeOH}. Electrochemical impedance spectroscopy (EIS) at -0.93 V shows that CoPc/SWCNT has less charge transfer resistance than CoPc/15 and CoPc/50, indicating more facile substrate reduction with CoPc/SWCNT (Appendix Figure A18).

To examine the role of SWCNT's electronic structure, we used metallic and semiconducting SWCNTs (SWCNT-M or SWCNT-S) as supports for catalyst preparation. SWCNT-M and SWCNT-S show distinct UV absorption at 600-800 nm and 900-1100 nm for the M_{11} and S_{22} peaks, respectively (Appendix Figure A19). CoPc/SWCNT-M and SWCNT-S exhibit similar FE_{MeOH} and j_{MeOH} to those of CoPc/SWCNT at -0.93 V (Appendix Figure A20d), suggesting the SWCNT electronic structure does not play a

major role in steering the multielectron reduction.

To highlight the necessity of the CoPc-SWCNT interfacial configuration, we covalently anchored CoPc to the surface of SWCNT (Appendix Figure A20a), leading to a flat CoPc vertically bound to SWCNT (f-CoPc-SWCNT). The N1s XPS peak of f-CoPc-SWCNT exhibits no peak splitting and the out-of-plane deformation signal does not emerge (Appendix Figure A20b,c); these features are distinct from CoPc/SWCNT but similar to pristine CoPc. Moreover, the f-CoPc-SWCNT only reaches 15.5% FE_{MeOH} and a j_{MeOH} of 1.6 mA cm^{-2}, which i>s similar to the performance of CoPc/50 (Appendix Figure A20d).

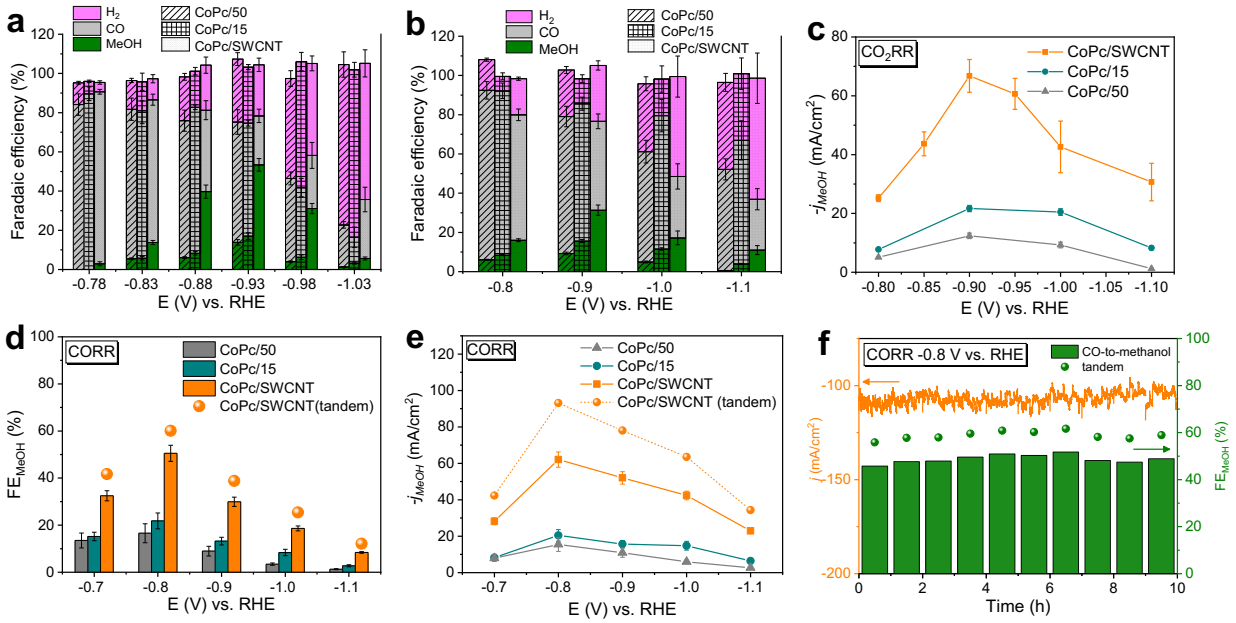

Figure 2.3: FE of MeOH, CO and H_2 in (**a**) H-cell with 0.5 M $KHCO_3$ as electrolyte and (**b**) flow cell with 0.1 M KOH + 3 M KCl as electrolyte. (**c**) j_{MeOH} of CoPc/SWCNT, CoPc/15 and CoPc/50 catalysts in a flow cell under CO_2 atmosphere. (**d**) FE_{MeOH} and (**e**) j_{MeOH} of CoPc/SWCNT, CoPc/15 and CoPc/50 in a flow cell under CO atmosphere. (**f**) long-term stability and corresponding FE_{MeOH} of CoPc/SWCNT at -0.8 V vs. RHE.

2.3.3 High Current Density in CO_2RR and CORR Using a Flow Cell

The CO_2RR current density is limited in the H-cell by low CO_2 solubility and mass transport in aqueous electrolyte. In order to achieve higher j_{MeOH}, we constructed a flow cell featuring a gas diffusion electrode (Appendix Figure A21). In the flow cell, 0.1 M KOH + 3 M KCl (instead of $KHCO_3$) was used as the catholyte to improve j_{MeOH} and suppress HER at high potential[10,30,31]. The total current density in the flow cell is substantially higher (Appendix Figure A22) than that of the H-cell at all applied potentials. The maximum j_{MeOH} of CoPc/SWCNT reaches 66.8 mA cm^{-2} with a 31.3% FE_{MeOH} at -0.9 V vs. RHE, which is 7.6 times that of j_{MeOH} in the H-cell (Figure3b and Figure 2.3c). The maximum j_{MeOH} of CoPc/15 and CoPc/50 are 21.7 mA cm^{-2} (15.6% FE_{MeOH}) and 9.3 mA cm^{-2} (9.3% FE_{MeOH}) at -0.9 V vs. RHE, respectively. Additionally, CoPc/SWCNT exhibits a stable total current density with no loss for 20 min at various potentials (Appendix Figure A23). Even at 200 mA cm^{-2} (-0.9 V vs. RHE), the FE_{MeOH} is maintained at ~26% for 10 h without decay (Appendix Figure A23 and 24).

Since the electrochemical reduction of CO_2 to MeOH is a multistep process with CO being the important intermediate[9], MeOH production will be inhibited by *H and *CO_2 adsorption. Competition with *CO_2 adsorption can be resolved by a tandem reaction. Specifically, CO_2 can be first reduced to CO with >95% FE, and then the produced CO can be further reduced to MeOH in a second electrolyzer free of CO_2 in alkaline media. We conducted direct CO reduction in a flow cell identical to the parent CO_2RR process, except that CO was used as the feed gas to achieve higher FE_{MeOH} and j_{MeOH}. For

CoPc/SWCNT, j_{MeOH} reaches 62.1 mA cm^{-2} at -0.8 V_{RHE} with a corresponding FE_{MeOH} of 50.5% (Figure 2.3d and Appendix Figure A25). This corresponds to a FE_{MeOH} of 60.1% for the tandem reaction, assuming a 95% FE_{CO} from CO_2. CoPc/15 and CoPc/50 achieve j_{MeOH}s of only 20.5 mA cm^{-2} and 15.5 mA cm^{-2} with FE_{MeOH}s of 21.8% and 16.6%, respectively (Figure 2.3e and Appendix Figure A26). Moreover, CORR with CoPc/SWCNT maintains a total current density of 100 mA cm^{-2} at a FE_{MeOH} of ~50% for 10 h (Figure 2.3f and Appendix Figure A27).

An extremely high applied potential would over-reduce the Pc ligand, resulting in deactivation via demetallation[9]. After the stability test, the Raman spectrum confirms the presence of the SWCNT and the curved CoPc structure. The UV-vis absorption spectrum and X-ray diffraction patterns of CoPc/SWCNT display no new peaks related to cobalt metal or cobalt oxide, indicating no demetallation (Appendix Figure A28).

2.4 Computational Results

2.4.1 CoPc Immobilized on a CNT

We find that binding the CoPc catalyst to the CNT walls changes the geometric and electronic structure. To further investigate this, we employed MD calculations using the Universal Force Field (UFF)[32]. These MD simulations used the polarizable charge equilibration (PQEq)[33] scheme for electrostatics and the RexPoN universal nonbond (UNB)[34] van der Waals interactions (UFF is used solely for valence terms). Using UFF + PQEq + UNB allows us to obtain molecular geometries at the accuracy level of high-

quality quantum mechanics while at the cost of classical mechanics. PQEq + UNB's ability to accurately capture non-bond geometries has been proven previously for several crystal systems[34].

We estimate that the smallest SWCNTs in our experiments have a diameter of ~2 nm. To model the SWCNT, we use a large $C_{116}H_{28}$ graphitic sheet with curvature matching that of a SWCNT with 2 nm diameter (Appendix Figure A29 and 30); the 116 C atoms provide ample surface area for coordinating CoPc. We then placed a flat CoPc catalyst within van der Waals distance of the outside of the SWCNT. With the H atoms of the SWCNT frozen, we optimized the geometry of the CoPc when near the outside of the SWCNT wall. The MD simulation shows that the CoPc curves around the $C_{116}H_{28}$ such that the curvature of the catalyst and the CNT are equal. Additionally, the curved plane of the catalyst lies ~3.11 Å from the wall of the SWCNT, indicating significant pi-pi stacking between the catalyst and the SWCNT. Fixing the peripheral H of CoPc to maintain the pristine CoPc structure, however, results in a longer Co-$C_{116}H_{28}$ distance, which suggests a weaker Co-CNT interaction. We also explored how CoPc interacts with a large, flat sheet of carbon, which represents the MWCNT. In this case, the CoPc plane remained parallel to the flat $C_{116}H_{28}$ sheet with the distance between the two planes being ~3.37 Å. When instead we used 2D periodic graphene, the inter-plane distance is still predicted to be 3.37 Å. Thus, we conclude that the flat or curved $C_{116}H_{28}$ sheet properly mimics the graphene or SWCNT. The predicted structures from our MD calculations agree well with our QM calculations and with our experimental spectroscopic data for

curved and flat CoPc structures as shown in Figure 2.2e,f and Appendix Table A1. Moreover, DFT at the PBE-D3 level of theory predicts flat CoPc to reside 3.39 Å from graphene, in excellent agreement with the prediction. This justifies our claim that PQEq + UNB accurately captures non-bond geometries.

In addition to the geometric distortion of CoPc upon binding to the SWCNT, we observe a shift in the N 1s indicating electronic structure distortion. DFT predicts 4 degenerate N 1s orbitals at -381.16 eV below the vacuum energy. Forcing the complex into the curved geometry breaks the degeneracy of the N 1s orbitals. Specifically, the 4 orbitals now range from -381.44 eV to -381.36 eV (0.08 eV variation). The N 1s orbitals are also stabilized in the curved complex by an average of -0.24 eV, indicating increased binding energy as observed in experiment (Figure 2.2b).

2.4.2 Enhanced CO Absorption

The differing CO_2RR selectivity between curved and flat CoPc hints a change in the CO absorption step. To explore this, we applied Grand Canonical DFT to examine the energetics as a function of chemical potential. Our Grand Canonical Potential Kinetics (GCPK) method[35] keeps the applied potential constant for the initial and product states of each reaction step, just as in experiment (see Methods for more details). For CoPc on the SWCNT, we use the curved CoPc generated from the MD simulation as the starting point. For CoPc on the MWCNT, we start with the typical CoPc catalyst with D_{4h} symmetry. Liao and coworkers[36] recently suggested that at -1.0 V vs. RHE (-1.4 V vs.

SHE at pH=6.8), the CoPc catalyst is spontaneously reduced to $CoPcH_4$ in water. Specifically, the 4 outward N of the Pc ligand are hydrogenated (hence PcH_4) with a free energy change of -2.92 eV relative to CoPc at 298.15 K. Thus, for our calculations we hydrogenate the 4 outward N of the Pc ligand for both curved and flat $CoPcH_4$. These hydrogenations are not likely to cause Co dementalization since the reductions do not occur at the Co-N sites.

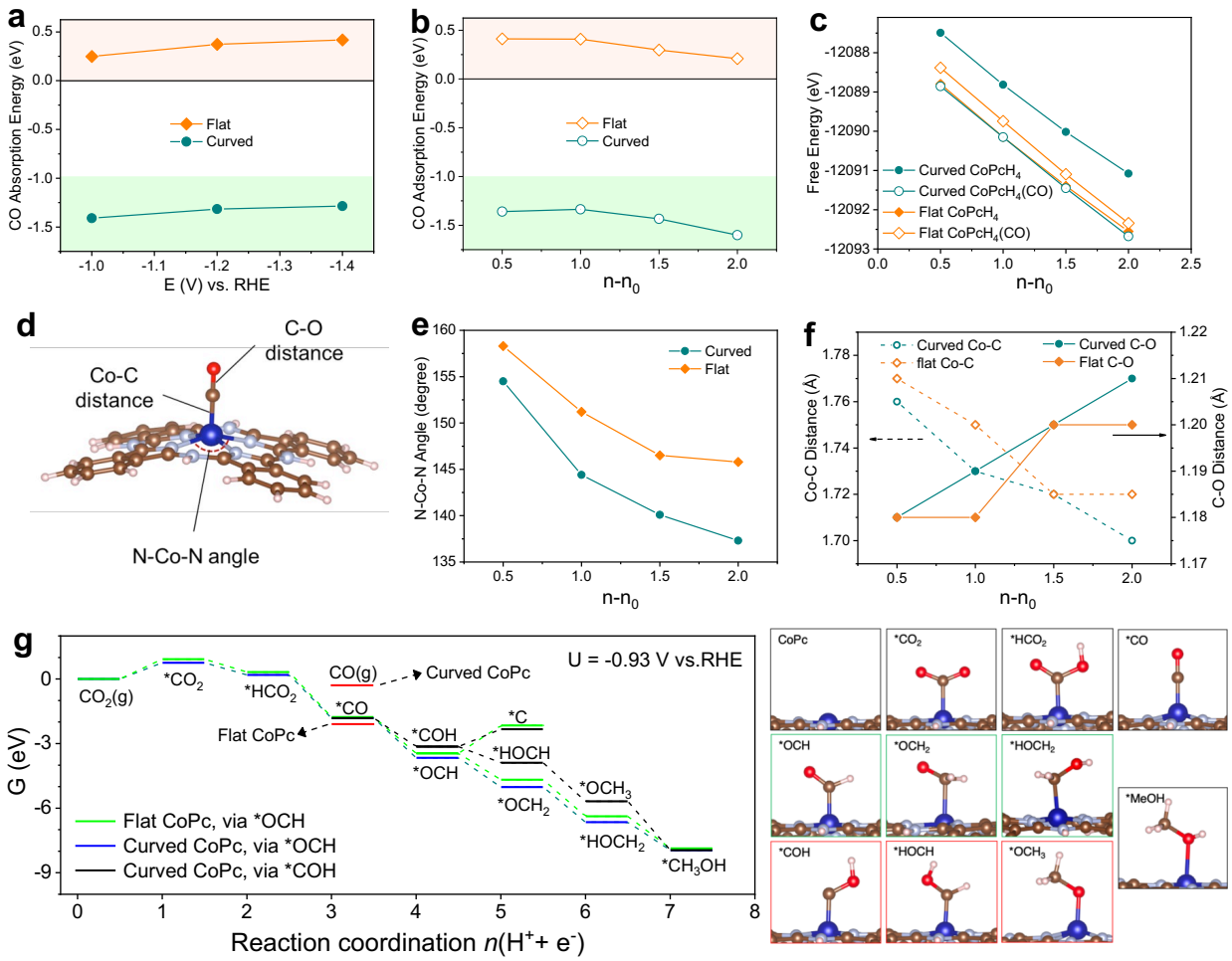

Figure 2.4: (**a**) Absorption energy versus potential (U_{RHE}, V) and (**b**) n-n_0, where n is the number of electrons added (n-n_0 = 1 indicates 1 electron has been added to the neutral system). (**c**) Free energies of curved and flat $CoPcH_4$ with and without CO adsorption versus n-n_0. (**d**) Representative N-Co-N angle and

Co-C and C-O distances of $CoPcH_4$. **(e)** N-Co-N angle (degrees) versus n-n_0 for the curved and flat structures. (**f**) Co-C and C-O distances (Å) versus n-n_0. (**g**) Free Energies (eV) at U = -0.93 V vs. RHE and pH = 7 for CO_2 reduction to methanol on curved and flat CoPc. ΔG_C and ΔG_F are reaction step free energies for the curved and flat CoPc, respectively. For flat CoPc it is favorable for CO to desorb so it is not available for subsequent steps toward MeOH. For curved CoPc, it is not favorable to desorb CO, making it available for production of MeOH. Green boxes indicate the preferred intermediates and red boxes indicate the higher-energy intermediates.

The CO absorption energy as a function of applied potential is shown in Figure 2.4a,b. We see that for the calculated potential window, the curved CoPc has stronger CO binding than the flat CoPc. At -1.0 V vs. RHE, the curved $CoPcH_4$ binds CO by -1.41 eV and the flat $CoPcH_4$ binds CO by 0.25 eV. Thus, for flat $CoPcH_4$, CO production leads to immediate CO desorption, making further steps to MeOH unlikely. For curved $CoPcH_4$, the CO remains bound to the catalyst, enabling further transformation to MeOH; this agrees with the experiment, in which curved CoPc is selective towards MeOH while flat CoPc is selective towards CO.

In Figure 2.4c, the curved $CoPcH_4$ is higher in energy than the flat analog due to the induced strain. However, the curved $CoPcH_4$(CO) is lower in energy than the flat analog, because the strain makes for favorable CO binding. These two factors lead towards improved CO binding for curved CoPc, which ultimately improves MeOH selectivity.

The distortion of the square pyramidal $CoPcH_4$(CO) geometry on the SWCNT is likely due to strong spin-orbit coupling in the d^7 configuration[37]. The 4-coordinate planar Co (II) ion has degenerate d_{xz} and d_{yz} orbitals which lie below the singly occupied d_{xy}. Upon binding to the SWCNT, the Co distorts out of the N basal plane, swapping the d_{xz} and

d_{yz} orbitals with the d_{xy} orbital, so that d_{xy} becomes doubly occupied lying below the doubly occupied d_{xz} and singly occupied d_{yz}.

We evaluated the geometries of the curved and flat $CoPcH_4(CO)$ intermediates at varying charge to understand how CO binding affinity changes with potential. We investigated the N-Co-N angle, the Co-C distance, and the C-O distance (Figure 2.4d). At all charges, the curved $CoPcH_4(CO)$ maintains a smaller N-Co-N angle than the flat analog, indicating more out-of-plane distortion (Figure 2.4e). For both cases, the angle decreases as additional electrons are introduced (potential becomes more negative). This is likely because electrons are occupying the d_{yz} orbital, and to minimize overlap with the in-plane p orbitals of the ligand, the Co distorts axially out of plane. The curved $CoPcH_4(CO)$ maintains a shorter Co-C distance for all charges until $n\text{-}n_0 = 1.5$, where the Co-C distance is 1.72 Å for both flat and curved cases (Figure 2.4f). As electrons are added, the Co-C distance decreases, indicating stronger binding of Co to C. In this potential range, the first orbitals filled are d_{yz} and d_{z^2}, both of which can participate in bonding to CO. Because Co is more distorted in the curved case, these d orbitals are more easily occupied due to decreased overlap with the PcH_4 in-plane p orbitals, leading to more facile binding to CO. The curved $CoPcH_4(CO)$ maintains a longer C-O distance for all charges except for $n\text{-}n_0 = 1.5$, where the C-O distance is 1.20 Å for both the curved and flat $CoPcH_4(CO)$. As bonding between Co and C increases, the C=O bond becomes activated, increasing the bond distance. We consider this C=O bond activation desirable since it makes it easier to reduce CO, increasing selectivity towards MeOH. Because the

C-O distance is longer in the curved $CoPcH_4(CO)$, CO reduction and further conversion to MeOH will be more facile.

We explored the entire mechanism for the reduction of CO_2 to methanol on the curved and flat CoPc molecules using grand-canonical DFT (Figure 2.4g). The conditions of U = -0.93 V vs. RHE and pH = 7 were chosen to match that of experiment. The reduction of CO_2 to CO is straight forward: CO_2 binds to Co to form bent $*CO_2$, which is then reduced to form *HOCO. *HOCO undergoes an additional reduction at the protonated O to liberate a H_2O and form *CO. At this point, for the flat CoPc, it is favorable for CO to desorb so subsequent steps to form $OHCH_3$ are not relevant. However, *CO is much more strongly bonding to SWCNT, favoring reduction at C to form *OCH or at O to form *COH. For the curved and flat CoPc, we find *OCH to be more stable at -0.93 V vs. RHE. Reduction of *OCH can lead to either $*OCH_2$ (reduction at C) or *HOCH (reduction at O), while reduction of *COH leads to *HOCH. DFT predicts $*OCH_2$ to be more stable than *HOCH. At -0.93 V vs. RHE, O of $*OCH_2$ carries negative charge, which permits C to make a covalent bond to Co; this ultimately keeps $*OCH_2$ from desorbing to form formaldehyde. From $*OCH_2$, the next reduction can yield either $*HOCH_2$ or $*OCH_3$. At -0.93 V vs. RHE, $*HOCH_2$ is more stable. The final reduction yields methanol (*MeOH), which can be formed from $*HOCH_2$ or $*OCH_3$. The overall reduction of CO_2 to *MeOH is -7.97 for the curved CoPc, with the highest-energy intermediate being $*CO_2$. The most important reaction step for CO vs. MeOH formation is reduction of *CO to *OCH. We see that for the curved CoPc, this step is -1.84 eV. We note that methane is often

competitive with methanol formation during CO_2RR. However, the methane mechanism usually requires multi-site catalysts such that intermediates like *C can coordinate to multiple catalyst centers[38,39]. Because CoPc is a single-site catalyst, *C would be severely undercoordinated, resulting in a high energy. Similarly, C_{2+} products also require multi-site catalysts,[38,39] and we do not observe them experimentally. Calculations on methane-forming pathways can be found in the **Methane Formation** section of the supporting information.

In situ attenuated total reflectance-surface enhanced infrared absorption spectroscopy (ATR-SEIRAS; no iR-compensation) was performed to further characterize the reaction intermediates. (Appendix Figure A31). For CoPc/SWCNT, we found a C-H stretching mode at ~3010 cm^{-1}, which could be from *OCH_2 or *$HOCH_2$. We also observe the aldehyde C-H stretch at ~2765 cm^{-1}, which emerges at approximately -0.7 V and becomes stronger at higher overpotentials. For CoPc/50, we do not detect obvious signals between 2600–3200 cm^{-1}, likely because the poor *CO absorption prohibits subsequent reduction beyond *CO. A previous study showed that formaldehyde is a possible intermediate in methanol formation, based on the observation of a methanol signal from formaldehyde reduction[10]. Our ART-SEIRAS experiments supplemented with theoretical calculations explicitly confirm the *OCH_2 pathway for methanol production, in which the curved CoPc induced by SWCNT plays an indispensable role.

2.5 Extended Application of SWCNT Induced Distortion to Other Molecular Catalysts

We extended the concept of CNT-induced molecular distortion to enhance catalytic performance of other molecular systems. We investigated the oxygen reduction reaction (ORR) activity of FePc/SWCNT in O_2-saturated 0.1 M KOH via measurements on a rotating disk electrode (RDE). Linear sweep voltammetry (LSV, Figure 2.5a) indicates that FePc/SWCNT achieves higher activity than FePc/MWCNT, with a more positive onset (E_{onset}) and half-wave potential ($E_{1/2}$) than all other samples. The $E_{1/2}$ of FePc/SWCNT is 0.93 V, which is 40 mV more positive than FePc/15, FePc/50, and Pt/C. We calculated the average electron transfer number (n) from the LSV curves with different rotation rates using Koutecky-Levich (K-L) plots (Appendix Figure A32)[40]. We find $n = 3.98$ for FePc/SWCNT, close to the theoretical limit of 4.00 for a four-electron reduction process. In comparison, FePc/15 and FePc/50 show $n = 3.87$, indicating that curved FePc performs ORR more rapidly (Figure 2.5b).

We also measured the CO_2RR performance of NiPc with three different diameter CNTs in an H-cell containing CO_2-saturated 0.5 M $KHCO_3$. All samples lead only to gas products with similar FE_{CO} (Appendix Figure A33). However, as shown in Figure 2.5c and 5d, the NiPc/SWCNT shows higher current density and CO turnover frequency (TOF_{CO}) in CO_2RR performance than NiPc/15 and NiPc/50.

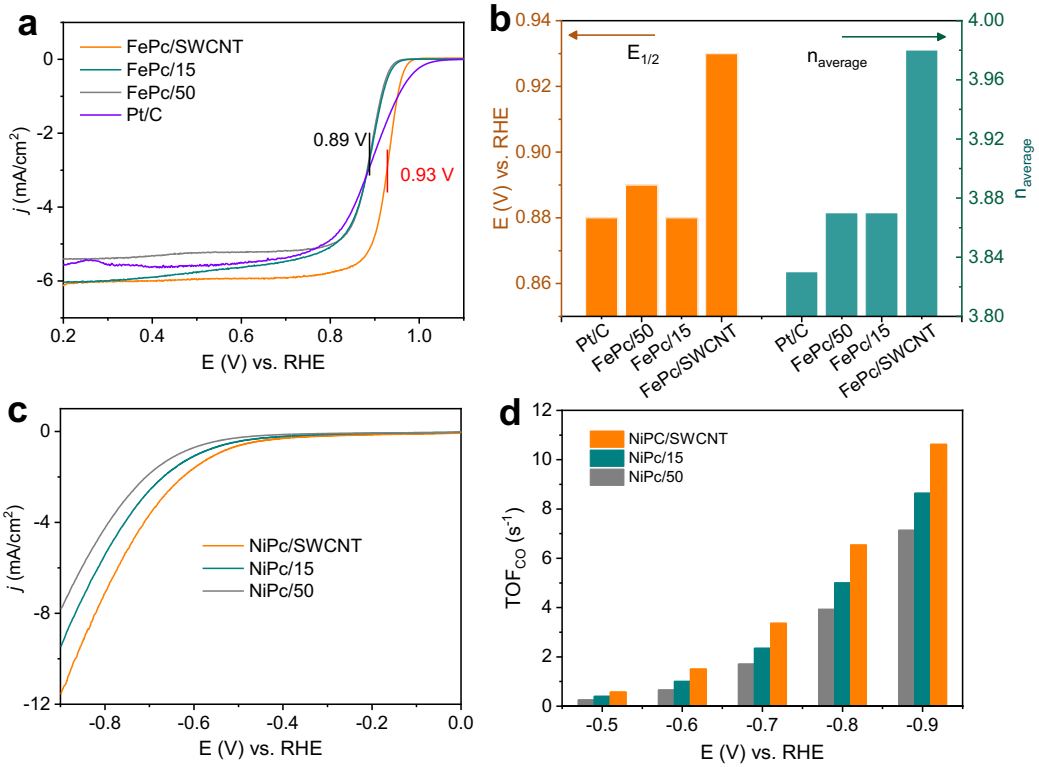

Figure 2.5: (**a**) ORR LSV curves and (**b**) comparison of half-wave potentials and average electron transfer number of FePc/SWCNT, FePc/15, FePc/50 and commercial Pt/C catalysts in O_2-saturated 0.1 M KOH electrolyte. (**c**) CO_2RR LSV curves and (**d**) TOF_{CO} values of NiPc/SWCNT, NiPc/15 and NiPc/50 in CO_2-saturated 0.5 M $KHCO_3$ electrolyte using H-cell.

2.6 Conclusions

CNTs have been widely used as supports to prevent sintering and agglomeration of nanoparticles, and as conductive substrates for electrochemical applications. Our work shows a new role of CNTs for inducing Å-scale molecular distortions to tailor catalytic activity. Using CoPc monodispersed on CNTs, we demonstrated the benefit of geometrically distorted CoPc on electrocatalysis, confirmed by various spectroscopic data, MD simulations, and DFT calculations. We show that for CO_2RR, CoPc/SWCNT can achieve 53.4% FE_{MeOH} with excellent durability, which is dramatically improved over

conventional CoPc/MWCNT. In a flow cell configuration, we achieved a j_{MeOH} of 66.8 mA cm^{-2} with FE_{MeOH} of 31.3% in CO_2 atmosphere and a j_{MeOH} of 62.1 mA cm^{-2} with FE_{MeOH} of 50.5% in CO atmosphere. We reach a total FE_{MeOH} of 60.0% with the CO_2RR-CORR tandem reaction. Our MD and DFT studies find that this performance is enabled by the strong CO adsorption on CoPc/SWCNT, which facilitates production of MeOH instead of CO. These results explain why CO is the prevailing product in most CoPc literature, where the substrates are often wide CNTs or graphitic carbon. We also show the different activities of ORR for FePc and CO_2RR for NiPc, which change with CNT support. Our study may prompt future investigation of curvature-dependent reactivity for other molecular catalysts at the nanometer scale.

2.7 Acknowledgements

RY acknowledges support from Guangdong Basic and Applied Basic Research Fund (2022A1515011333), Hong Kong Research Grant Council (21300620, 11307120) and State Key Laboratory of Marine Pollution (SKLMP/IRF/0029). CBM and WAG acknowledge support from the Liquid Sunlight Alliance, which is supported by the U.S. Department of Energy, Office of Science, Office of Basic Energy Sciences, Fuels from Sunlight Hub under Award Number DE-SC0021266. BZT acknowledges support from Shenzhen Key Laboratory of Functional Aggregate Materials (ZDSYS20211021111400001), the Science Technology Innovation Commission of Shenzhen Municipality (KQTD20210811090142053, JCYJ20220818103007014). We thank Wei Zhai, Lixin Wang for help with Raman

characterization, and Wanpeng Li for his assistance with HR-TEM image.

2.8 Methods

2.8.1 Preparation of CoPc/SWCNT catalysts

All CNTs were bought from XFNANO, Co., Ltd. and SWCNT (synthesized by a floating catalysts chemical vapor deposition method and contained both semiconducting and metallic) was pretreated in 6 mol L^{-1} HCl solution for 12 h to remove any metal impurities. After that, the SWCNT sample was filtrated, washed with deionized water and freeze-dried. Then 20 mg of the purified SWCNT was subsequently dispersed in 20 ml of DMF using sonication. Then, an appropriate amount of cobalt (II) phthalocyanine (J&K Scientific Ltd) dissolved in 5 ml DMF was added to the SWCNT suspension. The mixture was sonicated for 30 min to obtain a well-mixed suspension, which was further stirred at room temperature for 24 h. Subsequently, the mixture was centrifuged, and the precipitate was washed with DMF, ethanol and DI water. Finally, the precipitate was lyophilized to yield the final product. The samples with CNT substrates of different diameters SWCNT, 4–6 nm, 5–15 nm, 10–20 nm, 20–30 nm and >50 nm was denoted as CoPc/SWCNT, CoPc/5, CoPc/10, CoPc/15, CoPc/25, CoPc/50 respectively. The CoPc/SWCNT-M and CoPc/SWCNT-S were prepared with pure metallic and semiconductor SWCNTs (XFN13-2 and XFN08-2) as the substrates, respectively. The f-CoPc-SWCNT was synthesized through a modified covalent strategy[45]. The weight percentage of metal in all MPc/CNTs composites are ~0.22% determined by ICP test.

2.8.2 Preparation of FePc/SWCNT and NiPc/SWCNT catalysts

The preparation process of FePc/SWCNT and NiPc/SWCNT are same as above, except that CoPc is replaced by FePc and NiPc. The samples with different CNT diameters substrates of 10-20 and >50 nm was denoted as FePc/15, FePc/50, NiPc/15 and NiPc/50 respectively.

2.8.3 Materials characterization

The morphology of samples was characterized using transmission electron microscopy (TEM, Philips Technai 12) equipped with energy dispersive X-ray spectroscopy. ICP-atomic emission spectroscopy (ICP-OED) measurements were conducted on Optima 8000 spectrometer. Samples were digested in hot concentrated HNO_3 for 1 h and diluted to desired concentrations. UV-vis spectrum was performed on a Shimadzu 1700 spectrophotometer in ethanol solution with a concentration of 1×10^{-5} mol mL^{-1}. The X-ray photoelectron spectroscopy data were collected on a Thermo ESCALAB 250Xi spectrometer equipped with a monochromatic AlK radiation source (1486.6 eV, pass energy 20.0 eV). The data were calibrated with C 1s 284.6 eV. Raman spectra were collected using a LabRAM HR800 laser confocal micro-Raman spectrometer with a laser wavelength of 514.5 nm. Scanning transmission electron microscopy was characterized on a double spherical-aberration-corrected FEI Themis Z microscope at 60 kV.

X-ray absorption fine spectroscopy (XAFS) measurements were performed in the fluorescence mode using a Lytle detector at beamline 01C1 of National Synchrotron Radiation Research Center (NSRRC) in Taiwan. The electron storage ring was operated at 1.5 GeV with a constant current of ~ 360 mA. A Si (111) Double Crystal Monochromator (DCM) was used to scan the photon energy. XANES analysis were conducted using the Athena software based on the IFEFFIT program[41] to determine the structural environment of Co atoms. Averaged XAS spectra were first normalized to the absorption edge height, and the background was removed using the automatic background subtraction routine AUTOBK implemented in the Athena software[42]. A reference foil of Co foil was used for energy calibration of the monochromator, which was applied to all spectra. The Co K-edge calibration was set to the first inflection point of the reference foil, set at 7709 eV for easy comparison with other work[43]. Quantitative information on the radial distribution of neighboring atoms surrounding Co atoms was derived from the extended absorption fine structure (EXAFS) data. An established data reduction method was used to extract the EXAFS χ-functions from the raw experimental data using the IFEFFIT software.

2.8.4 Electrochemical measurements

H-cell, catalyst ink was prepared by dispersing 2 mg of catalyst in 1 mL of ethanol with 20 μL 5 wt.% Nafion solution (Sigma Aldrich, Nafion 117, 5 wt.%) and sonicated for

1 h. Then 200 μL of the ink was drop-casted on the glassy carbon working electrode and subsequently dried naturally. The loading was 0.4 mg/cm^2. The electrochemical performance was carried out in a customized glass H-cell. A platinum and Ag/AgCl were used as the counter and reference electrodes, respectively. The working electrode was separated from the counter electrode by the Nafion-117 membrane (Fuel Cell Store). Before use, the Ag/AgCl reference was calibrated as reported[44,45]. All potentials in this study were converted to the reversible hydrogen electrode (RHE) according to the Nernst equation (E (vs. RHE) = E (vs. Ag/AgCl) + 0.231+0.0592×pH). The 10 mL of 0.5 M $KHCO_3$ solution electrolyte was added into the working and counter compartment, respectively. The cell was purged with high-purity CO_2 gas (Linde, 99.999 %, 20 sccm) for 30 min prior to and throughout the duration of all electrochemical measurements. The electrochemical measurements were controlled and recorded with a CHI 650E potentiostat. The automatic iR (85%) compensation was used. Gas-phase products were quantified by an online gas chromatograph (Ruimin GC 2060, Shanghai) equipped with a methanizer, a Hayesep-D capillary column, a flame ionization detector (FID) for CO, and a thermal conductivity detector (TCD) for H_2. The CO_2 flow rate was controlled at 3 sccm using a standard series mass flow controller (Alicat Scientific mc-50 sccm). The liquid products were quantified after electrocatalysis using ^{1}H NMR spectroscopy with solvent (H_2O) suppression. 450 μL of electrolyte was mixed with 50 μL of a solution of 10 mM dimethyl sulfoxide (DMSO) in D_2O as internal standards for the ^{1}H NMR analysis. The concentration of MeOH was calculated using the ratio of the area of the MeOH peak (at

a chemical shift of 3.32 ppm) to that of the DMSO internal standard. Electrolyte of $^{13}CO_2$ in 0.5 M K$H^{13}CO_3$ were prepared by bubbling $^{13}CO_2$ into 0.5 M KOH for more than 30 minutes.

For CO_2RR flow electrolysis, in order to get a good FE_{MeOH} in the flow cell, CoPc/SWCNT with high CoPc loading catalysts was prepared using a CVD-type procedure according to our previous work[23]. Then 5 mg catalysts mixed with 40 μL Nafion solution were deposited in 2 mL ethanol and sonicated for 1 h to form uniform ink and then drop-casting on 1×2.5 cm^2 GDL (Sigracet-28BC) (mass loading of the sample: 1 mg/cm^2). GDL with catalysts as a CO_2RR cathode. A platinum and Ag/AgCl were used as the counter and reference electrodes, respectively. The cathode chamber and anode chamber were separated by Nafion-117 membrane (Fuel Cell Store). The CO_2 gas flow with 10 sccm flow rate was conducted on the cathode side while 0.1 M KOH+3 M KCl and 1 M KOH electrolyte at 5 mL/min flow rate was circulated in cathode and anode chamber, respectively. The cathode electrolyte was collected in a flask with an ice bath for NMR testing.

For CORR flow electrolysis, the working electrode preparation process and cell device are the same as the CO_2RR flow cell, except that the feed gas is changed to CO.

For FePc/CNT ORR measurement, 2 mg of catalyst was dispersed in 1 mL of solution containing 0.882 mL of ethanol and 0.098 mL of water and 20 μL of 5 wt.% Nafion solution, which was sonicated for 1 h to form a homogeneous catalyst ink. All the catalysts were cast onto the RDE (diameter 5 cm) with a loading amount of 0.2 mg/cm^2.

RDE tests were performed in O_2 saturated 0.1 mol/L KOH solution with a scan rate of 10 mV/s between 1.1 V and 0.2 V at different rotating rates using PINE 636 rotating-disk electrode system and CHI650 workstation. Ag/AgCl and Pt were used as reference and counter electrodes, respectively. All potentials were converted to the reversible hydrogen electrode (RHE).

The electron transfer number (n) was determined by the Koutecky-Levich equation:

$$\frac{1}{J} = \frac{1}{J_L} + \frac{1}{J_K} = \frac{1}{B\omega^{\frac{1}{2}}} + \frac{1}{J_K}$$

$$B = 0.62nFC_0D_0^{\frac{2}{3}}V^{-\frac{1}{6}}$$

where J is the measured current density, J_K and J_L are the kinetic and limiting current densities, ω is the angular velocity of the disk, n is the overall number of electrons transferred in oxygen reduction, F is the Faraday constant (96485 C/mol), C_0 is the bulk concentration of O_2 (1.2×10^{-6} mol cm^{-3}), D_0 is the diffusion coefficient of O_2 in 0.1 M KOH (1.9×10^{-5} cm^2 s^{-1}), and V is the kinematic viscosity of the electrolyte (0.01 cm^2 s^{-1}).

For NiPc/CNT CO_2RR measurement, 2 mg of catalyst in 1 mL of ethanol with 20 μL 5 wt.% Nafion solution and sonicated 1 h to form a homogeneous catalyst ink. All the catalysts were drop-cast onto carbon paper (Toray, TGP-H-060, Fuel Cell Store) (diameter of 0.5 inch) with a 0.4 mg/cm^2 loading. The electrochemical performance was carried out in a customized three-compartment cell, as previously reported[15,46]. A platinum foil and Ag/AgCl leak-free reference (LF-2, Innovative Instrument Inc.) were used as the counter

and reference electrode, respectively. The working electrode was separated from the counter electrode by the Nafion-117 membrane. The electrolyte was 0.5 M $KHCO_3$.

In situ ATR-SEIRAS was measured at a PerkinElmer spectrum 100 spectrometer equipped with a mercury cadmium telluride (MCT) detector, a variable angle specular reflectance accessory (Veemax III, Pike Technologies), and a one-compartment cell (LingLu Instruments Co., China) including a Pt counter electrode, an Ag/ AgCl reference electrode, a gas inlet port, and a gas outlet port. A catalyst-coated Si ATR crystal with Au film underlayer is placed in the cell as the working electrode. Before electrochemical measurements, the electrolyte (0.5M $KHCO_3$ saturated with CO_2) was injected into the cell and purged with high-purity CO_2 (99.999%) for 15 min. A CHI1242C potentiostat was employed to record the electrochemical response. The spectrum was collected step-wisely from -0.2 V to -1.1 V vs RHE with a dwell time of 3 min at each potential.

2.8.5 Computational Methods

Molecular dynamics simulations were performed using the LAMMPS software[47]. For these simulations we used the Universal Force Field (UFF) for valence interactions (bond, angle, and dihedral terms) combined with the RexPoN[48] universal nonbond potentials (UNB) to describe van der Waals interactions, and the polarizable charge equilibrium (PQEq) scheme for electrostatics. To represent the nanotube surface, we used a $C_{116}H_{28}$ sheet. To mimic a MWCNT, we used flat $C_{116}H_{28}$. To mimic the SWCNT, the $C_{116}H_{28}$ was bent to match the curvature of a 2 nm diameter SWCNT. To maintain the overall

curvature of the graphitic sheet, the edge hydrogens were fixed. To minimize the CNT-CoPc systems we used conjugate gradients followed by the steepest descent.

Density Functional Theory geometry optimizations were performed using VASP 5.4.4[49] with the solvation module[50]. For the curved species, the edge H atoms of the Pc ligand were fixed to maintain the curvature. Spin polarization was allowed during optimization. We used the PBE[51] functional with the D3[52] empirical correction for London dispersion forces. The kinetic energy cutoff was set to 500 eV, the wavefunction cutoff was set to 1E-5 eV, and the force cutoff was set to 0.03 eV/Å. All VASP optimizations were in a 20 $Å^3$ box with a 1x1x1 K point Monkhorst Pack grid.

To obtain the energy as a function of applied potential, we performed single point energy calculations using JDFTx[53] with the CANDLE[54] solvation model. Because our systems are finite (non-periodic), we were able to perform vibrational frequency calculations using Jaguar[55] v10.9, to obtain mode-dependent entropies, zero point energies, and enthalpies at 298.15 K.

In the Grand Canonical Potential (*GCP*) method, we first calculate the free energy *(F)* as a function of the number of electrons (n). *F(n)* includes the librational and vibrational contributions to the zero point energy, entropy, and enthalpy at 298.15 K. *F(n)* has a quadratic form, which we write as Equation 1:

$$F(n) = a(n - n_0)^2 + b(n - n_0) + c \quad (1)$$

where the a, b, and c parameters are fitted to the QM calculations. Here a should be positive to obtain a stable system (minima as opposed to maxima at $n = n_0$) and n_0 is the

number of explicit electrons for a neutral system (explicit because we utilize pseudopotentials). The quadratic form of *F(n)* is strictly verified in our calculations.

Then we use the Legendre transformation on *F(n)* to obtain Equation 2:

$$G(n;U) = F(n) - ne(U_{SHE} - U). \qquad (2)$$

We then minimize G with respect to U with a simple derivative:

$$\frac{\mathrm{d}G(n;U)}{\mathrm{d}n} = 0 \; or \; \mu_e = e(U_{SHE} - U) = \frac{\mathrm{d}F(n)}{\mathrm{d}n}. \qquad (3)$$

This leads to

$$\begin{aligned} GCP(U) &= minG(n;U) = \min\big(F(n) - ne(U_{SHE} - U)\big) \\ &= -\frac{1}{4a}\big(b - \mu_{e,SHE} + \mathrm{eU}\big)^2 + c - n_0\mu_{e,SHE} + n_0 eU \end{aligned} \qquad (4)$$

which can be written as

$$GCP(U) = -\frac{C_{diff}}{2}(U - U_{PZC})^2 + n_0 eU + F_0 - n_0\mu_{e,SHE} \qquad (5)$$

where C_{diff} is the differential capacitance and U_{PZC} is U at the point of zero charge. When the *GCP* is at its minimum, there is an inverse relationship between n and applied potential (C_{diff} has a positive value), meaning adding electrons makes the applied potential more negative. The GCP method assumes a metallic system. However, our CoPc systems have finite HOMO-LUMO gaps since the conductive CNTs are not explicitly included. We have done previous GCP with a similar inconsistency and found excellent agreement between the predicted and experimental onset potentials and current vs. applied potential, validating the use of GCP for finite-gap systems deposited on conducting supports.[55] Although *H is also competing,[56,57] it is not pertinent to our main result. Indeed, we found that *H adsorption does not change significantly under different potentials (Appendix

Figure A35).

2.9 References

1. Yang, S. et al. Tuning the Optical, Magnetic, and Electrical Properties of $ReSe_2$ by Nanoscale Strain Engineering. *Nano Lett.* **15**, 1660–1666 (2015).
2. Levy, N. et al. Strain-Induced Pseudo–Magnetic Fields Greater than 300 Tesla in Graphene Nanobubbles. *Science.* **329**, 544–547(2010).
3. Zeng, M. et al. Bandgap Tuning of Two-Dimensional Materials by Sphere Diameter Engineering. *Nat. Mater.* **19**, 528–533 (2020).
4. Li, H. et al. Activating and Optimizing MoS_2 Basal Planes for Hydrogen Evolution through the Formation of Strained Sulphur Vacancies. *Nat. Mater.* **15**, 48–53 (2016).
5. Nam, D. H. et al. Molecular Enhancement of Heterogeneous CO_2 Reduction. *Nat. Mater.* **19**, 266–276 (2020).
6. Navarro-Jaén, S. et al. Highlights and Challenges in the Selective Teduction of Carbon Dioxide to Methanol. *Nat. Rev. Chem.* **5**, 564–579 (2021).
7. Boutin, E. & Robert, M. Molecular Electrochemical Reduction of CO_2 beyond Two Electrons. *Trends Chem.* **3**, 359–372 (2021).
8. Kapusta, S. & Hackerman, N. Carbon Dioxide Reduction at a Metal Phthalocyanine Catalyzed Carbon Electrode. *J. Electrochem. Soc.* **131**, 1511–1514 (1984).
9. Wu, Y., Jiang, Z., Lu, X., Liang, Y. & Wang, H. Domino Electroreduction of CO_2 to Methanol on a Molecular Catalyst. *Nature* **575**, 639–642 (2019).
10. Boutin, E. et al. Aqueous Electrochemical Reduction of Carbon Dioxide and Carbon Monoxide into Methanol with Cobalt Phthalocyanine. *Angew. Chem. Int. Ed.* **58**,

16172–16176 (2019).

11. Chang, Q. et al. Metal-Coordinated Phthalocyanines as Platform Molecules for Understanding Isolated Metal Sites in the Electrochemical Reduction of CO_2. *J. Am. Chem. Soc.* **144**, 16131–16138 (2022).

12. Zhang, X. et al. Highly Selective and Active CO_2 Reduction Electrocatalysts Based on Cobalt Phthalocyanine/carbon Nanotube Hybrid Structures. *Nat. Commun.* **8**, 14675 (2017).

13. Han, N. et al. Supported Cobalt Polyphthalocyanine for High-Performance Electrocatalytic CO_2 Reduction. *Chem* **3**, 652–664 (2017).

14. Zhu, M., Ye, R., Jin, K., Lazouski, N. & Manthiram, K. Elucidating the Reactivity and Mechanism of CO_2 Electroreduction at Highly Dispersed Cobalt Phthalocyanine. *ACS Energy Lett.* **3**, 1381–1386 (2018).

15. Song, Y. et al. Zwitterionic Ultrathin Covalent Organic Polymers for High-Performance Electrocatalytic Carbon Dioxide Reduction. *Appl. Catal. B Environ.* **284**, 119750 (2021).

16. Kobayashi, N., Fukuda, T., Ueno, K. & Ogino, H. Extremely Non-Planar Phthalocyanines with Saddle or Helical Conformation: Synthesis and Structural Characterizations. *J. Am. Chem. Soc.* **123**, 10740–10741 (2001).

17. Fukuda, T., Homma, S. & Kobayashi, N. Deformed Phthalocyanines: Synthesis and Characterization of Zinc Phthalocyanines Bearing Phenyl Substituents at the 1-, 4-,

8-, 11-, 15-, 18-, 22-, and/or 25-Positions. *Chem. - A Eur. J.* **11**, 5205–5216 (2005).

18. Alvarez, L. et al. One-Dimensional Molecular Crystal of Phthalocyanine Confined into Single-Walled Carbon Nanotubes. *J. Phys. Chem. C* **119**, 5203–5210 (2015).

19. Liu, Z., Zhang, X., Zhang, Y. & Jiang, J. Theoretical Investigation of the Molecular, Electronic Structures and Vibrational Spectra of a Series of First Transition Metal Phthalocyanines. *Spectrochim. Acta - Part A Mol. Biomol. Spectrosc.* **67**, 1232–1246 (2007).

20. Wang, X. H., Zheng, C. C. & Ning, J. Q. Influence of Curvature Strain and Van der Waals Force on the Inter-Layer Vibration Mode of WS_2 Nanotubes: A Confocal Micro-Raman Spectroscopic Study. *Sci. Rep.* **6**, 6–11 (2016).

21. Zhang, J. et al. How to Manipulate Through-Space Conjugation and Clusteroluminescence of Simple AIEgens with Isolated Phenyl Rings. *J. Am. Chem. Soc.* **143**, 9565–9574 (2021).

22. Krichevsky, D. M. et al. Magnetic Nanoribbons with Embedded Cobalt Grown Inside Single-Walled Carbon Nanotubes. *Nanoscale* **14**, 1978–1989 (2022).

23. Tian, P. et al. Curvature-Induced Electronic Tuning of Molecular Catalysts for CO_2 Reduction. *Catal. Sci. Technol.* **11**, 2491–2496 (2021).

24. Papageorgiou, N. et al. Physics of Ultra-Thin Phthalocyanine Films on Semiconductors. *Prog. Surf. Sci.* **77**, 139–170 (2004).

25. Palmgren, P. et al. Strong Interactions in Dye-Sensitized Interfaces. *J. Phys. Chem. C* **2**, 5972–5977 (2008).

26. Wu, X. et al. Molecularly Dispersed Cobalt Phthalocyanine Mediates Selective and Durable CO_2 Reduction in a Membrane Flow Cell. *Adv. Funct. Mater.* **32**, 2107301 (2022).

27. Pan, Y. et al. Design of Single-Atom Co-N5 Catalytic Site: A Robust Electrocatalyst for CO_2 Reduction with Nearly 100% CO Selectivity and Remarkable Stability. *J. Am. Chem. Soc.* **140**, 4218–4221 (2018).

28. Han, G. et al. Substrate Strain Tunes Operando Geometric Distortion and Oxygen Reduction Activity of CuN_2C_2 Single-Atom Sites. *Nat. Commun.* **12**, 6335 (2021).

29. Kuhl, K. P. et al. Electrocatalytic Conversion of Carbon Dioxide to Methane and Methanol on Transition Metal Surfaces. *J. Am. Chem. Soc.* **136**, 14107–14113 (2014).

30. Zhang, X. et al. Selective and High Current CO_2 Electro-Reduction to Multicarbon Products in Near-Neutral KCl Electrolytes. *J. Am. Chem. Soc.* **143**, 3245–3255 (2021).

31. Gu, J. et al. Modulating Electric Field Distribution by Alkali Cations for CO_2 Electroreduction in Strongly Acidic Medium. *Nat. Catal.* **5**, 268–276 (2022).

32. Rappé, A. K., Casewit, C. J., Colwell, K. S., Goddard, W. A. & Skiff, W. M. UFF, a Full Periodic Table Force Field for Molecular Mechanics and Molecular Dynamics Simulations. *J. Am. Chem. Soc.* **114**, 10024–10035 (1992).

33. Naserifar, S., Brooks, D. J., Goddard, W. A. & Cvicek, V. Polarizable Charge Equilibration Model for Predicting Accurate Electrostatic Interactions in Molecules

and Solids. *J. Chem. Phys.* **146**, 124117 (2017).

34. Naserifar, S. et al. Accurate Non-Bonded Potentials Based on Periodic Quantum Mechanics Calculations for use in Molecular Simulations of Materials and Systems. *J. Chem. Phys.* **151**, 154111 (2019).

35. Sundararaman, R., Goddard, W. A. & Arias, T. A. Grand Canonical Electronic Density-Functional Theory: Algorithms and Applications to Electrochemistry. *J. Chem. Phys.* **146**, 114104 (2017).

36. Shi, L. Le, Li, M., You, B. & Liao, R. Z. Theoretical Study on the Electro-Reduction of Carbon Dioxide to Methanol Catalyzed by Cobalt Phthalocyanine. *Inorg. Chem.* **61**, 16549–16564 (2022).

37. Jurca, T. et al. Single-Molecule Magnet Behavior with a Single Metal Center Enhanced through Peripheral Ligand Modifications. *J. Am. Chem. Soc.* **133**, 15814–15817 (2011).

38. Birdja, Y. Y. et al. Advances and Challenges in Understanding the Electrocatalytic Conversion of Carbon Dioxide to Fuels. *Nat. Energy* **4**, 732–745 (2019).

39. Nitopi, S. et al. Progress and Perspectives of Electrochemical CO_2 Reduction on Copper in Aqueous Electrolyte. *Chem. Rev.* **119**, 7610–7672 (2019).

40. Chen, K. et al. Iron Phthalocyanine with Coordination Induced Electronic Localization to Boost Oxygen Reduction Reaction. *Nat. Commun.* **11**, 4173 (2020).

41. Ravel, B., & Newville, M. A. T. H. E. N. A. ATHENA, ARTEMIS, HEPHAESTUS: Data Analysis for X-ray Absorption Spectroscopy using IFEFFIT. *Journal of*

synchrotron radiation. **12**, 537-541 (2005).

42. Newville, M. IFEFFIT: interactive XAFS analysis and FEFF fitting. *Journal of synchrotron radiation*. **8**, 322-324 (2001).

43. Mathisen, K. et al. An In Situ XAS Study of the Cobalt Rhenium Catalyst for Ammonia Synthesis. *Top. Catal.* **61**, 225–239 (2018).

44. Song, Y. et al. Atomically Thin, Ionic Covalent Organic Nanosheets for Stable, High-Performance Carbon Dioxide Electroreduction. *Adv. Mater.* **34**, 2110496 (2022).

45. Ye, R. et al. In Situ Formation of Metal Oxide Nanocrystals Embedded in Laser-Induced Graphene. *ACS Nano* **9**, 9244–9251 (2015).

46. Su, J. et al. Building a Stable Cationic Molecule/Electrode Interface for Highly Efficient and Durable CO_2 Reduction at an Industrially Relevant Current. *Energy Environ. Sci.* **14**, 483–492 (2021).

47. Thompson, A. P. et al. LAMMPS – a Flexible Simulation Tool for Particle-based Materials Modeling at the Atomic, Meso, and Continuum Scales. *Comput. Phys. Commun.* **271**, 108171 (2022).

48. Naserifar, S. & Goddard, W. A. The Quantum Mechanics-based Polarizable Force Field for Water Simulations. *J. Chem. Phys.* **149**, (2018).

49. Allouche, A. Software News and Updates Gabedit — A Graphical User Interface for Computational Chemistry Softwares. *J. Comput. Chem.* **32**, 174–182 (2012).

50. Mathew, K., Sundararaman, R., Letchworth-Weaver, K., Arias, T. A. & Hennig, R.

G. Implicit Solvation Model for Density-Functional Study of Nanocrystal Surfaces and Reaction Pathways. *J. Chem. Phys.* **140**, (2014).

51. Perdew, J. P., Burke, K. & Ernzerhof, M. Generalized Gradient Approximation Made Simple. *Phys. Rev. Lett.* **77**, 3865–3868 (1996).

52. Grimme, S., Antony, J., Ehrlich, S. & Krieg, H. A Consistent and Accurate ab initio Parametrization of Density Functional Dispersion Correction (DFT-D) for the 94 Elements H-Pu. *J. Chem. Phys.* **132**, (2010).

53. Sundararaman, R. et al. JDFTx: Software for Joint Density-Functional Theory. *SoftwareX* **6**, 278–284 (2017).

54. Sundararaman, R. & Goddard, W. A. The Charge-Asymmetric Nonlocally Determined Local-electric (CANDLE) Solvation Model. *J. Chem. Phys.* **142**, (2015).

55. Bochevarov, A. D. et al. Jaguar: A High-Performance Quantum Chemistry Software Program with Strengths in Life and Materials Sciences. *Int. J. Quantum Chem.* **113**, 2110–2142 (2013).

56. Song, J. et al. Reaction Mechanism and Strategy for Optimizing the Hydrogen Evolution Reaction on Single-Layer 1T′ WSe_2 and WTe_2 Based on Grand Canonical Potential Kinetics. *ACS Appl. Mater. Interfaces* **13**, 55611–55620 (2021).

57. Bagger, A., Ju, W., Varela, A. S., Strasser, P. & Rossmeisl, J. Electrochemical CO_2 Reduction: A Classification Problem. *ChemPhysChem* **18**, 3266–3273 (2017).

58. Bagger, A., Ju, W., Varela, A. S., Strasser, P. & Rossmeisl, J. Electrochemical CO_2 Reduction: Classifying Cu Facets. *ACS Catal.* **9**, 7894–7899 (2019).

Chapter 3

Improving Iron Phthalocyanine Electrocatalytic Oxygen Reduction via Molecular Curvature

Reproduced with permission from:

Jianjun Su, Yun Song, Libei Huang, Yong Liu, Geng Li, Yinger Xin, Pei Xiong, Molly Meng-Jung Li, Haoran Wu, Minghui Zhu, Hao Ming Chen, Jianyu Zhang, Ben Zhong Tang, Marc Robert, Ruquan Ye, William A. Goddard III. *Molecular Strain Accelerates Electron Transfer for Enhanced Oxygen Reduction. submitted to Sci. Adv.)*

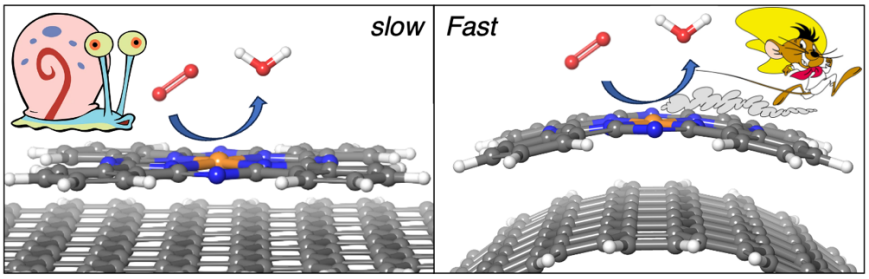

Figure 3.0: Table of Contents figure. © Warner bros., Nickelodeon.

3.1 Abstract

Single-walled carbon nanotubes (SWCNTs) have been shown to induce curvature in molecular catalysts, which results in modulated catalytic activity relative to the molecular catalysts on multi-walled carbon nanotubes (MWCNTs). Here we examine how inducing curvature in iron phthalocyanine (FePc) enhances the performance of the

electrocatalytic oxygen reduction reaction (ORR). We use Density Functional Theory (DFT) to predict the reaction mechanism for the 4-electron reduction of O_2 towards water. Several key deviations between the curved and flat reaction mechanisms ultimately suggest that ORR is accelerated when the curved FePc electrocatalyst is in contact with the curved SWCNT support. This agrees with experimental evidence that shows ORR on FePc/SWCNT is more rapid than ORR on FePc/MWCNT.

3.2 Introduction

In order to achieve a sustainable future, tremendous innovations in energy generation and utilization are necessary. Specifically, we must seek methods that exploit renewable energy sources. Such energy sources (such as wind, solar, or hydroelectric) have the capacity for producing "green" electrons, which in turn can be used for electrochemical reactions to afford renewable fuels. Moreover, the chemical energy released by combusting these fuels must be converted to useful electrical energy; such a conversion requires a fuel cell, which typically involves the electrochemical oxidation of the fuel (i.e., hydrogen, methanol, ethanol, etc.).[1–4]

Many fuel cell devices revolve around the oxygen reduction reaction (ORR), in which molecular oxygen undergoes a four-electron reduction to generate two equivalents of H_2O, according to Reaction 1.[5–7] It is also possible for molecular oxygen to undergo a

partial reaction in which a two-electron reduction generates hydrogen peroxide (H_2O_2, Reaction 2). The equilibrium potential (U_0) for the 4-electron reduction is equal to 1.23 V[8] while U_0 for the 2-electron reduction is equal to 0.70 V.

$$O_2 + 4\,H^+ + 4\,e^- \rightarrow 2\,H_2O \quad \text{(Reaction 1)}$$

$$O_2 + 2\,H^+ + 2\,e^- \rightarrow H_2O_2 \quad \text{(Reaction 2)}$$

Amongst the numerous fuel cell platforms, proton exchange membranes (PEMs) hold significant promise due to their high efficiency and zero-emission nature.[3,4,9,10] However, low-temperature PEMs are limited by the performance of the ORR catalyst on which they rely, such that development of improved ORR catalysts is imperative for improved PEMs.[11,12]

The industry-standard ORR catalysts are Pt group materials (PGMs), which as of 2017 were capable of achieving activities beyond 0.125 g/kW @ 150 kPa (whole cell) and mass activities beyond 0.6 A/mg @ 0.9 $V_{iR\text{-free}}$.[13,14] However, PGM-containing fuel cells are relatively expensive by virtue of having Pt. The DOE estimated that >50% of the cost for a Pt-based membrane electrode assembly originates from the Pt catalyst.[15–17] Additionally, Pt is susceptible to durability issues, such as dissolution, sintering, and nanoparticle formation, all of which result in catalyst deactivation.[18]

Fe-based materials have shown great promise for replacing PGMs in fuel cell devices, thanks in part to their high catalytic ORR performance and relatively low cost.[7,9,19–21] However, the best Fe-based ORR catalyst (as of 2019) was limited to 0.021 A/cm^2 @ 0.9 $V_{iR\text{-}free}$, which is less than half of the DOE's 2025 target of 0.044 A/cm^2 @ 0.9 $V_{iR\text{-}free}$. Additionally, Fe-based ORR catalysts are conventionally found in the form of nitrogen-doped carbon materials, which suffer from durability issues that preclude their use in practical PEM frameworks. On the bright side, this leaves plenty of room for further optimization of Fe-containing ORR catalysts.

We previously showed that the selectivity of Cobalt phthalocyanine (CoPc)-catalyzed CO_2 reduction can be steered by changing the radius of the carbon nanotube (CNT) support.[22] Typically, electrochemical CO_2 reduction catalyzed by CoPc on wide, multiwalled CNTs (MWCNTs) produces almost entirely CO and H_2.[23] However, when the diameter of a single-walled CNT (SWCNT) support becomes sufficiently small, strong pi-pi interaction between the SWCNT and CoPc induces distortion of the molecular catalyst, which in turn steers selectivity away from CO and diverts it towards methanol. The impetus for the dramatic selectivity shift appeared to be the result of improved CO binding to the CoPc catalyst; stronger binding increases the residence time of CO on the catalyst, which improves the odds of CO being further reduced towards methanol, as opposed to CO simply desorbing as in the case of CoPc on MWCNTs. Using the

CoPc/SWCNT results as inspiration, we also investigated FePc/SWCNT for electrochemical ORR. Our initial results revealed that FePc/SWCNT's ORR half-wave potential ($E_{1/2}$) was 0.93 V, which is 40 mV more positive than FePc/MWCNT and even Pt/C. We calculated the average electron transfer number (n) from linear sweep voltammetry at different rotation rates. We found $n = 3.98$, which is nearly equal to the theoretical limit of $n = 4$ for a 4-electron reduction, indicating the FePc/SWCNT reduces O_2 to 2 H_2O with extraordinary efficiency. Herein, we expand on the initial results reported previously for FePc-catalyzed ORR on SWCNTs vs. MWCNTs.

3.3 Methods

Periodic Density Functional Theory (DFT) calculations were performed using the Vienna Ab initio Simulation Package (VASP) version 6.3.2.[24] Optimizations were initially carried out using the PBE generalized gradient approximation (GGA) functional,[25] along with Grimme's D3BJ empirical correction for London Dispersion interactions.[26] All optimizations featured Projector Augmented Wave (PAW) pseudopotentials for all atoms.[27] The plane wave basis set cutoff was set to 500 eV, and a 1 x 1 x 1 K point grid was used. We also used VASP to calculate phonons via the finite difference method. Phonons at 298.15 K were used to predict thermochemical properties such as zero-point energy and entropy. A Hubbard U correction of 5 eV was used for Fe to account for

correlated d electrons that are not properly described by vanilla GGA functionals like PBE.[28]

VASP geometry minimizations were followed by solution-phase single point energy calculations, which were carried out using the JDFTx software package.[29] JDFTx solvent calculations included implicit water solvation via the CANDLE linear solvation model.[30] Coulomb interactions were truncated in all 3 cartesian directions to avoid artificial interactions of the FePc with itself in adjacent periodic images.

Hybrid DFT calculations were performed using the ORCA v5.0.4 quantum chemistry software.[31] Structural optimizations were first performed with the B3LYP functional[32] augmented with the D3BJ empirical correction for London dispersion forces. Following B3LYP structural optimizations, single-point energy calculations were performed with Head-Gordon's ωB97M-V range-separated functional,[33] which includes VV10 nonlocal correlation.[34] In all calculations, the def2-TZVP basis set was used.[35] All calculations also featured implicit water solvent via ORCA's Conductor-like Polarizable Continuum Model (CPCM).[36]

To capture how the reaction free energy surface changes with applied potential, we also computed Grand Canonical Potential (GCP) free energies.[37] GCP is computed by taking the Legendre transform of Gibbs free energy with respect to number of electrons (N_e), such that the conjugate variable that appears is the chemical potential, μ.[38] For

GCP to serve as a thermodynamic potential, N_e must be equilibrated to match the desired applied voltage. This is achieved by self-consistently varying N_e in order to match the fermi energy to the applied voltage, as in Equation 3.1). The Computational Hydrogen Electrode (CHE) method is used for the hydrogen reference, in which the potential of a proton-electron pair is equivalent to the free energy of $\frac{1}{2}$ H_2 at standard conditions.

$$\mu = \frac{dG(N_e)}{N_e} = e(U_{SHE} - U) \quad \text{(Equation 3.1)}$$

3.4 Results and Discussion

3.4.1 Characterization

We begin our study by examining the impact of curvature on the FePc molecule using range-separated DFT (ωB97M-V / def2-TZVP). This DFT methodology predicts the ground-state FePc to be a triplet (2 unpaired electrons), followed by the quintet state (4 unpaired electrons) and then the singlet state (0 unpaired electrons). We find that in terms of electronic energy, the triplet lies -1.02 eV below the quintet, and the quintet lies -0.13 eV below the singlet. For the curved FePc, the triplet lies -0.63 eV below the quintet and the quintet lies -0.60 eV below the singlet. Previous studies have reported different spin ground states depending on the functional and basis set used.[42] Different functionals

and basis sets have also given rise to different symmetry breakings. This indicates that the ground-state FePc is susceptible to 2nd order Jahn-Teller distortion, which stems from nearly degenerate states interacting. X-ray photoelectron spectroscopy (XPS) results of CoPc found that distortion of the molecule resulted in N 1s peak splitting and shift. We expect that distortion of the FePc molecule should also result in splitting of the N 1s peaks. We probed the 8 N 1s peaks of FePc; in the flat FePc (representative of FePc/MWCNT) 4 degenerate N 1s orbitals lie at -395.71 eV and the remaining 4 degenerate N 1s orbitals are found at -395.26 eV (Figure 3.1a). Upon distortion of the FePc, the 4 degenerate orbitals at -395.71 split slightly to range from -395.63 to -390.76 eV (˜0.13 eV deviation). The 4 degenerate orbitals previously found at -395.26 eV also split, ranging from -395.17 to -395.31 eV (˜0.13 eV deviation) upon molecular distortion. We suspect that the N 1s orbitals belonging to N far from the distortion axis undergo little to no change. On the other hand, N 1s orbitals belonging to N close the distortion axis undergo noticeable change, likely because the local nuclear geometry of these N atoms is altered (Figure 3.1b). We find that curving the FePc results in +0.40 eV of strain (i.e., $\Delta E_{flat \rightarrow curved} = +0.40$ eV). Analysis of the frontier orbitals reveals that the HOMO-LUMO gap is also altered by curvature. The flat FePc has a HOMO-LUMO gap of 4.60 eV, but upon curvature, the HOMO-LUMO gap increases to 4.80 eV (+0.20 eV decrease). This is a result of the β HOMO becoming stabilized while the β LUMO is simultaneously

destabilized upon curvature; the β HOMO decreases in energy by –0.12 eV and the β LUMO increases by +0.08 eV. We also compute the Mulliken charges of the FePc molecule. The Fe Mulliken charge in the flat molecule is +0.26, but upon molecular distortion the Fe charge drops slightly to +0.23, indicative of a small amount of electron transfer from the phthalocyanine to the Fe center.

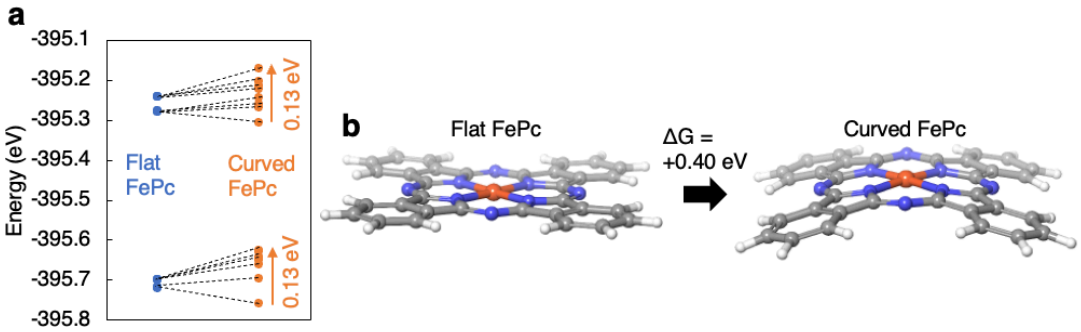

Figure 3.1: (**a**) Nitrogen 1s orbital energies for flat and curved FePc. (**b**) DFT-optimized structures for flat and curved FePc and $FePcH_4$. Orange atom is Fe, blue atoms are N, grey atoms are C, and white atoms are H.

In a previous study on CoPc-catalyzed CO_2 reduction, Liao *et al.* claimed that at -1.0 V vs. RHE and a slightly acidic pH of 6.8, the 4 outward N of the phthalocyanine are hydrogenated, forming $CoPcH_4$ with a total free energy change of -2.92 eV.[43] However, under basic conditions (pH = 13) and within the potential window for ORR (+0.8 - +1.0 V vs. RHE), we do not expect the FePc to undergo hydrogenations at the 4 outer N to form $FePcH_4$.

3.4.2 FePc Oxygen Reduction Mechanism

We carried out Grand Canonical Quantum Mechanics calculations to understand how the FePc-catalyzed ORR mechanism changes with applied potential. These FePc calculations were performed in a 20 x 20 x 20 Å periodic box and featured dipole corrections to account for FePc being non-periodic.

The ORR mechanism is initiated by coordination of molecular O_2 to the FePc catalyst center to form *OO.[7,44] Following adsorption, ORR can proceed through either the dissociative or associative pathway. In the dissociative pathway, adsorption of O_2 is followed immediately by O–O bond breaking to generate $(*O)_2$. This pathway conventionally requires two catalyst sites to accommodate the two *O. Since FePc is a single site catalyst, it is extremely unlikely that ORR will occur through the dissociative pathway; this has been established by previous first principles calculations on Fe-based ORR catalysts. The associative pathway is far more likely for FePc ORR: *OO undergoes a proton-coupled electron transfer (PCET) to generate the *OOH intermediate, in which the PCET occurs at the distal O. Following formation of *OOH, an additional PCET at the distal O generates *O and affords an equivalent of water. Alternatively, PCET at the proximal O generates *HOOH.[45] If the mechanism proceeds through the *O intermediate, the subsequent PCET produces *OH. If the mechanism instead proceeds through *HOOH, the subsequent PCET still yields *OH, but delays the formation of the equivalent water

until *OH formation. The next PCET forms $*OH_2$, which subsequently liberates from FePc to afford the second equivalent water and regenerate the catalyst starting state. Alternatively, *OH can undergo a single electron transfer (SET) to afford a free OH^-; this pathway is plausible given the high pH environment. The mechanism in whole is comprised of 6 steps: coordination of O_2, 4 PCETs, and then desorption of the final water product. The 6-step ORR mechanism for flat and curved FePc as functions of applied potential are displayed in Figure 3.2.

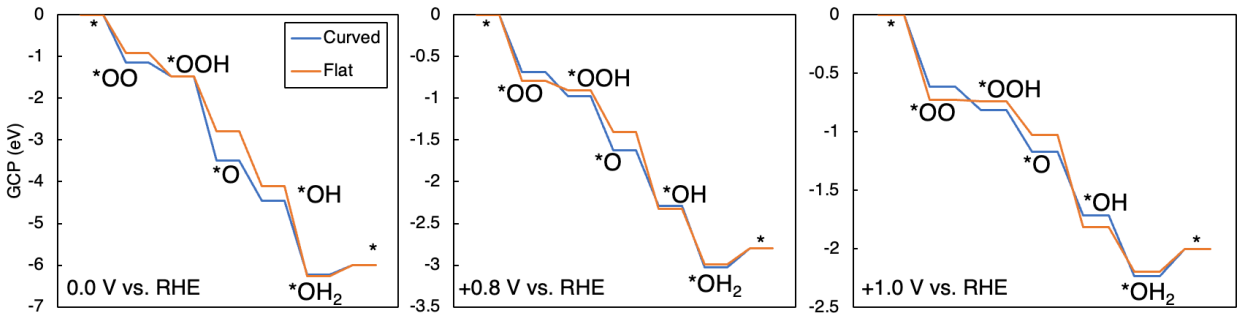

Figure 3.2: Grand Canonical Potential free energies at 298 K for flat and curved FePc at 0.0, +0.8, and +1.0 V vs. RHE.

According to the Grand Canonical Potential free energy landscapes in Figure 3.2, the rate-limiting step at +1.0 V vs. RHE is the desorption of the second H_2O. For the flat FePc the desorption of the second H_2O is uphill +0.19 eV; for the curved FePc, this step is uphill +0.23 eV. The rate-limiting step is more uphill for the curved FePc, which suggests that the curved FePc would less rapidly catalyze ORR compared to flat FePc; this is the opposite of what is observed experimentally. Additionally, the rate of ORR is potential-

dependent, indicating that the rate-limiting step should involve an electron transfer. These calculations on FePc-catalyzed ORR suggest that the rate-limiting step is purely chemical, which means that the present model and method are not properly describing the ORR catalyzed by FePc monodispersed on CNTs.

3.4.3 FePc-C_{24} Oxygen Reduction Mechanism

We have now calculated the ORR mechanism using just the FePc molecule and with PBE as the DFT functional. From these preliminary calculations in *3.4.2*, we established that PBE-predicted ORR via solely the FePc molecule does not yield the experimentally observed ORR enhancement of FePc/SWCNT over FePc/MWCNT. This suggests two primary issues with the initial approach:

- The DFT method is insufficient. Grand Canonical DFT with the PBE functional has produced excellent results in the past. However, the electronic structures of Fe and Fe-oxides are not always captured correctly by PBE. The strongly correlated nature of Fe's *d* electrons poses a problem that is not handled properly with PBE. PBE+U is the most common attempt to remedy the situation, although addition of the on-site U parameter is essentially a small patch to a much more involved problem.
- The model is insufficient. In our previous study on CoPc-catalyzed CO_2 reduction, the CoPc molecule alone was sufficient for elucidating the observed selectivity

difference between CoPc/SWCNT and CoPc/MWCNT. In the present case, the observed enhancement is not improved selectivity but improved rate. The ORR rate is highly influenced by the efficiency of electron transfer and will therefore be highly influenced by the conducting CNT support.

With these issues identified, we now calculate the ORR mechanism using Head-Gordon's ωB97M-V range-separated meta-GGA functional, which has been shown to outperform other leading functionals. We note that in the original 2016 paper, Head-Gordon warns against using ωB97M-V when correlation is significant. However, recent studies utilizing the functional have demonstrated its maintained accuracy, despite Head-Gordon's forewarning. Thus, we approach FePc ORR using ωB97M-V with cautious optimism. To remedy the issue of the model, we include a coronene molecule ($C_{24}H_{12}$) as a surrogate for the CNT support. Previous computational studies on FePc ORR suggest that catalysis is modulated by an axial ligand effect. Therefore, we place curved and flat coronenes under the curved and flat FePc molecules (FePc-C_{24}) and evaluated these systems for ORR (Figure 3.3).

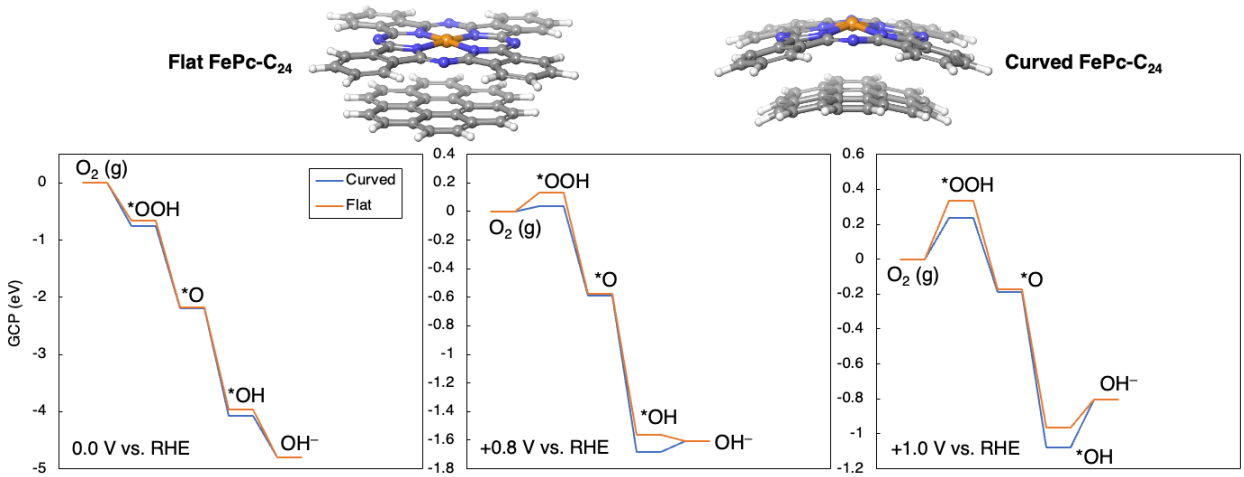

Figure 3.3: Grand canonical free energies at 298 K for flat and curved FePc-C_{24} at 0.0, +0.8, and +1.0 V vs. RHE.

For FePc-C_{24}, DFT calculations suggest that the most facile ORR pathway is initiated by PCET to O_2 (g) which forms the *OOH intermediate. The *OOH intermediate undergoes the second PCET to afford the *O intermediate and generate the first water. In the penultimate step, *O undergoes the third PCET to afford the *OH intermediate. Finally, *OH undergoes a SET to generate a free OH^-. At 0.0 V vs. RHE, this mechanism is precipitously downhill, with an overall free energy change of -4.18 eV; this is expected given the substantial overpotential at 0.0 V vs. RHE. The curved and flat FePc-C_{24} mechanisms are essentially identical, with only small deviations originating from the *OOH and *OH intermediates. However, at +0.8 V vs. RHE the flat and curved mechanisms present some finite deviation. Specifically, the first PCET to convert O_2 (g) to *OOH is nearly 0.2 eV more uphill for the flat system compared to the curved system. Additionally, the final SET that converts *OH to OH^- is downhill -0.04 eV for the flat

catalyst yet uphill +0.07 eV for the curved catalyst. At +1.0 V vs. RHE the flat and curved mechanisms are markedly different. At +1.0 V vs. RHE, the initial PCET to convert O_2 (g) to *OOH is uphill +0.33 eV and +0.24 eV for the flat and curved FePc-C_{24} systems, respectively. Moreover, the final conversion of *OH to OH^- is uphill +0.15 eV for flat FePc-C_{24} and +0.27 eV uphill for the curved analog. At +1.0 V vs. RHE, the most endergonic step for the flat FePc-C_{24} is O_2 (g) → *OOH which is uphill +0.33 eV. At the same potential, the most endergonic step for the curved FePc-C_{24} is *OH → OH^- which is uphill +0.27 eV. The difference in these two ΔG's is 0.06 eV, which agrees with the $\Delta E_{1/2}$ of 0.07 V (0.952 V for FePc/SWCNT vs. 0.879 V for FePc/50, see *3.4.5* below). The fact that these two energies originate from different steps in the reaction suggests a difference in the rate-limiting step, which may support the experimentally observed difference in Tafel slope between FePc/SWCNT (35.7 mV dec^{-1}) and FePc/50 (56.4 mV dec^{-1}).

3.4.4 Reaction Intermediate Adsorption Trends

Nørskov and coworkers previously reported scaling relationships amongst the ORR reaction intermediates for noble metal catalysis.[8] Scaling was originally based on the adsorption energy of the *O intermediate (ΔG_O), but more modern studies have diverted attention towards the adsorption energy of *OH (ΔG_{OH}), which typically exhibits better

scaling with adsorption of *OOH (ΔG_{OOH}). Our present calculations along with previous calculations on Fe in nitrogen-doped graphene (Fe-NDG) show that Fe-based catalysts also follow these trends, although with some deviation from the noble metals (Figure 3.4).

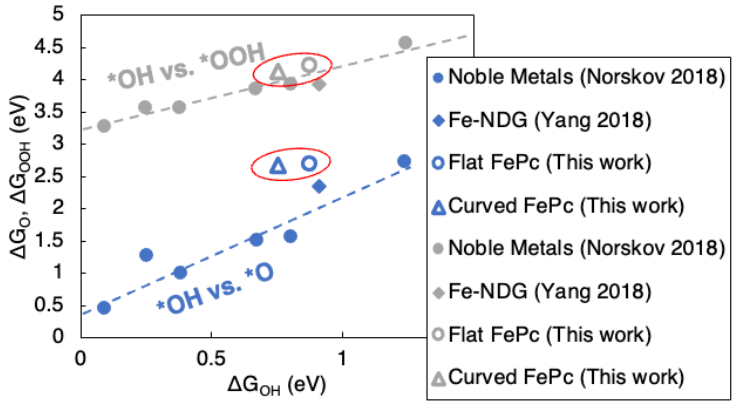

Figure 3.4: Binding energies of flat and curved FePc-C_{24} relative to conventional metal catalysts. Blue indicates *OH vs. *O binding and grey indicates *OH vs. *OOH binding. Closed circles represent conventional noble metals, diamonds represent Fe in nitrogen-doped graphene (Fe-NDG), open circles are flat FePc-C_{24}, and open triangles are curved FePc-C_{24}.

For *OH vs. *OOH scaling, the noble metals follow the relation: $\Delta G_{OOH} = \Delta G_{OH} + 3.2$. It appears that the Fe-based catalysts are well behaved in this regime and abide by the same relation. For *OH vs. *O scaling, the noble metals roughly follow the relation: $\Delta G_O = 1.7\Delta G_{OH} + 0.4$. No such relation is found for the curved and flat FePc-C_{24}. The flat and curved FePc-C_{24} systems have *OH and *O binding energies that correlate positively, as was found for the noble metals, but the linear trend is different, nonetheless. The flat and curved FePc-C_{24} binding energies scale as: $\Delta G_O = 0.1\Delta G_{OH} + 2.6$. This result indicates that the *O binding energy is essentially independent of the *OH binding

energy. We note that this linear trend is based off only 2 data points, such that we should not rely heavily on this linear regression. The well-behaved relationship between ΔG_{OOH} and ΔG_{OH} was proposed to be a result of the *OH and *OOH intermediates making nearly identical single bonds to the metal catalysts. We indeed find this to be the case for the flat and curved FePc-C_{24} systems (Figure 3.5).

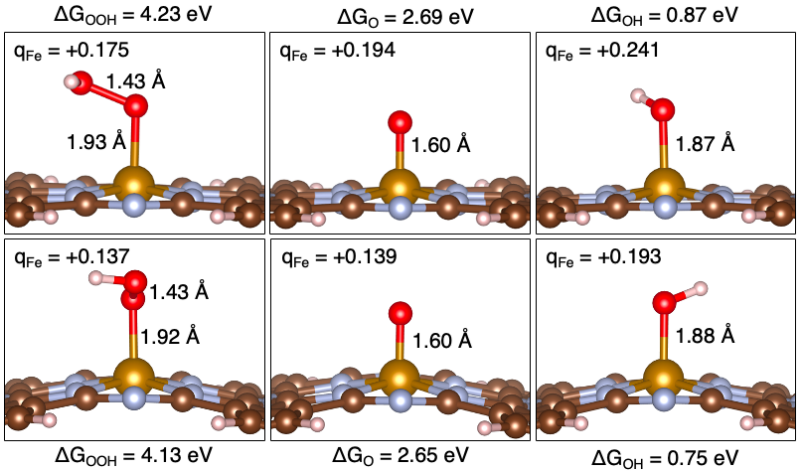

Figure 3.5: DFT-optimized *OOH, *O, and *OH intermediates for flat (above) and curved (below) FePc-C_{24}, accompanied by binding energies. Fe Mulliken charges denoted by q_{Fe}.

For the flat FePc-C_{24}, *OOH makes a Fe–O bond of 1.93 Å, while *OH makes a notably shorter Fe–O bond of 1.87 Å. The *OOH and *OH binding differ slightly more for the curved FePc-C_{24}, which bonds to *OOH and *OH with Fe–O distances of 1.92 and 1.88 Å, respectively. ΔG_O is very similar for the flat and curved FePc-C_{24}, equaling +2.69 and +2.65 eV for the two systems, respectively. The similarity in ΔG_O is reflected by the geometry of the *O intermediate; in both the curved and flat *O intermediates, the Fe–O

distance is 1.60 Å. ΔG_{OOH} and ΔG_{OH} vary more dramatically between the flat and curved systems. Specifically, ΔG_{OOH} is +4.23 eV for the flat FePc-C_{24} and +4.13 eV for the curved. ΔG_{OH} for the flat and curved FePc-C_{24} are +0.87 and +0.75 eV, respectively.

3.4.5 Experimental Results

FePc on different sized CNTs was prepared in the same way CoPc was prepared on different sized CNTs (see Section *2.8.1*).

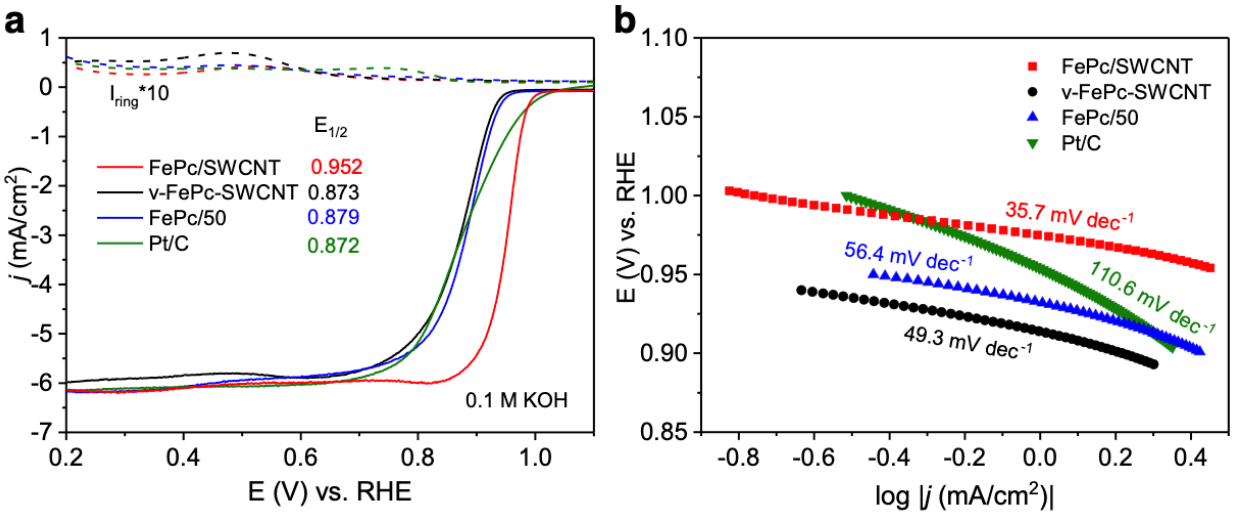

Figure 3.6: Linear Sweep Voltammetry curves comparing the ORR half-wave potentials (**a**) and Tafel slopes (**b**) for FePc/SWCNT, v-FePc/SWCNT (FePc is covalently bound to SWCNT), FePc/50 (MWCNT with 50 nm diameter), and commercial Pt/C.

Linear Sweep Voltammetry (LSV) curves (Figure 3.6a) indeed show ORR catalyzed by FePc/SWCNT to be more performant that FePc/MWCNT and commercial Pt/C. Specifically, $E_{1/2}$ = +0.872 V for Pt/C and +0.879 V for FePc/MWCNT. For

FePc/SWCNT, $E_{1/2}$ = +0.952 V, which is the highest $E_{1/2}$ ever reported for ORR. Moreover, the difference in $E_{1/2}$ between FePc/SWCNT and FePc/MWCNT is ~0.07 V, which is congruent with the computationally predicted $\Delta\Delta G$ of 0.05 V. Figure 3.6b depicts the Tafel slopes for the various ORR catalysts. The Tafel slope for Pt/C-catalyzed ORR is 110.6 mV/dec, while FePc/MWCNT-catalyzed ORR yields a Tafel slope of 56.4 mV/dec. FePc/SWCNT-catalyzed ORR results in a Tafel slope of 35.7 mV/dec, which is the lowest of the catalysts tested, indicating that FePc/SWCNT beholds the most rapid electron transfer. The fact that the Tafel slopes are dramatically different between FePc/SWCNT and FePc/MWCNT also suggests a change in the potential-determining step. This agrees with the computationally predicted reaction mechanisms, in which the potential-determining step for flat FePc-C_{24} was the conversion of O_2 → *OOH while the potential-determining step for curved FePc-C_{24} was the conversion of *OH → OH^-.

3.5 Conclusions

We have shown in the past that different-sized carbon nanotube supports can modulate the selectivity and performance and certain molecular electrocatalysts. The present study reveals how FePc monodispersed on single-walled carbon nanotubes results in accelerated electron transfer, which gives rise to accelerated oxygen reduction relative to FePc on multi-walled carbon nanotubes. For the flat FePc-C_{24}, the conversion of O_2 (g) to *OOH is rate-limiting at +1.0 V vs. RHE with a free energy change of +0.33 eV. For

the curved FePc-C_{24}, *OH → OH^- is rate-limiting with a free energy change of +0.27 eV. The observed ΔΔG of 0.06 eV aligns with the observed difference in $E_{1/2}$ (0.07 V). Moreover, the change in the rate-limiting step (O_2 (g) → *OOH for flat and *OH → OH^- for curved) lends support to the change in experimental Tafel slope (35.7 and 56.4 mA/cm^2 for FePc/SWCNT and FePc/50, respectively). DFT calculations suggest that the accelerated ORR is due to more efficient electron transfer between the curved FePc and the curved coronene support, as evidenced by Mulliken charge analysis. Overall, the curved FePc-C_{24} exhibits a more facile ORR mechanism than Flat FePc-C_{24}, which agrees with experimental findings that FePc/SWCNT more rapidly catalyzes ORR than FePc/MWCNT.

3.6 References

(1) Vesborg, P. C. K.; Jaramillo, T. F. Addressing the Terawatt Challenge: Scalability in the Supply of Chemical Elements for Renewable Energy. *RSC Adv.* **2012**, *2*, 7933–7947. https://doi.org/10.1039/c2ra20839c.

(2) Debe, M. K. Electrocatalyst Approaches and Challenges for Automotive Fuel Cells. *Nature* **2012**, *486*, 43–51. https://doi.org/10.1038/nature11115.

(3) Glibin, V. P.; Cherif, M.; Vidal, F.; Dodelet, J.-P.; Zhang, G.; Sun, S. Non-PGM Electrocatalysts for PEM Fuel Cells: Thermodynamic Stability and DFT

Evaluation of Fluorinated FeN 4 -Based ORR Catalysts. *J. Electrochem. Soc.* **2019**, *166* (7), F3277–F3286. https://doi.org/10.1149/2.0341907jes.

(4) Jung, N.; Chung, D. Y.; Ryu, J.; Yoo, S. J.; Sung, Y. E. Pt-Based Nanoarchitecture and Catalyst Design for Fuel Cell Applications. *Nano Today* **2014**, *9* (4), 433–456. https://doi.org/10.1016/j.nantod.2014.06.006.

(5) She, Z. W.; Kibsgaard, J.; Dickens, C. F.; Chorkendorff, I.; Nørskov, J. K.; Jaramillo, T. F. Combining Theory and Experiment in Electrocatalysis: Insights into Materials Design. *Science (80-.).* **2017**, *355* (6321). https://doi.org/10.1126/science.aad4998.

(6) Song, D.; Hu, C.; Gao, Z.; Yang, B.; Li, Q.; Zhan, X.; Tong, X.; Tian, J. Metal–Organic Frameworks (MOFs) Derived Materials Used in Zn–Air Battery. *Materials (Basel).* **2022**, *15* (17), 5837. https://doi.org/10.3390/ma15175837.

(7) Wang, W.; Jia, Q.; Mukerjee, S.; Chen, S. Recent Insights into the Oxygen-Reduction Electrocatalysis of Fe/N/C Materials. *ACS Catal.* **2019**, *9* (11), 10126–10141. https://doi.org/10.1021/acscatal.9b02583.

(8) Kulkarni, A.; Siahrostami, S.; Patel, A.; Nørskov, J. K. Understanding Catalytic Activity Trends in the Oxygen Reduction Reaction. *Chemical Reviews*. 2018. https://doi.org/10.1021/acs.chemrev.7b00488.

(9) Kramm, U. I.; Lefèvre, M.; Larouche, N.; Schmeisser, D.; Dodelet, J. P. Correlations

between Mass Activity and Physicochemical Properties of Fe/N/C Catalysts for the ORR in PEM Fuel Cell via 57Fe Mössbauer Spectroscopy and Other Techniques. *J. Am. Chem. Soc.* **2014**, *136* (3), 978–985. https://doi.org/10.1021/ja410076f.

(10) Lefèvre, M.; Dodelet, J. P.; Bertrand, P. Molecular Oxygen Reduction in PEM Fuel Cells: Evidence for the Simultaneous Presence of Two Active Sites in Fe-Based Catalysts. *J. Phys. Chem. B* **2002**, *106* (34), 8705–8713. https://doi.org/10.1021/jp020267f.

(11) Gasteiger, H. A.; Kocha, S. S.; Sompalli, B.; Wagner, F. T. Activity Benchmarks and Requirements for Pt, Pt-Alloy, and Non-Pt Oxygen Reduction Catalysts for PEMFCs. *Appl. Catal. B Environ.* **2005**, *56* (1–2), 9–35. https://doi.org/10.1016/j.apcatb.2004.06.021.

(12) Gasteiger, H. A.; Markovic, N. M. Just a Dream or Future Reality? *Science (80-.).* **2009**, *324* (5923), 48–49. https://doi.org/10.1126/science.1172083.

(13) Energy, U. S. D. of. No Title. *Transmission Facilitation Program*. 2012. https://doi.org/https://www.

energy.gov/sites/prod/files/2014/12/f19/fcto_myrdd_full_ document.pdf.

(14) Energy, U. S. D. of. No Title. *Transmission Facilitation Program*. 2017. https://doi.org/https://www.

energy.gov/sites/prod/files/2017/11/f46/FCTT_Roadmap_Nov_

2017_FINAL.pdf.

(15) Nie, Y.; Li, L.; Wei, Z. Recent Advancements in Pt and Pt-Free Catalysts for Oxygen Reduction Reaction. *Chem. Soc. Rev.* **2015**, *44*, 2168–2201. https://doi.org/10.1039/c4cs00484a.

(16) Voiry, D.; Shin, H. S.; Loh, K. P.; Chhowalla, M. Low-Dimensional Catalysts for Hydrogen Evolution and CO2 Reduction. *Nat. Rev. Chem.* **2018**, *2* (0105). https://doi.org/10.1038/s41570-017-0105.

(17) Xia, W.; Mahmood, A.; Liang, Z.; Zou, R.; Guo, S. Earth-Abundant Nanomaterials for Oxygen Reduction. *Angew. Chemie - Int. Ed.* **2016**, *55* (8), 2650–2676. https://doi.org/10.1002/anie.201504830.

(18) Li, M.; Zhao, Z.; Cheng, T.; Fortunelli, A.; Chen, C. Y.; Yu, R.; Zhang, Q.; Gu, L.; Merinov, B. V.; Lin, Z.; Zhu, E.; Yu, T.; Jia, Q.; Guo, J.; Zhang, L.; Goddard, W. A.; Huang, Y.; Duan, X. Ultrafine Jagged Platinum Nanowires Enable Ultrahigh Mass Activity for the Oxygen Reduction Reaction. *Science (80-.).* **2016**, *354* (6318), 1414–1419. https://doi.org/10.1126/science.aaf9050.

(19) Ju, W.; Bagger, A.; Wang, X.; Tsai, Y.; Luo, F.; Möller, T.; Wang, H.; Rossmeisl, J.; Varela, A. S.; Strasser, P. Unraveling Mechanistic Reaction Pathways of the Electrochemical CO2 Reduction on Fe-N-C Single-Site Catalysts. *ACS Energy Lett.* **2019**, *4* (7), 1663–1671. https://doi.org/10.1021/acsenergylett.9b01049.

(20) Bezerra, C. W. B.; Zhang, L.; Lee, K.; Liu, H.; Marques, A. L. B.; Marques, E. P.; Wang, H.; Zhang, J. A Review of Fe-N/C and Co-N/C Catalysts for the Oxygen Reduction Reaction. *Electrochim. Acta* **2008**, *53* (15), 4937–4951. https://doi.org/10.1016/j.electacta.2008.02.012.

(21) Zhang, S.; Zhang, H.; Liu, Q.; Chen, S. Fe-N Doped Carbon Nanotube/Graphene Composite: Facile Synthesis and Superior Electrocatalytic Activity. *J. Mater. Chem. A* **2013**, *1* (10), 3302–3308. https://doi.org/10.1039/c2ta01351g.

(22) Su, J.; Iii, C. B. M.; Song, Y.; Huang, L.; Liu, Y.; Li, G.; Xin, Y.; Xiong, P.; Li, M. M.-J.; Chen, H. M.; Tang, B. Z.; Robert, M.; Iii, W. A. G.; Ye, R. Improving Molecular Catalyst Activity Using Strain-Inducing Carbon Nanotube Supports. *ChemRxiv* **2022**. https://doi.org/0.26434/chemrxiv-2022-r9r22.

(23) Wu, Y.; Jiang, Z.; Lu, X.; Liang, Y.; Wang, H. Domino Electroreduction of CO2 to Methanol on a Molecular Catalyst. *Nature* **2019**, *575*, 639–642. https://doi.org/10.1038/s41586-019-1760-8.

(24) Marqués Arias, M. Vienna Ab-Initio Simulation Package. *Univ. Edinburgh* **2009**.

(25) Perdew, J. P.; Burke, K.; Ernzerhof, M. Generalized Gradient Approximation Made Simple. *Phys. Rev. Lett.* **1996**, *77* (18), 3865–3868. https://doi.org/10.1103/PhysRevLett.77.3865.

(26) Grimme, S.; Antony, J.; Ehrlich, S.; Krieg, H. A Consistent and Accurate Ab Initio

Parametrization of Density Functional Dispersion Correction (DFT-D) for the 94 Elements H-Pu. *J. Chem. Phys.* **2010**, *132* (15), 154104. https://doi.org/10.1063/1.3382344.

(27) Joubert, D. From Ultrasoft Pseudopotentials to the Projector Augmented-Wave Method. *Phys. Rev. B - Condens. Matter Mater. Phys.* **1999**. https://doi.org/10.1103/PhysRevB.59.1758.

(28) Brena, B.; Puglia, C.; De Simone, M.; Coreno, M.; Tarafder, K.; Feyer, V.; Banerjee, R.; Göthelid, E.; Sanyal, B.; Oppeneer, P. M.; Eriksson, O. Valence-Band Electronic Structure of Iron Phthalocyanine: An Experimental and Theoretical Photoelectron Spectroscopy Study. *J. Chem. Phys.* **2011**, *134* (7). https://doi.org/10.1063/1.3554212.

(29) Sundararaman, R.; Letchworth-Weaver, K.; Schwarz, K. A.; Gunceler, D.; Ozhabes, Y.; Arias, T. A. JDFTx: Software for Joint Density-Functional Theory. *SoftwareX* **2017**, *6*, 278–284. https://doi.org/10.1016/j.softx.2017.10.006.

(30) Sundararaman, R.; Goddard, W. A. The Charge-Asymmetric Nonlocally Determined Local-Electric (CANDLE) Solvation Model. *J. Chem. Phys.* **2015**, *142* (064107). https://doi.org/10.1063/1.4907731.

(31) Neese, F.; Wennmohs, F.; Becker, U.; Riplinger, C. The ORCA Quantum Chemistry Program Package. *J. Chem. Phys.* **2020**, *152* (22), 224108.

https://doi.org/10.1063/5.0004608.

(32) Becke, A. D. Density-Functional Thermochemistry. III. The Role of Exact Exchange. *J. Chem. Phys.* **1993**, *98* (7), 5648–5652. https://doi.org/10.1063/1.464913.

(33) Mardirossian, N.; Head-Gordon, M. ω B97M-V: A Combinatorially Optimized, Range-Separated Hybrid, Meta-GGA Density Functional with VV10 Nonlocal Correlation. *J. Chem. Phys.* **2016**, *144* (21), 214110. https://doi.org/10.1063/1.4952647.

(34) Vydrov, O. A.; Van Voorhis, T. Nonlocal van Der Waals Density Functional: The Simpler the Better. *J. Chem. Phys.* **2010**, *133* (24), 244103. https://doi.org/10.1063/1.3521275.

(35) Weigend, F.; Ahlrichs, R. Balanced Basis Sets of Split Valence, Triple Zeta Valence and Quadruple Zeta Valence. *Phys. Chem. Chem. Phys.* **2005**, *7*, 3297–3305.

(36) Barone, V.; Cossi, M. Quantum Calculation of Molecular Energies and Energy Gradients in Solution by a Conductor Solvent Model. *J. Phys. Chem. A* **1998**, *102* (11), 1995–2001. https://doi.org/10.1021/jp9716997.

(37) Sundararaman, R.; Goddard, W. A.; Arias, T. A. Grand Canonical Electronic Density-Functional Theory: Algorithms and Applications to Electrochemistry. *J. Chem. Phys.* **2017**. https://doi.org/10.1063/1.4978411.

(38) Huang, Y.; Nielsen, R. J.; Goddard, W. A. Reaction Mechanism for the Hydrogen Evolution Reaction on the Basal Plane Sulfur Vacancy Site of MoS 2 Using Grand Canonical Potential Kinetics. *J. Am. Chem. Soc.* **2018**, *140* (48), 16773–16782. https://doi.org/10.1021/jacs.8b10016.

(39) Rappé, A. K.; Casewit, C. J.; Colwell, K. S.; Goddard, W. A.; Skiff, W. M. UFF, a Full Periodic Table Force Field for Molecular Mechanics and Molecular Dynamics Simulations. *J. Am. Chem. Soc.* **1992**, *11425* (10024–10035). https://doi.org/10.1021/ja00051a040.

(40) Naserifar, S.; Brooks, D. J.; Goddard, W. A.; Cvicek, V. Polarizable Charge Equilibration Model for Predicting Accurate Electrostatic Interactions in Molecules and Solids. *J. Chem. Phys.* **2017**. https://doi.org/10.1063/1.4978891.

(41) Naserifar, S.; Oppenheim, J. J.; Yang, H.; Zhou, T.; Zybin, S.; Rizk, M.; Goddard, W. A. Accurate Non-Bonded Potentials Based on Periodic Quantum Mechanics Calculations for Use in Molecular Simulations of Materials and Systems. *J. Chem. Phys.* **2019**, *151* (15). https://doi.org/10.1063/1.5113811.

(42) Marom, N.; Kronik, L. Density Functional Theory of Transition Metal Phthalocyanines, II: Electronic Structure of MnPc and FePc - Symmetry and Symmetry Breaking. *Appl. Phys. A Mater. Sci. Process.* **2009**, *95* (1), 165–172. https://doi.org/10.1007/s00339-008-5005-1.

(43) Shi, L. Le; Li, M.; You, B.; Liao, R. Z. Theoretical Study on the Electro-Reduction of Carbon Dioxide to Methanol Catalyzed by Cobalt Phthalocyanine. *Inorg. Chem.* **2022**, *61* (42), 16549–16564. https://doi.org/10.1021/acs.inorgchem.2c00739.

(44) Liang, W.; Chen, J.; Liu, Y.; Chen, S. Density-Functional-Theory Calculation Analysis of Active Sites for Four-Electron Reduction of O2 on Fe/N-Doped Graphene. *ACS Catal.* **2014**, *4* (11), 4170–4177. https://doi.org/10.1021/cs501170a.

(45) Choi, C. H.; Choi, W. S.; Kasian, O.; Mechler, A. K.; Sougrati, M. T.; Brüller, S.; Strickland, K.; Jia, Q.; Mukerjee, S.; Mayrhofer, K. J. J.; Jaouen, F. Unraveling the Nature of Sites Active toward Hydrogen Peroxide Reduction in Fe-N-C Catalysts. *Angew. Chemie - Int. Ed.* **2017**, *56* (30), 8809–8812. https://doi.org/10.1002/anie.201704356.

(46) Abrahams, S. C.; Collin, R. L.; Lipscomb, W. N. The Crystal Structure of Hydrogen Peroxide. *Acta Crystallogr.* **1951**, *4* (1), 15–20. https://doi.org/10.1107/s0365110x51000039.

Chapter 4

Dual Atoms Catalysts for Rapid Electrochemical Reduction of CO to Ethylene

Reproduced with permission from:

Yuyin Li, Zhengtang Luo, William A. Goddard III. *Dual atom catalysts for rapid electrochemical reduction of CO to ethylene, Nano Energy,* **2024**, *118, 108966*

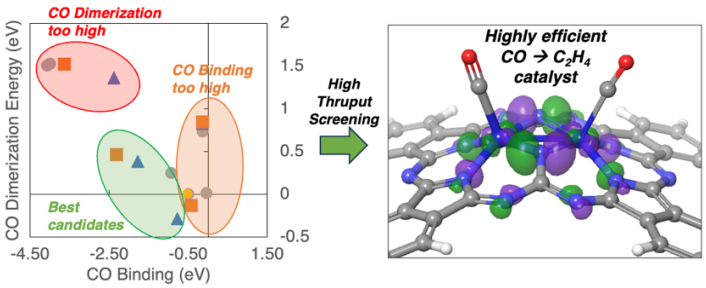

Figure 4.0: Table of contents figure

4.1 Abstract

Strong CO adsorption and facile CO dimerization are the key challenges in electrochemical CO_2 reduction towards multi-carbon (C_{2+}) products. We recently showed that CoPc immobilized on a single-walled carbon nanotube can selectively reduce CO_2 to

methanol. This is enabled through molecular strain, which dramatically improves the CO adsorption energy to CoPc, which in turn facilitates methanol formation. We now examine the extended Phthalocyanine (Pc_{Ex}) **dual atom catalyst (DAC),** which is intrinsically strained and contains two catalyst centers, making it a candidate for reducing CO to C_{2+} products. Using Quantum Mechanics (QM), we screened 20 elements embedded in the Pc_{Ex}, seeking catalysts with weak hydrogen binding, strong CO binding, and facile CO dimerization. We identified Fe, Ru, Co, and Ir as the best performers and subsequently evaluated the entire CO to C_2H_4 mechanism (9 steps) using each of these elements as catalysts. In terms of limiting potential and overall exergonicity, we identified $CoPc_{Ex}$ as the best catalyst, followed by $IrPc_{Ex}$. We then examined the full CO to C_2H_4 mechanism on the bimetallic $IrCoPc_{Ex}$ catalyst using grand canonical QM to obtain the reaction energetics as a function of applied potential. We conclude that the bimetallic $IrCoPc_{Ex}$ is most promising for efficiently converting CO to ethylene.

4.2 Introduction

Climate change has been a direct result of increased anthropogenic CO_2 levels in the earth's atmosphere.[1,2] To combat the negative effects on our environment, research and development of CO_2 capture and transformation strategies are imperative.[3–6] One promising solution towards a carbon-neutral economy is electrochemical CO_2 reduction

(eCO_2R), in which CO_2 is reduced to useful, value-added products.[7,8] The electrochemical nature of the reduction process means that the required energy input can be sourced from green energy, such as electrons generated via solar or wind power. While this method appears enticing, numerous issues with cost, efficiency, and selectivity, keep eCO_2R from being commercially or industrially viable. Even if we ignore the cost of eCO_2R, the lack of reaction selectivity poses a problem. Ideally, eCO_2R should generate multi-carbon (C_{2+}) products such as ethylene (C_2H_4) or ethanol (C_2H_6). These products could serve as high energy density liquid fuels or feedstocks for polymers, rendering them far more desirable than other eCO_2R products like methane or carbon monoxide (CO). However, eCO_2R is rarely selective towards C_{2+} products, with major products including CO and/or H_2, the latter resulting from the undesired Hydrogen evolution reaction (HER). A large portion of current eCO_2R research has been devoted towards maximizing the amount of C_{2+} products formed during eCO_2R. The only catalyst showing appreciable quantities of C_{2+} products is Cu metal, but even Cu metal cannot reliably produce mainly C_{2+} products.[9] This results from numerous factors with Cu metal, including: reactant concentrations, applied potential, electrode microenvironment, and electrode structure.

Single atom catalysts (SACs) have been studied thoroughly over the past decade, finding uses in numerous electrochemical reactions including electrochemical oxygen reduction,[10] nitrogen reduction,[11] and eCO_2R.[12,13] To go one step beyond SACs, we

introduce a second catalyst center. Dual atom catalysts (DACs) have received abundant attention recently, as they are capable of doubled metal loading relative to SACs, which could hypothetically increase catalytic performance.[14] Additionally, the larger footprint of DACs provides more opportunity for strain engineering, which we found extremely useful in the case of Cobalt Phthalocyanine (CoPc) on single-walled carbon nanotubes (SWCNT, see below for further details).[15] DACs have already been proposed for use in dehydrogenation reactions,[16] oxygen reduction,[17] nitrogen and nitrate reduction,[18,19] and even eCO_2R.[20]

We set our aim on the CO reduction reaction (CORR). It was recently showed that a Pd_2 DAC was capable of reaching 98.2% faradic efficiency (FE) towards CO at -0.85 V vs. RHE, proving that DACs can reduce CO_2 to CO.[21] However, for reduction towards C_{2+} products, we seek a catalyst that reduces CO all the way to C_2H_4. This requires the catalyst to bind CO sufficiently strongly to facilitate dimerization of two adsorbed CO molecules, forming a covalent C–C bond. These two barriers are perhaps the biggest issues facing eCO_2R and CORR towards C_{2+} products. Most catalysts bind CO weakly, such that once it's formed from CO_2, it desorbs. In the case that a catalyst does bind CO strongly, the dimerization step typically requires a large energy barrier, so that CO is more likely to desorb or be reduced towards CH_4 or methanol (CH_3OH) rather than dimerizing; while these products are not necessarily undesired, C_{2+} products are preferred.

We recently demonstrated that when CoPc SAC is immobilized on single-walled carbon nanotubes (SWCNTs), it's eCO_2R selectivity is dramatically altered, producing CH_3OH as the main product instead of CO (the main product when CoPc is immobilized on a conventional graphitic support or on multi-walled carbon nanotubes). This change in mechanism resulted from molecular distortion induced in the CoPc by the SWCNT, which improved the CO binding energy and ultimately steered the selectivity towards value-added CH_3OH product. This result inspired us to investigate the extended Phthalocyanine (Pc_{Ex}) DAC platform for CO reduction towards C_{2+} products (Figure 4.1). We investigate a selection of 20 transition metals (TMs) and main group elements for the purpose of CORR towards C_{2+} products. We begin by evaluating hydrogen binding and CO binding for all 20 Pc_{Ex} catalysts, providing us with an idea of how selective the catalyst will be for CORR vs. HER. We then evaluate CO dimerization energies for all 20 catalysts, allowing us to anticipate which catalysts will actually dimerize adsorbed CO. For our best four candidates, we next calculated the entire mechanism (9 steps) for converting 2 CO to C_2H_4. We combined the two best elements to form a bimetallic Pc_{Ex} catalyst, and investigated the CO to C_2H_4 mechanism as a function of applied potential, using our Grand Canonical quantum mechanics method.

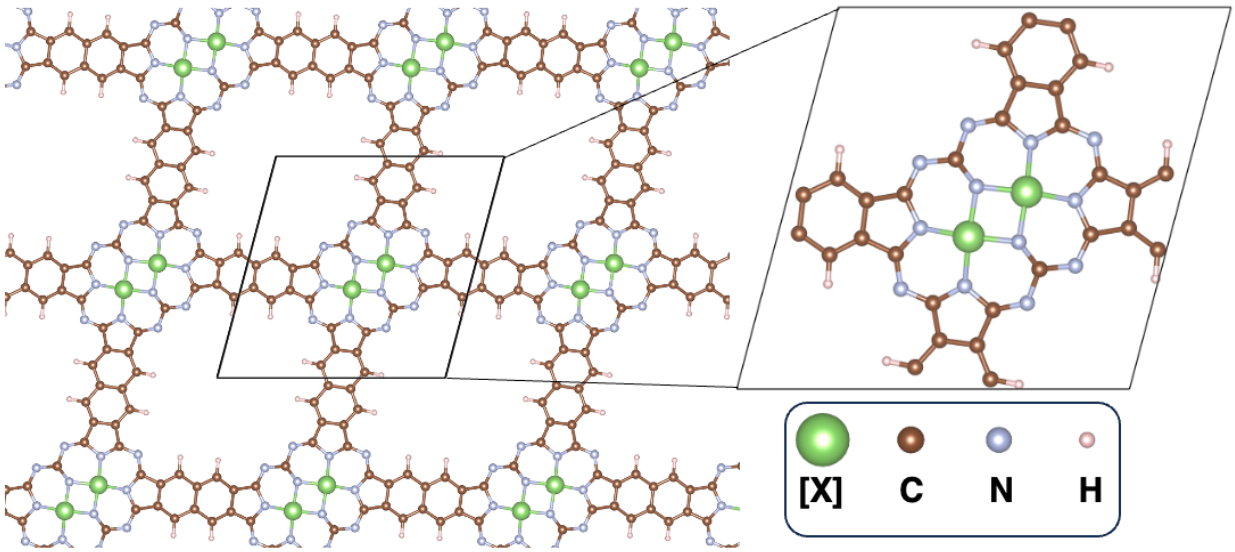

Figure 4.1: Extended Phthalocyanine (Pc_{Ex}) periodic structure. Green atoms denoted as [X] represent the catalyst center (can be either transition metal or main group), brown are carbon, light blue are nitrogen, and white are hydrogen.

4.3 Methods

All DFT structure optimizations were performed using the Vienna Ab Initio Simulation Package (VASP) version 6.3.2.[22] Initial optimizations were performed using the PBE[23] flavor GGA functional with the D3BJ correction for London Dispersion forces.[24] Projector Augmented Wave (PAW) pseudopotentials[25] were used to describe all atoms, and a plane wave basis set cutoff of 520 eV was chosen. All calculations were spin-polarized, with initial magnetics moments aligned to high spin. Structural optimizations featured gamma-centered 3 x 3 x 1 K point grids to sample the Brillouin zone. VASP was also used to calculate phonons at 298.15 K.

Structural optimizations were followed by rigorous solution-phase energy calculations using the JDFTx software.[26] All JDFTx calculations featured implicit water solvent as implemented via the CANDLE solvation model.[27,28] Because we are dealing with 2D structures, coulomb interactions in the direction orthogonal to the catalyst plane were truncated. This eliminates any artificial coulomb interactions between the 2D catalyst and its periodic images.

Hybrid DFT calculations were performed using the Jaguar v10.9 software by Schrodinger Inc.[29] For consistency, structures were optimized at the PBE-D3BJ level, along with the 6-311G** basis set for non-metals using the LAV3P** large-core effective core potential for metals.[30–33] Following structure optimizations, single-point energies were performed using the meta-NGA MN15 functional by Truhlar.[34] MN15 has been demonstrated to accurately capture multireference and noncovalent interactions in complex molecules.[ref]

Grand Canonical Potential (GCP, Equation 4.1) energies were calculated to determine how the reactions change with applied potential.[35] GCP introduces the Legendre Transform of the Gibbs free energy with respect to number of electrons (N_e), in which the conjugate variable is the chemical potential (μ).

$$GCP = G - \mu N_e = H - TS - \mu N_e \quad \text{(Equation 4.1)}$$

To obtain GCP energies, we first compute Gibbs free energies at varying N_e. We fit these data points to a quadratic curve, in which the 2^{nd}, 1^{st}, and 0^{th}-order coefficients relate to the differential capacitance, the potential of zero charge, and the free energy at neutral charge, respectively. From these coefficients we predict the reaction free energies as a function of applied potential, U.

4.4 Results and Discussion

4.4.1 Hydrogen Binding

Previous theoretical work on the Pc_{Ex} DAC revealed that many TMs and main group elements are thermodynamically stable in the Pc_{Ex} framework relative to their bulk structures.[19] Thus, we did not examine thermodynamic stability of these DACs, proceeding directly to investigate key CORR descriptors. The key descriptors and their relevant equations are as follows:

- Hydrogen Binding Energy: 2 * + H_2 → 2 *H
- Binding Energy of 2 CO: 2 * + 2 CO → 2 *CO
- CO Dimerization Energy: 2 *CO → *OCCO

In which * indicates an open catalyst site, *H is an adsorbed hydrogen atom, *CO is an adsorbed CO molecule, and *OCCO is an adsorbed OCCO that bridges the two catalyst sites. For the remainder of this study, we omit the *, such that all species are assumed to be adsorbed unless otherwise noted. These reactions are also depicted in Figure 4.2.

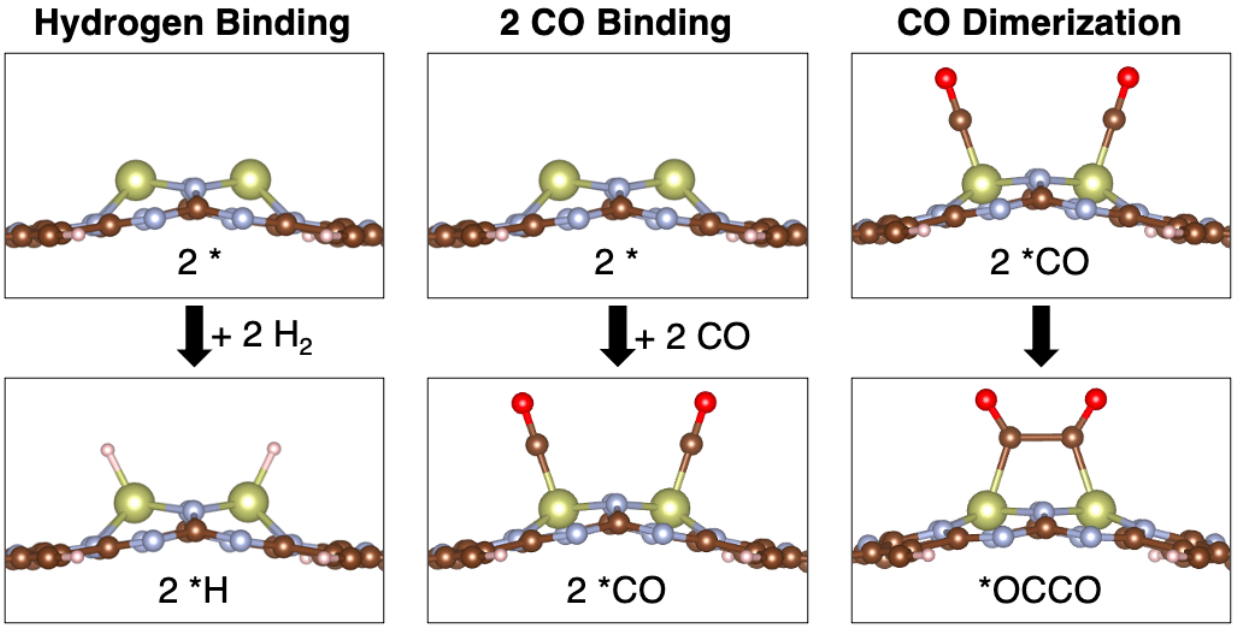

Figure 4.2: Representative Hydrogen binding, 2 CO binding, and CO dimerization reactions for the extended Phthalocyanine dual atom catalyst.

CORR typically competes with the hydrogen evolution reaction (HER), in which 2 solvent waters are converted to OH^- while evolving an equivalent of H_2, according to Reaction 4.1. This reaction also occurs at low pH via hydronium cation instead of water (Reaction 4.2).

$$2\,H_2O + 2\,e^- \rightarrow H_2 + 2\,OH^- \qquad \text{(Reaction 4.1)}$$

$$2\,H_3O^+ + 2\,e^- \rightarrow H_2 + 2\,H_2O \qquad \text{(Reaction 4.2)}$$

For practical purposes, we seek to catalyze CORR in aqueous media, such that water is inevitably present at the catalyst site (assuming no hydrophobic film has been deposited on the catalyst). Moreover, these reduction reactions require protons, such that low pH is also desired. While low pH does theoretically accelerate CORR kinetics, it simultaneously accelerates HER; thus highly-selectivity CORR is typically performed at high pH, at the cost of retarded kinetics. This stems from the fact that CO and H compete for catalyst binding.[36] To improve the likelihood of CORR and the inhibition of HER, we seek a catalyst that disfavors hydrogen binding. Table 4.1 contains the Gibbs free energies for binding two H (one H per catalyst site) to the Pc_{Ex} DAC. H binding energies are also depicted in Figure 4.1a. Our selected TM and main group elements have H binding energies ranging from +4.03 (Ag) to -2.08 eV (W), with each transition metal row (3d, 4d, 5d) trending towards more endergonic binding with more d electrons. From these results, we must be wary of the early transition metals, as they are predicted to strongly bind hydrogen, such that they would likely be selective towards HER.

Table 4.1: Gibbs free energies at 298.15 K for 2 H binding, 2 CO binding, and CO dimerization (eV).

Catalyst	2 H Binding (eV)	2 CO Binding (eV)	CO Dimerization (eV)
Ti	0.60	-1.64	--
Cr	0.01	-2.19	--
Mn	0.06	-2.39	1.36
Fe	-0.17	-1.76	0.38
Co	0.45	-0.77	-0.29
Ni	2.51	-0.14	0.83
Cu	3.95	-0.09	--
Mo	-1.35	-3.63	1.52
Ru	-0.68	-2.32	0.46
Rh	0.50	-0.42	-0.13
Pd	1.91	-0.13	0.84
Ag	4.03	-0.10	--
W	-2.08	-3.98	1.52
Re	-1.74	-4.06	1.50
Ir	0.38	-0.92	0.24
Pt	1.40	-0.10	0.72
Au	4.01	-0.03	0.01
Ga	0.51	-0.48	0.00
Sn	-0.18	--	0.23
Bi	3.49	0.30	--

4.4.2 CO Binding

As stated previously, a stellar CORR catalyst should disfavor H binding in order to inhibit HER and steer selectivity towards reduction of CO. However, this catalyst must also be capable of binding CO with moderate exergonicity.[37] A catalyst that disfavors CO

binding will not be capable of adsorbing CO long enough for the CO to be reduced.[38] In the case of the Pc_{Ex} DAC, a poor CO binding will preclude the possibility of 2 CO's dimerizing, since CO desorption would occur before the endergonic dimerization step. Alternatively, the catalyst should not bind CO too strongly; overly exergonic CO binding may result in poisoning of the catalyst with subsequent deactivation. In the context of CO binding, the perfect CORR catalyst should bind CO with a free energy of slightly more than -0.25 eV. Given the ~35 entropy units of the CO molecule, -0.25 eV ensures that CO stays adsorbed to the catalyst but is still vulnerable to reduction or dimerization.

Table 4.1 contains the Gibbs free energies of 2 CO binding (one CO per catalyst site). 2 CO Binding energies range from +0.30 eV (Bi) to -4.06 eV (Re). 2 CO binding over our 20 cases averaged -1.31 eV (-0.65 eV per CO), indicating that the Pc_{Ex} DAC should selectively bind CO over H. 2 CO binding energies are also displayed in Figure 4.3b. Non-trivial trends emerge when 2 CO binding energies are distinguished by their elemental types. For the early 3d TMs (Ti through Mn), 2 CO binding becomes more negative when going across the row. However, the late 3d TMs exhibit the opposite; from Mn to Cu, 2 CO binding becomes less negative when going across the row. No inflection point is found in the case of the 4d TMs; proceeding from Mo across to Ag leads only to less negative 2 CO binding. The same is found for 5d TMs (W through Au), although the Re 2 CO binding is slightly more negative than for W. Finally, no obvious trend is

observed for the main group elements investigated. Of the 20 elements screened, the following elements had 2 CO binding energies weaker than -0.50 eV (-0.25 eV per CO): Ni, Cu, Rh, Pd, Ag, Pt, Au, Ga, and Bi. Because these catalysts will likely favor CO adsorption over CORR or CO dimerization, we exclude them from further investigation. We note that Cu falls into this group, which is surprising given that Cu metal is the only catalyst known to convert CO_2 to C_2H_4 with a faradic efficiency (FE) exceeding 5%.[39] This is likely because Cu resides in the +2 oxidation state when placed in the Pc_{Ex}, as opposed to metal Cu in which Cu is relatively reduced. On the other hand, we find that several elements bind CO too strongly, such that the catalyst would likely be poisoned in experiment. TMs such as Mo, W, and Re, exhibit 2 CO binding energies more negative than -3 eV, such that we immediately exclude them from further investigation for CORR.

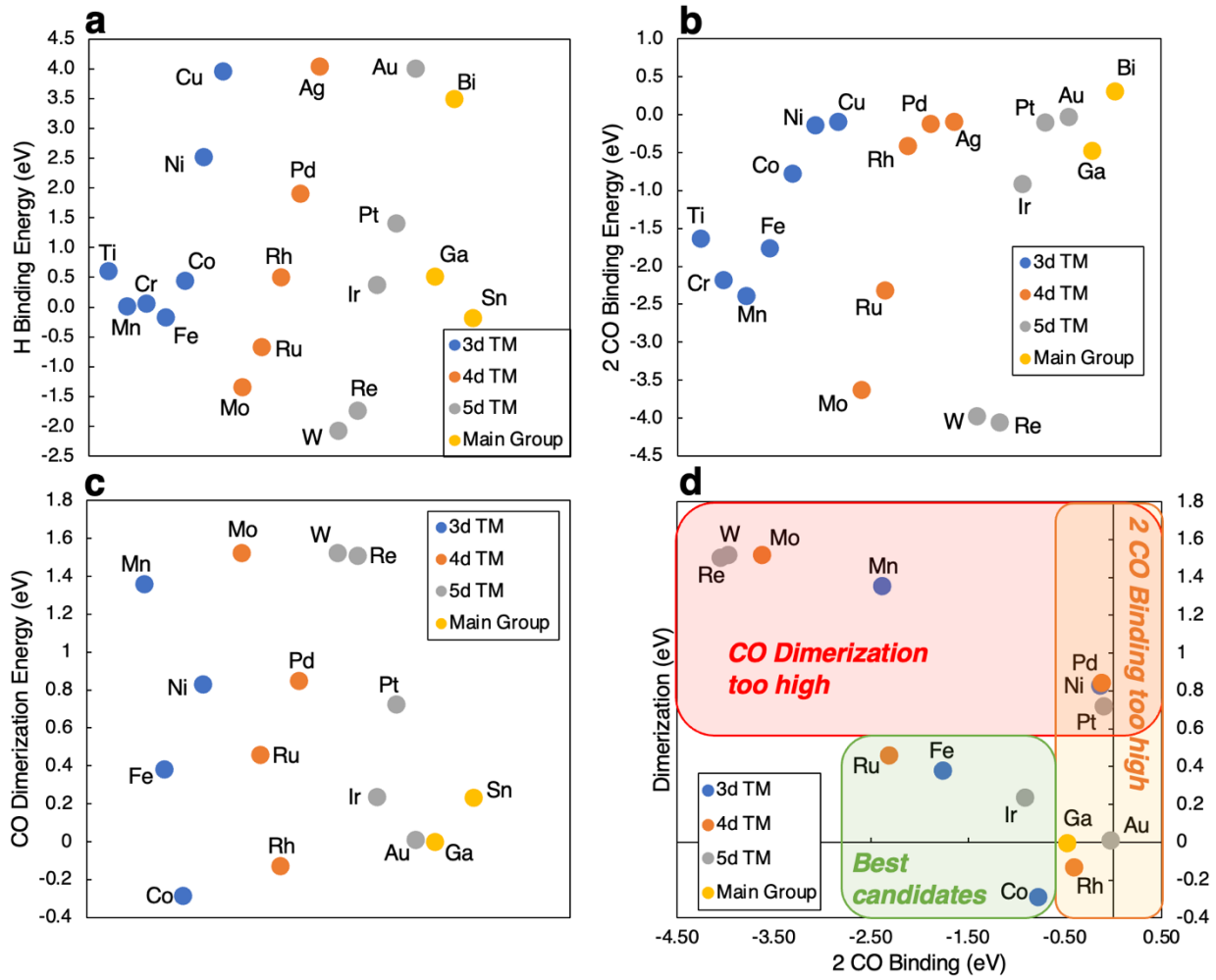

Figure 4.3: (**a**) H Binding energies at 298.15 K in eV for the 20 screened elements. 3d, 4d, and 5d TM correspond to the first, second, and third row transition metals, respectively. (**b**) 2 CO Binding energies at 298.15 K in eV for the 20 screened elements. Only Sn is omitted as we were unable to converge the 2 CO-adsorbed structure. (**c**) CO Dimerization energies at 298.15 K in eV for the 20 screened elements. Ti, Cr, Cu, Ag, and Bi are omitted here since we were unable to converge their adsorbed OCCO structures. (**d**) CO binding energies versus CO Dimerization energies. The orange region defines the area in which 2 CO Binding is too high, such that the CO would likely desorb from the catalyst. The red region defines the area in which CO Dimerization is too high, such that elements in this region would not likely form the OCCO species from 2 CO. Ti, Cr, Cu, Ag, Sn, and Bi are omitted since these elements did not simultaneously have 2 CO Binding and CO Dimerization energies.

4.4.3 CO Dimerization

Perhaps the most important descriptor for determining if a catalyst will convert CO to multi-carbon (C_{2+}) products is the CO dimerization barrier.[40] The rate-determining

step (RDS) for Cu-catalyzed CO_2RR towards C_{2+} products is widely accepted to be the CO dimerization step, in which two adsorbed *CO on adjacent sites covalently link to generate an adsorbed *OCCO.[41–43] This step is purely chemical (i.e., does not require a proton or electron), although many studies find that the dimerization does depend on applied potential;[44] this apparent inconsistency will be addressed in section *3.4*. Regardless, we seek rapid CORR towards C_{2+} products, so that more exergonic CO dimerization is desired. Because the CO dimerization transition state is too costly to calculate for the purposes of high throughput screening, we instead consider the dimerization thermodynamics (i.e., Gibbs free energy of dimerization).

Table 4.1 contains the CO dimerization free energies; these energies are also displayed in Figure 4.3c. CO dimerization free energies range from +1.52 eV (W) to -0.29 eV (Co), with an average of +0.61 eV. The dimerization energies appear to follow a column-dependent trend. Specifically, group IX elements (Co, Rh Ir) all have relatively low dimerization energies (-0.29 eV, -0.13 eV, +0.23 eV, respectively). All group X elements (Ni, Pd, Pt) have high dimerization energies (+0.83 eV, +0.84 eV, +0.72 eV, respectively) while all elements from groups VI (Cr, Mo, W) and XI (Cu, Ag, Au) were not capable of stabilizing the *OCCO intermediate. For the main group elements, Ga CO dimerization is predicted to be thermoneutral (0.00 eV). Sn is an odd case; we were able to locate the *OCCO intermediate but not the preceding 2 CO intermediate, suggesting

that Sn spontaneously dimerizes 2 CO yet paradoxically refusing to bind CO. Finally, DFT predicts that Bi cannot stabilize the *OCCO intermediate.

With the 2 CO binding energies and CO dimerization energies tabulated, we plot 2 CO binding versus CO dimerization in Figure 4.3d. We desire a catalyst that binds 2 CO with moderate exergonicity while simultaneously dimerizing CO with strong exergonicity. In figure 4.3c, we immediately exclude elements residing in the right-hand portion (orange hue), as these elements bind CO weakly, and will likely not be selective towards CORR. Furthermore, we immediately exclude elements in the upper portion (red hue), as these elements are not likely to dimerize CO towards C_{2+} products. We therefore focus on elements found in the lower left (green hue); these elements (Fe, Ru, Co, Ir) exhibit moderately strong CO binding and moderately low dimerization energies. Along with their favorable heats of formation and hydrogen binding energies (except for Ru which had a rather exergonic hydrogen binding energy of -0.68 eV), we deem these elements the best candidates for CORR towards C_{2+} products. These elements being the best candidates is not unexpected, since they have previously found use in other electrochemical reactions including nitrogen and nitrate reduction,[45–47] oxygen evolution and reduction,[48–51] and CO_2 reduction.[52,53]

4.4.4 CO Reduction Mechanism towards Ethylene

CORR towards C_2H_4 is typically initiated via the CO dimerization step, which we investigated in section *3.3* above. Dimerization yields the OCCO intermediate, which next undergoes a simple proton-coupled electron transfer (PCET) at one of the oxygens to generate the HOCCO intermediate. Previous reports on this mechanism find that the next PCET occurs at the opposite oxygen to generate the symmetric HOCCOH intermediate. The next PCET occurs at either oxygen to generate the HOCC intermediate and liberate a free water molecule. Given that the carbon opposite the oxygen in HOCC is now severely undercoordinated, the next PCET occurs at said carbon to yield HOCCH. The following PCET occurs at the oxygen to product CCH and liberate another equivalent water molecule. The proceeding PCET can generate either HCCH or CCH_2, although previous studies on Cu metal find CCH_2 to be favored.[41] The proceeding PCET generates $HCCH_2$, and the final PCET affords the desired C_2H_4 product, thus completing the overall reaction to convert 2 CO to C_2H_4 (Reaction 4.3, which assumes the hydronium ion as the proton source).

$$2\,CO + 8\,H_3O^+ + 8\,e^- \rightarrow\ C_2H_4 + 10\,H_2O \quad \text{(Reaction 4.3)}$$

We calculated the 9-step reaction (dimerization + 8 PCETs) to convert 2 CO to C_2H_4 using our best elements (Fe, Ru, Co, Ir). The free energy landscapes for

converting 2 CO to C_2H_4 via $FePc_{Ex}$, $RuPc_{Ex}$, $CoPc_{Ex}$, and $IrPc_{Ex}$ are depicted in Figure 4.4.

Beginning with Fe, DFT predicts the limiting potential (U_{limit}) of $FePc_{Ex}$ to be +0.97 V, corresponding to the conversion of HOCCOH to HOCC + H_2O. This coincides with HOCC being the highest energy intermediate, residing at +1.90 eV above the 2 CO starting state. The overall conversion of 2 CO to C_2H_4 on $FePc_{Ex}$ is downhill -1.53 eV.

For $RuPc_{Ex}$, DFT predicts a U_{limit} of +1.37 V. Similar to the Fe case, this corresponds to the conversion of HOCCOH to HOCC, with HOCC being the highest-energy intermediate at +2.15 eV above the 2 CO starting state. $RuPc_{Ex}$ converts 2 CO to C_2H_4 with an overall free energy of -0.97 eV.

$CoPc_{Ex}$ converts 2 CO to C_2H_4 with a U_{limit} of +0.83 V. This again corresponds to the HOCC intermediate, which lies +1.41 eV above the 2 CO starting state. DFT predicts $CoPc_{Ex}$ to convert 2 CO to C_2H_4 with a free energy of -2.52 eV.

Finally, $IrPc_{Ex}$ has a U_{limit} of +1.06 V, such that the corresponding HOCC intermediate lies +1.99 eV above the 2 CO reference. The conversion of 2 CO to C_2H_4 on $IrPc_{Ex}$ is -2.37 eV downhill.

We note that despite previous studies that found the reduction mechanism to proceed through CCH_2 on Cu, for the DAC we find that HCCH is preferred over CCH_2

for all four catalysts. Specifically, HCCH is lower in energy than CCH_2 by -0.28, -0.12, -0.82, and -0.34 eV for Fe, Ru, Ir, and Co, respectively.

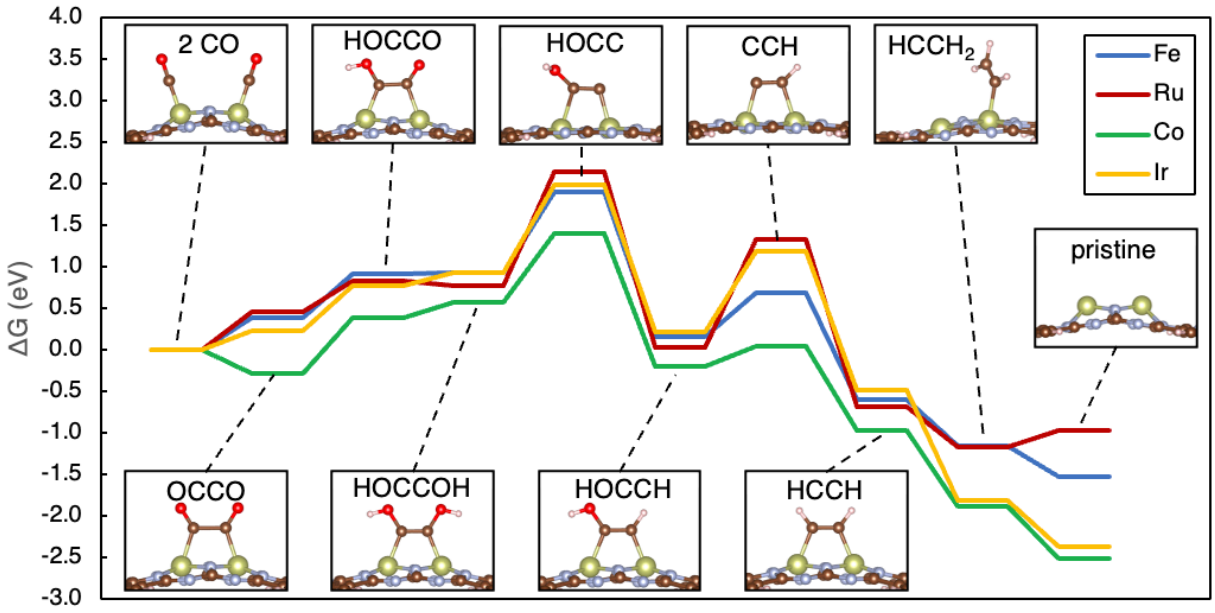

Figure 4.4: Gibbs free energies at 298.15 K for converting 2 CO to C_2H_4 via the $FePc_{Ex}$, $RuPc_{Ex}$, CoPcEx, and $IrPc_{Ex}$ dual atom catalysts. $\frac{1}{2}$ H_2 is used as the hydrogen reference. The steps that convert HOCCOH to HOCC and HOCCH to CCH both afford an equivalent of water, and the step that converts $HCCH_2$ to pristine substrate affords a free C_2H_4 molecule.

$CoPc_{Ex}$ exhibits the best energetics for CORR to C_2H_4, due primarily to its negative CO dimerization energy, which is in stark contrast to the other elements that all exhibit positive dimerization energies. This key departure from the other elements merits further analysis. We previously mentioned the inconsistency with CO dimerization, in which the dimerization barrier changes with applied potential, despite the reaction step being purely chemical (no proton or electron required). This phenomenon results from charge

accumulation on the catalyst centers that donates into the incipient C–C bond, such that the dimerization step is pseudo-electrochemical. With this knowledge, we calculate the Löwdin atomic populations, which act as a surrogate for atomic charge accumulation.[54] In the OCCO intermediates, Fe, Ru, and Ir have Löwdin oxidation states of +0.037, +0.023, and +0.077 respectively; Co has a Löwdin oxidation state of -0.101. The Co atoms are substantially more negative, which we hypothesize allows Co to donate charge density more easily into the carbon p orbitals, facilitating exergonic C–C bond formation.

4.4.5 Bimetallic Mechanism

Heterogeneous catalysts are often doped with co-catalyst species to modulate their catalytic properties towards enhanced CO_2RR or CORR. Through co-catalyst doping, novel combinations of multiple metal types have been investigated for enhanced catalytic performance.[55,56] Having differing metal types in the active site introduces asymmetry in the nuclear and electronic structure, which may well enhance reactions that proceed through asymmetric binding motifs. We envisage a hypothetical bimetallic active site, in which the differing metals work synergistically to induce a dipole between the two carbons of the two adsorbed CO molecules. Said dipole may polarize the carbon p orbitals, resulting in facile dimerization towards OCCO. With this idea in mind, we investigated a bimetallic Pc_{Ex} for enhanced CORR towards C_2H_4.

For the bimetallic Pc_{Ex} DAC we chose Ir and Co, as they performed the best out of the 4 elements tested in section *3.4* for CORR towards C_2H_4. The $IrCoPc_{Ex}$ binds 2 CO with a free energy of -0.78 eV and dimerizes CO with a free energy of 0.00 eV (Figure 4.5). This indicates that the bimetallic catalyst binds CO with the same strength as the parent Co catalyst and weaker than the parent Ir catalyst. Moreover, the bimetallic catalyst more readily dimerizes CO than the parent Ir catalyst, but less readily than the parent Co catalyst. We calculated the 9-step conversion of 2 CO to C_2H_4 using $IrCoPc_{Ex}$ as the substrate. Figure 4.5 depicts the free energy landscape for $IrCoPc_{Ex}$-catalyzed CORR, with the parent $IrPc_{Ex}$ and $CoPc_{Ex}$ overlayed for comparison. We see that introduction of asymmetry in the catalyst induces improved reduction energetics. As was found for all the other catalysts, HOCC is the highest-energy intermediate in the reaction path, at +1.05 eV above the starting state. However, $IrCoPc_{Ex}$ leads to $U_{\text{limit}} = +0.87$ V for formation of the CCH intermediate. The overall conversion of 2 CO to C_2H_4 is downhill -2.51 eV for $IrCoPc_{Ex}$, which is comparable to that of the parent $CoPc_{Ex}$ catalyst. While the bimetallic catalyst did not improve CO dimerization beyond the value of -0.29 eV for Co, we found that modulating the metal type caused a shift in the reaction mechanism, such that U_{limit} now corresponds to CCH formation instead of HOCC formation. Visual inspection of the HOCC intermediate on $IrCoPc_{Ex}$ reveals that the intermediate is substantially stabilized by desorbing from the Co and binding solely to Ir, resulting in a

C–C triple bond (Figure 4.5). Comparison with HOCC on the parent $IrPc_{Ex}$ and $CoPc_{Ex}$ reveals that the Ir catalyst binds HOCC in the conventional manner with one carbon bound to each metal center. However, $CoPc_{Ex}$ also binds HOCC through only 1 metal center, such that a C–C triple bond is formed. Evidently, this preferred HOCC binding orientation substantially stabilizes the HOCC intermediate relative to the conventional binding mode. A similar phenomenon is observed for the CCH intermediate on $CoPc_{Ex}$; instead of binding to both catalyst centers through both carbons, the CCH species desorbs from one of the Co to bind to just one Co, resulting in a C–C triple bond and significant strain relief (Figure 4.5).

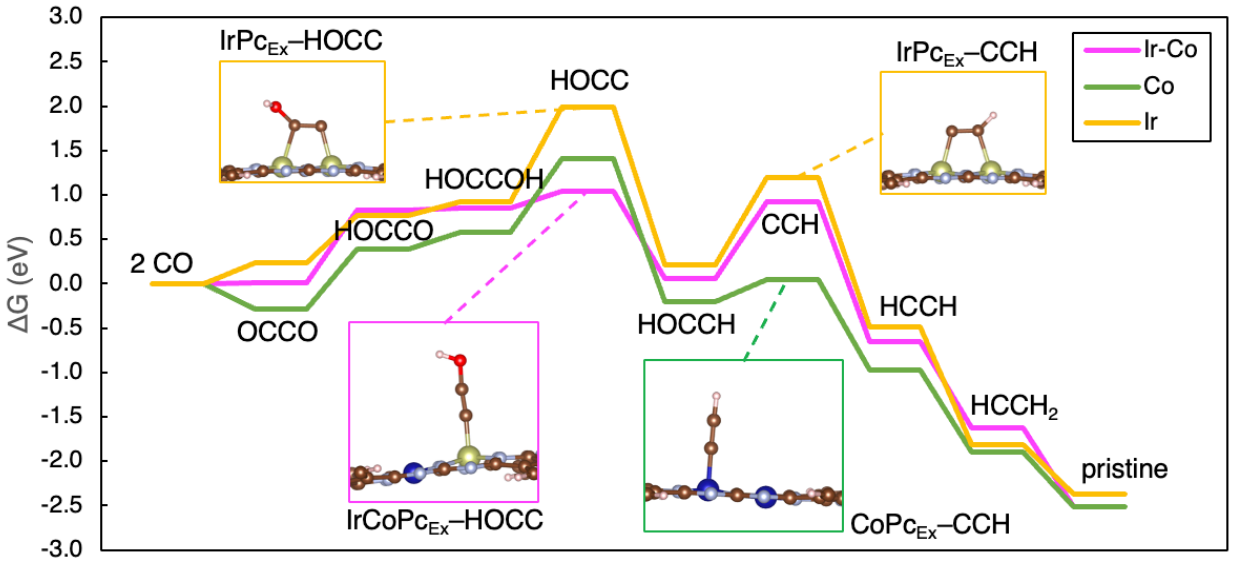

Figure 4.5: Gibbs free energies at 298.15 K for converting 2 CO to C_2H_4 via the $CoPc_{Ex}$, $IrPc_{Ex}$, and $IrCoPc_{Ex}$ dual atom catalysts.

In reality, the catalyst would be anchored to some conducting support which feeds the catalyst the electrons necessary for reducing CO to C_2H_4. In order to account for an applied potential, we now calculate the reaction mechanism via the Grand Canonical Potential (GCP) method which does all steps at the same applied potential (standard QM does all steps at the same charge). The GCP method has been utilized previously to elucidate potential-dependent free energy landscapes, leading to excellent agreement with experiment.[57,58] The 2 CO to C_2H_4 mechanism is depicted in Figure 4.6 at applied potentials of 0.0, -0.3, -0.6, and -1.0 V vs. RHE. Note that we now include the step for adsorbing 2 CO in order to elucidate the CO binding energy as a function of potential.

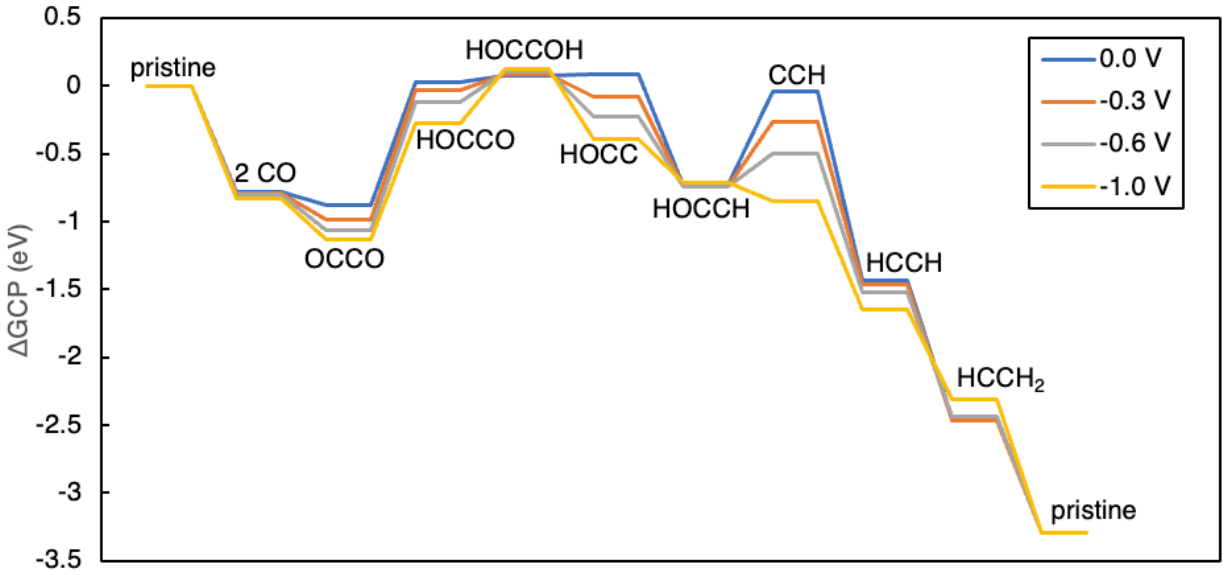

Figure 4.6: Grand Canonical Potential energies at 298.15 K for various applied potentials (versus RHE) at a pH of 7.

The reference states in the GCP landscapes are the pristine $IrCoPc_{Ex}$ catalysts, free of adsorbates. The GCP energies reveal that the applied potential modulates the thermodynamic stability of only some reaction intermediates. Take for example the HOCCOH and CCH intermediates; at all potentials, the HOCCOH intermediate remains ~0.1 eV above the reference state, yet CCH varies by over 0.8 eV as the potential changes from 0.0 to -1.0 V vs. RHE. Moreover, decreasing the potential to -1.0 V vs. RHE yields an exergonic conversion of HOCCH to CCH. Specifically, the conversion of HOCCH to CCH is at -0.6 V vs. RHE is +0.23 eV, but at -1.0 V vs. RHE, this conversion is now -0.13 eV. It is interesting to note that at all potentials investigated, CO dimerization is negative, despite the CO dimerization energy being thermoneutral at 0 charge. This is likely because the 0-charge case corresponds to a positive applied potential. Indeed, GCP reveals that for the OCCO intermediate, 0.0 V vs. RHE corresponds to a fractional charge of -0.7 electrons. Overall, the DFT GCP energies predict that for nearly all elementary steps in the reaction, making the potential more negative yields more exergonicity, making the conversion of CO to C_2H_4 via the $IrCoPc_{Ex}$ achievable under reducing conditions.

4.5 Conclusions

DACs contain an additional layer of complexity beyond conventional SACs, which may enable them to catalyze more intricate chemical reactions like the reduction of CO_2

or CO to multi-carbon products. We used Density Functional Theory to screen 20 select transition metal and main group elements for hydrogen binding, CO binding, and CO dimerization. Of these 20 elements, we identified Fe, Ru, Co, and Ir as the best candidates for converting CO to ethylene. Specifically, Fe, Ru, Co, and Ir had 2 CO binding energies of -1.76, -2.32, -0.77, and -0.92 eV, respectively. We attribute these exergonic CO binding energies to the distortion inherent to the Pc_{Ex} platform. The Fe, Ru, Co, and Ir CO dimerization energies are +0.38, +0.46, -0.29, and +0.24 eV, respectively. Löwdin population analysis suggests that the CO dimerization energy is negative for $CoPc_{Ex}$ as a result of the Co being negatively charged, in contrast to the other elements which hold positive charges. The negatively charged Co atoms transfer electron density into the incipient C–C bond, resulting in more facile CO dimerization.

We predicted the energetics for the 9-step reaction mechanisms for CO to C_2H_4 conversion using $FePc_{Ex}$, $RuPc_{Ex}$, $CoPc_{Ex}$, and $IrPc_{Ex}$ as catalysts. These catalysts had limiting potentials of +0.97, +1.38, +0.83, and +1.06 V respectively, all corresponding to the conversion of HOCCOH to HOCC. This coincides with HOCC being the highest energy intermediate, residing at +1.90, +2.15, +1.41, and +1.99 eV relative to the 2 CO reference state for the four catalysts. $CoPc_{Ex}$ has the lowest limiting potential and the lowest HOCC energy, making it the best monometallic Pc_{Ex} catalyst examined for converting CO to C_2H_4.

We then examined the conversion of CO to C_2H_4 using a bimetallic Pc_{Ex} catalyst. For this bimetallic DAC, we chose Ir and Co as active sites since they exhibited the best CO binding and CO dimerization energies of the elements screened. The bimetallic $IrCoPc_{Ex}$ catalyzes the reaction with a limiting potential of +0.87 V, which now corresponds to the conversion of HOCCH to CCH. The highest energy intermediate is still the HOCC species, which lies +1.04 eV above the 2 CO starting state. Despite the limiting potential of $IrCoPc_{Ex}$ being slightly higher than for the parent $CoPc_{Ex}$, the overall reaction mechanism is more thermodynamically feasible since the highest energy intermediate (CCH @ +1.04 eV) for $IrCoPc_{Ex}$ lies below the highest energy intermediate (HOCC @ +1.41 eV) of $CoPc_{Ex}$ by over ~0.37 eV. Analysis of HOCC intermediates for $IrCoPc_{Ex}$ and $CoPc_{Ex}$ reveals that the carbon bonded to oxygen prefers to desorb from the adjacent metal site, effectively forming a C–C triple bond and alleviating strain and undercoordination that the conventional HOCC intermediate must typically endure.

Finally, we used Grand Canonical Potential DFT to calculate the $IrCoPc_{Ex}$-catalyzed conversion of CO to C_2H_4 as a function of applied potential. Some reaction intermediates remain untouched with varying potential, although some intermediates see dramatic change in thermodynamic stability. The conversion of HOCCH to CCH (which is responsible for the limiting potential at 0 charge) shifts from highly endergonic (+0.69 eV) at 0.0 V vs. RHE to slightly exergonic (-0.13 eV) at -1.0 V vs. RHE, such that the

limiting potential shifts from the HOCCH → CCH step at 0.0 V vs. RHE to the OCCO → HOCCO step at -1.0 V vs. RHE.

Our calculations reveal that the Ir and Co-based extended phthalocyanine dual atom catalysts may be suitable for rapid and selective reduction of CO towards the desired C_2H_4, thanks to their strong CO binding and facile CO dimerization.

4.6 References

(1) Foote, E. Circumstances Affecrting the Heat of the Sun's Rays. *Am. J. Sci. Arts* **1856**, *22* (66), 383–384.

(2) Liu, Z.; Deng, Z.; Davis, S. J.; Giron, C.; Ciais, P. Monitoring Global Carbon Emissions in 2021. *Nat. Rev. Earth Environ.* **2022**, *3*, 217–219. https://doi.org/10.1038/s43017-022-00285-w.

(3) Yu, K. M. K.; Curcic, I.; Gabriel, J.; Tsang, S. C. E. Recent Advances in CO2 Capture and Utilization. *ChemSusChem* **2008**, *1* (11), 893–899. https://doi.org/10.1002/cssc.200800169.

(4) Koytsoumpa, E. I.; Bergins, C.; Kakaras, E. The CO2 Economy: Review of CO2 Capture and Reuse Technologies. *J. Supercrit. Fluids* **2018**, *132*, 3–16. https://doi.org/10.1016/j.supflu.2017.07.029.

(5) Musgrave, C. B.; Prokofjevs, A.; Goddard, W. A. Phosphine Modulation for

Enhanced CO2Capture: Quantum Mechanics Predictions of New Materials. *J. Phys. Chem. Lett.* **2022**, *13* (48), 11183–11190. https://doi.org/10.1021/acs.jpclett.2c03145.

(6) Xu, Y.; Zheng, M.; Musgrave, C. B. I. I. I.; Zhang, L.; Goddard, W. A. I. I. I.; Bukowski, B. C.; Liu, Y. Assessing the Kinetics of Quinone–CO2 Adduct Formation for Electrochemically Mediated Carbon Capture. *ACS Sustain. Chem. Eng.* **2023**. https://doi.org/10.1021/acssuschemeng.3c03321.

(7) Hori, Y.; Kikuchi, K.; Murata, A.; Suzuki, S. Production of Methane and Ethylene in Electrochemical Reduction of Carbon Dioxide at Copper Electrode in Aqueous Hydrogencarbonate Solution. *Chem. Lett.* **1986**, *15* (6), 897–898. https://doi.org/10.1246/cl.1986.897.

(8) Lewis, N. S.; Nocera, D. G. Powering the Planet: Chemical Challenges in Solar Energy Utilization. *Proc. Natl. Acad. Sci. U. S. A.* **2006**, *103* (43), 15729–15735. https://doi.org/10.1073/pnas.0603395103.

(9) Nitopi, S.; Bertheussen, E.; Scott, S. B.; Liu, X.; Engstfeld, A. K.; Horch, S.; Seger, B.; Stephens, I. E. L.; Chan, K.; Hahn, C.; Nørskov, J. K.; Jaramillo, T. F.; Chorkendorff, I. Progress and Perspectives of Electrochemical CO2 Reduction on Copper in Aqueous Electrolyte. *Chem. Rev.* **2019**, *119* (12), 7610–7672. https://doi.org/10.1021/acs.chemrev.8b00705.

(10) Wan, C.; Duan, X.; Huang, Y. Molecular Design of Single-Atom Catalysts for Oxygen Reduction Reaction. *Adv. Energy Mater.* **2020**, *10* (14), 1903815. https://doi.org/10.1002/aenm.201903815.

(11) Liu, X.; Jiao, Y.; Zheng, Y.; Jaroniec, M.; Qiao, S. Z. Building Up a Picture of the Electrocatalytic Nitrogen Reduction Activity of Transition Metal Single-Atom Catalysts. *J. Am. Chem. Soc.* **2019**, *141* (24), 9664–9672. https://doi.org/10.1021/jacs.9b03811.

(12) Yang, X. F.; Wang, A.; Qiao, B.; Li, J.; Liu, J.; Zhang, T. Single-Atom Catalysts: A New Frontier in Heterogeneous Catalysis. *Acc. Chem. Res.* **2013**, *46* (8), 1740–1748. https://doi.org/10.1021/ar300361m.

(13) Li, M.; Wang, H.; Luo, W.; Sherrell, P. C.; Chen, J.; Yang, J. Heterogeneous Single-Atom Catalysts for Electrochemical CO2 Reduction Reaction. *Adv. Mater.* **2020**, *32* (34), 2001848. https://doi.org/10.1002/adma.202001848.

(14) Li, R.; Wang, D. Superiority of Dual-Atom Catalysts in Electrocatalysis: One Step Further Than Single-Atom Catalysts. *Adv. Energy Mater.* **2022**, *12* (9), 2103564. https://doi.org/10.1002/aenm.202103564.

(15) Su, J.; Iii, C. B. M.; Song, Y.; Huang, L.; Liu, Y.; Li, G.; Xin, Y.; Xiong, P.; Li, M. M.-J.; Chen, H. M.; Tang, B. Z.; Robert, M.; Iii, W. A. G.; Ye, R. Improving Molecular Catalyst Activity Using Strain-Inducing Carbon Nanotube Supports.

ChemRxiv **2022**. https://doi.org/0.26434/chemrxiv-2022-r9r22.

(16) Yan, H.; Lin, Y.; Wu, H.; Zhang, W.; Sun, Z.; Cheng, H.; Liu, W.; Wang, C.; Li, J.; Huang, X.; Yao, T.; Yang, J.; Wei, S.; Lu, J. Bottom-up Precise Synthesis of Stable Platinum Dimers on Graphene. *Nat. Commun.* **2017**, *8* (1070). https://doi.org/10.1038/s41467-017-01259-z.

(17) Zhang, L.; Fischer, J. M. T. A.; Jia, Y.; Yan, X.; Xu, W.; Wang, X.; Chen, J.; Yang, D.; Liu, H.; Zhuang, L.; Hankel, M.; Searles, D. J.; Huang, K.; Feng, S.; Brown, C. L.; Yao, X. Coordination of Atomic Co-Pt Coupling Species at Carbon Defects as Active Sites for Oxygen Reduction Reaction. *J. Am. Chem. Soc.* **2018**, *140* (34), 10757–10763. https://doi.org/10.1021/jacs.8b04647.

(18) Zhang, L.; Fan, G.; Xu, W.; Yu, M.; Wang, L.; Yan, Z.; Cheng, F. Isolated Diatomic Zn-Fe in N-Doped Carbon for Electrocatalytic Nitrogen Reduction to Ammonia. *Chem. Commun.* **2020**, *56*, 11957–11960. https://doi.org/10.1039/d0cc04843g.

(19) Rehman, F.; Kwon, S.; Musgrave, C. B.; Tamtaji, M.; Goddard, W. A.; Luo, Z. High-Throughput Screening to Predict Highly Active Dual-Atom Catalysts for Electrocatalytic Reduction of Nitrate to Ammonia. *Nano Energy* **2022**, *103b*, 107866. https://doi.org/10.1016/j.nanoen.2022.107866.

(20) Ouyang, Y.; Shi, L.; Bai, X.; Li, Q.; Wang, J. Breaking Scaling Relations for Efficient Co2 Electrochemical Reduction through Dual-Atom Catalysts. *Chem. Sci.*

2020, *11*, 1807–1813. https://doi.org/10.1039/c9sc05236d.

(21) Zhang, N.; Zhang, X.; Kang, Y.; Ye, C.; Jin, R.; Yan, H.; Lin, R.; Yang, J.; Xu, Q.; Wang, Y.; Zhang, Q.; Gu, L.; Liu, L.; Song, W.; Liu, J.; Wang, D.; Li, Y. A Supported Pd2 Dual-Atom Site Catalyst for Efficient Electrochemical CO2 Reduction. *Angew. Chemie - Int. Ed.* **2021**, *60* (24), 13388–13393. https://doi.org/10.1002/anie.202101559.

(22) Marqués Arias, M. Vienna Ab-Initio Simulation Package. *Univ. Edinburgh* **2009**.

(23) Perdew, J. P.; Burke, K.; Ernzerhof, M. Generalized Gradient Approximation Made Simple. *Phys. Rev. Lett.* **1996**, *77* (18), 3865–3868. https://doi.org/10.1103/PhysRevLett.77.3865.

(24) Grimme, S.; Antony, J.; Ehrlich, S.; Krieg, H. A Consistent and Accurate Ab Initio Parametrization of Density Functional Dispersion Correction (DFT-D) for the 94 Elements H-Pu. *J. Chem. Phys.* **2010**, *132* (15), 154104. https://doi.org/10.1063/1.3382344.

(25) Joubert, D. From Ultrasoft Pseudopotentials to the Projector Augmented-Wave Method. *Phys. Rev. B - Condens. Matter Mater. Phys.* **1999**. https://doi.org/10.1103/PhysRevB.59.1758.

(26) Sundararaman, R.; Letchworth-Weaver, K.; Schwarz, K. A.; Gunceler, D.; Ozhabes, Y.; Arias, T. A. JDFTx: Software for Joint Density-Functional Theory. *SoftwareX*

2017, *6*, 278–284. https://doi.org/10.1016/j.softx.2017.10.006.

(27) Sundararaman, R.; Goddard, W. A. The Charge-Asymmetric Nonlocally Determined Local-Electric (CANDLE) Solvation Model. *J. Chem. Phys.* **2015**, *142* (064107). https://doi.org/10.1063/1.4907731.

(28) Mathew, K.; Sundararaman, R.; Letchworth-Weaver, K.; Arias, T. A.; Hennig, R. G. Implicit Solvation Model for Density-Functional Study of Nanocrystal Surfaces and Reaction Pathways. *J. Chem. Phys.* **2014**, *140* (084106). https://doi.org/10.1063/1.4865107.

(29) Bochevarov, A. D.; Harder, E.; Hughes, T. F.; Greenwood, J. R.; Braden, D. A.; Philipp, D. M.; Rinaldo, D.; Halls, M. D.; Zhang, J.; Friesner, R. A. Jaguar: A High-Performance Quantum Chemistry Software Program with Strengths in Life and Materials Sciences. *Int. J. Quantum Chem.* **2013**, *113* (18), 2110–2142. https://doi.org/10.1002/qua.24481.

(30) Hariharan, P. C.; Pople, J. A. The Influence of Polarization Functions on Molecular Orbital Hydrogenation Energies. *Theor. Chim. Acta* **1973**, *28* (3), 213–222. https://doi.org/10.1007/BF00533485.

(31) Hehre, W. J.; Ditchfield, K.; Pople, J. A. Self-Consistent Molecular Orbital Methods. XII. Further Extensions of Gaussian-Type Basis Sets for Use in Molecular Orbital Studies of Organic Molecules. *J. Chem. Phys.* **1972**, *56* (5), 2257–2261.

https://doi.org/10.1063/1.1677527.

(32) Kahn, L. R.; Goddard, W. A. Ab Initio Effective Potentials for Use in Molecular Calculations. *J. Chem. Phys.* **1972**, *56* (6), 2685–2701. https://doi.org/10.1063/1.1677597.

(33) Roy, L. E.; Hay, P. J.; Martin, R. L. Revised Basis Sets for the LANL Effective Core Potentials. *J. Chem. Theory Comput.* **2008**, *4* (7), 1029–1031. https://doi.org/10.1021/ct8000409.

(34) Yu, H. S.; He, X.; Li, S. L.; Truhlar, D. G. MN15: A Kohn-Sham Global-Hybrid Exchange-Correlation Density Functional with Broad Accuracy for Multi-Reference and Single-Reference Systems and Noncovalent Interactions. *Chem. Sci.* **2016**, *7*, 5032–5051. https://doi.org/10.1039/c6sc00705h.

(35) Sundararaman, R.; Goddard, W. A.; Arias, T. A. Grand Canonical Electronic Density-Functional Theory: Algorithms and Applications to Electrochemistry. *J. Chem. Phys.* **2017**. https://doi.org/10.1063/1.4978411.

(36) Voiry, D.; Shin, H. S.; Loh, K. P.; Chhowalla, M. Low-Dimensional Catalysts for Hydrogen Evolution and CO2 Reduction. *Nat. Rev. Chem.* **2018**, *2* (0105). https://doi.org/10.1038/s41570-017-0105.

(37) Abild-Pedersen, F.; Andersson, M. P. CO Adsorption Energies on Metals with Correction for High Coordination Adsorption Sites - A Density Functional Study.

Surf. Sci. **2007**, *601* (7), 1747–1753. https://doi.org/10.1016/j.susc.2007.01.052.

(38) Watkins, N. B.; Schiffer, Z. J.; Lai, Y.; Musgrave, C. B. I. I. I.; Atwater, H. A.; Goddard, W. A. I. I. I.; Agapie, T.; Peters, J. C.; Gregoire, J. M. Hydrodynamics Change Tafel Slopes in Electrochemical CO2 Reduction on Copper. *ACS Energy Lett.* **2023**, *8* (5), 2185–2192. https://doi.org/10.1021/acsenergylett.3c00442.

(39) Kuhl, K. P.; Cave, E. R.; Abram, D. N.; Jaramillo, T. F. New Insights into the Electrochemical Reduction of Carbon Dioxide on Metallic Copper Surfaces. *Energy Environ. Sci.* **2012**, *5* (7050). https://doi.org/10.1039/c2ee21234j.

(40) Montoya, J. H.; Shi, C.; Chan, K.; Nørskov, J. K. Theoretical Insights into a CO Dimerization Mechanism in CO2 Electroreduction. *J. Phys. Chem. Lett.* **2015**, *6*, 2032–2037. https://doi.org/10.1021/acs.jpclett.5b00722.

(41) Lum, Y.; Cheng, T.; Goddard, W. A.; Ager, J. W. Electrochemical CO Reduction Builds Solvent Water into Oxygenate Products. *J. Am. Chem. Soc.* **2018**, *140*, 9337–9340. https://doi.org/10.1021/jacs.8b03986.

(42) Xiao, H.; Goddard, W. A.; Cheng, T.; Liu, Y. Cu Metal Embedded in Oxidized Matrix Catalyst to Promote CO2 Activation and CO Dimerization for Electrochemical Reduction of CO2. *Proc. Natl. Acad. Sci. U. S. A.* **2017**, *114* (26), 6685–6688. https://doi.org/10.1073/pnas.1702405114.

(43) Wu, Z.-Z.; Zhang, X.-L.; Niu, Z.-Z.; Gao, F.-Y.; Yang, P.-P.; Chi, L.-P.; Shi, L.;

Wei, W.-S.; Liu, R.; Chen, Z.; Hu, S.; Zheng, X.; Gao, M.-R. Identification of Cu(100)/Cu(111) Interfaces as Superior Active Sites for CO Dimerization During CO2 Electroreduction. *J. Am. Chem. Soc.* **2022**, *144* (1), 259–269. https://doi.org/10.1021/jacs.1c09508.

(44) Kastlunger, G.; Wang, L.; Govindarajan, N.; Heenen, H. H.; Ringe, S.; Jaramillo, T.; Hahn, C.; Chan, K. Using PH Dependence to Understand Mechanisms in Electrochemical CO Reduction. *ACS Catal.* **2022**, *12* (8), 4344–4357. https://doi.org/10.1021/acscatal.1c05520.

(45) Li, P.; Jin, Z.; Fang, Z.; Yu, G. A Single-Site Iron Catalyst with Preoccupied Active Centers That Achieves Selective Ammonia Electrosynthesis from Nitrate. *Energy Environ. Sci.* **2021**, *14*, 3522–2531. https://doi.org/10.1039/d1ee00545f.

(46) Wu, Z. Y.; Karamad, M.; Yong, X.; Huang, Q.; Cullen, D. A.; Zhu, P.; Xia, C.; Xiao, Q.; Shakouri, M.; Chen, F. Y.; Kim, J. Y. (Timothy); Xia, Y.; Heck, K.; Hu, Y.; Wong, M. S.; Li, Q.; Gates, I.; Siahrostami, S.; Wang, H. Electrochemical Ammonia Synthesis via Nitrate Reduction on Fe Single Atom Catalyst. *Nat. Commun.* **2021**, *12* (1), 1–10. https://doi.org/10.1038/s41467-021-23115-x.

(47) Rehman, F.; Kwon, S.; Hossain, M. D.; Musgrave, C. B.; Goddard, W. A.; Luo, Z. Reaction Mechanism and Kinetics for N2 Reduction to Ammonia on the Fe-Ru Based Dual-Atom Catalyst. *J. Mater. Chem. A* **2022**, *10*, 23323–23331.

https://doi.org/10.1039/d2ta06826e.

(48) Wang, W.; Jia, Q.; Mukerjee, S.; Chen, S. Recent Insights into the Oxygen-Reduction Electrocatalysis of Fe/N/C Materials. *ACS Catal.* **2019**, *9* (11), 10126–10141. https://doi.org/10.1021/acscatal.9b02583.

(49) Xiao, M.; Gao, L.; Wang, Y.; Wang, X.; Zhu, J.; Jin, Z.; Liu, C.; Chen, H.; Li, G.; Ge, J.; He, Q.; Wu, Z.; Chen, Z.; Xing, W. Engineering Energy Level of Metal Center: Ru Single-Atom Site for Efficient and Durable Oxygen Reduction Catalysis. *J. Am. Chem. Soc.* **2019**, *141* (50), 19800–19806. https://doi.org/10.1021/jacs.9b09234.

(50) Liu, C.; Geer, A. M.; Webber, C.; Musgrave, C. B.; Gu, S.; Johnson, G.; Dickie, D. A.; Chabbra, S.; Schnegg, A.; Zhou, H.; Sun, C. J.; Hwang, S.; Goddard, W. A.; Zhang, S.; Gunnoe, T. B. Immobilization of "Capping Arene" Cobalt(II) Complexes on Ordered Mesoporous Carbon for Electrocatalytic Water Oxidation. *ACS Catal.* **2021**, *11* (24), 15068–15082. https://doi.org/10.1021/acscatal.1c04617.

(51) Geer, A. M.; Liu, C.; Musgrave, C. B.; Webber, C.; Johnson, G.; Zhou, H.; Sun, C.-J.; Dickie, D. A.; Goddard, W. A.; Zhang, S.; Gunnoe, T. B. Noncovalent Immobilization of Pentamethylcyclopentadienyl Iridium Complexes on Ordered Mesoporous Carbon for Electrocatalytic Water Oxidation. *Small Sci.* **2021**, *1* (11), 2100037. https://doi.org/10.1002/smsc.202100037.

(52) Sun, X.; Chen, C.; Liu, S.; Hong, S.; Zhu, Q.; Qian, Q.; Han, B.; Zhang, J.; Zheng, L. Aqueous CO2 Reduction with High Efficiency Using α-Co(OH)2-Supported Atomic Ir Electrocatalysts. *Angew. Chemie - Int. Ed.* **2019**, *131* (14), 4717–4721. https://doi.org/10.1002/anie.201900981.

(53) Wu, Y.; Jiang, Z.; Lu, X.; Liang, Y.; Wang, H. Domino Electroreduction of CO2 to Methanol on a Molecular Catalyst. *Nature* **2019**, *575*, 639–642. https://doi.org/10.1038/s41586-019-1760-8.

(54) Löwdin, P. O. Quantum Theory of Many-Particle Systems. I. Physical Interpretations by Means of Density Matrices, Natural Spin-Orbitals, and Convergence Problems in the Method of Configurational Interaction. *Phys. Rev.* **1955**, *97* (1474). https://doi.org/10.1103/PhysRev.97.1474.

(55) He, T.; Santiago, A. R. P.; Kong, Y.; Ahsan, M. A.; Luque, R.; Du, A.; Pan, H. Atomically Dispersed Heteronuclear Dual-Atom Catalysts: A New Rising Star in Atomic Catalysis. *Small* **2022**, *18* (12), 2106091. https://doi.org/10.1002/smll.202106091.

(56) Fu, J.; Dong, J.; Si, R.; Sun, K.; Zhang, J.; Li, M.; Yu, N.; Zhang, B.; Humphrey, M. G.; Fu, Q.; Huang, J. Synergistic Effects for Enhanced Catalysis in a Dual Single-Atom Catalyst. *ACS Catal.* **2021**, *11* (4), 1952–1961. https://doi.org/10.1021/acscatal.0c05599.

(57) Liu, C.; Qian, J.; Ye, Y.; Zhou, H.; Sun, C. J.; Sheehan, C.; Zhang, Z.; Wan, G.; Liu, Y. S.; Guo, J.; Li, S.; Shin, H.; Hwang, S.; Gunnoe, T. B.; Goddard, W. A.; Zhang, S. Oxygen Evolution Reaction over Catalytic Single-Site Co in a Well-Defined Brookite TiO2 Nanorod Surface. *Nat. Catal.* **2021**. https://doi.org/10.1038/s41929-020-00550-5.

(58) Huang, Y.; Nielsen, R. J.; Goddard, W. A. Reaction Mechanism for the Hydrogen Evolution Reaction on the Basal Plane Sulfur Vacancy Site of MoS 2 Using Grand Canonical Potential Kinetics. *J. Am. Chem. Soc.* **2018**, *140* (48), 16773–16782. https://doi.org/10.1021/jacs.8b10016.

Part II:
Molecular Design for Improved Methane Oxidation

Chapter 5

Partial Oxidation of Methane Enabled by Decatungstate Photocatalysis Coupled to Free Radical Chemistry

Reproduced with permission from:

Kaeleigh Olsen, Nichole S. Liebov, John T. Groves, William Goddard III, T. Brent Gunnoe. *Partial Oxidation of Methane Enabled by Decatungstate Photocatalysis Coupled to Free Radical Chemistry, ACS Catalysis*, **2023**, 13, 9, 6382-6395

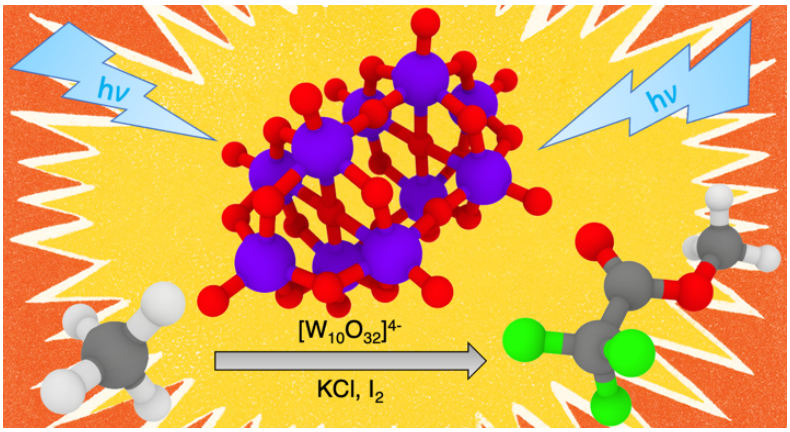

Figure 5.0: Table of contents figure

5.1 Abstract

The decatungstate anion, $[W_{10}O_{32}]^{4-}$ or DT, is a useful photocatalyst for organic transformations involving C–H functionalization. Herein, we leverage the unique photoredox properties of DT to generate chlorine radical from chloride ion for the photochemical partial oxidation of methane. Under optimized conditions, the DT-chloride-iodine ensemble achieves methane to methyl trifluoroacetate conversion with $>$ 350 photocatalyst turnovers at ~60% yield based on methane in trifluoroacetic acid solvent. Methyl trifluoroacetate exhibits excellent stability under reaction conditions with minimal amounts of degradation ($<$ 6%) detected after 41 hours. Using Density Functional Theory calculations, we propose a mechanism that involves synergistic relationships among the DT, chloride and iodine species with the following key features: (1) photoredox electron transfer reactions of DT with Cl^- to generate Cl•, (2) reaction of photo-excited DT with methane to generate methyl radicals via net hydrogen atom abstraction, (3) a Cl/I radical-based pathway in which methane is converted to MeTFA, and (4) reoxidation of reduced DT species by dioxygen. This mechanism takes advantage of the unique redox potential of DT and the ability of DT to mediate both electron transfer and hydrogen atom transfer reactions, ultimately generating an efficient pathway for aerobic methane partial oxidation.

5.2 Introduction

Conversion of light alkanes from natural gas into value-added chemicals is a cornerstone of the chemical industry. The development of new catalytic processes for the direct conversion of methane (and other light alkanes) to higher-value liquid products is important for the increased use of stranded natural gas as well as other sources (*e.g.*, biogas) of methane and light alkanes.[1-3] Highly desired processes include the direct partial oxidation of methane, ethane and propane to liquid products, so called direct gas-to-liquid (GTL) conversions, with a particular focus on methane-to-methanol. Given the substantial global natural gas reserves[4] which account for ~25% of global energy, there is enormous potential for direct GTL technologies. Additionally, these reserves are often in stranded locations, where at-wellhead GTL conversion is most desirable.

Current commercial methods for indirect methane-to-methanol conversion involve the highly energy- and capital-intensive methane reforming reaction ($H_2O + CH_4 \rightarrow CO + 3\ H_2$) followed by Fischer-Tropsch chemistry to produce methanol or longer chain hydrocarbons.[5, 6] A more desirable alternative is the direct mono-oxidation of methane by $\frac{1}{2}\ O_2$ to produce methanol. While methane partial oxidation using $\frac{1}{2}\ O_2$ is thermodynamically favorable, challenges include (1) overcoming the large activation barrier required to break a non-polar C–H bond of methane (bond dissociation energy ~105 kcal/mol), and (2) evading over-oxidation of methanol, due to methanol's weaker C–H bonds (96 kcal/mol) compared to methane.[7, 8]

Radical-based chemistry, such as catalytic oxychlorination, offers a route for C–H functionalization of light alkanes to produce functionalized products (Equation 1).[9-13] Unfortunately, such processes often suffer from the over-oxidation dilemma, again due to weaker C–H bonds in the product (*e.g.*, 101 kcal/mol for CH_3Cl).[14] In fact, methane conversion using catalytic oxychlorination is often limited to $< 10\%$ in order for high selectivity to be achieved.[15]

$$CH_4 + HX + 1/2\ O_2 \xrightarrow[\text{heat}]{\text{catalyst}} CH_3X + H_2O \qquad (1)$$

Shilov's electrophilic Pt(II) catalysis was an early example of catalytic methane mono-functionalization, but this process suffered from the requirement of stoichiometric Pt(IV) oxidant.[16] The Catalytica process pioneered by Periana and coworkers achieved methane to methyl bisulfate conversion with $> 70\%$ yield and $> 90\%$ selectivity, using the key strategy of protecting of the mono-functionalized product toward over oxidation by the electron-withdrawing bisulfate group. However, the energy requirements for the separation of product from oleum and reconcentration of sulfuric acid was a challenge for potential commercialization.[17, 18] Molecular iodine has been shown to functionalize light alkanes in oleum, but this approach could not be extended to non-superacidic media.[19, 20] Main group compounds, such as $Tl(TFA)_3$ and $Pb(TFA)_4$, and hypervalent iodine, namely

$(C_6F_5)I^{III}(TFA)_2$, have been shown to functionalize light alkanes in non-superacidic solvent, albeit stoichiometrically.[21, 22]

Metal-exchanged zeolites (*e.g.*, copper) are capable of methane oxidation to methanol.[23-30] However, these catalysts typically do not yield high methane conversion with high selectivity. Also, methanol extraction requires significant dilution for separation, which typically destroys the active site, requiring subsequent high-temperature oxidation for catalyst restoration.[31]

To improve product yields, we and other groups have pursued a strategy to circumvent over-oxidation through installing a protecting group in the functionalized alkyl product.[32, 33] For example, we reported the thermal (100-235 ^{o}C) partial oxidation of light alkanes (methane, ethane, propane) in trifluoroacetic acid (HTFA) by chloride-iodate and chloride-periodate systems via a method termed oxyesterification (OxE). OxE produced the corresponding alkyl esters (RTFA) with $>$ 20% yield relative to the alkanes and $>$ 80% selectivity towards mono-oxidized products.[34, 35] We discovered that the ester moiety protects the products from subsequent oxidation, thus permitting production of the corresponding alcohol, along with regeneration of HTFA through hydrolysis.[36, 37] Oxygen-recyclable cobalt and manganese catalysts have also been shown to effectively oxidize methane in HTFA.[38-40] Recently, we reported the use of molecular Mn oxides and Mn salts for methane partial oxidation along with a mechanistic study.

Several groups have reported photo-driven C–H functionalization for which the generation of chlorine radical from chloride appears to be a key step. Germane here, several examples of such reactions that are successful for unactivated hydrocarbons (e.g., cyclohexane) have been reported.[42-46] Using the strategy of generating chlorine from chloride, we recently pursued photo-driven light alkane functionalization. Higher yields were obtained for the chloride-iodate OxE process under photo-catalytic conditions (~50% yield was achieved for methane) compared to yields for the analogous thermally driven reaction.[47] We also reported that $Fe(TFA)_3$ mediates photo-driven hydrocarbon functionalization.[48] The Schelter and Goldberg groups recently reported photo-driven, aerobic alkane iodination in acetonitrile using catalytic $[^nBu_4N]Cl$.[49]

Polyoxometalates (POMs) have emerged as a widely successful class of photocatalysts for organic transformations due to their ability to perform both electron transfer (ET) and hydrogen atom transfer (HAT) reactions.[50-53] The decatungstate anion ($[W_{10}O_{32}]^{4-}$ or DT) is currently employed as a HAT photocatalyst because of its ready availability and the array of C–H bonds it can cleave.[54-59] Furthermore, DT has been used for a variety of $C(sp^3)$–H functionalizations, including C–C bond formations and oxidation reactions.[60-74] Laudadio and coworkers reported the functionalization of light alkanes (*e.g.*, methane, ethane, propane, isobutane) to C–C coupled products using DT in a photocatalytic flow system.[63] In a separate report, Laudadio and coworkers reported DT-

mediated selective oxidation of aliphatic substrates to ketone-containing products.[64] Figure 5.1 depicts the structure of the DT salt, TBADT [TBA = $(^{n}Bu_4N)_4$], and its ability to perform HAT in its photoexcited state; here DT•• denotes the suspected excited triplet state (referred to in previous publications as wO or DT*)[71] and HDT• denotes the species after HAT.

Because our previously reported thermal and photo-initiated OxE processes for light alkane functionalization are proposed to rely on HAT,[36, 37, 47] we hypothesized that the addition of DT as a photo-driven HAT reagent may accelerate the mono-oxidation of light alkanes to alkyl esters in a chloride-iodine system.

Of particular interest was the possibility that photo-excited DT could also generate chlorine atoms, Cl•, under these reaction conditions due to the very high reduction potential of DT••.[57] There have been a number of recent advances in the photogeneration of Cl•, including photoreduction of metal chlorides[44, 48, 75-80] and photoredox oxidation of chloride ion (Cl^-).[81-84] As noted above, photogeneration of chlorine has been used to functionalize unactivated hydrocarbons.[42-46] DT is robust under acidic conditions and has a high quantum yield for photoexcitation, but it has not been employed for the generation of Cl• as a C–H activation mediator. Herein, we report experimentally and validate computationally the use of DT as a photocatalyst for methane partial oxidation in the presence of chloride and iodine to form methyl trifluoroacetate (MeTFA) and methyl

chloride (MeCl or CH_3Cl). In our best case, this DT-chloride-iodine aerobic process achieved methane to MeTFA conversion with > 350 photocatalyst turnovers (TOs) and ~60% yield based on methane.

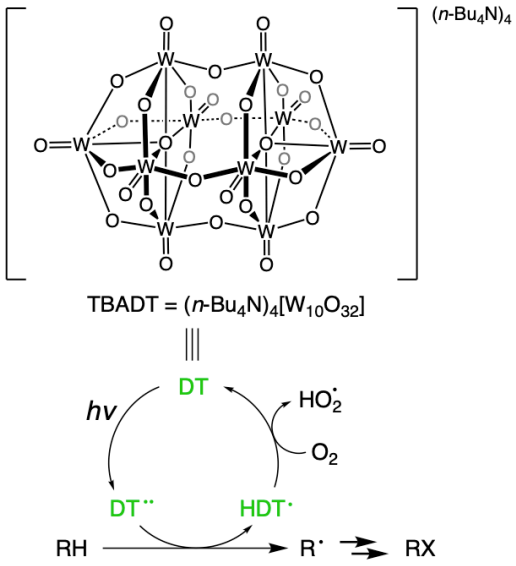

Figure 5.1: Simplified scheme showing capability of photoexcited decatungstate (DT●●) for hydrogen atom abstraction from a generic alkane (RH). HDT● denotes the radical species following hydrogen atom abstraction.

5.3 Results and Discussion

5.3.1 Reagent Screening and Optimization

An initial screening of the photochemical reactivity of an aerobic mixture of TBADT (0.014 mmol) and KCl (0.67 mmol) in HTFA (8 mL) pressurized with 100 psig of methane (~24 mmol) resulted in the formation of 0.043 ± 0.015 mmol of MeX (X = TFA, Cl) after 24 h of mercury arc lamp irradiation. This corresponds to a yield of 0.18 ± 0.071% and a 42:1 ratio of MeTFA to MeCl. Herein, percent yields are reported with respect to methane, and all data are the result of a minimum of three separate experiments with standard deviations. Product formation was determined by ^{1}H NMR spectroscopy and referenced against a known amount of either HOAc or CH_3NO_2 as an internal standard. When TBADT was ground using a mortar and pestle before addition to the reactor (with all other conditions unchanged), 0.10 ± 0.008 mmol of MeX was produced in 0.43 ± 0.027% yield with a 33:1 ratio of MeTFA to MeCl (Figure 5.2). The corresponding TOs of TBADT were 3.1 ± 1.1 and 7.3 ± 0.58 when TBADT was unground and ground, respectively. The increased product formation and the decreased standard deviation using the ground TBADT suggests that smaller particle size increased TBADT's solubility in HTFA.

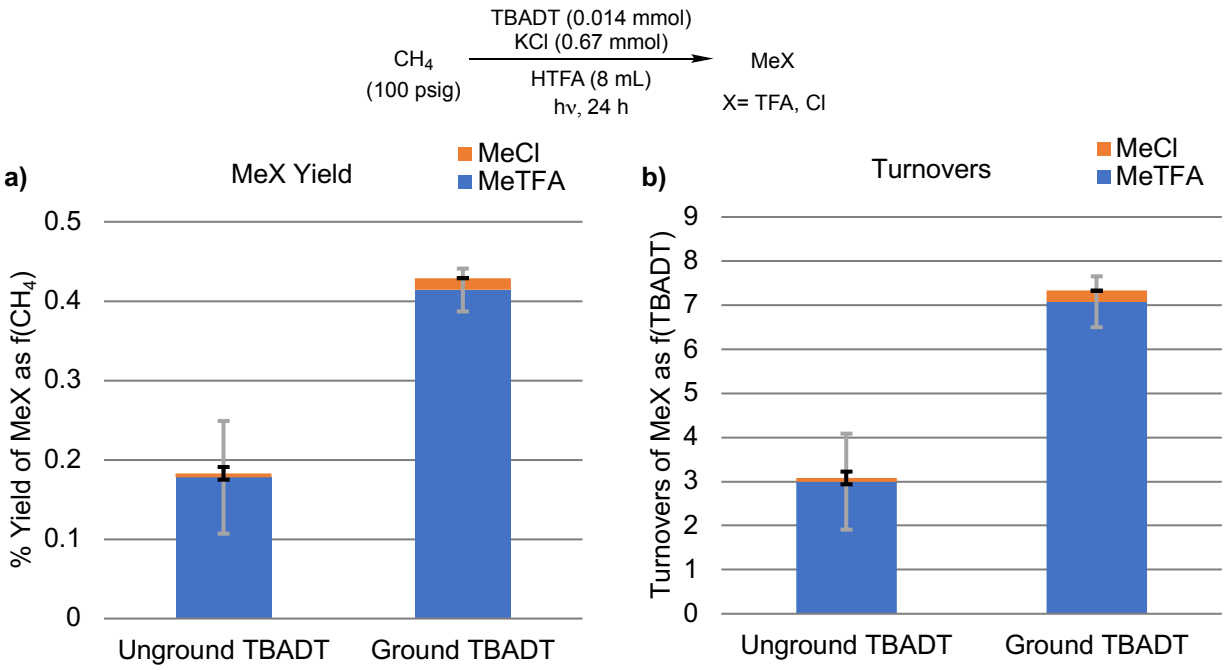

Figure 5.2: Initial screening for the photochemical functionalization of methane by TBADT (0.014 mmol) and KCl (0.67 mmol) in HTFA after 24 h of mercury arc lamp irradiation. TBADT was either used directly or ground before addition to the reactor. MeX (X = TFA, Cl) is plotted as methane conversion (**a**) and catalytic turnovers based on TBADT (**b**). Each bar graph represents the average of a minimum of three independent experiments with error bars depicting the standard deviation of the three experiments.

The analogous reaction to that shown in Figure 5.1 but in the absence of KCl produced no MeTFA; this is likely because no radical traps are present to quench $CH_3\bullet$ (see below for mechanism discussion). Various loadings of KCl were tested, and it was observed that doubling the KCl loading from 0.67 mmol to 1.34 mmol had a positive effect on MeX yield; however, increasing the KCl loading to 2.68 mmol had minimal effect, within deviation, on MeX yield (Figure 5.3a). Using 1.34 mmol of KCl, various loadings of TBADT were tested, with the optimal amount of TBADT being 0.007 mmol, as this maximized MeX yield (Figure 5.3b).

In our previous reports of light alkane partial oxidation using iodate as the oxidant, mechanistic studies indicated that I_2 is likely generated *in situ* from iodate and serves to trap alkyl radicals in solution.[36] Thus, I_2 was explored as a reaction additive in our TBADT photochemistry. We found 0.025 mmol of I_2 to be optimal, as this loading maximized MeX yield (Figure 5.3c). The addition of TBADT, KCl and I_2 in their optimized loadings in 8 mL HTFA led to the formation of 0.45 ± 0.030 mmol of MeX in 1.9 ± 0.078% yield with a 4.2:1 ratio of MeTFA to MeCl after 24 h of mercury arc lamp irradiation. This MeX formation as a function of TBADT corresponds to 64 ± 4.3 TOs. These optimized reagent loadings in 8 mL HTFA and 100 psig CH_4 will be referred to as the standard aerobic reaction conditions throughout the remainder of this contribution.

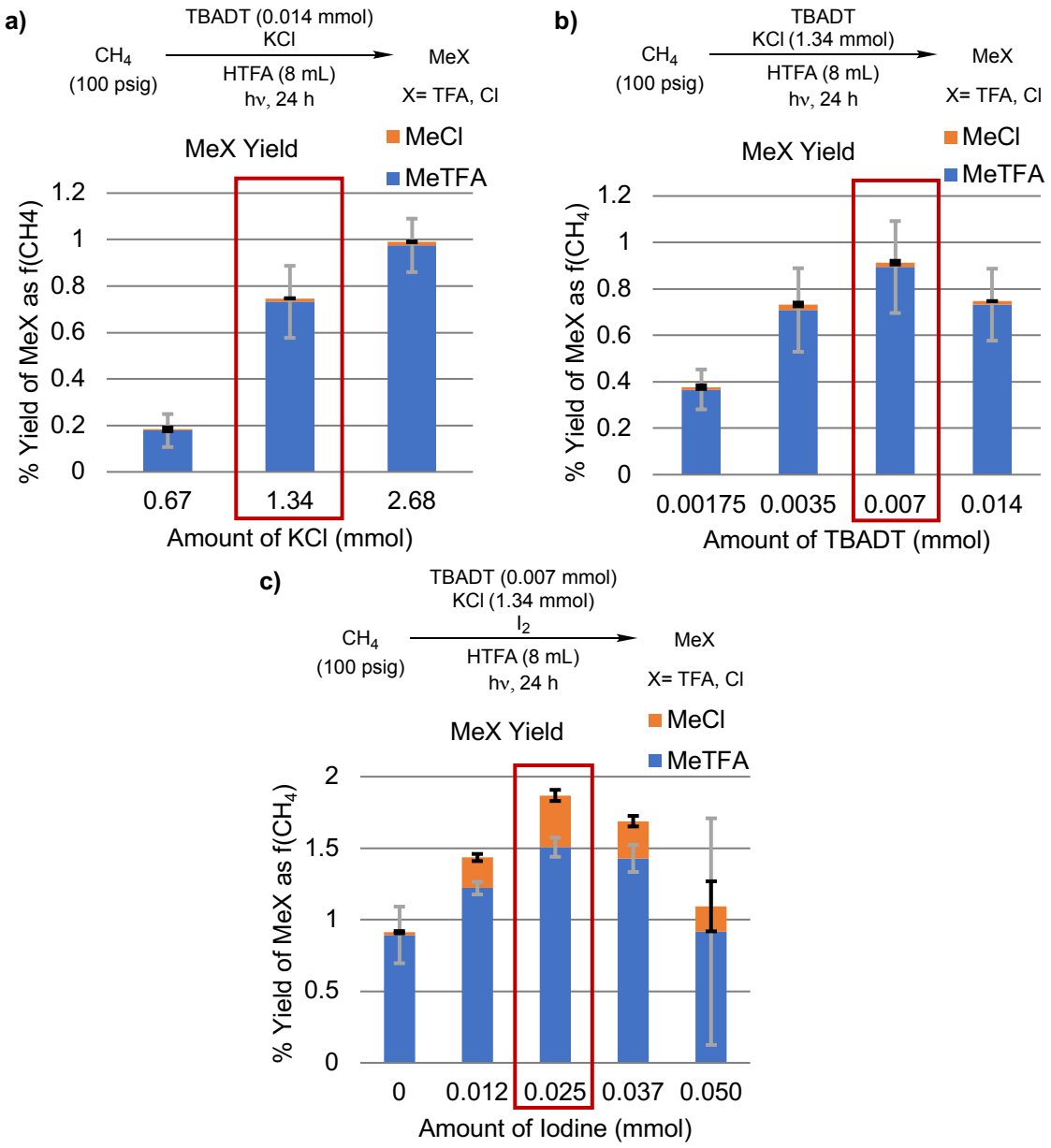

Figure 5.3: MeX (X = TFA, Cl) yield at various loadings of KCl (**a**), TBADT (**b**), and I_2 (**c**). Red boxes indicate optimal reagent loadings in the standard aerobic reaction conditions. Each bar graph represents the average of at least three independent experiments with error bars depicting the standard deviations.

Other combinations of TBADT, KCl and/or I_2 in HTFA led to decreased CH_4 functionalization (Table 1). For the reaction of KCl and I_2, it was found that iodine loading is crucial for MeX production. Specifically, increasing the loading of I_2 to 0.050

mmol with 1.34 mmol of KCl led to no MeX production within standard deviation (Table 1, Entry 4). However, halving the amount of I_2 to 0.025 mmol with 1.34 mmol KCl (corresponding to standard aerobic reaction conditions) led to substantial MeX formation (Table 5.1, Entry 5). The investigation of the background reaction of 1.34 mmol of KCl and 0.025 mmol of I_2 for methane functionalization in HTFA is described in Appendix D. The bimodal nature of MeX production as a function of time for this background reaction can be seen in Figure D5. The bifurcated results hint that radical chain processes for MeX formation are possible, but the initiation of such reactions is highly dependent on factors that we could not identify nor control.

Table 5.1: MeX (X = TFA, Cl) yields for the control reactions of remaining combinations of reagents.[a]

Entry	Reagents	% Yield of MeTFA	% Yield of MeCl
1	TBADT (0.007 mmol), I_2 (0.025 mmol)	0.13 ± 0.069	0
2	KCl (1.34 mmol)	0.36 ± 0.069	0.010 ± 0.0088
3	I_2 (0.025 mmol)	0.50 ± 0.16	0
4	KCl (1.34 mmol), I_2 (0.050 mmol)	0.010 ± 0.010	0
5	KCl (1.34 mmol), I_2 (0.025 mmol)	1.7 ± 0.26	0.42 ± 0.063

[a] The reagents were added to 8 mL HTFA, pressurized with 100 psig CH_4, and irradiated with a mercury arc lamp for 24 h. Each entry line represents the average of at least three independent experiments reported with their standard deviations.

Additional control reactions were performed. When heated (180 ºC for 3 h) without irradiation, TBADT (0.014 mmol) and KCl (1.34 mmol) in HTFA (8 mL) with 100 psig CH_4 resulted in no MeX formation. When the standard aerobic reaction conditions were pressurized with 100 psig Ar instead of CH_4 and subjected to a mercury arc lamp for 24 h, MeX production was not observed. Minimal methane functionalization ($< 0.03\%$ yield) occurred when KBr was used in place of KCl under the standard aerobic reaction conditions. When the standard aerobic reaction conditions were instead subjected to fume hood LED lighting or a 370 nm LED lamp, CH_4 functionalization occurred, albeit at much slower rates and with lower yields. Acetic acid (HOAc) was explored as a solvent alternative to HTFA. With pure HOAc as solvent, MeX formation was not observed. Using HOAc and HTFA solvent mixtures, the chemistry was not clean enough to extract meaningful results.

Using standard aerobic reaction conditions, CH_4 pressure was varied (Figure 5.4). At lower methane pressures, MeX yield based on methane was improved in the TBADT–KCl–I_2 system. For example, reacting TBADT (0.007 mmol), KCl (1.34 mmol) and I_2 (0.025 mmol) with 15 psig of methane (~4 mmol) afforded 0.35 ± 0.0057 mmol of MeX in 8.9 ± 0.58% yield with a 6.4:1 ratio of MeTFA to MeCl after 24 h of reaction. This MeX formation as a function of TBADT corresponds to 50 ± 0.82 TOs. This is the highest

conversion achieved with this system under aerobic conditions and without the inclusion of dioxygen.

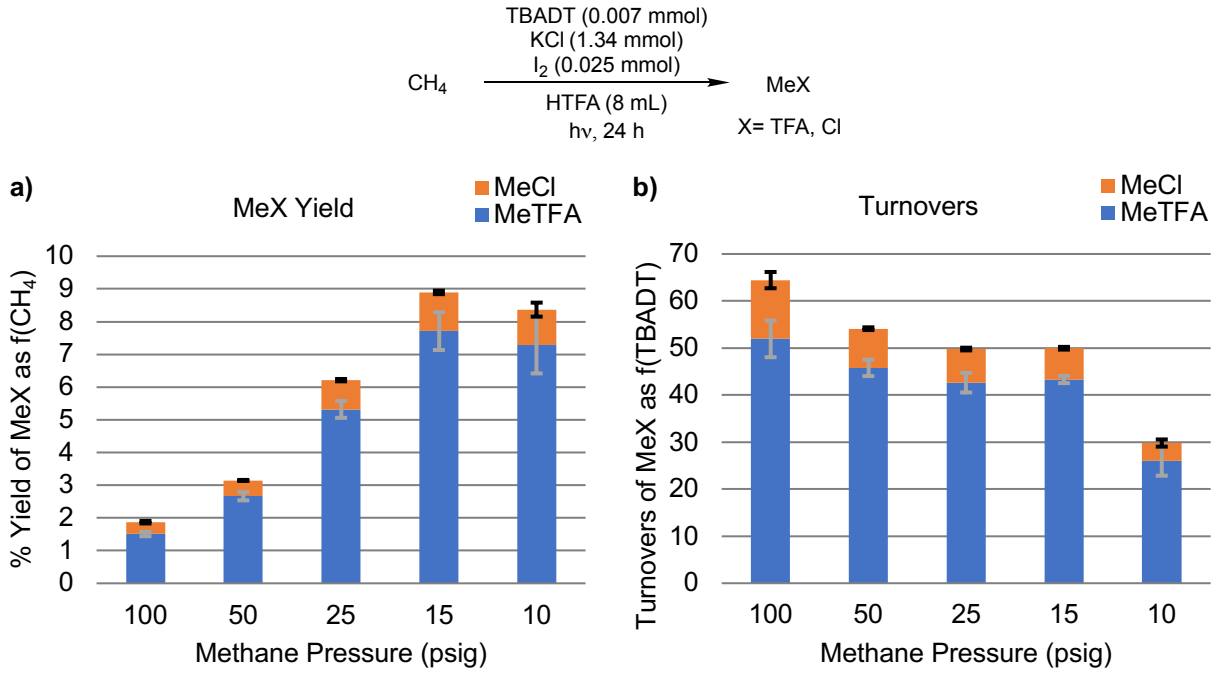

Figure 5.4: The effect of methane pressure on methane conversion (**a**) and the corresponding catalyst TOs (**b**). Each bar graph represents the average of at least three independent experiments with error bars depicting the standard deviations.

5.3.2 MeTFA Stability, Kinetics of Methane Functionalization and Photocatalyst Re-oxidation with Dioxygen

Product stability was explored under standard aerobic reaction conditions with the addition of 0.35 mmol MeTFA at time t = 0 h and pressurization with 100 psig Ar in

place of CH_4. MeTFA was found to be stable under these conditions with $> 94\%$ MeTFA remaining after 41 h (Figure 5.5).

Using standard aerobic reaction conditions, the time of mercury arc lamp irradiation was varied to explore CH_4 oxidation as a function of time (Figure 5.5). According to product formation versus time, it appears that MeX formation halts at t ≅ 21 h. However, the exact time is difficult to discern due to the large deviations inherent to the photoreactions. The lack of further product formation after t ≅ 21 h could indicate depletion of the limiting reagent. At t ≅ 21 h, 0.44 ± 0.010 mmol of MeX was present. This corresponds to ~62 ± 1.5 TOs of TBADT and consumption of ~32% of starting KCl.

Using the standard aerobic reaction conditions, the reagents were added to the reactor in air and then sealed. It was speculated that the dioxygen present in the headspace of the reactor was fully consumed at t ≅ 21 h, thus preventing photocatalyst re-oxidation. The amount of dioxygen estimated to be in the headspace was calculated to be ~ 0.75 mmol. Thus, at t ≅ 21 h, the concentration of dioxygen likely becomes too low to re-oxidize TBADT. This speculation is further supported by the blue color of the post-reaction solutions, indicative of spent decatungstate in its reduced form.

We began our studies on dioxygen dependence by varying the amount of dioxygen present in the reactor headspace before the start of the reaction. It has been shown that dioxygen is incapable of quenching DT••, such that catalyst deactivation by dioxygen is

very unlikely.[85] This was achieved by purging the reaction solution with either dinitrogen or dioxygen. Purging was performed by bubbling the respective gas into the reaction solution for 1 minute after charging the reactor with TBADT, KCl, I_2 and HTFA and before pressurizing with CH_4. When the solution was purged with dinitrogen, no MeX was produced (Scheme 5.1b). When the solution was purged with dioxygen, 0.90 ± 0.30 mmol MeX was produced after 24 h of irradiation (Scheme 5.1c). Scheme 5.1 details a comparison of these solution-purged reactions to the standard aerobic reaction. These results provide support for dioxygen as the limiting reagent, in which dioxygen re-oxidizes spent TBADT back to its active form.

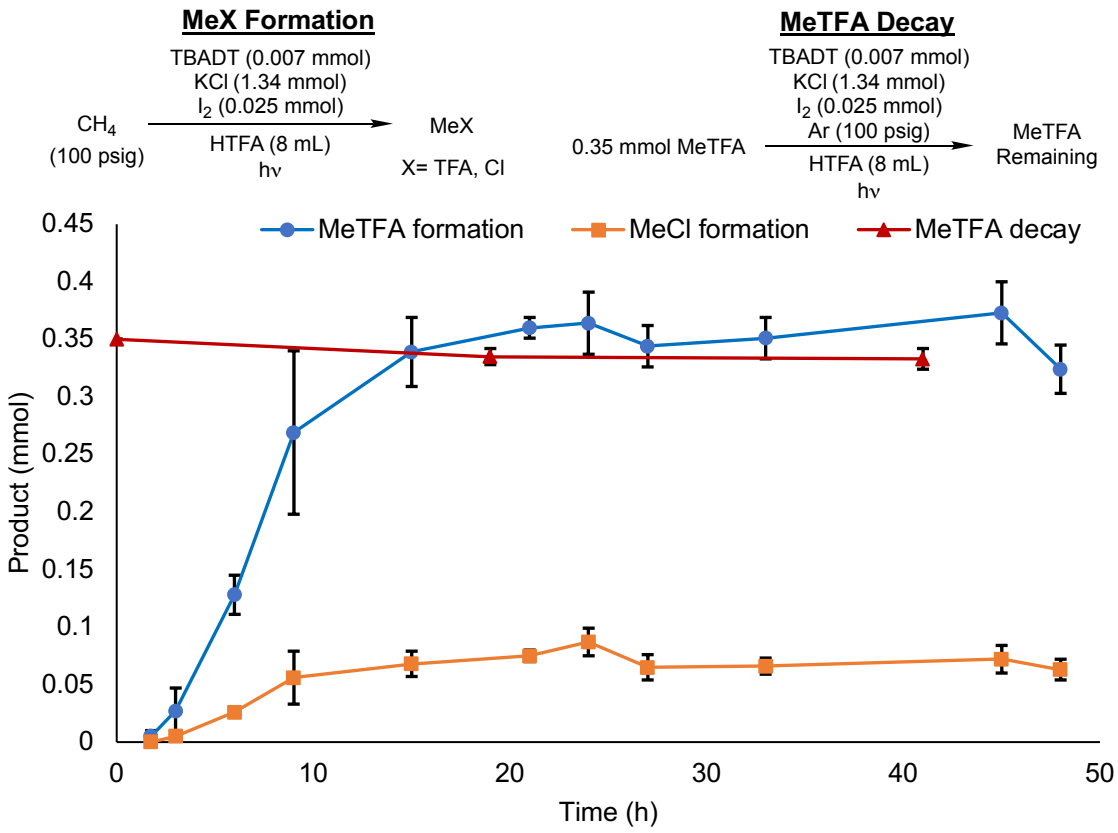

Figure 5.5: Methane functionalization and MeTFA decay under standard aerobic reaction conditions with TBADT, KCl and I_2 as a function of time. Each data point represents the average of at least three independent experiments with error bars depicting the standard deviations.

Additional experiments were performed to further probe the re-oxidation of TBADT by dioxygen. After irradiation of the high methane conversion aerobic reaction conditions (15 psig CH_4) for 24 h, dioxygen top pressure was added to the reactors, followed by further irradiation. A series of experiments were performed in which we modulated the amount of dioxygen added, the number of dioxygen pressurizations and the amount of irradiation time between dioxygen top pressure additions. In many of these experiments, the formation of MeCl could not be accurately quantified due to signal

broadening in the ^{1}H NMR spectra (see Figure D3 for representative ^{1}H NMR spectrum). A preliminary re-oxidation reaction as well as the optimal re-oxidation reaction are displayed in Scheme 5.2, along with the high methane conversion aerobic reaction for comparison. We note that the optimal re-oxidation experiment reached the pressure limitations of the reaction vessel. Because dioxygen is our limiting reagent under these conditions, it is feasible that MeX formation will continue with additional dioxygen if a reactor with a higher pressure limit or continuous-flow of dioxygen is used.

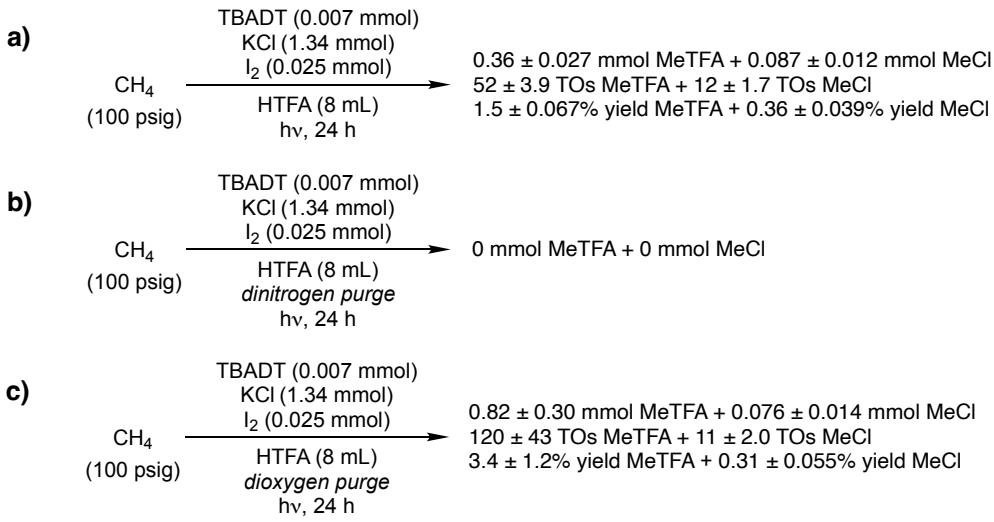

Scheme 5.1: Effect of differing concentrations of dioxygen on MeX (X = TFA, Cl) production reported as mmol of product, catalyst turnovers, and percent yield. **a** = standard aerobic reaction conditions; **b** = dinitrogen-purged reaction solution; **c** = dioxygen-purged reaction solution. Each reaction scheme represents the average of at least three independent experiments reported with their standard deviation.

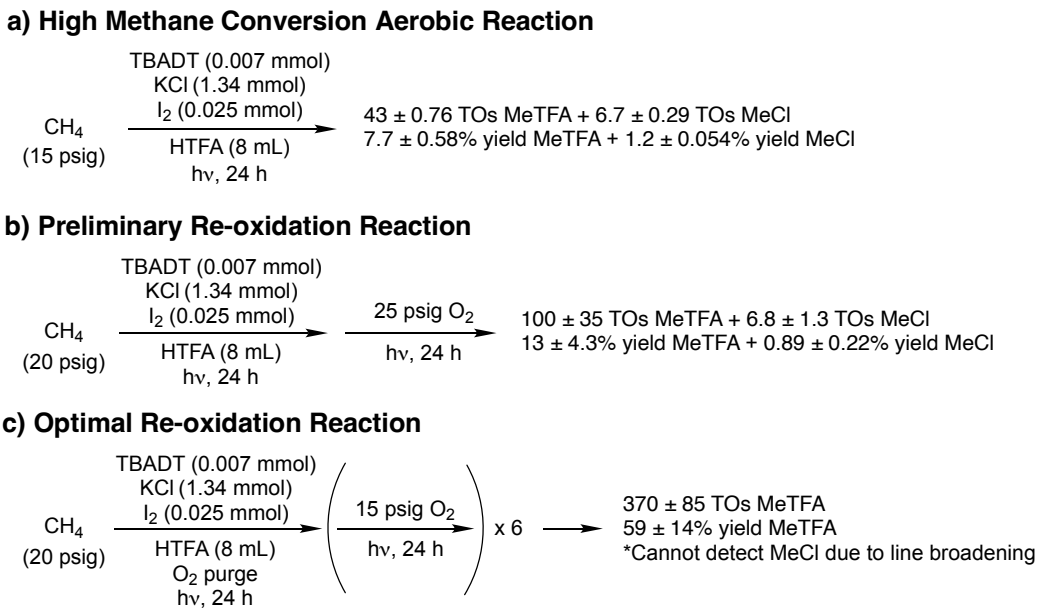

Scheme 5.2: Comparison of high methane conversion aerobic methane to MeX (X = TFA, Cl) reaction with standard reagent loadings (**a**) to preliminary re-oxidation reaction with standard reagent loadings (**b**) and optimal re-oxidation reaction with standard reagent loadings (**c**). Results are reported as catalyst TOs and percent yields based on methane. Each reaction scheme represents the average of at least three independent experiments reported with their standard deviation.

In an effort to circumvent the pressure limitations of the reactors described above with dioxygen, non-gaseous additives were explored as potential co-oxidants, such as copper salts and peroxides. None of the copper salts explored ($CuCl_2 \bullet xH_2O$, $Cu(OAc)_2 \bullet xH_2O$ [OAc = $C_2H_3O_2^-$], $Cu(TFA)_2 \bullet xH_2O$) nor $K_2S_2O_8$ had any beneficial effect on product formation (Figure D4). Alkyl peroxides (tert-butyl hydroperoxide, di-tert-butyl peroxide) were then explored as potential co-oxidants, resulting in $> 100\%$ yield of MeX (Table D1). However, this $> 100\%$ MeX yield was due to peroxide decomposition for which photo-induced cleavage of the peroxide O–O bond followed by decomposition

leads to the production of methyl radicals and acetone (see Appendix D for details).[86, 87] When hydrogen peroxide (which is unable to generate methyl radicals) was used, no improvement of MeX yield (within deviation) was observed relative to the high methane conversion aerobic reaction. The large deviations for these reactions can be explained by photodecomposition. UV irradiation initiates O–O bond cleavage to hydroxyl radicals which form water and dioxygen through a radical chain mechanism, leading to differing concentrations of these three compounds in reaction solution.[88] Overall, no solids or liquids were identified as effective co-oxidants.

5.3.3 Mechanistic Studies based on Density Functional Theory

DT's involvement in the chemistry is not trivial. DT is primarily known for its ability to perform HAT on alkanes to generate alkyl radicals. In the present case, this could be HAT to convert methane to $CH_3\bullet$, which has been previously observed.[63] We initially considered that DT also abstracts H from HTFA to form TFA•. However, HTFA's polarity mismatch with DT[56] and strong O–H BDE (113.7 kcal/mol) would make HAT of the HTFA O–H bond by DT unlikely.[89] If we assume that HCl is generated through HAT from methane by Cl•, it is plausible that DT undergoes a HAT with HCl to regenerate the Cl•. However, the difference in pK_a between H-TFA and H-Cl is > 6 units, such that HCl would likely deprotonate to form Cl^-. An alternative path for Cl^-

would be to undergo electron transfer (ET) with DT•• to again form Cl• and reduce DT•• to DT•$^{-}$.[83, 90] We propose a two-fold involvement of DT in the methane oxidation chemistry. First, active DT•• abstracts hydrogen from CH_4 to form CH_3•. Second, DT•• oxidizes Cl^- to Cl•; Cl• can either directly react with CH_4 via HAT, or associate with a Cl^- to form a Cl_2•$^-$ radical trap. With these considerations in mind, we propose the mechanism depicted in Figure 5.6.

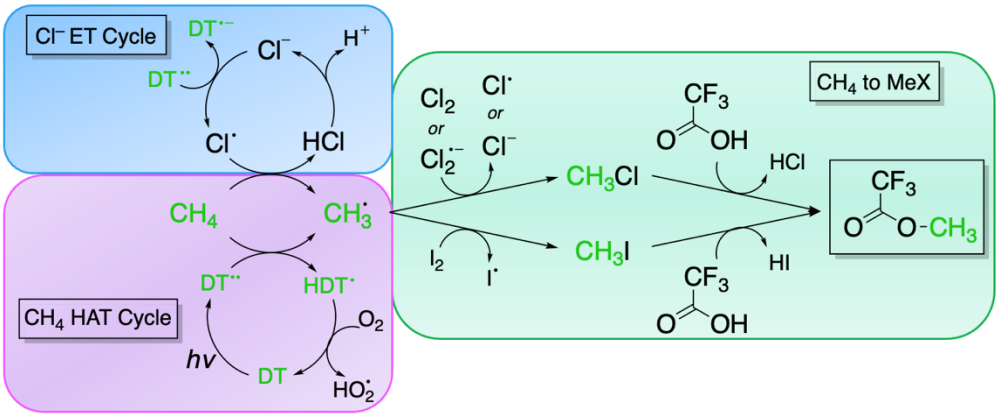

Figure 5.6: Global mechanism for methane oxidation towards MeX. The mechanism can be partitioned into 3 sub-mechanisms working synergistically. The first sub-mechanism (green, labeled CH_4 to MeX) is the Cl/I radical-based pathway in which methane (or CH_3• after HAT) is converted to MeTFA and MeCl (CH_3Cl in figure). The second sub-mechanism (blue, labelled Cl^- ET Cycle) is the DT•• + Cl^- ET to generate Cl•. The third sub-mechanism (purple, labelled CH_4 HAT Cycle) is the HAT of CH_4 with DT•• or Cl• to generate CH_3•.

We probed the mechanism for CH_4 conversion to MeTFA hypothesized in Figure 5.6 using quantum mechanics (QM) calculations at the DFT level. We begin with the first sub-mechanism, which involves the actual conversion of CH_4 to MeTFA. With Cl• as the HAT agent and I_2 as the radical trap, the sub-mechanism occurs as such:

- CH_4 reacts with Cl• to generate CH_3• and HCl
- CH_3• is then trapped by I_2 to form CH_3I and I•
- CH_3I reacts with HTFA to form MeTFA and leave HI

The free energy surface for this pathway is detailed in Scheme 5.3.

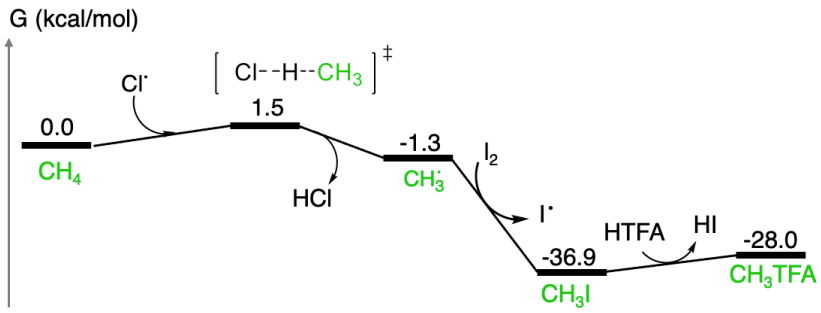

Scheme 5.3: DFT Free energies at 298 K for the conversion of methane to MeTFA within the Cl/I system.

5.3.4 Cl-Based Radical Mechanism

The barrier required for HAT between CH_4 and Cl• to produce CH_3• and HCl is calculated to be 1.5 kcal/mol above the methane starting state, while the reaction step is overall downhill by -1.3 kcal/mol. Following formation of CH_3•, molecular I_2 reacts to form CH_3I and I•. DFT predicts this step to be barrierless and exergonic by -35.6 kcal/mol, which places CH_3I at -36.9 kcal/mol below the methane starting state. Following the formation of CH_3I, MeTFA can now form by an S_N2 solvolysis reaction with HTFA. In this reaction step, the divalent O of HTFA acts as a nucleophile and attacks the C of

CH_3I, forming $HTFA^+$-CH_3 and I^-. The now trivalent O of $HTFA^+$-CH_3 gives up H^+ to I^-, forming HI and the desired MeTFA product. DFT predicts that this conversion of HTFA and MeI to MeTFA and HI is uphill 8.9 kcal/mol. In this sub-mechanism, the overall conversion of CH_4 to MeTFA is -28.0 kcal/mol when Cl• is the HAT agent with I_2 as the radical trap.

5.3.5 Iodine-Free Radical Mechanism

It is important that we also consider the chemistry in the absence of iodine, since this is the condition of some experiments. In the absence of iodine, we observe that oxidation of CH_4 to MeTFA still occurs, however with decreased turnovers. This is likely because without iodine, Cl_2 or $Cl_2•^-$ (which forms when Cl• and Cl^- associate)[91] serve as the radical trapping agent, in which CH_3Cl is formed instead of CH_3I.[36] Because Cl^- is a poorer leaving group than I^-, CH_3Cl + HTFA solvolysis to form HCl and MeTFA is likely retarded. However, HAT between CH_4 and Cl• is not affected by the absence of iodine. The free-energy pathway is depicted in Scheme 5.4. As noted, HAT between CH_4 and Cl• remains unchanged with a barrier of 1.5 kcal/mol, resulting in the alkyl radical and HCl at -1.3 kcal/mol. Trapping of the alkyl radical with Cl_2 is downhill -34.0 kcal/mol, resulting in formation of CH_3Cl at -35.3 kcal/mol. With $Cl_2•^-$, radical trapping is downhill -46.3 kcal/mol, resulting in CH_3Cl and Cl^- at -47.6 kcal/mol. Like the case with CH_3I, we

propose CH_3Cl follows an S_N2 solvolysis pathway with HTFA to generate MeTFA and HCl. Solvolysis between CH_3Cl and HTFA is uphill 4.7 kcal/mol, resulting in HCl and the desired MeTFA at -30.6 kcal/mol (-42.8 when $Cl_2\bullet^-$ is the radical trap). While solvolysis with MeCl (4.7 kcal/mol) is thermodynamically more accessible than MeI (8.9 kcal/mol), the actual kinetics for MeCl solvolysis will be slower because the $HTFA^+$-CH_3 + Cl^- ion pair is less stable than the iodine analog, on account of Cl^- being a worse leaving group than I^-.

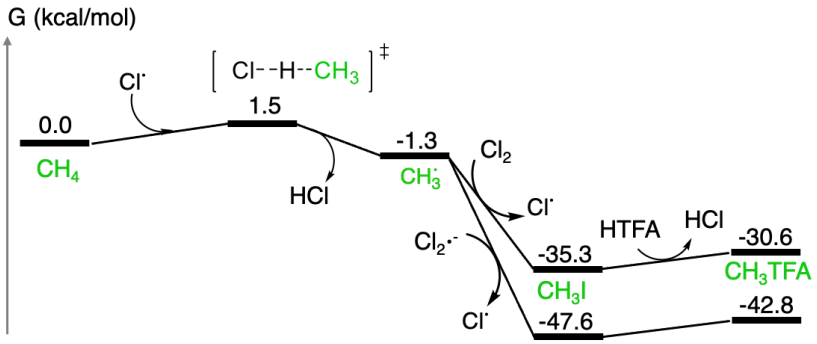

Scheme 5.4: DFT Free energies at 298 K for the conversion of methane to MeTFA in the absence of I_2.

5.3.6 Decatungstate Integration

Previous reports have shown that ground state DT, specifically NaDT and TBADT, can be photoexcited by 365-390 nm light to a highly active HAT reagent.[57, 68, 92, 93] The absorption spectrum for DT anion shows a large peak at 324 nm, corresponding to a HOMO-LUMO transition, also marked by ligand to metal charge transfer (LMCT).[94,

[95] This photoexcitation is likely a closed-shell singlet to open-shell singlet transition of DT in which the SOMOs reside on the oxygens. The open-shell singlet relaxes from the Franck-Condon point to the open-shell singlet minima in < 1 ps.[57] This excited singlet reportedly decays via an intersystem crossing to the active triplet state which is more stable due to the exchange interaction. This active triplet state is formed with a quantum yield of 0.5-0.6 and exists for 55 ± 20 ns in acetonitrile.[57, 96-101] The triplet state (DT••) has radical character on the electrophilic oxygens, such that it can readily pull H atoms off neighboring molecules (like CH_4 and HCl) to generate radicals when the substrate oxidation potential is above +2.44 V vs. saturated calomel electrode (SCE).[57] When the oxidation potential is below +2.44 V vs. SCE, the complex is expected to perform ET; this is the regime in which DT oxidizes Cl^- to Cl•.[91] Following ET, protonation of DT• from the medium would result in HDT• with an overall doublet spin. Previously published experimental evidence shows that after reacting, the solution containing DT turns dark blue with strong absorption bands in the 600-800 nm range; which we interpret as the formal reduction of W in DT.[85, 90, 93, 95, 102-104] The species responsible for the blue color occurs after relatively long periods of time and is not active in catalysis. For our purposes, we focus on the singlet ground state DT, the lowest-lying triplet DT•• and the reacted HDT•.

We calculate that the initial excitation of DT to the lowest-lying triplet DT•• requires 43.5 kcal/mol; experimentally this excitation arises through irradiation by 365-390 nm light. For simplicity, we set DT•• as the reference state of 0.0 kcal/mol in Scheme 5.5. Spin density analysis reveals significant unpaired spin on the bridging oxygens in DT••. Oddly, the terminal oxos exhibit little spin density, contrary to previous beliefs that the terminal oxos are responsible for HAT.[57] To confirm this finding, we analyzed the hydrogen binding (HB) energies for the 5 unique oxygens of DT•• (Figure 5.7).

DT Site	H-binding Energy (kcal/mol)
1	-29.0
2	-47.3
3	-35.0
4	-47.7
5	-41.4

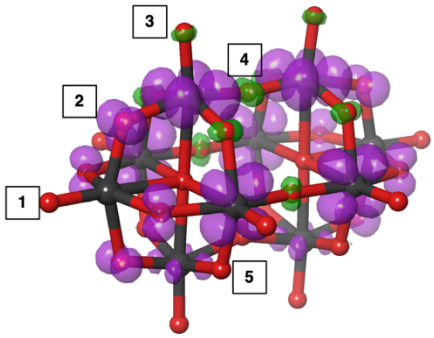

Figure 5.7: Spin-density diagram for the lowest-lying triplet decatungstate (purple=α, green=β) and hydrogen-binding energies (kcal/mol) for the 5 unique oxygen sites. The oxygen and tungsten atoms are red and grey, respectively.

We define the HB energy as the free energy of the reaction H• + DT•• → HDT•. Sites 2, 4, and 5 are bridging oxygens and sites 1 and 3 are terminal oxos. As the spin density analysis suggests, binding H• to the bridging oxygen sites was most favorable. The HB energy to sites 2, 4, and 5 are -47.3, -47.7, and -41.4 kcal/mol respectively. In contrast, the HB energy to sites 1 and 3 are -29.0 and -35.0 kcal/mol respectively, indicating that binding H to the terminal oxos is significantly less favorable. Overall, site 4 provides the best HB energy while site 1 is the worst. Thus site 4 would appear responsible for the HAT since it binds H the strongest, but we note that site 4 is not easily accessible due to the two adjacent oxo groups. For example, CH_4 would not readily undergo HAT with site 4 because the adjacent oxos would repel the molecule due to Pauli Repulsion. Instead, we propose that HAT occurs through site 2. Site 2 is easily accessible for HAT and provides the second-best HB energy, only 0.4 kcal/mol less than site 4. Ravelli and coworkers also proposed that site 4 is shielded and therefore not active for HAT.[57] Site 1 was previously believed to be the active HAT site because it contributes more to the shape of the HOMO-1 orbital compared to site 2 (HOMO-1 is where the unpaired spin resides), and because its geometric parameters match that of HAT with a triplet carbonyl in which the process occurs in-plane with the C=O bond. We claim that

the difference between sites 1 and 2 for HOMO-1 contribution is small and that both sites provide geometric parameters suitable for HAT with a carbonyl. This combined with site 2's more favorable HB energy leads us to propose that site 2 is responsible for HAT.

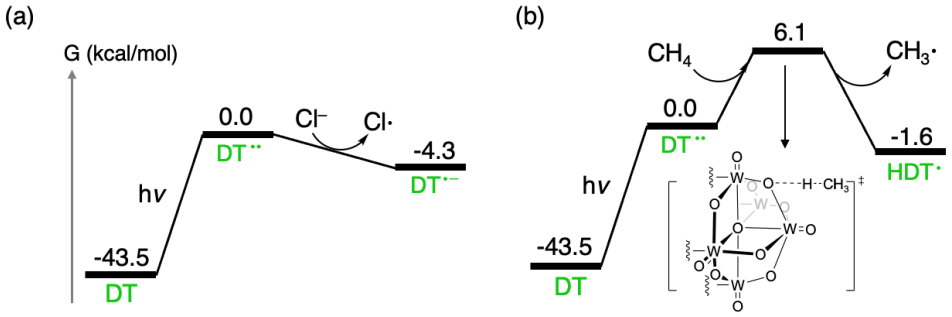

Scheme 5.5: DFT Free energies at 298 K for **(a)** the generation of Cl• through ET of Cl^- with DT•• and **(b)** for the generation of CH_3• through HAT of CH_4 with DT••.

Scheme 5.5 shows ET to DT•• from Cl^- to form Cl• and HAT to DT•• from CH_4 to form CH_3•; preceding these steps is the photoexcitation of DT to DT••, which DFT predicts requires 43.5 kcal/mol. For simplicity, we choose DT•• to be the reference state at 0.0 kcal/mol. DFT predicts ET to DT•• from Cl^- is downhill -4.3 kcal/mol.[90, 105] Following ET, DT•$^-$ would protonate to form HDT• (not shown). We find that HAT from CH_4 to DT•• is -1.6 kcal/mol downhill with a transition state barrier of 6.1 kcal/mol above the DT•• reference state. Subsequent regeneration of DT from HDT• is achieved through oxidation by dioxygen.

5.3.7 Decatungstate Regeneration by Dioxygen

HAT leads to the HDT• species which can undergo further re-oxidation to regenerate the DT catalyst and funnel H towards H_2O. Given the presence of dioxygen (O_2) in the reaction vessel, the first step is likely a HAT in which triplet O_2 pulls H off HDT• to generate HO_2• and a ground state singlet DT. The HO_2• can then pull another H off an additional equivalent of HDT• to generate HOOH. We envision that during catalysis, there exists a pool of O–H containing species such as OH•, HOOH, HO_2•, etc. These species can react in numerous ways, making it difficult to predict exactly how O_2 and HOOH may funnel towards a thermodynamic sink. However, our previous study on peroxide radical chemistry revealed that in a large ensemble of O–H-containing species, the reactions that occur most are (1) HOOH + OH• → HO_2• + H_2O and (2) HOOH + HO_2• → OH• + O_2 + H_2O.[106] Both reactions consume an HOOH and produce an H_2O. We hypothesize that upon formation of HOOH from HO_2•, either of these two reactions can consume the HOOH to form H_2O. This H_2O formation mechanism is depicted in Scheme 5.6.

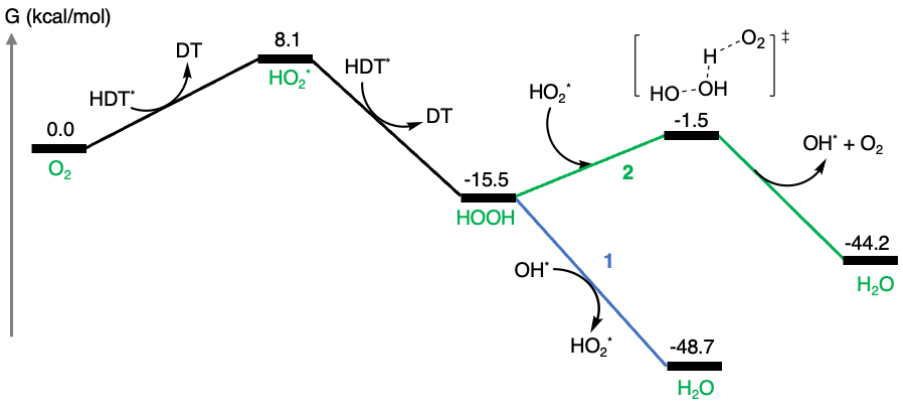

Scheme 5.6: DFT Free energies at 298 K for the conversion of dioxygen to H_2O and the regeneration of the DT ground state.

Starting with triplet O_2, HAT to pull H off the doublet HDT• to regenerate ground state singlet DT while forming HO_2• is uphill 8.1 kcal/mol. HO_2• can now perform a secondary HAT on an additional HDT• to form HOOH plus another singlet DT; this step is downhill to -15.5 kcal/mol. Formation of HOOH opens numerous avenues for a plethora of possible reaction steps. However, we believe the most likely reactions that can occur are either (1) HOOH + OH• → HO_2• + H_2O or (2) HOOH + HO_2• → OH• + O_2 + H_2O. Reaction 1 is barrierless to form HO_2• and H_2O at -48.7 kcal/mol. Reaction 2 requires a barrier of -1.5 kcal/mol (or 14.0 kcal/mol relative to preceding HOOH intermediate) and is downhill to form OH•, O_2, and H_2O at -44.2 kcal/mol. Overall, this sub-mechanism converts O_2 to H_2O and regenerates 2 ground-state DT from 2 HDT•. We note that this mechanism does not account for DT's reduced -5 or -6 states that are observed in experiment. We believe these states are formed via non-catalytic electron transfer side reactions that do not contribute to the catalytic methane oxidation

chemistry. Indeed, previous experimental studies claim that these -5 and -6 states are formed over long time periods and are not catalytic.[57]

5.3.8 Reaction Tolerance to Water

The DFT-predicted reaction mechanism suggests $HO_2\bullet$ formation from the re-oxidation of HDT• by O_2, which eventually funnels to the formation of H_2O. Thus, reaction tolerance to water was experimentally probed. Varying equivalents of water were added at the start of the reaction under our standard aerobic reaction conditions to quantify the effect on the amount of MeX produced. The formation of MeX is plotted against equivalents of added water relative to TBADT in Figure 5.8. At 1,000 equivalents of water relative to TBADT (7.0 mmol H_2O), there is no effect on MeX production. At 10,000 equivalents of water relative to TBADT (70 mmol H_2O), MeX production is shut down. Thus, water must become detrimental to the reaction at a loading greater than 1,000 equivalents and less than or equal to 10,000 equivalents and should be considered as a potential detriment in reactions for which TBADT TOs exceed 1,000.

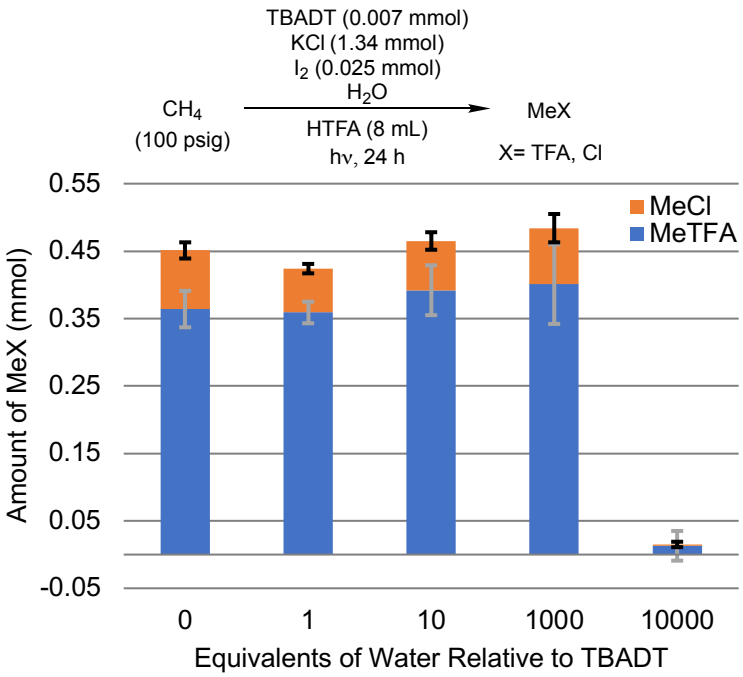

Figure 5.8: Amount of MeX (X = TFA, Cl) produced under standard aerobic reaction conditions in which varying amounts of water were added to the start of the reaction. Equivalents of water are reported with respect to TBADT. Each bar graph represents the average of at least three independent experiments with error bars depicting the standard deviation of the three experiments.

5.4 Conclusions

We have demonstrated the partial oxidation of methane using a photochemically driven process comprised of catalytic TBADT, chloride and iodine in HTFA. Under aerobic conditions, MeX yield reached ~9%. Kinetic studies revealed a dependence on dioxygen concentration. Re-oxidation experiments with dioxygen led us to achieve methane to MeTFA conversion with $>$ 350 TOs based on TBADT and ~60% yield based on methane when optimized. MeTFA was shown to be stable under standard reaction conditions, with $>$ 94% remaining after 41 h.

Density Functional Theory calculations were used to determine the reaction mechanism, which validates our proposal that photo and radical chemistry synergistically perform methane functionalization. Based on the DFT calculations and experiments, we propose a radical pathway in which a hydrogen atom is abstracted from methane by a chlorine atom or by triplet DT•• to generate a methyl radical, which is then trapped by some chlorine or iodine species (Cl_2, $Cl_2\bullet^-$, I_2) to generate a methyl halide.[36] From there, HTFA undergoes S_N2 solvolysis with the methyl halide to form the desired ester product, MeTFA. The chlorine radicals in this mechanism are generated through electron transfer from chloride anion to DT••. We propose that after ET by DT•• and subsequent protonation, dioxygen re-oxidizes HDT• and subsequently forms water.

The addition of DT to the chloride-iodine system presents a novel strategy for the photo-driven partial oxidation of methane towards MeTFA. DT's remarkable quantum efficiency and HAT reactivity provides synergy with the free radical chemistry of chloride and iodine, affording the desired MeTFA product which maintains excellent stability.

5.5 Experimental Methods

CAUTION. Many of the reagents and conditions described herein are particularly hazardous. Appropriate safety measures should be taken and appropriate personal protective equipment should be worn when handling strong acids, especially in large

volumes. Broadband mercury arc lamps are dangerous to the skin and eyes, and even a brief exposure can result in permanent damage. The lamps must only be turned on while encased in an enclosure that precludes exposure to the naked eye. Cool to room temperature water must always be recirculated around the lamp to prevent uncontrolled overheating; this is especially important when conducting reactions containing mixtures of methane and air or dioxygen.

General Comments and Materials. All reactions were carried out under ambient atmosphere unless indicated otherwise. Methane, oxygen, nitrogen, and argon were purchased from GTS-Welco and used as received. Potassium chloride, potassium bromide, iodine, trifluoroacetic acid ($> 99.9\%$), glacial acetic acid, nitromethane, copper(II) acetate hydrate, copper(II) chloride hydrate, copper(II) trifluoroacetate hydrate, potassium persulfate, di-tert-butyl peroxide, tert-butyl hydroperoxide, hydrogen peroxide, and trifluoroacetic anhydride were purchased commercially and used as received. Tetrabutylammonium decatungstate (TBADT) was synthesized and characterized according to literature procedure, for which the reagents were purchased commercially and used as received.[107] High pressure reaction vessels were constructed from Fisher-Porter tubes, purchased from Andrews Glass, and custom-built reactor tops were constructed from Swagelok stainless steel fittings (see Figure D2). These reaction vessels can be safely pressurized to 250 psig at room temperature. The photolysis enclosure was

constructed with a power supply feeding a broadband mercury arc lamp. The mercury arc lamp was nested in a quartz immersion well in which cool to room temperature DI water (15-40 ^{o}C) was recirculated through at all times the lamp was powered on. The power supply (450-watt, product #7830-60), Hanovia mercury arc lamp (medium pressure, 450 watt, 121.92 mm arc length, 244.35 mm overall length, product #7825-34), and quartz immersion well (product #7854-27) were purchased from Ace Glass. The mercury arc lamp is quoted to irradiate ~ 40-48% in the ultraviolet spectral range, ~ 40-43% in the visible spectral range, and the remainder in the infrared spectral range. Mercury arc lamps were replaced every 1,000 hours. NMR analysis was performed using either a Varian Inova 500 or 600 MHz spectrometer. ^{1}H NMR data of reaction mixtures were obtained with a capillary of C_6D_6 as the internal lock reference. Chemical shifts are reported relative to the internal standards of either CH_3NO_2 (d 4.18) or HOAc (d 2.04). UV-vis spectral measurements of TBADT were collected on a Cary 60 UV-vis spectrometer. Samples were prepared in 1 cm square quartz cuvettes.

General Procedure for Photochemical Methane Functionalization. Reactions were performed in triplicate. Each Fisher-Porter reactor was charged with a stir bar and solid reagents (TBADT, KCl, I_2) followed by 8 mL HTFA. Unless specified otherwise, TBADT was ground with a mortar and pestle prior to adding to the reactor. The reactors were sealed under air and weighed. The reactors were then pressurized with methane and

weighed again. The amount of methane added was quantified by the difference in mass before and after methane addition. The reactors were then added to a photolysis enclosure, each positioned 16 cm from the mercury arc lamp with uniform stirring. Reaction time was started 15 minutes following lamp turn on to account for lamp warm up time to reach full intensity. After the reaction, the lamp was turned off and the photolysis chamber was kept closed for at least one minute to ensure the lamp was safely powered off. The reactors were removed, weighed to probe for leaks, and cooled in front of a fan for at least 15 minutes. The reactors were then vented in a fume hood, 20 µL of internal standard (either CH_3NO_2 or HOAc) was added to each reaction, and the reaction mixtures were thoroughly stirred. An aliquot from each reaction mixture was removed and centrifuged, from which the supernatant of each was added to an NMR tube containing a sealed capillary containing C_6D_6. The products were analyzed by ^{1}H NMR spectroscopy. See Figure D1 for a sample ^{1}H NMR spectrum.

MeTFA Stability Under Photochemical Conditions. Reactions were performed in triplicate. Each Fisher-Porter reactor was charged with 0.007 mmol TBADT, 1.34 mmol KCl, 0.025 mmol I_2, and a stir bar followed by 8 mL HTFA and 0.35 mmol of MeTFA. The reactors were sealed under air, pressurized with 100 psig Ar, and weighed. The reactors were then added to a photolysis enclosure, each positioned 16 cm from the mercury arc lamp with uniform stirring. Reaction time was started 15 minutes following

lamp turn on to account for lamp warm up time to reach full intensity. After the reaction, the lamp was turned off and the photolysis chamber was kept closed for at least one minute to ensure the lamp was safely powered off. The reactors were removed, weighed to probe for leaks, and cooled in front of a fan for at least 15 minutes. The reactors were then vented in a fume hood, 20 µL of internal standard (either CH_3NO_2 or HOAc) was added to each reaction, and the reaction mixtures were thoroughly stirred. An aliquot from each reaction mixture was removed and centrifuged, from which the supernatant of each was added to an NMR tube containing a sealed capillary containing C_6D_6. The products were analyzed by ^1H NMR spectroscopy.

Experiments Involving Dinitrogen/Dioxygen Purges. Reactions were performed in triplicate. Each Fisher-Porter reactor was charged with 0.007 mmol TBADT, 1.34 mmol KCl, 0.025 mmol I_2, and a stir bar followed by 8 mL HTFA. The reactor tops were fitted to the reactors but not sealed. Using a long needle, the respective gas was bubbled through each reaction solution one at a time. Following one minute of bubbling, the needle was removed and the reactor valve was quickly sealed. The reactors were weighed, pressurized with 100 psig methane, and weighed again. The amount of methane added was quantified by the difference in mass before and after methane addition. The reactors were then added to a photolysis enclosure, each positioned 16 cm from the mercury arc lamp with uniform stirring. Reaction time was started 15 minutes following lamp turn on to account for lamp

warm up time to reach full intensity. After 24 h of reaction, the lamp was turned off and the photolysis chamber was kept closed for at least one minute to ensure the lamp was safely powered off. The reactors were removed, weighed to probe for leaks, and cooled in front of a fan for at least 15 minutes. The reactors were then vented in a fume hood, 20 µL of internal standard (either CH_3NO_2 or HOAc) was added to each reaction, and the reaction mixtures were thoroughly stirred. An aliquot from each reaction mixture was removed and centrifuged, from which the supernatant of each was added to an NMR tube containing a sealed capillary containing C_6D_6. The products were analyzed by ^1H NMR spectroscopy.

Re-oxidation Experiments with Dioxygen. Reactions were performed in triplicate. Each Fisher-Porter reactor was charged with 0.007 mmol TBADT, 1.34 mmol KCl, 0.025 mmol I_2, and a stir bar followed by 8 mL HTFA. Reactors were either sealed under air or purged with dioxygen. The reactors were weighed, pressurized with methane and weighed again. The amount of methane added was quantified by the difference in mass before and after methane addition. The reactors were then added to a photolysis enclosure, each positioned 16 cm from the mercury arc lamp with uniform stirring. Reaction time was started 15 minutes following lamp turn on to account for lamp warm up time to reach full intensity. After the reaction, the lamp was turned off and the photolysis chamber was kept closed for at least one minute to ensure the lamp was safely powered off. The reactors

were removed, weighed to probe for leaks, and cooled in front of a fan for at least 15 minutes. The reactors were then pressurized with dioxygen top pressure and weighed again. The amount of dioxygen added was quantified by the difference in mass before and after dioxygen addition. The reactors were then subjected again to the mercury arc lamp. This process of adding additional dioxygen top pressure and re-subjecting to the mercury arc lamp was repeated as detailed in each set of reaction conditions. Following the last dioxygen addition and irradiation, the reactors were removed, weighed to probe for leaks, and cooled in front of a fan for at least 15 minutes. The reactors were then vented in a fume hood, 20 µL of internal standard (either CH_3NO_2 or HOAc) was added to each reaction, and the reaction mixtures were thoroughly stirred. An aliquot from each reaction mixture was removed and centrifuged, from which the supernatant of each was added to an NMR tube containing a sealed capillary containing C_6D_6. The products were analyzed by ^1H NMR spectroscopy.

5.6 Computational Methods

All Density Functional Theory calculations were performed within the Jaguar software package version 10.9 from Schrodinger Inc. Structures were first optimized using the PBE flavor of DFT including the Grimme-Becke-Johnson (GBJ) D3 correction for London dispersion. W and I atoms were treated with the Los Alamos **large-core** triple-

zeta pseudopotential augmented with polarization and diffuse functions (LAV3P*+ in Jaguar). All other atoms were treated with the 6-31+G(d) basis set. PBE-D3 geometry optimizations were followed by additional single-point energy (SPE) calculations with implicit solvent. SPEs were calculated with the M06-2X functional using the GBJ D3 dispersion correction. For the SPE, W and I were described with the Los Alamos **small-core** triple-zeta potential augmented with polarization and diffuse functions; all other atoms were described with the 6-311++G(d,p) basis set (LACV3P**++ in Jaguar). Solvent effects were included through the PBF Poisson Boltzmann continuum model with parameters matching trifluoroacetic acid. Frequency calculations were performed at the M06-2X-D3/LACV3P**++ level to predict thermochemical properties (zero-point energy, entropy, and temperature correction to enthalpy) at 298K and to confirm intermediate and transition states.

5.7 References

1. Olah, G. A.; Goeppert, A.; Prakash, G. K. S., *Beyond Oil and Gas: The Methanol Economy*. Wiley-VCH: Weinheim, Germany, 2009.

2. Gunsalus, N. J.; Koppaka, A.; Park, S. H.; Bischof, S. M.; Hashiguchi, B. G.; Periana, R. A., Homogeneous Functionalization of Methane. *Chem. Rev.* **2017,** *117* (13), 8521-8573.

3. Dummer, N. F.; Willock, D. J.; He, Q.; Howard, M. J.; Lewis, R. J.; Qi, G.; Taylor, S. H.; Xu, J.; Bethell, D.; Kiely, C. J.; Hutchings, G. J., Methane Oxidation to Methanol. *Chem. Rev.* **2022**.

4. *BP Statistical Review of World Energy 2022*. 71st ed.; BP: London, 2022.

5. Zakaria, Z.; Kamarudin, S. K., Direct Conversion Technologies of Methane to Methanol: An Overview. *Renewable and Sustainable Energy Reviews* **2016,** *65*, 250-261.

6. Schwach, P.; Pan, X.; Bao, X., Direct Conversion of Methane to Value-Added Chemicals over Heterogeneous Catalysts: Challenges and Prospects. *Chem. Rev.* **2017,** *117* (13), 8497-8520.

7. Tang, P.; Zhu, Q.; Wu, Z.; Ma, D., Methane activation: The past and future. *Energy Environ. Sci.* **2014,** *7* (8), 2580-2591.

8. Ravi, M.; Ranocchiari, M.; van Bokhoven, J. A., The Direct Catalytic Oxidation of Methane to Methanol—A Critical Assessment. *Angew. Chem. Int. Ed.* **2017,** *56* (52), 16464-16483.

9. Lin, R.; Amrute, A. P.; Pérez-Ramírez, J., Halogen-Mediated Conversion of Hydrocarbons to Commodities. *Chem. Rev.* **2017,** *117* (5), 4182-4247.

10. Zichittella, G.; Paunović, V.; Amrute, A. P.; Pérez-Ramírez, J., Catalytic Oxychlorination versus Oxybromination for Methane Functionalization. *ACS Catal.* **2017,** *7* (3), 1805-1817.

11. Podkolzin, S. G.; Stangland, E. E.; Jones, M. E.; Peringer, E.; Lercher, J. A., Methyl Chloride Production from Methane over Lanthanum-Based Catalysts. *J. Am. Chem. Soc.* **2007,** *129* (9), 2569-2576.

12. Wang, K. X.; Xu, H. F.; Li, W. S.; Zhou, X. P., Acetic acid synthesis from methane by non-synthesis gas process. *Journal of Molecular Catalysis A: Chemical* **2005,** *225* (1), 65-69.

13. Paunović, V.; Zichittella, G.; Moser, M.; Amrute, A. P.; Pérez-Ramírez, J., Catalyst design for natural-gas upgrading through oxybromination chemistry. *Nat. Chem.* **2016,** *8* (8), 803-809.

14. Tschuikow-Roux, E.; Paddison, S., Bond dissociation energies and radical heats of formation in CH3Cl, CH2Cl2, CH3Br, CH2Br2, CH2FCl, and CHFCl2. *Int. J. Chem. Kinet.* **1987,** *19* (1), 15-24.

15. Breed, A.; Doherty, M. F.; Gadewar, S.; Grosso, P.; Lorkovic, I. M.; McFarland, E. W.; Weiss, M. J., Natural gas conversion to liquid fuels in a zone reactor. *Catalysis Today* **2005,** *106* (1), 301-304.

16. Shilov, A. E.; Shul'pin, G. B., Activation of C−H Bonds by Metal Complexes. *Chem. Rev.* **1997,** *97* (8), 2879-2932.

17. Periana, R. A.; Taube, D. J.; Gamble, S.; Taube, H.; Satoh, T.; Fujii, H., Platinum Catalysts for the High-Yield Oxidation of Methane to a Methanol Derivative. *Science* **1998,** *280* (5363), 560-564.

18. Chen, S.-S.; Koppaka, A.; Periana, R. A.; Ess, D. H., Theory and Experiment Demonstrate that Sb(V)-Promoted Methane C–H Activation and Functionalization Outcompete Superacid Protonolysis in Sulfuric Acid. *J. Am. Chem. Soc.* **2021,** *143* (43), 18242-18250.

19. Periana, R. A.; Mirinov, O.; Taube, D. J.; Gamble, S., High yield conversion of methane to methyl bisulfate catalyzed by iodine cations. *Chem. Commun.* **2002**, 2376-2377.

20. Gang, X.; Zhu, Y.; Birch, H.; Hjuler, H. A.; Bjerrum, N. J., Iodine as catalyst for the direct oxidation of methane to methyl sulfates in oleum. *Appl. Catal. A* **2004,** *261* (1), 91-98.

21. Hashiguchi, B. G.; Konnick, M. M.; Bischof, S. M.; Gustafson, S. J.; Devarajan, D.; Gunsalus, N.; Ess, D. H.; Periana, R. A., Main-Group Compounds Selectively Oxidize Mixtures of Methane, Ethane, and Propane to Alcohol Esters. *Science* **2014,** *343* (6176), 1232-1237.

22. Konnick, M. M.; Hashiguchi, B. G.; Devarajan, D.; Boaz, N. C.; Gunnoe, T. B.; Groves, J. T.; Gunsalus, N.; Ess, D. H.; Periana, R. A., Selective CH Functionalization of Methane, Ethane, and Propane by a Perfluoroarene Iodine(III) Complex. *Angew. Chem. Int. Ed.* **2014,** *53* (39), 10490-10494.

23. Groothaert, M. H.; Smeets, P. J.; Sels, B. F.; Jacobs, P. A.; Schoonheydt, R. A., Selective Oxidation of Methane by the Bis(μ-oxo)dicopper Core Stabilized on ZSM-5 and Mordenite Zeolites. *J. Am. Chem. Soc.* **2005,** *127* (5), 1394-1395.

24. Woertink, J. S.; Smeets, P. J.; Groothaert, M. H.; Vance, M. A.; Sels, B. F.; Schoonheydt, R. A.; Solomon, E. I., A [Cu2O]2+ core in Cu-ZSM-5, the active site in the oxidation of methane to methanol. *Proc. Nat. Acad. Sci. USA* **2009,** *106* (45), 18908-18913.

25. Alayon, E. M.; Nachtegaal, M.; Ranocchiari, M.; van Bokhoven, J. A., Catalytic conversion of methane to methanol over Cu–mordenite. *Chem. Commun.* **2012,** *48* (3), 404-406.

26. Vanelderen, P.; Snyder, B. E.; Tsai, M. L.; Hadt, R. G.; Vancauwenbergh, J.; Coussens, O.; Schoonheydt, R. A.; Sels, B. F.; Solomon, E. I., Spectroscopic definition of the copper active sites in mordenite: selective methane oxidation. *J. Am. Chem. Soc.* **2015,** *137* (19), 6383-6392.

27. Grundner, S.; Markovits, M. A.; Li, G.; Tromp, M.; Pidko, E. A.; Hensen, E. J.; Jentys, A.; Sanchez-Sanchez, M.; Lercher, J. A., Single-site trinuclear copper oxygen clusters in mordenite for selective conversion of methane to methanol. *Nat. Commun.* **2015,** *6*, 7546.

28. Ipek, B.; Lobo, R. F., Catalytic conversion of methane to methanol on Cu-SSZ-13 using N2O as oxidant. *Chem. Commun.* **2016,** *52* (91), 13401-13404.

29. Pappas, D. K.; Martini, A.; Dyballa, M.; Kvande, K.; Teketel, S.; Lomachenko, K. A.; Baran, R.; Glatzel, P.; Arstad, B.; Berlier, G.; Lamberti, C.; Bordiga, S.; Olsbye, U.; Svelle, S.; Beato, P.; Borfecchia, E., The Nuclearity of the Active Site for Methane to Methanol Conversion in Cu-Mordenite: A Quantitative Assessment. *J. Am. Chem. Soc.* **2018,** *140* (45), 15270-15278.

30. Brezicki, G.; Kammert, J. D.; Gunnoe, T. B.; Paolucci, C.; Davis, R. J., Insights into the Speciation of Cu in the Cu-H-Mordenite Catalyst for the Oxidation of Methane to Methanol. *ACS Catal.* **2019,** *9* (6), 5308-5319.

31. Kulkarni, A. R.; Zhao, Z.-J.; Siahrostami, S.; Nørskov, J. K.; Studt, F., Cation-exchanged zeolites for the selective oxidation of methane to methanol. *Catalysis Science & Technology* **2018,** *8* (1), 114-123.

32. Walling, C.; Mayahi, M. F., Some Solvent and Structural Effects in Free Radical Chlorination. *J. Am. Chem. Soc.* **1959,** *81* (6), 1485-1489.

33. Tedder, J. M., Which Factors Determine the Reactivity and Regioselectivity of Free Radical Substitution and Addition Reactions? *Angew. Chem. Int. Ed.* **1982,** *21* (6), 401-410.

34. Fortman, G. C.; Boaz, N. C.; Munz, D.; Konnick, M. M.; Periana, R. A.; Groves, J. T.; Gunnoe, T. B., Selective monooxidation of light alkanes using chloride and iodate. *J. Am. Chem. Soc.* **2014,** *136* (23), 8393-8401.

35. Kalman, S. E.; Munz, D.; Fortman, G. C.; Boaz, N. C.; Groves, J. T.; Gunnoe, T. B., Partial oxidation of light alkanes by periodate and chloride salts. *Dalton Trans.* **2015,** *44* (12), 5294-5298.

36. Schwartz, N. A.; Boaz, N. C.; Kalman, S. E.; Zhuang, T.; Goldberg, J. M.; Fu, R.; Nielsen, R. J.; Goddard, W. A.; Groves, J. T.; Gunnoe, T. B., Mechanism of Hydrocarbon Functionalization by an Iodate/Chloride System: The Role of Ester Protection. *ACS Catal.* **2018,** *8* (4), 3138-3149.

37. Fu, R.; Nielsen, R. J.; Liebov, N. S.; Goddard, W. A., III; Gunnoe, T. B.; Groves, J. T., DFT Mechanistic Study of Methane Mono-Esterification by Hypervalent Iodine Alkane Oxidation Process. *Journal of Physical Chemistry C* **2019,** *123* (25), 15674-15684.

38. Vargaftik, M. N.; Stolarov, I. P.; Moiseev, I. I., Highly selective partial oxidation of methane to methyl trifluoroacetate. *Journal of the Chemical Society, Chemical Communications* **1990,** (15), 1049-1050.

39. Chen, W.; Kocal, J. A.; Brandvold, T. A.; Bricker, M. L.; Bare, S. R.; Broach, R. W.; Greenlay, N.; Popp, K.; Walenga, J. T.; Yang, S. S.; Low, J. J., Manganese oxide catalyzed methane partial oxidation in trifluoroacetic acid: Catalysis and kinetic analysis. *Catalysis Today* **2009,** *140* (3), 157-161.

40. Tang, R.; Kochi, J. K., Cobalt(III) trifluoroacetate: An electron transfer oxidant. *Journal of Inorganic and Nuclear Chemistry* **1973,** *35* (11), 3845-3856.

41. Coutard, N.; Musgrave, C. B., III; Moon, J.; Liebov, N. S.; Nielsen, R. M.; Goldberg, J. M.; Li, M.; Jia, X.; Lee, S.; Dickie, D. A.; Schinski, W. L.; Wu, Z.; Groves, J. T.; Goddard, W. A., III; Gunnoe, T. B., Manganese Catalyzed Partial Oxidation of Light Alkanes. *ACS Catal.* **2022,** *12* (9), 5356-5370.

42. Deng, H. P.; Zhou, Q.; Wu, J., Microtubing-Reactor-Assisted Aliphatic C-H Functionalization with HCl as a Hydrogen-Atom-Transfer Catalyst Precursor in Conjunction with an Organic Photoredox Catalyst. *Angew. Chem. Int. Ed.* **2018,** *57* (39), 12661-12665.

43. Gonzalez, M. I.; Gygi, D.; Qin, Y.; Zhu, Q.; Johnson, E. J.; Chen, Y.-S.; Nocera, D. G., Taming the Chlorine Radical: Enforcing Steric Control over Chlorine-Radical-Mediated C–H Activation. *J. Am. Chem. Soc.* **2022,** *144* (3), 1464-1472.

44. Yang, Q. M.; Wang, Y. H.; Qiao, Y. S.; Gau, M.; Carroll, P. J.; Walsh, P. J.; Schelter, E. J., Photocatalytic C-H activation and the subtle role of chlorine radical complexation in reactivity. *Science* **2021,** *372* (6544), 847-+.

45. Li, Z.; Luo, L.; Li, M.; Chen, W.; Liu, Y.; Yang, J.; Xu, S.-M.; Zhou, H.; Ma, L.; Xu, M.; Kong, X.; Duan, H., Photoelectrocatalytic C–H halogenation over an oxygen vacancy-rich TiO2 photoanode. *Nat. Commun.* **2021,** *12* (1), 6698.

46. Panetti, G. B.; Yang, Q.; Gau, M. R.; Carroll, P. J.; Walsh, P. J.; Schelter, E. J., Discovery and mechanistic investigation of photoinduced sp3 C–H activation of hydrocarbons by the simple anion hexachlorotitanate. *Chem Catalysis* **2022,** *2* (4), 853-866.

47. Liebov, N. S.; Goldberg, J. M.; Boaz, N. C.; Coutard, N.; Kalman, S. E.; Zhuang, T.; Groves, J. T.; Gunnoe, T. B., Selective Photo-Oxygenation of Light Alkanes Using Iodine Oxides and Chloride. *ChemCatChem* **2019,** *11* (20), 5045-5054.

48. Coutard, N.; Goldberg, J. M.; Valle, H. U.; Cao, Y.; Jia, X.; Jeffrey, P. D.; Gunnoe, T. B.; Groves, J. T., Aerobic Partial Oxidation of Alkanes Using Photodriven Iron Catalysis. *Inorg. Chem.* **2022,** *61* (2), 759-766.

49. Hirscher, N. A.; Ohri, N.; Yang, Q.; Zhou, J.; Anna, J. M.; Schelter, E. J.; Goldberg, K. I., A Metal-Free, Photocatalytic Method for Aerobic Alkane Iodination. *J. Am. Chem. Soc.* **2021,** *143* (46), 19262-19267.

50. Gumerova, N. I.; Rompel, A., Synthesis, structures and applications of electron-rich polyoxometalates. *Nat. Rev. C hem.* **2018,** *2* (2).

51. Pope, M. T.; Müller, A., Polyoxometalate Chemistry: An Old Field with New Dimensions in Several Disciplines. *Angewandte Chemie International Edition in English* **1991,** *30* (1), 34-48.

52. Long, D.-L.; Burkholder, E.; Cronin, L., Polyoxometalate clusters, nanostructures and materials: From self assembly to designer materials and devices. *Chem. Soc. Rev.* **2007,** *36* (1), 105-121.

53. Dupré, N.; Rémy, P.; Micoine, K.; Boglio, C.; Thorimbert, S.; Lacôte, E.; Hasenknopf, B.; Malacria, M., Chemoselective Catalysis with Organosoluble Lewis Acidic Polyoxotungstates. *Chemistry – A European Journal* **2010,** *16* (24), 7256-7264.

54. Tzirakis, M. D.; Lykakis, I. N.; Orfanopoulos, M., Decatungstate as an efficient photocatalyst in organic chemistry. *Chem. Soc. Rev.* **2009,** *38* (9), 2609-2621.

55. Ravelli, D.; Protti, S.; Fagnoni, M., Decatungstate Anion for Photocatalyzed "Window Ledge" Reactions. *Acc. Chem. Res.* **2016,** *49* (10), 2232-2242.

56. Ravelli, D.; Fagnoni, M.; Fukuyama, T.; Nishikawa, T.; Ryu, I., Site-Selective C–H Functionalization by Decatungstate Anion Photocatalysis: Synergistic Control by Polar and Steric Effects Expands the Reaction Scope. *ACS Catal.* **2018,** *8* (1), 701-713.

57. De Waele, V.; Poizat, O.; Fagnoni, M.; Bagno, A.; Ravelli, D., Unraveling the Key Features of the Reactive State of Decatungstate Anion in Hydrogen Atom Transfer (HAT) Photocatalysis. *ACS Catal.* **2016,** *6* (10), 7174-7182.

58. Cheung, K. P. S.; Sarkar, S.; Gevorgyan, V., Visible Light-Induced Transition Metal Catalysis. *Chem. Rev.* **2022,** *122* (2), 1543-1625.

59. Holmberg-Douglas, N.; Nicewicz, D. A., Photoredox-Catalyzed C-H Functionalization Reactions. *Chem. Rev.* **2022,** *122* (2), 1925-2016.

60. Sarver, P. J.; Bacauanu, V.; Schultz, D. M.; DiRocco, D. A.; Lam, Y. H.; Sherer, E. C.; MacMillan, D. W. C., The merger of decatungstate and copper catalysis to enable aliphatic C(sp(3))-H trifluoromethylation. *Nat. Chem.* **2020,** *12* (5), 459-467.

61. Schultz, D. M.; Lévesque, F.; DiRocco, D. A.; Reibarkh, M.; Ji, Y.; Joyce, L. A.; Dropinski, J. F.; Sheng, H.; Sherry, B. D.; Davies, I. W., Oxyfunctionalization of the Remote C—H Bonds of Aliphatic Amines by Decatungstate Photocatalysis. *Angew. Chem. Int. Ed.* **2017,** *56* (48), 15274-15278.

62. Wu, W.; Fu, Z.; Tang, S.; Zou, S.; Wen, X.; Meng, Y.; Sun, S.; Deng, J.; Liu, Y.; Yin, D., (nBu4N)4W10O32-catalyzed selective oxygenation of cyclohexane by

molecular oxygen under visible light irradiation. *Applied Catalysis B: Environmental* **2015,** *164*, 113-119.

63. Laudadio, G.; Deng, Y.; van der Wal, K.; Ravelli, D.; Nuño, M.; Fagnoni, M.; Guthrie, D.; Sun, Y.; Noël, T., C(sp3)-H functionalizations of light hydrocarbons using decatungstate photocatalysis in flow. *Science* **2020,** *369* (6499), 92-96.

64. Laudadio, G.; Govaerts, S.; Wang, Y.; Ravelli, D.; Koolman, H. F.; Fagnoni, M.; Djuric, S. W.; Noël, T., Selective C(sp3)–H Aerobic Oxidation Enabled by Decatungstate Photocatalysis in Flow. *Angew. Chem. Int. Ed.* **2018,** *57* (15), 4078-4082.

65. Halperin, S. D.; Fan, H.; Chang, S.; Martin, R. E.; Britton, R., A Convenient Photocatalytic Fluorination of Unactivated C–H Bonds. *Angew. Chem. Int. Ed.* **2014,** *53* (18), 4690-4693.

66. Perry, I. B.; Brewer, T. F.; Sarver, P. J.; Schultz, D. M.; DiRocco, D. A.; MacMillan, D. W. C., Direct arylation of strong aliphatic C–H bonds. *Nature* **2018,** *560* (7716), 70-75.

67. Murphy, J. J.; Bastida, D.; Paria, S.; Fagnoni, M.; Melchiorre, P., Asymmetric catalytic formation of quaternary carbons by iminium ion trapping of radicals. *Nature* **2016,** *532* (7598), 218-222.

68. Zeng, J.; Torigoe, T.; Kuninobu, Y., Control of Site-Selectivity in Hydrogen Atom Transfer by Electrostatic Interaction: Proximal-Selective C(sp3)–H Alkylation of 2-

Methylanilinium Salts Using a Decatungstate Photocatalyst. *ACS Catal.* **2022,** *12* (5), 3058-3062.

69. Capaldo, L.; Bonciolini, S.; Pulcinella, A.; Nuño, M.; Noël, T., Modular allylation of C(sp3)–H bonds by combining decatungstate photocatalysis and HWE olefination in flow. *Chem. Sci.* **2022,** *13* (24), 7325-7331.

70. Wang, Y.-T.; Shih, Y.-L.; Wu, Y.-K.; Ryu, I., Site-Selective C(sp3)-H Alkenylation Using Decatungstate Anion as Photocatalyst. *Adv. Synth. Catal.* **2022,** *364* (5), 1039-1043.

71. Capaldo, L.; Ravelli, D.; Fagnoni, M., Direct Photocatalyzed Hydrogen Atom Transfer (HAT) for Aliphatic C-H Bonds Elaboration. *Chem. Rev.* **2022,** *122* (2), 1875-1924.

72. Golden, D. L.; Suh, S. E.; Stahl, S. S., Radical C(sp(3))-H functionalization and cross-coupling reactions. *Nat. Rev. C hem.* **2022,** *6* (6), 405-427.

73. Pulcinella, A.; Mazzarella, D.; Noël, T., Homogeneous catalytic C(sp3)–H functionalization of gaseous alkanes. *Chem. Commun.* **2021,** *57* (78), 9956-9967.

74. Ye, Z. Q.; Lin, Y. M.; Gong, L., The Merger of Photocatalyzed Hydrogen Atom Transfer with Transition Metal Catalysis for C-H Functionalization of Alkanes and Cycloalkanes. *Eur. J. Org. Chem.* **2021,** *2021* (40), 5545-5556.

75. Wang, Y. H.; Yang, Q. M.; Walsh, P. J.; Schelter, E. J., Light-mediated aerobic oxidation of C(sp(3))-H bonds by a Ce(iv) hexachloride complex. *Org. Chem. Front.* **2022,** *9* (10), 2612-2620.

76. Panetti, G. B.; Yang, Q.; Gau, M. R.; Carroll, P. J.; Walsh, P. J.; Schelter, E. J., Discovery and mechanistic investigation of photoinduced sp3 C−H activation of hydrocarbons by the simple anion hexachlorotitanate. *Chem. Catal.* **2022,** *2*, 853−866.

77. Gonzalez, M. I.; Gygi, D.; Qin, Y. Z.; Zhu, Q. L.; Johnson, E. J.; Chen, Y. S.; Nocera, D. G., Taming the Chlorine Radical: Enforcing Steric Control over Chlorine-Radical-Mediated C-H Activation. *J. Am. Chem. Soc.* **2022,** *144* (3), 1464-1472.

78. Gygi, D.; Gonzalez, M. I.; Hwang, S. J.; Xia, K. T.; Qin, Y. Z.; Johnson, E. J.; Gygi, F.; Chen, Y. S.; Nocera, D. G., Capturing the Complete Reaction Profile of a C-H Bond Activation. *J. Am. Chem. Soc.* **2021,** *143* (16), 6060-6064.

79. Troian-Gautier, L.; Turlington, M. D.; Wehlin, S. A. M.; Maurer, A. B.; Brady, M. D.; Swords, W. B.; Meyer, G. J., Halide Photoredox Chemistry. *Chem. Rev.* **2019,** *119* (7), 4628-4683.

80. Shields, B. J.; Doyle, A. G., Direct C(sp(3))-H Cross Coupling Enabled by Catalytic Generation of Chlorine Radicals. *J. Am. Chem. Soc.* **2016,** *138* (39), 12719-12722.

81. Deng, H. P.; Zhou, Q.; Wu, J., Microtubing-Reactor-Assisted Aliphatic C-H Functionalization with HCl as a Hydrogen-Atom-Transfer Catalyst Precursor in Conjunction with an Organic Photoredox Catalyst. *Angewandte Chemie-International Edition* **2018,** *57* (39), 12661-12665.

82. Li, P.; Deetz, A. M.; Hu, J.; Meyer, G. J.; Hu, K., Chloride Oxidation by One- or Two-Photon Excitation of N-Phenylphenothiazine. *J. Am. Chem. Soc.* **2022,** *144*, 17604−17610.

83. Rohe, S.; Morris, A. O.; McCallum, T.; Barriault, L., Hydrogen Atom Transfer Reactions via Photoredox Catalyzed Chlorine Atom Generation. *Angew. Chem. Int. Ed.* **2018,** *57* (48), 15664-15669.

84. Zidan, M.; Morris, A. O.; McCallum, T.; Barriault, L., The Alkylation and Reduction of Heteroarenes with Alcohols Using Photoredox Catalyzed Hydrogen Atom Transfer via Chlorine Atom Generation. *Eur. J. Org. Chem.* **2020,** *2020* (10), 1453-1458.

85. Ermolenko, L. P.; Delaire, J. A.; Giannotti, C., Laser flash photolysis study of the mechanism of photooxidation of alkanes catalyzed by decatungstate anion. *J. Chem. Soc., Perkin Trans. 2* **1997,** (1), 25-30.

86. McMillan, G.; Wijnen, M. H. J., Reactions of Alkoxy Radicals v. Photolysis of Di-t-butyl peroxide. *Can. J. Chem.* **1958,** *36*, 1227-1232.

87. Brook, J. H. T., Reaction of Hydrocarbons with Tert.-butoxy Radicals. *Trans. Faraday Soc.* **1957,** *53*, 327-332.

88. Luňák, S.; Sedlák, P., Photoinitiated reactions of hydrogen peroxide in the liquid phase. *Journal of Photochemistry and Photobiology A: Chemistry* **1992,** *68* (1), 1-33.

89. St. John, P. C.; Guan, Y.; Kim, Y.; Kim, S.; Paton, R. S., Prediction of organic homolytic bond dissociation enthalpies at near chemical accuracy with sub-second computational cost. *Nat. Commun.* **2020,** *11* (1), 2328.

90. Texier, I.; Delaire, J. A.; Giannotti, C., Reactivity of the charge transfer excited state of sodium decatungstate at the nanosecond time scale. *Phys. Chem. Chem. Phys.* **2000,** *2* (6), 1205-1212.

91. Lei, Y.; Lei, X.; Westerhoff, P.; Zhang, X.; Yang, X., Reactivity of Chlorine Radicals (Cl• and Cl2•–) with Dissolved Organic Matter and the Formation of Chlorinated Byproducts. *Environ. Sci. Technol.* **2021,** *55* (1), 689-699.

92. Capaldo, L.; Ravelli, D., Decatungstate as Direct Hydrogen Atom Transfer Photocatalyst for SOMOphilic Alkynylation. *Org. Lett.* **2021,** *23* (6), 2243-2247.

93. Tanielian, C., Decatungstate photocatalysis. *Coord. Chem. Rev.* **1998,** *178-180*, 1165-1181.

94. Hill, C. L., Introduction of functionality into unactivated carbon-hydrogen bonds. Catalytic generation and nonconventional utilization of organic radicals. *Synlett* **1995,** (2), 127.

95. Duncan, D. C.; Netzel, T. L.; Hill, C. L., Early-Time Dynamics and Reactivity of Polyoxometalate Excited States. Identification of a Short-Lived LMCT Excited State and a Reactive Long-Lived Charge-Transfer Intermediate following Picosecond Flash Excitation of [W10O32]4- in Acetonitrile. *Inorg. Chem.* **1995,** *34* (18), 4640-4646.

96. Ravelli, D.; Dondi, D.; Fagnoni, M.; Albini, A.; Bagno, A., Electronic and EPR spectra of the species involved in [W10O32]4− photocatalysis. A relativistic DFT investigation. *Phys. Chem. Chem. Phys.* **2013,** *15* (8), 2890-2896.

97. Duncan, D. C.; Fox, M. A., Early Events in Decatungstate Photocatalyzed Oxidations: A Nanosecond Laser Transient Absorbance Reinvestigation. *J. Phys. Chem. A* **1998,** *102* (24), 4559-4567.

98. Kothe, T.; Martschke, R.; Fischer, H., Photoreactions of the decatungstate anion W10O324- with organic substrates in solution studied by EPR and kinetic absorption spectroscopy: an example for the persistent radical effect. *J. Chem. Soc., Perkin Trans. 2* **1998,** (3), 503-508.

99. Tanielian, C.; Schweitzer, C.; Seghrouchni, R.; Esch, M.; Mechin, R., Polyoxometalate sensitization in mechanistic studies of photochemical reactions: The

decatungstate anion as a reference sensitizer for photoinduced free radical oxygenations of organic compounds. *Photochemical & Photobiological Sciences* **2003,** *2* (3), 297-305.

100. Tanielian, C.; Seghrouchni, R.; Schweitzer, C., Decatungstate Photocatalyzed Electron-Transfer Reactions of Alkenes. Interception of the Geminate Radical Ion Pair by Oxygen. *J. Phys. Chem. A* **2003,** *107* (8), 1102-1111.

101. Tanielian, C.; Lykakis, I. N.; Seghrouchni, R.; Cougnon, F.; Orfanopoulos, M., Mechanism of decatungstate photocatalyzed oxygenation of aromatic alcohols: Part I. Continuous photolysis and laser flash photolysis studies. *Journal of Molecular Catalysis A: Chemical* **2007,** *262* (1), 170-175.

102. Tanielian, C.; Duffy, K.; Jones, A., Kinetic and Mechanistic Aspects of Photocatalysis by Polyoxotungstates: A Laser Flash Photolysis, Pulse Radiolysis, and Continuous Photolysis Study. *J. Phys. Chem. B* **1997,** *101* (21), 4276-4282.

103. Texier, I.; Delouis, J. F.; Delaire, J. A.; Giannotti, C.; Plaza, P.; Martin, M. M., Dynamics of the first excited state of the decatungstate anion studied by subpicosecond laser spectroscopy. *Chem. Phys. Lett.* **1999,** *311*, 139-145.

104. Chemseddine, A.; Sanchez, C.; Livage, J.; Launay, J. P.; Fournier, M., Electrochemical and photochemical reduction of decatungstate: a reinvestigation. *Inorg. Chem.* **1984,** *23* (17), 2609-2613.

105. Armstrong, D. A.; Huie, R. E.; Koppenol, W. H.; Lymar, S. V.; Merényi, G.; Neta, P.; Ruscic, B.; Stanbury, D. M.; Steenken, S.; Wardman, P., Standard electrode potentials involving radicals in aqueous solution: inorganic radicals (IUPAC Technical Report). *Pure Appl. Chem.* **2015,** *87* (11-12), 1139-1150.

106. Ilyin, D. V.; Goddard, W. A.; Oppenheim, J. J.; Cheng, T., First-principles–based reaction kinetics from reactive molecular dynamics simulations: Application to hydrogen peroxide decomposition. *Proc. Nat. Acad. Sci. USA* **2019,** *116* (37), 18202-18208.

107. Protti, S.; Ravelli, D.; Fagnoni, M.; Albini, A., Solar light-driven photocatalyzed alkylations. Chemistry on the window ledge. *Chem. Commun.* **2009,** (47), 7351-7353.

Chapter 6

Manganese Catalyzed Partial Oxidation of Light Alkanes

Reproduced with permission from:

N Coutard, J Moon, N Liebov, RJ Nielsen, J Goldberg, M Li, X Jia, W Schinski, Z Wu, JT Groves, WA Goddard III, TB Gunnoe. *Manganese Catalyzed Partial Oxidation of Light Alkanes, ACS Catalysis,* **2022**, 12, 9, 5356-5370

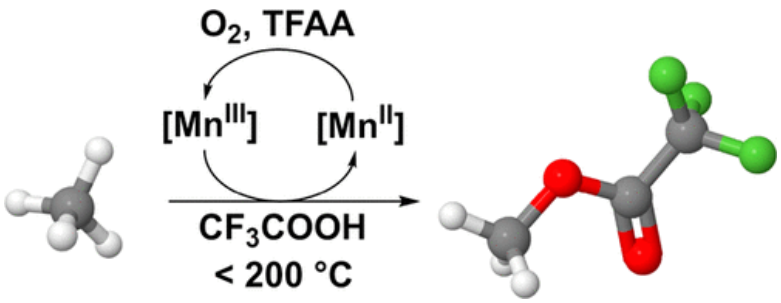

Figure 6.0: Table of contents figure

6.1 Abstract

The catalytic partial oxidation of methane is achieved at low temperatures (< 200 °C) using manganese oxides and manganese salts in mixtures of trifluoroacetic acid and trifluoroacetic anhydride. Dioxygen is used as the *in situ* terminal oxidant. For Mn oxides

(*e.g.*, MnO_2, Mn_2O_3 and Mn_3O_4), we studied stoichiometric methane partial oxidation in HTFA (TFA = trifluoroacetate). Using a Mn trifluoroacetate salt, at 180 °C and under 25 psig of methane, product selectivity for the mono-oxidized product methyl trifluoroacetate (MeTFA) is observed to be $>$ 90% at ~35% methane conversion at approximately 6 turnovers. Under our catalytic methane oxidation reaction conditions, MeTFA is stable against over-oxidation, which explains the likely high selectivity at conversions $>$ 15%. Using combined experimental studies and DFT calculations, a mechanism involving soluble and molecular Mn species in the catalytic cycle is proposed. The proposed reaction pathway involves initial activation of Mn^{II} by dioxygen, cleavage of a methane C–H bond by a Mn^{III} hydroxo intermediate, rebound of the methyl radical to generate MeTFA, and finally regeneration of the starting Mn^{II} complex. Also, this process is shown to be applicable to the oxidation of ethane, favoring the mono-oxidized product ethyl trifluoroacetate (EtTFA) and reaching ~46% conversion.

6.2 Introduction

Methane, the primary component of natural gas, is a potent greenhouse gas that traps up to 35 times more heat than CO_2 and is often flared at wellheads when it cannot be transported with existing infrastructure.[1] As a result, it has been estimated that ~300 million tons of CO_2 are released into the atmosphere annually without any valorization of

the flared methane.[2] Consequently, although methane is primarily used as an energy source through combustion and as a precursor for the chemical industry,[3] its use is limited by the stranding of a large proportion of available methane in remote locations.[4]

A potential solution to the wasteful practice of natural gas flaring is the chemical conversion of the light alkanes from natural gas into readily transported liquids through a gas to liquid (GTL) process. Currently, the prominent GTL method for methane upgrading involves its initial over-oxidation to syngas (*i.e.*, synthesis gas, a mixture of CO and H_2) followed by subsequent conversion of CO and H_2 to products such as methanol. Steam reforming of methane to form syngas is energy and capital intense, which renders its use for distributed natural gas conversion impractical. Thus, there is a need for processes amenable for small-scale and distributed GTL to convert light alkanes from natural gas, such as methane, to value-added products.

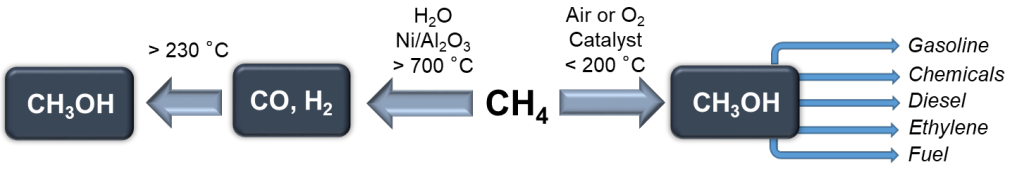

Figure 6.1: Comparison of current route to convert methane to methanol (left) to desired direct partial oxidation of methane to form methanol (right).

Methanol stands as a choice target for a value-added product from methane as it is a versatile liquid chemical that can be either transformed into other valuable chemicals (*e.g.*, methyl acrylate, ethylene, propylene) or used directly as a standalone fuel, in

gasoline blends or converted to diesel fuel.[5] The development of efficient and selective catalytic strategies to directly convert methane directly to liquid products such as methanol, without the need for initial formation of syngas, to enable efficient use of this resource is economically important.

While the overall reaction of methane with dioxygen to yield methanol is exothermic and exergonic, the strong C–H bonds (BDE = 104 kcal/mol) of methane and the covalent nature of the C–H bonds result in a significant kinetic barrier for methane C–H bond activation.[6] Mechanisms for C–H bond breaking of methane include radical pathways that involve hydrogen atom abstraction by a high-energy radical species to generate an alkyl radical intermediate[7] as well as transition metal-mediated C–H activation (*e.g.*, electrophilic substitution, oxidative addition, 1,2-addition across metal-heteroatom bonds and σ-bond metathesis) in which case the substrate first coordinates to a metal center before C–H bond cleavage.[5a, 8] A second fundamental challenge is catalyst selectivity for C–H bond activation of methane over that of methanol, or that of an intermediate product (Me–X), since the C–H bonds of these downstream products are often weaker than the C–H bonds in methane, making methane over-oxidation a common complication.[5e, 6b, 8d]

Oxyhalogenation strategies for methane valorization typically occur through radical pathways that are selective for mono-functionalization only at low conversions.[9] In these processes, HX (X = Cl or Br) and O_2 generate alkyl halide products, usually with

a heterogeneous catalyst.[7] While oxyhalogenation uses O_2 as the terminal oxidant, it typically suffers from low selectivity at even moderate conversions (even $<$ 15-20%) as the radical intermediates are often highly reactive given the weaker C–H bonds found in the formed alkyl halides, leading to over-oxidation.[10]

In another strategy, electrophilic metal complexes have been used to form mono-oxidized products with more electron-deficient C–H bonds than those of CH_4.[11] The initial discovery of this chemistry, reported by Shilov and coworkers, utilizes Pt^{II} chloride as catalyst to yield methanol or methyl chloride directly from methane but, in the original process, Pt^{IV} was used as a sacrificial oxidant.[11b, 11c, 11f, 11g, 12] These discoveries led to the development of the Catalytica process, which uses Pt(II) ligated by 2,2'-bipyrimidine in oleum at temperatures $<$ 220 °C, achieving $>$ 90% selectivity at $>$ 70% conversion to mono-oxidized methyl bisulfate.[13] The produced methyl bisulfate has been estimated to be ~100 times less reactive than methane toward further oxidation.[6a, 14] However, slow catalytic rates, water intolerance, and the energy required for product separation from oleum complicated commercialization of the Catalytica process.[15]

Previous work in our groups identified a process for the selective oxidation of light alkanes, including methane, at high conversions and selectivity using iodine oxides and catalytic amounts of chloride at moderate temperatures in acidic solvent.[16] Our mechanistic analysis of this reactivity demonstrated how polar effects favored homolysis

of the C–H bond of methane over those of the mono-ester products.[17] Most recently, we reported the translation of this thermal chemistry to photo-driven processes with high selectivity at high conversions for the mono-oxidation of methane, ethane and propane in HTFA (trifluoroacetic acid, TFA = trifluoroacetate) to yield alkyl esters.[18] In all of our previous results, a significant limitation is the use of sacrificial oxidants that cannot be easily regenerated using dioxygen, either *in* or *ex situ.* By shifting our research to transition metals, we hoped to enable aerobic regeneration of active sites.

While the use of molecular Co precursors for methane activation in HTFA has been studied,[19] there is, to the best of our knowledge, little precedent regarding the use of molecular Mn oxides or related complexes for solution-phase methane activation, and no detailed mechanistic investigation has been reported.[20] The Mn cluster of photosystem II is able to oxidize water to produce molecular dioxygen.[21] Synthetic Mn complexes, some of which yield high-valent Mn oxo species are able to activate O_2 and C–H bonds.[22] High-valent manganese oxo complexes have also shown high activity for the oxygenation, halogenation and azidation of C–H bonds with BDEs as high as that of cyclohexane (BDE = 100.0 kcal/mol).[23] $Mn(OAc)_3$ was reported to be active for methane activation in HTFA, albeit with sub-stoichiometric activity.[19a] A relevant article describes the use of Mn oxides for stoichiometric methane oxidation.[24] Herein, we demonstrate examples of selective, catalytic light alkane partial oxidation using either Mn oxides or Mn salts as

precursors, both stoichiometric and catalytic, and we propose a reaction mechanism based on combined DFT calculations and experimental studies that accounts for the observed results. Methane conversions up to ~35% are reached while maintaining selectivity for the mono-oxidized ester product.

6.3 Results and Discussion

6.3.1 Stoichiometric Activity of Mn Oxides for Light Alkane Oxidation

We combined methane with MnO_2 and I_2 in HTFA, in the presence and absence of a chloride source, and observed conversion of methane to methyl trifluoroacetate (MeTFA) in ~65% yield (calculated as yield = $\frac{n_{MeTFA}}{n_{Mn}} \times 100$) at 180°C. For our previously reported light alkane oxidation using iodine oxides,[16a, 17a, 25] both iodine and catalytic amounts of chloride were beneficial;[17a] however, using MnO_2 neither chloride nor iodine is required to observe the conversion of methane to MeTFA in reactions set up in air. These results indicate that the mechanism of methane functionalization using MnO_2 is likely different from the proposed reaction pathway using iodate and periodate. For the iodate/periodate mediated alkane partial oxidation, we speculated on the role of chlorine and IO_2 radical species for homolytic C–H bond breaking,[16c] but here, in contrast, we speculate that Mn sites could be directly involved in breaking the methane C–H bond (see below). The presence of I_2, while not required for activity, appears to accelerate the

reaction through the removal of an initial induction period. Based on evidence discussed below, we propose that the role of I_2 is to convert heterogeneous MnO_2 into a soluble form of Mn. After approximately 1 hour in the presence of I_2, or 3 hours in its absence, the reaction reached completion with a yield of about 65% per Mn equivalent.

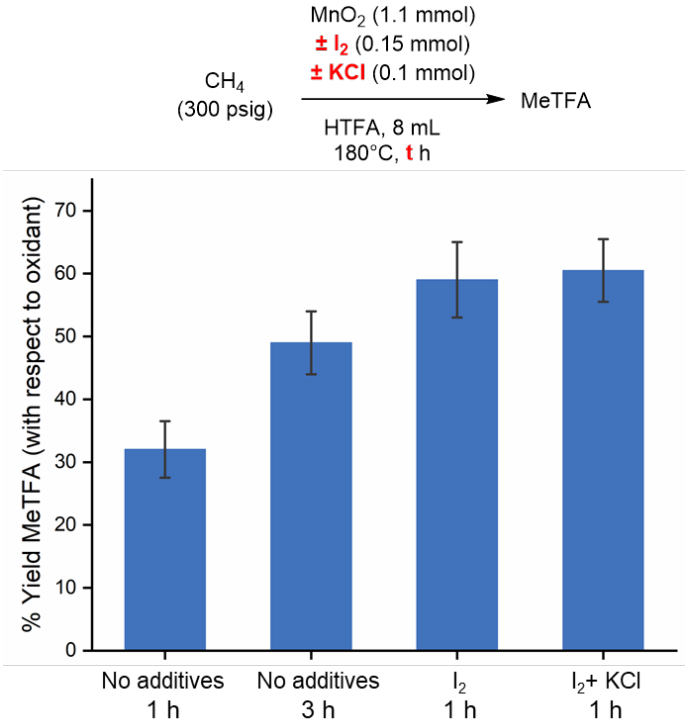

Figure 6.2: Conversion of methane to MeTFA using MnO_2 as stoichiometric oxidant with and without I_2 or KCl. Conditions: CH_4 (300 psig, 27 ± 1.3 mmol), KCl (0.1 mmol, if added), MnO_2 (1.1 mmol), I_2 (0.15 mmol), HTFA (8 mL), 180 °C, 1 or 3 h. Error bars denote standard deviations based on at least three independent experiments.

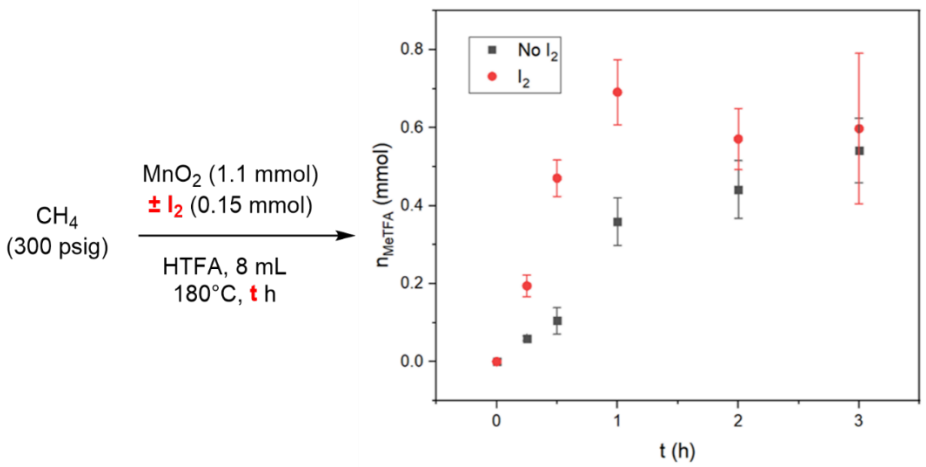

Figure 6.3: Effect of I_2 on the kinetics of MeTFA formation from methane oxidation in HTFA. Conditions: CH_4 (300 psig), MnO_2 (1.1 mmol), I_2 (0.15 mmol, if added), HTFA (8 mL), 180 °C. Error bars denote standard deviations based on at least three independent experiments.

Under these conditions, other Mn oxides (Mn_2O_3 and Mn_3O_4) showed similar activity for methane oxidation, even in the absence of air or dioxygen. Adding dioxygen or air to these reactions, with or without added I_2, did not improve yields and did not enable catalytic turnover, which differs from previously reported results based on Mn catalysis (Figure E1).[24] The similar yields observed using either Mn_3O_4, Mn_2O_3 or MnO_2 suggest that the different Mn precursors likely lead to the same or very similar reaction pathway that funnels to a homogeneous reaction independent of oxide phase or surface topology. Furthermore, as Mn^{IV}, Mn^{III} and $Mn^{II,III}$ oxides are active for methane oxidation but Mn^{II} oxide is not, it is likely that active oxides converge after the reaction to a spent oxidant

state containing Mn^{II} (see below). Thus, a key to catalytic aerobic methane oxidation seemed to be aerobic recycling of reduced Mn^{II} (see below).

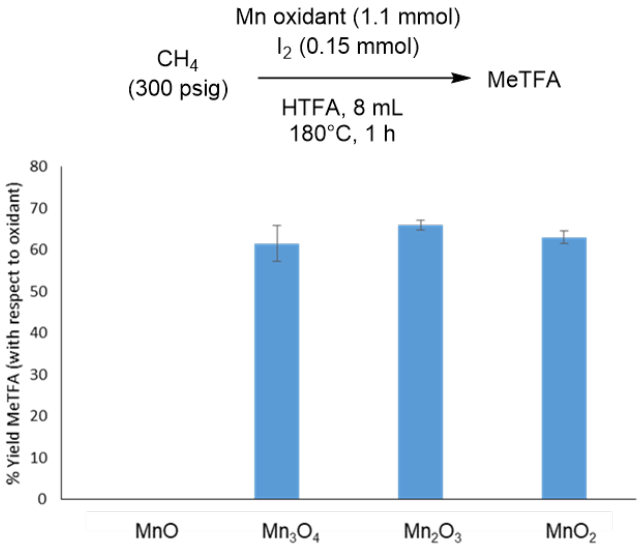

Figure 6.4: Screening of Mn oxides for methane functionalization. Conditions: CH_4 (300 psig), Mn source (1.1 mmol of Mn_xO_y), I_2 (0.15 mmol), HTFA (8 mL), 180 °C, 1 h, anaerobic (purged with 1 atm N_2). Error bars denote standard deviation based on three experiments. Yields = $\frac{n_{MeTFA}}{n_{Oxidant}} \times 100$.

Of particular interest, the formed MeTFA is stable under reaction conditions that convert methane to MeTFA. Monitoring the concentration of MeTFA at 140 °C shows > 80% of the MeTFA remaining after 16 hours (the temperature was decreased to 140 °C from 180 °C to accurately assess the kinetics). The plots of MeTFA production versus decay cannot be used to directly compare reaction rates as the concentration of methane in solution is different from MeTFA. However, the relative rates of decay and functionalization can be obtained from the slopes of the plots of MeTFA decay and

production over time to provide an estimate of the relative rates of methane and MeTFA conversion. Under our conditions, using the linear fit of the MeTFA production that was forced through zero (ignoring a possible induction period), the ratio of methane functionalization to MeTFA decay with MnO_2/I_2 is approximately 35:1. Using a linear fit of the data through four hours without forcing the fit through zero (accounting for an induction period), the ratio of methane functionalization to MeTFA decay is higher, approximately 54:1. With the conservative estimate of methane functionalization being at least 35 times faster than MeTFA decay under our conditions, we expect high selectivity from this system even as methane conversion is increased (see below).

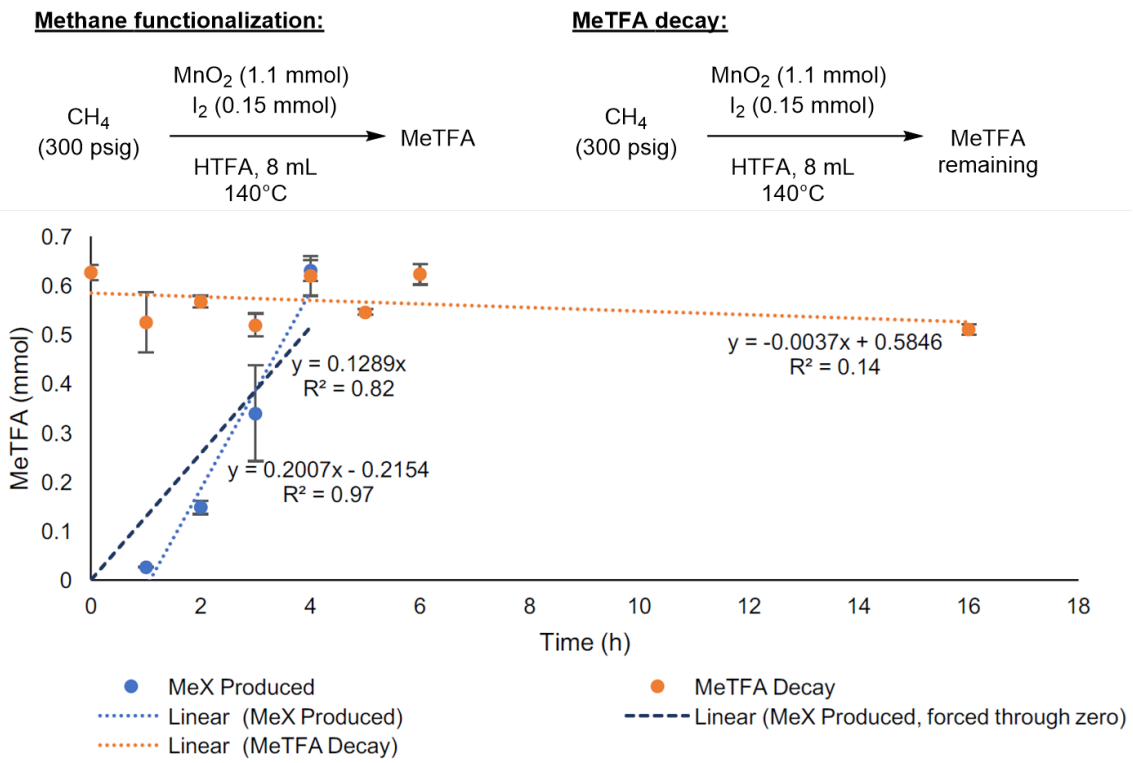

Figure 6.5: Methane functionalization versus MeTFA decay using MnO_2/I_2. Methane functionalization conditions: CH_4 (300 psig), MnO_2 (1.1 mmol), I_2 (0.15 mmol), HTFA (8 mL), 140 °C. MeTFA decay conditions: MeTFA (0.63 mmol), Ar (300 psig), MnO_2 (1.1 mmol), I_2 (0.15 mmol), HTFA (8 mL), 140 °C. Each data point is a separate experiment. Error bars denote standard deviations based on at least three independent experiments. The temperature was decreased to 140 °C from 180 °C to allow a more precise evaluation of the kinetic parameters.

As a result of optimizing reaction conditions to improve conversion, we found that using Mn_2O_3 as an oxidant, with a lower methane pressure and increased loading of Mn oxidant and I_2, and a slightly increased reaction temperature (185 °C), up to 19% methane conversion to MeTFA was observed (Scheme). While these results were encouraging, these conditions are suboptimal as the yield per equivalent of oxidant is low. Also, we considered that solvent decomposition could become problematic in the presence of large concentrations of Mn oxidant, as a blackening of the solution and increase in viscosity

were observed. Because the Mn solution is typically colourless with and without filtration, the blackened solution is not due to formation of a Mn oxide suspension.

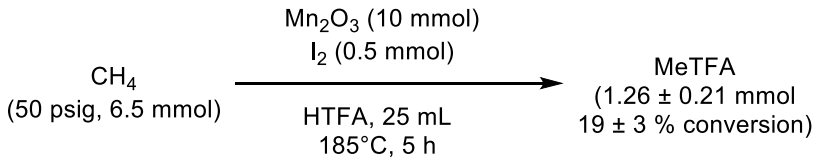

Scheme 6.1: High conversion of methane to MeTFA using Mn_2O_3. Conditions: CH_4 (50 psig) Mn_2O_3 (10 mmol), I_2 (0.5 mmol), HTFA (25 mL), 185 °C, 5 h. Standard deviation was calculated based on at least three separate experiments. The temperature and reaction time were increased to improve yield.

We assessed the effectiveness of ethane functionalization using MnO_2 (Scheme). For ethane, 57% conversion was observed with 81% selectivity observed towards EtTFA and 19% towards 1,2-bis(trifluoroacetate)ethane, the mono- and bis-oxidized products, respectively. Of note, the mono-oxidized product is favored over the bis-oxidized product, which highlights the selectivity of this process for the activation of strong C–H bonds over some weaker C–H bonds. We explain this selectivity by the protective role played by the ester of EtTFA on neighboring C–H bonds, as described in previous work by our groups.[17a] Previously, we have proposed that while the BDE of the C–H bond of an esterified alkyl is lower than that of the corresponding alkane, the ester moiety in fact protects neighboring C–H bonds from over oxidation by making reaction intermediates less polar and hence less thermodynamically favored in a strongly polar solvent such as HTFA. This protecting effect is less prevalent as the distance between a C–H bond and the ester moiety

increases, favoring in the case of ethane the formation of 1,2-bis(trifluoroacetate)ethane over 1,1-bis(trifluoroacetate)ethane.

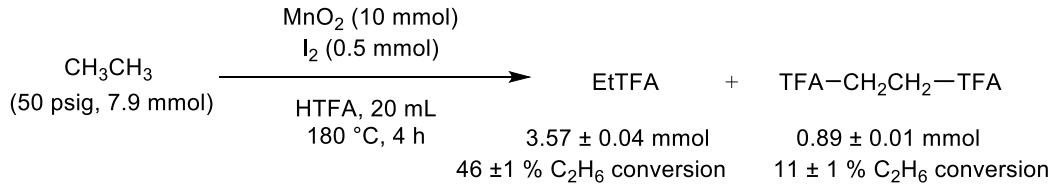

Scheme 6.2: Functionalization of ethane using MnO_2. Conditions: C_2H_6 (50 psig) MnO_2 (10 mmol), I_2 (0.5 mmol), HTFA (20 mL), 180 °C, 4 h. Standard deviations were calculated based on at least three separate experiments.

Since obtaining catalytic turnover is the desired end goal for these reactions, we attempted to characterize the spent state of the oxidant to find ways to recycle it. After using MnO_2 to convert methane to MeTFA, the soluble fraction of the reaction obtained by filtration to remove any remaining MnO_2 was evaporated to yield the reduced (or spent) oxidant as a white powder, termed "$MnOx_{red}$" herein. After drying, $MnOx_{red}$ was assayed under atmospheres of either N_2 or O_2 for further methane oxidation, but proved unreactive in both cases (Scheme). X-ray photoelectron spectroscopy (XPS) showed that $MnOx_{red}$ contained Mn in the +II oxidation state, evidenced by the Mn3s and Mn p peaks. The energy splitting of Mn 3s is 6.4 eV, indicating oxidation state of Mn is +II in the $MnOx_{red}$. In addition, the Mn 2p region shown in Fig. 6 consists of a spin-orbit doublet of Mn $2p_{1/2}$ and Mn $2p_{3/2}$ located at 653.8 and 641.8 eV, and a typical "shake-up" satellite feature at 647 eV, characterizing the existence of Mn^{II}.[26]

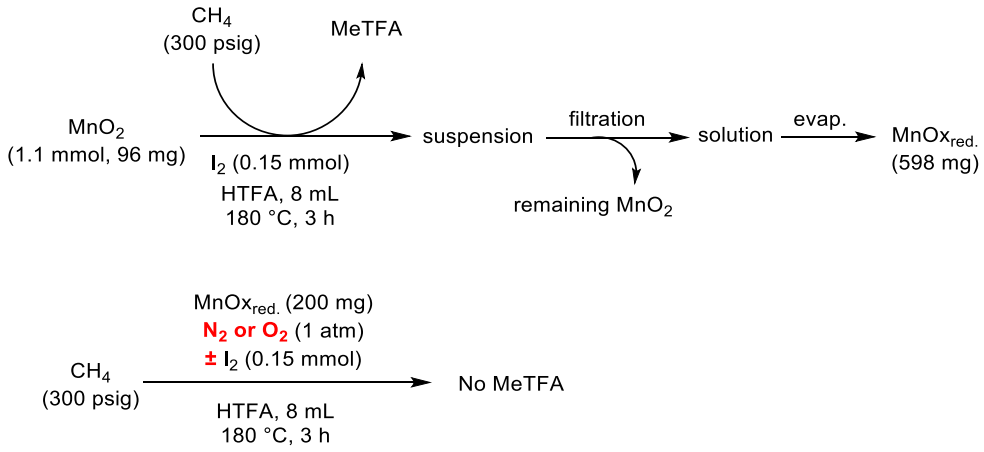

Scheme 6.3: $MnOx_{red}$ cannot be used to functionalize methane in the presence of N_2 or O_2 and with or without added I_2. Conditions: CH_4 (300 psig), $MnOx_{red.}$ (200 mg), I_2 (0 or 0.15 mmol), HTFA (8 mL), O_2 or N_2 (1 atm), 180 °C, 3 h. The reactions and workup shown at the top of the scheme were under anaerobic conditions and using dinitrogen.

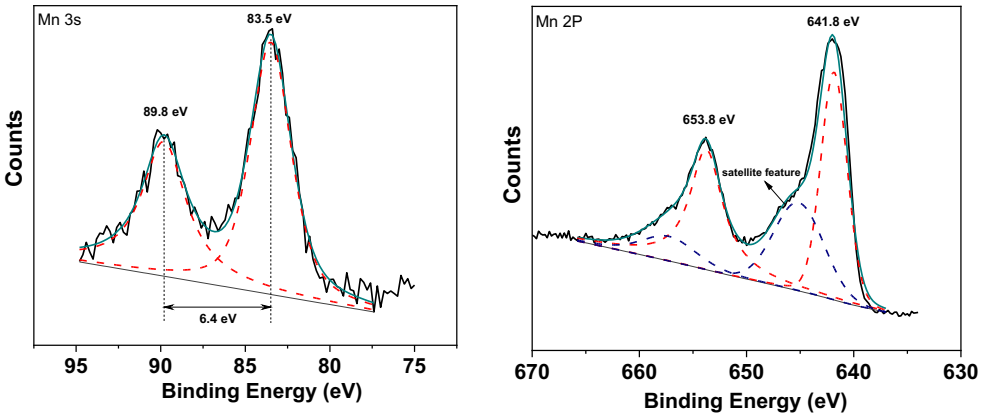

Figure 6.6: Left: the splitting of the Mn 3s peak in the XPS spectrum of $MnOx_{red}$ can be used to assess the oxidation state of Mn in that sample.[26a] Right: a "shake-up" satellite feature on the Mn 2p peak at ~ 647 eV (pink line, right) is characteristic of Mn^{II}.

6.3.2 Catalytic Methane Oxidation using Dioxygen

Since XPS data indicated that $MnOx_{red}$ contained Mn^{II}, and since we observed that exposing $MnOx_{red}$ to O_2 did not enable activity for methane oxidation, we tried using O_2 to activate Mn^{II} oxide (manganous oxide, MnO) and a bimetallic trifluoroacetate Mn^{II}

salt, $Mn_2(HTFA)_4(TFA)_4$. The molecular complex $Mn_2(HTFA)_4(TFA)_4$ was synthesized following a published procedure.[27] While MnO is inactive for methane functionalization under a dinitrogen atmosphere, the addition of O_2 enabled methane oxidation to form MeTFA, albeit in low yields. This was also true of $Mn_2(HTFA)_4(TFA)_4$, but the yield of MeTFA is substantially higher than when using MnO. Since both MnO and $Mn_2(HTFA)_4(TFA)_4$ are precursors for methane functionalization under aerobic conditions, we do not believe that either of these forms of Mn^{II} are a major component of $MnOx_{red}$. Furthermore, while addition of 1 atm O_2 rendered these Mn^{II} compounds active for methane oxidation, further increasing the amount of O_2 did not result in catalytic turnover, with yields remaining sub-stoichiometric, leading us to conclude that these Mn species, after O_2 activation and reaction with methane, converge towards an inactive form of Mn, possibly the same $MnOx_{red}$ described above. Of note, the reaction using $Mn_2(HTFA)_4(TFA)_4$ reaches completion much faster than that using MnO, which remains incomplete after 3 hours (35% yield is obtained after 6 h). This leads us to conclude that the solubilization of Mn oxides (see above) is a kinetically limiting factor, and that starting the reaction with the already soluble $Mn_2(HTFA)_4(TFA)_4$ removes an initial induction period, similar to the observed effect of adding I_2 to Mn oxides. These results strengthen our hypothesis that the oxidation of methane and ethane by Mn oxides takes place with a molecular Mn complex in what is likely a homogeneous process (see below).

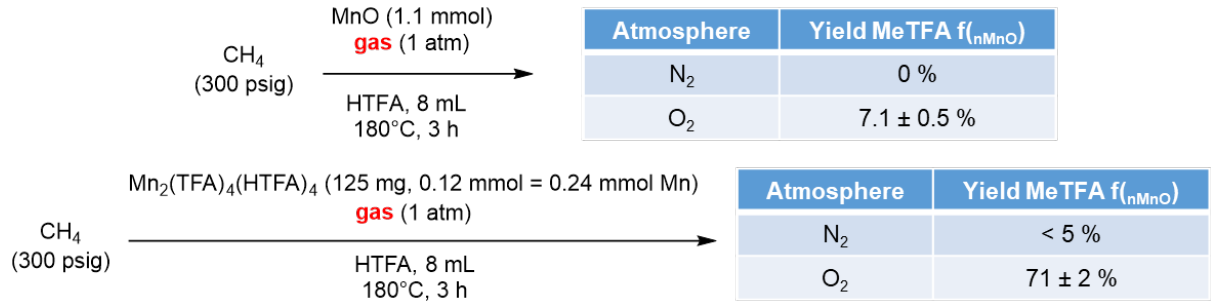

Figure 6.7: MnO and $Mn_2(HTFA)_4(TFA)_4$ can be activated by O_2 for methane oxidation. Conditions: CH_4 (300 psig), HTFA (8 mL), 180 °C, 3 h (see reaction conditions in the figure). Standard deviations were calculated based on at least three independent experiments.

One possible source of poisoning of the active Mn catalysts could be the generation of water as byproduct of the methane oxidation. Water has been shown to inhibit catalytic oxidation of methane to MeTFA by cobalt salts.[19a] Indeed, it is possible that instead of direct formation of MeTFA from methane, MeOH could be formed and undergo solvolysis with HTFA *in situ* to yield MeTFA and water (Scheme), as solvolysis of MeOH to MeTFA was observed to occur promptly in pure HTFA even at room temperature (see Figure E2). However, adding water showed almost no effect on the activity of $Mn_2(HTFA)_4(TFA)_4$ for stoichiometric methane oxidation, with only a slightly larger standard deviation observed and yields overall remaining approximately the same (Scheme). Furthermore, in reaction conditions containing silica (SiO_2) as a desiccant, no improvement in yields of MeTFA was observed (Figure E3). We hypothesize that rather than forming free water, the reaction could yield a hydroxo group that remains

coordinated to Mn, poisoning the metal and preventing it from turning over catalytically (Scheme).

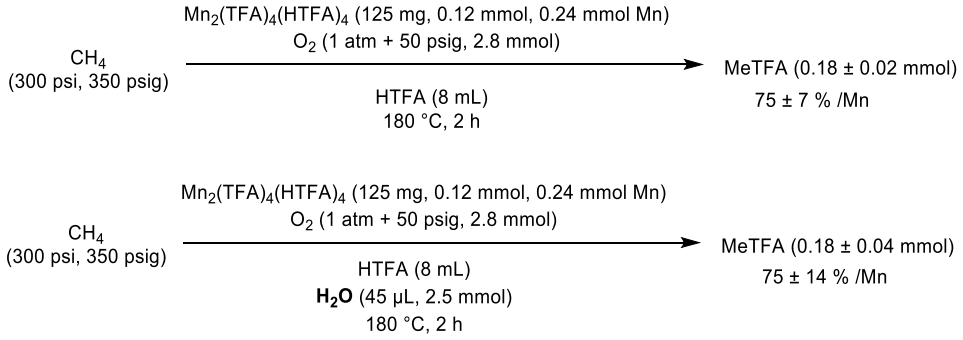

Scheme 6.4: Experiments to probe the effect of H_2O on the activity of $Mn_2(HTFA)_4(TFA)_4$ for methane oxidation in the presence of O_2. Conditions: CH_4 (300 psi, or 350 psig as it was pressurized after pressurizing with 50 psig O_2), HTFA (8 mL), 180 °C, 2 h. Standard deviations are based on at least three independent experiments.

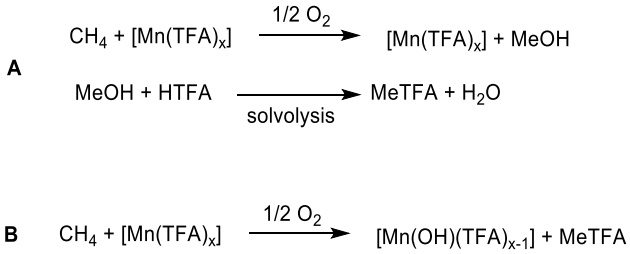

Scheme 6.5: Possible pathways for the oxidation of methane to MeTFA using a $[Mn(TFA)_x]$ complex as the active center in HTFA. The reaction might proceed either through formation of MeOH followed by solvolysis, forming water as a byproduct (**A**), or direct formation of MeTFA, leaving a hydroxo ligand on the Mn (**B**).

$MnOx_{red}$ samples resulting from the oxidation of methane with either MnO_2, Mn_2O_3, MnO or $Mn_2(HTFA)_4(TFA)_4$ were obtained as shown above (Scheme). Since we were unable to grow crystals of $MnOx_{red}$ large enough for single-crystal X-ray diffraction and

UV-Vis spectroscopy was inconclusive, we attempted to further characterize $MnOx_{red}$ using X-ray Absorption Spectroscopy (XAS). The X-ray absorption near edge structure (XANES) spectra of all reacted $MnOx_{red}$ samples are shown in Figure 6.8 (left) in addition to the spectra from a few Mn references.

Using the Mn references, Mn in each oxidation state shows distinctly different features with a stronger white line for the Mn species in lower formal oxidation states. The Mn absorption edges of all the reacted samples are located between Mn(II) and Mn(III), but most are closer to that of Mn(II). In the extended X-ray absorption fine structure (EXAFS) spectra (Figure 6.8, right) side, similar features at 1.6 Å and 3.1 Å (before phase correction) were observed for all the reacted Mn samples, supporting our suggestion that all Mn precursors converge to the same or similar spent oxidant.

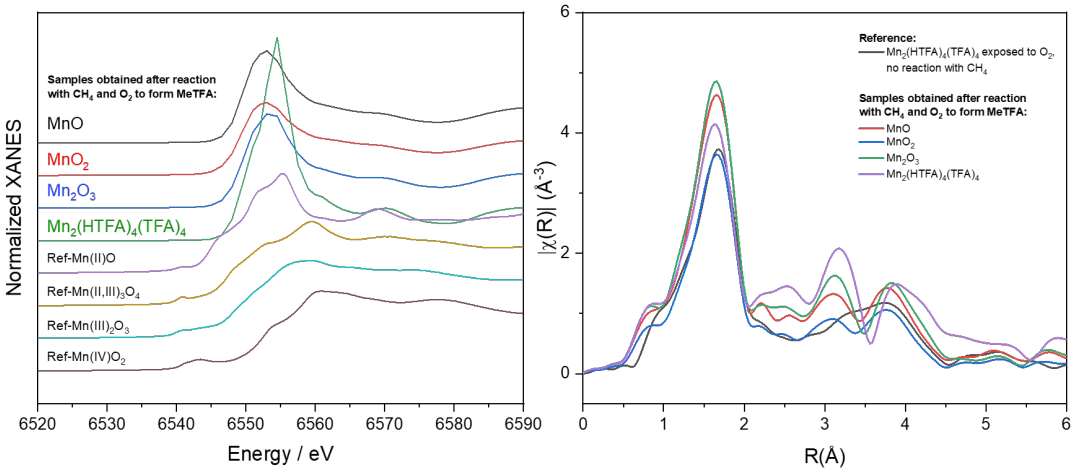

Figure 6.8: Plot of XANES (left) and the R-space EXAFS (right) data for the Mn K-edge of different samples of "spent" Mn oxidant from reactions with methane.

6.3.3 Enabling Catalytic Turnover

In the presence of trifluoroacetic anhydride (TFAA) and O_2, we observed catalytic turnover using MnO_2 for methane oxidation to MeTFA in HTFA with ~16% conversion and ~1.4 turnovers (TOs) per Mn atom after 4 hours (Scheme .6). Since we demonstrated that water is not likely detrimental to the activity of Mn oxides or $Mn_2(HTFA)_4(TFA)_4$, and that the addition of a desiccant did not improve activity (Figure E3), we believe the role of TFAA is not that of a desiccant, but rather that TFAA might enable the reactivation of $MnOx_{red}$. With the incorporation of TFAA, using $Mn_2(HTFA)_4(TFA)_4$ as precursor we were able to reach a methane conversion to MeTFA of ~34% with ~6 TOs per Mn atom or ~12 TOs per starting Mn dimer (Scheme).

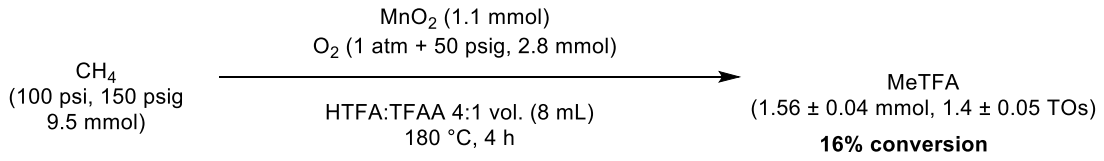

Scheme 6.6: TFAA enables catalytic turnover using MnO_2 for methane oxidation in the presence of O_2. Conditions: CH_4 (100 psi or 150 psig as it was pressurized after pressurizing with 50 psig O_2), HTFA:TFAA 4:1 vol. ratio (8 mL), 180 °C, 4 h. Standard deviations were calculated based on at least three independent experiments.

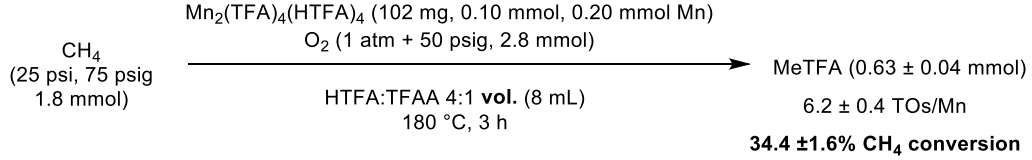

Scheme 6.7: Using $Mn_2(HTFA)_4(TFA)_4$ for the conversion of methane to MeTFA in the presence of O_2. Conditions: CH_4 (25 psi or 75 psig as it was pressurized after pressurizing with 50 psig O_2), HTFA:TFAA 4:1 vol. ratio (8 mL), 180 °C, 3 h. Standard deviations were calculated based on at least three independent experiments.

Under the conditions of Scheme , we investigated the selectivity of the reaction. Injection of the headspace of the reactor in GC-TCD revealed the presence of CO_2 (3.05 mmol), but CO was not observed (Figure E4). To assess whether CO_2 originates from HTFA or TFAA degradation or methane over-oxidation, an experiment was performed under similar conditions using $^{13}CH_4$ enriched methane. While the conditions of the experiment had to be adapted on account of the low pressure in the commercial $^{13}CH_4$ cylinder, 20% conversion to $^{13}CH_3TFA$ was observed, as assessed by ^1H NMR spectroscopy. The resultant headspace from this labelled reaction was injected into a GC-TCD to assess the overall amount of formed CO_2, and into a GC-MS to assess the ratio of formed $^{12}CO_2/^{13}CO_2$. We found that 1.4% of the CO_2 was $^{13}CO_2$, close to the natural abundance of ^{13}C (1.1%), leading to the conclusion that most of the CO_2 was formed from degradation of HTFA or TFAA rather than from over-oxidation of $^{13}CH_4$. This information, taken with the fact that we did not observe any intermediate oxidation products (e.g., CO, HCO_2H, HC(O)H) and that MeTFA is quite stable under reaction conditions provides strong evidence that this reaction is very selective ($> 90\%$) for methane mono-oxidation to MeTFA. Furthermore, the methane to MeTFA conversion was found to scalable with ~40% methane conversion to MeTFA observed in a 300 mL reactor (Figure E5).

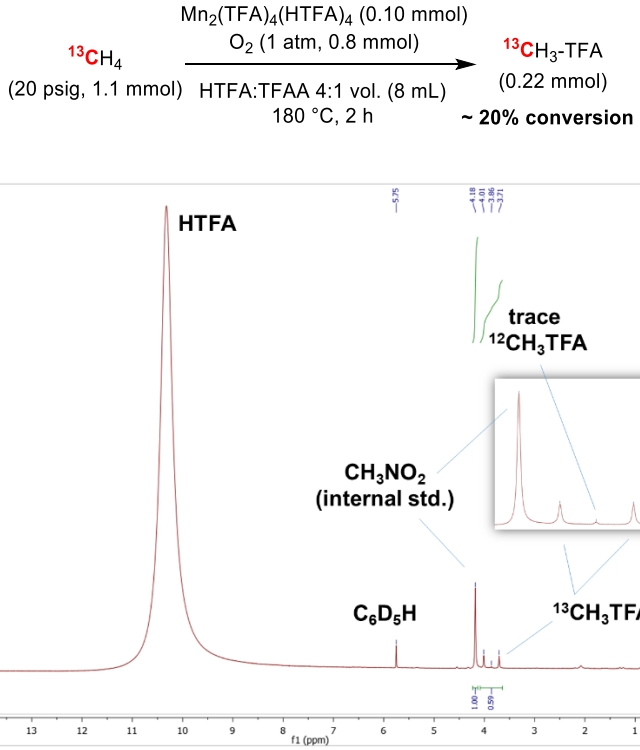

Figure 6.9: ^{1}H NMR spectrum from the reaction with $^{13}CH_4$. Conditions: $^{13}CH_4$ (20 psig), HTFA:TFAA 4:1 vol. ratio (8 mL), 180 °C, 2 h. A doublet for $^{13}CH_3TFA$ peak centred around 3.86 ppm is observed because of the ^{13}C-^{1}H coupling ($^{1}J_{13C\text{-}1H}$ = 150 Hz). Trace $^{12}CH_3TFA$ is observed at 3.86 ppm, resulting from the incomplete isotopic enrichment of $^{13}CH_4$.

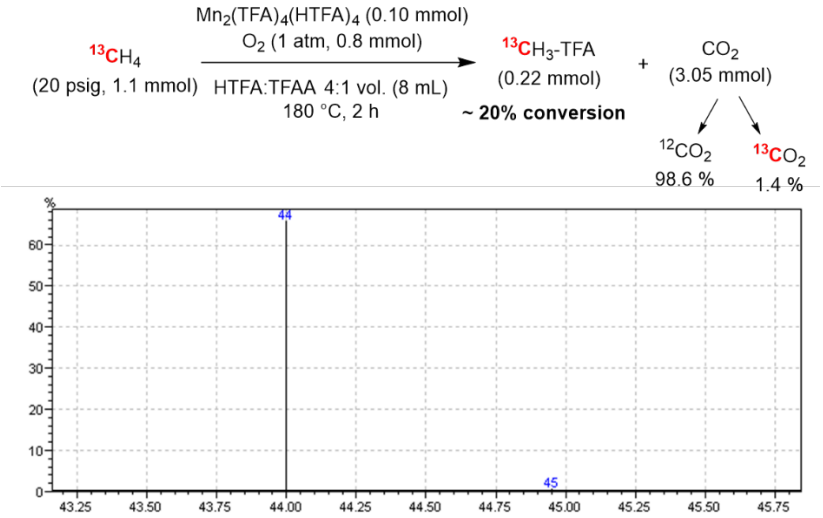

Figure 6.10: Reaction of $Mn_2(TFA)_4(HTFA)_4$ with $^{13}CH_4$ and GC-MS showing the m/z 44 ($^{12}CO_2$) and 45 ($^{13}CO_2$) signals. These data indicate that 1.4% of CO_2 in the headspace of the reaction is $^{13}CO_2$. Overall CO_2 was quantified using GC-TCD. Conditions: $^{13}CH_4$ (20 psig), 0.10 mmol $Mn_2(TFA)_4(HTFA)_4$, HTFA:TFAA 4:1 vol. ratio (8 mL), 180 °C, 2 h.

6.3.4 Elucidation of the Catalytic Mechanism

Experimental results provide insight into a possible catalytic mechanism. We have shown that the starting coordination environment is the binuclear $Mn_2(TFA)_4(HTFA)_4$, which has been isolated experimentally and characterized through single crystal X-ray diffraction. XAS studies have shown that this binuclear species undergoes ligand exchange when exposed to O_2, resulting in no significant change in the formal oxidation state, suggesting that Mn^{IV} and Mn^{V} are not formed and that the Mn in the catalytic cycle remains mostly as Mn^{II} and/or Mn^{III}. Additionally, the EXAFS data indicate the likely presence of 7 oxygen atoms within the first solvent shell of the Mn centers after the complex was exposed to O_2. This decreased coordination number upon exposure to O_2 from 8 to 7 is suggestive of the loss of the bimetallic character of the Mn complex to generate a monometallic Mn complex with de-ligation of two bridging TFA ligands, possibly replaced by a bridging O_2 (Figure 6.11). We hypothesize that this bridging O_2 would then undergo homolysis to yield two monometallic Mn complexes with either oxo or hydroxo ligands, as previously proposed for bimetallic Mn complexes reacting with O_2.[22a, 28] With this hypothesis as a starting point, we utilized Density Functional Theory

(DFT) quantum mechanical calculations to probe possible pathways for Mn-catalyzed partial oxidation of methane to MeTFA.

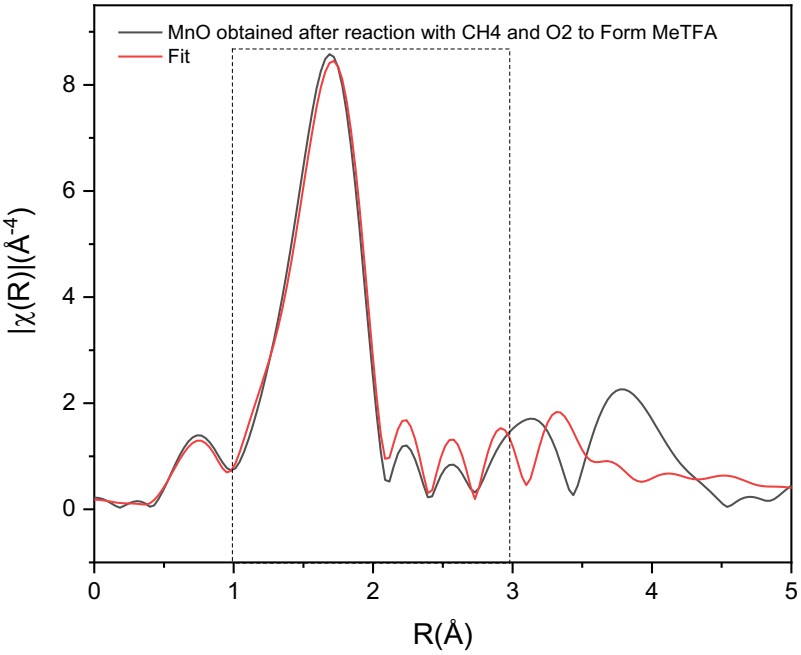

Figure 6.11: R-space data of spent oxidant obtained after reaction of MnO with CH_4 and O_2 to form MeTFA and fitting between 1Å and 3Å to obtain the coordination number of first coordination shell.

We examined the Mn^{III}, Mn^{IV}, and Mn^{V} barriers for hydrogen atom transfer (HAT) from methane to the Mn catalyst. Our DFT calculations utilized the MN15 functional[29] and the LACV3P**++ basis set;[30] more details can be found in the Methods section. Mn^{II}, Mn^{III}, Mn^{IV}, and Mn^{V} were modeled as sextet, quintet, quartet, and triplet, respectively. The $Mn^{III}(OH)(TFA)_2(HTFA)$ species has an HAT barrier of 14.3 kcal/mol; the $Mn^{III}(O)(TFA)(HTFA)_2$ has an HAT barrier of 18.6 kcal/mol (Figure E11). The HAT

barriers for $Mn^{IV}(O)(TFA)_2(HTFA)$ and $Mn^{IV}(OH)(TFA)_3$ are 8.9 and 15.3 kcal/mol, respectively. The HAT barriers for $Mn^{V}(O)(TFA)_3$ and $Mn^{V}(OH)(TFA)_4$ are 7.5 and 8.8 kcal/mol, respectively. The Mn^{IV} and Mn^{V} species have lower barriers than Mn^{III} for HAT from methane. However, formation of Mn^{IV} and Mn^{V} species was ruled out by XAS analysis (see above) and DFT calculations. Namely, the oxidation of the ground state Mn^{II} to either the Mn^{IV} or Mn^{V} species is too uphill in free energy. For example, oxidation of $Mn^{II}(TFA)_2(HTFA)_2$ to $Mn^{IV}(O)(TFA)_2(HTFA)_2$ by $\frac{1}{2}$ triplet O_2 is uphill 50.8 kcal/mol. Even under oxidizing conditions (applied potential of 1.85 V vs. SHE and a pH of -3), the oxidation of $Mn^{II}(TFA)_2(HTFA)(H_2O)$ to $Mn^{IV}(TFA)_3(OH)$ is uphill 25 kcal/mol (Figure E6). Thus, we rule out Mn^{IV} and Mn^{V} as potential catalysts and proceed with the full mechanistic study using the $Mn^{III}(OH)(TFA)_2(HTFA)$ as the active catalyst. The stoichiometry of the overall reaction is depicted in Scheme 6.8.

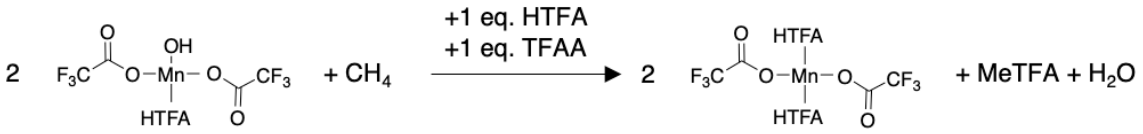

Scheme 6.8: The overall reaction for conversion of methane to MeTFA involving two equivalents of $Mn^{III}(OH)(TFA)_2(HTFA)$. The reaction requires one equivalent of TFAA and 1 equivalent of HTFA. Two HTFA molecules are consumed during the reaction; however, one molecule of HTFA is also generated.

The energy of $Mn^{III}(OH)(TFA)_2(HTFA)$ (**A**) is set to 0.0 kcal/mol since it is the likely Mn starting state. Beginning with $Mn^{III}(OH)(TFA)_2(HTFA)$, HAT from CH_4 to generate the methyl radical and $Mn^{II}(OH_2)(TFA)_2(HTFA)$ (**TS1**, quintet) requires a barrier of 14.3 kcal/mol. The formation of $Mn^{II}(OH_2)(TFA)_2(HTFA)$ and methyl radical is exergonic, releasing 7.7 kcal/mol (**B** + **C2**). $Mn^{II}(OH_2)(TFA)_2(HTFA)$ is then expected to undergo solvolysis in HTFA to yield $Mn^{II}(TFA)_2(HTFA)_2$ and a free water molecule (**D2**). Starting from $Mn^{II}(OH_2)(TFA)_2(HTFA)$, this process is uphill 7.2 kcal/mol. The generation of methyl radical opens several avenues towards formation of MeTFA. The methyl radical is unlikely to react with a free TFA^- anion in solution (see Figure E7), as this would require a free energy barrier of 23.8 kcal/mol relative to the Mn^{III} starting state. We find that it is more likely that the methyl radical reacts with a TFA ligand bound to the Mn center. This pathway would generate the MeTFA product, while reducing Mn^{III} to Mn^{II}, and this step is predicted by our calculations to occur with a large thermodynamic driving force. We examined the reaction between a methyl radical and a TFA ligand already bound to one equivalent of $Mn^{III}(OH)(TFA)_2(HTFA)$ to generate $Mn^{II}(OH_2)(TFA)(HTFA)(MeTFA)$ (**C1**, sextet). This pathway requires a free energy barrier of 13.6 kcal/mol and is -62.3 kcal/mol downhill; we found that upon formation, MeTFA simultaneously dissociates from the Mn center, leaving an open coordination site. Following MeTFA formation at -62.3 kcal/mol, the open coordination site on the Mn is

occupied by HTFA to generate $Mn^{II}(OH)(TFA)(HTFA)_2$ (**D1**), which we propose is likely the major component of $MnOx_{Red}$ (see above). The coordination of HTFA to $Mn^{II}(OH)(TFA)(HTFA)$ is calculated to be favorable by -15.9 kcal/mol, resulting in a free MeTFA and $Mn^{II}(OH)(TFA)(HTFA)_2$ at -78.1 kcal/mol relative to $Mn^{III}(OH)(TFA)_2(HTFA)$.

At this point, the conversion of CH_4 to MeTFA is complete with a reduction of two equivalents of Mn^{III} to Mn^{II}, which bears a hydroxo ligand that needs to be displaced to generate $Mn^{II}(TFA)_2(HTFA)_2$. In the absence of TFAA, experimental results suggest that this conversion does not happen, limiting the theoretical maximum yield of the reaction to the quantitative formation of MeTFA as a function of the amount of Mn (yield = $\frac{n_{MeTFA}}{n_{Mn}} \times 100$). In the presence of TFAA, displacement of the hydroxo ligand is expected to occur through reaction of Mn^{II}-OH with a TFAA molecule to generate a TFA ligand bound to the Mn and a free HTFA molecule in a reaction analogous to a simple hydrolysis of TFAA, but reacting with Mn^{II}-OH rather than H-OH. The reaction of TFAA with $Mn^{II}(OH)(TFA)(HTFA)_2$ to generate free HTFA and $Mn(TFA)_2(HTFA)_2$ (**E**) is 26.3 kcal/mol downhill. With this reaction, $MnOx_{Red}$ reacts to form $Mn^{II}(TFA)_2(HTFA)_2$, two equivalents of which form our starting catalyst precursor, $Mn_2(TFA)_4(HTFA)_4$, and the reaction is able to turn over. The proposed overall catalytic reaction and the corresponding free energy surface are shown in Scheme 6.9. One step in the reaction that we did not

include above is the oxidation of the catalyst by O_2. Our experiments clearly show that O_2 oxidizes Mn in solution at ambient and elevated conditions. However, DFT struggles to replicate the facile Mn oxidation by O_2. We attribute this to inability of DFT to describe the triplet ground state of O_2.[31] Consequently, we did not investigate in detail the oxidation of Mn(II) by O_2 with DFT.

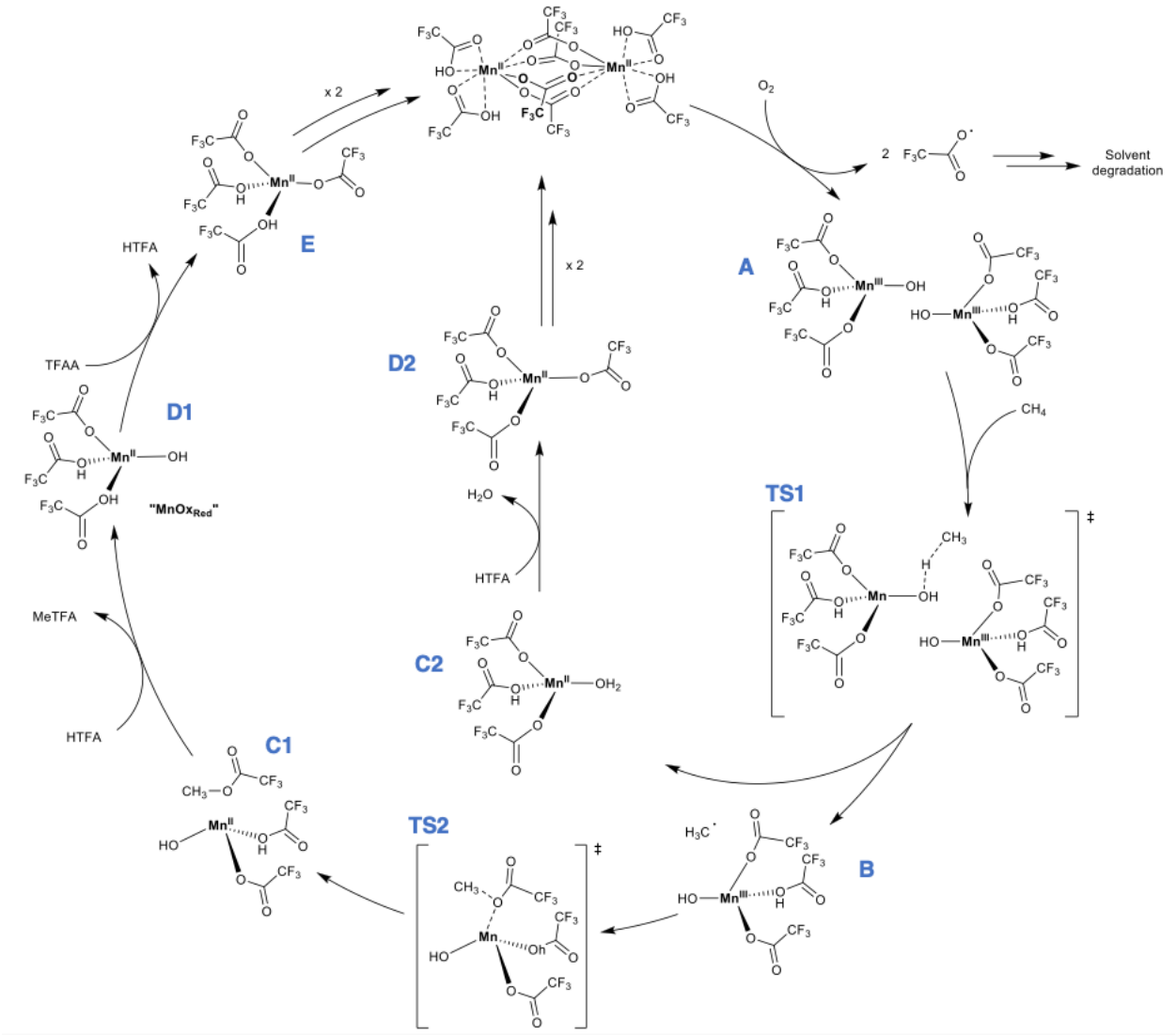

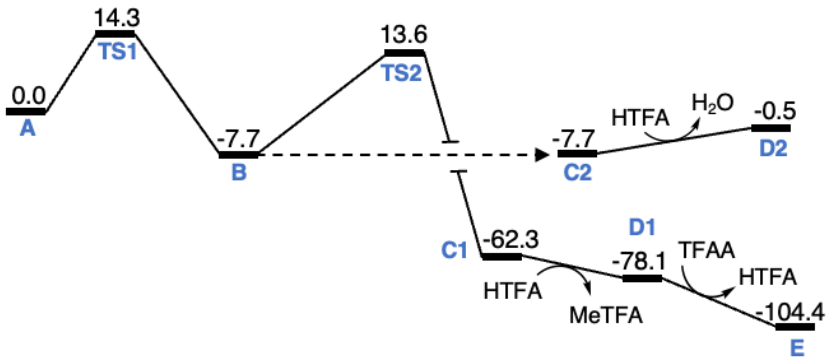

Scheme 6.9: Proposed catalytic cycle for the oxidation of methane to MeTFA, with activation of $Mn_2(HTFA)_4(TFA)_4$, formation of a Mn-OH containing species regenerated through reaction with TFAA to yield $Mn_2(HTFA)_4(TFA)_4$. DFT-predicted free energies at 473.15 K are shown below the overall cycle.

One potential issue with the Mn mediated alkane partial oxidation in HTFA is the selectivity of Mn towards MeTFA formation versus solvent decomposition. We experimentally observed formation of 0.22 mmol MeTFA over 2 hours at 180 °C; the same experiment also produced 3.01 mmol of CO_2 with $>$ 98.6% of the CO_2 arising from solvent decomposition, making solvent degradation a key issue to be addressed. Energetics for the solvent decomposition mechanism are depicted in Figure E9.

6.4 Conclusions

We report the use of simple manganese precursors for the selective, catalytic oxidation of light alkanes towards mono-esters. Of particular interest, dioxygen is found to act as the terminal oxidant in the catalytic oxidation of methane to MeTFA using $Mn_2(HTFA)_4(TFA)_4$ as catalyst with nearly 35% methane conversion and near quantitative selectivity observed at 6 catalytic turnovers (per Mn atom, 12 TOs based on

the Mn dimer, $Mn_2(HTFA)_4(TFA)_4$). The MeTFA formed is found to be stable under reaction conditions. Using isotopic labeling experiments, EXAFS and DFT calculations, we propose a mechanism that accounts for the observed results and renders explicit the contributions of solvent and Mn active center. In the proposed reaction pathway, a Mn(III) hydroxide complex is responsible for methane C–H bond breaking, which is followed by rebound of methyl radical to generate MeTFA. We find that addition of trifluoroacetic anhydride is necessary to recycle the molecular Mn catalyst to the starting state, $Mn_2(HTFA)_4(TFA)_4$.

6.5 Experimental Methods

Many of the reagents and conditions described herein are hazardous. Trifluoroacetic acid (HTFA) is highly corrosive and should be handled inside a fume hood with long nitrile gloves covering up to the elbow. Dioxygen/hydrocarbon mixtures can be explosive. Appropriate safety procedures should be consulted prior to handling concentrated acids, strong oxidants, and mixtures of hydrocarbon substrates and dioxygen.

General considerations. All reactions were carried out under ambient atmosphere unless otherwise stated. Trifluoroacetic acid (HTFA), trifluoroacetic anhydride(TFAA), manganese(IV) dioxide (MnO_2), manganous(II) oxide (MnO), dimanganese(III) trioxide (Mn_2O_3), manganese(II) chloride ($MnCl_2$), trimanganese(II, III) tetraoxide (Mn_3O_4), silica gel (SiO_2), nitromethane (CH_3NO_2), glacial acetic acid (HOAc), iodine (I_2), and potassium

chloride (KCl) were purchased from commercial sources and used as received. To be used as a desiccant, SiO_2 was dried overnight in a vacuum oven at 125 °C, purged with three dinitrogen/vacuum cycles and used immediately. Methane, ethane, oxygen and argon were purchased from GTS-Welco and used as received. ^{13}C-methane was purchased from Sigma in a low-pressure lecture bottle and used as received.

Assessment of methane oxidation. Under standard conditions, an 8 mL high pressure reactor fabricated in house was charged with a stir bar, specified oxidant and HTFA (8 mL, 104.5 mmol). The reactor was then sealed and pressurized with alkane (methane or ethane) at 300 psig. The reactors were placed on a stir plate and heated to 180°C unless otherwise mentioned. Following the reaction, the reactor was cooled under air flow over 30 minutes. Internal standard, either CH_3NO_2 or HOAc, was added to the reaction mixture in a known concentration to allow for quantification of products by ^{1}H NMR.[17a, 18a] ^{1}H NMR spectra were recorded on a Bruker 500 MHz NMR spectrometer, using a capillary tube filled with C_6D_6 as an internal lock reference. Chemical shifts in HTFA are reported relative to CH_3NO_2 (^{1}H NMR δ 4.18 ppm) added after the reaction. Unless otherwise mentioned, reactions were carried out in air. When air was excluded, the reactors were charged using a N_2 glove box and Schlenk line using N_2 degassed HTFA. When needed, dry O_2 was added by bubbling the vessel for 10 minutes and if necessary, pressurized O_2 was added. When needed, N_2-degassed H_2O was added through cannula

transfer from a N_2-purged Schlenk flask. For other experiments, including attempts at high conversion of alkane to alkyl ester and in order to reach catalytic turnover, these standard reaction conditions were modified as described below.

High conversion conditions. For high conversion under stoichiometric conditions, the reactor was pressurized with a lower amount of methane (20-50 psig) and the amount of oxidant (Mn_2O_3) was increased to a large excess (10 mmol), along with that of iodine (0.5 mmol). Reactor temperature was increased to 185°C, and reaction time extended to 5 hours. For catalytic reaction conditions and high conversion under catalytic conditions, the solvent was 8 mL of a 4:1 vol. mixture of HTFA and TFAA rather than neat HTFA. Reaction time was in some cases shortened from 5 h to 4 h.

Assessment of MeTFA stability under reaction conditions. For assessment of the stability of MeTFA in the presence of MnO_2, a pressure reactor was charged with a stir bar, MeTFA (0.63 mmol), MnO_2 (1.1 mmol), I_2 (0.15 mmol), and HTFA (8 mL). The reactor was sealed and pressurized with argon and heated to 140°C. Following the reaction, the reactor was cooled and vented. Internal standard was added to the reaction mixture, and the mixture was stirred. An aliquot was removed for centrifugation, and the supernatant was used for ^{1}H NMR analysis.

Synthesis of $Mn_2(HTFA)_4(TFAA)_4$. $Mn_2(HTFA)_4(TFAA)_4$ was synthesized following a published procedure,[27] and crystals were characterized by single-crystal X-Ray

diffraction. Briefly, $MnCl_2$ was heated in a mixture of HTFA and TFAA over 72 to 96 hours, and $Mn_2(HTFA)_4(TFAA)_4$ crystallized out of solution upon cooling. This synthesis was amenable to a multiple gram scale.

GC-TCD for overall quantification of CO_2 in the headspace. GC-TCD data were obtained with a Shimadzu GC-2014 instrument equipped with a 500 mL injection loop in which the sample passed through three columns in series (Hayesep T 80/100 mesh 0.5 m × 2.0 mm, Supelco 60/80 Mesh 5 Å molecular sieve 2.0 m × 2.1 mm, and Hayesep Q 80/100 mesh 1.5 m × 2.0 mm). The detector temperature was 200 °C, the current was 100 mA and the column temperature was 75 °C. Injector temperature was 68 °C. The resulting integration yielded an amount of CO_2 as a volumetric fraction of total headspace, using independently measured calibration curves established from standards prepared with known volumetric fractions of CO_2 in CH_4. Consistent detector response was observed when using CO_2/CH_4 mixtures or CO_2/N_2 mixtures or CO_2/O_2 mixtures, with a given % vol. of CO_2 yielding statistically identical peak integration. These volumetric fractions were then converted to an amount of substance using total headspace volume, measured by submitting the sampling bag to Archimedes' principle. CO_2 elutes at 1.8 min.

GC-MS for isotopic ratio determination of CO_2 in the headspace. GC/MS was performed using a Shimadzu GCMS-QP2010 Plus system with a Restek RT-Qbond 30 m

× 8 mm fused silica PLOT column with 8 μm thickness using electron impact ionization. A portion (1 mL) of the headspace was injected to GC−MS to determine the amount of $^{13}CO_2$ produced. GC-MS Parameters: starting temperature: 40 °C; time at starting temp: 3 min; ramp: 20 °C/min up to 200 °C; flow rate (carrier): 3.01 mL/min (He); split ratio: 10:1; inlet temperature: 200 °C; detector ion source temperature: 200 °C, interface temperature: 230 °C. CO_2 elutes at 2.97 min.

XPS. A PHI Versaprobe III Imaging X-ray Photoelectron Spectrometer (XPS) was used for compositional and chemical analysis of the sample near-surface region. The base pressure of this instrument is $< 10^{-8}$ Pa. Data was collected from a 200 μm spot over a range of 1100 – 0 eV in 1 eV steps at a pass energy of 55 eV (energy resolution = ~1% of pass energy), with a dwell time of 50 ms over 8 cycles. Dual neutralization of the surface during analysis was provided by simultaneous irradiation with an electron flood-gun and low energy (10 eV) Ar ions.

EXAFS. Samples for EXAFS were prepared as follows: 8 mL high pressure reactors were charged with a stir bar, 1.1 mmol of Mn oxidant (MnO, MnO_2, Mn_2O_3 or $Mn_2(HTFA)_4(TFA)_4$) and HTFA (8 mL, 104.5 mmol). The reactors were sealed and pressurized with 300 psig of methane, then placed on a stir plate and heated to 180 °C for 4 hours. Following the reaction, the amount of formed MeTFA was assessed as described above and the remaining reaction medium was worked up under N_2 atmosphere: first it

was filtered to remove solids, then the bulk of the solvent was removed under reduced pressure before thorough drying for 14 hours in a vacuum oven at 60 °C. The obtained powders were stored under Ar until they were characterized by X-ray absorption spectroscopy. X-ray absorption spectra were collected with transmission mode at beamline 12-BM-B at the Advanced Photon Source of Argonne National Laboratory, which is equipped with a fixed-exit, double-crystal Si (111) monochromator with Pt coated toroidal and flat mirrors. The beam was detuned by 30% to reduce harmonic content of the beam. A reference X-ray absorption spectrum of Mn K-edge spectrum was simultaneously collected using Mn foil. X-ray absorption data was analyzed using IFEFFIT-Athena and Artemis.

Single crystal X-ray diffraction. A colorless plate-like crystal of $Mn_2(TFA)_4(HTFA)_4$ was coated with Paratone oil and mounted on a MiTeGen MicroLoop. The X-ray intensity data were measured on a Bruker Kappa APEXII Duo system equipped with a fine-focus sealed tube (Mo K_α, $\lambda = 0.71073$ Å) and a graphite monochromator. The total exposure time was 9.38 hours. The frames were integrated with the Bruker SAINT software package[32] using a narrow-frame algorithm. Data were corrected for absorption effects using the Multi-Scan method (SADABS).[32] The structure was solved and refined using the Bruker SHELXTL Software Package[33] within APEX3[32] and OLEX2.[34] Non-hydrogen atoms were refined anisotropically. Hydrogen atoms were located in the electron density

map and refined isotropically. Two CF_3 groups were found to be disordered. The relative occupancies of each position were freely refined, with constraints and restraints anisotropic displacement parameters and bond lengths of the disordered atoms. Crystallographic data is summarized in the Table E2. CCDC 2131612 contains the supplementary crystallographic data for this paper. This data can be obtained free of charge from The Cambridge Crystallographic Data Centre via https://www.ccdc.cam.ac.uk/structures.

6.6 Computational Methods

All DFT calculations were performed using the Jaguar v10.9 software by Schrodinger Inc. Structure optimizations were performed using MN15 flavour of DFT. Non-metal atoms were described using the 6-311G**++ basis set, while metal atoms (Mn) were described by the Los Alamos small-core pseudopotential augmented with diffuse and polarization functions (designated LACV3P**++ in Jaguar). Ultra-fine DFT grids were used for all calculations. Frequency calculations at 473 K were performed at the MN15/LACV3P**++ level in order to predict thermochemical properties such as enthalpies and entropies. Frequency calculations also served to confirm intermediates (no imaginary mode) and transition states (1 imaginary mode). All calculations included implicit solvent treatment. Solvent effects were implemented via the Poisson-Boltzmann

finite element method (PBF). A probe radius of 1.40 angstroms and a bulk dielectric constant of 8.55 were used to describe an HTFA solvent.

6.7 References

1. Caulton, D. R.; Shepson, P. B.; Cambaliza, M. O. L.; McCabe, D.; Baum, E.; Stirm, B. H., Methane Destruction Efficiency of Natural Gas Flares Associated with Shale Formation Wells. *Environmental Science & Technology* **2014,** *48* (16), 9548-9554.

2. Alvarez, R. A.; Zavala-Araiza, D.; Lyon, D. R.; Allen, D. T.; Barkley, Z. R.; Brandt, A. R.; Davis, K. E.; Herndon, S. C.; Jacob, D. J.; Karion, A.; Kort, E. A.; Lamb, B. K.; Lauvaux, T.; Maasakkers, J. D.; Marchese, A. J.; Omara, M.; Pacala, S. W.; Townsend-Small, A.; Wofsy, S. C.; Hamburg, S. P., Assessment of methane emissions from the U.S. oil and gas supply chain. *Science* **2018,** *361*, 186-188.

3. Lunsford, J. H., Catalytic conversion of methane to more useful chemicals and fuels: a challenge for the 21st century. *Catal. Today* **2000,** *63* (2–4), 165-174.

4. Golombok, M.; Teunissen, W., A Chemical Alternative to Natural Gas Flaring. *Ind. Eng. Chem. Res.* **2003,** *42*, 5003-5006.

5. (a) Webb, J. R.; Bolaño, T.; Gunnoe, T. B., Catalytic Oxy-Functionalization of Methane and Other Hydrocarbons: Fundamental Advancements and New Strategies. *ChemSusChem* **2011,** *4* (1), 37-49; (b) Olah, G. A.; Goeppert, A.; Prakash, G. K. S., *Beyond Oil and Gas: The Methanol Economy, Second Edition*. Wiley: 2009; (c) Olah, G. A., Crossing Conventional Boundaries in Half a Century of Research. *The Journal of*

Organic Chemistry **2005,** *70* (7), 2413-2429; (d) Baek, J.; Rungtaweevoranit, B.; Pei, X.; Park, M.; Fakra, S. C.; Liu, Y.-S.; Matheu, R.; Alshmimri, S. A.; Alshehri, S.; Trickett, C. A.; Somorjai, G. A.; Yaghi, O. M., Bioinspired Metal–Organic Framework Catalysts for Selective Methane Oxidation to Methanol. *J. Am. Chem. Soc.* **2018,** *140* (51), 18208-18216; (e) Liu, W.-C.; Baek, J.; Somorjai, G. A., The Methanol Economy: Methane and Carbon Dioxide Conversion. *Top. Catal.* **2018,** *61* (7), 530-541.

6. (a) Gunsalus, N. J.; Koppaka, A.; Park, S. H.; Bischof, S. M.; Hashiguchi, B. G.; Periana, R. A., Homogeneous Functionalization of Methane. *Chem. Rev.* **2017,** *117* (13), 8521-8573; (b) Ravi, M.; Ranocchiari, M.; van Bokhoven, J. A., The Direct Catalytic Oxidation of Methane to Methanol—A Critical Assessment. *Angew. Chem. Int. Ed.* **2017,** *56* (52), 16464-16483; (c) Olivos-Suarez, A. I.; Szécsényi, À.; Hensen, E. J. M.; Ruiz-Martinez, J.; Pidko, E. A.; Gascon, J., Strategies for the Direct Catalytic Valorization of Methane Using Heterogeneous Catalysis: Challenges and Opportunities. *ACS Catalysis* **2016,** *6* (5), 2965-2981.

7. Horn, R.; Schlögl, R., Methane Activation by Heterogeneous Catalysis. *Catal. Lett.* **2015,** *145* (1), 23-39.

8. (a) Gunnoe, T. B., Metal-Mediated Carbon-Hydrogen Bond Activation. In *Physical Inorganic Chemistry: Reactions, Processes, and Appications*, Bakac, A., Ed. John Wiley & Sons: Hoboken, New Jersey, 2010; pp 495-549; (b) Feray, L.; Kuznetsov, K.; Renaud,

P., Hydrogen Atom Abstraction. In *Radicals in Organic Synthesis*, Renaud, P.; Sibi, M. P., Eds. Wiley-VCH: New York, NYvolu, 2008; Vol. 2; (c) Webb, J. R.; Burgess, S. A.; Cundari, T. R.; Gunnoe, T. B., Activation of carbon–hydrogen bonds and dihydrogen by 1,2-CH-addition across metal–heteroatom bonds. *Dalton Trans.* **2013,** *42* (48), 16646-16665; (d) Meng, X.; Cui, X.; Rajan, N. P.; Yu, L.; Deng, D.; Bao, X., Direct Methane Conversion under Mild Condition by Thermo-, Electro-, or Photocatalysis. *Chem* **2019,** *5* (9), 2296-2325; (e) Han, B.; Yang, Y.; Xu, Y.; Etim, U. J.; Qiao, K.; Xu, B.; Yan, Z., A review of the direct oxidation of methane to methanol. *Chinese Journal of Catalysis* **2016,** *37* (8), 1206-1215; (f) Stahl, S. S.; Labinger, J. A.; Bercaw, J. E., Homogeneous Oxidation of Alkanes by Electrophilic Late Transition Metals. *Angew. Chem. Int. Ed.* **1998,** *37* (16), 2180-2192; (g) Crabtree, R. H., Alkane C–H activation and functionalization with homogeneous transition metal catalysts: a century of progress—a new millennium in prospect. *J. Chem. Soc., Dalton Trans.* **2001,** (17), 2437-2450; (h) Lersch, M.; Tilset, M., Mechanistic Aspects of C−H Activation by Pt Complexes. *Chem. Rev.* **2005,** *105* (6), 2471-2526; (i) Cavaliere, V. N.; Mindiola, D. J., Methane: a new frontier in organometallic chemistry. *Chem. Sci.* **2012,** *3* (12), 3356-3365.

9. Lin, R.; Amrute, A. P.; Pérez-Ramírez, J., Halogen-Mediated Conversion of Hydrocarbons to Commodities. *Chem. Rev.* **2017,** *117*, 4182-4247.

10. Zichittella, G.; Paunović, V.; Amrute, A. P.; Pérez-Ramírez, J., Catalytic Oxychlorination versus Oxybromination for Methane Functionalization. *ACS Catalysis* **2017,** *7* (3), 1805-1817.

11. (a) Periana, R. A.; Taube, D. J.; Gamble, S.; Taube, H.; Satoh, T.; Fujii, H., Platinum Catalysts for the High-Yield Oxidation of Methane to a Methanol Derivative. *Science* **1998,** *280* (5363), 560-564; (b) Shilov, A. E.; Shul'pin, G. B., Activation of C−H Bonds by Metal Complexes. *Chem. Rev.* **1997,** *97* (8), 2879-2932; (c) Shteinman, A. A., Shilov alkane platinum chemistry: 45 years. *Journal of Organometallic Chemistry* **2015,** *793*, 34-40; (d) Periana, R. A.; Taube, D. J.; Evitt, E. R.; Löffler, D. G.; Wentrcek, P. R.; Voss, G.; Masuda, T., A Mercury-Catalyzed, High-Yield System for the Oxidation of Methane to Methanol. *Science* **1993,** *259* (5093), 340-343; (e) Jones, C.; Taube, D.; Ziatdinov, V. R.; Periana, R. A.; Nielsen, R. J.; Oxgaard, J.; Goddard III, W. A., Selective Oxidation of Methane to Methanol Catalyzed, with C-H Activation, by Homogeneous, Cationic Gold. *Angew. Chem. Int. Ed.* **2004,** *43* (35), 4626-4629; (f) Goldshleger, N.; Tyabin, M.; Shilov, A.; Shteinman, A., Activation of saturated hydrocarbons-deuterium-hydrogen exchange in solutions of transition metal complexes. *Russian Journal of Physical Chemistry* **1969,** *43* (8), 1222-+; (g) Shilov, A. E.; Shteinman, A. A., Activation of saturated hydrocarbons by metal complexes in solution. *Coord. Chem. Rev.* **1977,** *24* (2), 97-143; (h) Hodges, R. J.; Webster, D. E.; Wells, P. B., The activation of saturated

hydrocarbons by transition-metal complexes in solution. Part I. Hydrogen–deuterium exchange in alkanes catalysed by potassium tetrachloroplatinate(II) in acetic acid. *Journal of the Chemical Society A: Inorganic, Physical, Theoretical* **1971,** (0), 3230-3238.

12. (a) Crabtree, R. H., Organometallic alkane CH activation. *J. Organomet. Chem.* **2004,** *689* (24), 4083-4091; (b) Crabtree, R. H., A. E. Shilov's influence on early work in organometallic CH activation and functionalization. *J. Organomet. Chem.* **2015,** *793*, 41-46; (c) Labinger, J. A.; Bercaw, J. E., Mechanistic studies on the Shilov system: A retrospective. *J. Organomet. Chem.* **2015,** *793*, 47-53.

13. (a) Ahlquist, M.; Nielsen, R. J.; Periana, R. A.; Goddard III, W. A., Product Protection, the Key to Developing High Performance Methane Selective Oxidation Catalysts. *J. Am. Chem. Soc.* **2009,** *131* (47), 17110-17115; (b) Periana, R. A.; Taube, D. J.; Gamble, S.; Taube, H.; Satoh, T.; Fujii, H., Platinum Catalysts for the High-Yield Oxidation of Methane to a Methanol Derivative. *Science* **1998,** *280*, 560-564.

14. (a) Ahlquist, M.; Nielsen, R. J.; Periana, R. A.; Goddard Iii, W. A., Product Protection, the Key to Developing High Performance Methane Selective Oxidation Catalysts. *J. Am. Chem. Soc.* **2009,** *131* (47), 17110-17115; (b) Mironov, O. A.; Bischof, S. M.; Konnick, M. M.; Hashiguchi, B. G.; Ziatdinov, V. R.; Goddard, W. A.; Ahlquist, M.; Periana, R. A., Using Reduced Catalysts for Oxidation Reactions: Mechanistic Studies

of the "Periana-Catalytica" System for CH4 Oxidation. *J. Am. Chem. Soc.* **2013,** *135* (39), 14644-14658.

15. (a) Conley, B. L.; Tenn, W. J.; Young, K. J. H.; Ganesh, S. K.; Meier, S. K.; Ziatdinov, V. R.; Mironov, O.; Oxgaard, J.; Gonzales, J.; Goddard, W. A.; Periana, R. A., Design and study of homogeneous catalysts for the selective, low temperature oxidation of hydrocarbons. *Journal of Molecular Catalysis a-Chemical* **2006,** *251* (1-2), 8-23; (b) Michalkiewicz, B.; Ziebro, J.; Tomaszewska, M., Preliminary Investigation of Low Pressure Membrane Distillation of Methyl Bisulphate from Its Solutions in Fuming Sulphuric Acid Combined with Hydrolysis to Methanol. *J. Membr. Sci.* **2006,** *286* (1), 223-227.

16. (a) Fortman, G. C.; Boaz, N. C.; Munz, D.; Konnick, M. M.; Periana, R. A.; Groves, J. T.; Gunnoe, T. B., Selective Monooxidation of Light Alkanes Using Chloride and Iodate. *J. Am. Chem. Soc.* **2014,** *136* (23), 8393-8401; (b) Kalman, S. E.; Munz, D.; Fortman, G. C.; Boaz, N. C.; Groves, J. T.; Gunnoe, T. B., Partial Oxidation of Light Alkanes by Periodate and Chloride Salts. *Dalton Trans.* **2015,** *44*, 5294-5298; (c) Fu, R.; Nielsen, R. J.; Liebov, N. S.; Goddard, W. A.; Gunnoe, T. B.; Groves, J. T., DFT Mechanistic Study of Methane Mono-Esterification by Hypervalent Iodine Alkane Oxidation Process. *J. Phys. Chem. C* **2019,** *123* (25), 15674-15684.

17. (a) Schwartz, N. A.; Boaz, N. C.; Kalman, S. E.; Zhuang, T.; Goldberg, J. M.; Fu, R.; Nielsen, R. J.; Goddard, W. A.; Groves, J. T.; Gunnoe, T. B., Mechanism of Hydrocarbon Functionalization by an Iodate/Chloride System: The Role of Ester Protection. *ACS Catalysis* **2018,** *8* (4), 3138-3149; (b) Periana, R. A.; Mirinov, O.; Taube, D. J.; Gamble, S., High Yield Conversion of Methane to Methyl Bisulfate Catalyzed by Iodine Cations. *Chem. Commun.* **2002,** (20), 2376-2377.

18. (a) Liebov, N. S.; Goldberg, J. M.; Boaz, N. C.; Coutard, N.; Kalman, S. E.; Zhuang, T.; Groves, J. T.; Gunnoe, T. B., Selective Photo-Oxygenation of Light Alkanes Using Iodine Oxides and Chloride. *ChemCatChem* **2019,** *11* (20), 5045-5054; (b) Hirscher, N. A.; Ohri, N.; Yang, Q.; Zhou, J.; Anna, J. M.; Schelter, E. J.; Goldberg, K. I., A Metal-Free, Photocatalytic Method for Aerobic Alkane Iodination. *J. Am. Chem. Soc.* **2021,** *143* (46), 19262-19267.

19. (a) Strassner, T.; Ahrens, S.; Muehlhofer, M.; Munz, D.; Zeller, A., Cobalt-Catalyzed Oxidation of Methane to Methyl Trifluoroacetate by Dioxygen. *Eur. J. Inorg. Chem.* **2013,** *2013* (21), 3659-3663; (b) Vargaftik, M. N.; Stolarov, I. P.; Moiseev, I. I., Highly selective partial oxidation of methane to methyl trifluoroacetate. *J. Chem. Soc., Chem. Commun.* **1990,** (15), 1049-1050.

20. Munz, D.; Strassner, T., Alkane C–H Functionalization and Oxidation with Molecular Oxygen. *Inorg. Chem.* **2015,** *54* (11), 5043-5052.

21. (a) Umena, Y.; Kawakami, K.; Shen, J.-R.; Kamiya, N., Crystal structure of oxygen-evolving photosystem II at a resolution of 1.9 Å. *Nature* **2011,** *473* (7345), 55-60; (b) Requena, L.; Bornemann, S., Barley (Hordeum vulgare) oxalate oxidase is a manganese-containing enzyme. *The Biochemical journal* **1999,** *343 Pt 1* (Pt 1), 185-190; (c) Holley, A. K.; Bakthavatchalu, V.; Velez-Roman, J. M.; St Clair, D. K., Manganese superoxide dismutase: guardian of the powerhouse. *International journal of molecular sciences* **2011,** *12* (10), 7114-7162.

22. (a) Mayfield, J. R.; Grotemeyer, E. N.; Jackson, T. A., Concerted proton–electron transfer reactions of manganese–hydroxo and manganese–oxo complexes. *Chem. Commun.* **2020,** *56* (65), 9238-9255; (b) Larson, V. A.; Battistella, B.; Ray, K.; Lehnert, N.; Nam, W., Iron and manganese oxo complexes, oxo wall and beyond. *Nature Reviews Chemistry* **2020,** *4* (8), 404-419; (c) Deville, C.; Padamati, S. K.; Sundberg, J.; McKee, V.; Browne, W. R.; McKenzie, C. J., O2 Activation and Double C⊠H Oxidation by a Mononuclear Manganese(II) Complex. *Angew. Chem. Int. Ed.* **2016,** *55* (2), 545-549; (d) Sahu, S.; Goldberg, D. P., Activation of Dioxygen by Iron and Manganese Complexes: A Heme and Nonheme Perspective. *J. Am. Chem. Soc.* **2016,** *138* (36), 11410-11428.

23. (a) Wu, X.; Seo, M. S.; Davis, K. M.; Lee, Y.-M.; Chen, J.; Cho, K.-B.; Pushkar, Y. N.; Nam, W., A Highly Reactive Mononuclear Non-Heme Manganese(IV)–Oxo Complex That Can Activate the Strong C–H Bonds of Alkanes. *J. Am. Chem. Soc.* **2011,**

133 (50), 20088-20091; (b) Li, X.-X.; Guo, M.; Qiu, B.; Cho, K.-B.; Sun, W.; Nam, W., High-Spin Mn(V)-Oxo Intermediate in Nonheme Manganese Complex-Catalyzed Alkane Hydroxylation Reaction: Experimental and Theoretical Approach. *Inorg. Chem.* **2019,** *58* (21), 14842-14852; (c) Liu, W.; Cheng, M.-J.; Nielsen, R. J.; Goddard, W. A.; Groves, J. T., Probing the C–O Bond-Formation Step in Metalloporphyrin-Catalyzed C–H Oxygenation Reactions. *ACS Catalysis* **2017,** *7* (6), 4182-4188; (d) Huang, X.; Zhuang, T.; Kates, P. A.; Gao, H.; Chen, X.; Groves, J. T., Alkyl Isocyanates via Manganese-Catalyzed C–H Activation for the Preparation of Substituted Ureas. *J. Am. Chem. Soc.* **2017,** *139* (43), 15407-15413; (e) Huang, X.; Bergsten, T. M.; Groves, J. T., Manganese-Catalyzed Late-Stage Aliphatic C–H Azidation. *J. Am. Chem. Soc.* **2015,** *137* (16), 5300-5303; (f) Liu, W.; Huang, X.; Cheng, M.-J.; Nielsen, R. J.; Goddard, W. A.; Groves, J. T., Oxidative Aliphatic C-H Fluorination with Fluoride Ion Catalyzed by a Manganese Porphyrin. *Science* **2012,** *337* (6100), 1322-1325; (g) Tian, Z.; Fattahi, A.; Lis, L.; Kass, S. R., Cycloalkane and Cycloalkene C—H Bond Dissociation Energies. *J. Am. Chem. Soc.* **2006,** *128* (51), 17087-17092.

24. Chen, W.; Kocal, J. A.; Brandvold, T. A.; Bricker, M. L.; Bare, S. R.; Broach, R. W.; Greenlay, N.; Popp, K.; Walenga, J. T.; Yang, S. S.; Low, J. J., Manganese oxide catalyzed methane partial oxidation in trifluoroacetic acid: Catalysis and kinetic analysis. *Catal. Today* **2009,** *140* (3), 157-161.

25. Kalman, S. E.; Munz, D.; Fortman, G. C.; Boaz, N. C.; Groves, J. T.; Gunnoe, T. B., Partial oxidation of light alkanes by periodate and chloride salts. *Dalton Trans.* **2015,** *44* (12), 5294-5298.

26. (a) Biesinger, M. C.; Payne, B. P.; Grosvenor, A. P.; Lau, L. W. M.; Gerson, A. R.; Smart, R. S. C., Resolving surface chemical states in XPS analysis of first row transition metals, oxides and hydroxides: Cr, Mn, Fe, Co and Ni. *Appl. Surf. Sci.* **2011,** *257* (7), 2717-2730; (b) Toupin, M.; Brousse, T.; Bélanger, D., Influence of Microstucture on the Charge Storage Properties of Chemically Synthesized Manganese Dioxide. *Chem. Mater.* **2002,** *14* (9), 3946-3952.

27. Guntlin, C. P.; Zund, T.; Kravchyk, K. V.; Worle, M.; Bodnarchuk, M. I.; Kovalenko, M. V., Nanocrystalline FeF_3 and MF_2 (M = Fe, Co, and Mn) from metal trifluoroacetates and their Li(Na)-ion storage properties. *J. Mater. Chem. A* **2017,** *5* (16), 7383-7393.

28. Brewer, K. J.; Calvin, M.; Lumpkin, R. S.; Otvos, J. W.; Spreer, L. O., Synthesis, structure, and characterization of a mixed-valence manganese(III)-manganese(IV) bis(.mu.-oxo) complex with a macrocyclic tetraaza ligand. *Inorg. Chem.* **1989,** *28* (25), 4446-4451.

29. Yu, H. S.; He, X.; Li, S. L.; Truhlar, D. G., MN15: A Kohn–Sham global-hybrid exchange–correlation density functional with broad accuracy for multi-reference and single-reference systems and noncovalent interactions. *Chem. Sci.* **2016,** *7* (8), 5032-5051.

30. Roy, L. E.; Hay, P. J.; Martin, R. L., Revised Basis Sets for the LANL Effective Core Potentials. *J Chem Theory Comput* **2008,** *4* (7), 1029-31.

31. (a) Busch, M.; Ahlberg, E.; Panas, I., Electrocatalytic oxygen evolution from water on a Mn(iii–v) dimer model catalyst—A DFT perspective. *Phys. Chem. Chem. Phys.* **2011,** *13* (33), 15069-15076; (b) Brazzolotto, D.; Cantú Reinhard, F. G.; Smith-Jones, J.; Retegan, M.; Amidani, L.; Faponle, A. S.; Ray, K.; Philouze, C.; de Visser, S. P.; Gennari, M.; Duboc, C., A High-Valent Non-Heme μ-Oxo Manganese(IV) Dimer Generated from a Thiolate-Bound Manganese(II) Complex and Dioxygen. *Angew. Chem. Int. Ed.* **2017,** *56* (28), 8211-8215; (c) Valentine, A. M.; Stahl, S. S.; Lippard, S. J., Mechanistic Studies of the Reaction of Reduced Methane Monooxygenase Hydroxylase with Dioxygen and Substrates. *J. Am. Chem. Soc.* **1999,** *121* (16), 3876-3887.

32. Bruker (2012). Saint; SADABS; APEX3. Bruker AXS Inc., M., Wisconsin, USA.

33. Sheldrick, G. M., SHELXT - Integrated space-group and crystal-structure determination. *Acta Crystallographica Section A* **2015,** *71* (1), 3-8.

Part III:
Other Assorted Studies

Chapter 7

Phosphine Modulation for Enhanced CO_2 Capture: Quantum Mechanics Predictions of New Materials

Reproduced with permission from:

A Prokofjevs, WA Goddard III. *Phosphine Modulation for Enhanced CO_2 Capture: Quantum Mechanics Predictions of New Materials, J. Phys. Chem. Lett.*, **2022**, 13, 48, 11183-11190

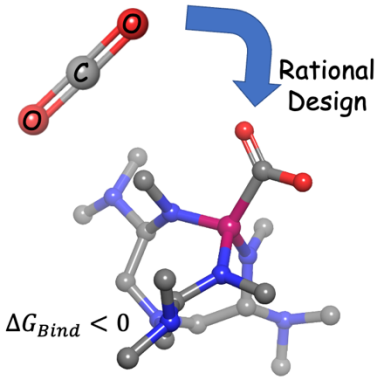

Figure 7.0: Table of contents figure

7.1 Abstract

It is imperative to develop efficient CO_2 capture and activation technologies to combat the rising levels of deleterious greenhouse gases in the atmosphere. Using Quantum

Mechanics methods (Density Functional Theory), we propose and evaluate several metal-free and metal-containing phosphines that provide strong CO_2 binding under ambient conditions. Depending on the electron donating capacity of the phosphine and the ability of the P-bound ligands to hydrogen bond to the CO_2, we find that the CO_2 binding can be as strong as -18.6 kcal/mol downhill, which should be quite adequate for ambient conditions. We explore some modifications of the phosphine to improve CO_2 binding, and we elucidate which chemical descriptors correlate directly with CO_2 binding energy. Specifically, we find that charge accumulation on the CO_2 unit of the CO_2-bound adduct has the greatest correlation with CO_2 binding affinity. Finally, we probe the mechanism for CO_2 reduction to CO and methanol in aqueous media.

7.2 Introduction

The rapid development of modern society has required a massive increase in global energy production. This increased energy consumption has been addressed by escalated utilization of nonrenewable fossil fuels,[1] ultimately leading to climate change induced by greenhouse gas emissions. Prominent among these greenhouse gases is carbon dioxide (CO_2), the ubiquitous product which is generated in numerous industrial processes, including fossil fuel generation.[2] To remediate the impact on the environment, it is highly desirable to have a working technology for sequestering CO_2 under ambient conditions,

followed by chemical reaction converting the captured CO_2 into commodity chemicals.[3] Taking inspiration from bio-inspired processes is artificial photosynthesis, which uses (photo)electrochemistry to catalytically convert CO_2 to value-added hydrocarbon fuels.[4] In these processes, solar-thermal water splitting is often used to generate the 'green' electrons.[5] Unfortunately, electrochemical CO_2 reduction to multi-carbon products remains challenging given the complexity of the reaction and also the propensity to generate side products, such as H_2 and CO.[6] In the meantime, an alternative method for reducing atmospheric CO_2 levels is to simply capture and store CO_2.

CO_2 physisorption is known for many materials; however, to activate the CO_2 and generate the bent intermediate required for subsequent chemical modification requires more extreme conditions. The most simplistic yet robust approach for CO_2 binding is via formation of Lewis base adducts.[7] Indeed, electron-rich species such as strong organic and inorganic nucleophiles and transition metal complexes are capable of binding CO_2.[8] However, organocatalysts for CO_2 capture remain rare, and their affinity for CO_2 binding is often low, precluding their use for subsequent CO_2 conversion. Additionally, many complexes that bind CO_2 do so reversibly,[9,10] and are thus not easily adaptable for transforming CO_2 into useful fuels and products.

In this study, we utilize Density Functional Theory (DFT) to propose and evaluate several classes of phosphines aimed at strong binding of CO_2. We analyze what features

may lead towards increased CO_2 capture, and then we elucidate a possible mechanism for conversion of CO_2 to methanol on our best phosphine.

7.3 Results and Discussion

7.3.1 CO2 Binding Affinities

We desire molecules that form a strong bond to the carbon of CO_2, since a stronger bond to C likely weakens the CO_2's C=O bond, making conversion of the trapped CO_2 molecule more facile.[11] Heterogeneous species such as microporous phosphine oxides[12] and P-doped graphitic carbon nitrides have been studied for CO_2 capture and conversion,[13] to products such as CO, CH_4, and H_2. Moreover, Dielmann et al. have found that P(NI*i*Pr)$_3$ (NI*i*Pr = 1,3-diisopropyl-4,5-dimethylimidazolin-2-ylidenamino) can capture and even split CO_2, while resisting thermal decarboxylation.[14]

Given the widespread interest in using amines for CO_2 capture applications, we sought to explore the suitability of phosphines for the same task. While most organophosphines do not bind CO_2 under normal conditions, a few scattered experimental reports suggest this to be a clear possibility, thus demanding theoretical investigation. Here we propose a family of phosphine molecules that we predict will bind CO_2 strongly for storage and for potential conversion to value-added products. Our initial selection of phosphines is shown in Figure 7.1.

- Phosphine **1** contains a bidentate 1,2-diamine ligand that forms a 5-membered ring with P.
- Phosphine **2** contains a highly electron-rich monodentate guanidine ligand.[15]
- Phosphine **3**, the familiar Verkade base,[16,17] has a tridentate ligand that forms a [3.3.3]-bicyclic framework with P and N atoms at the bridgehead positions.
- Silaphosphine **4** contains 5-, 4-, and 3-membered rings, with 4, 2, and 2 P atoms, respectively. Bridging these rings are two tetrahedral Si centers; **4** actually contains 4 unique P centers. This compound caught our attention due to the high content of electron-rich P and Si centers.
- Similarly, the related spirocyclic Ge counterpart **5** has 3 unique P sites among the 5- and 3-membered rings.
- **6,** the known anion of the dimethylphosphine BH_3 complex, features another potential approach for increasing the electron density at the P center.

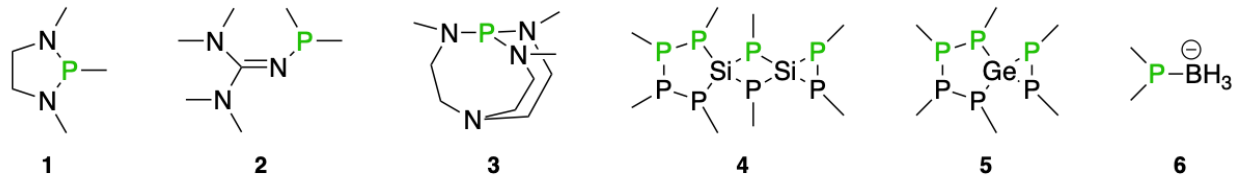

Figure 7.1: phosphines evaluated for CO_2 capture. Green indicates unique P sites.

To assess the feasibility of capturing CO_2 with the proposed phosphine species, we utilized Density Functional Theory (DFT) quantum mechanics calculations. In particular, we used the highly accurate M06-2X[18] meta-GGA functional accompanied by the D3 empirical correction for dispersion.[19] In this study, we also include the effects of THF solvent via the PBF Poisson Boltzmann implicit solvent model. More details on computational methods can be found in the computational methods section below.

The natural first step to evaluating CO_2 capture is the thermodynamic driving force to bind CO_2 to the phosphine center. Depending on the subsequent steps in the reaction, we may seek a phosphine that binds CO_2 with a large driving force (more downhill in free energy)[20] or a phosphine that is thermoneutral with its CO_2-bound adduct (neither downhill nor uphill in free energy).[21] As stated above, we presume that a greater thermodynamic driving force will likely yield a lower barrier. The CO_2 binding energies (ΔG), along with Mulliken charges for the P atom and the CO_2 unit of the CO_2-bound adduct are reported in Table 7.1. The CO_2 binding energy is calculated as:

$$\Delta G = G_{P-CO_2} - G_P - G_{CO_2}$$

where G_{P-CO_2}, G_P, and G_{CO_2} are the free energies of the CO_2-bound phosphine adduct, the phosphine, and CO_2, respectively.

Table 7.1: CO_2 binding energies (kcal/mol) for the proposed phosphines at 298.15 K in THF. The Mulliken charge for the P atom and for the CO_2 unit are included.

Species	CO_2 Binding (ΔG, kcal/mol)	P Charge (Q_P,e)	CO_2 Charge (Q_{CO2}, e)
1	2.9	+0.828	-0.758
2	-6.0	+0.540	-0.761
3	-2.7	+1.170	-0.883
4_1	Too Unstable	--	--
4_2	Too Unstable	--	--
4_3	10.7	-0.122	-0.476
4_4	11.7	-0.012	-0.589
5_1	Too Unstable	--	--
5_2	12.2	-0.151	-0.371
5_3	11.5	-0.008	-0.455
6	-16.4	+0.487	-0.893

Binding CO_2 to **1** is uphill 2.9 kcal/mol in free energy at 298.15 K. In **1a** (the CO_2-bound adduct of **1**), there is significant positive charge on P (+0.828) and significant negative charge on the CO_2 (-0.758), indicating formation of a zwitterion.

We find that **2** readily captures CO_2 with a binding energy of -6.0 kcal/mol. Here **2a** features a P with a +0.540 charge and a CO_2 with a -0.761 charge, again indicating the presence of a zwitterion, although the charge difference between P and CO_2 is less pronounced than in the case of **1a**.

We find that species **3** also binds CO_2 favorably with a ΔG of -2.7 kcal/mol to form **3a**. With CO_2 bound, **3a** has a +1.17 charge on P and a -0.883 charge on CO_2, making **3a** a potent zwitterion.

In the case of species **4**, the 8 total P yield 4 unique sites by symmetry. The first site (**4_1**) is P in a 3-membered ring containing another P and a Si. We were unable to bind CO_2 to this site. The second site (**4_2**) is P in a 4-membered ring containing another P and 2 Si. Similar to **4_1**, **4_2** is not capable of capturing CO_2. Site **4_3** is P in a 5-membered ring that contains 3 other P and a Si; here the P site is adjacent to a P and the Si. **4_3** binds CO_2 with a ΔG of 10.7 kcal/mol. In **4_3a**, P has a -0.122 charge and CO_2 has a -0.476 charge; both charges are negative which likely contributes to the highly endergonic CO_2 binding. Site **4_4** is similar to site **4_3** except that P is now adjacent to 2 other P. Binding CO_2 to site **4_4** is uphill 11.7 kcal/mol. In **4_4a**, the P charge is -0.012 and the CO_2 charge is -0.589.

Species **5** has 6 total P's and 3 unique sites by symmetry. **5_1** is P in the 3-membered ring containing 2 P's and Ge. **5_2** is the site in the 5-membered ring containing 2 other

P and Ge; here P is adjacent to another P and the Ge. **5_3** is also in the 5-membered ring but bound to 2 other P. Similar to **4_1**, **5_1** cannot bind CO_2. Sites **5_2** and **5_3** bind CO_2 with free energies of 12.2 and 11.5 kcal/mol, respectively. **5_2a** features negative charges on P and CO_2: P has a -0.151 charge and CO_2 has a -0.371 charge. **5_3a** has a -0.008 charge on P and a -0.455 charge on CO_2. In **4_4a** and **5_3a** the P charge is virtually 0.

Finally, species **6** which contains the anionic $-BH_3^-$ unit binds CO_2 very strongly with a free energy change of -16.4 kcal/mol. This is by far the most exergonic bind energy, likely because the anion donates electron density to the P, making P more Lewis basic and therefore more likely to bond to CO_2. In **6a** the P charge is +0.487 and the CO_2 unit holds a charge of -0.893. While metal salts of secondary phosphine BH_3 complexes have been reported previously,[22,23] their ability to bind CO_2 has not been documented in the literature. Nevertheless, if the accompanying counterion (e.g. Na^+ or Li^+) does not disrupt its ability to bind CO_2, phosphine-borane anions related to **6** can be expected to exhibit outstanding CO_2 capture performance. The substantial hydricity of **6** suggests that a hydride can be transferred directly to CO_2 to generate a formate anion (HCO_2^-). This hydride transfer is 6.9 kcal/mol uphill, suggesting an alternative path for CO_2 transformation. We will analyze the anionic phosphine-borane family for CO_2 capture in a future study. Of the neutral phosphines examined (i.e. excluding species **6**), **2** yields the

most exergonic CO_2 binding energy while **5_2** yields the most endergonic. Further, species **3** exhibits the most pronounced zwitterionic character. The zwitterionic character correlates with the electronegativity of the atoms bonded to P in the parent complexes. **3** is the most zwitterionic with 3 N's bound to P, followed by **1** which has 2 N's bound to P, followed then by **2** which has a single N-P bond. Neither **4** nor **5** produce CO_2-bound adducts with zwitterionic character since all atoms bound to P sites are less electronegative than P. The DFT-optimized structures with CO_2 bound are shown in Figure 7.2.

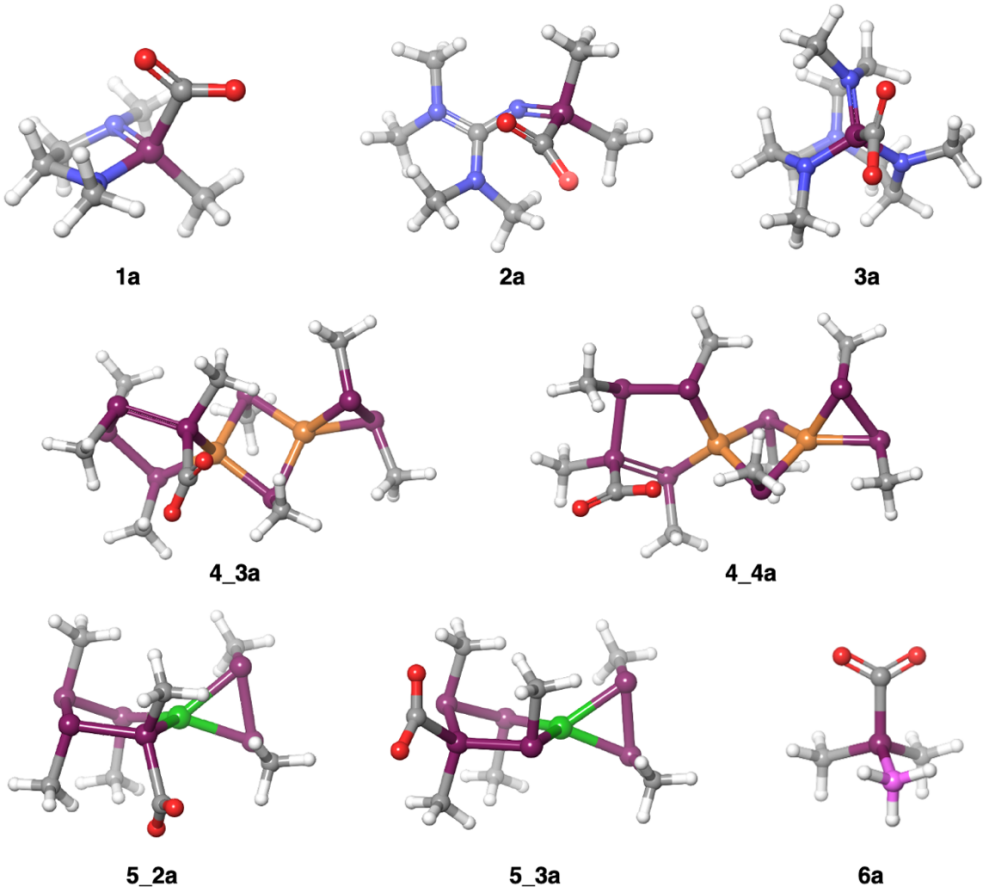

Figure 7.2: DFT-optimized phosphines with CO_2 bound. Purple atoms are P, blue atoms are N, orange are Si, green are Ge, and pink is B. Bonds are depicted to show molecular structure and do not represent the true bond orders.

7.3.2 CO_2 Binding in Different Solvents

Using species **2** as a template, we investigated the effect of solvent on CO_2 binding.[24] In water (dielectric constant = 80.37 and probe radius = 1.40 Å) the CO_2 binding is exergonic -5.12 kcal/mol. In acetonitrile (dielectric constant = 36.64 and probe radius = 2.18 Å) the CO_2 binding is exergonic -8.27 kcal/mol. The difference in CO_2 binding energy upon switching from tetrahydrofuran (THF, dielectric constant = 7.6, probe radius = 2.52 Å) to acetonitrile is made more exergonic by 2.24 kcal/mol; conversely, switching from THF to water makes CO_2 binding more endergonic by 0.91 kcal/mol. Previous studies regarding solvent effects have predicted that CO_2-bound adducts with larger dipole moments are more stabilized by solvent.[25,26] Previous work by Alkorta and coworkers found that increased dielectric constant leads to a more negative binding energy, meaning that the CO_2 binding energy trend should be: water (largest dielectric constant) < acetonitrile < tetrahydrofuran (smallest dielectric constant). However, our results for **2** break this trend; we instead find the binding energy trend to be: acetonitrile < tetrahydrofuran < water.

7.3.3 Ligand Addition for Enhanced CO_2 Binding

Species **2** features only a single 1,1,3,3-tetramethylguanidinium (TMG) ligand.[27] It is plausible that addition of one or two more of these TMG ligands would increase the CO_2 binding energy even further. Indeed, adding one additional TMG ligand to make **2.1** improves the CO_2 binding energy to -7.9 kcal/mol. In **2.1a** the P charge has increased to +0.778 (from +0.540 in **2**). Adding a third TMG to form **2.2** further improves CO_2 binding to -13.9 kcal/mol. This agrees with Alkorta's previous phosphine study that found increasing the number of guanidine ligands generally makes CO_2 binding energy more negative. In **2.2a** the P charge has increased to +1.010. We find that the magnitude of the zwitterion charge separation increases as additional TMG ligands are added. The P-CO_2 charge difference (Q_P-Q_{CO2}) increases from 1.301 in **2a** to 1.616 in **2.1a** to 1.921 in **2.2a**. The O-C-O angle is also observed to decrease from 132.6° to 131.2° to 130.1° in **2a**, **2.1a**, and **2.2a** respectively.

With **2.2** as our new gold standard, we can compare to previously reported phosphines used for capturing CO_2. Dielmann and coworkers reported the experimental realization and subsequent DFT-computed CO_2 binding of a phosphine containing two 1,3-diisopropyl-4,5-dimethylimidazolin-2-ylidenamino (NI*i*Pr) ligands and an isopropyl group.[9] We find their P(*i*Pr)(NI*i*Pr)$_2$ complex to capture CO_2 with an exergonicity of -12.4 kcal/mol at 298 K; here the P has a +0.944 charge and the CO_2 has a -0.852 charge,

such that the P-CO_2 charge difference is 1.796. The P(*i*Pr)(NI*i*Pr)$_2$ complex has exceptional binding to CO_2, however, **2.2** binds CO_2 -1.5 kcal/mol more strongly. Additionally, **2.2a** has already been synthesized and characterized, making its use for CO_2 transformation quite feasible.[28]

7.3.4 Hydrogen-binding Motifs for Increased CO_2 Afffinity

The TMG ligand (1,1,3,3-tetramethylguanidinium) features four methyl groups bound through two sp^2 nitrogens. A natural extension of the TMG ligand is to swap out the methyl moieties for functional groups capable of hydrogen bond donation to the oxygens of the incoming CO_2.[29] Currently, the optimal geometry of **2.2a** precludes any hydrogen bonding or favorable Van der Waals interactions between the TMG methyl groups and the oxygens of the bent CO_2 component. However, the thermodynamic driving force for CO_2 capture can be further improved by swapping the methyl groups for groups that could stabilize the CO_2-bound adduct through direct Van der Waals stabilization. As a proof of concept, we modify the TMG ligands by swapping out singular methyl groups with

- ethyl groups, -CH_2CH_3 (**2.2.1**),
- aminomethyl groups, -CH_2NH_2 (**2.2.2**), and
- methoxy groups, -CH_2OH (**2.2.3**).

Based on typical hydrogen bonding trends, we expect **2.2.1** (in which methyls are replaced with ethyls) will not make any significant Van der Waals coordination in the CO_2 bound adduct.

2.2.2, in which methyls are replaced with aminomethyl groups, is likely to form hydrogen bonds with the incoming CO_2 through the NH_2 components, given the increased electronegativity of nitrogen. We believe **2.2.2**'s ability to form hydrogen bonds will increase the exergonic nature of CO_2 binding relative to the parent **2.2** phosphine.

Finally, **2.2.3** should form the strongest hydrogen bonds with the incoming CO_2 given the presence of -OH components on the methoxy groups; the increased strength of the hydrogen bonds should significantly stabilize the bound CO_2, such that CO_2 binding for **2.2.3** should be very exergonic. The DFT-optimized structures for **2.2.1a**, **2.2.2a**, and **2.2.3a** are depicted in Figure 7.3.

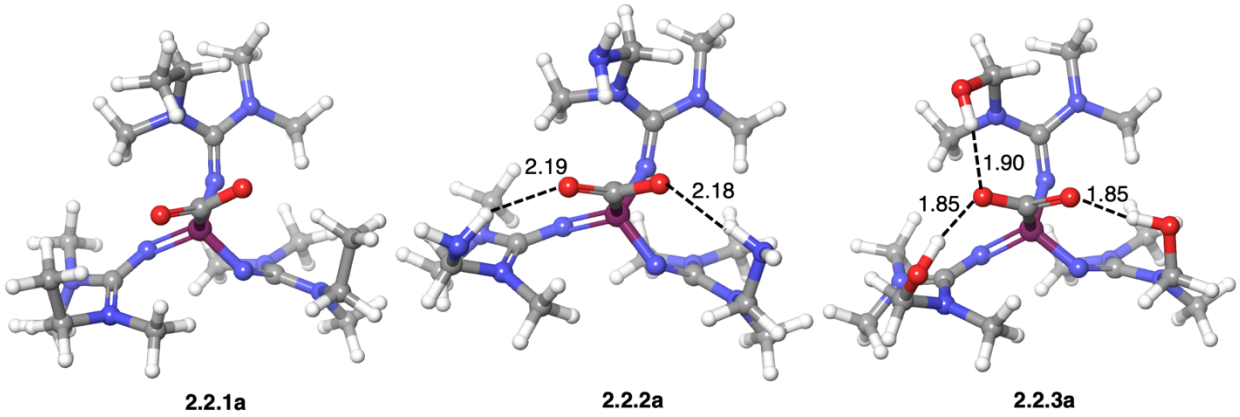

Figure 7.3: DFT-optimized structures for CO2-bound phosphines with singular methyl groups on each TMG ligand replaced by ethyl, aminomethyl, and methoxy groups (**2.2.1a**, **2.2.2a**, **2.2.3a**, respectively). Hydrogen bonds are denoted by dashed lines with lengths in Å).

In **2.2.1a**, there is no significant hydrogen bonding or favorable Van der Waals interactions between the bound CO_2 and the ethyl groups. The shortest distance between the CO_2 and an ethyl H is 2.42 Å, which may indicate a weak London Dispersion attraction with the H pointed towards the O's lone pair instead of toward O's nucleus. Regardless, the free energy for **2.2.1** to bind CO_2 is -12.4 kcal/mol, which is identical to that of the **2.2** parent compound, such that functionalization of TMG with ethyl groups offers no improvement. For phosphine **2.2.2**, addition of the three new aminomethyl groups enables two hydrogen bonds to be formed with the bound CO_2. Both hydrogen bonds are slightly elongated at 2.18 and 2.19 Å, suggesting they are somewhat weak relative to an ideal NH--O hydrogen bond. The free energy to bind CO_2 to **2.2.2** is -14.8 kcal/mol; this is an -2.4 kcal/mol improvement over the parent phosphine **2.2**, confirming that introducing hydrogen bonds to the CO_2 constituent increases the exergonicity of CO_2 binding. Since primary amines are known to capture CO_2, it is also possible the newly introduced amino moieties directly bind CO_2. Bonding CO_2 directly to an amino moiety of **2.2.2** is uphill 2.3 kcal/mol. This alternative path is therefore not competitive with direct binding of CO_2 to P.

Finally, **2.2.3**, which contains methoxy groups, makes three strong hydrogen bonds with the bound CO_2. Two methoxy's direct their hydrogens to one O and the third methoxy directs its H to the other O. The hydrogen bond distances are 1.85, 1.85, and 1.90 Å, indicative of appreciable attraction between the methoxy's and the CO_2 component. The free energy to bind CO_2 to **2.2.3** is -18.6 kcal/mol, reflective of the substantial stabilization induced by the methoxy constituents. This binding free energy is a -6.2 kcal/mol improvement over the parent **2.2** phosphine making it the strongest CO_2-binding phosphine reported here. The presence of the alcohol groups also presents the opportunity for alternative pathways towards CO2 activation. First, CO_2 can bind directly to the OH moiety. For **2.2.3**, CO2 binding directly to the O atom of the OH group is downhill -12.9 kcal/mol. Interestingly, in this CO_2 binding process, the OH spontaneously transfers its H to a neighboring N. This N is bound to P, such that P is reduced in this path. The key feature of this process that makes it exergonic is the spontaneous H transfer to P. In **2.2.2**, the analogous CO_2 binding to the amine did not yield a spontaneous H transfer, such that the process was endergonic. **2.2.3** also presents a pathway in which P acts as a superbase to deprotonate the OH moiety, followed by binding of CO_2 to the now deprotonated O. Deprotonation of OH by P is uphill 2.4 kcal/mol. Subsequent binding of CO_2 to the deprotonated O is downhill -7.44 kcal/mol, such that the net process is downhill -5.0

kcal/mol (2.4 + -7.4). Because binding of CO_2 directly to P of **2.2.3** is downhill -18.6 kcal/mol, this alternative path is not likely competitive.

7.3.5 Correlating CO_2 Binding with Computed Observables

In an attempt to predict CO_2 binding energy from the parent phosphines or the CO_2-bound adducts, we tried to correlate the CO_2 binding energy with various geometric and electronic parameters calculated from quantum mechanics. Of the 10 parameters screened, the CO_2 angle of the CO_2-bound adduct, the overall charge of the CO_2 in the bound adduct, and the change in P charge from parent phosphine to CO_2-bound product all showed the greatest linear correlations with CO_2 binding energy (R^2 = 0.82, 0.83, and 0.80, respectively). No parameter showed definitive correlation with CO_2 binding, and thus we cannot use any one parameter to predict CO_2 binding affinity. However, it appears that these three parameters can serve as general heuristics for predicting whether or not a phosphine will favorably bind CO_2. The correlations of CO_2 binding energy with these 3 screened parameters are shown in Figure 7.4. All 10 screened parameters can be found in the Appendix F.

The O-C-O angle is a natural descriptor for binding affinity given that it provides a direct geometric quantification of how much a bound CO_2 has deviated from the initial angle of 180°. Previous studies with N-heterocyclic carbenes and semiconductor oxides have also

shown correlation O-C-O bending with binding affinity.[30–32] The phosphines that most strongly bind CO_2 bend the CO_2 to nearly 120°, indicating sp^2 hybridization on the C; the phosphines that bind weakly to CO_2 decrease the angle to only ~140°.

CO_2 charge is an electronic descriptor that captures the charge transfer from the phosphine. Here, increased charged transfer reflects stronger binding; the phosphine that binds CO_2 the strongest donates nearly a full charge to the CO_2 unit.

Finally, the change in P charge from the parent state to CO_2-bound state captures the change in the phosphine that most prominently correlates with CO_2 binding; the previous two descriptors only captured single-state features.

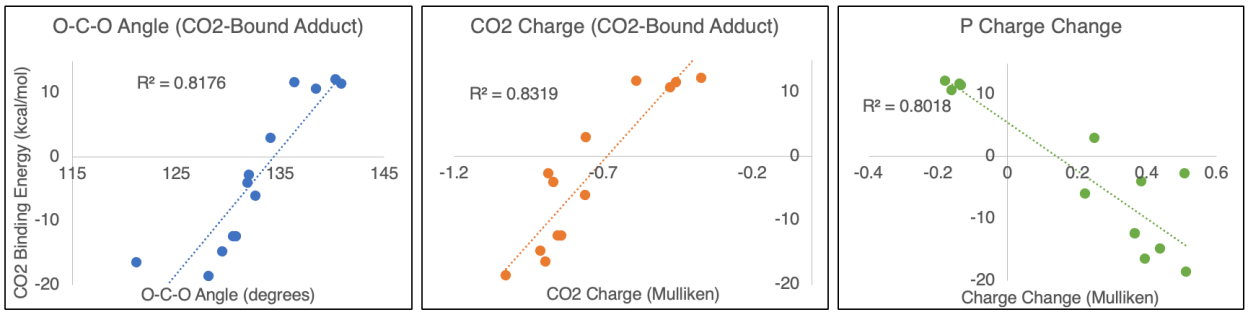

Figure 7.4: Correlation of CO_2 binding energy (y axes, kcal/mol) with the screened parameters that showed the greatest linear correlation with CO_2 binding. Charges and charge changes are Mulliken charges, and angles are degrees. Linear trendlines are shown with their R^2 values.

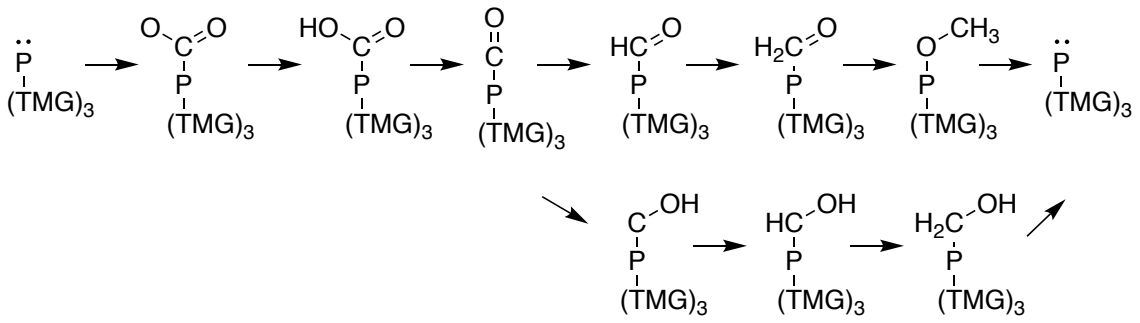

Scheme 7.1: Reaction mechanism for CO_2 reduction to methanol starting from species **2.2** (TMG = 1,1,3,3-tetramethylguanidinium).

7.3.6 CO_2 Reduction Towards Methanol

Despite phosphine **2.2.3** having the most exergonic CO_2 binding energy, the synthesis of a TMG ligand with a methyl group substituted with a methoxy group would likely require some development on the synthesis side before experimental realization. However, the base TMG ligand is experimentally accessible, making phosphine **2.2** a plausible species for experimental CO_2 capture. Since species **2.2** also exhibits the most exergonic CO_2 binding energy before TMG ligand modulation, we investigated the mechanism for the CO_2 reduction reaction (CO_2RR) towards methanol (Scheme 7.1).[33] The reaction proceeds through a series of proton-coupled electron transfers (PCETs) such that CO_2 undergoes 6 total reductions to form methanol and a water.[34,35] Starting with the bound *CO_2, initial reaction at an oxygen generates *HOCO. The second reaction step occurs at the same oxygen, generating *CO and liberating a water molecule. At this point *CO can either desorb from the phosphine to generate a free CO or undergo further

reduction. Further reduction can lead towards either *HCO (reaction at the carbon) or *COH (reaction at the oxygen). Reduction of these intermediates can generate either *H_2CO or *HCOH, and reduction of these yields either *H_3CO or *H_2COH. Finally, the 6^{th} reduction generates the desired methanol product. The free energy surface for CO_2RR to methanol via species **2.2** is shown in Figure 7.5. Here $\frac{1}{2}$ H_2 is used as the reference for hydrogen.

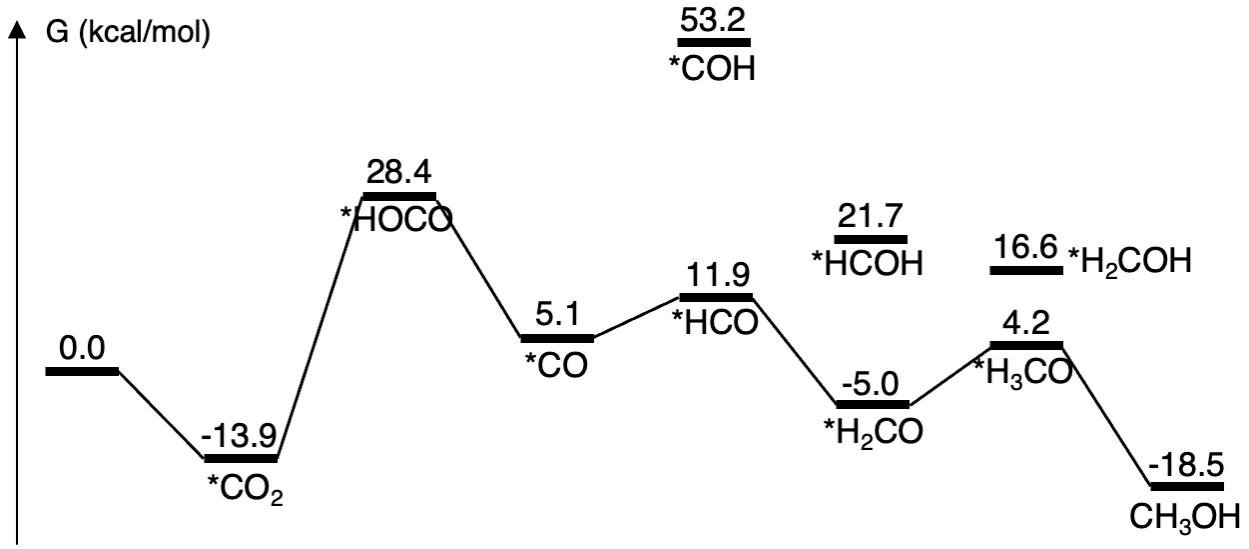

Figure 7.5: DFT free energies at 298.15 K for the conversion of CO_2 to methanol using **2.2**. $\frac{1}{2}$ H_2 in vacuum is used as the reference hydrogen source. Energies are in kcal/mol. The first state at 0.0 kcal/mol is the pristine phosphine precursor.

The pristine **2.2** species is set as the ground state at 0.0 kcal/mol. The CO_2-bound adduct lies -13.9 kcal/mol below the ground state. The first reduction to make *HOCO is uphill to 28.4 kcal/mol, followed by the second reduction that yields adsorbed *CO and a water at 5.1 kcal/mol. In the *HOCO intermediate, the Mulliken spin densities of the C and P atoms are 0.54 and 0.17 respectively, indicating that the formal reduction occurs at the C. Upon *CO formation, the complex can either undergo CO desorption to generate a free *CO (3.1 kcal/mol, not shown), or further reduction to *HCO (11.9 kcal/mol) or *COH (53.2 kcal/mol). We see that *HCO is favored over *COH; this is likely because *HCO satisfies the valences of C and O while *COH leaves the C undercoordinated. In *HCO, the C and P atoms have spin densities of 0.56 and 0.14 respectively, again indicating that the reduction occurs at C. In *COH, the C and P spin densities are 0.80 and 0.12; the more pronounced spin density on C is attributed to C's undercoordination. The fourth reduction can generate either $*H_2CO$ or *HCOH; these species occur at -5.0 and 21.7 kcal/mol, respectively. The fifth reduction can generate either $*H_3CO$ (4.2 kcal/mol) or $*H_2COH$ (16.6 kcal/mol), and the 6th and final reduction yields the desired methanol (CH_3OH) product at -18.5 kcal/mol relative to the ground state phosphine. Clearly the reduction to methanol prefers the *HCO → $*H_2CO$ → H_3CO pathway. However, this is rendered somewhat irrelevant since the CO desorption step is -2.0 kcal/mol (3.1 – 5.1), indicating that this phosphine would generate primarily CO gas.

7.4 Conclusions

In this work we evaluated several phosphines for the purpose of exergonic CO_2 capture. Among the first phosphines studies, CO_2 binding ranged from +12.2 to -16.4 kcal/mol, the worst being the Ge-based phosphine and the best being a phosphine with an anionic Boron-based ligand. This anionic phosphine-borane molecule exhibited such excellent CO_2 binding affinity, that a future study will be conducted focusing on just this family of phosphines. Of the neutral phosphines evaluated (e.g. excluding **6**), species **2**, which contains a guanidium ligand (denoted TMG), exhibited the best CO_2 binding energy of -6.0 kcal/mol.

Using **2** as a template, we explored the effect of solvent, and found that in water, CO_2 binding is less exergonic (-5.1 kcal/mol), while in acetonitrile CO_2 binding is more exergonic (-8.3 kcal/mol). We then modified phosphine **2** by adding additional TMG ligands, and found that addition of one TMG (**2.1**) improves CO_2 binding to -7.9 kcal/mol, while addition of two TMGs (**2.2**) improves binding to -13.9 kcal/mol. We then modified the three TMG ligands of **2.2** by replacing single methyl groups with functional groups capable of hydrogen bonding. When methyl groups are substituted with methoxy groups (**2.2.3**), CO2 binding improves to -18.6 kcal/mol.

We then screened 10 phosphine descriptors to see what features may correlate with CO_2 binding. The descriptors with the best linear fit are the O-C-O angle in the CO_2-bound adduct, the charge of the CO2 unit in the CO2-bound adduct, and the change in P charge from the parent phosphine to the CO2-bound state.

Finally, we explored the mechanism for converting CO_2 to methanol using **2.2** as the catalyst. At 298.15 K and neutral pH, the reaction overall is downhill -18.5 kcal/mol. However, highest-lying intermediate is the *HOCO species, which lies 28.4 kcal/mol above the resting state pristine phosphine. Because the preceding intermediate is $*CO_2$ which lies -13.9 kcal/mol below the resting state, a barrier of over 42 kcal/mol would be required to turn this reaction over, making this reaction unlikely to occur at ambient conditions.

This study provides new insights and design principles for the purpose of engineering novel phosphines towards improved CO_2 capture and transformation. The demonstration of highly exergonic CO_2 capture by metal-free phosphine opens new avenues to catalyst design that leverage the molecular phosphine platform.

7.5 Computational Methods

All Density Functional Theory calculations were performed using the Jaguar v10.9 software by Schrodinger Inc.[36] All calculations utilized the M06-2X meta-GGA functional[37] with the D3 empirical correction for London Dispersion forces.[19] Almost all

atoms were described by the 6-311G Pople basis set,[38] augmented with polarization and diffuse functions. Atoms not described by 6-311G**++ (Ge) were modeled using the Los Alamos small-core pseudopotential[39] augmented with polarization and diffuse functions (designated LACV3P**++ in Jaguar).

All calculations included an implicit solvent treatment described by the Poisson Boltzmann (PBF) continuum model.[40] Unless otherwise noted, solvent parameters matching tetrahydrofuran (dielectric constant = 7.6, probe radius = 2.52 Å) were used. For acetonitrile solvent, we used a dielectric constant of 36.64 and a probe radius of 2.18 Å.

Frequency calculations were performed to confirm all geometries were true minima (no negative eigenmodes in Hessian) and to compute thermochemical properties such as enthalpy (H), entropy (S) , and free energies (G). Because librational modes are hindered in solvent media, we corrected our free energies by reducing translational and rotational entropy modes by 50%. That is, G was calculated via $G = H - T * (0.5 * (S_{trans} + S_{rot}) + S_{vib})$ Where S_{trans}, S_{rot}, and S_{vib} are the translational, rotational, and vibrational entropies, respectively. T was chosen to be 298 K.

7.6 References

(1) Wuebbles, D. J.; Jain, A. K. Concerns about Climate Change and the Role of Fossil Fuel Use. *Fuel Process. Technol.* **2001**, *71*, 99–119.

(2) Boden, T. a; Marland, G.; Andres, R. J. Global, Regional, and National Fossil-Fuel CO2 Emissions. *Carbon Dioxide Inf. Anal. Cent. Oak Ridge Natl. Lab. USA Oak Ridge TN Dep. Energy* **2009**.

(3) Yu, K. M. K.; Curcic, I.; Gabriel, J.; Tsang, S. C. E. Recent Advances in CO2 Capture and Utilization. *Chem. Sus. Chem.* **2008**, *1*, 893–899.

(4) Gust, D.; Moore, T. A.; Moore, A. L. Solar Fuels via Artificial Photosynthesis. *Acc. Chem. Res.* **2009**, *42*, 1890–1898.

(5) Muhich, C. L.; Ehrhart, B. D.; Al-Shankiti, I.; Ward, B. J.; Musgrave, C. B.; Weimer, A. W. A Review and Perspective of Efficient Hydrogen Generation via Solar Thermal Water Splitting. *Wiley Interdiscip. Rev. Energy Environ.* **2016**, *5*, 261–287.

(6) Nitopi, S.; Bertheussen, E.; Scott, S. B.; Liu, X.; Engstfeld, A. K.; Horch, S.; Seger, B.; Stephens, I. E. L.; Chan, K.; Hahn, C.; Nørskov, J. K.; Jaramillo, T. F.; Chorkendorff, I. Progress and Perspectives of Electrochemical CO2 Reduction on Copper in Aqueous Electrolyte. *Chem. Rev.* **2019**, *119*, 7610–7672.

(7) Chi, J. J.; Johnstone, T. C.; Voicu, D.; Mehlmann, P.; Dielmann, F.; Kumacheva, E.; Stephan, D. W. Quantifying the Efficiency of CO2 Capture by Lewis Pairs. *Chem. Sci.* **2017**, *8*, 3270–3275.

(8) Murphy, L. J.; Robertson, K. N.; Kemp, R. A.; Tuononen, H. M.; Clyburne, J. A.

C. Structurally Simple Complexes of CO2. *Chem. Commun.* **2015**, *51*, 3942–3956.

(9) Buß, F.; Mehlmann, P.; Mück-Lichtenfeld, C.; Bergander, K.; Dielmann, F. Reversible Carbon Dioxide Binding by Simple Lewis Base Adducts with Electron-Rich Phosphines. *J. Am. Chem. Soc.* **2016**, *138*, 1840–1843.

(10) Dickie, D. A.; Barker, M. T.; Land, M. A.; Hughes, K. E.; Clyburne, J. A. C.; Kemp, R. A. Rapid, Reversible, Solid-Gas and Solution-Phase Insertion of CO2 into In-P Bonds. *Inorg. Chem.* **2015**, *54*, 11121–11126.

(11) Stephan, D. W.; Erker, G. Frustrated Lewis Pair Chemistry: Development and Perspectives. *Angew. Chemie - Int. Ed.* **2015**, *54*, 6400-6441.

(12) Qiao, S.; Huang, W.; Du, Z.; Chen, X.; Shieh, F. K.; Yang, R. Phosphine Oxide-Based Conjugated Microporous Polymers with Excellent CO2 Capture Properties. *New J. Chem.* **2015**, *39*, 136–141.

(13) Liu, B.; Ye, L.; Wang, R.; Yang, J.; Zhang, Y.; Guan, R.; Tian, L.; Chen, X. Phosphorus-Doped Graphitic Carbon Nitride Nanotubes with Amino-Rich Surface for Efficient CO2 Capture, Enhanced Photocatalytic Activity, and Product Selectivity. *ACS Appl. Mater. Interfaces* **2018**, *10*, 4001–4009.

(14) Mehlmann, P.; Mück-Lichtenfeld, C.; Tan, T. T. Y.; Dielmann, F. Tris(Imidazolin-2-Ylidenamino)Phosphine: A Crystalline Phosphorus(III) Superbase That Splits Carbon Dioxide. *Chem. - A Eur. J.* **2017,** *23,* 5929-5933.

(15) Wünsche, M. A.; Mehlmann, P.; Witteler, T.; Buß, F.; Rathmann, P.; Dielmann, F. Imidazolin-2-Ylidenaminophosphines as Highly Electron-Rich Ligands for Transition-Metal Catalysts. *Angew. Chemie - Int. Ed.* **2015**, *54*, 11857–11860.

(16) Tang, J. sheng; Verkade, J. G. An Improved Synthesis of the Strong Base P(MeNCH2CH2)3N. *Tetrahedron Lett.* **1993**, *34*, 2903–2904.

(17) Johnstone, T. C.; Wee, G. N. J. H.; Stephan, D. W. Accessing Frustrated Lewis Pair Chemistry from a Spectroscopically Stable and Classical Lewis Acid-Base Adduct. *Angew. Chemie - Int. Ed.* **2018**, *57,* 5881-5884.

(18) Zhao, Y.; Truhlar, D. G. The M06 Suite of Density Functionals for Main Group Thermochemistry, Thermochemical Kinetics, Noncovalent Interactions, Excited States, and Transition Elements: Two New Functionals and Systematic Testing of Four M06-Class Functionals and 12 Other Function. *Theor. Chem. Acc.* **2008**, *120*, 215–241.

(19) Grimme, S.; Antony, J.; Ehrlich, S.; Krieg, H. A Consistent and Accurate Ab Initio Parametrization of Density Functional Dispersion Correction (DFT-D) for the 94 Elements H-Pu. *J. Chem. Phys.* **2010**, *132*, 154104.

(20) Kwon, H. J.; Kim, H. W.; Rhee, Y. M. On the Mechanism of Irreversible Carbon Dioxide Binding with a Frustrated Lewis Pair: Solvent-Assisted Frustration and Transition-State Entropic Encouragement. *Chem. - A Eur. J.* **2011**, *17*, 6501–6507.

(21) Mömming, C. M.; Otten, E.; Kehr, G.; Fröhlich, R.; Grimme, S.; Stephan, D. W.; Erker, G. Reversible Metal-Free Carbon Dioxide Binding by Frustrated Lewis Pairs. *Angew. Chemie - Int. Ed.* **2009**, *48*, 6643–6646.

(22) Staubitz, A.; Robertson, A. P. M.; Sloan, M. E.; Manners, I. Amine-and Phosphine-Borane Adducts: New Interest in Old Molecules. *Chem. Rev.* **2010**, *110*, 4023–4078.

(23) Kuchen, W.; Buchwald, H. Zur Kenntnis Der Organophosphorverbindungen, III. Umsetzungen Mit Diphenylphosphin-natrium. *Chem. Ber.* **1959**, *92*, 227-231.

(24) N.Borhani, T.; Wang, M. Role of Solvents in CO2 Capture Processes: The Review of Selection and Design Methods. *Renew. Sustain. Energy Rev.* **2019**, *114*, 109299.

(25) Alkorta, I.; Trujillo, C.; Sánchez-Sanz, G.; Elguero, J. Solvent and Substituent Effects on the Phosphine + CO2 Reaction. *Inorganics* **2018**, *6*, 110.

(26) Sánchez-Sanz, G.; Alkorta, I.; Elguero, J.; Trujillo, C. Sequestration of CO2 by Phosphatrane Molecules. *ChemPhysChem* **2019**, *20*, 3195-3200.

(27) Fiorani, G.; Guo, W.; Kleij, A. W. Sustainable Conversion of Carbon Dioxide: The Advent of Organocatalysis. *Green Chem.* **2015**, *17*, 1375-1389.

(28) Buß, F.; Röthel, M. B.; Werra, J. A.; Rotering, P.; Wilm, L. F. B.; Daniliuc, C. G.; Löwe, P.; Dielmann, F. Tris(Tetramethylguanidinyl)Phosphine: The Simplest Non-Ionic Phosphorus Superbase and Strongly Donating Phosphine Ligand. *Chem. - A Eur. J.* **2022,** *28*, e202104021.

(29) Williams, N. J.; Seipp, C. A.; Brethomé, F. M.; Ma, Y. Z.; Ivanov, A. S.; Bryantsev, V. S.; Kidder, M. K.; Martin, H. J.; Holguin, E.; Garrabrant, K. A.; Custelcean, R. CO2 Capture via Crystalline Hydrogen-Bonded Bicarbonate Dimers. *Chem.* **2019**, *5*, 719–730.

(30) Wang, Z.; Wang, F.; Xue, X. S.; Ji, P. Acidity Scale of N-Heterocyclic Carbene Precursors: Can We Predict the Stability of NHC-CO2 Adducts? *Org. Lett.* **2018**, *20*, 6041-6045.

(31) Yang, L.; Wang, H. Recent Advances in Carbon Dioxide Capture, Fixation, and Activation by Using N-Heterocyclic Carbenes. *ChemSusChem* **2014**, *1*, 893-899.

(32) Mazheika, A.; Wang, Y. G.; Valero, R.; Viñes, F.; Illas, F.; Ghiringhelli, L. M.; Levchenko, S. V.; Scheffler, M. Artificial-Intelligence-Driven Discovery of Catalyst Genes with Application to CO2 Activation on Semiconductor Oxides. *Nat. Commun.* **2022**, *13*, 419.

(33) Kar, S.; Goeppert, A.; Prakash, G. K. S. Integrated CO2 Capture and Conversion to Formate and Methanol: Connecting Two Threads. *Acc. Chem. Res.* **2019**, *52*, 2892–2903.

(34) Ju, W.; Bagger, A.; Wang, X.; Tsai, Y.; Luo, F.; Möller, T.; Wang, H.; Rossmeisl, J.; Varela, A. S.; Strasser, P. Unraveling Mechanistic Reaction Pathways of the Electrochemical CO2 Reduction on Fe-N-C Single-Site Catalysts. *ACS Energy Lett.*

2019, *4*, 1663–1671.

(35) Huff, C.; Sanford, M. S. Cascade Catalysis for the Homogeneous Hydrogenation of CO2 to Methanol. *J. Am. Chem. Soc.* **2011**, *133*, 18122–18125.

(36) Bochevarov, A. D.; Harder, E.; Hughes, T. F.; Greenwood, J. R.; Braden, D. A.; Philipp, D. M.; Rinaldo, D.; Halls, M. D.; Zhang, J.; Friesner, R. A. Jaguar: A High-Performance Quantum Chemistry Software Program with Strengths in Life and Materials Sciences. *Int. J. Quantum Chem.* **2013**, *113*, 2110–2142.

(37) Zhao, Y.; Truhlar, D. G. Density Functionals with Broad Applicability in Chemistry. *Acc. Chem. Res.* **2008**, *41*, 157–167.

(38) Hehre, W. J.; Ditchfield, K.; Pople, J. A. Self-Consistent Molecular Orbital Methods. XII. Further Extensions of Gaussian-Type Basis Sets for Use in Molecular Orbital Studies of Organic Molecules. *J. Chem. Phys.* **1972**, *56*, 2257–2261.

(39) Kahn, L. R.; Goddard, W. A. Ab Initio Effective Potentials for Use in Molecular Calculations. *J. Chem. Phys.* **1972**, *56*, 2685–2701.

(40) Friedrichs, M.; Zhou, R.; Edinger, S. R.; Friesner, R. A. Poisson-Boltzmann Analytical Gradients for Molecular Modeling Calculations. *J. Phys. Chem. B* **1999**, *103*, 3057–3061.

Chapter 8

Electrochemical Nitrate Reduction Catalyzed by 2D MBenes

Reproduced with permission from:

WA Goddard III. *Electrochemical Nitrate Reduction Catalyzed by Two-Dimensional Transition Metal Borides, J. Phys. Chem. Lett.*, **2024**, *15, 7, 1899-1907*

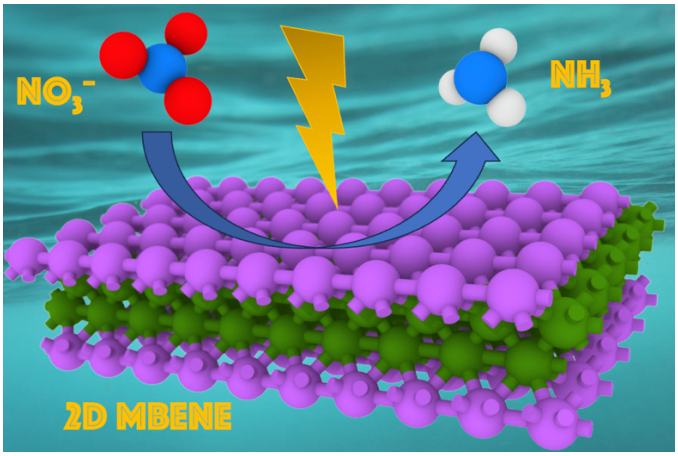

Figure 8.0: Table of contents figure

8.1 Abstract

Nitrate reduction towards ammonia aides in restoring the nitrogen cycle, which is currently far from equilibrium due to human impacts such as the Haber Bosch process. We systematically investigated 2D transition metal borides (MBenes) for the efficient

conversion of nitrate to ammonia. MBenes have been previously shown to bind oxygen with extraordinary strength, which should translate towards selective adsorption of nitrate in aqueous media. Using Density Functional Theory, we screened MBenes by first computing their nitrate and water adsorption energies, seeking materials with strong nitrate binding and weak water binding. We identified MnB, CrB, and VB as the best materials for the selective adsorption of nitrate and proceeded by computing their free energy landscapes for converting nitrate to ammonia. Of the three candidates, CrB requires the lowest overpotential, making it the best candidate. In an attempt to further decrease the overpotential, we doped the CrB MBene with secondary transition metals, and found the addition of Mn to the active site further reduced the overpotential. We then computed the reaction mechanism grand canonically to observe the effect of applied potential on the free energy landscape.

8.2 Introduction

One of the largest sources of greenhouse gas emissions is the generation of ammonia (NH_3) through the Haber Bosch process, in which nitrogen and hydrogen are combined at high temperature and pressure (400 - 600 °C, 150 - 350 atm).[1] The hydrogen sourced for the Haber Bosch reaction is generated via steam methane reformation ($CH_4 + H_2O \rightarrow CO + 3\ H_2$), in which ungodly amounts of CO and CO_2 are generated as undesired

byproducts.[2] The electrochemical reduction of nitrogen-based species to afford ammonia is a desirable alternative to the Haber Bosch process due primarily to the sourcing of green electrons for driving ammonia formation.[3,4] Much attention has been devoted towards the electrochemical reduction of N_2 to ammonia, given the abundance of N_2 in the atmosphere and the several modalities in which the reduction reaction is performed (noble metals,[5,6] organic polymers,[7] molten salts[8]). However, electrochemical N_2 reduction is inherently difficult given the extreme strength (~9.75 eV) of N_2's apolar, triple bond. Moreover, N_2 reduction is most desirably performed in aqueous media, which introduces hydrogen evolution as a competing reaction path. Electrochemical N_2 reduction generally sees an improved faradic efficiency at elevated temperatures (400 – 500 °C), although the increased selectivity is overshadowed by the decreased partial current density that arises due to poisoning of the catalyst by the ammonia product, which in turn gives rise to undesired ammonia decomposition.[9]

A promising alternative to electrochemical N_2 reduction is the reduction of the nitrate anion (NO_3^-).[10] The removal and conversion of nitrate is a challenge that must be faced in order to enclose the nitrogen cycle.[11] Nitrate release is of particularly high consequence because it's leaching into soil results in contamination of nearby bodies of water and the eventual destruction of local ecosystems. A common practice is the "denitrification" of wastewater streams in which nitrate contained within the wastewater

is converted to N_2.[12] While this is necessary for decreasing the high levels of nitrate in water supplies, a more elegant solution would be converting the nitrate directly to ammonia, effectively eliminating the $NO_3^- \rightarrow N_2 \rightarrow NH_3$ steps from the nitrogen cycle.

Compared to the strength of N_2's triple bond, nitrate's N=O bond is a measly 2.11 eV which renders nitrate more suitable for reductive activation. The field of nitrate reduction typically focuses on precious group metal (PGM) catalysts, PGM-free catalysts, and metal-free catalysts. Ni, Co, and Pd are the elements most often seen for PGM catalysts,[13] although Ti, Cr, Mn, V, and Pt have also been seen implemented in single and dual-atom catalysts for nitrate reduction.[14,15] Ru,[16] Pd,[17–19] and Pt[20–22] appear to be the frontrunners for PGM-based nitrate reduction, although their high price and currently insufficient electrocatalytic properties preclude their use for industrial nitrate reduction, although recent ventures in catalyst co-doping may open new avenues for PGM-based nitrate reduction.[23] Because Fe, Co, and Cu are traditionally considered non-precious metals, they fall into their own PGM-free category. Regardless of their label, Fe,[24–27] Co,[28–32] and Cu[16,33–36] catalysts show promise for selective nitrate reduction, with Cu nanosheets achieving >99% FE to ammonia.[37] However, these high FEs are accompanied by sub-mg per hour production rates per mg of catalyst, which is far below any industrially relevant production rate.

2D materials have recently garnered attention for use in electrochemical reactions and gas sorption. MXenes, which are derived from A-etching of MAX-phase materials (layered ternary carbides or nitrides), have already been shown to catalyze electrochemical hydrogen evolution,[38] CO_2 reduction,[39] and even nitrogen reduction.[40] A natural extension of the 2D MXene platform is the 2D Mbene, which is analogously derived via A-etching of MAB-phase materials (Figure 8.1).[41–45] The key difference in the MBene platform is the underlying boride structure, in contrast to MXene's carbide layer. Mbenes have recently been explored for electrocatalysis, showing potential for oxygen and hydrogen evolution,[46–49] as well as for use in carbon capture.[50] Unlike MXenes, MBenes do not require surface passivation, making them more preferable for applications in heterogeneous catalysis.[51] The impetus for investigating MBenes towards nitrate reduction is the fact that they bind oxygen with exceptional strength. Additionally, the transition metal atoms exposed on the MBene surfaces have in-plane spacing commensurate with the O-O distances of nitrate. These two factors suggest that MBenes may provide ideal surfaces for strong binding of nitrate, which will hopefully give way towards selective nitrate reduction. Herein, we leverage Density Functional Theory calculations to explore and validate different transition metal MBenes for the facile conversion of nitrate to ammonia.

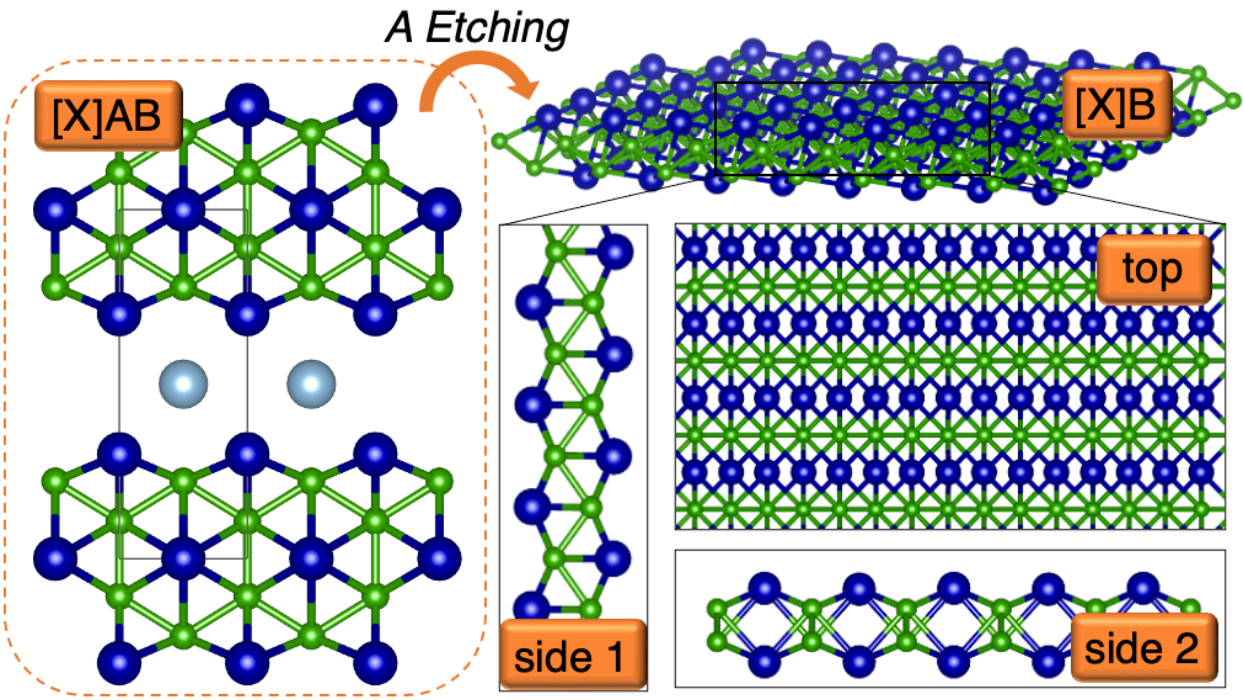

Figure 8.1: Illustration of the MAB-phase precursor (with formula [X]AB where [X] = transition metal) which can be A-etched to form 2D MBenes of the formula [X]B. Green, blue, and light-blue atoms are boron, [X], and Al, respectively.

8.3 Methods

The Vienna Ab initio Simulation Package (VASP) version 6.3.2 was used for all Density Functional Theory (DFT) geometry optimizations.[52] All structures were first optimized in VASP with the PBE functional[53] and the Grimme D3BJ empirical correction for London Dispersion interactions.[54] All atoms were described using Projector Augmented Wave (PAW) pseudopotentials[55] with a global planewave energy cutoff of 520 eV. To avoid antiferromagnetic states, all calculations featured polarized spins, with the initial

magnetic moments all aligned to high spin. All slab calculations featured gamma-centered 3 x 5 x 1 K point meshes. VASP was also used to compute the phonon spectra at 298.15 K in order to predict thermochemical properties such as zero-point energies and entropies.

Following the geometry optimizations performed in VASP, high-accuracy solution-phase energies were computed using the JDFTx plane-wave code.[56] These solution-phase computations featured implicit solvent treatment as modeled by the CANDLE solvation method.[57] Solvation parameters were chosen to match that of liquid water. Coulomb interactions were truncated in the direction orthogonal to the MBene plane, such that spurious, axial interactions of the MBene with itself are eliminated.

8.4 Results and Discussion

8.4.1 Nitrate versus Water Adsorption

Nitrate reduction is often performed in the potential window of 0.0 to -1.0 V vs RHE and usually at neutral to basic pH. Competitive hydrogen evolution would normally pose a threat to nitrate reduction but because MBenes preferably bind oxygen over hydrogen, reduction of water to generate H_2 is unlikely to occur under nitrate-reducing conditions. However, strong oxygen binding will make water adsorption favorable, which may compete with nitrate reduction via competitive adsorption.

We initiate our study by computing the nitrate binding energies and water adsorption energies on our ground-state MBene surfaces. We started with 13 MBene structures that were previously determined to be stable according to a phonon band structure analysis (0 imaginary frequencies indicating structural stability).[58] We computed the nitrate and water binding energies according to the following reactions:

1. $2 * + NO_3^- \rightarrow *NO_3^-$
2. $2 * + 2\ H_2O \rightarrow 2\ *H_2O$

where * indicates an open catalyst site, $*NO_3^-$ is an adsorbed nitrate, and $*H_2O$ is an adsorbed water. Note that the adsorption of nitrate requires 2 open catalyst sites while each water requires 1; this is because the nitrate binds to two transition metals simultaneously via two of the three oxygen atoms, while water binds to just one transition metal atom in the conventional fashion. For clarity, the adsorptions of nitrate and water are depicted in Figure 8.2.

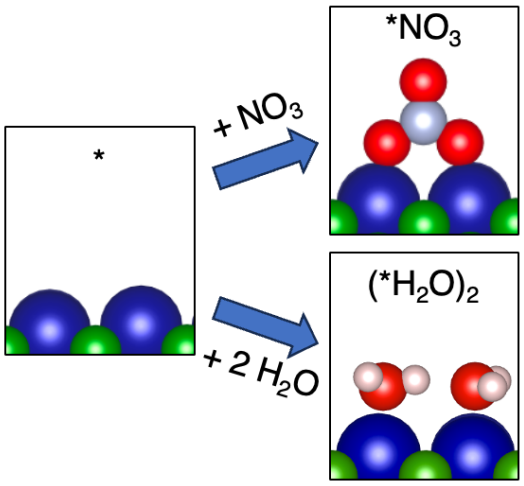

Figure 8.2: Depiction of nitrate (NO_3^-) and water (H_2O) adsorption on the pristine MBene surface. The grey atom denotes nitrogen and the red atoms denote oxygen.

The nitrate and water adsorption energies are listed in Table 8.1. Of the 13 MBenes initially screened, the Co, Ru, Re, and Os catalysts were discarded due to structural instability upon nitrate binding. Specifically, upon binding nitrate to these MBenes, the MBenes underwent substantial geometric rearrangement, resulting in destruction of the parent MBene geometry. The remaining nine MBenes maintained their form upon binding of nitrate and water. As expected, all MBenes bind nitrate with exceptional strength. The weakest nitrate binding is held by FeB which binds nitrate by -4.34 eV. The strongest nitrate binding is held by TiB in which nitrate is adsorbed to the catalyst by -5.62 eV. All Mbenes bind nitrate with exceptional strength, to an extent in which poisoning of the catalyst by nitrate could be an issue (see below for further discussion). Water adsorption is also thermodynamically favorable on the MBene surfaces, although nitrate binding is

stronger across the board. DFT predicts the MnB catalyst to bind water the weakest at -1.07 eV for 2 waters. On the other hand, DFT predicts the WB catalyst to bind water the strongest at -1.88 eV for 2 waters.

Table 8.1: Predicted Nitrate and water adsorption free energies at 298.15 K in eV.

Element	ΔG_{*NO3}	$\Delta G_{(*H2O)2}$
Tc	-4.45	-1.60
Ti	-5.62	-1.53
Mn	-4.44	-1.07
Fe	-4.34	-1.56
Cr	-4.87	-1.53
V	-5.35	-1.52
Nb	-5.15	-1.58
W	-5.08	-1.88
Mo	-4.93	-1.56

Because all MBenes bind nitrate so strongly, we need not worry about desorption; if anything, we should be concerned about catalyst poisoning by nitrate. Because the Gibbs free energy drops so precipitously upon nitrate adsorption, it is possible that the

$*NO_3^-$ state acts as a thermodynamic sink, such that neither desorption nor further reduction can occur. To test this hypothesis, we also computed the $*HNO_3$ state, which will reveal whether the $*NO_3^-$ intermediate acts as a thermodynamic sink or is capable of further reduction towards ammonia. The free energies for converting $*NO_3^-$ to $*HNO_3$ can be found in Table F31 of Appendix F. DFT predicts that the conversion of $*NO_3^-$ to $*HNO_3$ is downhill in free energy for almost all MBenes. The MnB and CrB MBenes convert $*NO_3^-$ to $*HNO_3$ with almost no change in free energy (+0.07 and 0.00 eV, respectively). The conversion of $*NO_3^-$ to $*HNO_3$ is endergonic +0.59 eV for FeB, making it the only MBene for which the reduction of $*NO_3^-$ to $*HNO_3$ is uphill in free energy.

8.4.2 Nitrate Reduction Mechanism

At this stage, we have computed the adsorption energies for nitrate and water species, as well as computed the free energy changes for reducing $*NO_3^-$ to $*HNO_3$. We find that nitrate and water binding energies are strong for all catalysts, and that all catalysts except FeB can theoretically convert $*NO_3^-$ to $*HNO_3$. To eliminate some MBenes from consideration, we look primarily towards water binding energies. Since nitrate reduction will be performed in aqueous media, a big concern would be blocking of catalyst sites by water. Therefore, we should seek the catalysts with the weakest water

binding. Of the MBenes screened, the MnB, CrB, and VB catalysts hold the weakest water binding energies. Specifically, the MnB, CrB, and VB catalysts bind two waters with free energies of -1.07, -1.53, and -1.52 eV, respectively. These three catalysts bind nitrate strongly and are capable of converting $*NO_3^-$ to $*HNO_3$, making them the best candidates for further exploration.

We now explore the reaction mechanisms for converting nitrate to ammonia. The entire conversion requires 9 reduction steps. For the purposes of computing thermodynamic free energy changes, we assume these reduction steps occur in the forms of proton-coupled electron transfers or PCETs. In aqueous media, the resting state of the catalyst is likely the MBene with adsorbed water. The first step is to desorb two waters and adsorb nitrate. With nitrate present, the first PCET generally occurs at the oxygen furthest from the catalyst surface, generating $*HNO_3$. The next PCET can either (i) occur at the same oxygen to afford $*NO_2$ and liberate a water, or (ii) occur at one of the oxygens bound to the MBene surface to afford $*NO_2H*OH$. From here the mechanism begins to branch due to the multiple sites where PCET can occur. The most likely reaction sequences that can occur are depicted in Figure 8.3.

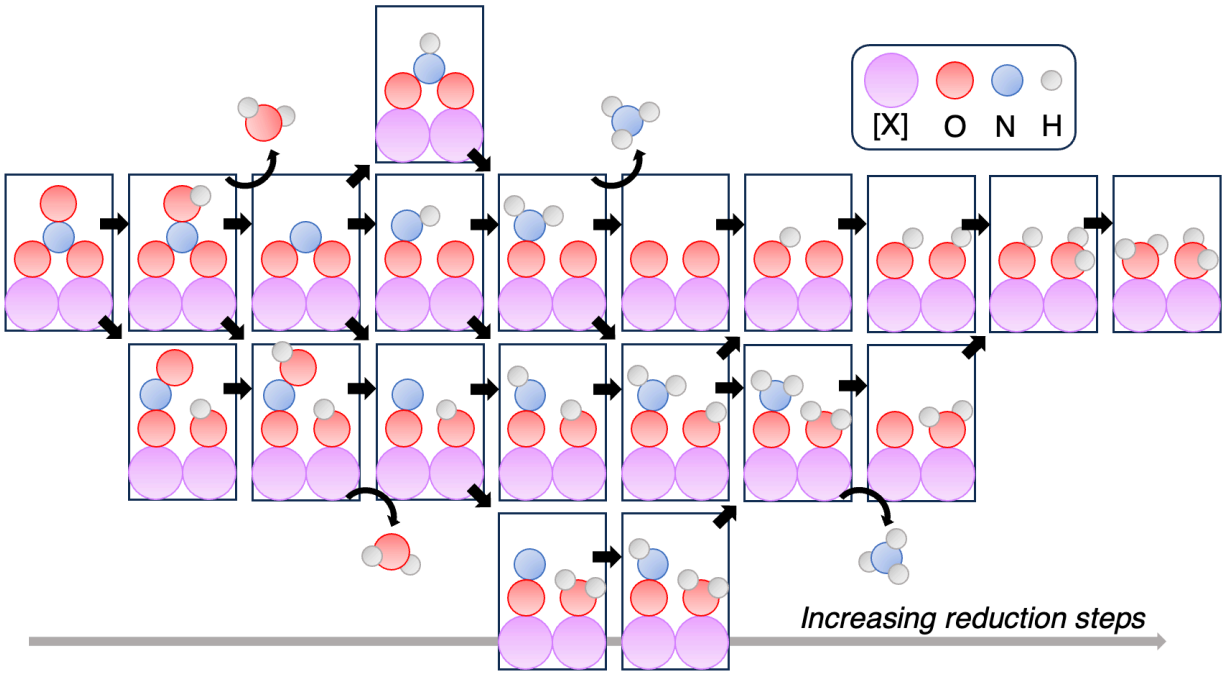

Figure 8.3: Common reaction sequence for nitrate reduction to ammonia. As depicted, the overall reaction to convert nitrate to ammonia and 2 waters requires 9 reduction steps. This diagram neglects the adsorption of nitrate and desorption of water. Straight arrows denote steps in which proton-coupled electron transfers occur.

The reaction mechanisms for MnB, CrB, and VB-catalyzed conversion of nitrate to ammonia are illustrated in Figure 8.4. As stated above, all catalysts in reality would proceed through the sequence: 2 $*H_2O$ → * → $*NO_3^-$ → $*HNO_3$. However, to compare the total free energy changes for converting nitrate to ammonia, we initiate the reaction mechanism with the pristine * state and terminate the mechanism with the 2 $*H_2O$ state.

For MnB, the second PCET to the $*HNO_3$ intermediate generates $*NO_2*H_2O$, which is more thermodynamically stable than $*NO_2$ + H_2O by -0.38 eV; this is trivial given that

the energy difference is the desorption of water. The third PCET converts *NO_2*H_2O to *NO_2H+ H_2O; this intermediate is more stable than *NOH*O by -2.08 eV, due mostly to the entropic gain of liberating the free water molecule. The fourth and fifth PCETs follow the sequence *NO_2H → *NOH_2*O → *NOH_2*OH. The sixth PCET converts *NOH_2*OH to *O*OH and liberates the desired ammonia product. From here, the seventh through ninth PCETs occur as *O*OH → $(*OH)_2$ → *OH*H_2O → $(*H_2O)_2$. The overall change in free energy for this reaction is -8.97 eV, with the potential-limiting step being the conversion of *NO_2*H_2O to *NO_2H which is uphill +0.66 eV.

CrB proceeds through a different mechanism than MnB. Skipping straight to *HNO_3, the second PCET generates *NO_2 + H_2O, which is -0.36 eV more stable than *NO_2H*OH. This is in contrast to MnB where *NO_2*H_2O was more stable than *NO_2 + H_2O; the key difference is that for MnB, the water was formed on the surface, but for CrB, the water is formed from the oxygen furthest from the CrB surface, such that the water goes towards solution as opposed to towards any open surface site. The third PCET converts *NO_2 to *NOH*O, which is -0.84 eV more stable than *NO*OH. This is again in contrast to MnB which prefers the formation of *NO_2H over *NOH*O. The remainder of the mechanism is identical to MnB. From *NOH*O, the proceeding PCETs occur via the sequence: *NOH*O → *NOH_2*OH → *NOH_2*OH → *O*OH → $(*OH)_2$ → *OH*H_2O → $(*H_2O)_2$. The total free energy change for CrB-catalyzed conversion of nitrate to

ammonia is -9.43 eV. Here the potential-limiting step is the final conversion of *OH*H_2O to $(*H_2O)_2$, which is uphill +0.38 eV.

VB converts nitrate to ammonia through a pathway nearly identical to the path for CrB with the exception of the second PCET. Following formation of *HNO_3, the second PCET generates *NO_2H*OH, which is -0.82 eV more stable than the *NO_2 + H_2O state. The remaining PCETs follow the same sequence as the third through ninth PCETs that the CrB catalyst undergoes: *NOH*O → *NOH_2*O → *NOH_2*OH → *O*OH → $(*OH)_2$ → *OH*H_2O → $(*H_2O)_2$. The VB catalyst converts nitrate to ammonia with an overall free energy change of -9.42 eV, which is nearly identical to that of the CrB catalyst. VB also has the same potential-limiting step as CrB which is the conversion of *OH*H_2O to $(*H_2O)_2$, although VB requires +0.84 eV for this step.

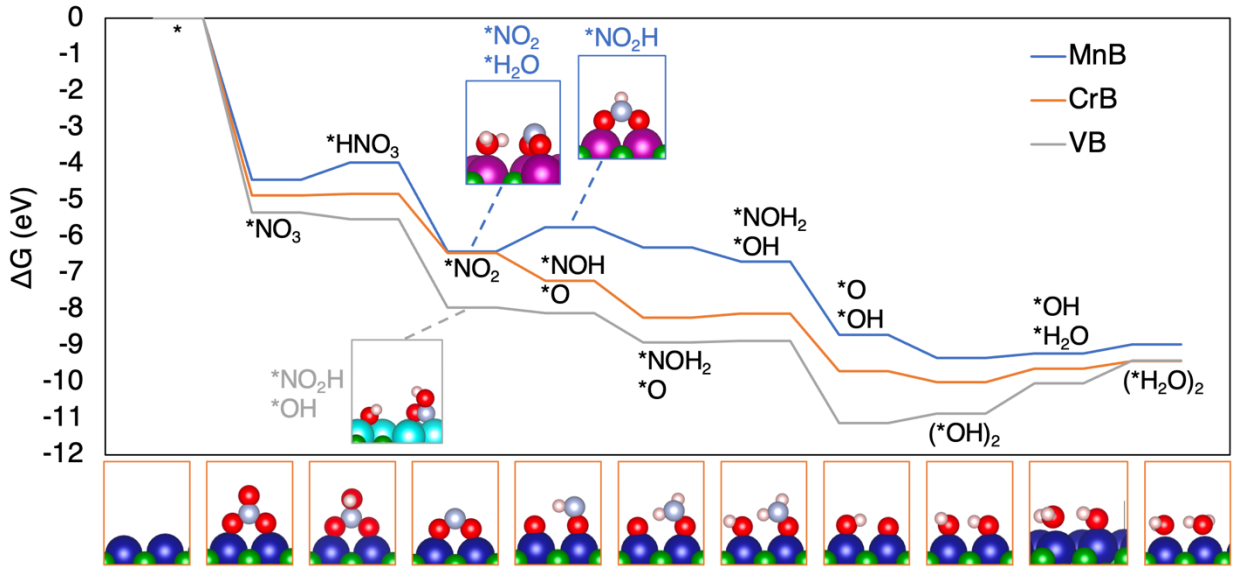

Figure 8.4: Free energy landscapes at 298.15 K for the conversion of nitrate to ammonia using MnB (blue), CrB (orange), and VB (grey). The bottom images outlined in orange depict the reaction intermediates for the CrB-catalyzed reaction. The blue and grey-outlined images in the inset depict intermediates for the MnB and VB-catalyzed reactions that deviate from those in the CrB reaction.

To summarize briefly, DFT predicts that the MnB, CrB, and VB MBenes convert nitrate to ammonia with overall free energy changes of -8.97, -9.43, and -9.42 eV respectively, which is in line with an electrochemical reaction consisting of 9 reduction steps. The potential-limiting step for MnB was the conversion of $*NO_2*H_2O$ to $*NO_2H$ which is uphill +0.66 eV. For CrB the conversion of $*OH*H_2O$ to $(*H_2O)_2$ was potential-limiting, requiring a free energy change of +0.38 eV. The conversion of $*OH*H_2O$ to $(*H_2O)_2$ was also the potential-limiting step for VB, requiring a free energy change of +0.84 eV. These DFT-predicted energetics suggest that CrB is the best catalyst for electrochemically converting nitrate to ammonia, due primarily to its low limiting potential.

VB converts nitrate to ammonia through a mechanism nearly identical to CrB, yet the energetics are notably worse. It appears that VB's decreased performance is due to overly strong binding of oxygen. Once *OH are formed on the VB surface, strong V-O bonding makes it difficult to convert *OH to $*H_2O$ since the protonation requires breaking

the V-O bond. This is evidenced by the highly endergonic conversions of $(*OH)_2$ to $*OH*H_2O$ and $*OH*H_2O$ to $(*H2O)_2$, since both steps break a V-O bond.

In the case of MnB, the reaction mechanism deviates from the CrB and VB mechanisms during the second and third PCETs; this deviation in the path also marks MnB's potential-limiting conversion of $*NO_2*OH$ to $*NO_2H$. The endergonicity of converting $*NO_2*OH$ to $*NO_2H$ can be deconvoluted into the desorption of H_2O from the surface and PCET to the $*NO_2$ fragment to form $*NO_2H$. Because the desorption of H_2O is canonically a chemical step and not electrochemical, we should exclude the water desorption energy from this step and focus solely on the energy required for PCET to convert the $*NO_2$ fragment to $*NO_2H$. If we subtract the water desorption energy (+0.53 eV) from the free energy change of converting $*NO_2*OH$ to $*NO_2H$ (+0.66 eV), we arrive at +0.13 eV, which suggests that MnB may be comparable to CrB for reducing nitrate to ammonia.

8.4.3 MBene Doping for Enhanced Electroreduction

CrB establishes itself as the best MBene for reducing nitrate to ammonia. We question if the reaction energetics can be further improved via substitutional doping. Given that several of the reaction intermediates involve binding to multiple sites on the

MBene surface, replacement of one of the Cr centers with a different transition metal could provide more thermodynamically favorable PCETs and ultimately more facile production of ammonia. To identify which metals may improve upon CrB's nitrate to ammonia energetics, we started by evaluating the $(*OH)_2$ → $*OH*H_2O$ → $(*H_2O)_2$ reaction sequence, which encompasses the two potential-limiting steps for CrB. For each of the transition metals originally screened in this study, we embedded said metal in the place of one Cr in the CrB active site. We then computed the free energy change for the two PCETs required to convert $(*OH)_2$ to $(*H_2O)_2$; the energy to beat is +0.59 eV which is the sum of the free energy changes for the parent CrB catalyst to convert $(*OH)_2$ to $*OH*H_2O$ (+0.38 eV) and $*OH*H_2O$ to $(*H_2O)2$ (+0.21 eV). The free energy changes for converting $(*OH)_2$ to $(*H_2O)_2$ for the various doped CrB MBenes can be found in Table F32 of Appendix F. Amongst the 9 doped CrB MBenes, the best energetics were held by Ru and Mn-doped CrB. Specifically, doping CrB with Ru decreased the free energy change of converting $(*OH)_2$ to $(*H_2O)_2$ to +0.11 eV, and doping CrB with Mn decreased the free energy change to +0.54 eV. The Mn doping did not provide a significant improvement beyond the parent CrB, but given that the MnB catalyst was the second best candidate for electrochemical nitrate reduction (second only to CrB), the Mn-doped CrB poses an interesting possibility for further improved catalysis.

Equipped with the result that doping of CrB with Ru and Mn decreases the endergonicity of the potential-limiting reaction steps, we now compute the entire reaction mechanisms for Ru and Mn-doped CrB catalysts. Because the active sites now contain two different metals, the catalyst is now asymmetric such that several of the PCETs that occur along the reaction path now produce different conformers dependent on the location of the PCET; this is in contrast to the parent CrB catalyst which maintained a symmetric active site, which eliminated several reaction intermediate possibilities via symmetry. For simplicity, we only discuss the lowest-energy conformations of the Ru and Mn-doped CrB catalysts. The reaction paths are displayed in Figure 8.5.

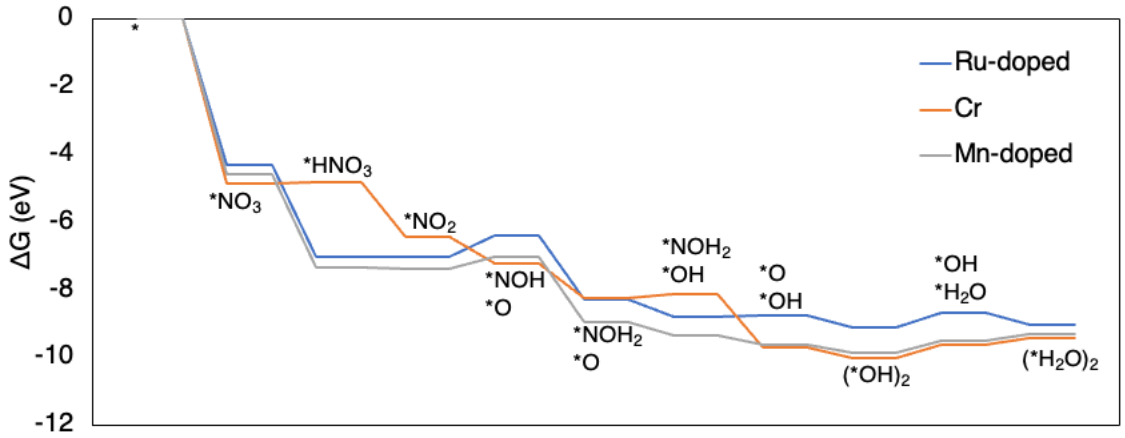

Figure 8.5: Free energy landscapes at 298.15 K for the conversion of nitrate to ammonia using CrB (orange), the Ru-doped CrB (blue), and the Mn-doped CrB (grey).

Recall that for the parent CrB MBene the overall free energy change is -9.43 eV and the potential-limiting step is converting $(*OH)_2$ to $*OH*H_2O$ which is uphill +0.38 eV. When doped with Ru, the overall free energy change is -9.02 eV, which is +0.41 eV less exergonic than the parent CrB catalyst. While the conversion of $(*OH)_2$ → $(*H_2O)_2$ is now only uphill +0.11 eV, when deconstructed into the two separate $(*OH)_2$ → $*OH*H_2O$ and $*OH*H_2O$ → $(*H_2O)_2$ steps, we discover that the free energy gain is due solely to the latter step, which is downhill -0.35 eV. However, the preceding $(*OH)_2$ → $*OH*H_2O$ step is substantially uphill at +0.46 eV, which is greater than the parent CrB's +0.38 eV. Moreover, we find that the conversion of $*NO_2$ → *NOH*O is actually more endergonic at +0.63 eV, such that $*NO_2$ to *NOH*O is potential-limiting for Ru-doped CrB instead of $(*OH)_2$ → $*OH*H_2O$. These results suggest that doping of CrB with Ru offers no improvement towards the conversion of nitrate to ammonia.

Doping the CrB MBene with a Mn atom results in an overall free energy change of -9.32 eV for converting nitrate to ammonia. This free energy change is -0.30 eV better than the Ru-doped CrB but +0.11 eV worse than the parent CrB. As seen previously, the conversion of $(*OH)_2$ → $(*H_2O)_2$ is uphill +0.54 eV which is a slight improvement over the parent CrB. When deconstructed into the $(*OH)_2$ → $*OH*H_2O$ and $*OH*H_2O$ → $(*H_2O)_2$ steps we arrive at free energy changes of +0.33 and +0.21 eV, respectively, which is an improvement beyond the original CrB which required +0.38 and +0.21 eV for these

steps. Similar to the Ru-doped CrB, the $*NO_2$ → *NOH*O step becomes a competitively endergonic step, requiring +0.33 eV for the Mn-doped CrB.

8.4.4 Grand Canonical Free Energies for Mn-doped CrB

In experiment, nitrate reduction is typically performed at negative bias. Sargent et al. previously reported nitrate reduction to ammonia using Cu-Ni alloys at -0.1 V vs. RHE, achieving 99% faradic efficiency (FE) at -90 mA/cm^2.[59] Using strained Ru nanoclusters, Li and coworkers reported ~100% FE to ammonia at -120 mA/cm^2 when performed at -0.2 V vs. RHE.[23] To understand how Mn-doped CrB catalyzes the reaction at different applied potentials, we now compute the free energy landscape using grand canonical DFT (GC-DFT).[60] This is achieved by computing the reaction intermediates at varying electron count, and then applying a Legendre transform to convert from constant-electron to constant-potential. By fitting the free energy vs number of electrons to a 2^{nd}-order polynomial, we extract such other features as the differential capacitance, potential at zero-charge, and free energy at zero charge.[61,62] The free energy landscapes at relevant applied potentials are shown in Figure 8.6. We note that in the GC-DFT formalism, the system is coupled to an electron bath, which adds and removes electrons depending on

the potential. Because of this feature, it is not necessary for the system to include an explicit conducting support.

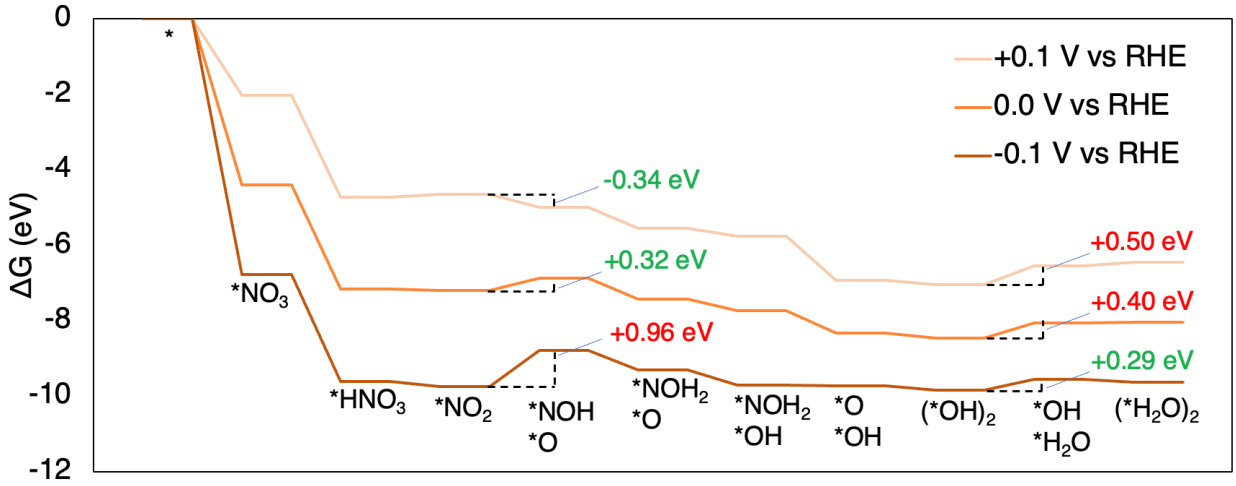

Figure 8.6: Free energy landscapes at 298.15 K for the conversion of nitrate to ammonia at applied potentials of +0.1, 0.0, and -0.1 V vs RHE using the Mn-doped CrB MBene.

Previous experimental studies on nitrate reduction were performed near -0.1 V vs RHE so we computed the nitrate to ammonia reaction mechanisms at +0.1, 0.0, and -0.1 V vs RHE. At these potentials, we observe no change in the reaction mechanism relative to the 0-charge state. At +0.1 V vs RHE, the total free energy change for converting nitrate to ammonia is -6.47 eV. At potentials of 0.0 and -0.1 V vs RHE, the total free energy change decreases to -8.05 and -9.63 eV, respectively; these values are again in line with the 9-step reduction process.

At +0.1, 0.0, and -0.1 V vs RHE, the free energy drops dramatically at the * → $*NO_3^-$ and $*HNO_3$ steps. The proceeding PCET to form $*NO_2$ is nearly thermoneutral in this potential window. Upon formation of $*NO_2$, the next PCET shifts the free energy change significantly from +0.1 to -0.1 V vs RHE. At +0.1, 0.0, and -0.1 V vs RHE, $*NO_2$ → *NOH*O is downhill -0.34, +0.32, and +0.96 eV, respectively. The following 4 PCETS are all downhill within the potential window, which brings us to the $(*OH)_2$ → $*OH*H_2O$ step. At +0.1, 0.0, and -0.1 V vs RHE, this step is +0.50, +0.40, and +0.29 eV, respectively. When comparing these energies to the energies for $*NO_2$ → *NOH*O at the same potentials, we discover that the potential-limiting step changes as the potential shifts from 0.0 to -0.1 V vs RHE. At 0.0 V vs RHE the potential-limiting step is $(*OH)_2$ → $*OH*H_2O$ which requires +0.40 eV; at -0.1 V vs RHE the potential-limiting step becomes $*NO_2$ → *NOH*O which requires +0.96 eV. Analysis of the $*NO_2$ → *NOH*O and $(*OH)_2$ → $*OH*H_2O$ free energy changes versus applied potential reveals the $*NO_2$ → *NOH*O step to become more positive with more negative potential, while the $(*OH)_2$ → $*OH*H_2O$ step becomes more negative with more negative potential. These two potential-limiting steps are inversely proportional, suggesting that the optimal potential should be selected as the potential where the free energies for these steps intersect. The intersection occurs at -0.01 V vs RHE, where the free energy change for both steps is +0.37 eV.

8.5 Conclusions

Electrochemical nitrate reduction is crucial for rebalancing the global nitrogen cycle and ensuring a sustainable future. In this study we evaluate 2D MBene materials for facile electrochemical reduction of nitrate to ammonia. We demonstrate the plausibility of the MBene catalyst for generating ammonia at modest applied potential. We started with 13 different MBenes and found that of the 9 MBenes capable of adsorbing nitrate, the MnB, CrB, and VB catalysts exhibited moderate nitrate binding and weak water binding, making them the best candidates for converting nitrate to ammonia. The entire 10-step reaction mechanism was then computed for the MnB, CrB, and VB catalysts. Density Functional Theory predicts the free energy changes for the potential-limiting steps to be +0.66, +0.38, and +0.84 eV for these catalysts, respectively. The CrB reaction energetics are superior to the MnB and VB catalysts, with the potential-limiting steps originating from the $(*OH)_2$ → $*OH*H_2O$ → $(*H_2O)_2$ reaction sequence. We then doped the CrB MBene with other transition metals in an attempt to improve the $(*OH)_2$ → $*OH*H_2O$ → $(*H_2O)_2$ energetics. DFT predicts that doping CrB with Ru and Mn lowers the free energy requirements for the potential-limiting steps, with the Mn-doped CrB providing the best overall energetics. Finally, we computed the Mn-doped CrB free energy landscape grand canonically to understand how the reaction mechanism changes with applied potential. We found that the optimal potential to operate at is -0.01 V vs RHE which

provides a potential-limiting free energy change of +0.37 eV which originates both from the conversion of $*NO_2$ → $*NOH*O$ and $(*OH)_2$ → $*OH*H_2O$.

We consider this letter a proof of concept which should act as a foundation for further exploration on MBene-catalyzed nitrate reduction. Follow-up studies should investigate the effect of increasing MBene thickness, as well as consideration of surface oxidation and vacancy formation.

8.6 References

(1) Kandemir, T.; Schuster, M. E.; Senyshyn, A.; Behrens, M.; Schlögl, R. The Haber-Bosch Process Revisited: On the Real Structure and Stability of "Ammonia Iron" under Working Conditions. *Angew. Chemie - Int. Ed.* **2013**, *52* (48), 12723–12726.

(2) Barelli, L.; Bidini, G.; Gallorini, F.; Servili, S. Hydrogen Production through Sorption-Enhanced Steam Methane Reforming and Membrane Technology: A Review. *Energy* **2008**, *33* (4), 554–570.

(3) Zhao, X.; Hu, G.; Chen, G. F.; Zhang, H.; Zhang, S.; Wang, H. Comprehensive Understanding of the Thriving Ambient Electrochemical Nitrogen Reduction Reaction. *Adv. Mater.* **2021**, *33* (33), 2007650.

(4) Foster, S. L.; Bakovic, S. I. P.; Duda, R. D.; Maheshwari, S.; Milton, R. D.; Minteer,

S. D.; Janik, M. J.; Renner, J. N.; Greenlee, L. F. Catalysts for Nitrogen Reduction to Ammonia. *Nat. Catal.* **2018**, *1* (7), 490–500.

(5) Rehman, F.; Kwon, S.; Hossain, M. D.; Musgrave, C. B.; Goddard, W. A.; Luo, Z. Reaction Mechanism and Kinetics for N2 Reduction to Ammonia on the Fe-Ru Based Dual-Atom Catalyst. *J. Mater. Chem. A* **2022**, *10*, 23323–23331.

(6) Skúlason, E.; Bligaard, T.; Gudmundsdóttir, S.; Studt, F.; Rossmeisl, J.; Abild-Pedersen, F.; Vegge, T.; Jónsson, H.; Nørskov, J. K. A Theoretical Evaluation of Possible Transition Metal Electro-Catalysts for N2 Reduction. *Phys. Chem. Chem. Phys.* **2012**, *14*, 1235–1245.

(7) Furuya, N.; Yoshiba, H. Electroreduction of Nitrogen to Ammonia on Gas-Diffusion Electrodes Modified by Metal Phthalocyanines. *J. Electroanal. Chem.* **1989**, *272* (1–2), 263–266.

(8) Musgrave, C. B.; Morozov, S.; Schinski, W. L.; Goddard, W. A. Reduction of N2to Ammonia by Phosphate Molten Salt and Li Electrode: Proof of Concept Using Quantum Mechanics. *J. Phys. Chem. Lett.* **2021**, *12* (6), 1696–1701.

(9) Qian, J.; An, Q.; Fortunelli, A.; Nielsen, R. J.; Goddard, W. A. Reaction Mechanism and Kinetics for Ammonia Synthesis on the Fe(111) Surface. *J. Am. Chem. Soc.* **2018**, *140* (20), 6288–6297.

(10) van Langevelde, P. H.; Katsounaros, I.; Koper, M. T. M. Electrocatalytic Nitrate

Reduction for Sustainable Ammonia Production. *Joule* **2021**, *5* (2), 290–294.

(11) Rosca, V.; Duca, M.; DeGroot, M. T.; Koper, M. T. M. Nitrogen Cycle Electrocatalysis. *Chem. Rev.* **2009**, *109* (6), 2209–2244.

(12) Duca, M.; Koper, M. T. M. Powering Denitrification: The Perspectives of Electrocatalytic Nitrate Reduction. *Energy Environ. Sci.* **2012**, *5*, 9726–9742.

(13) Liang, X.; Zhu, H.; Yang, X.; Xue, S.; Liang, Z.; Ren, X.; Liu, A.; Wu, G. Recent Advances in Designing Efficient Electrocatalysts for Electrochemical Nitrate Reduction to Ammonia. *Small Struct.* **2023**, *4* (6), 2200202.

(14) Lv, L.; Shen, Y.; Liu, J.; Meng, X.; Gao, X.; Zhou, M.; Zhang, Y.; Gong, D.; Zheng, Y.; Zhou, Z. Computational Screening of High Activity and Selectivity TM/g-C3N4 Single-Atom Catalysts for Electrocatalytic Reduction of Nitrates to Ammonia. *J. Phys. Chem. Lett.* **2021**, *12* (45), 11143–11150.

(15) Rehman, F.; Kwon, S.; Musgrave, C. B.; Tamtaji, M.; Goddard, W. A.; Luo, Z. High-Throughput Screening to Predict Highly Active Dual-Atom Catalysts for Electrocatalytic Reduction of Nitrate to Ammonia. *Nano Energy* **2022**, *103B*, 107866.

(16) Chen, F. Y.; Wu, Z. Y.; Gupta, S.; Rivera, D. J.; Lambeets, S. V.; Pecaut, S.; Kim, J. Y. T.; Zhu, P.; Finfrock, Y. Z.; Meira, D. M.; King, G.; Gao, G.; Xu, W.; Cullen, D. A.; Zhou, H.; Han, Y.; Perea, D. E.; Muhich, C. L.; Wang, H. Efficient

Conversion of Low-Concentration Nitrate Sources into Ammonia on a Ru-Dispersed Cu Nanowire Electrocatalyst. *Nat. Nanotechnol.* **2022**, *17*, 759–767.

(17) Lim, J.; Liu, C. Y.; Park, J.; Liu, Y. H.; Senftle, T. P.; Lee, S. W.; Hatzell, M. C. Structure Sensitivity of Pd Facets for Enhanced Electrochemical Nitrate Reduction to Ammonia. *ACS Catal.* **2021**, *11* (12), 7568–7577.

(18) Soares, O. S. G. P.; Pereira, M. F. R.; Órfão, J. J. M.; Faria, J. L.; Silva, C. G. Photocatalytic Nitrate Reduction over Pd-Cu/TiO2. *Chem. Eng. J.* **2014**, *251*, 123–130.

(19) Prüsse, U.; Vorlop, K. D. Supported Bimetallic Palladium Catalysts for Water-Phase Nitrate Reduction. *J. Mol. Catal. A Chem.* **2001**, *173* (1–2), 313–328.

(20) Taguchi, S.; Feliu, J. M. Kinetic Study of Nitrate Reduction on Pt(1 1 0) Electrode in Perchloric Acid Solution. *Electrochim. Acta* **2008**, *53* (10), 3626–3634.

(21) Wang, Z.; Young, S. D.; Goldsmith, B. R.; Singh, N. Increasing Electrocatalytic Nitrate Reduction Activity by Controlling Adsorption through PtRu Alloying. *J. Catal.* **2021**, *395*, 143–154.

(22) Dima, G. E.; Beltramo, G. L.; Koper, M. T. M. Nitrate Reduction on Single-Crystal Platinum Electrodes. *Electrochim. Acta* **2005**, *50* (21), 4318–4326.

(23) Li, J.; Zhan, G.; Yang, J.; Quan, F.; Mao, C.; Liu, Y.; Wang, B.; Lei, F.; Li, L.; Chan, A. W. M.; Xu, L.; Shi, Y.; Du, Y.; Hao, W.; Wong, P. K.; Wang, J.; Dou, S.

X.; Zhang, L.; Yu, J. C. Efficient Ammonia Electrosynthesis from Nitrate on Strained Ruthenium Nanoclusters. *J. Am. Chem. Soc.* **2020**, *142* (15), 7036–7046.

(24) Wu, Z. Y.; Karamad, M.; Yong, X.; Huang, Q.; Cullen, D. A.; Zhu, P.; Xia, C.; Xiao, Q.; Shakouri, M.; Chen, F. Y.; Kim, J. Y. (Timothy); Xia, Y.; Heck, K.; Hu, Y.; Wong, M. S.; Li, Q.; Gates, I.; Siahrostami, S.; Wang, H. Electrochemical Ammonia Synthesis via Nitrate Reduction on Fe Single Atom Catalyst. *Nat. Commun.* **2021**, *12*, 2870.

(25) Mossa Hosseini, S.; Ataie-Ashtiani, B.; Kholghi, M. Nitrate Reduction by Nano-Fe/Cu Particles in Packed Column. *Desalination* **2011**, *276* (1–3), 214–221.

(26) Postma, D. Kinetics of Nitrate Reduction by Detrital Fe(II)-Silicates. *Geochim. Cosmochim. Acta* **1990**, *54* (3), 903–908.

(27) Huang, C. P.; Wang, H. W.; Chiu, P. C. Nitrate Reduction by Metallic Iron. *Water Res.* **1998**, *32* (8), 2257–2264.

(28) Deng, X.; Yang, Y.; Wang, L.; Fu, X. Z.; Luo, J. L. Metallic Co Nanoarray Catalyzes Selective NH3 Production from Electrochemical Nitrate Reduction at Current Densities Exceeding 2 A Cm−2. *Adv. Sci.* **2021**, *8* (7), 2004523.

(29) Fu, W.; Du, X.; Su, P.; Zhang, Q.; Zhou, M. Synergistic Effect of Co(III) and Co(II) in a 3D Structured Co3O4/Carbon Felt Electrode for Enhanced Electrochemical Nitrate Reduction Reaction. *ACS Appl. Mater. Interfaces* **2021**, *13* (24), 28348–

28358.

(30) Fan, X.; Zhao, D.; Deng, Z.; Zhang, L.; Li, J.; Li, Z.; Sun, S.; Luo, Y.; Zheng, D.; Wang, Y.; Ying, B.; Zhang, J.; Alshehri, A. A.; Lin, Y.; Tang, C.; Sun, X.; Zheng, Y. Constructing Co@TiO2 Nanoarray Heterostructure with Schottky Contact for Selective Electrocatalytic Nitrate Reduction to Ammonia. *Small* **2023**, *19* (17), 2208036.

(31) Zhang, S.; Li, M.; Li, J.; Song, Q.; Liu, X. High-Ammonia Selective Metal-Organic Framework-Derived Co-Doped Fe/Fe2O3 Catalysts for Electrochemical Nitrate Reduction. *Proc. Natl. Acad. Sci. U. S. A.* **2022**, *119* (6), e2115504119.

(32) Gao, J.; Jiang, B.; Ni, C.; Qi, Y.; Zhang, Y.; Oturan, N.; Oturan, M. A. Non-Precious Co3O4-TiO2/Ti Cathode Based Electrocatalytic Nitrate Reduction: Preparation, Performance and Mechanism. *Appl. Catal. B Environ.* **2019**, *254*, 391–402.

(33) Wu, K.; Sun, C.; Wang, Z.; Song, Q.; Bai, X.; Yu, X.; Li, Q.; Wang, Z.; Zhang, H.; Zhang, J.; Tong, X.; Liang, Y.; Khosla, A.; Zhao, Z. Surface Reconstruction on Uniform Cu Nanodisks Boosted Electrochemical Nitrate Reduction to Ammonia. *ACS Mater. Lett.* **2022**, *4* (4), 650–656.

(34) Zhu, T.; Chen, Q.; Liao, P.; Duan, W.; Liang, S.; Yan, Z.; Feng, C. Single-Atom Cu Catalysts for Enhanced Electrocatalytic Nitrate Reduction with Significant

Alleviation of Nitrite Production. *Small* **2020**, *16* (49), 2004526.

(35) Teng, M.; Ye, J.; Wan, C.; He, G.; Chen, H. Research Progress on Cu-Based Catalysts for Electrochemical Nitrate Reduction Reaction to Ammonia. *Ind. Eng. Chem. Res.* **2022**, *61* (40), 14731–14746.

(36) Hu, T.; Wang, C.; Wang, M.; Li, C. M.; Guo, C. Theoretical Insights into Superior Nitrate Reduction to Ammonia Performance of Copper Catalysts. *ACS Catal.* **2021**, *11* (23), 14417–14427.

(37) Fu, X.; Zhao, X.; Hu, X.; He, K.; Yu, Y.; Li, T.; Tu, Q.; Qian, X.; Yue, Q.; Wasielewski, M. R.; Kang, Y. Alternative Route for Electrochemical Ammonia Synthesis by Reduction of Nitrate on Copper Nanosheets. *Appl. Mater. Today* **2020**, *19*, 100620.

(38) Kang, Z.; Khan, M. A.; Gong, Y.; Javed, R.; Xu, Y.; Ye, D.; Zhao, H.; Zhang, J. Recent Progress of MXenes and MXene-Based Nanomaterials for the Electrocatalytic Hydrogen Evolution Reaction. *J. Mater. Chem. A* **2021**, *9*, 6089–6108.

(39) Cao, S.; Shen, B.; Tong, T.; Fu, J.; Yu, J. 2D/2D Heterojunction of Ultrathin MXene/Bi2WO6 Nanosheets for Improved Photocatalytic CO2 Reduction. *Adv. Funct. Mater.* **2018**, *28* (21), 1800136.

(40) Sun, J.; Kong, W.; Jin, Z.; Han, Y.; Ma, L.; Ding, X.; Niu, Y.; Xu, Y. Recent

Advances of MXene as Promising Catalysts for Electrochemical Nitrogen Reduction Reaction. *Chinese Chem. Lett.* **2020**, *31* (4), 953–960.

(41) Kota, S.; Sokol, M.; Barsoum, M. W. A Progress Report on the MAB Phases: Atomically Laminated, Ternary Transition Metal Borides. *Int. Mater. Rev.* **2020**, *65* (4), 226–255.

(42) Khazaei, M.; Wang, J.; Estili, M.; Ranjbar, A.; Suehara, S.; Arai, M.; Esfarjani, K.; Yunoki, S. Novel MAB Phases and Insights into Their Exfoliation into 2D MB. *Nanoscale* **2019**, *11*, 11305–11314.

(43) Ozdemir, I.; Kadioglu, Y.; Üzengi Aktürk, O.; Yuksel, Y.; Akinci; Aktürk, E. A New Single-Layer Structure of MBene Family: Ti2B. *J. Phys. Condens. Matter* **2019**, *31*, 505401.

(44) Zhang, H.; Xiang, H.; Dai, F. zhi; Zhang, Z.; Zhou, Y. First Demonstration of Possible Two-Dimensional MBene CrB Derived from MAB Phase Cr2AlB2. *J. Mater. Sci. Technol.* **2018**, *34* (11), 2022–2026.

(45) Sahu, R.; Bogdanovski, D.; Achenbach, J. O.; Zhang, S.; Hans, M.; Primetzhofer, D.; Schneider, J. M.; Scheu, C. Direct MoB MBene Domain Formation in Magnetron Sputtered MoAlB Thin Films. *Nanoscale* **2021**, *13*, 18077–18083.

(46) Li, F.; Tang, Q. First-Principles Calculations of TiB MBene Monolayers for Hydrogen Evolution. *ACS Appl. Nano Mater.* **2019**, *2* (11), 7220–7229.

(47) Wang, E.; Zhang, B.; Zhou, J.; Sun, Z. High Catalytic Activity of MBenes-Supported Single Atom Catalysts for Oxygen Reduction and Oxygen Evolution Reaction. *Appl. Surf. Sci.* **2022**, *604*, 154522.

(48) Li, B.; Wu, Y.; Li, N.; Chen, X.; Zeng, X.; Arramel; Zhao, X.; Jiang, J. Single-Metal Atoms Supported on MBenes for Robust Electrochemical Hydrogen Evolution. *ACS Appl. Mater. Interfaces* **2020**, *12* (8), 9261–9267.

(49) Sun, X.; Zheng, J.; Gao, Y.; Qiu, C.; Yan, Y.; Yao, Z.; Deng, S.; Wang, J. Machine-Learning-Accelerated Screening of Hydrogen Evolution Catalysts in MBenes Materials. *Appl. Surf. Sci.* **2020**, *526*, 146522.

(50) Ozkan, M.; Quiros, K. A. M.; Watkins, J. M.; Nelson, T. M.; Singh, N. D.; Chowdhury, M.; Namboodiri, T.; Talluri, K. R.; Yuan, E. Curbing Pollutant CO2 by Using Two-Dimensional MXenes and MBenes. *Chem* **2023**, *10*, 1–41.

(51) Mir, S. H.; Yadav, V. K.; Singh, J. K. Efficient CO2Capture and Activation on Novel Two-Dimensional Transition Metal Borides. *ACS Appl. Mater. Interfaces* **2022**, *14* (26), 29703–29710.

(52) Kresse, G.; Furthmüller, J. Efficiency of Ab-Initio Total Energy Calculations for Metals and Semiconductors Using a Plane-Wave Basis Set. *Comput. Mater. Sci.* **1996**, *6* (1), 15–50.

(53) Perdew, J. P.; Burke, K.; Ernzerhof, M. Generalized Gradient Approximation Made

Simple. *Phys. Rev. Lett.* **1996**, *77* (18), 3865–3868.

(54) Grimme, S.; Antony, J.; Ehrlich, S.; Krieg, H. A Consistent and Accurate Ab Initio Parametrization of Density Functional Dispersion Correction (DFT-D) for the 94 Elements H-Pu. *J. Chem. Phys.* **2010**, *132* (15), 154104.

(55) Joubert, D. From Ultrasoft Pseudopotentials to the Projector Augmented-Wave Method. *Phys. Rev. B - Condens. Matter Mater. Phys.* **1999**, *59* (1758).

(56) Sundararaman, R.; Letchworth-Weaver, K.; Schwarz, K. A.; Gunceler, D.; Ozhabes, Y.; Arias, T. A. JDFTx: Software for Joint Density-Functional Theory. *SoftwareX* **2017**, *6*, 278–284.

(57) Sundararaman, R.; Goddard, W. A. The Charge-Asymmetric Nonlocally Determined Local-Electric (CANDLE) Solvation Model. *J. Chem. Phys.* **2015**, *142* (064107).

(58) Yuan, H.; Li, Z.; Yang, J. Transition-Metal Diboride: A New Family of Two-Dimensional Materials Designed for Selective CO2 Electroreduction. *J. Phys. Chem. C* **2019**, *123* (26), 16294–16299.

(59) Wang, Y.; Xu, A.; Wang, Z.; Huang, L.; Li, J.; Li, F.; Wicks, J.; Luo, M.; Nam, D. H.; Tan, C. S.; Ding, Y.; Wu, J.; Lum, Y.; Dinh, C. T.; Sinton, D.; Zheng, G.; Sargent, E. H. Enhanced Nitrate-to-Ammonia Activity on Copper-Nickel Alloys via Tuning of Intermediate Adsorption. *J. Am. Chem. Soc.* **2020**, *142* (12), 5702–5708.

(60) Sundararaman, R.; Goddard, W. A.; Arias, T. A. Grand Canonical Electronic Density-Functional Theory: Algorithms and Applications to Electrochemistry. *J. Chem. Phys.* **2017**, *146*, 114104.

(61) Huang, Y.; Nielsen, R. J.; Goddard, W. A. Reaction Mechanism for the Hydrogen Evolution Reaction on the Basal Plane Sulfur Vacancy Site of MoS 2 Using Grand Canonical Potential Kinetics. *J. Am. Chem. Soc.* **2018**, *140* (48), 16773–16782.

(62) Su, J.; Musgrave, C. B.; Song, Y.; Huang, L.; Liu, Y.; Li, G.; Xin, Y.; Xiong, P.; Li, M. M. J.; Wu, H.; Zhu, M.; Chen, H. M.; Zhang, J.; Shen, H.; Tang, B. Z.; Robert, M.; Goddard, W. A.; Ye, R. Strain Enhances the Activity of Molecular Electrocatalysts via Carbon Nanotube Supports. *Nat. Catal.* **2023**, *6*, 818–828.

Chapter 9

The Reaction Mechanism Underlying Pd(II) Catalyzed Oxidative Coupling of Ethylene and Benzene to Form Styrene: Identification of a cyclic Mono-Pd^{II} Bis-Cu^{II} Complex as the Active Catalyst

Reproduced with permission from:

MT Bennett, JF Ellena, DA Dickie, TB Gunnoe, WA Goddard III. *Reaction Mechanism Underlying Pd(II)-Catalyzed Oxidative Coupling of Ethylene and Benzene to Form Styrene: Identification of a Cyclic Mono-Pd^{II} Bis-Cu^{II} Complex as the Active Catalyst,* *Organometallics*, **2022**, 41, 15, 1988-2000

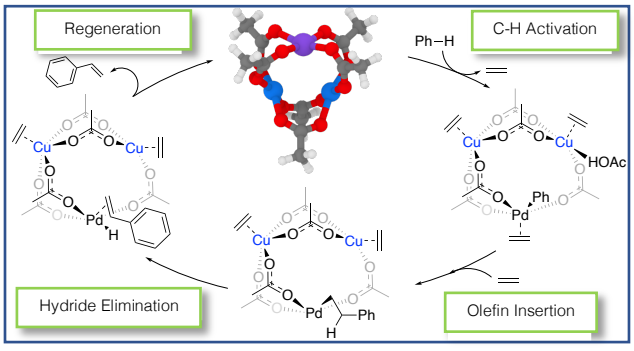

Figure 9.0: Table of contents figure

9.1 Abstract

A recent advance in the synthesis of alkenylated arenes was the demonstration that the $Pd(OAc)_2$ catalyst precursor gives $> 95\%$ selectivity towards styrene from ethylene and benzene under optimized conditions using excess Cu(II) carboxylate as the *in situ* oxidant (*Organometallics* **2019**, *38*, 3532-3541). To understand the mechanism underlying this catalysis, we applied Density Functional Theory (DFT) calculations in combination with experimental studies. From DFT calculations we determined the lowest energy multi-metallic Pd and Pd-Cu mixed metal species as possible catalyst precursors. From the various structures, we determined the cyclic heterotrinuclear complex $PdCu_2(\boxtimes\text{-}OAc)_6$ to be the global minimum in Gibbs free energy under conditions of excess Cu(II). For cyclic $PdCu_2(\boxtimes\text{-}OAc)_6$ and the parent $[Pd(\mu\text{-}OAc)_2]_3$, we evaluated the barriers for benzene C–H activation through concerted metalation deprotonation (CMD). The $PdCu_2(\boxtimes\text{-}OAc)_6$ cyclic trimer leads to a CMD barrier of 33.5 kcal/mol while the $[Pd(\mu\text{-}OAc)_2]_3$ species leads to a larger CMD barrier at > 35 kcal/mol. This decrease in the CMD barrier arises from insertion of Cu(II) into the trimetallic species. Because cyclic $PdCu_2(\mu\text{-}OAc)_6$ is likely the predominant species under experimental conditions (the Cu to Pd ratio is 480:1 at the start of catalysis) with a predicted CMD barrier within the range of the experimentally determined activation barrier, we propose that cyclic $PdCu_2(\boxtimes\text{-}OAc)_6$ is the Pd species responsible for catalysis and report a full reaction mechanism based on DFT calculations.

For catalytic conversion of benzene and ethylene to styrene at 120 °C using $Pd(OAc)_2$ as catalyst precursor and $Cu(OPiv)_2$ (OPiv = pivalate) as oxidant, an induction period of ~1 hour was observed, followed by catalysis with a turnover frequency of ~2.3×10^{-3} s^{-1}. *In situ* ^1H NMR spectroscopy experiments indicate that during the induction period, $Pd(OAc)_2$ is likely converted to cyclic $PdCu_2(\eta^2\text{-}C_2H_4)_3(\mu\text{-}OPiv)_6$, which is consistent with the calculations and consistent with the proposal that the active catalyst is the ethylene-coordinated heterotrinuclear complex cyclic-$PdCu_2(\eta^2\text{-}C_2H_4)_3(\mu\text{-}OPiv)_6$.

9.2 Introduction

The addition of arene C–H bonds across olefin C=C bonds is a useful approach for synthesis of alkylated and alkenylated arenes.[1–10] A common method to alkylate arenes is acid-mediated catalysis, using either a Friedel-Crafts or zeolite-based catalytic process, with an olefin or alkyl halide to directly generate an alkyl arene.[11,12] A common issue with acid-mediated arene alkylation is polyalkylation of the arene, which can result in formation of undesired products that necessitate energy intense distillation and catalytic trans-alkylation to optimize the yield of the mono-alkyl arene.[3,13–16] Also, in the case of substituted α-olefins, Friedel-Crafts alkylation involves carbocation rearrangements that result in formation of *m*-aryl alkanes ($m > 1$). Thus, 1-aryl alkanes (or the corresponding alkenes) generally cannot be produced in high yield with Friedel-Crafts or related acid-

mediated catalysis. The alternative method of transition metal-mediated olefin hydroarylation (or oxidative dehydrogenative coupling to produce alkenyl arenes) provides a methodology for synthesis of alkyl and alkenyl arenes with selectivities that are often distinct from acid catalyzed processes.[8-47]

Recent studies of arene alkylation or alkenylation involving unfunctionalized hydrocarbons such as ethylene and benzene with Ru(II),[17–23] Pt(II),[24–29] Ir(III),[30–35] Rh(I),[36–44] or Ni(II)[45,46] catalyst precursors provided insight toward understanding reaction mechanisms. Studies involving unactivated hydrocarbons to give anti-Markovnikov products, such as the Ni catalyst[45] reported by Hartwig and coworkers and new Rh[36–38] catalyzed processes, have also begun to emerge.

Palladium catalysts have been reported to mediate the hydroarylation of alkynes with the use of carbene ligands[47–49] and for alkene arylation using boronic esters.[50,51] In addition, palladium-catalyzed oxidative alkenylation of arenes (i.e., the Fujiwara-Moritani reaction[52]) has been reported; however, this process often requires directing groups, thus limiting the scope of possible reactants and products.[47,48,50–57] The production of styrene from Pd(II) catalyst precursors with Cu(II) oxidants through oxidative coupling of olefins and arenes can also suffer from low selectivity due to formation of vinyl ester and stilbene side products. For example, $Pd(OAc)_2$ catalyzes styrene formation from benzene, ethylene and $Cu(OAc)_2$.[39] However, poor catalyst selectivity under the initially reported conditions

led to formation of ~2.5 times more vinyl acetate than styrene. Fujiwara and coworkers also reported styrene synthesis from $Pd(OAc)_2$, but the conditions were not catalytic (~60% yield based on Pd).[52] Pd-catalyzed vinyl acetate formation has been demonstrated under both homogeneous and heterogenous conditions by Maseras and coworkers,[56] suggesting the styrene and vinyl acetate pathways are highly competitive. In 2019, we reported conditions that provide > 95% selectivity towards styrene from ethylene and benzene using $Pd(OAc)_2$ as the catalyst precursor (Scheme 9.1).[53] These reactions were studied with stoichiometric Cu(II) under anaerobic conditions, with Cu(II) as the limiting reagent, and using dioxygen or air as the oxidant, which allows recycling of Cu(II) (see below).

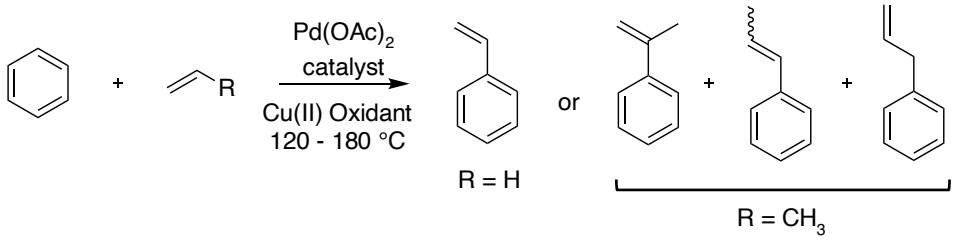

Scheme 9.1. Process for Pd-catalyzed oxidative dehydrogenative coupling from benzene and ethylene (R = H) or propylene (R = CH_3) to afford styrene or other alkenyl benzenes.

Herein, we report density functional theory (DFT) quantum mechanics studies with complementary experimental studies to identify the likely active Pd catalyst for styrene formation from benzene, ethylene and Cu(II) carboxylate. Most interesting is that we find

the active catalyst to be a cyclic heterotrinuclear $PdCu_2$ complex. Following identification of this active species, we use DFT to predict reaction kinetics for various steps of the catalytic cycle. The agreement between DFT studies and experimental results, including *in situ* ^{1}H NMR spectroscopy, validates the proposed mechanism. The proposed cyclic $PdCu_2$ catalyst, formed upon reaction of PdX_2 (X = carboxylate such as acetate or pivalate) with excess $Cu(OPiv)_2$, is reminiscent of recently proposed active catalysts involving mixed Rh/Cu and Pd/Ag complexes.[44,58,59] These studies plus our new results suggest that mixed metallic active catalysts may be common when using late transition metals in combination with metal-based oxidants such as Cu(II) and Ag(I). Thus, identifying such active catalysts and understanding how they influence the barriers to catalysis are of fundamental importance.

9.3 Results and Discussion

We expected that the Pd-catalyzed formation of styrene from benzene, ethylene and Cu(II) at elevated temperatures would involve the commonly invoked oxidative olefin hydroarylation pathway (Scheme 9.2).[6-31] In this catalytic cycle, the first step is typically coordination of an arene to the active site followed by arene C–H activation to form a metal-aryl bond with dissociation of a carboxylic acid (when starting from a catalyst that has an acetate or other carboxylate ligand).[39,41,52,53,60,61] Dissociation of the carboxylic acid

then opens a site on the metal for olefin coordination. Hence, after dissociation of the carboxylic acid, an olefin can coordinate and insert into the metal-aryl bond via an olefin insertion step. Subsequent β-hydride elimination produces the alkenylated arene product and reaction of the resulting metal-hydride with an oxidant can regenerate the starting catalyst species. In our catalysis, excess Cu(II) carboxylate is present at ~480 times the concentration of Pd. This high concentration is used because Cu(II) serves as an in situ oxidant much like the Wacker process for ethylene oxidation. In the absence of Cu(II) and under anaerobic conditions, styrene formation is not observed. The net reaction is:

$$C_6H_6 + C_2H_4 + 2Cu(OAc)_2 \rightarrow \text{styrene} + 2\ Cu(OAc) + 2\ HOAc$$

Separate reaction of Cu(OAc) and HOAc with O_2 reforms $Cu(OAc)_2$:

$$\tfrac{1}{2}\ O_2 + 2\ Cu(OAc) + 2\ HOAc \rightarrow H_2O + 2\ Cu(OAc)_2$$

The formation of acetic acid likely occurs upon reaction of a Pd–H intermediate with $Cu(OAc)_2$ to generate a product with a Pd–OAc group and HOAc. Such reactions are well precedented in Wacker oxidation chemistry using $CuCl_2$ rather than $Cu(OAc)_2$.

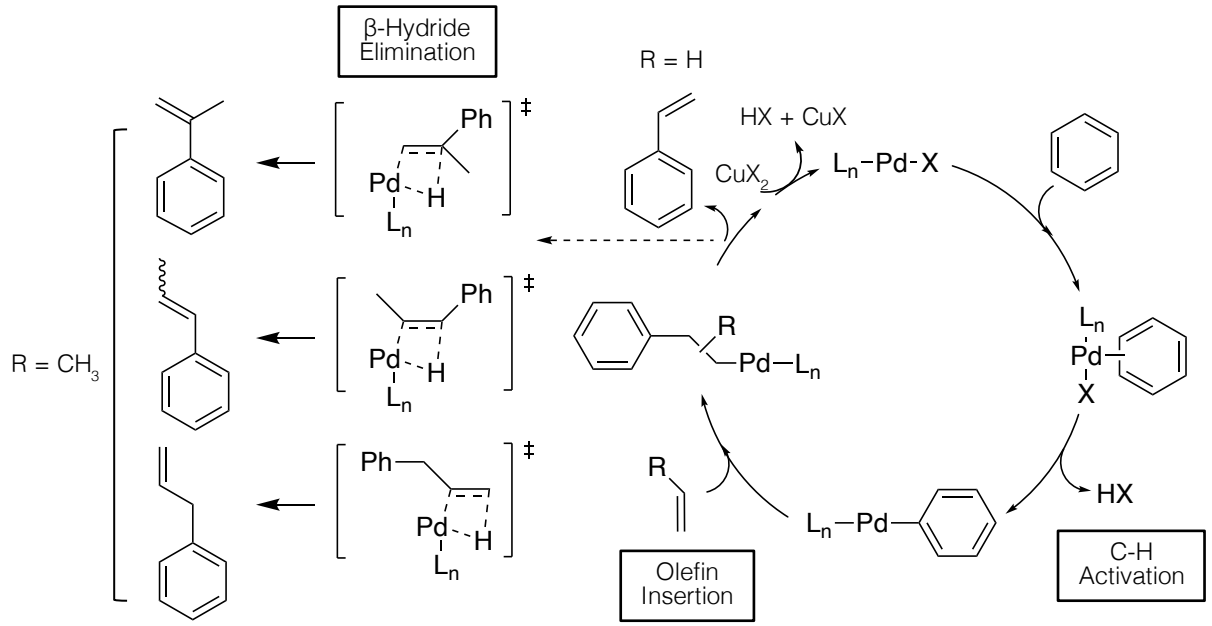

Scheme 9.2. General catalytic cycle for Pd-mediated oxidative arene alkenylation. This catalytic cycle consists of C–H activation, olefin insertion, β-hydride elimination, and conversion of the resulting Pd–H complex back to starting catalyst. Linear and branched (i.e., anti-Markovnikov and Markovnikov products) alkenyl benzene products (far left) can be synthesized through the use of alkyl-substituted olefins (here, the α-olefin is propylene when R = CH_3). When R = H, styrene is formed.

9.3.1 Structural Identification of Ground State Pd Complex

The first step in discovering the mechanism of the previously reported Pd-catalyzed styrene formation[53] is identifying the ground state of the active species. The experimental

Pd starting material has the stoichiometry $Pd(OAc)_2$ (OAc = acetate) where Pd is in the formal +2 oxidation state. It is possible that this starting Pd species is mononuclear (as written), binuclear $(Pd(\mu\text{-}OAc)_2)_2$, or even cyclic trinuclear $(Pd(\mu\text{-}OAc)_2)_3$.[48,58,59,62,63] Because free ethylene is present in solution, we can also envision that any of these species might involve coordinated ethylene, which we consider in our calculations. In addition to ethylene, excess $Cu(OPiv)_2$ (OPiv = pivalate) is present in the starting reaction mixture at ~480 times the concentration of Pd. Thus, multi-metallic Pd/Cu complexes with bridging carboxylate ligands are also candidates for the ground state active catalyst.[64,65] To consider all these possibilities, we calculated the relative free energies of 12 possible Pd species with varying geometries and stoichiometries, including bimetallic Pd/Cu complexes that result from the reaction of Pd(II) with $Cu(OAc)_2$ (Scheme S4 in Supporting Information). The lowest-energy species are shown in Scheme 9.3; the complexes with 3 metals (Pd_3, Pd_2Cu, $PdCu_2$, and Cu_3) are modeled in the lowest energy cyclic form. Although previous styrene formation experiments used OPiv as the ligand, we use OAc instead for our calculations since the carboxylate identity should not affect the DFT-calculated energetics and OAc is smaller and faster to calculate. Note that all free energies refer to Gibbs free energies.

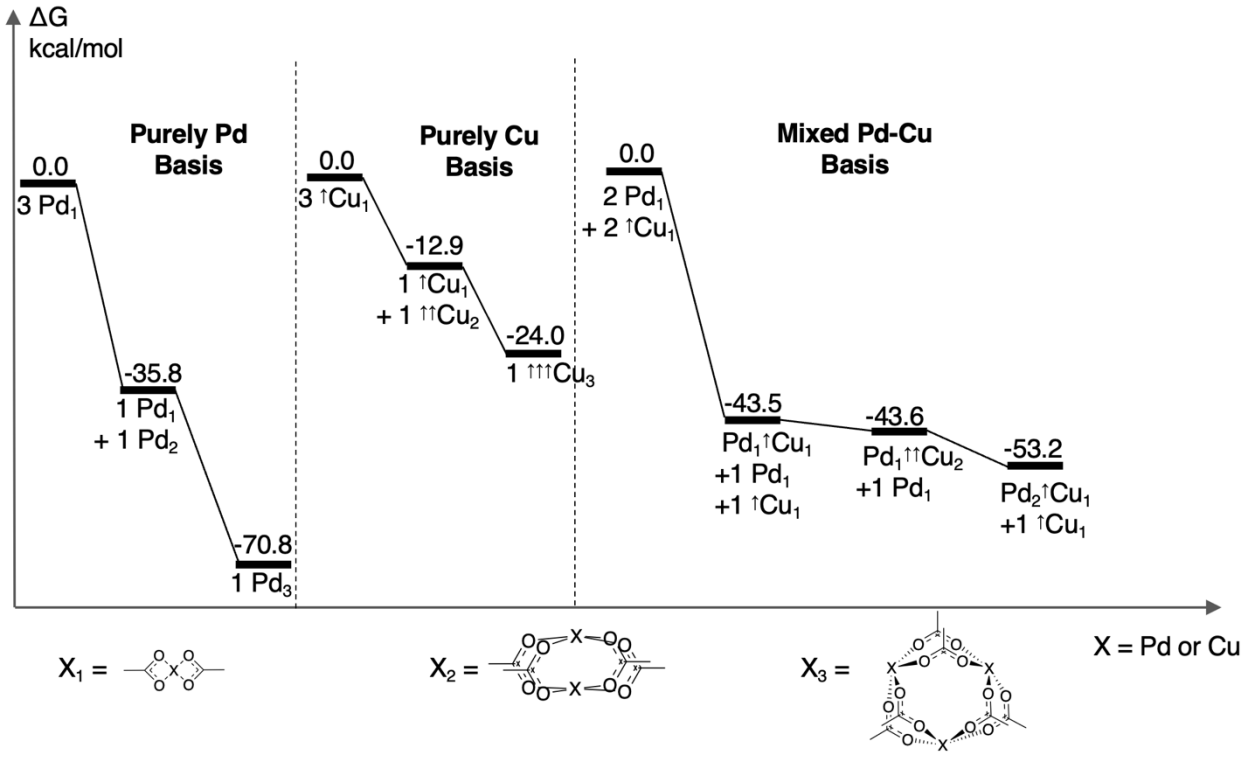

Scheme 9.3. DFT free energies calculated at 423 K for the lowest-energy Pd and Pd/Cu species for catalytic reactions using $Pd(OAc)_2$ and $Cu(OAc)_2$. Note that the bases here are not the same and thus the zeroes in free energy are not equivalent. The basis on the left is 3 Pd monomers, the basis for the middle is 3 Cu monomers, and the basis for the right is 2 Pd monomers and 2 Cu monomers. Superscript up arrows denote unpaired spins.

To arrive at the free energies in Scheme 9.3, we start with the ground state of the pure $Pd(OAc)_2$ and $Cu(OAc)_2$ species. With a basis of 3 Pd_1, the mononuclear, binuclear, and trinuclear $Pd(OAc)_2$ species have relative free energies of 0.0, -35.8, and -70.8 kcal/mol. Similar to $Pd(OAc)_2$, the Cu(II) species is square planar and can possibly adopt the mononuclear configuration (as written), binuclear $[Cu(\mu\text{-}OAc)_2]_2$, or cyclic trinuclear

$[Cu(\mu\text{-}OAc)_2]_3$.[66–68] Cu(II) is a doublet spin state so that the mononuclear species is a doublet spin state, the binuclear species is a triplet, and the trinuclear species is a quartet. Our DFT calculations find that the mononuclear, binuclear, and trinuclear Cu species have relative free energies of 0.0, -12.9, and -24.0 kcal/mol, respectively (with a basis of 3 Cu_1). We also investigated the mononuclear quartet, binuclear singlet, and trinuclear doublet. The quartet $Cu(OAc)_2$ lies 97.7 kcal/mol above the doublet, the singlet $[Cu(\mu\text{-}OAc)_2]_2$ lies 15.4 kcal/mol above the triplet, and the doublet $[Cu(\mu\text{-}OAc)_2]_3$ lies 0.2 kcal/mol above the quartet. Moreover, with a basis of two $Pd(OAc)_2$ monomers and two $Cu(OAc)_2$ monomers, the lowest energy species that can be formed are the heterobinuclear $PdCu(\boxtimes\text{-}OAc)_4$ at -43.5 kcal/mol, the cyclic heterotrinuclear $PdCu_2(\boxtimes\text{-}OAc)_6$ at -43.6 kcal/mol, or the cyclic heterotrinuclear $Pd_2Cu(\boxtimes\text{-}OAc)_6$ at -53.2 kcal/mol. Note that the bases in Scheme 9.3 are different (3 Pd_1 monomers for the left, 3 Cu_1 monomers for the middle, 2 of each monomer for the right), such that the zeroes in free energy cannot be directly compared. However, the experiments necessitate a Cu to Pd ratio of ≥ 240:1. We can assess the total free energies for the various cyclic trimers as follows, assuming a 240:1 Cu:Pd ratio:

- 240 Cu_3 + 1 Pd_3 ; G = -5830.8 kcal/mol
- 239 Cu_3 + 1 Pd_2Cu + 1 $PdCu_2$; G = -5832.7 kcal/mol
- 239.5 Cu_3 + 1.5 Pd_2Cu ; G = -5827.8 kcal/mol

- 238 Cu_3 + 3 $PdCu_2$; G = -5842.8 kcal/mol

This analysis confirms that under experimental conditions there is a strong thermodynamic driving force to form cyclic $PdCu_2$, such that equilibrium consists primarily of the Cu-rich cyclic $PdCu_2(\mu\text{-}OAc)_6$ species. The DFT-optimized structure for cyclic $PdCu_2(\mu\text{-}OAc)_6$ is depicted in Figure 9.1.

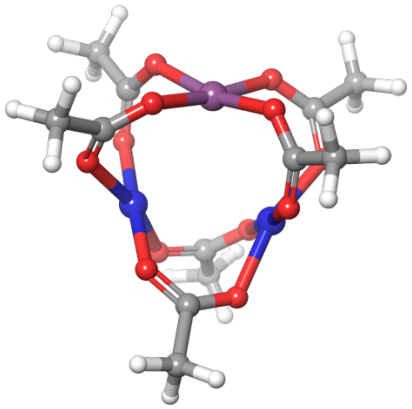

Figure 1. DFT-optimized structure of $PdCu_2(\mu\text{-}OAc)_6$ (**A**) (Pd in purple and Cu in blue). Each Cu has an unpaired spin.

Our finding of a stable heteronuclear Pd/Cu complex is consistent with a recent analysis of Rh-catalyzed styrene formation, for which the active species was identified as a noncyclic heterotrinuclear Rh-Cu-Rh species in which the three square planar metal centers are bridged by four OAc ligands.[44] Also, Houk and coworkers examined heteronuclear Pd-Ag species and discovered a similar trend[58] in which substitution of $Pd(OAc)_2$ with Ag(OAc) in $Pd_2(\mu\text{-}OAc)_2(\kappa^2\text{-}OAc)_2$ to generate $PdAg(\mu\text{-}OAc)_2(\kappa^2\text{-}OAc)$

resulted in -3.7 kcal/mol of stabilization. Schaefer and coworkers reported Pd-catalyzed C–H activation using the heterobimetallic $PdAg(\mu\text{-}OAc)_3$ and noted the multi-metallic nature to be a key driving force for catalysis.[59] Similar to Houk and Schaefer, we indeed find inclusion of Cu(II) to stabilize the heteronuclear Pd/Cu complex. Specifically, the reaction in which two Pd units in $[Pd(\mu\text{-}OAc)_2]_3$ are replaced by two Cu units to form cyclic $PdCu_2(\mu\text{-}OAc)_6$ (i.e., $[Pd(\mu\text{-}OAc)_2]_3 + 2/3 *[Cu(\mu\text{-}OAc)_2]_3 \rightarrow PdCu_2(\mu\text{-}OAc)_6 + 2/3*[Pd(\mu\text{-}OAc)_2]_3$), is downhill -8.0 kcal/mol, giving rise to -4.0 kcal/mol stabilization per Cu inserted.

We note that the mixed Pd_2Cu and $PdCu_2$ acetate moieties have both been observed simultaneously in experiment. Thornton and Sloan previously discovered the presence of $Pd_2Cu(\mu\text{-}OAc)_6$ and $PdCu_2(\mu\text{-}OAc)_6$ when exposing $[Pd(\mu\text{-}OAc)_2]_3$ to excess $[Cu(\boxtimes\text{-}OAc)_2(H_2O)]_2$.[62] However, their reported 54% yield of the Pd_2Cu configuration and 26% yield of the $PdCu_2$ required a Cu:Pd molar ratio of 3:1. Our experiment uses a Pd:Cu ratio of $\geq$ 240:1 so that virtually all Pd and Cu will form $PdCu_2$ complexes. The equilibrium thermodynamics between these complexes can be found in the Supporting Information.

9.3.2 C–H Activation of Benzene by Lowest Energy Pd Complexes

We discovered that the predominant Pd species under our conditions of ≥ 240 times Cu(II) excess is the heterotrinuclear cyclic $PdCu_2(\mu\text{-}OAc)_6$. We examined this candidate for catalytic styrene formation by calculating its performance for the benzene C–H activation step, which is expected to be the rate determining step (RDS) of Pd-catalyzed styrene production.[12,53,58,59,61,69,70] Benzene C–H activation can occur through several different pathways. For late transition metal complexes, the dominant mechanisms for C–H activation are oxidative addition, concerted metalation deprotonation (CMD) and electrophilic substitution.[71] Pd catalysis using $Pd(OAc)_2$ has been established to occur through CMD, in which a coordinated carboxylate promotes deprotonation of the C–H bond to form a Pd–C bond and release a carboxylic acid.[12] In the present chemistry, CMD occurs when benzene is deprotonated by a coordinated OAc ligand while simultaneously forming a Pd–C_{phenyl} bond. Thus, CMD results in the formation of a Pd(II)–Ph bond and acetic acid (HOAc). With these considerations in mind, we evaluated the CMD barrier for $PdCu_2(\mu\text{-}OAc)_6$, **A** (Scheme 9.4). We also calculated the CMD barrier for **C**, the homotrinuclear $[Pd(\mu\text{-}OAc)_2]_3$ complex to determine how the inclusion of Cu(II) affects the energetics of benzene C–H activation.

We attempted to calculate benzene C–H activation via an oxidative addition pathway, but in all cases the calculations optimized to the CMD transition state (see Supporting Information).

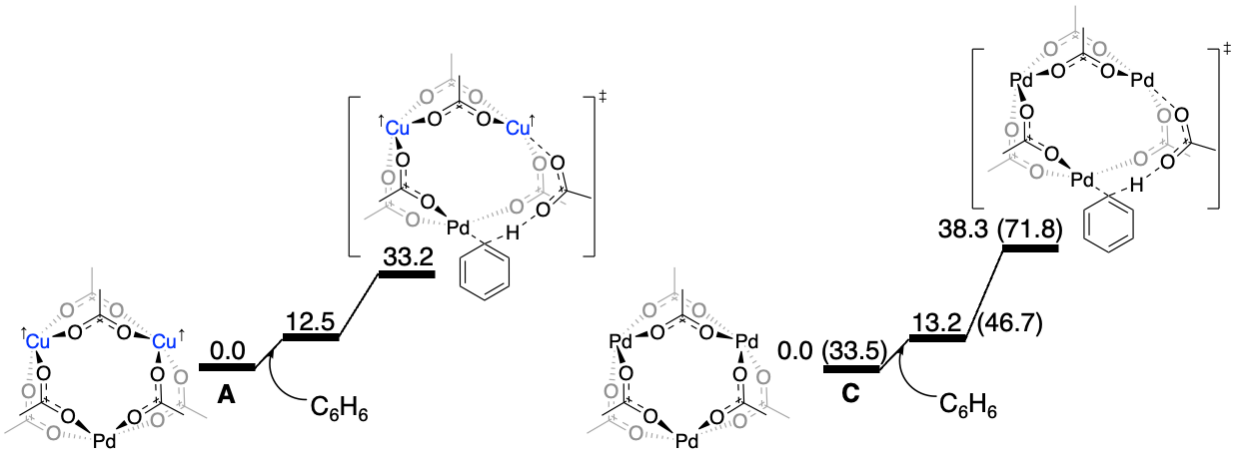

Scheme 9.4. DFT free energies calculated at 423 K for benzene coordination and concerted metalation deprotonation barriers using $PdCu_2(\mu\text{-}OAc)_6$ and $(Pd(\mu\text{-}OAc)_2)_3$ (**A** and **C**, respectively). The values in parentheses for **C** are with respect to the global ground state **A**. Superscript up arrows denote unpaired spins. The free energies of **A** and **C** are set to zero.

For the $PdCu_2$ species **A** and the Pd_3 species **C**, DFT predicts CMD barriers of 33.2 and 38.3 kcal/mol, respectively. Thus, including two Cu in the parent Pd_3 complex reduces the CMD barrier by 5.1 kcal/mol, enabling facile C-H activation of benzene. In both **A** and **C**, CMD requires an OAc ligand to break its bridging character to allow for the η^2-coordination of benzene to Pd. The C–H bond breaking CMD step occurs after coordination of benzene to Pd. Figure 9.2 shows the DFT-optimized CMD transition state geometries for **A** and **C**; the overall geometries of **A_CMD** and **C_CMD** are similar.

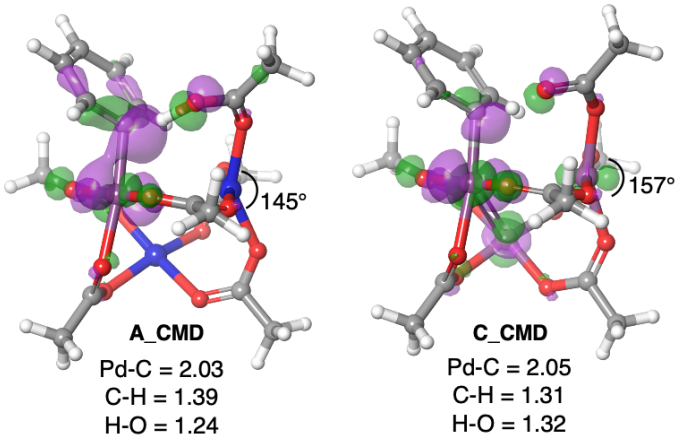

Figure 9.2. DFT-optimized transition states for concerted metalation deprotonation (CMD) for the $PdCu_2$ and Pd_3 complexes, **A** and **C**. Significant interatomic distances are included in Å. Pd–C denotes the distance between the active Pd and the adjacent C of benzene; C–H is the distance between the same benzene C and the transiting H; H–O distance is between the transiting H and the adjacent O of the acetate base. The highest-occupied molecular orbitals (HOMOs) are shown. Each Cu has an unpaired spin.

Using DFT, we found the heterobinuclear PdCu and cyclic heterotrinuclear Pd_2Cu species also have decreased CMD barriers relative to the Pd_3 complex **C** (see Supporting Information), again indicating that inclusion of Cu(II) reduces the barrier for C–H activation. This is consistent with our previously study of Rh catalysis in which inclusion of Cu(II) in the catalyst complex leads to a lower barrier for C–H activation,[44] along with other steps in the catalytic cycle (albeit the Rh-mediated C–H activation was calculated to occur through stepwise oxidative addition-reductive elimination as opposed to CMD).

The three important bond distances (Pd–C, C–H and H–O) are nearly the same amongst the two CMD transition states in Figure 9.2, suggesting they play no role in decreasing the CMD barrier for the $PdCu_2$ complex **A**. One explanation for the lower CMD barrier for **A** is that the square planar Cu distorts toward a tetrahedral geometry to accommodate the incoming strain required for the OAc to accept H from benzene. Indeed the O–Pd–O angle in **C_CMD** is 157° while the analogous O–Cu–O in **A_CMD** is 145°. An orbital analysis of the CMD states reveals that in **A_CMD**, the HOMO is concentrated near the Pd center such that neither of the non-reactive Cu atoms display any HOMO character. In **C_CMD**, both non-reactive Pd d_{z^2} orbitals contribute to the HOMO character. Furthermore, the HOMO of **A_CMD** is delocalized over the Pd--C—H unit while the HOMO of **C_CMD** is localized on the Pd and the C atom. These observations demonstrate how the presence of Cu(II) serves to bring down the activation barrier for the key C–H activation step.

9.3.3 Experimental Studies of Styrene Formation with $Pd(OAc)_2$ as the Catalyst Precursor

The kinetics of styrene production from benzene and ethylene using $Pd(OAc)_2$ as the catalyst precursor were studied experimentally at 120 °C in the presence of 480 eq. $Cu(OPiv)_2$, 960 eq. HOPiv and 50 psig (344 kPa) of ethylene (Figure 9.3). An induction

period of ~1 hour was observed under these reaction conditions, followed by a region of linear product formation versus time with a turnover frequency (TOF) of ~2.6 $\times$ 10^{-3} s^{-1} in the linear region (the TOF was calculated using the difference in styrene amount at the 2.5-hour and 4.5-hour time points). We note that a statistically identical induction period was obtained using $Pd(OPiv)_2$ as the catalyst precursor, suggesting that the induction period is not likely the result of carboxylate exchange (Figure H1). Further, below we propose that the induction period could be due to the formation of $PdCu_2(\eta^2\text{-}C_2H_4)_3(\mu\text{-}X)_6$ (X = OAc or OPiv), which data indicate forms under reaction conditions. We have isolated a solid from heating (55 °C) $Pd(OPiv)_2$, 6 eq. $Cu(OPiv)_2$ and 50 psig (344 kPa) of ethylene, and using this solid to set up a catalytic reaction reveals no induction period (Figure 9.3). Using material prepared at otherwise identical conditions, but in the absence of ethylene, as the catalyst precursor gave a similar induction period to use of $Pd(OAc)_2$, suggesting that ethylene is necessary to form the active catalyst (Figure H2). These findings are consistent with our proposal that $PdCu_2(\eta^2\text{-}C_2H_4)_3(\mu\text{-}OPiv)_6$ is the active catalyst (see below for more details on the characterization of $PdCu_2(\eta^2\text{-}C_2H_4)_3(\mu\text{-}OPiv)_6$ and $PdCu_2(\mu\text{-}OPiv)_6$). Performing catalysis with a $Cu(OPiv)_2$ loading of 48 eq. gave a color change from blue to colorless and ~24 TOs of styrene after 3 hours, consistent with 2 equivalents of Cu(II) being necessary for each turnover of styrene (Figure H3).

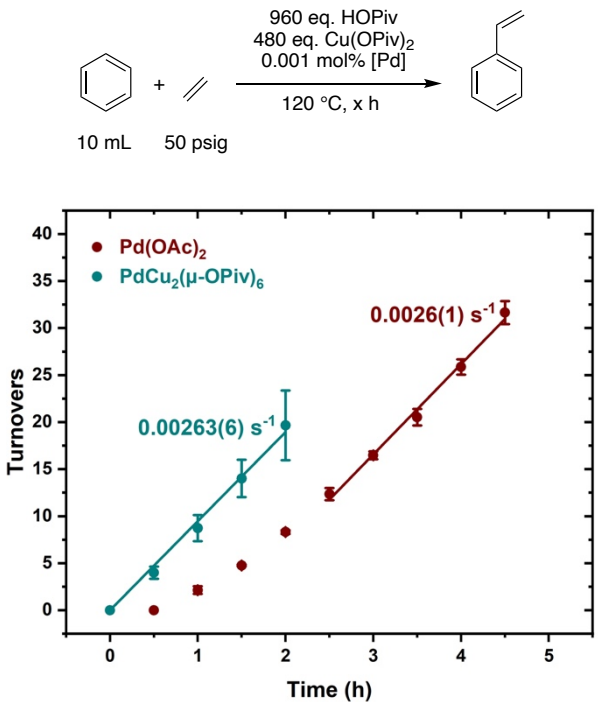

Figure 9.3. Kinetics of styrene production from benzene and ethylene using $Pd(OAc)_2$ or isolated $PdCu_2(\mu\text{-}OPiv)_6$ as the catalyst precursor. Reaction conditions: 10 mL benzene, 0.001 mol% (relative to benzene) $Pd(OAc)_2$ or $PdCu_2(\mu\text{-}OPiv)_6$, 480 eq. $Cu(OPiv)_2$ (relative to Pd), 960 eq. HOPiv (relative to Pd), 50 psig (344 kPa) ethylene, 120 °C. Turnovers were calculated by GC-FID relative to the internal standard hexamethylbenzene. Each data point is the average of three independent experiments and error bars represent the standard deviation for the three experiments.

To understand the nature of the observed induction period and identify the initially formed Pd species, we carried out *in situ* ^{1}H NMR spectroscopy experiments. Heating $Pd(OPiv)_2$ in benzene-d_6 at 120 °C in the presence of 72 eq. of $Cu(OPiv)_2$ and 144 eq. of HOPiv resulted in slow consumption of $Pd(OPiv)_2$, but led to no observable new species by ^{1}H NMR after 5 hours (Figures S7 and S8). At otherwise identical conditions, the

presence of 50 psig (344 kPa) ethylene enabled the conversion of $Pd(OPiv)_2$ to a new complex over a 3-hour time period (Figure 9.4); changes in the ^1H NMR spectrum are consistent with this conversion. Specifically, the broad resonance due to *tert*-butyl groups at 2.86 ppm broadened and shifted to 2.31 ppm and the ethylene peak at 5.25 ppm broadened and shifted to 5.22 ppm (Figure H4). DFT calculations predict $PdCu_2(\mu\text{-}OAc)_6$ as the most stable species among several possible pure Pd and mixed Pd/Cu complexes (see above). Also, as discussed below, we have obtained further NMR data that are consistent with the new Pd complex being $PdCu_2(\eta^2\text{-}C_2H_4)_3(\mu\text{-}OPiv)_6$. The proposed formation of cyclic $PdCu_2(\mu\text{-}OPiv)_6$ and cyclic $PdCu_2(\eta^2\text{-}C_2H_4)_3(\mu\text{-}OPiv)_6$ (see below for more discussion) is consistent with previous observations by Thornton and Sloan.[62] In addition to the formation of a new complex, the *in situ* ^1H NMR spectroscopy experiments show the catalytic formation of vinyl pivalate and styrene-d_5 (Figure H5 and Figure H6).

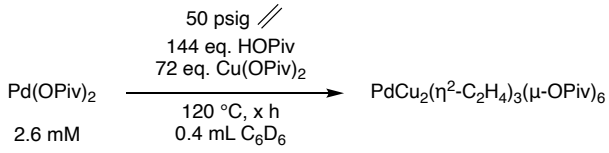

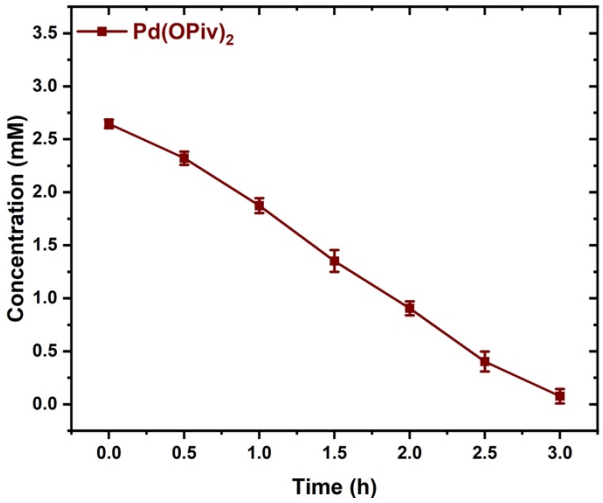

Figure 9.4. Kinetics of $Pd(OPiv)_2$ consumption to form $PdCu_2(\eta^2\text{-}C_2H_4)_3(\mu\text{-}OPiv)_6$ determined by ^1H NMR spectroscopy. Reaction conditions: 2.6 mM $Pd(OPiv)_2$, 0.3 mL benzene-d_6, 72 eq. of $Cu(OPiv)_2$ (relative to Pd), 144 eq. of HOPiv, 50 psig (344 kPa) of ethylene, 120 °C. Each data point is the average of three independent experiments and error bars represent the standard deviation for the three experiments.

In an attempt to isolate putative $PdCu_2(\mu\text{-}OPiv)_6$ or $PdCu_2(\eta^2\text{-}C_2H_4)_3(\mu\text{-}OPiv)_6$, $Pd(OPiv)_2$ and 4 eq. of $Cu(OPiv)_2$ were heated at 55 °C in 10 mL of benzene in the presence of 50 psig (344 kPa) ethylene for 48 hours. The reaction temperature was maintained until a color change from dark blue to light green was observed, which indicated consumption of a majority of $Cu(OPiv)_2$ in the solution. After removal of benzene *in vacuo*, the residue was extracted with pentane and filtered. The pentane extract was dried and then dissolved in CD_2Cl_2. The data collected, in combination with the computational modeling results (see above), are consistent with the isolation of

$PdCu_2(\mu\text{-}OPiv)_6$. The ^1H NMR spectrum of the pentane extract showed a new broad singlet at ~3.17 ppm (Figure H9, bottom spectrum) and a second broad peak at 1.50 ppm. The resonances do not appear when reacting $Pd(OPiv)_2$ with ethylene in the absence of $Cu(OPiv)_2$. The intensity of the 1.50 ppm peak increased when HOPiv was added to the sample and the peak is assigned to the *tert*-butyl protons of HOPiv. Saturation transfer and NOESY (EXSY) experiments indicated chemical exchange between the protons that resonate at 3.17 ppm and those that resonate at 1.50 ppm, indicating that the peak at 3.17 ppm can be assigned to OPiv bound to a new species (Figure H16). At low temperatures the resonance at 3.17 ppm splits into two broad signals that integrate to an approximate 2:1 ratio upon decreasing the temperature to -80 °C (Figure H10). We tentatively assign these resonances as the two distinct *tert*-butyl groups of $PdCu_2(\mu\text{-}OPiv)_6$. ^1H NMR signals consistent with an ethylene ligand were not observed, indicating that ethylene ligands are removed under reduced pressure during work-up. An additional peak at 0.99 ppm is assigned to OPiv functionalities of the ill-defined Cu(OPiv) species that form as the result of vinyl pivalate and styrene production.

We grew crystals from the pentane extract described above by slow evaporation of a benzene solution. The structure determined from single crystal X-ray diffraction has a pseudo-three-fold rotational symmetry and therefore each of the metal sites was modeled as a mixture of Cu and Pd (Figure H19). Free refinement of the relative occupancies of

the metal sites converged at a 1.88:1.12 Cu:Pd ratio. This is consistent with the 2:1 Cu:Pd ratio of the expected $PdCu_2(\mu\text{-}OPiv)_6$ product, but other possibilities such as co-crystallization of the two homo-trimetallic species cannot be completely ruled out on the basis of the crystallographic data due to the disorder caused by the pseudosymmetry. However, the combination of single crystal X-ray diffraction data and NMR (NOESY, EXSY and saturation transfer) data are consistent with the isolation of $PdCu_2(\mu\text{-}OPiv)_6$.

We attempted to observe and isolate $PdCu_2(\eta^2\text{-}C_2H_4)_3(\mu\text{-}OPiv)_6$. Adding 10 psig (69 kPa) of ethylene to an NMR sample of $PdCu_2(\mu\text{-}OPiv)_6$ resulted in the observation of a time-averaged signal for free ethylene and a coordinated ethylene (Figure H9, middle spectrum). This time-averaged peak shifts downfield upon addition of 50 psig (344 kPa) ethylene (Figure H9, top spectrum). For the solution of $PdCu_2(\eta^2\text{-}C_2H_4)_3(\mu\text{-}OPiv)_6$, the resonance observed at room temperature that is assigned to a time average of an ethylene ligand and free ethylene is split at -80 °C and exchange peaks between free ethylene and the ethylene ligand were observed by NOESY (EXSY) spectroscopy at -80 °C (Figure H17). We propose that the second ethylene peak can be assigned primarily to ethylene coordinated to Cu(I), because its integration is inconsistent with it being in the same complex as the *tert*-butyl resonance centered at 3.5 ppm. The peaks assigned to *tert*-butyl protons of OPiv ligands coalesce at a lower temperature in the presence of ethylene than in its absence suggesting that they undergo faster exchange when ethylene is present.

From this, we conclude that $PdCu_2(\eta^2\text{-}C_2H_4)_3(\mu\text{-}OPiv)_6$ likely forms in the presence of ethylene, but the ethylene ligand was not observed by ^1H NMR spectroscopy, perhaps due to rapid exchange or to poor solubility of the complex in CD_2Cl_2 at -80 °C resulting in a poor signal to noise ratio. To support the formation of $PdCu_2(\mu\text{-}OPiv)_6$ and $PdCu_2(\eta^2\text{-}C_2H_4)_3(\mu\text{-}OPiv)_6$, we performed spin-lattice relaxation measurements. These experiments were complicated by the fluxionality of the complexes, precluding estimation of proton-Cu(II) distances as was done previously for $Rh_2Cu(\eta^2\text{-}C_2H_4)_4(\mu\text{-}OPiv)_4$ (Figures S13-S15, Table S4).[44]

9.3.5 Calculated Mechanism for Styrene Formation with cyclic $PdCu_2(\eta^2\text{-}C_2H_4)_3(\mu\text{-}OPiv)_6$ as Catalyst

We have established triplet-spin cyclic $PdCu_2(\mu\text{-}OAc)_6$ (**A**) as the lowest energy species among the several complexes evaluated. Additionally, we predict that benzene C–H activation by **A** occurs through a CMD barrier of 33.5 kcal/mol, which is markedly lower than the 38.3 kcal/mol barrier required for the Pd_3 complex **C** to activate benzene.[53] These findings, in combination with our new experimental results and previous studies by Thornton and Sloan[62] provide evidence that the cyclic $PdCu_2$ complex **A** is the active catalyst for the oxidative coupling of benzene and ethylene to form styrene.

We now evaluate the full mechanism for the conversion of benzene and ethylene to styrene using **A** as the active catalyst. The free energy landscape for styrene formation catalyzed by $PdCu_2(\mu\text{-}OAc)_6$ (**A**) is depicted in Scheme 9.5 and discussed below. As noted below, ethylene coordination to **A** generates our proposed catalyst resting state, cyclic $PdCu_2(\eta^2\text{-}C_2H_4)_3(\mu\text{-}OAc)_6$ (or $PdCu_2(\eta^2\text{-}C_2H_4)_3(\mu\text{-}OPiv)_6$ when $Cu(OPiv)_2$ is used as the oxidant).

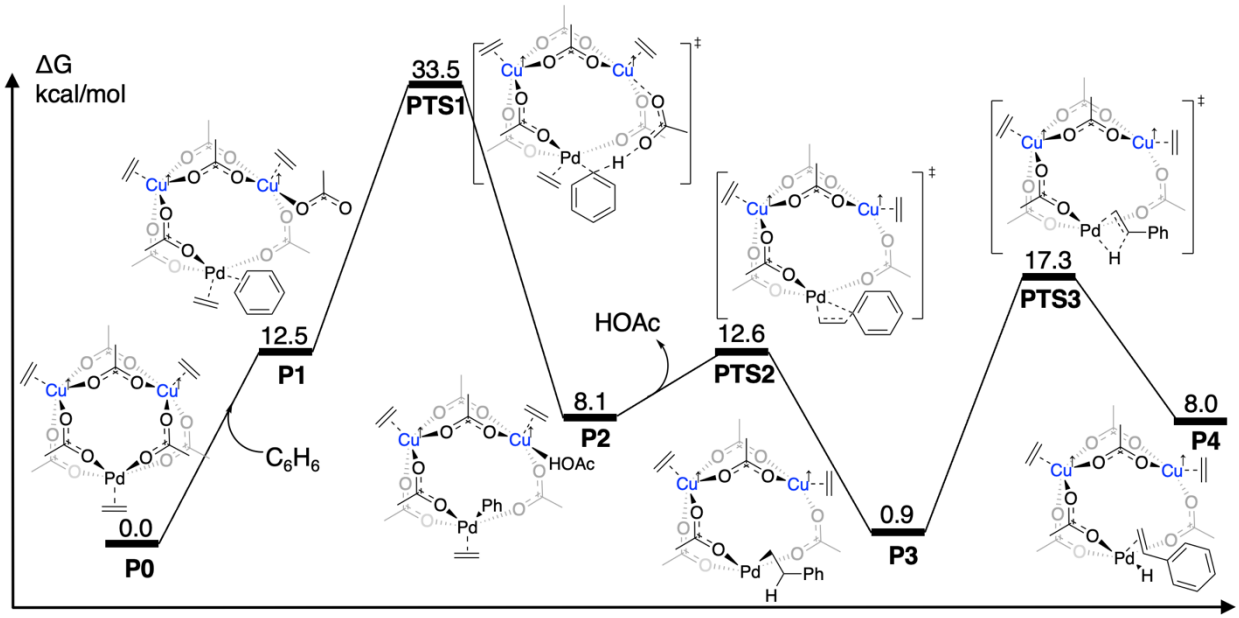

Scheme 9.5. DFT free energies calculated at 423 K for the styrene formation mechanism catalyzed by cyclic $PdCu_2(\mu\text{-}OAc)_6(C_2H_4)_3$. The free energy of this starting complex (**P0**) is set to zero. Superscript up arrows denote unpaired spins.

For the reference state at 0.0 kcal/mol, we start with cyclic $PdCu_2(\eta^2\text{-}C_2H_4)_3(\mu\text{-}OAc)_6$ (**P0**), which we believe is the experimentally observed species under catalytic conditions. **P0** is a ground state singlet with the triplet lying 20.5 kcal/mol above the ground state. Three additional equivalents of ethylene are included in **P0** that are not present in **A**; our DFT calculations revealed that the additional ethylene ligands stabilize the olefin insertion and β-hydride elimination transition states. Due to this stabilization and because we have experimental evidence that ethylene binds to the complex, the additional ethylene ligands are included for the mechanism evaluation.

Breaking an OAc bridge in **P0** to accommodate η^2-coordination of benzene is uphill by 12.5 kcal/mol (**P1**). This is expected since it is favorable for OAc to bridge Pd and Cu, and because coordination of the benzene to Pd likely disrupts the arene aromaticity.[72–76] Following benzene coordination, the complex undergoes C–H activation through CMD, which we have already found requires a free energy barrier of 33.5 kcal/mol (**PTS1**). The formation of a Pd–Ph bond and formation of coordinated HOAc results in an intermediate state (**P2**) at 8.1 kcal/mol. The ethylene axially coordinated to Pd in **P2** has a calculated C=C bond distance of 1.35 Å, indicating nominal Pd-to-ethylene backbonding. Ethylene insertion into the Pd–Ph bond occurs with a transition state barrier of 12.5 kcal/mol (**PTS2**) relative to the starting point **P0**, but the calculated olefin insertion barrier is only 4.5 kcal/mol above the preceding intermediate **P2**. Dissociation of HOAc occurs during

the ethylene insertion step, in which the relatively bulky alkyl arene being formed bullies HOAc out of the coordination site on the adjacent Cu (Figure 9.5). Formation of the alkyl arene ligand results in a free energy of 0.9 kcal/mol (**P3**) relative to the starting state. After formation of **P3**, the complex undergoes β-hydride elimination with a barrier of 17.3 kcal/mol (**PTS3**) relative to **P0**. Typically, β-hydride elimination is facile relative to ethylene insertion. However, the present case provides an example in which β-hydride elimination requires a significant activation barrier. This is attributed to the fact that the active Pd center in **P3** has all four coordination sites occupied, such that the incoming hydride would disrupt a Pd–OAc donor-acceptor coordination in order to form the Pd–H bond. β-hydride elimination affords the styrene product and the Pd–H bond at 8.0 kcal/mol (**P4**). Per expectation, the CMD transition state energy is notably higher than the ethylene insertion and β-hydride elimination transition states; C–H activation therefore is our proposed rate-determining step. The formation of styrene is endergonic by 8.0 kcal/mol. To return **P4** to the starting state **P0**, **P4** must dissociate the styrene, and a proton must be abstracted to generate free HOAc. The complex then undergoes an oxidation by acetyl transfer, accompanied by coordination of an ethylene. For the overall reaction, benzene + ethylene + 2 $Cu(OAc)_2$ → Styrene + 2 Cu(OAc) + 2 HOAc, the reaction free energy is ΔG = -13.9 kcal/mol.

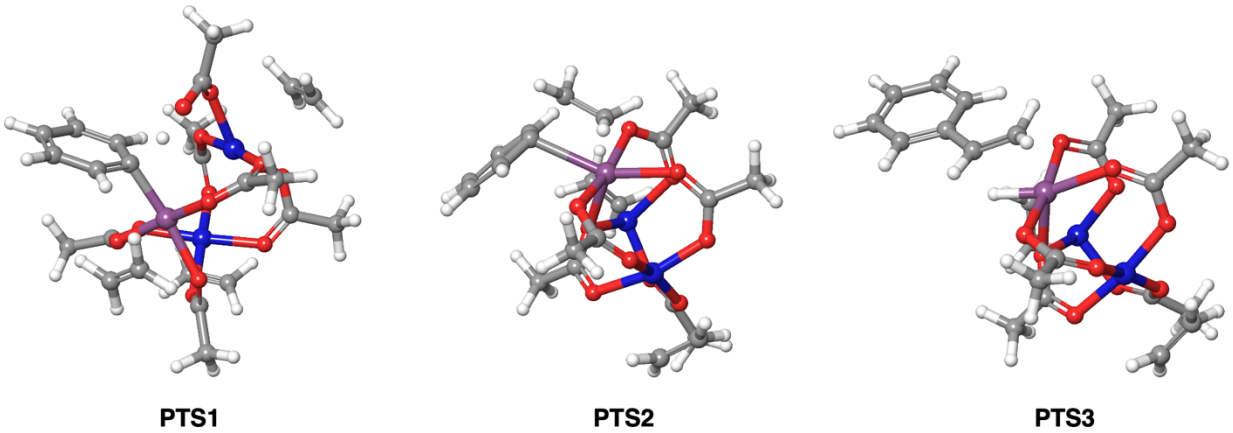

Figure 9.5. DFT-optimized concerted metalation deprotonation (**PTS1**), olefin insertion (**PTS2**) and β-hydride elimination (**PTS3**) transition states for $PdCu_2(\eta^2\text{-}C_2H_4)_3(\mu\text{-}OAc)_6$. Each Cu has an unpaired spin.

9.3.6 Comparison of Multi-Metallic $PdCu_2$ and Rh_2Cu Catalysts for Styrene Formation

At this point, we have proposed and validated a mechanism for Pd-catalyzed conversion of ethylene and benzene to styrene by the heterotrinuclear cyclic $PdCu_2(\eta^2\text{-}C_2H_4)_3(\mu\text{-}OAc)_6$ catalyst. We previously proposed a similar active catalyst, $Rh_2Cu(\eta^2\text{-}C_2H_4)_4(\mu\text{-}OAc)_4$, for the conversion of ethylene and benzene to styrene. Because Pd(II) and Rh(I) are isoelectronic (both d^8), we provide here a comparison of the two catalytic processes. In Scheme 9.6, we overlay our previously elucidated free energy surface (FES) for Rh-catalyzed styrene formation with the FES for Pd catalysis, and make several distinctions. Starting with benzene coordination, we see that **R1** lies 4.0 kcal/mol above **P1**. In **R1**, there is an additional energy cost of displacing an ethylene. However, **P1** has the additional cost of breaking the OAc ligand's bridging character. The largest difference

between Rh and Pd catalysis is the C–H activation step. Pd is calculated to undergo a CMD (**PTS1**) pathway for benzene C–H activation while Rh is calculated to activate benzene by oxidative addition (**RTS1**). Our calculations indicate that Rh provides a more facile route for benzene C–H activation in which **RTS1** and **RTS2** require 23.9 and 27.5 kcal/mol, while Pd requires 33.5 kcal/mol for CMD (**PTS1**). This is consistent with our experimental studies, where Rh has been observed to form styrene faster than Pd.[11] For Rh, we previously observed a substantial barrier for olefin insertion at 24.5 kcal/mol (**RTS2**) and a β-hydride elimination at 16.3 kcal/mol (**RTS3**). For Pd, the olefin insertion barrier is relatively small at 12.6 kcal/mol (**PTS2**) while the β-hydride elimination is 17.3 kcal/mol (**PTS3**). **RTS2** is believed to be highly energetic due to the Rh-aryl bond torsion required for ethylene insertion; no such torsion is required for **PTS2**. **PTS3** is high in energy because the fully coordinated Pd must accommodate the incoming H by relieving a nearby OAc of its donor-acceptor coordination. Overall, the Pd FES resides lower than the Rh FES for a majority of the reaction, but Rh provides a lower energy C–H activation (27.5 kcal/mol for Rh and 33.5 kcal/mol for Pd) and a more rapid overall catalytic process. Ultimately, in both Pd and Rh catalysis, the inclusion of Cu(II) in the active species enables the desired formation of styrene.

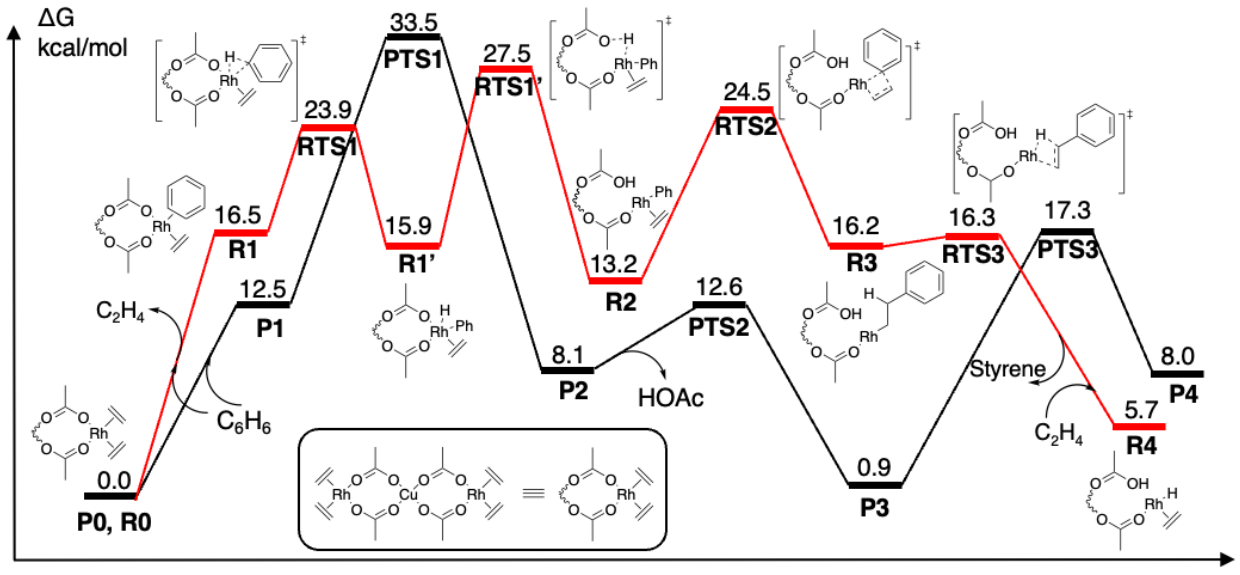

Scheme 9.6. Comparison of $PdCu_2(\eta^2\text{-}C_2H_4)_3(\mu\text{-}OAc)_6$ (**P0**) and $Rh_2Cu(\eta^2\text{-}C_2H_4)_4(\mu\text{-}OAc)_4$ (**R0**) for catalytic styrene formation at 423 K. The Pd-catalyzed path is in black while the Rh-catalyzed path is in red. The Rh complexes remain doublets along the surface while the Pd complexes remain triplets. The free energies of **P0** and **R0** are set to zero.

9.4 Conclusions

In this contribution we utilized DFT computations and experimental methods to elucidate the nature of the Pd catalyst for the oxidative conversion of benzene and ethylene to styrene (Scheme 9.7). Importantly, we propose that Cu(II) is a component of the active catalyst with Cu(II) carboxylates playing an important role beyond serving as the *in situ* oxidant.

We discovered that under our experimental conditions of 480 times excess Cu(II), the heterotrinuclear cyclic $PdCu_2(\mu\text{-}OAc)_6$ species likely predominates. Coordination of ethylene to this complex to form $PdCu_2(\eta^2\text{-}C_2H_4)_3(\mu\text{-}OAc)_6$ gives the proposed catalyst resting state. The calculated catalytic cycle has a rate-limiting benzene C–H activation barrier of 33.5 kcal/mol, which is consistent with previously observed experimental data. We consider that this discovery has broad impact; it illustrates an example of a heteronuclear transition metal complex that enables chemistry that is, according to our calculations, not otherwise feasible. The demonstration that cyclic $PdCu_2(\mu\text{-}OAc)_6$ enables formation of styrene opens new avenues to catalyst design that leverage the concept of a cyclic heteromultinuclear catalyst center.

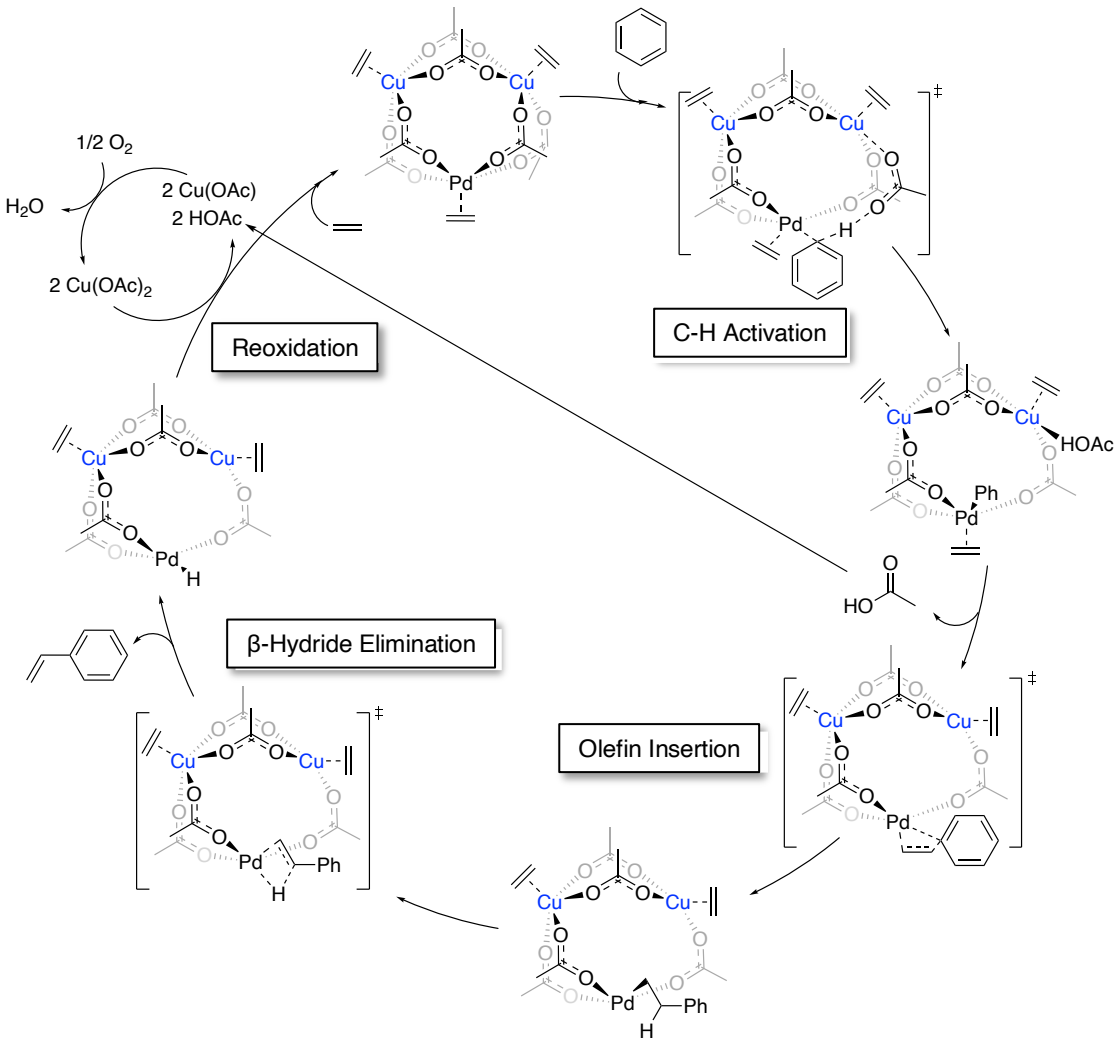

Scheme 9.7. The full catalytic cycle for the conversion of benzene and ethylene to styrene via the $PdCu_2(\eta^2\text{-}C_2H_4)_3(\mu\text{-}OAc)_6$ catalyst with $Cu(OAc)_2$ as *in situ* oxidant. Note that catalysis is typically performed anaerobically, where regeneration of $Cu(OAc)_2$ by O_2 is usually done separately. When the reaction is performed aerobically, product selectivity changes. All Cu have singular unpaired spins, such that all complexes are triplets. The recycling of Cu(I) and carboxylic acid to Cu(II) with dioxygen has been demonstrated in

a previous publication (reference 53). Thus, although studies herein are anaerobic with stoichiometric Cu(II), we have retained the dioxygen recycle in the overall mechanism.

9.5 Methods

9.5.1 Computational Methods

All quantum chemical calculations were performed using the Jaguar software package version 8.4 by Schrödinger Inc.[77] All structures were optimized using the B3LYP hybrid functional[78,79] with the Grimme-Becke-Johnson D3 empirical correction for London Dispersion.[80] The organic elements were treated with the triple-ζ 6-311G**++ basis set[81,82] while Pd was described using the Los Alamos small-core Effective Core Potential[83,84] (leaving 18 explicit electrons on Pd), LACV3P.

Vibrational frequency calculations were carried out to predict zero-point energies, enthalpies and entropies at catalytic conditions (150 °C) for all structures. These frequency calculations were also used to confirm local minima for stationary geometries and saddle points for transition states. We chose 150 °C (423 K) because the highest styrene selectivity was achieved at this temperature and above.[53]

For larger structures, geometries were first optimized in vacuum with the B3LYP functional using the large core LAV3P* ECP (10 explicit electrons for Pd) basis set, followed by re-optimization using B3LYP-D3 with the LAV3P**++ ECP basis set while

including implicit solvent. Smaller structures were optimized directly at the B3LYP-D3/LAV3P**++ level with implicit solvent. The two-step practice for large structures and the single-step practice for small structures both gave the same optimized structures, although the former method was found to be more computationally efficient for larger systems (depending on the initial guess).

To include the effect of solvation we apply the PBF Poisson-Boltzmann finite element method implicit solvation model.[85] The PBF model requires only two parameters to accurately describe an implicit solvent.[86] The parameters are the dielectric constant (ε) and the probe radius used to determine the solvent accessible surface, which is calculated via the formula $r = \sqrt[3]{3\Delta MW/4\pi N_A \rho}$ where MW is the molecular weight, N_A is Avogadro's number and ρ is the density. Here Δ represents the liquid packing density. To mimic benzene, we chose a dielectric constant of 2.284 and calculate a probe radius of 2.6 Å.

9.5.2 Experimental Methods

General Considerations. Unless otherwise noted, all procedures were carried out under an inert atmosphere using a nitrogen-filled glovebox or standard Schlenk techniques. Glovebox purity was maintained by periodic nitrogen purges (O_2 < 15 ppm). Benzene was dried by passage through a column of activated alumina. GC-FID was performed using a Shimadzu GC-2014 system with a 30 m x 90.25 mm HP5 column with 0.25 µm

film thickness. Styrene, vinyl pivalate, biphenyl, stilbene and phenyl pivalate production were monitored by GC-FID, and quantified using linear regression analysis of standard samples relative to the internal standard hexamethylbenzene. For the GC/FID instrument, the slope and correlation coefficient of the regression lines were 1.67 and 0.99 (styrene), 0.87 and 0.99 (trans-stilbene), 1.22 and 0.99 (phenyl pivalate) and 0.96 and 0.99 (biphenyl), respectively. ^{1}H NMR spectra were recorded on a Varian 500 MHz spectrometer, a Varian 600 MHz spectrometer, or a Bruker 600 MHz spectrometer. $Cu(OPiv)_2$ was synthesized by a previously reported method.[87] All other reagents were purchased from commercial sources and used as received.

Styrene Production Using $Pd(OAc)_2$ as Catalyst Precursor. A 30 mL stock solution of $Pd(OAc)_2$ (0.8 mg, 3.3 μmol) and hexamethylbenzene (5.4 mg, 33 μmol) was prepared. Next, 10 mL aliquots of this solution were combined with $Cu(OPiv)_2$ (143.7 mg, 538 μmol), HOPiv (110 mg, 1.07 mmol) in three dried Andrews Glass™ Labcrest® Fisher-Porter tubes with stir bars. The reactors were subsequently sealed and pressurized with 50 psig (344 kPa) of ethylene using a high-pressure line and heated at 120 °C. Note: reactors were kept behind a blast shield while under pressure and/or heated. Reactors were sampled every 30 minutes under an anerobic atmosphere using a long needle. Next, 0.25 mL aliquots of the reaction solution were combined with 0.5 mL benzene and washed with a

saturated aqueous solution of $NaHCO_3$ (1.5 mL). The organic layer was analyzed by GC-FID.

Styrene Production Using $PdCu_2(\mu\text{-}OPiv)_6$ as Catalyst Precursor. To a Fisher-Porter reactor, benzene (10 mL), $Pd(OPiv)_2$ (10.3 mg, 33.6 μmol) and 6 eq. of $Cu(OPiv)_2$ (53 mg, 198 μmol) were added. This mixture was stirred at 25 °C for 10 minutes to dissolve $Cu(OPiv)_2$ and $Pd(OPiv)_2$ and subsequently pressurized with 50 psig (344 kPa) of ethylene. The reactor was heated at 55 °C in an oil bath for 60 hours, and a color change from blue to green was observed due to the catalytic production of vinyl pivalate and styrene, which consumes $Cu(OPiv)_2$. A 1 mL aliquot of this solution, which contains the appropriate quantity of Pd atoms for three catalytic reactions (3.3 μmol), was dried *in vacuo* for 48 hours. To this dried solid, 30 mL of benzene and hexamethylbenzene (5.4 mg, 33 μmol) were added. Next, 10 mL aliquots of this solution were combined with $Cu(OPiv)_2$ (143.7 mg, 538 μmol) and HOPiv (110 mg, 1.07 mmol) in three dried Andrews Glass™ Labcrest® Fisher-Porter tubes with stir bars. Prior to beginning the catalytic reactions, reaction mixtures were analyzed by GC-FID. No styrene or vinyl pivalate was detected in any of the reaction mixtures. The reactors were subsequently sealed and pressurized with 50 psig (344 kPa) of ethylene using a high-pressure line and heated at 120 °C. Note: reactors were kept behind a blast shield while under pressure and/or heated. Reactors were sampled every 30 minutes under an anerobic atmosphere using a long

needle. Next, 0.25 mL aliquots of the reaction solution were combined with 0.5 mL benzene and washed with a saturated aqueous solution of $NaHCO_3$ (1.5 mL). The organic layer was analyzed by GC-FID. For the experiment using material synthesized in the absence of ethylene, benzene (10 mL), $Pd(OPiv)_2$ (10.3 mg, 33.6 μmol) and 6 eq. of $Cu(OPiv)_2$ (53 mg, 198 μmol) were added. This mixture was stirred at 25 °C for 10 minutes to dissolve $Cu(OPiv)_2$ and $Pd(OPiv)_2$ and subsequently pressurized with 50 psig (344 kPa) of dinitrogen. The reactor was heated at 55 °C in an oil bath for 96 hours, and no color change was observed. A 1 mL aliquot of this solution, which contains the appropriate quantity of Pd for three catalytic reactions, was combined with 29 mL benzene and (5.4 mg, 33 μmol) hexamethylbenzene. Aliquots (10 mL) of this solution were combined with $Cu(OPiv)_2$ (143.7 mg, 538 μmol) and HOPiv (110 mg, 1.07 mmol) in three dried Andrews Glass™ Labcrest® Fisher-Porter tubes with stir bars. Catalytic styrene production was carried out identically to the procedure detailed above.

NMR Experiments Probing Reaction of $Pd(OAc)_2$ and $Cu(OPiv)_2$ Without Ethylene. A 2.6 mM solution of $Pd(OPiv)_2$ (1.2 mg, 3.9 μmol) was prepared in 1.5 mL C_6D_6. To this solution, 5 eq. of hexamethyldisiloxane (HMDSO) (4 μL, 19 μmol), 72 eq. $Cu(OPiv)_2$ (74 mg, 280 μmol) and 144 eq. of HOPiv (57 mg, 560 μmol) were added. Next, 0.4 mL aliquots of this solution were added to three oven-dried J-Young tubes, which were sealed and removed from the glovebox. Dinitrogen {50 psig (344 kPa)} was added

using a high-pressure line, and the J-Young NMR tubes were heated at 120 °C in an oil bath. At each timepoint, the J-Young NMR tubes were cooled to room temperature and analyzed by ^{1}H NMR spectroscopy.

NMR Experiments Probing Reaction of $Pd(OAc)_2$ and $Cu(OPiv)_2$ with Ethylene. A 2.6 mM solution of $Pd(OPiv)_2$ (1.2 mg, 3.9 μmol) was prepared in 1.5 mL C_6D_6. To this solution, 5 eq. of HMDSO (4 μL, 19 μmol), 72 eq. of $Cu(OPiv)_2$ (74 mg, 280 μmol) and 144 eq. of HOPiv (57 mg, 560 μmol) were added. Next, 0.4 mL aliquots of this solution were added to three oven-dried J-Young NMR tubes, which were sealed and taken out of the glovebox. Ethylene {50 psig (344 kPa)} was added using a high-pressure line, and the NMR tubes were heated at 120 °C in an oil bath. At each timepoint, the NMR tubes were cooled to room temperature and analyzed by ^{1}H NMR spectroscopy.

Representative procedure for the synthesis of $PdCu_2(\mu\text{-}OPiv)_6$. To a Fisher-Porter reactor, benzene (5 mL), $Pd(OPiv)_2$ (15 mg, 50 μmol) and 4 eq. of $Cu(OPiv)_2$ (53 mg, 198 μmol) were added. This mixture was stirred at 25 °C for 10 minutes to dissolve $Cu(OPiv)_2$ and $Pd(OPiv)_2$, and subsequently pressurized with 50 psig (344 kPa) of ethylene. The reactor was heated at 55 °C in an oil bath for 48 hours, and a color change from blue to green was observed due to the catalytic production of vinyl pivalate and styrene, which consumes $Cu(OPiv)_2$. To consume remaining $Cu(OPiv)_2$, the reaction mixture was heated at 120 °C for 2 minutes, and a color change from green to brown was observed. Benzene

was removed from this solution *in vacuo*, and the residue was stirred with 10 mL of pentanes and filtered through a celite-loaded fine porosity frit. Pentane was removed from the filtrate *in vacuo*, leaving a yellow-brown residue.

Measurement of Concentration Dependence of Spin-Lattice Relaxation Rates for $PdCu_2(\mu\text{-}OPiv)_6$. The residue obtained from the above synthesis was dissolved in 0.9 mL C_6D_6, and 0.3 mL aliquots were added to three oven-dried J-Young NMR tubes in the glovebox. Relative concentration was varied by serial dilution of these samples. For each dilution, 0.15 mL of C_6D_6 were added in the glovebox. An inversion recovery (T1R) experiment was performed using a Bruker Advance III spectrometer operating at 600 MHz.

Representative Procedure for the *in situ* Synthesis of $PdCu_2(\eta^2\text{-}C_2H_4)_3(\mu\text{-}OPiv)_6$. The solid containing $PdCu_2(\mu\text{-}OPiv)_6$ was dissolved in 0.1 mL CD_2Cl_2 and pressurized with 10 psig (69 kPa) of ethylene in a J-Young tube.

Measurement of Spin-Lattice Relaxation Rates for $PdCu_2(\eta^2\text{-}C_2H_4)_3(\mu\text{-}OPiv)_6$. $PdCu_2(\eta^2\text{-}C_2H_4)_3(\mu\text{-}OPiv)_6$ was prepared *in situ* as described above with either 10 or 50 psig (69 or 344 kPa) of ethylene. An inversion recovery (T1R) experiment was performed at 25 °C using a Bruker Advance III spectrometer operating at 600.165 MHz or at -80 °C using a Varian spectrometer operating at 500 MHz.

9.6 References

(1) Kocal, J. A.; Vora, B. V.; Imai, T. Production of Linear Alkylbenzenes. *Appl. Catal. A Gen.* **2001**, *221* (1–1), 295–301. https://doi.org/10.1016/S0926-860X(01)00808-0.

(2) Olah, G. A.; Prakash, G. K. S.; Wade, K.; Molnár, Á.; Williams, R. E. *Hypercarbon Chemistry: Second Edition*; 2011. https://doi.org/10.1002/9781118016466.

(3) Wittcoff, H. A.; Reuben, B. G.; Plotkin, J. S. *Industrial Organic Chemicals: Third Edition*; 2013. https://doi.org/10.1002/9781118229996.

(4) de Almeida, J. L. G.; Dufaux, M.; Taarit, Y. Ben; Naccache, C. Linear Alkylbenzene. *J. Am. Oil Chem. Soc.* **1994**, *71* (7), 675–694. https://doi.org/10.1007/BF02541423.

(5) Garside, J. *Guide to the Business of Chemistry*; 2019.

(6) Čejka, J.; Wichterlová, B. Acid-Catalyzed Synthesis of Mono-and Dialkyl Benzenes over Zeolites: Active Sites, Zeolite Topology, and Reaction Mechanisms. *Catal. Rev. - Sci. Eng.* **2002**, *44* (3), 375–421. https://doi.org/10.1081/CR-120005741.

(7) Perego, C.; Ingallina, P. Recent Advances in the Industrial Alkylation of Aromatics: New Catalysts and New Processes. *Catal. Today* **2002**, *73* (1–2), 3–22. https://doi.org/10.1016/S0920-5861(01)00511-9.

(8) Perego, C.; Ingallina, P. Combining Alkylation and Transalkylation for

Alkylaromatic Production. *Green Chem.* **2004**, *6* (6), 274–279. https://doi.org/10.1039/b403277m.

(9) Perego, C.; Pollesel, P. Advances in Aromatics Processing Using Zeolite Catalysts. *Adv. Nanoporous Mater.* **2010**, *1* (1), 97–149. https://doi.org/10.1016/S1878-7959(09)00102-9.

(10) Gerzeliev, I. M.; Khadzhiev, S. N.; Sakharova, I. E. Ethylbenzene Synthesis and Benzene Transalkylation with Diethylbenzenes on Zeolite Catalysts. *Pet. Chem.* **2011**, *51* (1), 39–48. https://doi.org/10.1134/S0965544111010038.

(11) Gunnoe, T. B.; Schinski, W. L.; Jia, X.; Zhu, W. Transition-Metal-Catalyzed Arene Alkylation and Alkenylation: Catalytic Processes for the Generation of Chemical Intermediates. *ACS Catal.* **2020**, *10* (23), 14080–14092. https://doi.org/10.1021/acscatal.0c03494.

(12) Zhu, W.; Gunnoe, T. B. Advances in Group 10 Transition-Metal-Catalyzed Arene Alkylation and Alkenylation. *J. Am. Chem. Soc.* **2021**, *143* (18), 6746–6766. https://doi.org/10.1021/jacs.1c01810.

(13) NOAck, M.; Caro, J. Zeolite Membranes. In *Handbook of Porous Solids*; 2008. https://doi.org/10.1002/9783527618286.ch31b.

(14) Moodie, R. B. Electrophilic Aromatic Substitution. In *Organic Reaction*

Mechanisms, 1983: An Annual Survey Covering the Literature Dated December 1982 Through November 1983; 2007; pp 263–267. https://doi.org/10.1002/9780470066690.ch8.

(15) Rueping, M.; Nachtsheim, B. J. A Review of New Developments in the Friedel-Crafts Alkylation - From Green Chemistry to Asymmetric Catalysis. *Beilstein J. Org. Chem.* **2010**, *6* (6). https://doi.org/10.3762/bjoc.6.6.

(16) Bandini, M.; Melloni, A.; Umani-Ronchi, A. New Catalytic ApprOAches in the Stereoselective Friedel-Crafts Alkylation Reaction. *Angew. Chemie - Int. Ed.* **2004**, *43* (5), 550–556. https://doi.org/10.1002/anie.200301679.

(17) Foley, N. A.; Lee, J. P.; Ke, Z.; Gunnoe, T. B.; Cundari, T. R. Ru(Ll) Catalysts Supported by Hydridotris(Pyrazolyl)Borate for the Hydroarylation of Olefins: Reaction Scope, Mechanistic Studies, and Guides for the Development of Improved Catalysts. *Acc. Chem. Res.* **2009**, *42* (5), 585–597. https://doi.org/10.1021/ar800183j.

(18) Marty Lail , Christen M. Bell , David Conner, T. R. C.; T. Brent Gunnoe; Petersen, and J. L. Experimental and Computational Studies of Ru (II) Catalyzed Addition of Arene C-H Bonds to Olefins. *Organometallics* **2004**, *23* (21), 5007–5020. https://doi.org/https://doi.org/10.1021/om049404g.

(19) Burgess, S. A.; Joslin, E. E.; Gunnoe, T. B.; Cundari, T. R.; Sabat, M.; Myers, W.

H. Hydrophenylation of Ethylene Using a Cationic Ru(Ii) Catalyst: Comparison to a Neutral Ru(Ii) Catalyst. *Chem. Sci.* **2014**, *5* (11), 4355–4366. https://doi.org/10.1039/c4sc01665c.

(20) Lail, M.; Bell, C. M.; Conner, D.; Cundari, T. R.; Gunnoe, T. B.; Petersen, J. L. Experimental and Computational Studies of Ruthenium(II)-Catalyzed Addition of Arene C−H Bonds to Olefins. *Organometallics* **2004**, *23* (21), 5007–5020. https://doi.org/10.1021/om049404g.

(21) Jia, X.; Gary, J. B.; Gu, S.; Cundari, T. R.; Gunnoe, T. B. Oxidative Hydrophenylation of Ethylene Using a Cationic Ru(II) Catalyst: Styrene Production with Ethylene as the Oxidant. *Isr. J. Chem.* **2017**, *57* (10), 1037–1046. https://doi.org/10.1002/ijch.201700099.

(22) Schinkel, M.; Marek, I.; Ackermann, L. Carboxylate-Assisted Ruthenium(II)-Catalyzed Hydroarylations of Unactivated Alkenes through C-H Cleavage. *Angew. Chemie - Int. Ed.* **2013**, *52* (14), 3977–3980. https://doi.org/10.1002/anie.201208446.

(23) Lail, M.; Arrowood, B. N.; Gunnoe, T. B. Addition of Arenes to Ethylene and Propene Catalyzed by Ruthenium. *J. Am. Chem. Soc.* **2003**, *125* (25), 7506–7507. https://doi.org/10.1021/ja035076k.

(24) McKeown, B. A.; Foley, N. A.; Lee, J. P.; Gunnoe, T. B. Hydroarylation of

Unactivated Olefins Catalyzed by Platinum(II) Complexes. *Organometallics* **2008**, *27* (16), 4031–4033. https://doi.org/10.1021/om8006008.

(25) Clement, M. L.; Grice, K. A.; Luedtke, A. T.; Kaminsky, W.; Goldberg, K. I. Platinum(II) Olefin Hydroarylation Catalysts: Tuning Selectivity for the Anti-Markovnikov Product. *Chem. - A Eur. J.* **2014**, *20* (52), 17287–17291. https://doi.org/10.1002/chem.201405174.

(26) Luedtke, A. T.; Goldberg, K. I. Intermolecular Hydroarylation of Unactivated Olefins Catalyzed by Homogeneous Platinum Complexes. *Angew. Chemie - Int. Ed.* **2008**, *47* (40), 7694–7696. https://doi.org/10.1002/anie.200800524.

(27) McKeown, B. A.; Gonzalez, H. E.; Friedfeld, M. R.; Gunnoe, T. B.; Cundari, T. R.; Sabat, M. Mechanistic Studies of Ethylene Hydrophenylation Catalyzed by Bipyridyl Pt(II) Complexes. *J. Am. Chem. Soc.* **2011**, *133* (47), 19131. https://doi.org/10.1021/ja206064v.

(28) Suslick, B. A.; Liberman-Martin, A. L.; Wambach, T. C.; Tilley, T. D. Olefin Hydroarylation Catalyzed by (Pyridyl-Indolate)Pt(II) Complexes: Catalytic Efficiencies and Mechanistic Aspects. *ACS Catal.* **2017**, *7* (7), 4313–4322. https://doi.org/10.1021/acscatal.7b01560.

(29) Mckeown, B.; Prince, B.; Ramiro, Z.; Gunnoe, T.; Cundari, T. PtII-Catalyzed Hydrophenylation of α-Olefins: Variation of Linear/Branched Products as a

Function of Ligand Donor Ability. *ACS Catal.* **2014**, *4* (5), 1607–1615. https://doi.org/10.1021/cs400988w.

(30) Oxgaard, J.; Muller, R. P.; Goddard, W. A.; Periana, R. A. Mechanism of Homogeneous Ir(III) Catalyzed Regioselective Arylation of Olefins. *J. Am. Chem. Soc.* **2004**, *126* (1), 352–363. https://doi.org/10.1021/ja034126i.

(31) Bhalla, G.; Oxgaard, J.; Goddard, W. A.; Periana, R. A. Anti-Markovnikov Hydroarylation of Unactivated Olefins Catalyzed by a Bis-Tropolonato Iridium (III) Organometallic Complex. *Organometallics* **2005**, *24* (13), 3229–3232. https://doi.org/10.1021/om0501733.

(32) Pahls, D. R.; Allen, K. E.; Goldberg, K. I.; Cundari, T. R. Understanding the Effect of Ancillary Ligands on Concerted Metalation-Deprotonation by (DmPhebox)Ir(OAc)2(H2O) Complexes: A DFT Study. *Organometallics* **2014**, *33* (22), 6413–6419. https://doi.org/10.1021/om500752m.

(33) Matsumoto, T.; Periana, R. A.; Taube, D. J.; Yoshida, H. Regioselective Hydrophenylation of Olefins Catalyzed by an Ir(III) Complex. *J. Mol. Catal. A Chem.* **2002**, *180* (1–2), 1–18. https://doi.org/10.1016/S1381-1169(01)00390-9.

(34) Periana, R. A.; Liu, X. Y.; Bhalla, G. Novel Bis-Acac-O,O-Ir(III) Catalyst for Anti-Markovnikov, Hydroarylation of Olefins Operates by Arene CH Activation. *Chem. Commun.* **2002**, No. 24, 3000–3001. https://doi.org/10.1039/b208680h.

(35) Gao, Y.; Guan, C.; Zhou, M.; Kumar, A.; Emge, T. J.; Wright, A. M.; Goldberg, K. I.; Krogh-Jespersen, K.; Goldman, A. S. β-Hydride Elimination and C-H Activation by an Iridium Acetate Complex, Catalyzed by Lewis Acids. Alkane Dehydrogenation Cocatalyzed by Lewis Acids and [2,6-Bis(4,4-Dimethyloxazolinyl)-3,5-Dimethylphenyl]Iridium. *J. Am. Chem. Soc.* **2017**, *139* (18), 6338–6350. https://doi.org/10.1021/jacs.6b12995.

(36) Webster-Gardiner, M. S.; Chen, J.; Vaughan, B. A.; McKeown, B. A.; Schinski, W.; Gunnoe, T. B. Catalytic Synthesis of "Super" Linear Alkenyl Arenes Using an Easily Prepared Rh(I) Catalyst. *J. Am. Chem. Soc.* **2017**, *139* (15), 5474–5480. https://doi.org/10.1021/jacs.7b01165.

(37) Zhu, W.; Gunnoe, T. B. Advances in Rhodium-Catalyzed Oxidative Arene Alkenylation. *Acc. Chem. Res.* **2020**, *53* (4), 920–936. https://doi.org/10.1021/acs.accounts.0c00036.

(38) Chen, J.; Nielsen, R. J.; Goddard, W. A.; McKeown, B. A.; Dickie, D. A.; Gunnoe, T. B. Catalytic Synthesis of Superlinear Alkenyl Arenes Using a Rh(I) Catalyst Supported by a "Capping Arene" Ligand: Access to Aerobic Catalysis. *J. Am. Chem. Soc.* **2018**, *140* (49), 17007–17018. https://doi.org/10.1021/jacs.8b07728.

(39) Matsumoto, T.; Periana, R. A.; Taube, D. J. Oxidative Coupling of Olefins and Aromatics Using a Rhodium Catalyst and a Copper (II) Redox Agent. Patent

US6127590A, 2000.

(40) Vaughan, B. A.; Webster-Gardiner, M. S.; Cundari, T. R.; Gunnoe, T. B. A Rhodium Catalyst for Single-Step Styrene Production from Benzene and Ethylene. *Science (80-.).* **2015**, *348* (6233), 421–424. https://doi.org/10.1126/science.aaa2260.

(41) Matsumoto, T.; Periana, R. A.; Taube, D. J.; Yoshida, H. Direct Synthesis of Styrene by Rhodium-Catalyzed Oxidative Arylation of Ethylene with Benzene. *J. Catal.* **2002**, *206* (2), 272–280. https://doi.org/10.1006/jcat.2001.3471.

(42) Vaughan, B. A.; Khani, S. K.; Gary, J. B.; Kammert, J. D.; Webster-Gardiner, M. S.; McKeown, B. A.; Davis, R. J.; Cundari, T. R.; Gunnoe, T. B. Mechanistic Studies of Single-Step Styrene Production Using a Rhodium(I) Catalyst. *J. Am. Chem. Soc.* **2017**, *139* (4), 1485–1498. https://doi.org/10.1021/jacs.6b10658.

(43) Jia, X.; Frye, L. I.; Zhu, W.; Gu, S.; Gunnoe, T. B. Synthesis of Stilbenes by Rhodium-Catalyzed Aerobic Alkenylation of Arenes via C–H Activation. *J. Am. Chem. Soc.* **2020**, *142* (23), 10534–10543. https://doi.org/10.1021/jacs.0c03935.

(44) Musgrave, C. B.; Zhu, W.; Coutard, N.; Ellena, J. F.; Dickie, D. A.; Gunnoe, T. B.; Goddard, W. A. Mechanistic Studies of Styrene Production from Benzene and Ethylene Using [(η 2 -C 2 H 4) 2 Rh(μ-OAc)] 2 as Catalyst Precursor: Identification of a Bis-Rh I Mono-Cu II Complex As the Catalyst. *ACS Catal.* **2021**, *11* (9), 5688–

5702. https://doi.org/10.1021/acscatal.1c01203.

(45) Saper, N. I.; Ohgi, A.; Small, D. W.; Semba, K.; Nakao, Y.; Hartwig, J. F. Nickel-Catalysed Anti-Markovnikov Hydroarylation of Unactivated Alkenes with Unactivated Arenes Facilitated by Non-Covalent Interactions. *Nat. Chem.* **2020**, *12* (3), 276–283. https://doi.org/10.1038/s41557-019-0409-4.

(46) Qiu, Y.; Hartwig, J. F. Mechanism of Ni-Catalyzed Oxidations of Unactivated C(Sp3)-H Bonds. *J. Am. Chem. Soc.* **2020**, *142* (45), 19239–19248. https://doi.org/10.1021/jacs.0c09157.

(47) Biffis, A.; Tubaro, C.; Buscemi, G.; Basato, M. Highly Efficient Alkyne Hydroarylation with Chelating Dicarbene Palladium (II) and Platinum(II) Complexes. *Adv. Synth. Catal.* **2008**, *350* (1), 189–196. https://doi.org/10.1002/adsc.200700271.

(48) Viciu, M. S.; Stevens, E. D.; Petersen, J. L.; Nolan, S. P. N-Heterocyclic Carbene Palladium Complexes Bearing Carboxylate Ligands and Their Catalytic Activity in the Hydroarylation of Alkynes. *Organometallics* **2004**, *23* (15), 3752–3755. https://doi.org/10.1021/om049843f.

(49) Danopoulos, A. A.; Tsoureas, N.; Macgregor, S. A.; Smith, C. Phosphine- and Pyridine-Functionalized N-Heterocyclic Carbene Methyl and Allyl Complexes of Palladium. Unexpected Regiospecificity of the Protonation Reaction of the

Dimethyl Complexes. *Organometallics* **2007**, *26* (2), 253–263. https://doi.org/10.1021/om0608408.

(50) Liao, L.; Sigman, M. S. Palladium-Catalyzed Hydroarylation of 1,3-Dienes with Boronic Esters via Reductive Formation of π-Allyl Palladium Intermediates under Oxidative Conditions. *J. Am. Chem. Soc.* **2010**, *132* (30), 10209–10211. https://doi.org/10.1021/ja105010t.

(51) Iwai, Y.; Gligorich, K. M.; Sigman, M. S. Aerobic Alcohol Oxidation Coupled to Palladium-Catalyzed Alkene Hydroarylation with Boronic Esters. *Angew. Chemie - Int. Ed.* **2008**, *47* (17), 3219–3222. https://doi.org/10.1002/anie.200705317.

(52) Fujiwara, Y.; Moritani, I.; Danno, S.; Asano, R.; Teranishi, S. Aromatic Substitution of Olefins. VI. Arylation of Olefins with Palladium (II) Acetate. *J. Am. Chem. Soc.* **1969**, *91* (25), 7166–7169. https://doi.org/10.1021/ja01053a047.

(53) Jia, X.; Foley, A. M.; Liu, C.; Vaughan, B. A.; McKeown, B. A.; Zhang, S.; Gunnoe, T. B. Styrene Production from Benzene and Ethylene Catalyzed by Palladium(II): Enhancement of Selectivity toward Styrene via Temperature-Dependent Vinyl Ester Consumption. *Organometallics* **2019**, *38* (19), 3532–3541. https://doi.org/10.1021/acs.organomet.9b00349.

(54) Lyons, T. W.; Sanford, M. S. Palladium-Catalyzed Ligand-Directed C-H Functionalization Reactions. *Chem. Rev.* **2010**, *110* (2), 1147–1169.

https://doi.org/10.1021/cr900184e.

(55) Chen, X.; Engle, K. M.; Wang, D.-H.; Yu, J.-Q. Palladium(II)-Catalyzed C⊠H Activation/C⊠C Cross-Coupling Reactions: Versatility and Practicality. *Angew. Chemie Int. Ed.* **2009**, *48* (28), 5094–5115. https://doi.org/10.1002/anie.200806273.

(56) Plata, J. J.; García-Mota, M.; Braga, A. A. C.; López, N.; Maseras, F. Vinyl Acetate Synthesis on Homogeneous and Heterogeneous Pd-Based Catalysts: A Theoretical Analysis on the Reaction Mechanisms. *J. Phys. Chem. A* **2009**, *113* (43), 11758–11762. https://doi.org/10.1021/jp902929x.

(57) García-Cuadrado, D.; Braga, A. A. C.; Maseras, F.; Echavarren, A. M. Proton Abstraction Mechanism for the Palladium-Catalyzed Intramolecular Arylation. *J. Am. Chem. Soc.* **2006**, *128* (4), 1066–1067. https://doi.org/10.1021/ja056165v.

(58) Yang, Y. F.; Cheng, G. J.; Liu, P.; Leow, D.; Sun, T. Y.; Chen, P.; Zhang, X.; Yu, J. Q.; Wu, Y. D.; Houk, K. N. Palladium-Catalyzed Meta-Selective C-H Bond Activation with a Nitrile-Containing Template: Computational Study on Mechanism and Origins of Selectivity. *J. Am. Chem. Soc.* **2014**, *136* (1), 344–355. https://doi.org/10.1021/ja410485g.

(59) Anand, M.; Sunoj, R. B.; Schaefer, H. F. Non-Innocent Additives in a Palladium(II)-Catalyzed C-H Bond Activation Reaction: Insights into Multimetallic Active Catalysts. *J. Am. Chem. Soc.* **2014**, *136* (15), 5535–5538.

https://doi.org/10.1021/ja412770h.

(60) Balcells, D.; Clot, E.; Eisenstein, O. C-H Bond Activation in Transition Metal Species from a Computational Perspective. *Chem. Rev.* **2010**, *110* (2), 749–823. https://doi.org/10.1021/cr900315k.

(61) Davies, D. L.; Donald, S. M. A.; Macgregor, S. A. Computational Study of the Mechanism of Cyclometalation by Palladium Acetate. *J. Am. Chem. Soc.* **2005**, *127* (40), 13754–13755. https://doi.org/10.1021/ja052047w.

(62) Sloan, O. D.; Thornton, P. Mixed Copper(II)-Palladium(II) Acetates. *Inorganica Chim. Acta* **1986**, *120* (2), 173–175. https://doi.org/10.1016/S0020-1693(00)86105-8.

(63) Bakhmutov, V. I.; Berry, J. F.; Cotton, F. A.; Ibragimov, S.; Murillo, C. A. Non-Trivial Behavior of Palladium(II) Acetate. *Dalt. Trans.* **2005**, No. 11, 1989–1992. https://doi.org/10.1039/b502122g.

(64) Funes-Ardoiz, I.; Maseras, F. Cooperative Reductive Elimination: The Missing Piece in the Oxidative-Coupling Mechanistic Puzzle. *Angew. Chemie - Int. Ed.* **2016**, *55* (8), 2764–2767. https://doi.org/10.1002/anie.201510540.

(65) Funes-Ardoiz, I.; Maseras, F. Computational Characterization of the Mechanism for the Oxidative Coupling of Benzoic Acid and Alkynes by Rhodium/Copper and

Rhodium/Silver Systems. *Chem. - A Eur. J.* **2018**, *24* (47), 12383–12388. https://doi.org/10.1002/chem.201800627.

(66) Karaliota, A.; Kretsi, O.; Tzougraki, C. Synthesis and Characterization of a Binuclear Coumarin-3-Carboxylate Copper(II) Complex. *J. Inorg. Biochem.* **2001**, *84* (1–2), 33–37. https://doi.org/10.1016/S0162-0134(00)00214-2.

(67) Ozarowski, A. The Zero-Field-Splitting Parameter D in Binuclear Copper(II) Carboxylates Is Negative. *Inorg. Chem.* **2008**, *47* (21), 9760–9762. https://doi.org/10.1021/ic801560e.

(68) Karthik, K.; Qadir, A. M. Synthesis and Crystal Structure of a New Binuclear Copper(II) Carboxylate Complex as a Precursor for Copper(II) Oxide Nanoparticles. *J. Struct. Chem.* **2019**, *60*, 1126–1132. https://doi.org/10.1134/S002247661907014X.

(69) Spivey, A. C.; Tseng, C.-C.; Schatz, J.; Seler, M.; Seßler, M.; Sainsbury, M.; Shimada, K.; Koutentis, P. A.; Ioannidou, H. A.; Margaretha, P.; Hrtinger, S.; Ulrich, H.; Schnrch, M.; Hmmerle, J.; Stanetty, P.; Schnürch, M.; Hämmerle, J.; Zhang, J.; Waldvogel, S. R.; Joule, J. A.; Yorimitsu, H.; Shimizu, M.; Khartulyari, A.; Maier, M. E.; Fowler, L. S.; Sutherland, A.; Carbery, D.; Anderson, E. A.; Gockel, B.; Demchenko, A. V.; De Meo, C.; Coote, S. C.; Smith, L. H. S.; Procter, D. J.; Uemura, M.; Hari, Y.; Aoyama, T.; Shioiri, T.; Oishi, M.; Takikawa, H.;

Yamaguchi, M.; Araki, S.; Hirashita, T.; Yanagisawa, A.; Naka, H.; Saito, S.; Matsunaga, S.; Arai, T.; Landelle, G.; Paquin, J.-F.; Gleason, J. L.; Tiong, E. A.; Higashihara, T.; Ueda, M.; Merino, P.; Araki, S.; Hirashita, T. *Palladium-Catalyzed Cross-Coupling Reactions*; 2010. https://doi.org/10.1055/sos-sd-107-00124.

(70) Arndtsen, B. A.; Bergman, R. G. Usually Mild and Selective Hydrocarbon C-H Bond Activation with Positively Charged Iridium(III) Complexes. *Science (80-.).* **1995**. https://doi.org/10.1126/science.270.5244.1970.

(71) Liebov, N. S.; Gu, S.; McKeown, B. A.; Huang, X.; Boaz, N. C.; Brent Gunnoe, T.; Groves, J. T. Studies of C–H Activation and Functionalization: Combined Computational and Experimental Efforts to Elucidate Mechanisms, Principles, and Catalysts. In *Springer Series in Materials Science*; 2021; Vol. 284, pp 767–806. https://doi.org/10.1007/978-3-030-18778-1_34.

(72) Keane, J. M.; Harman, W. D. A New Generation of π-Basic Dearomatization Agents. *Organometallics* **2005**, *24* (8), 1786–1798. https://doi.org/10.1021/om050029h.

(73) Harman, W. D. The Activation of Aromatic Molecules with Pentaammineosmium(II). *Chem. Rev.* **1997**. https://doi.org/10.1021/cr940316n.

(74) Graham, P. M.; Meiere, S. H.; Sabat, M.; Harman, W. D. Dearomatization of Benzene, Deamidization of N,N-Dimethylformamide, and a Versatile New Tungsten

π Base. *Organometallics* **2003**, *22* (22), 4364–4366. https://doi.org/10.1021/om030560h.

(75) Meiere, S. H.; Brooks, B. C.; Gunnoe, T. B.; Sabat, M.; Harman, W. D. A Promising New Dearomatization Agent: Crystal Structure, Synthesis, and Exchange Reactions of the Versatile Complex TpRe(CO)(1-Methylimidazole)(H2-Benzene) (Tp = Hydridotris(Pyrazolyl)Borate). *Organometallics* **2001**, *20* (6), 1038–1040. https://doi.org/10.1021/om000900o.

(76) Tellers, D. M.; Skoog, S. J.; Bergman, R. G.; Gunnoe, T. B.; Harman, W. D. Comparison of the Relative Electron-Donating Abilities of Hydridotris(Pyrazolyl)Borate and Cyclopentadienyl Ligands: Different Interactions with Different Transition Metals. *Organometallics* **2000**. https://doi.org/10.1021/om000043o.

(77) Bochevarov, A. D.; Harder, E.; Hughes, T. F.; Greenwood, J. R.; Braden, D. A.; Philipp, D. M.; Rinaldo, D.; Halls, M. D.; Zhang, J.; Friesner, R. A. Jaguar: A High-Performance Quantum Chemistry Software Program with Strengths in Life and Materials Sciences. *Int. J. Quantum Chem.* **2013**, *113* (18), 2110–2142. https://doi.org/10.1002/qua.24481.

(78) Becke, A. D. Density-Functional Thermochemistry. III. The Role of Exact Exchange. *J. Chem. Phys.* **1993**, *98* (7), 5648–5652.

https://doi.org/10.1063/1.464913.

(79) Lee, C.; Yang, W.; Parr, R. G. Development of the Colle-Salvetti Correlation-Energy Formula into a Functional of the Electron Density. *Phys. Rev. B* **1988**, *37* (2), 785–789. https://doi.org/10.1103/PhysRevB.37.785.

(80) Grimme, S.; Antony, J.; Ehrlich, S.; Krieg, H. A Consistent and Accurate Ab Initio Parametrization of Density Functional Dispersion Correction (DFT-D) for the 94 Elements H-Pu. *J. Chem. Phys.* **2010**, *132* (15). https://doi.org/10.1063/1.3382344.

(81) Hariharan, P. C.; Pople, J. A. The Influence of Polarization Functions on Molecular Orbital Hydrogenation Energies. *Theor. Chim. Acta* **1973**, *28* (3), 213–222. https://doi.org/10.1007/BF00533485.

(82) Hehre, W. J.; Ditchfield, K.; Pople, J. A. Self-Consistent Molecular Orbital Methods. XII. Further Extensions of Gaussian-Type Basis Sets for Use in Molecular Orbital Studies of Organic Molecules. *J. Chem. Phys.* **1972**, *56* (5), 2257–2261. https://doi.org/10.1063/1.1677527.

(83) Kahn, L. R.; Goddard, W. A. Ab Initio Effective Potentials for Use in Molecular Calculations. *J. Chem. Phys.* **1972**, *56* (6), 2685–2701. https://doi.org/10.1063/1.1677597.

(84) Roy, L. E.; Hay, P. J.; Martin, R. L. Revised Basis Sets for the LANL Effective

Core Potentials. *J. Chem. Theory Comput.* **2008**, *4* (7), 1029–1031. https://doi.org/10.1021/ct8000409.

(85) Friedrichs, M.; Zhou, R.; Edinger, S. R.; Friesner, R. A. Poisson-Boltzmann Analytical Gradients for Molecular Modeling Calculations. *J. Phys. Chem. B* **1999**, *103* (16), 3057–3061. https://doi.org/10.1021/jp982513m.

(86) Tannor, D. J.; Marten, B.; Murphy, R.; Friesner, R. A.; Sitkoff, D.; Nicholls, A.; Honig, B.; Ringnald, M.; Goddard, W. A. Accurate First Principles Calculation of Molecular Charge Distributions and Solvation Energies from Ab Initio Quantum Mechanics and Continuum Dielectric Theory. *J. Am. Chem. Soc.* **1994**, *116* (26), 11875–11882. https://doi.org/10.1021/ja00105a030.

(87) Xie, L. H.; Suh, M. P. Flexible Metal-Organic Framework with Hydrophobic Pores. *Chem. - A Eur. J.* **2011**, *17* (49), 13653–13656. https://doi.org/10.1002/chem.201103078.

Chapter 10

Mechanistic Studies of Styrene Production from Benzene and Ethylene using $[(\eta^2\text{-}C_2H_4)_2Rh(\mu\text{-}OAc)]_2$ as Catalyst Precursor: Identification of a Multi-nuclear Bis-Rh^{I} Mono-Cu^{II} Complex as the Catalyst

Reproduced with permission from:

W Zhu, N Coutard, JF Ellena, DA Dickie, TB Gunnoe, WA Goddard III. *Mechanistic Studies of Styrene Production from Benzene and Ethylene using $[(\eta^2\text{-}C_2H_4)_2Rh(\mu\text{-}OAc)]_2$ as Catalyst Precursor: Identification of a Multi-nuclear Bis-Rh^{I} Mono-Cu^{II} Complex as the Catalyst*, *ACS Catalysis*, **2021**, 11, 9, 5688-5702

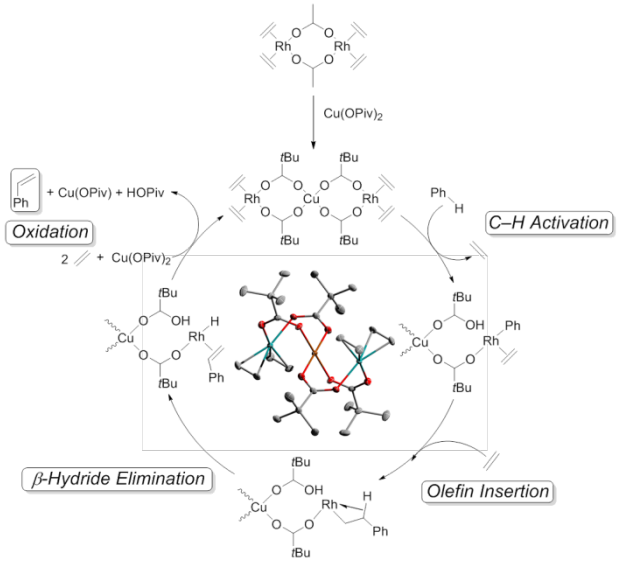

Figure 10.0: Table of contents figure

10.1 Abstract

We report a combined experimental and computational study focused on the mechanism of oxidative conversion of benzene and ethylene to styrene using $[(\eta^2\text{-}C_2H_4)_2Rh(\mu\text{-}OAc)]_2$ as the catalyst precursor in the presence of $Cu(OPiv)_2$ (OPiv = pivalate). We identify the catalyst resting state to be $[(\eta^2\text{-}C_2H_4)_2Rh^{I}(\mu\text{-}OPiv)_2]_2(\mu\text{-}Cu)$, which is a heterotrinuclear molecular complex in which a central Cu^{II} atom bridges two Rh moieties. At high Rh concentration in the presence of $Cu(OPiv)_2$ and pivalic acid (HOPiv), the trinuclear complex $[(\eta^2\text{-}C_2H_4)_2Rh^{I}(\mu\text{-}OPiv)_2]_2(\mu\text{-}Cu)$ converts to the binuclear Rh(II) complex $[(HOPiv)Rh^{II}(\mu\text{-}OPiv)_2]_2$, which has been identified by ^1H NMR spectroscopy and single crystal X-ray diffraction. The binuclear Rh(II) $[(HOPiv)Rh^{II}(\mu\text{-}OPiv)_2]_2$ is not a catalyst for styrene production, but under catalytic conditions

$[(HOPiv)Rh^{II}(\mu\text{-}OPiv)_2]_2$ can be partially converted to the active catalyst, the Rh-Cu-Rh complex $[(\eta^2\text{-}C_2H_4)_2Rh^{I}(\mu\text{-}OPiv)_2]_2(\mu\text{-}Cu)$, following an induction period of ~6 hours. Using quantum chemical calculations, we sampled possible mononuclear and binuclear Rh species, finding that the binuclear Rh(II) $[(HOPiv)Rh^{II}(\mu\text{-}OPiv)_2]_2$ paddle-wheel is a low energy global minimum, which is consistent with experimental observations that $[(HOPiv)Rh^{II}(\mu\text{-}OPiv)_2]_2$ is not a catalyst for styrene formation. Further, we investigated the mechanism of styrene production starting from $[(\eta^2\text{-}C_2H_4)_2Rh^{I}(\mu\text{-}OAc)_2]_2(\mu\text{-}Cu)$, $[(\eta^2\text{-}C_2H_4)_2Rh(\mu\text{-}OAc)]_2$, and $(\eta^2\text{-}C_2H_4)_2Rh(\kappa^2\text{-}OAc)$. For all reaction pathways studied, the predicted activation barriers for styrene formation from $[(\eta^2\text{-}C_2H_4)_2Rh(\mu\text{-}OAc)]_2$ and $(\eta^2\text{-}C_2H_4)_2Rh(\kappa^2\text{-}OAc)$ are too high compared to experimental kinetics. In contrast, the overall activation barrier for styrene formation predicted by DFT from the Rh-Cu-Rh complex$[(\eta^2\text{-}C_2H_4)_2Rh^{I}(\mu\text{-}OPiv)_2]_2(\mu\text{-}Cu)$ is in agreement with experimentally determined rates of catalysis. Based on these results, we conclude that incorporation of Cu(II) into the active Rh-Cu-Rh catalyst reduces the activation barrier for benzene C–H activation, O–H reductive elimination, and ethylene insertion into the Rh–Ph bond.

10.2 Introduction

Catalytic transformations that form C–C bonds are of substantial value for both large scale commodity processes and for fine chemical syntheses.[1-9] Acid-based catalysis via Brønsted acids or zeolite catalysts are common methods for C–C bond formation to form alkyl arenes. These reactions have been widely applied to industrial production of alkyl arenes and, ultimately, alkenyl arenes such as styrene. Alkyl and alkenyl arenes are precursors for a range of products including plastics, surfactants, elastomers, pharmaceuticals and fine chemicals.[10-13]

Acid-catalyzed arene alkylation has drawbacks that are inherent to the reaction mechanism (i.e., electrophilic aromatic substitution) such as limited reaction scope, inability to produce 1-aryl alkanes, and regioselectivity for alkylation of substituted arenes that is dictated by electronic effects of the substituents rather than catalyst directed.[14] Transition metal-mediated cross-coupling reactions are another widely used method to construct new C–C bonds, but, these reactions typically require the use of halogenated aromatic starting substrates and a stoichiometric amount of metal-containing reagents.[15-20]

In an approach that is complementary to acid-catalyzed arene alkylation, olefin hydroarylation can be achieved through transition metal mediated aromatic C–H activation and subsequent olefin insertion into metal-aryl bonds. This route provides

potential advantages over the traditional acid-based and C–C cross coupling methods.[5-9, 21, 22] Transition metal-catalyzed olefin hydroarylation offers opportunities to a) selectively synthesize linear 1-aryl alkane/alkenes by circumventing carbocation intermediates, b) directly produce unsaturated alkenyl arenes from arenes and olefins through a β-hydride elimination reaction step, c) alkenylate electron-deficient arene substrates, and d) inhibit polyalkylation. Molecular complexes based on Ru,[23-32] Pd,[33-38] Ni,[39, 40] Ir[41-46] and Pt[47-55] have been reported to catalyze olefin hydroarylation (to produce alkyl arenes) and oxidative olefin hydroarylation (to produce alkenyl arenes) using unactivated arenes and olefins. Our group and others have reported Rh catalyzed aromatic C—H activation[56-60] and arene alkenylation using hydrocarbon substrates,[35, 61-66] and we recently demonstrated oxidative olefin hydroarylation using $[(\eta^2\text{-}C_2H_4)_2Rh(\mu\text{-}OAc)]_2$ (**1**) as the catalyst precursor.[14, 67-73] These reactions incorporate the Rh catalyst precursor, arene, olefin and CuX_2 (X = carboxylate such as acetate, pivalate and 2-ethylhexanoate) and are generally heated between 150 °C and 165 °C. Potential advantages of the Rh-catalyzed alkenyl arene formation include: a) selectivity for linear 1-aryl alkenes (> 8:1 linear/branched ratio in most cases); b) broad substrate scope including electron-deficient arenes; c) under some reaction conditions, quantitative yield based on Cu(II) oxidants as the limiting reagent; d) aerobic oxidation by recycling Cu(II) with air, either during catalysis or in a step separate from catalysis. The presumed catalytic cycle involves Rh-mediated arene C–H

activation, olefin insertion into a Rh-aryl bond, β-hydride elimination to form a Rh-hydride bond and net dissociation of the alkenyl arene product. Reaction of the Rh hydride with Cu(II) carboxylate completes the catalytic cycle.[69]

Previous studies are consistent with a soluble Rh species as the active catalyst, and kinetic studies under some conditions revealed the possibility of a binuclear Rh species as an intermediate.[69, 70] Previous data from X-ray photoelectron spectroscopy (XPS) are consistent with a possible Rh(II) catalyst resting state, but due to ligand modification of binding energies, we noted that formal Rh(II) was not conclusive.[70] Despite our detailed previous studies, elucidation of the catalyst resting state has eluded us. The need for paramagnetic Cu(II), which limits the use of NMR spectroscopy under some catalytic conditions, has complicated *in situ* mechanistic studies. Thus, while some details of the Rh catalyzed arene alkenylation have been determined, the inability to determine the identity of the molecular catalyst has limited our ability to fully understand the catalysis and observed selectivity patterns. Herein, we report combined experimental and computational studies that provide evidence that the trimetallic complex $[(\eta^2\text{-}C_2H_4)_2Rh^{I}(\mu\text{-}OPiv)_2]_2(\mu\text{-}Cu)$ (**4**) is the catalyst resting state under our standard catalytic conditions. Further, we report evidence that the Rh/Cu/Rh core remains intact during catalysis, suggesting a role for Cu^{II} in addition to being an oxidant for the net removal of

two hydrogen atoms. Indeed, our DFT calculations reinforce that the presence of Cu^{II} in the active catalyst is essential to catalyst activity.

10.3 Results and Discussion

10.3.1 Experimental Comparison of Rh(I), (II) and (III) Catalyst Precursors

We probed catalytic styrene production using different molecular Rh complexes, in formal oxidation states Rh(I), Rh(II) and Rh(III), as catalyst precursors. The reactions were studied at 150 °C using the Rh catalyst precursor, benzene, ethylene (C_2H_4), $Cu(OPiv)_2$, and pivalic acid (HOPiv). HOPiv is added to increase the solubility of the $Cu(OPiv)_2$, which helps inhibit decomposition of the Rh(I) catalyst precursor to elemental Rh.[70] Also, HOPiv is beneficial for the recycling of Cu(I) to Cu(II) oxidants by dioxygen since carboxylic acid inhibits hydrolysis of Cu(I).[65] Under these conditions, the binuclear Rh(I) **1**, the binuclear Rh(II) $[(HOPiv)Rh(\mu\text{-}OPiv)_2]_2$ (**2**), and $RhCl_3$ (**3**) all act as catalyst precursors to produce styrene (Scheme 10.1 and Figure 10.1). Experiments revealed that the catalysis using complex **1** as the catalyst precursor produces styrene rapidly without an observable induction period under conditions studied (Figure 10.1). In contrast, catalysis with complex **3** as the catalyst precursor shows an induction period of approximately 1.5 hours, after which the rate of catalysis is similar to that using complex **1** as catalyst precursor. Calculating apparent turnover frequencies (TOFs), after any

induction period, showed nearly identical results using complexes **1** and **3** as the catalyst precursor: the apparent TOF using catalyst precursor **1** is ~1.1 × 10^{-1} s^{-1} using data between 0 h and 0.5 h, and the apparent TOF using catalyst precursor **3** is ~9.6 × 10^{-2} s^{-1} using data between 1.5 h and 2 h. The apparent TOFs are determined based on a binuclear Rh catalyst (see below). This result indicates that the active Rh catalyst from both precursors **1** and **3**, following an induction period for catalyst precursor **3**, are likely the same species. In contrast, catalysis using the binuclear Rh(II) complex **2** as the precursor showed a longer induction period (~6 hours) than catalyst precursor **3**. Also, catalysis using **2** as the catalyst precursor reveals a lower apparent TOF after the induction period of ~2.8 × 10^{-2} s^{-1} (the TOF was calculated using data between 7 h and 9 h when the TO versus time plots are linear).

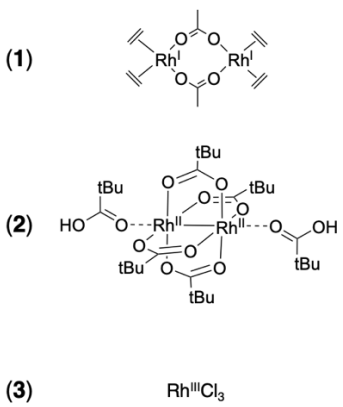

Scheme 10.1. Structures of three Rh catalyst precursors: binuclear Rh(I) $[(\eta^2\text{-}C_2H_4)_2Rh(\mu\text{-}OAc)]_2$ (**1**), binuclear Rh(II) $[(HOPiv)Rh(\mu\text{-}OPiv)_2]_2$ (**2**), and $RhCl_3$ (**3**).

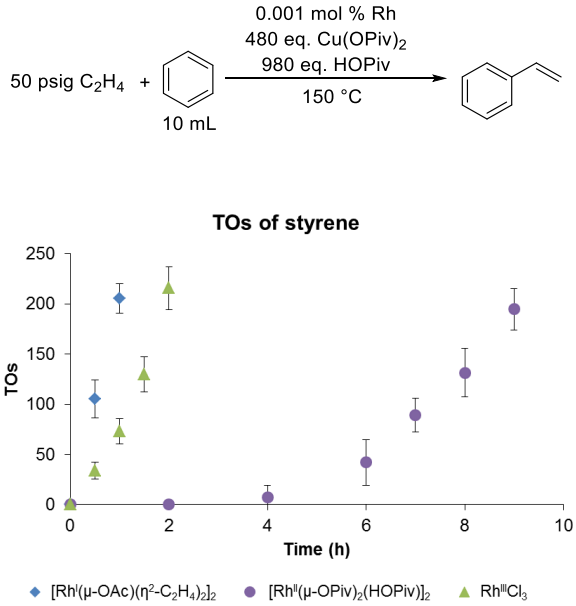

Figure 10.1. Comparison of turnovers (TOs) vs time plots for the conversion of benzene and ethylene to styrene using various molecular Rh catalyst precursors: $[(\eta^2\text{-}C_2H_4)_2Rh(\mu\text{-}OAc)]_2$ (**1**), $[(HOPiv)Rh(\mu\text{-}OPiv)_2]_2$ (**2**), and $RhCl_3$ (**3**). Each data point is the average of at least three separate experiments. Error bars represent the standard deviations based on a minimum of three independent experiments. Reaction conditions: 0.001 mol % of Rh (relative to benzene), 480 eq. $Cu(OPiv)_2$ (relative to Rh), 960 eq. HOPiv (relative to Rh), 10 mL benzene, 50 psig ethylene, 150 °C.

10.3.2 Characterization of Rh Resting State: Experimental Studies

We sought to experimentally identify the resting state of the Rh complex starting from complex **1**. For the conversion of benzene and ethylene to styrene, the catalytic reaction conditions involved the combination of complex **1**, benzene, ethylene, $Cu(OPiv)_2$

and pivalic acid (HOPiv).[69] Our initial studies monitored the transformation of complex **1** in the presence of $Cu(OPiv)_2$ and HOPiv in benzene-d_6 by *in situ* ^1H NMR spectroscopy (Scheme 10.2). As observed by ^1H NMR spectroscopy (Figure I1), approximately 10 minutes after combination of **1** with 24 equivalents of $Cu(OPiv)_2$ and 48 equivalents of HOPiv (relative to Rh) at room temperature, **1** (18.7 mM Rh) was consumed and a new broad peak was observed at ~4.0 ppm in the ^1H NMR spectrum. This indicates **1** was converted to a new Rh complex, which we have characterized (see below) as **4** (Scheme 10.2). After 12 hours at 120 °C in the presence of 50 psig ethylene, $Cu(OPiv)_2$ and HOPiv in benzene-d_6, intermediate **4** was converted to the binuclear paddle-wheel complex **2**, which was readily identified by ^1H NMR spectroscopy with a singlet at ~1.05 ppm (the resulting solution of **2** is labeled as solution A in discussions below). In the absence of ethylene, the formation of **2** was reproducible with high yields (91(5)% by ^1H NMR spectroscopy, based on 3 independent experiments with the standard deviation provided) and, as expected, accompanied by the release of ethylene (Figure I2). We confirmed the in situ formation of **2** by addition of independently prepared and isolated sample of **2** (prepared according to literature procedures[74] and confirmed by an X-ray diffraction study, Figure I3) to a reaction solution. In addition, catalytic styrene production using independently prepared **2** (5.60×10^{-4} mmol, 0.001 mol % Rh) and solution A (initially 5.60×10^{-4} mmol of **1** as precursors provided almost identical TOs vs time plots (Scheme

10.3). Also, both catalytic reactions showed a similar induction period and reactivity after the induction period (Figure 10.2). This result confirms that the majority of **1** is converted to **2** under the conditions shown in Scheme 10.2 and after 12 h at 120 °C.

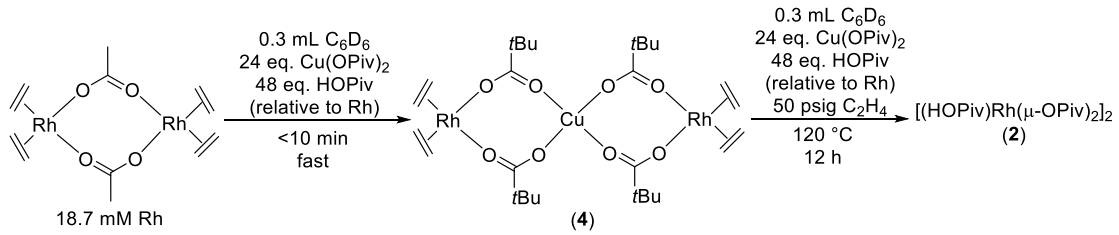

Scheme 10.2. Conversion of $[(\eta^2\text{-}C_2H_4)_2Rh(\mu\text{-}OAc)]_2$ (**1**) to $[(\eta^2\text{-}C_2H_4)_2Rh^I(\mu\text{-}OPiv)_2]_2(\mu\text{-}Cu)$ (**4**) at room temperature and $[(HOPiv)Rh(\mu\text{-}OPiv)_2]_2$ (**2**) at 120 °C under 50 psig ethylene.

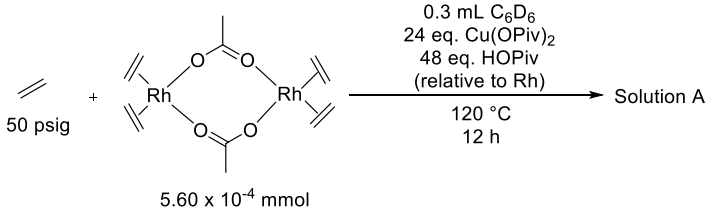

Scheme 10.3. Conversion of $[(\eta^2\text{-}C_2H_4)_2Rh(\mu\text{-}OAc)]_2$ to solution A {containing $[(HOPiv)Rh(\mu\text{-}OPiv)_2]_2$ (**2**)}.

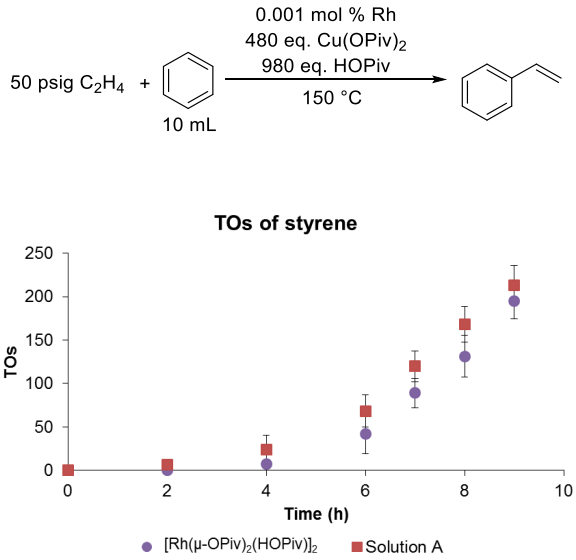

Figure 10.2. Comparison of turnovers (TOs) vs time plots for the conversion of benzene and ethylene to styrene using [(HOPiv)Rh(μ-OPiv)$_2$]$_2$ (**2**) and solution A (see above for description of solution A). Each data point is the average of at least three separate experiments and error bars represent the standard deviations based on these independent experiments. Reaction conditions: 0.001 mol % of Rh (relative to benzene), 480 eq. Cu(OPiv)$_2$ (relative to Rh), 960 eq. HOPiv (relative to Rh), 10 mL benzene, 50 psig ethylene, 150 °C.

We used single-crystal X-ray analysis to validate the structure of intermediate **4**. X-ray quality crystals of **4** were obtained by treating **1** with 1 equivalent of Cu(OPiv)$_2$ and 2 equivalents of HOPiv (relative to Rh) at room temperature. The resulting crystal was characterized as the heterometallic complex **4** with bridging pivalate groups between the Rh^{I} centers and Cu^{II} (Figure 10.3). Reported examples of structurally characterized trinuclear Rh$_2$Cu complexes are rare.[75-80] The distance between Rh and Cu atoms

(3.0095(5) Å) is longer than the sum of the covalent radii of rhodium (1.39 Å) and copper (1.27 Å) in cluster compounds[81] and is longer than the typical range of Rh-Cu bond lengths (2.5-2.6 Å) in this class of Rh_2Cu complexes.[77-79] Therefore, we believe little or no Rh–Cu bonding interaction is involved in **4**. The orientation of coordinated ethylene is perpendicular to the Rh coordination square plane, which is characteristic for d^8 $Rh^I(\eta^2$-$C_2H_4)$ complexes.[65, 82] Similar to other reported Rh(I) complexes with ethylene ligand,[65, 82] the C=C bond of coordinated ethylene in **4** is only slightly longer (1.393(6) and 1.402(6) Å) than that of free ethylene (1.330 Å),[83] suggesting substantial double bond character. The bond length of coordinated ethylene in **4** is slightly longer than that in reported **1** (1.35-1.40 Å).[80]

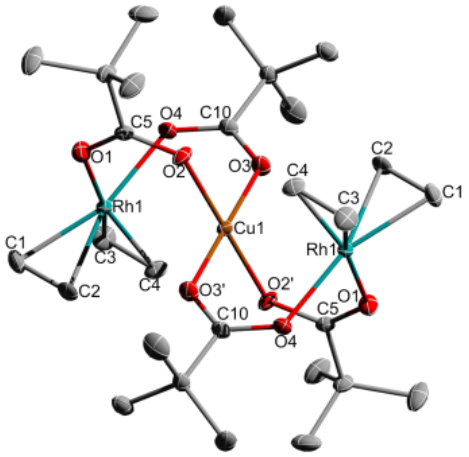

Figure 10.3. ORTEP of $[(\eta^2$-$C_2H_4)_2Rh^I(\mu$-OPiv$)_2]_2(\mu$-Cu) (**4**) (50% probability). H atoms are omitted for clarity. Selected bond lengths (Å): Cu1-O2 1.948(3), Cu1-O3 1.949(3), Rh1-O4 2.078(3), Rh1-C1 2.112(4),

Rh1-C2 2.118(3), Rh1-Cu1 3.0095(5), Rh1-O1 2.079(3), Rh1-C3 2.112(4), Rh1-C4 2.122(4), C1-C2 1.393(6), C3-C4 1.402(6). Selected bond angles (°): O4-Rh1-O1 87.78(11), C1-Rh1-C2 38.45(16), C1-Rh1-C3 88.43(18), C1-Rh1-C4 100.63(17), O4-Rh1-C1 160.42(14), O1-Rh1-C1 88.93(15), C3-Rh1-C4 38.66(16), O2'-Cu1-O3' 90.05(12), O2'-Cu1-O3 89.95(12), O1-C5-O2 125.9(3), O3-C10-O4 125.7(3).

To ascertain if complex **4** persists in solution, further NMR studies were conducted. Diffusion ordered spectroscopy experiments were not possible due to rapid spin relaxation of the ethylene protons of **4** (see Appendix I). This is likely due to a short average distance between the ethylene protons of **4** and the paramagnetic Cu^{II} atom (termed $C_2\mathbf{H}_4$–Cu distance). However, we were able to quantify the ethylene proton spin lattice relaxation rate (R_{1C2H4}).[84] R_{1C2H4} was measured as a function of concentration of **4** (Figure I10). The spin-lattice relaxation rate of the ethylene protons of a solution **4** (benzene-d_6) was plotted as a function of relative concentration (Figure I10, Appendix I). The intercept of this plot at 0 concentration ($141 \pm 7\ s^{-1}$) gives the pure intramolecular spin lattice relaxation rate for these protons.[85] Since the slope is small, meaning a weak dependence on concentration, we conclude that most or all of the spin lattice relaxation observed occurs from an intramolecular phenomenon, indicative that the paramagnetic center (Cu^{II}) and ethylene protons belong to the same molecule, supporting the persistence of **4** in solution.

Crystals of **4** were washed with pentane and dried under vacuum. The obtained solid was subjected to the reaction conditions where we observed the conversion of intermediate **4** to complex **2**: 24 equivalents of $Cu(OPiv)_2$ and 48 equivalents of HOPiv (relative to Rh, assuming the obtained solid is pure **4** at 120 °C for 12 hours). As expected, complete conversion of the obtained solid from crystals of **4** to **2** was observed by ^1H NMR spectroscopy (Figure I4). Catalytic styrene production using crystals of intermediate **4** showed statistically identical reactivity compared to the same reaction conditions using complex **1** as the catalyst precursor (Figure 10.4). Thus, we propose that **4** is a catalytically relevant intermediate that is rapidly formed from **1** under catalytic conditions, and **4** is likely the catalyst resting state for styrene production (see below for additional evidence). Catalysis using heterometallic complexes and clusters is widely-studied,[86-89] but examples of Rh-Cu catalyst systems are rare. One example we found is the use of a Rh-Cu cluster $Cu_2\{Rh_{12}(CO)_{30}\}$ as a catalyst for CO hydrogenation.[90]

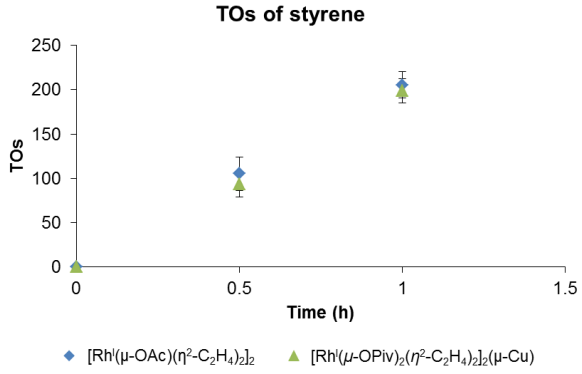

Figure 10.4. Comparison of TOs vs time plots for the conversion of benzene and ethylene to styrene using $[(\eta^2\text{-}C_2H_4)_2Rh(\boxtimes\text{-}OAc)]_2$ (**1**) and $[(\eta^2\text{-}C_2H_4)_2Rh^I(\mu\text{-}OPiv)_2]_2(\mu\text{-}Cu)$ (**4**). Each data point is the average of at least three separate experiments with error bars representing the standard deviations based on these independent experiments. Reaction conditions: 0.001 mol % of Rh (relative to benzene), 480 eq. $Cu(OPiv)_2$ (relative to Rh), 960 eq. HOPiv (relative to Rh), 10 mL benzene 50 psig ethylene, 150 °C.

Kinetic studies were performed for the conversion of **1** (18.7 mM Rh) to **2** at 21, 45, 50, and 60 °C. Given the rapid conversion of **1** to **4**, these studies provide kinetic data for the conversion of **4** to **2**. Kinetic plots were derived by monitoring the amount of complex **2** formed. The kinetic plots show a second-order dependence on concentration of **4** (Figure 10.5A and Figure I5). Activation parameters were obtained from an Eyring plot using the observed second-order rate constants (k_{obs}) at four different temperatures (Figure 10.5B). The $\Delta H^{\ddagger}$ and $\boxtimes S^{\ddagger}$ were determined to be 16(3) kcal/mol and -19(5) cal/(mol·K), respectively. In the absence of Cu(II), treating complex **1** with 100 equivalents of HOAc (relative to Rh) in C_6D_6 at room temperature reveals no reaction after 12 h. We conclude that carboxylic acid does not oxidize Rh(I) during the formation of **2**. Moreover, the decay of **4** shows a first-order dependence on concentration of HOPiv (Figures S6 and S7). In the absence of ethylene, the observed rate constants obtained at 45 and 50 °C were 8(2) x 10^{-3} and 1.2(4) x 10^{-2} mol·s^{-1}·L^{-1}, respectively, which are higher than the rate constants in the presence of 50 psig ethylene (3.6(6) x 10^{-3} and 4.6(8) x 10^{-3} mol·s^{-1}·L^{-1}) (Figure

10.6). The observed rate dependence on HOPiv and ethylene indicates that the dissociation of ethylene and coordination of HOPiv are both involved in kinetically relevant steps. Although details cannot be elucidated with the current data, the second-order dependence on Rh species and the negative $\boxtimes S^{\ddagger}$ value are consistent with the involvement of two molecules of **4** in what is likely a multi-step and complicated process.

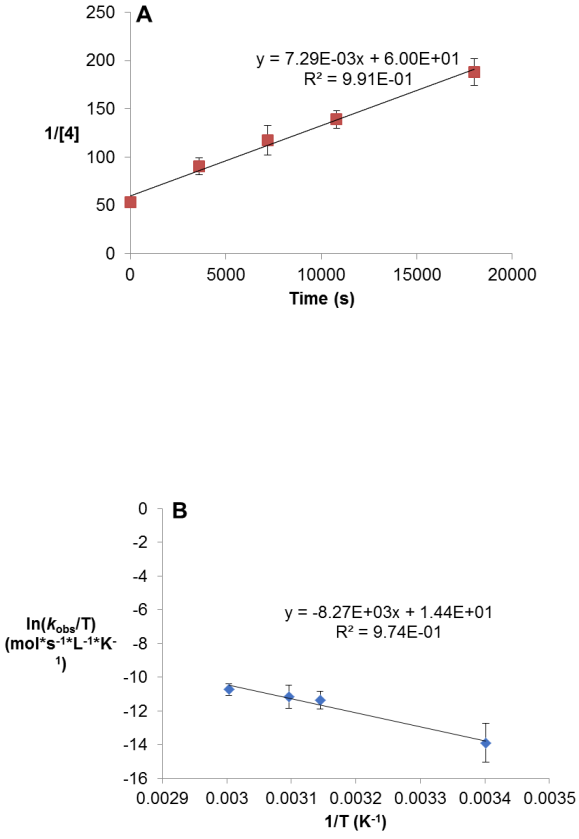

Figure 10.5. Representative kinetic plots (60 °C) (**A**) and Eyring plot (**B**) for conversion of $[(\eta^2\text{-}C_2H_4)_2Rh^{I}(\mu\text{-}OPiv)_2]_2(\mu\text{-}Cu)$ (**4**) to $[(HOPiv)Rh(\mu\text{-}OPiv)_2]_2$ (**2**) at 21, 45, 50, and 60 °C under ethylene. Reaction conditions: 9.35 mM of $[Rh(\kappa\text{-}OAc)(\eta^2\text{-}C_2H_4)_2]_2$ as starting material, 0.3 mL benzene-d_6, 24 eq. $Cu(OPiv)_2$

(relative to Rh), 48 eq. HOPiv (relative to Rh), 50 psig ethylene. The rate of decay of **4** is determined based on the amount of complex **2** formed. Each data point is the average of three separate experiments and error bars represent the standard deviations based these independent experiments.

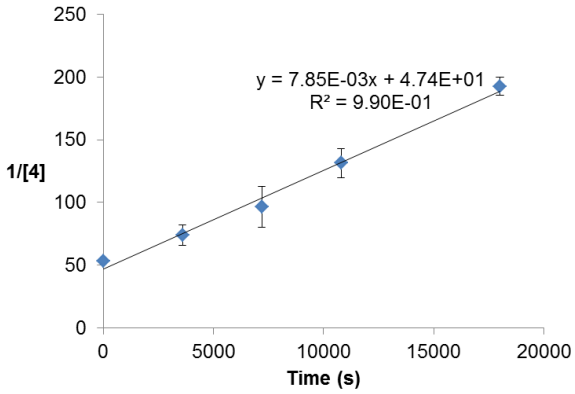

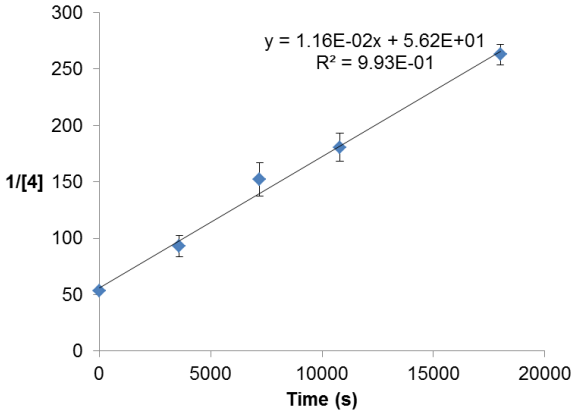

Figure 10.6. Kinetic plots for conversion of $[(\eta^2\text{-}C_2H_4)_2Rh^I(\mu\text{-}OPiv)_2]_2(\mu\text{-}Cu)$ (**4**) to $[(HOPiv)Rh(\mu\text{-}OPiv)_2]_2$ (**2**) at 45 (top) and 50 °C (bottom) in the absence of ethylene. Reaction conditions: 9.35 mM of $[(\eta^2\text{-}C_2H_4)_2Rh(\kappa\text{-}OAc)]_2$ as starting material, 0.3 mL benzene-d_6, 24 eq. $Cu(OPiv)_2$ (relative to Rh), 48 eq. HOPiv (relative to Rh). The rate of decay of **4** is determined based on the amount of complex **2** formed. Each data point is the average of three separate experiments and error bars represent the standard deviations based these independent experiments.

10.3.3 Characterization of Rh Resting State: Computational Studies

We deduced several points from the experimental results. First, **2** requires a significant induction period (approximately 6 h, Figure 10.2) to enter the catalytic cycle. After the induction period, catalytic styrene formation with **2** is slower than with the Rh(I) and Rh(III) precursors **1** and **3**, respectively. This hints that the binuclear Rh(II) **2** is *not directly involved* in the catalytic cycle for styrene formation. Second, **4,** which is rapidly formed by reacting **1** with $Cu(OPiv)_2$, is a viable catalyst resting state, consistent with the nearly identical TOs versus time as the Rh(I) precursor **1**. Third, Rh(III) precursor **3** is likely reduced to catalytically active **4** under the catalytic conditions, in agreement with induction period of ~1.5 hours and a nearly identical TOF as Rh(I) precursor **1** after the induction period. Finally, **4** can be converted to **2** at high Rh concentration, although this transformation must be slow under catalytic conditions. Binuclear Rh(II) **2** is more stable than Rh(I) precursors **1** and **4**. The reduction of **2** to **4** is likely slow and incomplete under

catalytic conditions (hence lower TOF after the induction period relative to the Rh(I) precursor **1**).

With these key factors realized, we computed free energies at 423 K (~150 °C) for several mononuclear and binuclear Rh species of varying oxidation states (Scheme 10.4). $Cu(OAc)_2$ was used as the oxidant but we anticipate similar DFT results for OAc and OPiv (and OAc is more computationally efficient). To model the redox chemistry in the catalytic process, we studied one-electron redox events, that is: $Rh^n + Cu^{II} \rightarrow Rh^{n+1} + Cu^{I}$. The calculated energetics for Rh oxidation is influenced by the modeling of Cu^{II} and Cu^{I} species. Our calculations indicate that the most stable Cu^{II} configuration is the $[Cu(\mu\text{-}OAc)_2]_3$ trimer while the most stable Cu^{I} species is mononuclear $Cu(\kappa^2\text{-}OAc)(HOAc)(\eta^2\text{-}C_2H_4)$. We therefore model Rh oxidation to occur through simultaneous reduction of trimeric $[Cu(\mu\text{-}OAc)_2]_3$ to produce dimeric $[Cu(\mu\text{-}OAc)_2]_2$ (which is the second most stable Cu^{II} configuration), liberating a monomeric CuOAc, which binds C_2H_4 and HOAc to form $Cu(\kappa^2\text{-}OAc)(HOAc)(\eta^2\text{-}C_2H_4)$ (see Appendix I for full details). Thus, we used these species in our calculations of Rh catalytic styrene formation.

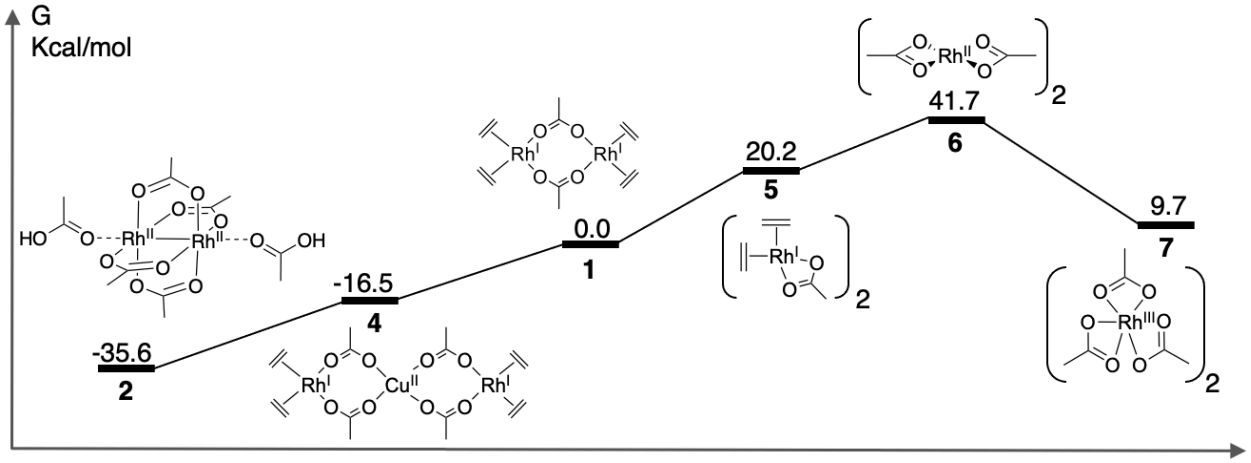

Scheme 10.4. B3LYP-D3 free energies at 423 K for (from left to right): $[(HOAc)Rh^{II}(\mu\text{-}OAc)_2]_2$ (**2**), $[(\eta^2\text{-}C_2H_4)_2Rh^{I}(\mu\text{-}OPiv)_2]_2(\mu\text{-}Cu)$ (**4**), $[(\eta^2\text{-}C_2H_4)_2Rh^{I}(\mu\text{-}OAc)]_2$ (**1**), $(\eta^2\text{-}C_2H_4)_2Rh^{I}(\kappa^2\text{-}OAc)$ (**5**), $Rh^{II}(\kappa^2\text{-}OAc)_2$ (**6**), and $Rh^{III}(\kappa^2\text{-}OAc)_3$ (**7**). Stoichiometric amounts of $[Cu^{II}(\mu\text{-}OAc)_2]_3$, of $[Cu^{II}(\mu\text{-}OAc)_2]_2$, $Cu^{I}(\kappa^2\text{-}OAc)(HOAc)(C_2H_4)$, C_2H_4, and HOAc were added to maintain the same number of atoms. Similarly, mononuclear complex energies were doubled to be consistent with the binuclear complexes. More details on Cu modeling and stoichiometry balancing can be found in the Additional Calculations section of Appendix I.

We set **1** as our reference state of 0.0 kcal/mol since it is the catalytic precursor for optimal catalysis. Scheme 10.4 confirms the relative free energies for Rh: the binuclear Rh(II) paddle-wheel with HOAc coordinated, complex **2**, is calculated to be lowest in energy, while the mononuclear Rh(II) species $Rh(\kappa^2\text{-}OAc)_2$ (**6**) is calculated to be the highest in energy. The energy difference between **2** and **4** is calculated to be 19.1 kcal/mol, but it is difficult to establish an accurate energy difference between **2** and **4** that can be used to predict the equilibrium. The conversion of **4** to **2** requires a two-electron reduction

of Rh (one electron for each Rh), but we have not experimentally elucidated the reducing agent, which could be in situ formed Cu(s), Cu(OAc), benzene or ethylene. For the calculations, we have Cu(OAc) as the reducing agent. The dissociation of the binuclear Rh(I) **1** to form two mononuclear Rh(I) species (**5**) is uphill 20.2 kcal/mol. Further oxidation of **5** by $[Cu(OAc)_2]_3$ is more unfavorable with two mononuclear Rh(II) complexes (**6**) 41.7 kcal/mol above **1**. However, oxidation of **6** to two mononuclear Rh(III)s $Rh(\kappa^2\text{-}OAc)_3$ (**7**) is downhill. Complex **7** is only 9.7 kcal/mol above **1**; this is expected considering Rh(III) forms an octahedral complex saturated with 18 electrons. DFT predicts oxidation of **1** to be favorable. Specifically, **2** is 40.9 kcal/mol below **1**. This supports the experimentally observed conversion of **1** to **4**, and ultimately to **2** at 120 °C after 12 h.

10.3.4 Mechanism of Styrene Formation: Computational Studies

From the computational results shown in Scheme 10.4, we conclude that **2** is stable and therefore inefficient for catalysis. This conclusion is supported by experimental studies using complex **2** as catalyst precursor (Figure 10.2), which reveals a substantial induction period as **2** is converted to an active catalyst. The calculations also suggest that reduction of **7** to **5** (with subsequent dimerization to **1**) will be energetically limited since **7** is more stable; this is supported by experimental data in which catalysis starting with Rh(III)

requires an induction period. These computational results in combination with our experimental observation of the formation of **4** prompted us to study catalytic styrene formation from **4**.

Starting from complex **4**, coordination of benzene is uphill 16.5 kcal/mol (Scheme 10.5). Another benzene could feasibly coordinate to the other Rh center through displacement of another ethylene, although this would cost an additional 16.5 kcal/mol. Benzene is significantly more prevalent than ethylene in solution such that this 16.5 kcal/mol is more mild; however the displacement is still endergonic. From the η^2-benzene adduct, the formation of a Rh-phenyl intermediate via C–H activation is likely to occur by either 1) C–H oxidative addition and O–H reductive coupling to form coordinated acetic acid (or, reductive elimination to form free acetic acid)[91-94] or 2) concerted metalation deprotonation (CMD).[2, 95-101] A previous study using mononuclear Rh(I) reported oxidative addition, reductive coupling, and CMD barriers of 24.4, 26.6, and 30.6 kcal/mol, respectively.[65] We expected **4** to follow the same trend in which stepwise oxidative addition/reductive coupling is energetically more viable than CMD. DFT predicts benzene C–H oxidative addition and O–H reductive coupling barriers of 23.9 and 27.5 kcal/mol (**TS4.1** and **TS4.2**). For CMD, DFT predicts a barrier of 28.5 kcal/mol (**TS4.1'**). Thus, our calculations indicate a slight preference for stepwise oxidative addition/reductive elimination. Using the calculated energetics, it is difficult to make a

strong case for either mechanism. Previous reports of Pd^{II}-acetate catalysis (isoelectronic with Rh^{I}) have offered the possibility of deprotonation by an external acetate ligand as opposed to intramolecular reductive coupling, the primary benefit being that no energy is required to liberate the HOAc from the catalyst.[102-105] This mechanism involving an external acetate is highly unlikely because excess HOPiv inhibits free acetates in solution, and because **4** does not require HOAc to dissociate after O–H bond formation. Indeed, deprotonation of **4c** by an external acetate results in a transition state free energy of 31.8 kcal/mol, making this path unfavorable (see Appendix I for more details).

With the unique nature of the Rh/Cu/Rh complex that mediates benzene C–H activation, we evaluated the transition states for oxidative addition and CMD (Figure 10.7). The oxidative addition transition state looks as expected (Figure 10.7, **TS4.1**); the transferring H is nearly halfway between the phenyl ring and the Rh with C–H and H–Rh distances of 1.65 and 1.66 Å. The new C–Rh bond is slightly long at 2.1 Å, indicating it is late in the transition. The structure overall is similar to the starting state with the exception of benzene. In contrast, the geometry of the CMD transition state (Figure 10.7, **TS4.1'**) appears severely distorted relative to the starting state. To accommodate the CMD process, a bridging acetate must break a bond with Cu, which moves Cu away from the Rh responsible for C–H activation. The C–H and H–Rh distances are 1.5 Å and 1.25 Å while the C–Rh distance is 2.11 Å, similar to in the oxidative addition transition state.

In the CMD geometry, the Rh–H distance is 2.36 Å, indicating that there is negligible interaction between Rh and H.

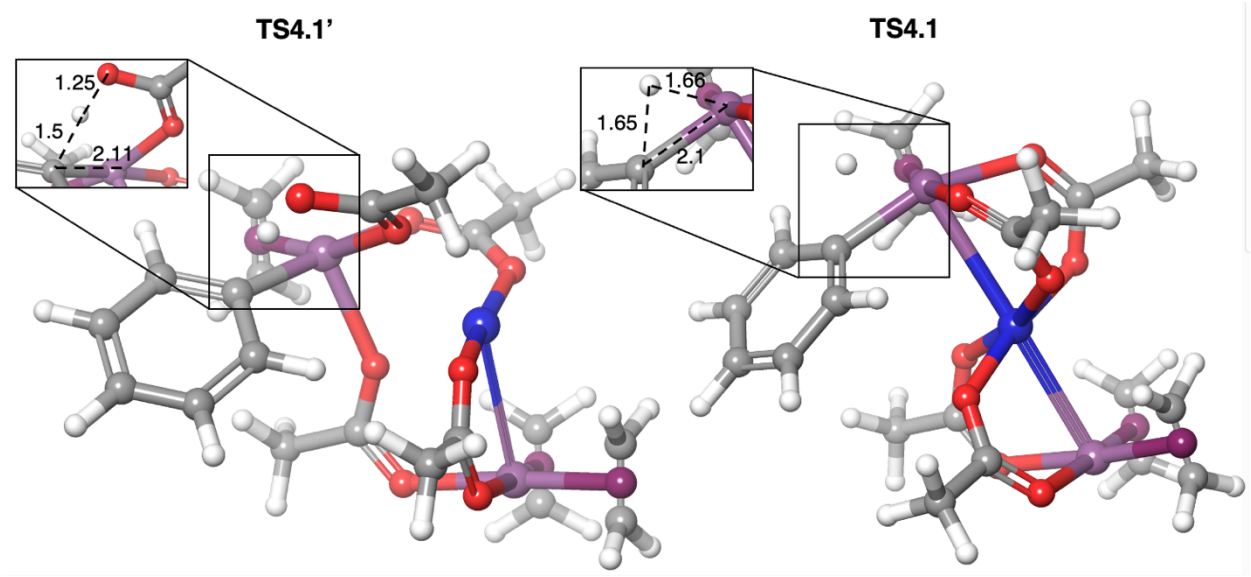

Figure 10.7. DFT-optimized concerted metalation deprotonation (**TS4.1'**, left) and oxidative addition (**TS4.1**, right) transition states for benzene C-H activation starting from $[(\eta^2\text{-}C_2H_4)_2Rh^I(\mu\text{-}OPiv)_2]_2(\mu\text{-}Cu)$ (**4**).

Following the benzene C–H activation, $Rh(\eta^2\text{-}C_2H_4)_2(\mu\text{-}OAc)_2Cu(HOAc)(\mu\text{-}OAc)Rh(Ph)(\eta^2\text{-}C_2H_4)$ (**4d**), the "$Rh(Ph)(\eta^2\text{-}C_2H_4)$" moiety *could* dissociate and bind two equivalents of ethylene to form mononuclear $Rh^I(Ph)(\eta^2\text{-}C_2H_4)_3$, HOAc and a $Rh(\eta^2\text{-}C_2H_4)_2(\mu\text{-}OAc)_2Cu(\boxtimes^2\text{-}OAc)$ heterodimer (**8**). This transformation is conceivably possible because **8** is stable (see below). However, DFT predicts the dissociation of $Rh^I(Ph)(\eta^2\text{-}C_2H_4)$ from **4d** to be uphill by 40.2 kcal/mol (**4d'**). Instead, we find the Rh/Cu/Rh

trimetallic product **4d** to be reasonable with an intermediate energy of 13.2 kcal/mol (Scheme 10.5). From **4d**, ethylene insertion into the Rh–Ph bond and β-hydride elimination result in transition state free energies of 24.5 and 16.3 kcal/mol (**TS4.3** and **TS4.4**). We could also envisage ethylene insertion following intermediate **4c** since the Rh-Ph bond is present alongside a coordinated ethylene. But, ethylene insertion following **4c** results in a transition state free energy of 40.3 kcal/mol, indicating the pathway is not favorable (see Appendix I for more details). Dissociation of styrene upon ligand exchange with ethylene yields free styrene and **4f** at 5.7 kcal/mol above the starting state. Subsequent reaction of **4f** with $Cu(OAc)_2$ can produce acetic acid and regenerate the starting catalyst **4**. Our calculations predict that the rate-determining step for catalytic styrene formation from **4** is the 27.5 kcal/mol barrier for reductive coupling to form coordinated acetic acid. On the other hand, the calculated activation barriers for C–H oxidative addition and ethylene insertion, at 23.9 kcal/mol and 24.5 kcal/mol, respectively, are very similar, making it difficult to predict the rate determining step with high confidence. The calculated activation barrier of 27.5 kcal/mol shows excellent agreement with the experimentally determined barrier of 26.9 kcal/mol (calculated from the 0.11 s^{-1} TOF at 150 °C via the Eyring equation).

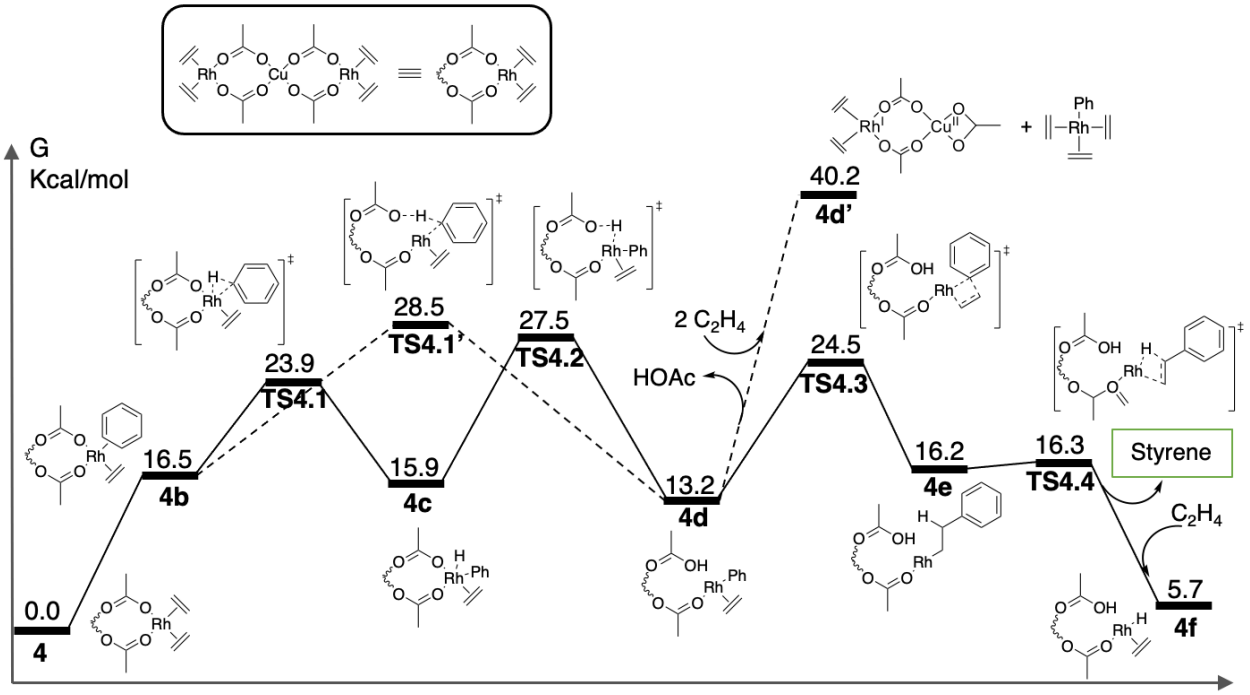

Scheme 10.5. B3LYP-D3 free energy profile at 423 K for styrene formation from $[Rh^{I}(\mu\text{-OPiv})_2(\eta^2\text{-}C_2H_4)_2]_2(\mu\text{-Cu})$ (**4**). The reductive coupling (**TS4.2**) is the rate-determining step with a free energy of 27.5 kcal/mol above the starting state. The DFT predicted 27.5 kcal/mol activation barrier is in excellent agreement with experiment.

Based on these combined experimental and computational results, we hypothesize that the Rh-Cu-Rh complex **4**, is the active catalyst for styrene formation. Further, experimental and computational data are consistent with the binuclear Rh(II) **2** being inactive for catalysis but thermodynamically favorable from **4** under catalytic conditions. But how does Rh avoid the formation of **2**? We propose that: 1) under catalytic conditions where Rh concentration is low (e.g., 0.112 mM Rh), the formation of **2**, which follows 2nd order kinetics in complex **4**, is slow. In contrast, in J-Young tube reactions monitored by

^{1}H NMR spectroscopy, the conversion of **1** to **2** is rapid due to higher Rh concentrations (18.7 mM Rh). 2) Under the catalytic conditions with reaction temperature of 150 °C, the catalytic reaction that involves **4** is competitive with the conversion of **4** to **2**.

10.3.5 The Role of Cu in the Catalytic Cycle

The inclusion of Cu(II) carboxylate into the binuclear Rh(I) **1** appears to provide the correct energetics for the catalytic formation of styrene. While Cu(II) addition to form **4** seems to inhibit oxidation to form the binuclear Rh(II) complex **2**, it is not immediately clear that Cu(II) more readily facilitates styrene formation over a Cu-free Rh species. To confirm this, we compared the styrene formation energetics using complex **4** with Cu-free species, namely C–H activation and ethylene insertion starting from Cu-free complexes **1** and **5**.

We began by investigating the mechanism of styrene formation starting with **1** (Scheme 10.6). Coordination of benzene to **1** is 20.3 kcal/mol uphill. Oxidative addition of benzene to Rh is 25.8 kcal/mol above the starting state, which is 1.9 kcal/mol above the oxidative addition starting with complex **4**. Reductive elimination to afford HOAc is 32.6 kcal/mol above **1**. The CMD barrier using **1** is predicted to be 39.2 kcal/mol above the starting state, reiterating that CMD might be disfavored for Rh. The following ethylene insertion is predicted to be 26.8 kcal/mol above the starting state, meaning

reductive elimination is the RDS in this route, similar to **4**. The reductive elimination barrier of 32.6 kcal/mol is too high with respect to the experimentally observed TOF of 0.11 s^{-1} at 150 °C, confirming that **1** is not likely the active catalyst.

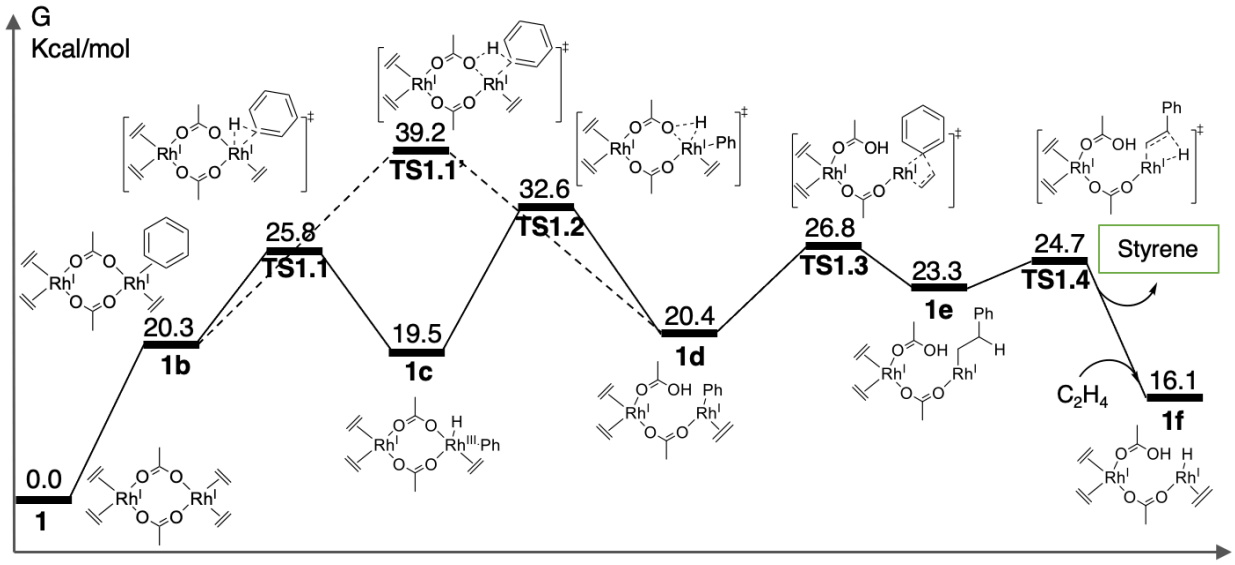

Scheme 10.6. B3LYP-D3 free energies at 423 K for key transition states towards styrene formation starting from $[Rh(\mu\text{-}OAc)(\eta^2\text{-}C_2H_4)_2]_2$ (**1**).

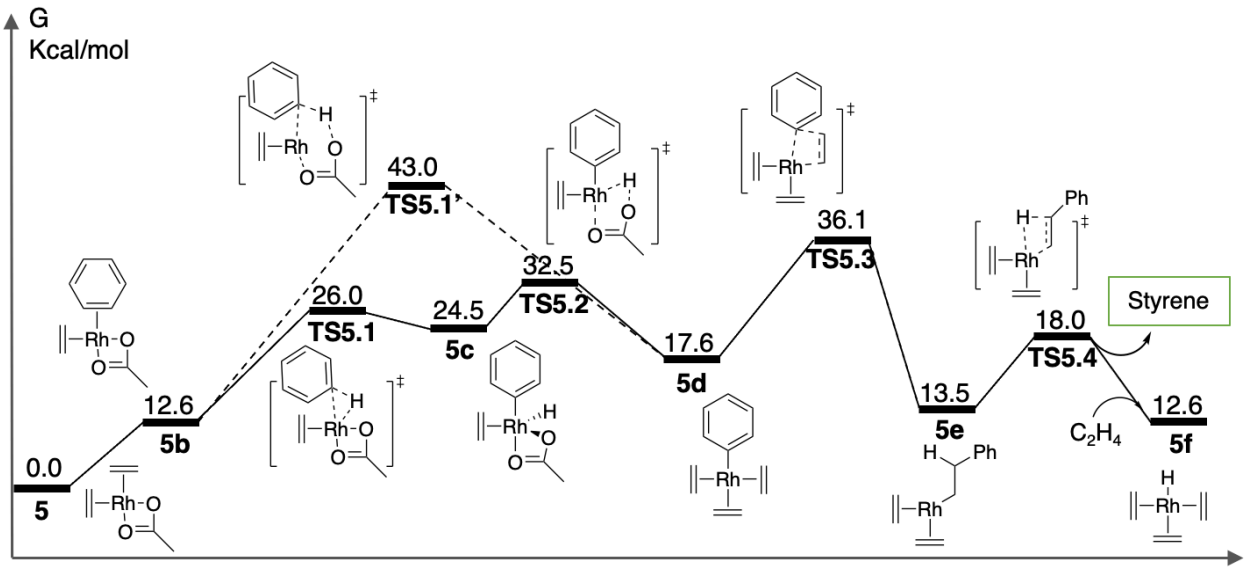

Scheme 10.7. B3LYP-D3 free energies at 423 K for key transition states towards styrene formation starting from Rh(κ^2-OAc)(η^2-C_2H_4)$_2$ (**5**).

We also explored the mechanism for styrene formation starting with the mononuclear Rh(I), **5** (Scheme 10.7). Coordination of benzene to **5** is uphill by 12.6 kcal/mol. Benzene coordination is expected to be more facile for **5** due to reduced steric clashing between the bulky benzene and neighboring ligands. Benzene C–H oxidative addition is calculated to have an activation energy of 26.0 kcal/mol while the O–H reductive elimination transition state to afford HOAc is 32.5 kcal/mol above the starting state. We see that reductive elimination from **5** presents too high a barrier relative to the 27.5 kcal/mol barrier for **4**. Similar to **4** and **1**, CMD is less favorable with a barrier of 43.0 kcal/mol above **5**. Subsequent ethylene insertion is predicted by DFT to be 36.1 kcal/mol above **5**. DFT

predicts both the O–H reductive elimination and ethylene insertion barriers for **5** to be less favorable than using **4**, revealing that **5** is not likely the active catalyst.

Our calculations of styrene formation starting from **1**, **4**, and **5** reveal that the most substantial difference in energetics is the O–H reductive coupling step with activation barrier of 32.6 kcal/mol starting from **1**, 27.5 kcal/mol starting from **4**, and 32.5 kcal/mol starting from **5** (compared to starting states). Thus, the calculated $\Delta\Delta G^{\ddagger}$'s for O–H reductive coupling is significant at 5.1 and 5.0 kcal/mol. Analysis of the reductive elimination transition states reveals a potential source of the differences in transition state energy (Figure 10.8). In **TS4.2**, the acetate that is involved in the O–H reductive coupling is coordinated to both Rh and Cu. Otherwise, there are no major differences in the three transition states for reductive coupling (Figure 10.8). Thus, the acetate/Cu interaction appears to facilitate reductive coupling, perhaps by withdrawing electron-density from Rh and favoring the formal Rh reduction. In intermediate **4c**, the acetate oxygen atoms adjacent to Rh have charges of -0.83 and -0.92 (Figure 10.8). In **1c**, these Rh-adjacent oxygen atoms have charges of -0.80 and -0.91. The hydride ligands of complexes **4c** and **1c** have charges of +0.12 and +0.17, respectively. These deviations are the same within the accuracy of Mulliken charges, so that we *cannot* conclude that Cu inclusion has significantly impacted the basicity of the acetate ligands or the acidity of the hydride ligand of **4c**. However, Mulliken charges reveal that the acetate ligand the transition state

for O–H coupling (**TS4.2**) is more negatively charged than the acetate ligand in **TS1.2**. The acetate oxygen atoms in **TS4.2** have calculated charges of -0.71 and -0.94 (where the -0.94 is the oxygen bridging Cu and Rh); the charge of the transferring hydrogen is +0.34. In **TS1.2**, the acetate oxygen atoms have charges of -0.47 and -0.74 (where the -0.47 is the oxygen bridging two Rh) while the transferring hydrogen has a charge of +0.26. Overall, the active acetate in **TS4.2** is more negatively charged than the active acetate in **TS1.2**. This suggests that inclusion of Cu might impose a structural change that makes the acetate ligand more basic and the hydrogen more acidic in the transition state for O–H bond formation. Indeed, DFT predicts distances of Rh–H = 1.66 Å and H–O = 1.35 Å in **TS4.2**. This is consistent with the relative energy of the reductive coupling Rh product compared to the starting state: 13.2 kcal/mol for **4d** (Scheme 10.5) and 20.4 kcal/mol for **1d** (Scheme 10.6). Computed Mulliken charges and bond distances both support the hypothesis that Cu inclusion in **TS4.2** enhances acetate basicity and hydrogen acidity, resulting in an improved reductive coupling barrier. Maseras and coworkers previously reported the inclusion of Cu^{II} in Rh catalysis, finding a cooperative reductive elimination step in which the key transition state contained both Cu and Rh.[106]

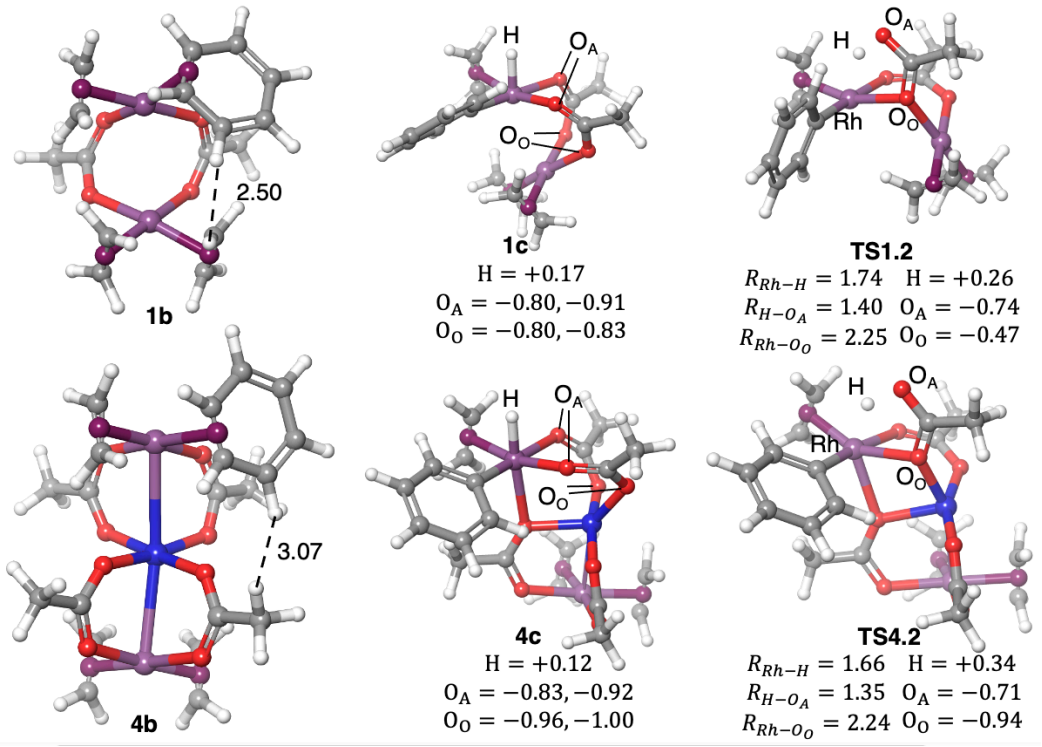

Figure 10.8. Structures **1b**, **1c**, **TS1.2**, **4b**, **4c**, and **TS4.2** as predicted by DFT. Mulliken charges are included for intermediates **1c** and **4c** and reductive coupling transition states **TS1.2** and **TS4.2**. Transition states also include significant bond distances in Å. **4c** and **1c** include Mulliken charges for both acetate ligands bound to Rh, while **TS4.2** and **TS1.2** include only the charges for the active acetate. O_A denotes the oxygens adjacent to the Rh and O_O denotes oxygens opposite Rh.

From our calculations, the largest deviation between catalysis using complex **1** versus complex **4** is the benzene coordination step. Displacement of ethylene by benzene is 16.5 kcal/mol for **4** and 20.3 kcal/mol for **1**. We attribute this difference to the steric repulsion between benzene and other ligands. Inspection of the calculated structure of complex **1b** shows significant steric repulsion between benzene and ethylene with a distance of 2.50 Å

between hydrogens (Figure 10.8). In **4b**, the closest hydrogen-hydrogen distance is 3.07 Å. This increased energy for benzene coordination in **1** effectively increases the energy of subsequent steps for catalysis. It is therefore useful to analyze the reductive coupling step relative to its preceding intermediate as opposed to the starting state. For **4**, the barrier for reductive coupling relative to its preceding intermediate (**TS4.2 - 4c**) is 11.6 kcal/mol. For **1**, the analogous barrier (**TS1.2 - 1c**) is 13.1 kcal/mol. The reductive coupling $\boxtimes\boxtimes G^{\ddagger}$ is 1.5 kcal/mol when the transition states are compared to their preceding intermediates. Recall that the global $\Delta\Delta G^{\ddagger}$ is 5.1 kcal/mol, where the 3.6 kcal/mol difference between these values appears to be due to the steric repulsion induced by benzene on neighboring ligands. The benefit of including Cu in the catalyst is likely two-fold. Cu inclusion likely (1) assists in relieving steric repulsion, facilitating benzene coordination from **4** by 3.6 kcal/mol relative to **1**, and (2) generates a more negatively charged acetate ligand and more acidic hydrogen in the reductive coupling transition state, lowering the barrier by 1.5 kcal/mol.

10.4 Conclusions

Catalytic styrene formation from benzene, ethylene and Cu(II) carboxylation using $[(\boldsymbol{\kappa}^2\text{-}C_2H_4)_2Rh(\mu\text{-}OAc)]_2$ (**1**), $[(HOPiv)Rh(\mu\text{-}OPiv)_2]_2$ (**2**), and $RhCl_3$ (**3**) as precursors reveals complex **1** as the optimal entry into the catalytic cycle. We have identified a Rh-

Cu-Rh species, $[(\eta^2\text{-}C_2H_4)_2Rh^I(\mu\text{-}OPiv)_2]_2(\mu\text{-}Cu)$ (**4**), as the likely catalyst resting state, showing that experimental and DFT calculations are consistent with this trimetallic core remaining intact through the entire catalytic cycle. Thus, Cu(II) not only serves as the oxidant for styrene production, but also appears to play a critical role in the active catalyst. The formation of **4** inhibits conversion of **1** to **2**, which is important since the stability of **2** renders it an inefficient catalyst precursor with a substantial induction period.

We confirmed the catalytic role of **4** by probing the styrene formation mechanism with DFT. Starting with **4**, DFT predicts a rate-limiting O–H reductive coupling barrier of 27.5 kcal/mol (from the starting state **4**). The calculations indicate that inclusion of Cu(II) in the active Rh catalyst promotes catalytic styrene formation by reducing the O–H reductive coupling barrier by 5.1 kcal/mol. It appears that the decreased barrier for **4** is due to electron polarization to Rh from neighboring acetate ligands that are formally bonded to the Cu; this effect is not present in **1**. Furthermore, the DFT-predicted barrier of 27.5 kcal/mol from **4** is in agreement with the experimentally observed TOF of 0.11 s^{-1} (which corresponds to a 26.9 kcal/mol barrier at 423 K using the Eyring equation). Given the common use of Cu(II) as an in situ oxidant in catalytic oxidation reactions, these results suggest that other catalysts might similarly include Cu(II) to form multi-metallic catalysts.

All Rh(I) species are treated as singlets with the degenerate d_{yz} and d_{xz} orbitals doubly occupied. Rh(III)s are treated as singlets with all t_{2g} orbitals doubly occupied. Cu(I)s are treated as singlets with t_{2g} and e_g orbitals all doubly occupied. Cu(II)s are treated as doublets with all d orbitals doubly occupied except the highest-lying singly occupied d_{x2-y2}.

10.5 Experimental Methods

General Considerations. Unless otherwise noted, reactions were performed under an atmosphere of dry nitrogen using standard Schlenk techniques and/or in a glovebox. Glovebox purity was maintained by periodic nitrogen purges and was monitored by an oxygen analyzer (O_2 concentration was $<$ 15 ppm for all reactions). All NMR reactions were performed using Wilmad medium wall precision low pressure/vacuum (LPV) NMR tube and pressurized with dinitrogen or ethylene using a high-pressure line. Benzene and *n*-pentane were dried by passage through columns of activated alumina. Tetrahydrofuran was dried via potassium-benzophenone/ketyl stills under dinitrogen atmosphere and stored in the nitrogen-filled glovebox over 4 Å molecular sieves. Benzene-d_6 was used as received and stored in the nitrogen-filled glovebox over 4Å molecular sieves. Ethylene was purchased in gas cylinders from GTS-Welco and used as received. All other reagents were purchased from commercial sources and used as received. **1** and its crystal was prepared

according to a literature procedure.[82] **2** and its crystal was prepared according to a literature procedure.[74] GC/FID was performed using a Shimadzu GC-2014 system with a 30 m x 90.25 mm HP5 column with 0.25 μm film thickness. Styrene production was quantified using linear regression analysis of gas chromatograms of standard samples of authentic products. A plot of peak area ratios versus molar ratios gave a regression line using hexamethylbenzene as the internal standard. The slopes and correlation coefficients of the regression lines were 1.67 and 0.99 respectively. Measurement of the ^{1}H spectra was performed on a Varian VNMRS 600 MHz spectrometer or a Bruker Avance III 800 MHz spectrometer. All ^{1}H spectra are referenced against residual proton signals (^{1}H NMR) of deuterated solvents. Spin-lattice relaxation experiments were performed on a Bruker III Avance 600 MHz spectrometer.

Styrene production using [(μ-OAc)Rh(η^2-C_2H_4)$_2$]$_2$, [(HOPiv)Rh(μ-OPiv)$_2$]$_2$ or [(η^2-C_2H_4)$_2$Rh^I(μ-OPiv)$_2$]$_2$(μ-Cu) as catalyst precursor and copper(II) pivalate as oxidant. A stock solution containing **1**, **2**, or **4** (0.0056 mmol, 0.001 mol % of Rh relative to benzene), hexamethylbenzene (0.073 g, 0.46 mmol), and benzene (200 mL) was prepared in a volumetric flask. Fisher-Porter reactors were charged with stock solution (10 mL), copper(II) pivalate (240 equiv. relative to Rh, 0.072 g, 0.27 mmol) and pivalic acid (480 equiv. relative to Rh, 0.0550 g, 0.539 mmol). The vessels were sealed, pressurized with ethylene (50 psig), and subsequently stirred and heated to 150 °C. To analyze reaction

mixture samples by GC-FID, the reactors were cooled to room temperature, sampled under N_2, recharged with gases, and reheated. Aliquots of the resulting solution ($<$ 100 μL) were washed with saturated sodium carbonate solution (0.25 mL). The aqueous and organic layers were separated. The resulting organic layers were analyzed by GC/FID.

Styrene production using $RhCl_3$ as catalyst precursor and copper(II) pivalate as oxidant. Under air, a stock solution containing rhodium chloride trihydrate (0.0118 g, 0.0449 mmol) and distilled water (2 mL) was prepared in a volumetric flask. Fisher-Porter reactors were charged with 0.05 mL stock solution (contains 0.0011 mmol Rh) and placed under dynamic vacuum at 40 °C for 2 hours to remove water. The Fisher-Porter reactors were then brought into the nitrogen-filled glovebox and charged with hexamethylbenzene (0.0182 g, 0.1121 mmol), additives (2000 eq. of relative to Rh), copper(II) pivalate (240 equiv. relative to Rh, 0.072 g, 0.27 mmol), pivalic acid (480 equiv. relative to Rh, 0.0550 g, 0.539 mmol) and benzene (10 mL). The vessels were sealed, pressurized with ethylene (50 psig), stirred and heated to 150 °C. To analyze reaction mixture samples by GC-FID, the reactors were cooled to room temperature, sampled under N_2, recharged with gases, and reheated. Aliquots of the resulting solution ($<$ 100 μL) were washed with saturated sodium carbonate solution (0.25 mL). The aqueous and organic layers were separated. The resulting organic layers were analyzed by GC/FID.

Styrene production using solution A and copper(II) pivalate as oxidant. A stock solution containing **1** (8.2 mg, 0.0373 mmol Rh) and benzene-d_6 (10 mL) was prepared in a volumetric flask. A J-Young pressure NMR tube was charged with stock solution (0.3 mL), copper(II) pivalate (24 equiv. relative to Rh, 7.2 mg, 0.027 mmol), pivalic acid (48 equiv. relative to Rh, 5.5 mg, 0.054 mmol). Each NMR tube was purged and pressurized with ethylene. Then the tube was heated in a 120 °C oil bath for 12 h. The J. Young tubes were taken out of the oil bath, cooled to room temperature and subsequently brought to the nitrogen-filled glovebox. In the glovebox, Fisher-Porter reactors were charged with solution from the J. Young tube reaction, hexamethylbenzene (0.0182 g, 0.112 mmol), copper(II) pivalate (240 equiv. relative to Rh, 0.072 g, 0.27 mmol) and pivalic acid (480 equiv. relative to Rh, 0.0550 g, 0.539 mmol). The vessels were sealed, pressurized with ethylene (50 psig), and subsequently stirred and heated to 150 °C. To analyze reaction mixture samples by GC-FID, the reactors were cooled to room temperature, sampled under N_2, recharged with gases, and reheated. Aliquots of the resulting solution (< 100 μL) were washed with saturated sodium carbonate solution (0.25 mL). The aqueous and organic layers were separated. The resulting organic layers were analyzed by GC/FID.

In situ ^{1}H NMR studies of conversion of $[(\mu\text{-OAc})\text{Rh}(\eta^2\text{-C}_2\text{H}_4)_2]_2$ to $[(\text{HOPiv})\text{Rh}(\mu\text{-OPiv})_2]_2$. A stock solution containing **1** (8.2 mg, 0.0373 mmol Rh, 18.7

mM Rh) and benzene-d_6 (2 mL) was prepared in a volumetric flask. A J-Young pressure NMR tube was charged with stock solution (0.3 mL), copper(II) pivalate (24 equiv. relative to Rh, 0.036 g, 0.135 mmol), pivalic acid (48 equiv. relative to Rh, 0.0275 g, 0.27 mmol) and hexamethyldisiloxane (HMDSO, internal standard). A ^{1}H NMR spectrum was obtained immediately after pressurizing each tube with N_2 (~20 psig). If needed, the tube was purged with ethylene to remove N_2 and pressurized with ethylene. Then the tube was heated in an oil bath. At each time point, the J. Young tubes were taken out of the oil bath and cooled to room temperature with water for NMR measurement. After ^{1}H NMR spectra were obtained, the J-Young tubes were put back into the oil bath. The relaxation delay time (d1) for ^{1}H NMR was set to 10 s. The rate of decay of **4** was determined based on the amount of **2** formed. Concentration of **2** were determined based on the integration ratio between the **2** peak and the HMDSO peak in the ^{1}H NMR spectra.

Generation of $[(\eta^2\text{-}C_2H_4)_2Rh^I(\mu\text{-}OPiv)_2]_2(\mu\text{-}Cu)$ (4). To a solution of **4** (4.9 mg, 0.0224 mmol Rh) in benzene (1 mL), copper(II) pivalate (1 equiv. relative to Rh, 6.5 mg, 0.0224 mmol) and pivalic acid (2 equiv. relative to Rh, 4.6 mg, 0.0448 mmol) were added. Crystals suitable for X-ray analysis were obtained by slowly evaporating benzene solvent. Crystals of **4** were washed with pentane and dried under vacuum. The obtained solid was collected for NMR and catalysis studies.

In Situ ^{1}H NMR Studies of conversion of [(η^2-C_2H_4)$_2$Rh^I(μ-OPiv)$_2$]$_2$(μ-Cu) to [(HOPiv)Rh(μ-OPiv)$_2$]$_2$. A J-Young pressure NMR tube was charged with benzene-d_6 (0.3 mL), **4** (2.2 mg, 18.7 mM Rh), hexamethyldisiloxane (HMDSO, internal standard). A ^{1}H NMR spectrum was obtained before the tube was changed with copper(II) pivalate (24 equiv. relative to Rh, 0.036 g, 0.135 mmol) and pivalic acid (48 equiv. relative to Rh, 0.0275 g, 0.27 mmol). Each NMR tube was pressurized with 20 psig N_2. Then the tube was heated in a 120 °C oil bath. ^{1}H NMR spectra were subsequently acquired after 12 hours.

Measurement of spin-lattice relaxation of [(η^2-C_2H_4)$_2$Rh^I(μ-OPiv)$_2$]$_2$(μ-Cu) (4). J-Young pressure NMR tubes were charged with dilute solutions of **4** in benzene-d_6 (450 μL) with relative concentrations of 1, 0.5 and 0.25. For each of these solutions, the spin-lattice relaxation time of the ^{1}H peak of the ethylene ligands of **4** (~4.0 ppm) was measured using an inversion recovery experiment (T1IR) with a Bruker Avance III spectrometer operating at 600.165 MHz.

10.6 References

1. Ritleng, V.; Sirlin, C.; Pfeffer, M. Ru-, Rh-, and Pd-Catalyzed C−C Bond Formation Involving C−H Activation and Addition on Unsaturated Substrates: Reactions and Mechanistic Aspects. *Chem. Rev.* **2002,** *102*, 1731-1770.

2. Ackermann, L. Carboxylate-Assisted Ruthenium-Catalyzed Alkyne Annulations by C–H/Het–H Bond Functionalizations. *Acc. Chem. Res.* **2014,** *47*, 281-295.

3. Hussain, I.; Singh, T. Synthesis of Biaryls through Aromatic C⊠H Bond Activation: A Review of Recent Developments. *Adv. Synth. Catal.* **2014,** *356*, 1661-1696.

4. Yang, J. Transition Metal Catalyzed Meta-C–H Functionalization of Aromatic Compounds. *Org. Biomol. Chem.* **2015,** *13*, 1930-1941.

5. Laurel, A. G.; Gunnoe, T. B. Developments in Catalytic Aromatic C-H Transformations: Promising Tools for Organic Synthesis. *Curr. Org. Chem.* **2005,** *9*, 671-685.

6. Lewis, J. C.; Bergman, R. G.; Ellman, J. A. Direct Functionalization of Nitrogen Heterocycles Via Rh-Catalyzed C−H Bond Activation. *Acc. Chem. Res.* **2008,** *41*, 1013-1025.

7. Jia, C.; Kitamura, T.; Fujiwara, Y. Catalytic Functionalization of Arenes and Alkanes Via C−H Bond Activation. *Acc. Chem. Res.* **2001,** *34*, 633-639.

8. Colby, D. A.; Bergman, R. G.; Ellman, J. A. Rhodium-Catalyzed C−C Bond Formation Via Heteroatom-Directed C−H Bond Activation. *Chem. Rev.* **2010,** *110*, 624-655.

9. Huang, Z.; Lim, H. N.; Mo, F.; Young, M. C.; Dong, G. Transition Metal-Catalyzed Ketone-Directed or Mediated C–H Functionalization. *Chem. Soc. Rev.* **2015,** *44*, 7764-7786.

10. Chen, S. S. *Kirk-Othmer Encyclopedia of Chemical Technology*; John Wiley & Sons, Inc.: Hoboken: NJ, 2000; p. 325-357.

11. Olah, G. A.; Molnár, Á. *Hydrocarbon Chemistry. 2nd Ed.*; Wiley-Interscience: Hoboken: NJ, 2003; p. 283.

12. Wittcoff, H. A.; Reuben, B. G.; Plotkin, J. S. Chemicals and Polymers from Ethylene. In *Industrial Organic Chemicals*; John Wiley & Sons, Inc.: Hoboken: NJ, 2004; p. 100-166.

13. Perego, C.; Pollesel, P. Advances in Aromatics Processing Using Zeolite Catalysts. *Advances in Nanoporous Materials*; Elsevier: 2010; Vol. 1, p. 97-149.

14. Zhu, W.; Gunnoe, T. B. Advances in Rhodium-Catalyzed Oxidative Arene Alkenylation. *Acc. Chem. Res.* **2020,** *53*, 920-936.

15. Negishi, E.-i.; Anastasia, L. Palladium-Catalyzed Alkynylation. *Chem. Rev.* **2003,** *103*, 1979-2018.

16. Stille, J. K. The Palladium-Catalyzed Cross-Coupling Reactions of Organotin Reagents with Organic Electrophiles. *Angew. Chem. Int. Ed.* **1986,** *25*, 508-524.

17. Beletskaya, I. P.; Cheprakov, A. V. The Heck Reaction as a Sharpening Stone of Palladium Catalysis. *Chem. Rev.* **2000,** *100*, 3009-3066.

18. Suzuki, A. Organoborates in New Synthetic Reactions. *Acc. Chem. Res.* **1982,** *15*, 178-184.

19. Varun, B. V.; Dhineshkumar, J.; Bettadapur, K. R.; Siddaraju, Y.; Alagiri, K.; Prabhu, K. R. Recent Advancements in Dehydrogenative Cross Coupling Reactions for C–C Bond Formation. *Tetrahedron Lett.* **2017,** *58*, 803-824.

20. Biffis, A.; Centomo, P.; Del Zotto, A.; Zecca, M. Pd Metal Catalysts for Cross-Couplings and Related Reactions in the 21st Century: A Critical Review. *Chem. Rev.* **2018,** *118*, 2249-2295.

21. McKeown, B. A.; Habgood, L. G.; Cundari, T. R.; Gunnoe, T. B.; Ackermann, L.; Gunnoe, T. B.; Habgood, L. G. Catalytic Hydroarylation of Carbon–Carbon Multiple Bonds; 2018; p. 1.

22. Andreatta, J. R.; McKeown, B. A.; Gunnoe, T. B. Transition Metal Catalyzed Hydroarylation of Olefins Using Unactivated Substrates: Recent Developments and Challenges. *J. Organomet. Chem.* **2011,** *696*, 305-315.

23. Weissman, H.; Song, X.; Milstein, D. Ru-Catalyzed Oxidative Coupling of Arenes with Olefins Using O2. *J. Am. Chem. Soc.* **2001,** *123*, 337-338.

24. Lail, M.; Arrowood, B. N.; Gunnoe, T. B. Addition of Arenes to Ethylene and Propene Catalyzed by Ruthenium. *J. Am. Chem. Soc.* **2003,** *125*, 7506-7507.

25. Lail, M.; Bell, C. M.; Conner, D.; Cundari, T. R.; Gunnoe, T. B.; Petersen, J. L. Experimental and Computational Studies of Ruthenium(II)-Catalyzed Addition of Arene C–H Bonds to Olefins. *Organometallics* **2004,** *23*, 5007-5020.

26. Foley, N. A.; Lail, M.; Gunnoe, T. B.; Cundari, T. R.; Boyle, P. D.; Petersen, J. L. Combined Experimental and Computational Study of TpRu{P(pyr)$_3$}(NCMe)Me (pyr = *N*-pyrrolyl): Inter- and Intramolecular Activation of C−H Bonds and the Impact of Sterics on Catalytic Hydroarylation of Olefin. *Organometallics* **2007,** *26*, 5507-5516.

27. Foley, N. A.; Lail, M.; Lee, J. P.; Gunnoe, T. B.; Cundari, T. R.; Petersen, J. L. Comparative Reactivity of TpRu(L)(NCMe)Ph (L = CO or PMe$_3$): Impact of Ancillary Ligand L on Activation of Carbon-Hydrogen Bonds Including Catalytic Hydroarylation and Hydrovinylation/Oligomerization of Ethylene. *J. Am. Chem. Soc.* **2007,** *129*, 6765–6781.

28. Foley, N. A.; Ke, Z.; Gunnoe, T. B.; Cundari, T. R.; Petersen, J. L. Aromatic C−H Activation and Catalytic Hydrophenylation of Ethylene by TpRu{P(OCH$_2$)$_3$CEt}(NCMe)Ph. *Organometallics* **2008,** *27*, 3007-3017.

29. Foley, N. A.; Lee, J. P.; Ke, Z.; Gunnoe, T. B.; Cundari, T. R. Ru(II) Catalysts Supported by Hydridotris(Pyrazolyl)Borate for the Hydroarylation of Olefins: Reaction Scope, Mechanistic Studies, and Guides for the Development of Improved Catalysts. *Acc. Chem. Res.* **2009,** *42*, 585.

30. Joslin, E. E.; McMullin, C. L.; Gunnoe, T. B.; Cundari, T. R.; Sabat, M.; Myers, W. H. Catalytic Hydroarylation of Ethylene Using TpRu(L)(NCMe)Ph (L = 2,6,7-Trioxa-1-phosphabicyclo[2,2,1]heptane): Comparison to TpRu(L′)(NCMe)Ph Systems (L′ = CO, PMe_3, $P(pyr)_3$, or $P(OCH_2)_3CEt$). *Organometallics* **2012,** *31*, 6851-6860.

31. Burgess, S. A.; Joslin, E. E.; Gunnoe, T. B.; Cundari, T. R.; Sabat, M.; Myers, W. H. Hydrophenylation of Ethylene Using a Cationic Ru(II) Catalyst: Comparison to a Neutral Ru(II) Catalyst. *Chem. Sci.* **2014,** *5*, 4355-4366.

32. Jia, X.; Gary, J. B.; Gu, S.; Cundari, T. R.; Gunnoe, T. B. Oxidative Hydrophenylation of Ethylene Using a Cationic Ru(II) Catalyst: Styrene Production with Ethylene as the Oxidant. *Isr. J. Chem.* **2017,** *57*, 1037-1046.

33. Fujiwara, Y.; Moritani, I.; Danno, S.; Asano, R.; Teranishi, S. Aromatic Substitution of Olefins. VI. Arylation of Olefins with Palladium(II) Acetate. *J. Am. Chem. Soc.* **1969,** *91*, 7166-7169.

34. Shue, R. S. Catalytic Coupling of Aromatics and Olefins by Homogeneous Palladium(II) Compounds under Oxygen. *J. Chem. Soc. D* **1971**, 1510-1511.

35. Matsumoto, T.; Periana, R. A.; Taube, D. J.; Yoshida, H. Direct Synthesis of Styrene by Rhodium-Catalyzed Oxidative Arylation of Ethylene with Benzene. *J. Catal.* **2002,** *206*, 272-280.

36. Yamada, T.; Sakakura, A.; Sakaguchi, S.; Obora, Y.; Ishii, Y. Oxidative Arylation of Ethylene with Benzene Catalyzed by $Pd(OAc)_2$/Heteropoly Acid/O_2 System. *New J. Chem.* **2008,** *32*, 738-742.

37. Kubota, A.; Emmert, M. H.; Sanford, M. S. Pyridine Ligands as Promoters in PdII/0-Catalyzed C–H Olefination Reactions. *Org. Lett.* **2012,** *14*, 1760-1763.

38. Jia, X.; Foley, A. M.; Liu, C.; Vaughan, B. A.; McKeown, B. A.; Zhang, S.; Gunnoe, T. B. Styrene Production from Benzene and Ethylene Catalyzed by Palladium(II): Enhancement of Selectivity toward Styrene Via Temperature-Dependent Vinyl Ester Consumption. *Organometallics* **2019,** *38*, 3532-3541.

39. Bair, J. S.; Schramm, Y.; Sergeev, A. G.; Clot, E.; Eisenstein, O.; Hartwig, J. F. Linear-Selective Hydroarylation of Unactivated Terminal and Internal Olefins with Trifluoromethyl-Substituted Arenes. *J. Am. Chem. Soc.* **2014,** *136*, 13098-13101.

40. Saper, N. I.; Ohgi, A.; Small, D. W.; Semba, K.; Nakao, Y.; Hartwig, J. F. Nickel-Catalysed Anti-Markovnikov Hydroarylation of Unactivated Alkenes with Unactivated Arenes Facilitated by Non-Covalent Interactions. *Nature Chemistry* **2020,** *12*, 276-283.

41. Matsumoto, T.; Taube, D. J.; Periana, R. A.; Taube, H.; Yoshida, H. Anti-Markovnikov Olefin Arylation Catalyzed by an Iridium Complex. *J. Am. Chem. Soc.* **2000,** *122*, 7414-7415.

42. Periana, R. A.; Liu, X. Y.; Bhalla, G. Novel Bis-Acac-O, O–Ir (III) Catalyst for Anti-Markovnikov, Hydroarylation of Olefins Operates by Arene Ch Activation. *Chem. Commun.* **2002**, 3000-3001.

43. Bhalla, G.; Liu, X. Y.; Oxgaard, J.; Goddard, W. A.; Periana, R. A. Synthesis, Structure, and Reactivity of O-Donor Ir(III) Complexes: C−H Activation Studies with Benzene. *J. Am. Chem. Soc.* **2005,** *127*, 11372-11389.

44. Bhalla, G.; Oxgaard, J.; Goddard, W. A.; Periana, R. A. Anti-Markovnikov Hydroarylation of Unactivated Olefins Catalyzed by a Bis-Tropolonato Iridium(III) Organometallic Complex. *Organometallics* **2005,** *24*, 3229-3232.

45. Bhalla, G.; Bischof, S. M.; Ganesh, S. K.; Liu, X. Y.; Jones, C. J.; Borzenko, A.; Tenn, W. J.; Ess, D. H.; Hashiguchi, B. G.; Lokare, K. S.; Leung, C. H.; Oxgaard, J.; Goddard, W. A.; Periana, R. A. Mechanism of Efficient Anti-Markovnikov Olefin Hydroarylation Catalyzed by Homogeneous Ir(III) Complexes. *Green Chem.* **2011,** *13*, 69-81.

46. Crisenza, G. E. M.; McCreanor, N. G.; Bower, J. F. Branch-Selective, Iridium-Catalyzed Hydroarylation of Monosubstituted Alkenes Via a Cooperative Destabilization Strategy. *J. Am. Chem. Soc.* **2014,** *136*, 10258-10261.

47. Luedtke, A. T.; Goldberg, K. I. Intermolecular Hydroarylation of Unactivated Olefins Catalyzed by Homogeneous Platinum Complexes. *Angew. Chem., Int. Ed.* **2008,** *47*, 7694-7696.

48. McKeown, B. A.; Foley, N. A.; Lee, J. P.; Gunnoe, T. B. Hydroarylation of Unactivated Olefins Catalyzed by Platinum(II) Complexes. *Organometallics* **2008,** *27*, 4031-4033.

49. McKeown, B. A.; Gonzalez, H. E.; Friedfeld, M. R.; Gunnoe, T. B.; Cundari, T. R.; Sabat, M. Mechanistic Studies of Ethylene Hydrophenylation Catalyzed by Bipyridyl Pt(II) Complexes. *J. Am. Chem. Soc.* **2011,** *133*, 19131-19152.

50. McKeown, B. A.; Gonzalez, H. E.; Friedfeld, M. R.; Brosnahan, A. M.; Gunnoe, T. B.; Cundari, T. R.; Sabat, M. Platinum(II)-Catalyzed Ethylene Hydrophenylation: Switching Selectivity between Alkyl- and Vinylbenzene Production. *Organometallics* **2013,** *32*, 2857-2865.

51. McKeown, B. A.; Gonzalez, H. E.; Gunnoe, T. B.; Cundari, T. R.; Sabat, M. Ptii-Catalyzed Ethylene Hydrophenylation: Influence of Dipyridyl Chelate Ring Size on Catalyst Activity and Longevity. *ACS Catal.* **2013,** *3*, 1165-1171.

52. McKeown, B. A.; Gonzalez, H. E.; Michaelos, T.; Gunnoe, T. B.; Cundari, T. R.; Crabtree, R. H.; Sabat, M. Control of Olefin Hydroarylation Catalysis Via a Sterically and Electronically Flexible Platinum(II) Catalyst Scaffold. *Organometallics* **2013,** *32*, 3903-3913.

53. Clement, M. L.; Grice, K. A.; Luedtke, A. T.; Kaminsky, W.; Goldberg, K. I. Platinum(II) Olefin Hydroarylation Catalysts: Tuning Selectivity for the Anti-Markovnikov Product. *Chem. - Eur. J.* **2014,** *20*, 17287-17291.

54. McKeown, B. A.; Prince, B. M.; Ramiro, Z.; Gunnoe, T. B.; Cundari, T. R. Pt^{II}-Catalyzed Hydrophenylation of α-Olefins: Variation of Linear/Branched Products as a Function of Ligand Donor Ability. *ACS Catal.* **2014,** *4*, 1607-1615.

55. Suslick, B. A.; Liberman-Martin, A. L.; Wambach, T. C.; Tilley, T. D. Olefin Hydroarylation Catalyzed by (Pyridyl-Indolate)Pt(II) Complexes: Catalytic Efficiencies and Mechanistic Aspects. *ACS Catal.* **2017,** *7*, 4313-4322.

56. Webster-Gardiner, M. S.; Fu, R.; Fortman, G. C.; Nielsen, R. J.; Gunnoe, T. B.; Goddard III, W. A. Arene C–H Activation Using Rh(I) Catalysts Supported by Bidentate Nitrogen Chelates. *Catal. Sci. Technol.* **2015,** *5*, 96-100.

57. Webster-Gardiner, M. S.; Piszel, P. E.; Fu, R.; McKeown, B. A.; Nielsen, R. J.; Goddard, W. A.; Gunnoe, T. B. Electrophilic Rh^{I} Catalysts for Arene H/D Exchange in

Acidic Media: Evidence for an Electrophilic Aromatic Substitution Mechanism. *J. Mol. Catal. A: Chem.* **2017,** *426*, 381-388.

58. O'Reilly, M. E.; Fu, R.; Nielsen, R. J.; Sabat, M.; Goddard, W. A.; Gunnoe, T. B. Long-Range C–H Bond Activation by Rh^{III}-Carboxylates. *J. Am. Chem. Soc.* **2014,** *136*, 14690-14693.

59. Fu, R.; O'Reilly, M. E.; Nielsen, R. J.; Goddard III , W. A.; Gunnoe, T. B. Rhodium Bis(Quinolinyl)Benzene Complexes for Methane Activation and Functionalization. *Chem. Eur. J.* **2015,** *21*, 1286-1293.

60. Kong, F.; Gu, S.; Liu, C.; Dickie, D. A.; Zhang, S.; Gunnoe, T. B. Effects of Additives on Catalytic Arene C–H Activation: Study of Rh Catalysts Supported by Bis-Phosphine Pincer Ligands. *Organometallics* **2020,** *39*, 3918-3935.

61. Hong, P.; Yamazaki, H. Rhodium Carbonyl-Catalyzed Activation of Carbon-Hydrogen Bonds for Application in Organic Synthesis.: V. Phenylation of Olefins with Benzenes. *J. Mol. Catal.* **1984,** *26*, 297-311.

62. Taube, D.; Periana, R.; Matsumoto, T. Oxidative Coupling of Olefins and Aromatics Using a Rhodium Catalyst and a Copper(II) Redox Agent. U.S. Patent 6127590A, 2000.

63. Matsumoto, T.; Yoshida, H. Oxidative Arylation of Ethylene with Benzene to Produce Styrene. *Chem. Lett.* **2000,** *29*, 1064-1065.

64. Zhu, W.; Gunnoe, T. B. Rhodium-Catalyzed Arene Alkenylation Using Only Dioxygen as the Oxidant. *ACS Catal.* **2020,** *10*, 11519-11531.

65. Chen, J.; Nielsen, R. J.; Goddard, W. A.; McKeown, B. A.; Dickie, D. A.; Gunnoe, T. B. Catalytic Synthesis of Superlinear Alkenyl Arenes Using a Rh(I) Catalyst Supported by a "Capping Arene" Ligand: Access to Aerobic Catalysis. *J. Am. Chem. Soc.* **2018,** *140*, 17007-17018.

66. Luo, Z.; Whitcomb, C. A.; Kaylor, N.; Zhang, Y.; Zhang, S.; Davis, R. J.; Gunnoe, T. B. Oxidative Alkenylation of Arenes Using Supported Rh Materials: Evidence That Active Catalysts Are Formed by Rh Leaching. *ChemCatChem* **2021,** *13*, 260-270.

67. Vaughan, B. A.; Webster-Gardiner, M. S.; Cundari, T. R.; Gunnoe, T. B. Organic Chemistry. A Rhodium Catalyst for Single-Step Styrene Production from Benzene and Ethylene. *Science* **2015,** *348*, 421-424.

68. Webster-Gardiner, M. S.; Chen, J.; Vaughan, B. A.; McKeown, B. A.; Schinski, W.; Gunnoe, T. B. Catalytic Synthesis of "Super" Linear Alkenyl Arenes Using an Easily Prepared Rh(I) Catalyst. *J. Am. Chem. Soc.* **2017,** *139*, 5474-5480.

69. Vaughan, B. A.; Khani, S. K.; Gary, J. B.; Kammert, J. D.; Webster-Gardiner, M. S.; McKeown, B. A.; Davis, R. J.; Cundari, T. R.; Gunnoe, T. B. Mechanistic Studies of Single-Step Styrene Production Using a Rhodium(I) Catalyst. *J. Am. Chem. Soc.* **2017,** *139*, 1485-1498.

70. Zhu, W.; Luo, Z.; Chen, J.; Liu, C.; Yang, L.; Dickie, D. A.; Liu, N.; Zhang, S.; Davis, R. J.; Gunnoe, T. B. Mechanistic Studies of Single-Step Styrene Production Catalyzed by Rh Complexes with Diimine Ligands: An Evaluation of the Role of Ligands and Induction Period. *ACS Catal.* **2019,** *9*, 7457-7475.

71. Liebov, N. S.; Zhu, W.; Chen, J.; Webster-Gardiner, M. S.; Schinski, W. L.; Gunnoe, T. B. Rhodium-Catalyzed Alkenylation of Toluene Using 1-Pentene: Regioselectivity to Generate Precursors for Bicyclic Compounds. *Organometallics* **2019,** *38*, 3860-3870.

72. Jia, X.; Frye, L. I.; Zhu, W.; Gu, S.; Gunnoe, T. B. Synthesis of Stilbenes by Rhodium-Catalyzed Aerobic Alkenylation of Arenes Via C–H Activation. *J. Am. Chem. Soc.* **2020,** *142*, 10534-10543.

73. Gunnoe, T. B.; Schinski, W. L.; Jia, X.; Zhu, W. Transition-Metal-Catalyzed Arene Alkylation and Alkenylation: Catalytic Processes for the Generation of Chemical Intermediates. *ACS Catal.* **2020,** *10*, 14080-14092.

74. Mikuriya, M.; Yamamoto, J.; Ishida, H.; Yoshioka, D.; Handa, M. Preparation and Crystal Structure of Tetrakis(μ-pivalato-O,O')bis[(pivalic acid-O)rhodium(II)]. *X-Ray Struct. Anal. Online* **2011,** *27*, 7-8.

75. Barnett, H. J.; Hill, A. F. A Dirhoda-Heterocyclic Carbene. *Angew. Chem. Int. Ed.* **2020,** *59*, 4274-4277.

76. Carriedo, G. A.; Howard, J. A. K.; Stone, F. G. A. Chemistry of Di- and Tri-Metal Complexes with Bridging Carbene or Carbyne Ligands. Part 24. Complexes of the Pentamethylcyclopentadienylcopper Group and the Crystal Structures of the Compounds [CuPtW(μ-$_3$CC$_6$H$_4$Me-4)(Co)$_2$(PMe$_3$)$_2$(H-C$_5$H$_5$)(H-C$_5$Me$_5$)] and [CuRh$_2$(μ-Co)$_2$(H-C$_5$Me$_5$)$_3$]. *J. Chem. Soc., Dalton Trans.* **1984**, 1555-1561.

77. Bachechi, F.; Bianchini, C.; Meli, A. X-Ray Structural Analyses of Copper(I) and Silver(I) Adducts of the Rh(III) Trihydride [(Triphos)RhH$_3$], with Triphos=CH$_3$C(CH$_2$PPh$_2$)$_3$. *Inorg. Chim. Acta* **1993,** *213*, 269-277.

78. Grazia Arena, C.; Faraone, F.; Lanfranchi, M.; Rotondo, E.; Tiripicchio, A. Steric Effects of the 2-(Diphenylphosphino)-6-Methoxypyridine Short-Bite Bridging Ligand in the Synthesis of Binuclear Complexes. Crystal and Molecular Structure of [Rh$_2$Cu(CO)$_2$(Ph$_2$PPyOMe)$_2$(μ-Cl)$_2$]BF$_4$.cntdot.CH$_2$Cl$_2$. *Inorg. Chem.* **1992,** *31*, 4797-4802.

79. Bruno, G.; Lo Schiavo, S.; Rotondo, E.; Piraino, P.; Faraone, F. Synthesis of Triangular Mixed-Metal Clusters by the Addition of Copper Electrophiles to an Electron-Rich Rhodium-Rhodium Bond. X-Ray Crystal Structures of [Rh$_2$(η-C$_5$H$_5$)$_2$(μ-Co)(μ-Ph$_2$PCH$_2$PPh$_2$)(μ-CuI)] and [Rh$_2$(η-C$_5$H$_5$)$_2$(μ-Co)(μ-Ph$_2$PCH$_2$PPh$_2$)(μ-AgO$_2$CCH$_3$)]. *Organometallics* **1987,** *6*, 2502-2507.

80. Tegethoff, M.; Roelfes, F.; Schulte to Brinke, C.; Tan, T. T. Y.; Kampert, F.; Jin, G.-X.; Hahn, F. E. Synthesis of Heterobimetallic Complexes by Coordination of Rhodium(III) and Iridium(III) Poly-N,O-NHC Complexes to Silver(I), Copper(II), and Zinc(II). *Organometallics* **2018,** *37*, 1801-1812.

81. Churchill, M. R.; Bezman, S. A.; Osborn, J. A.; Wormald, J. Synthesis and Molecular Geometry of Hexameric Triphenylphosphinocopper(I) Hydride and the Crystal Structure of $H_6Cu_6(PPh_3)_6$. $HCONMe_2$ [Hexameric Triphenylphosphino Copper(I) Hydride Dimethylformamide]. *Inorg. Chem.* **1972,** *11*, 1818-1825.

82. Werner, H.; Poelsma, S.; Schneider, M. E.; Windmüller, B.; Barth, D. Synthesis and Reactivity of Bis(Ethene) Rhodium(I) and Iridium(I) Carboxylato Complexes. *Chem. Ber.* **1996,** *129*, 647-652.

83. Craig, N. C.; Groner, P.; McKean, D. C. Equilibrium Structures for Butadiene and Ethylene: Compelling Evidence for Π-Electron Delocalization in Butadiene. *The Journal of Physical Chemistry A* **2006,** *110*, 7461-7469.

84. Krugh, T. R. Spin-Label-Induced Nuclear Magnetic Resonance Relaxation Studies of Enzymes. In *Spin Labeling, Theory and Applications*. Academic Press, New York; 1976; p. 339–372.

85. Jacob, J.; Baker, B.; Bryant, R. G.; Cafiso, D. S. Distance Estimates from Paramagnetic Enhancements of Nuclear Relaxation in Linear and Flexible Model Peptides. *Biophys. J.* **1999,** *77*, 1086-1092.

86. Das, D.; Mohapatra, S. S.; Roy, S. Recent Advances in Heterobimetallic Catalysis across a "Transition Metal–Tin" Motif. *Chem. Soc. Rev.* **2015,** *44*, 3666-3690.

87. Campos, J. Bimetallic Cooperation across the Periodic Table. *Nature Reviews Chemistry* **2020**.

88. Buchwalter, P.; Rosé, J.; Braunstein, P. Multimetallic Catalysis Based on Heterometallic Complexes and Clusters. *Chem. Rev.* **2015,** *115*, 28-126.

89. Mata, J. A.; Hahn, F. E.; Peris, E. Heterometallic Complexes, Tandem Catalysis and Catalytic Cooperativity. *Chemical Science* **2014,** *5*, 1723-1732.

90. Walker, W. E.; Brown, E. S.; Pruett, R. L. U.S. Patent 4,320,064, 1975, Union Carbide Co.

91. Jones, W. D.; Feher, F. J. The Mechanism and Thermodynamics of Alkane and Arene Carbon-Hydrogen Bond Activation in $(C_5Me_5)Rh(PMe_3)(R)H$. *J. Am. Chem. Soc.* **1984,** *106*, 1650-1663.

92. Vetter, A. J.; Flaschenriem, C.; Jones, W. D. Alkane Coordination Selectivity in Hydrocarbon Activation by [Tp'Rh(CNneopentyl)]: The Role of Alkane Complexes. *J. Am. Chem. Soc.* **2005,** *127*, 12315-12322.

93. Northcutt, T. O.; Wick, D. D.; Vetter, A. J.; Jones, W. D. Investigation of the Mechanism of Alkane Reductive Elimination and Skeletal Isomerization in Tp'Rh(CNneopentyl)(R)H Complexes: The Role of Alkane Complexes. *J. Am. Chem. Soc.* **2001,** *123*, 7257-7270.

94. Bergman, R. G. Activation of Alkanes with Organotransition Metal Complexes. *Science* **1984,** *223*, 902.

95. Gorelsky, S. I.; Lapointe, D.; Fagnou, K. Analysis of the Concerted Metalation-Deprotonation Mechanism in Palladium-Catalyzed Direct Arylation across a Broad Range of Aromatic Substrates. *J. Am. Chem. Soc.* **2008,** *130*, 10848-10849.

96. Sperger, T.; Sanhueza, I. A.; Kalvet, I.; Schoenebeck, F. Computational Studies of Synthetically Relevant Homogeneous Organometallic Catalysis Involving Ni, Pd, Ir, and Rh: An Overview of Commonly Employed DFT Methods and Mechanistic Insights. *Chem. Rev.* **2015,** *115*, 9532-9586.

97. Boutadla, Y.; Davies, D. L.; Macgregor, S. A.; Poblador-Bahamonde, A. I. Mechanisms of C–H Bond Activation: Rich Synergy between Computation and Experiment. *Dalton Trans.* **2009**, 5820-5831.

98. Webb, J. R.; Burgess, S. A.; Cundari, T. R.; Gunnoe, T. B. Activation of Carbon–Hydrogen Bonds and Dihydrogen by 1,2-CH-Addition across Metal–Heteroatom Bonds. *Dalton Trans.* **2013,** *42*, 16646-16665.

99. Gunnoe, T. B. Reactivity of Ruthenium(II) and Copper(I) Complexes That Possess Anionic Heteroatomic Ligands: Synthetic Exploitation of Nucleophilicity and Basicity of Amido, Hydroxo, Alkoxo, and Aryloxo Ligands for the Activation of Substrates That Possess Polar Bonds as Well as Nonpolar C–H and H–H Bonds. *Eur. J. Inorg. Chem.* **2007,** *2007*, 1177-1177.

100. Lapointe, D.; Fagnou, K. Overview of the Mechanistic Work on the Concerted Metallation–Deprotonation Pathway. *Chem. Lett.* **2010,** *39*, 1118-1126.

101. Ackermann, L. Carboxylate-Assisted Transition-Metal-Catalyzed C−H Bond Functionalizations: Mechanism and Scope. *Chem. Rev.* **2011,** *111*, 1315-1345.

102. Braga, A. A. C.; Ujaque, G.; Maseras, F. A DFT Study of the Full Catalytic Cycle of the Suzuki−Miyaura Cross-Coupling on a Model System. *Organometallics* **2006,** *25*, 3647-3658.

103. Gourlaouen, C.; Ujaque, G.; Lledós, A.; Medio-Simon, M.; Asensio, G.; Maseras, F. Why Is the Suzuki−Miyaura Cross-Coupling of sp^3 Carbons in A-Bromo Sulfoxide Systems Fast and Stereoselective? A DFT Study on the Mechanism. *J. Org. Chem.* **2009,** *74*, 4049-4054.

104. Besora, M.; Gourlaouen, C.; Yates, B.; Maseras, F. Phosphine and Solvent Effects on Oxidative Addition of CH_3Br to $Pd(PR_3)$ and $Pd(PR_3)_2$ Complexes. *Dalton Trans.* **2011,** *40*, 11089-11094.

105. Kragten, D. D.; van Santen, R. A.; Neurock, M.; Lerou, J. J. A Density Functional Study of the Acetoxylation of Ethylene to Vinyl Acetate Catalyzed by Palladium Acetate. *The Journal of Physical Chemistry A* **1999,** *103*, 2756-2765.

106. Funes-Ardoiz, I.; Maseras, F. Cooperative Reductive Elimination: The Missing Piece in the Oxidative-Coupling Mechanistic Puzzle. *Angew. Chem. Int. Ed.* **2016,** *55*, 2764-2767.

Appendix A

Appendix for: Improving Cobalt Phthalocyanine Catalyst Activity using Strain-Inducing Carbon Nanotube Supports

Reproduced with permission from:

Jianjun Su, Yun Song, Libei Huang, Yong Liu, Geng Li, Yinger Xin, Pei Xiong, Molly Meng-Jung Li, Haoran Wu, Minghui Zhu, Hao Ming Chen, Jianyu Zhang, Ben Zhong Tang, Marc Robert, William A. Goddard III, Ruquan Ye.

Nature Catalysis, **2023**, *6, 818 – 828 (Open Access).*

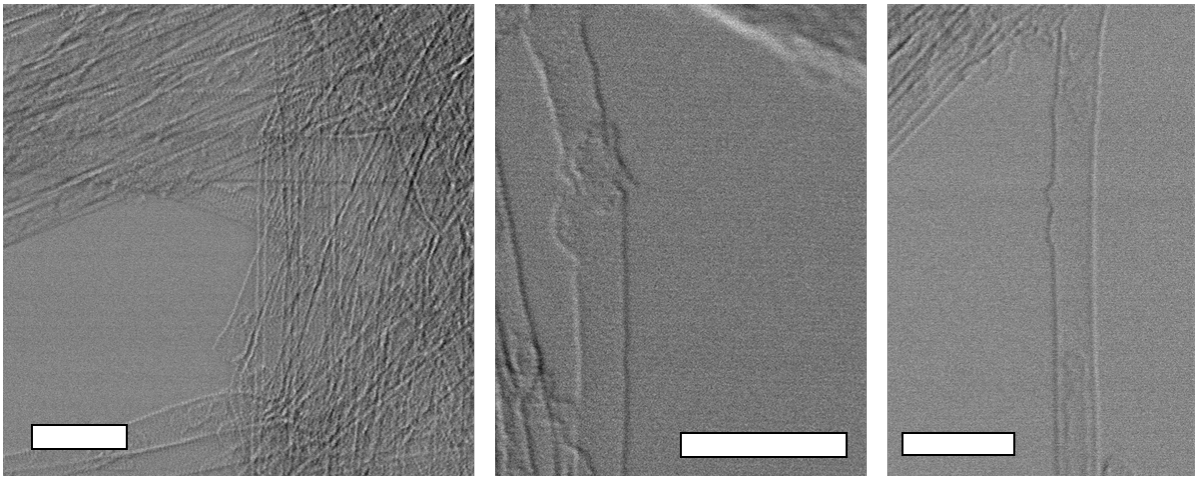

Figure A1: Additional TEM image of SWCNT. Scale bar: 5 nm.

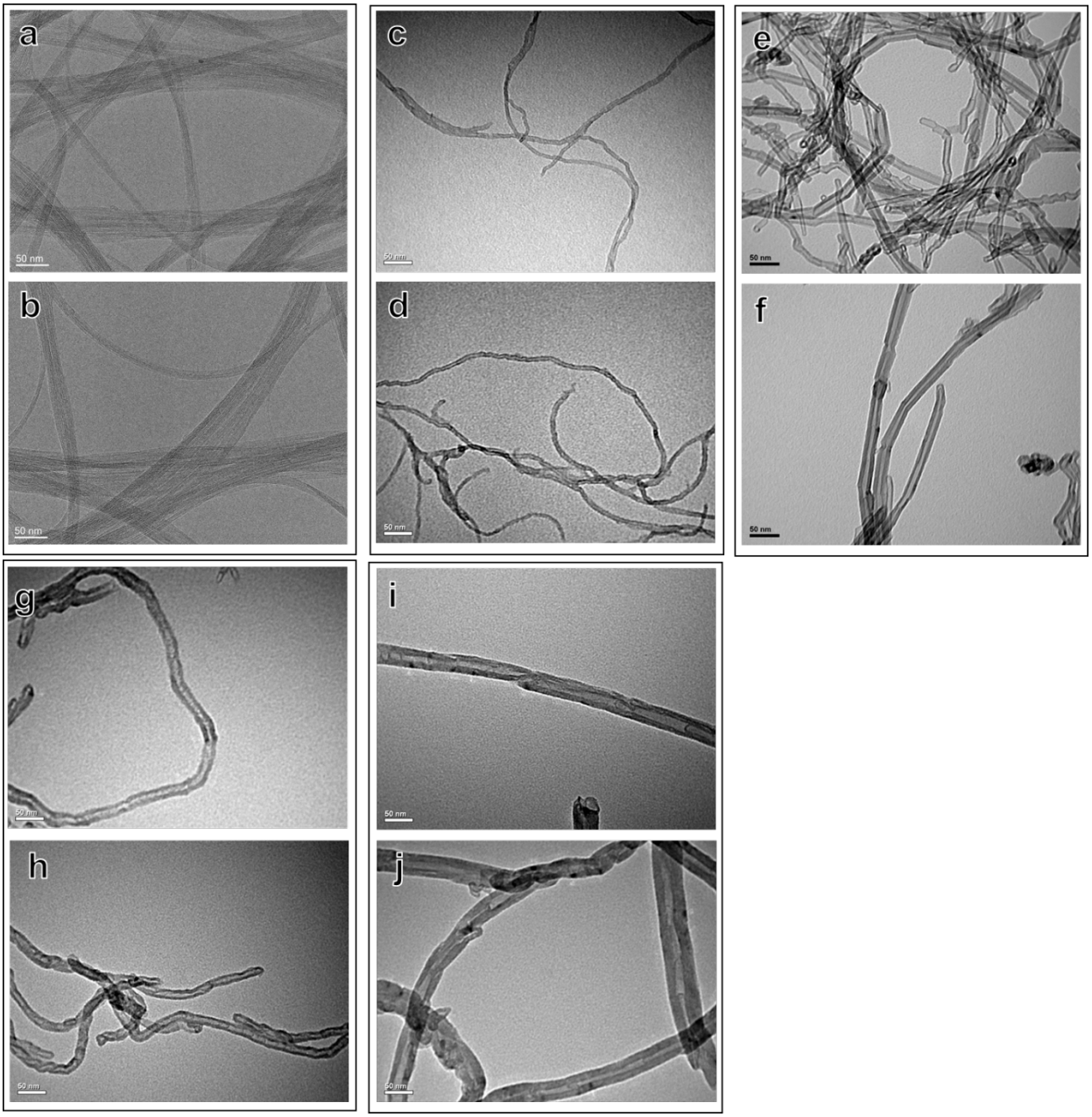

Figure A2: TEM images of (**a**), (**c**), (**e**), (**g**) and (**h**) MWCNT/5, MWCNT/10, MWCNT/15, MWCNT/25 and MWCNT/50. (**b**), (**d**), (**f**), (**h**) and (**j**) CoPc/5, CoPc/10, CoPc/15, CoPc/25 and CoPc/50.

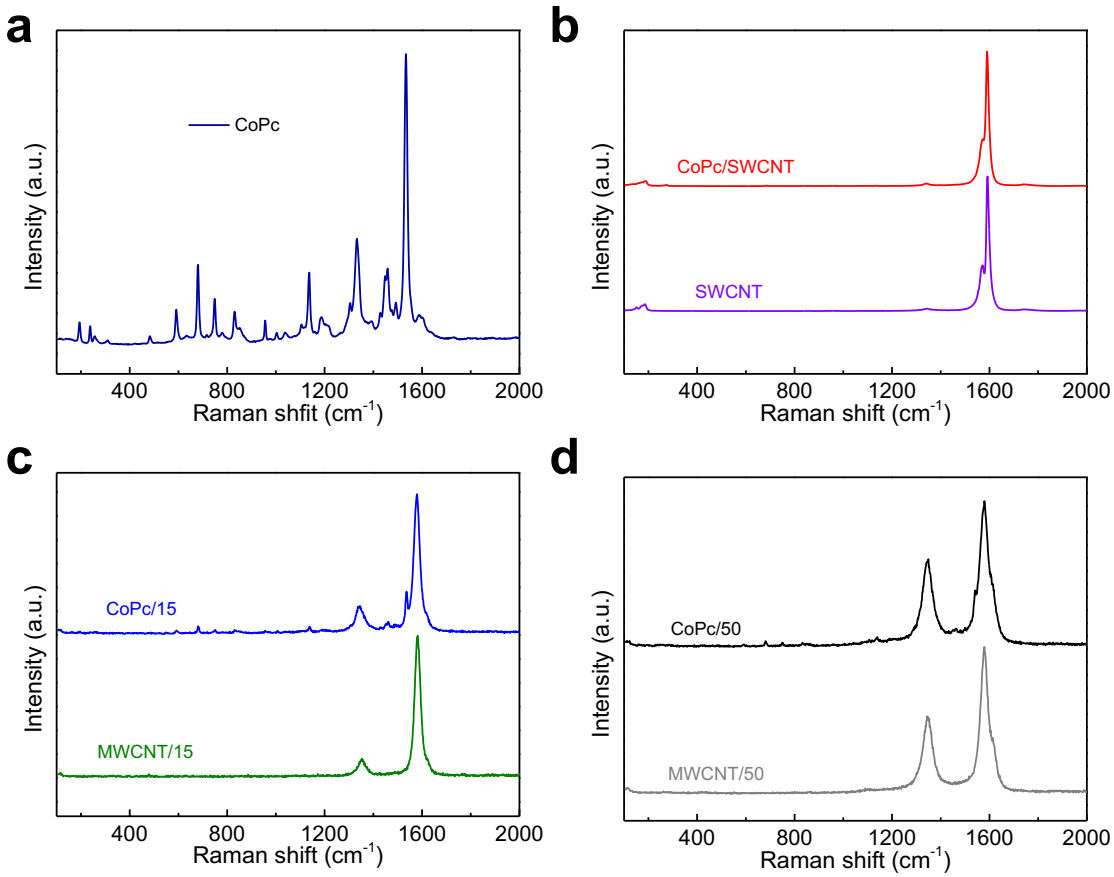

Figure A3: Raman spectrum of (**a**) CoPc, (**b**) CoPc/SWCNT and SWCNT, (**c**) CoPc/15 and MWCNT/15. (**d**) CoPc/50, MWCNT/50.

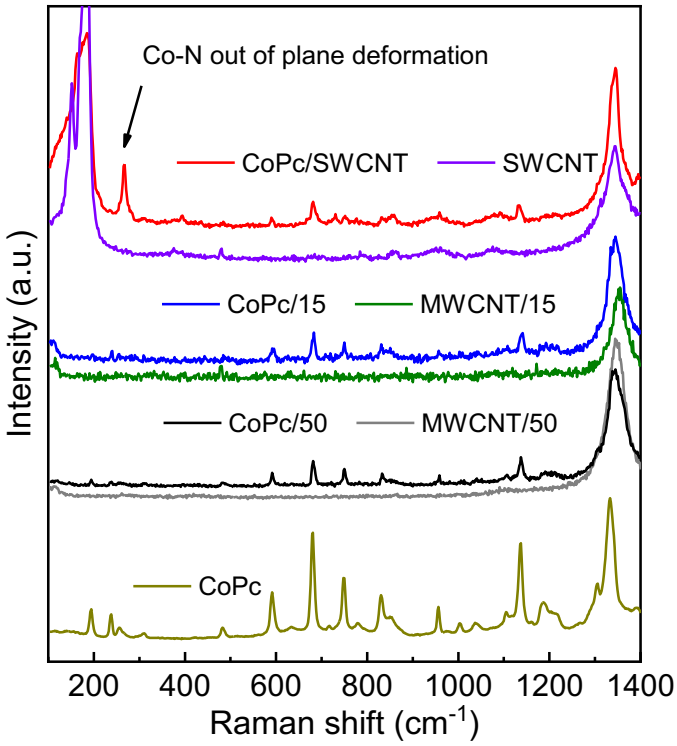

Figure A4: Enlarged Raman spectrum of CoPc/SWCNT, SWCNT, CoPc/15, MWCNT/15, CoPc/50, MWCNT/50 and CoPc.

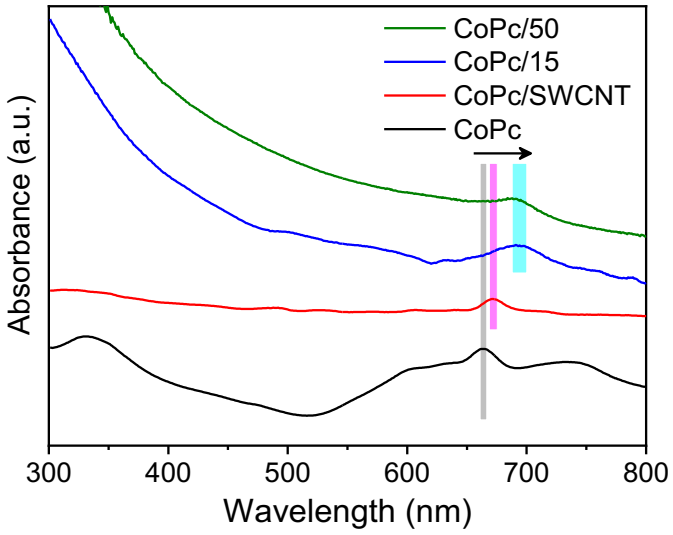

Figure A5: UV-vis of CoPc/SWCNT, CoPc/15, CoPc/50 and CoPc in ethanol solvent.

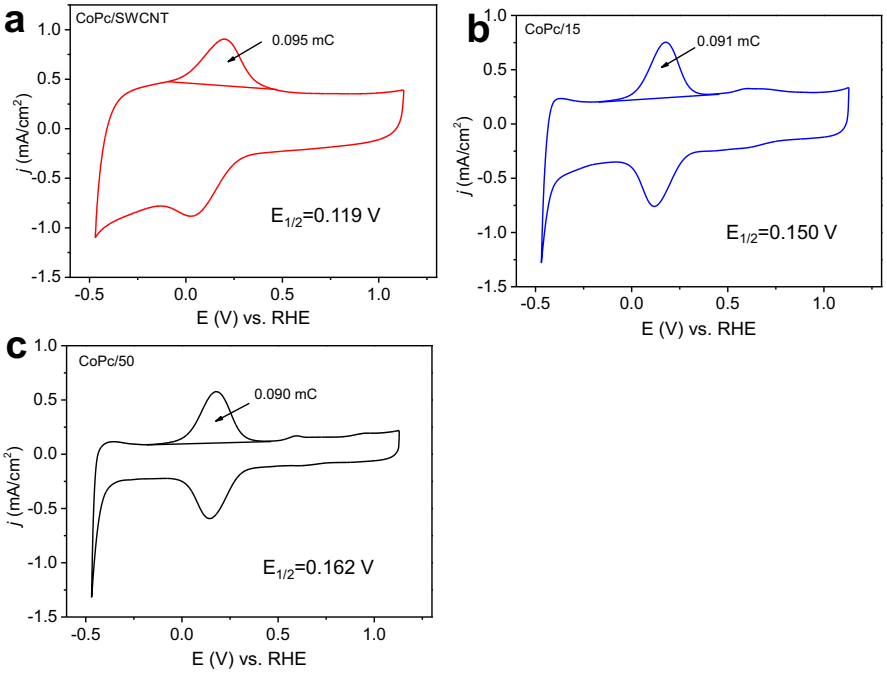

Figure A6: The CV curves of (**a**) CoPc/SWCNT, (**b**) CoPc/15 and (**c**) CoPc/50 under Ar-saturated 0.5 M $KHCO_3$ at a scan rate of 100 mV/s. The Q value is calculated by integrating the Co^{I}/Co^{II} oxidation peak.

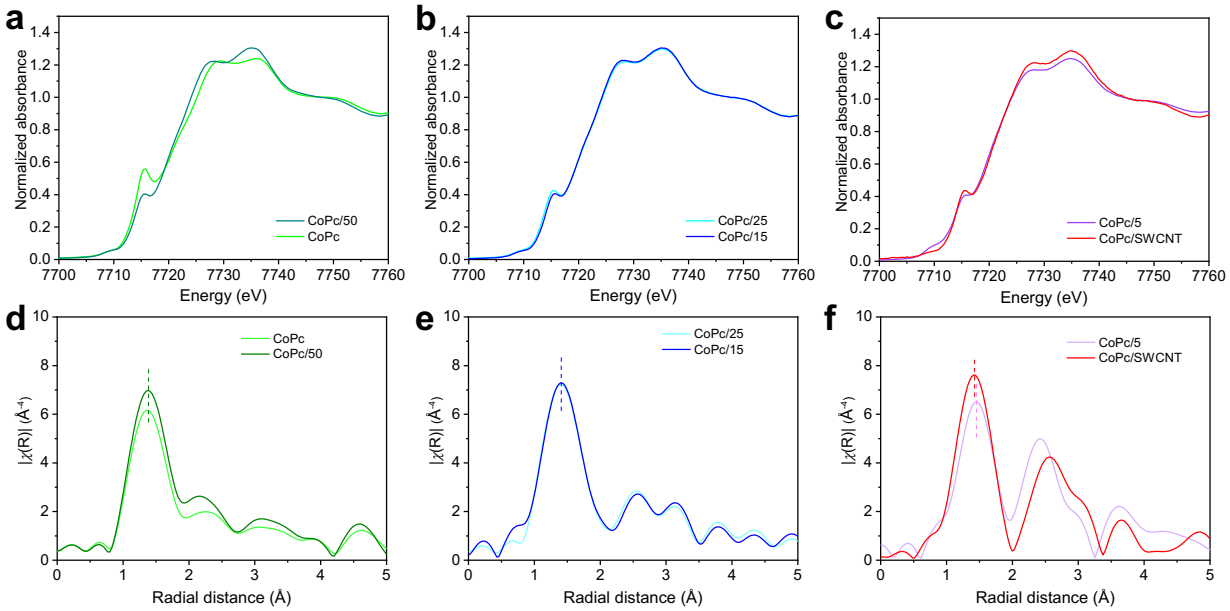

Figure A7: XANES Co K-edge (**a**), (**b**), (**c**) and FT-EXAFS (**d**), (**b**), (**f**) spectrum of CoPc and CoPc/50, CoPc/25 and CoPc/15, CoPc/5 and CoPc/SWCNT.

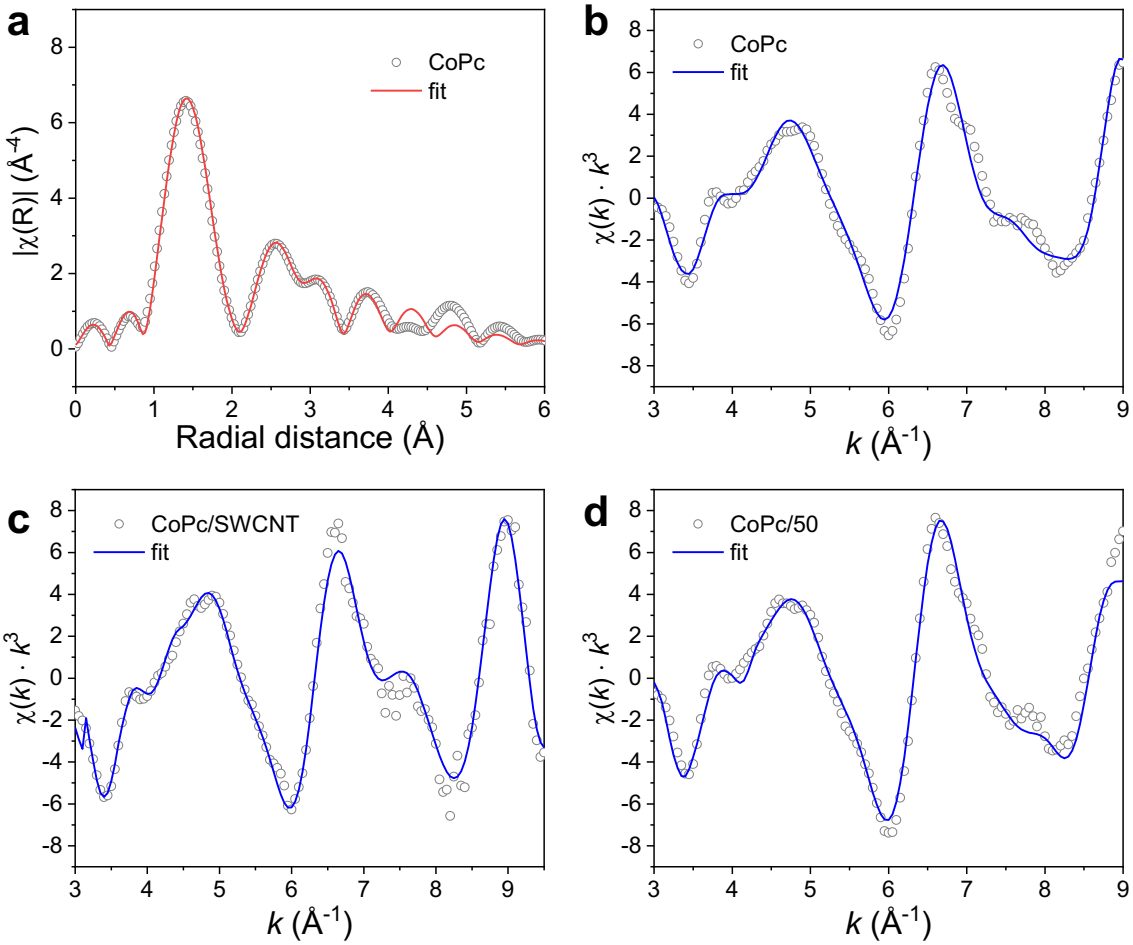

Figure A8: (**a**) EXAFS fitting at R space and (**b**) k space of CoPc. k space EXAFS fitting result of (**c**) CoPc/SWCNT and (d) CoPc/50.

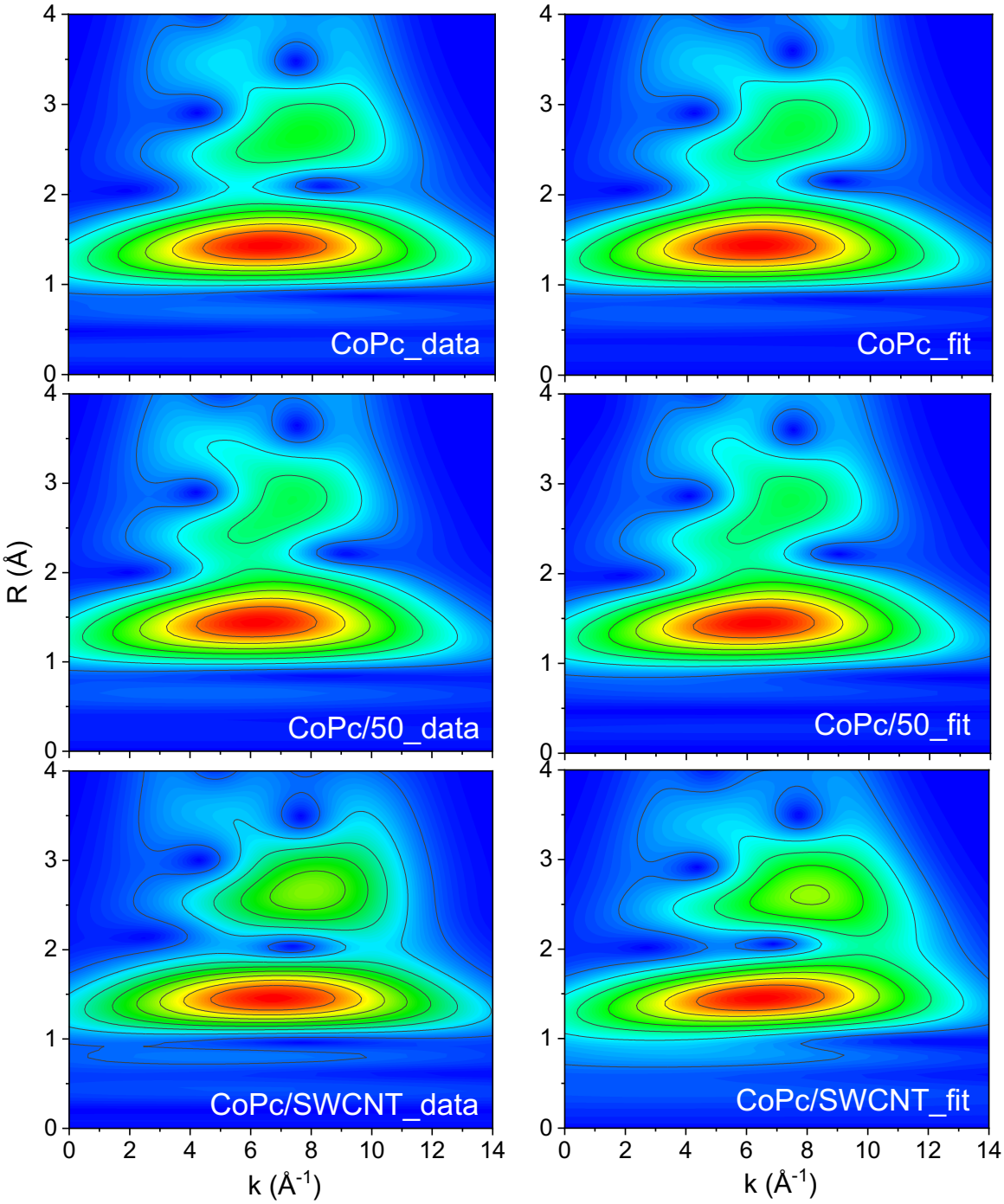

Figure A9: Wavelet transformation of EXAFS data and the fitting result.

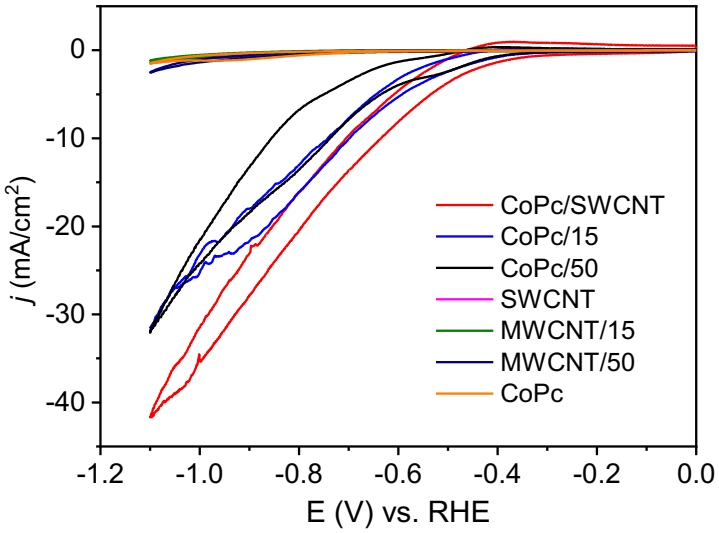

Figure A10: Electrochemical CO_2RR performance in H-cell (0.5 M $KHCO_3$ as electrolyte) with a CO_2 flow rate of 3 sccm. CV curves of CoPc/SWCNT, CoPc/15, CoPc/50 and control samples of SWCNT, MWCNT/15, MWCNT/50, CoPc acquired at a scan rate of 10 mV/s.

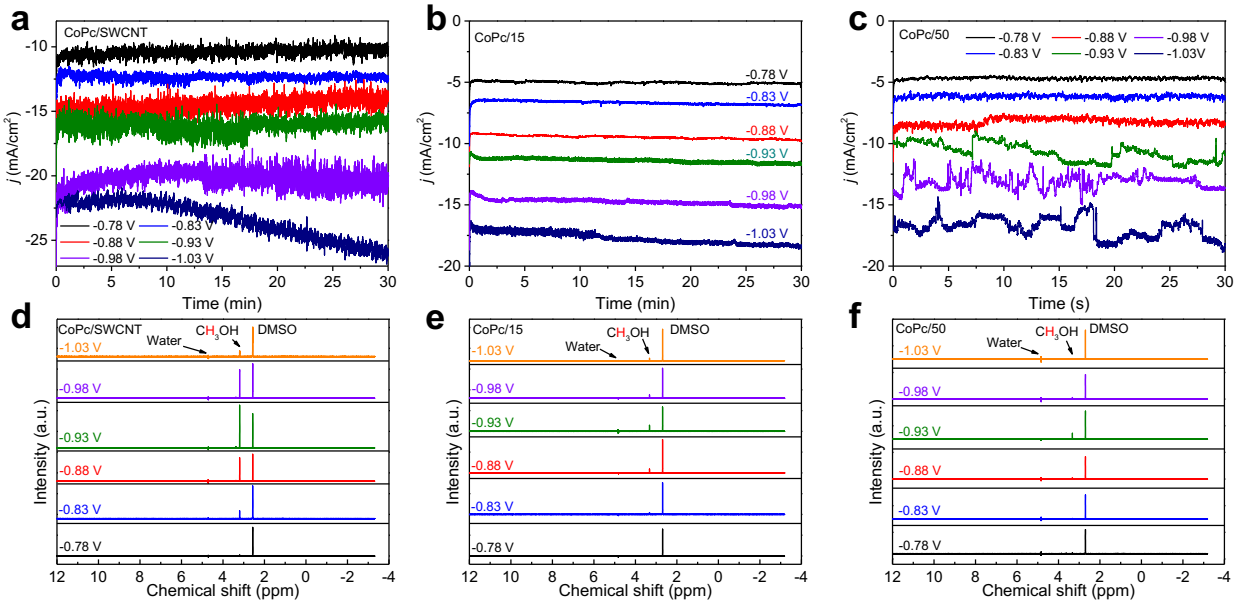

Figure A11: Chronoamperometric study (current density as a function of time) of (**a**), (**b**) and (**c**) CoPc/SWCNT, CoPc/15 and CoPc/50 using H-cell in 0.5 M $KHCO_3$ at different potentials. (**d**), (**e**) and (**f**) ^{1}H-NMR results of catholyte obtained from the CO_2RR at different potentials.

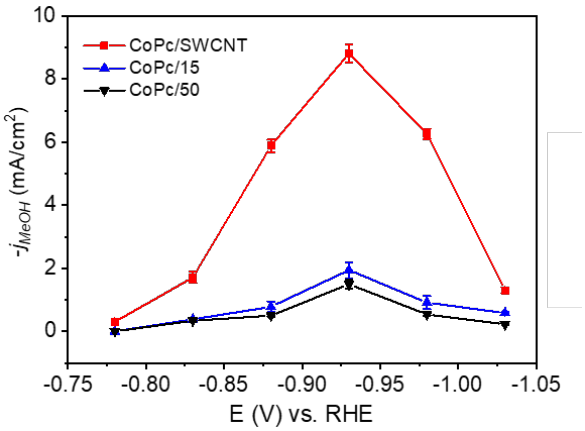

Figure A12: MeOH partial current density of CoPc/SWCNT, CoPc/15 and CoPc/50.

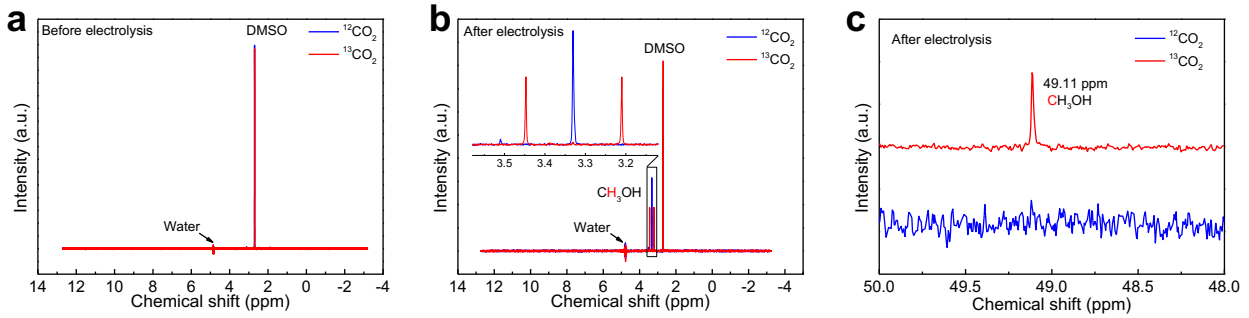

Figure A13: ^{1}H-NMR spectra of the electrolyte (**a**) before and (**b**) after controlled potential electrolysis. (**c**) ^{13}C-NMR spectra of the post-electrolysis electrolyte. The isotope labeled $^{13}CO_2$ reduction were tested at -0.88 V vs. RHE for 20 min in $^{12}CO_2$ and $^{13}CO_2$ using H-cell in 0.5 M $KH^{13}CO_3$ prepared from $^{13}CO_2$-saturated KOH.

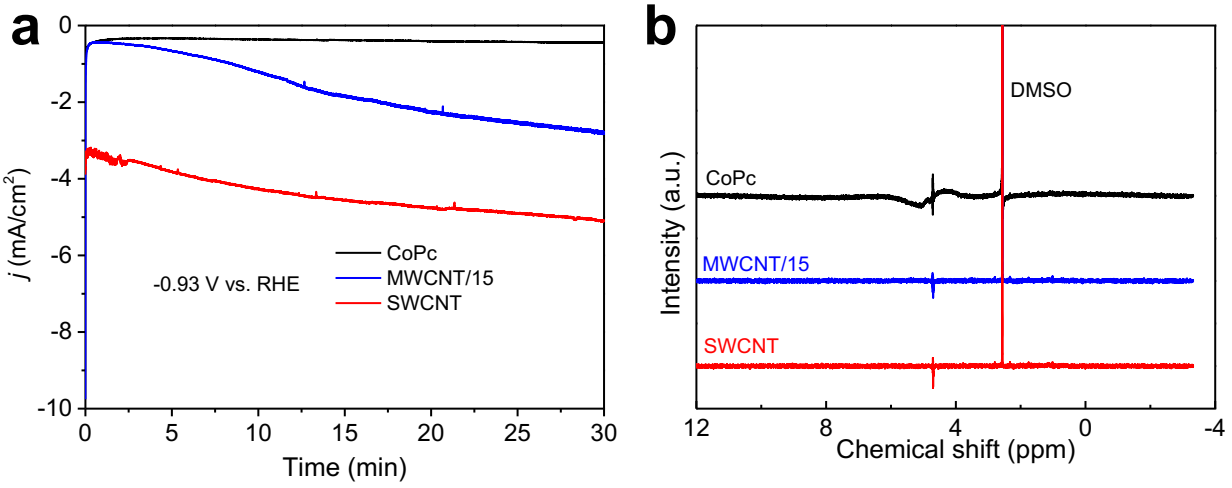

Figure A14: (**a**) Chronoamperometric curves and (**b**) corresponding ^{1}H-NMR results of bare CoPc, MWCNT/15 and SWCNT using H-cell in 0.5 M $KHCO_3$ at -0.93 V vs. RHE.

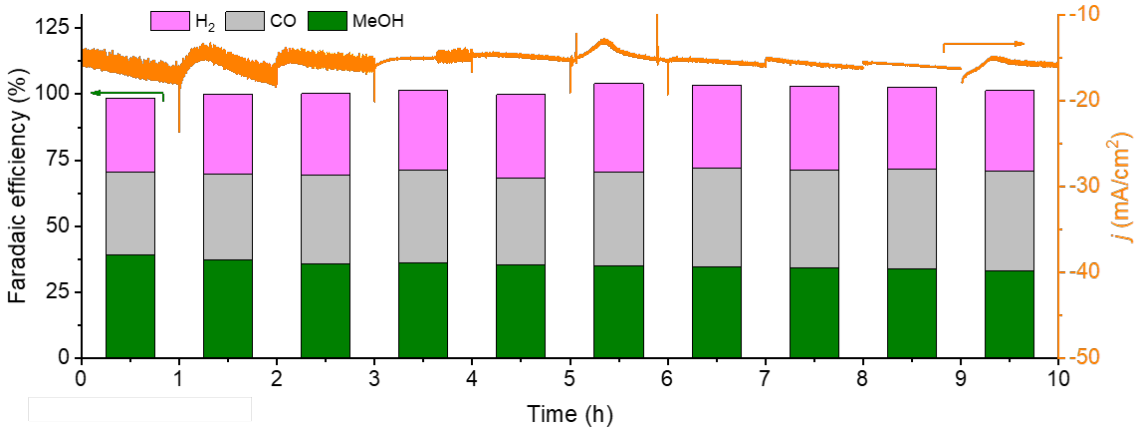

Figure A15: Stability testing and corresponding FE (CO, H_2 and MeOH) of CoPc/SWCNT at -0.88 V vs. RHE.

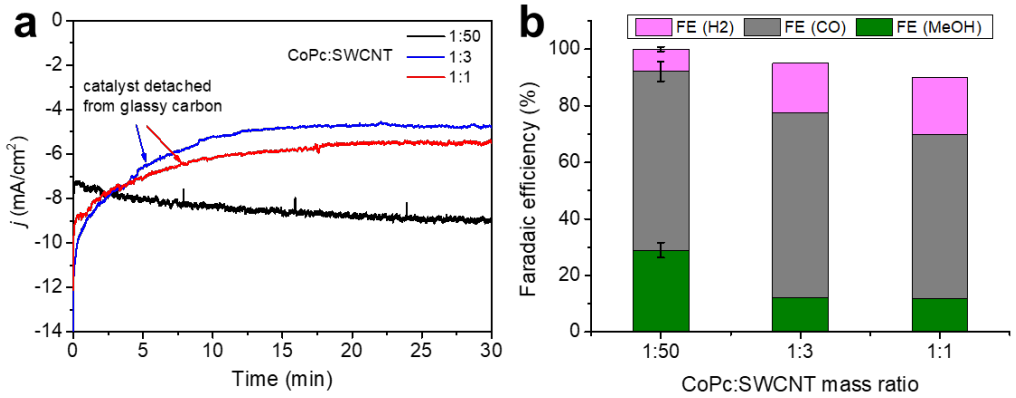

Figure A16: (**a**) Chronoamperometric curves and (**b**) FE (CO, H_2 and MeOH) of different CoPc loading samples using H-cell in 0.5 M $KHCO_3$ at -0.93 V vs. RHE.

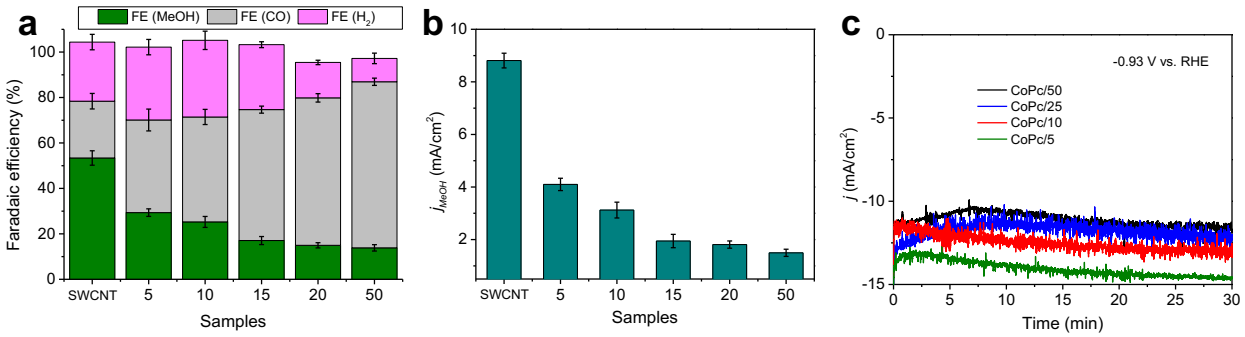

Figure A17: (**a**) FE (CO, H_2 and MeOH), (**b**) MeOH partial current density and (**c**) Chronoamperometric curves of different CNT diameter samples using H-cell in 0.5 M $KHCO_3$ at -0.93 V vs. RHE.

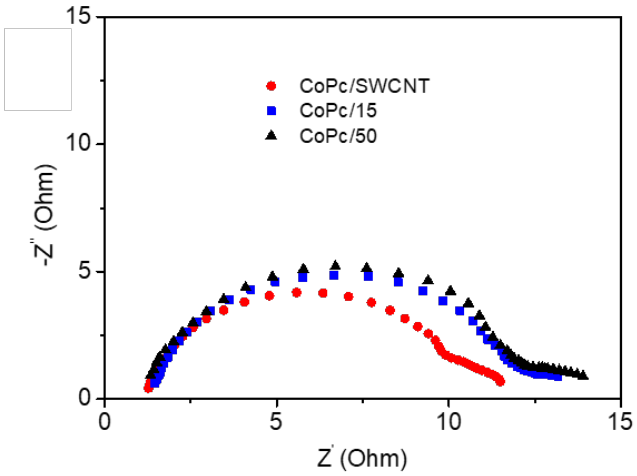

Figure A18: Nyquist plots of CoPc/SWCNT, CoPc/15 and CoPc/50, measured at −0.93 V vs. RHE in CO_2-saturated 0.5 M aqueous $KHCO_3$ electrolyte with a scanning frequency range from 200 kHz to 100 Hz and an A.C. amplitude of 5 mV.

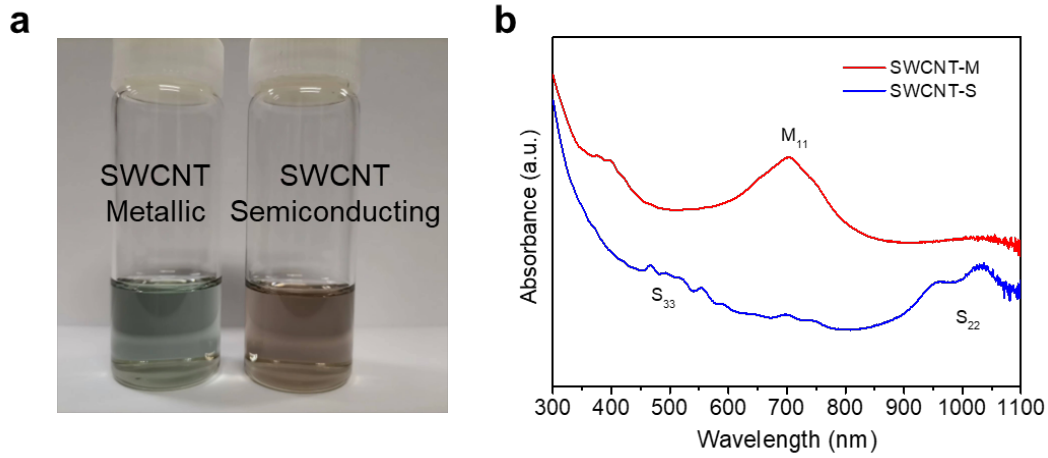

Figure A19: (**a**) Optical images and (**b**) UV-vis plots of SWCNT-M and SWCNT-S in DMF solvent.

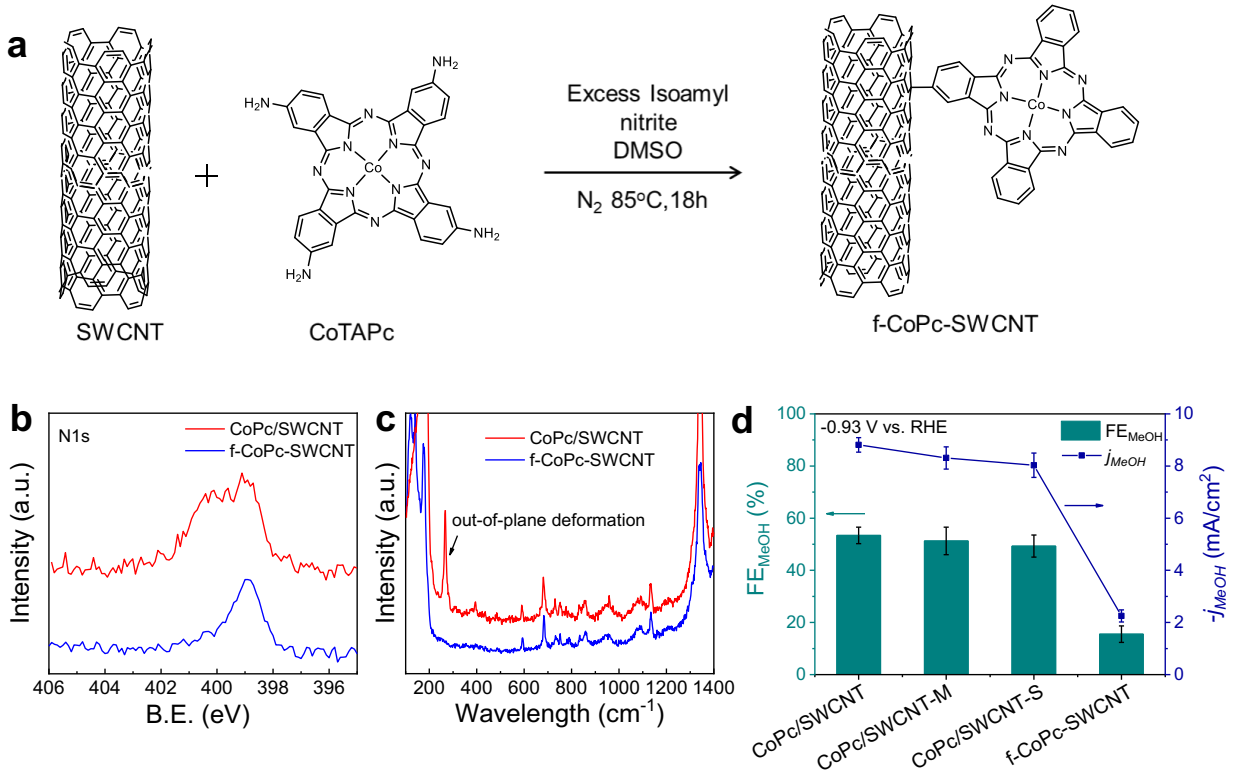

Figure A20: (**a**) Scheme for the synthesis of f-CoPc-SWCNT. (**b**) N 1s XPS spectra and (**c**) Raman spectra of f-CoPc-SWCNT and CoPc/SWCNT. (**d**) Comparing FE_{MeOH} and j_{MeOH} of CoPc/SWCNT, CoPc/SWCNT-M, CoPc/SWCNT-S and f-CoPc/SWCNT samples using H-cell in 0.5 M $KHCO_3$ at -0.93 V vs. RHE.

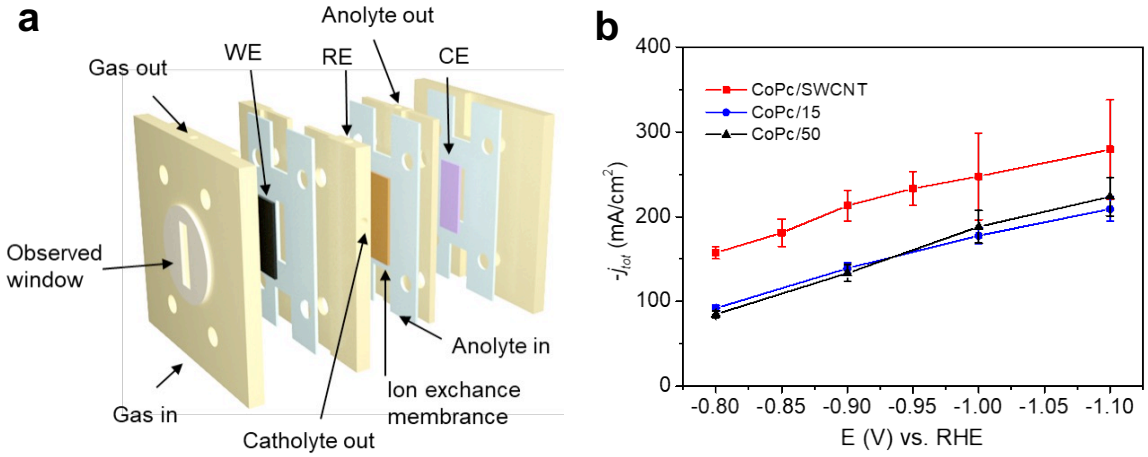

Figure A21: (**a**) Schematic illustration of the flow cell. (**b**) j_{tot} of electrochemical CO_2RR performance in flow cell configuration.

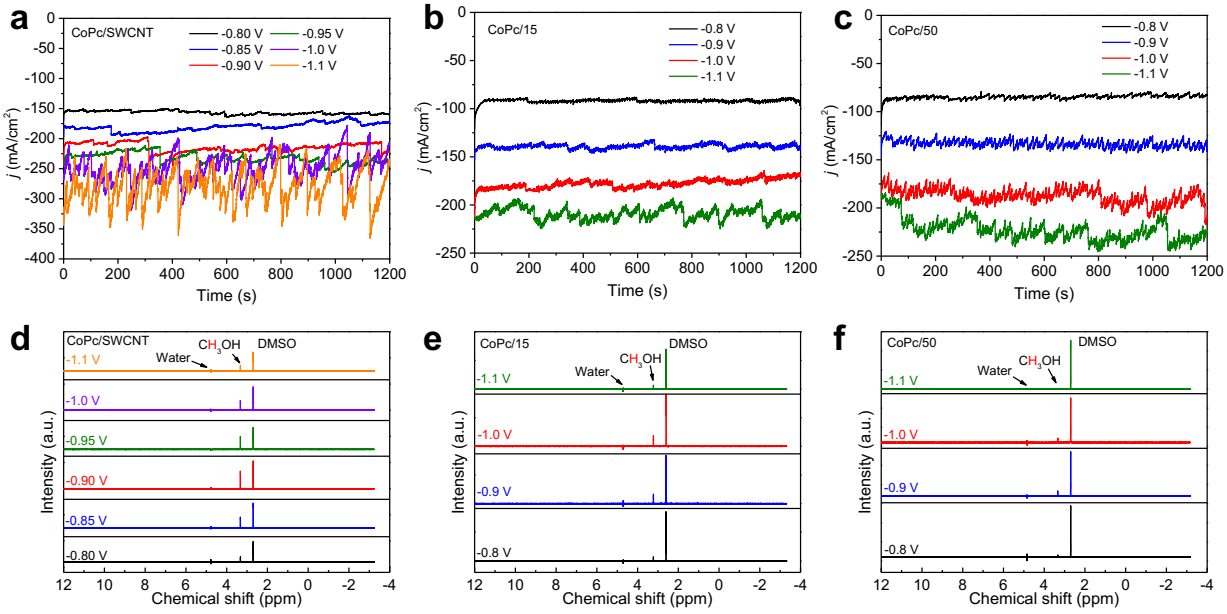

Figure A22: Chronoamperometric curves of (**a**), (**b**) and (**c**) CoPc/SWCNT, CoPc/15 and CoPc/50 in CO_2RR flow cell at different potentials. (**d**), (**e**) and (**f**) ^{1}H-NMR results of catholyte obtained at different potentials.

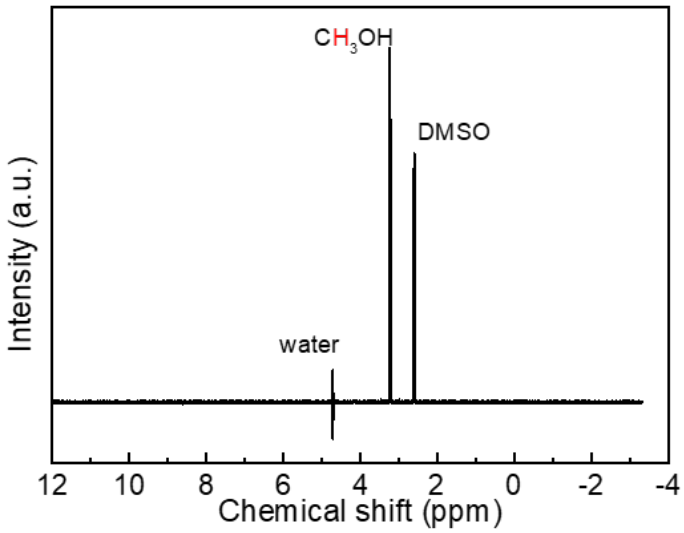

Figure A23: Typical CO_2RR ^{1}H-NMR result of stability test catholyte in first 1h using flow cell.

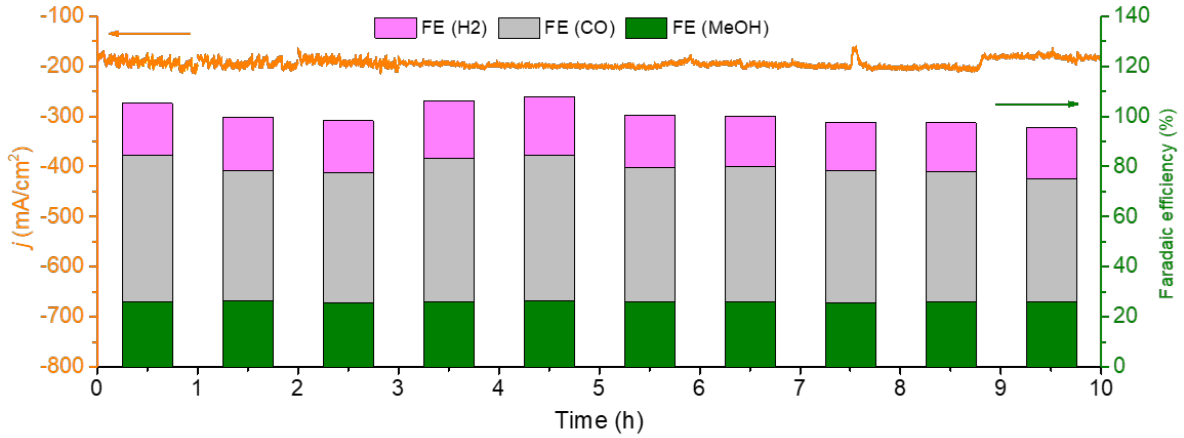

Figure A24: Long-term stability and corresponding FE (CO, H_2 and MeOH) of electrochemical CORR performance for CoPc/SWCNT at -0.9 V vs. RHE.

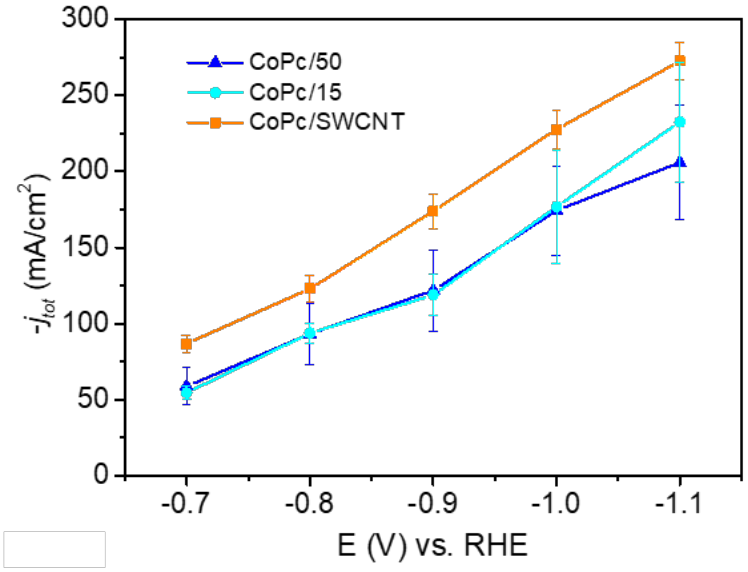

Figure A25: j_{tot} of electrochemical CORR performance in flow cell configuration.

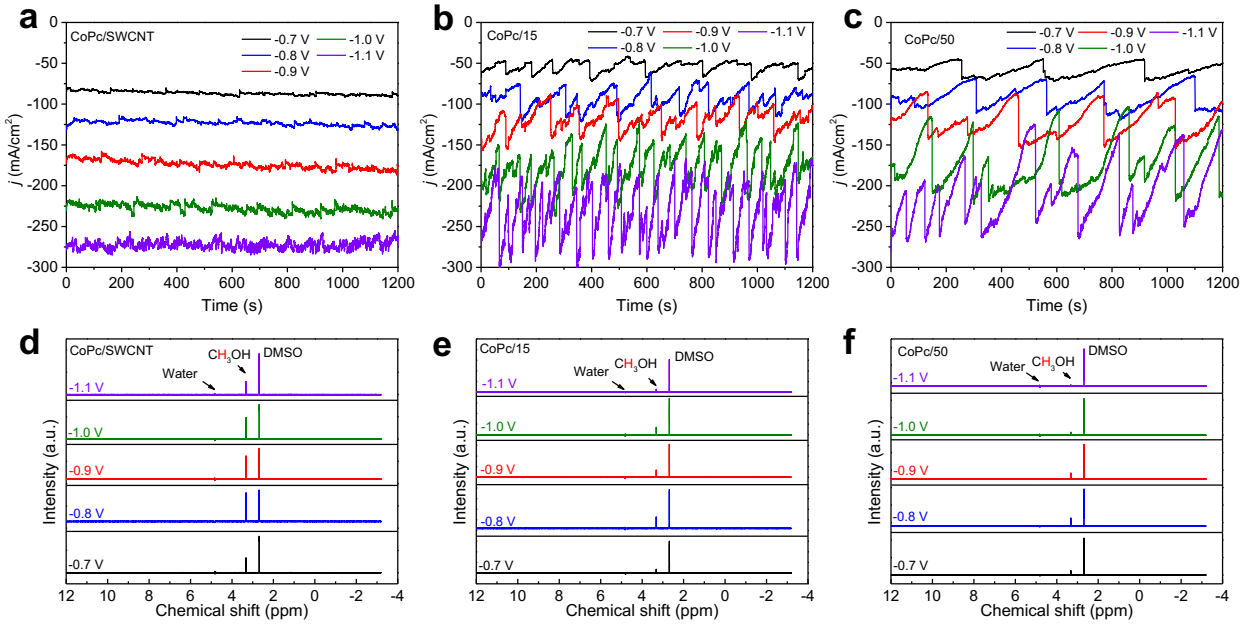

Figure A26: Chronoamperometric curves of (**a**), (**b**) and (**c**) CoPc/SWCNT, CoPc/15 and CoPc/50 in CORR flow cell at different potentials. (**d**), (**e**) and (**f**) ^{1}H-NMR results of catholyte obtained at different potentials.

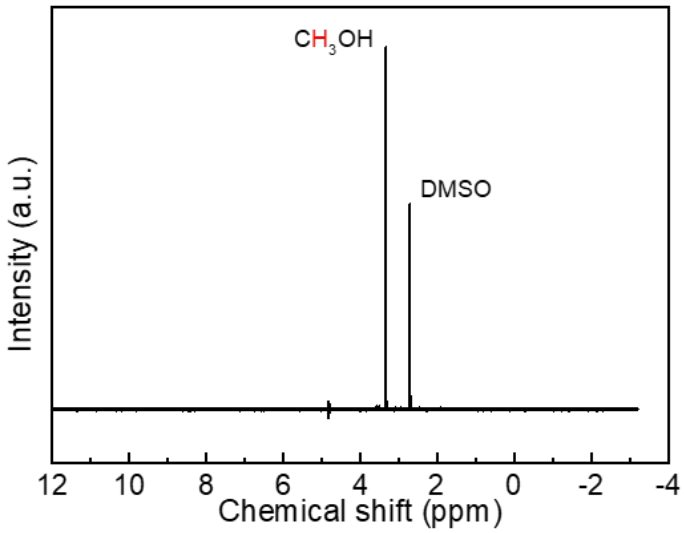

Figure A27: Typical CORR ^{1}H-NMR result of stability test catholyte in first 1h using flow cell.

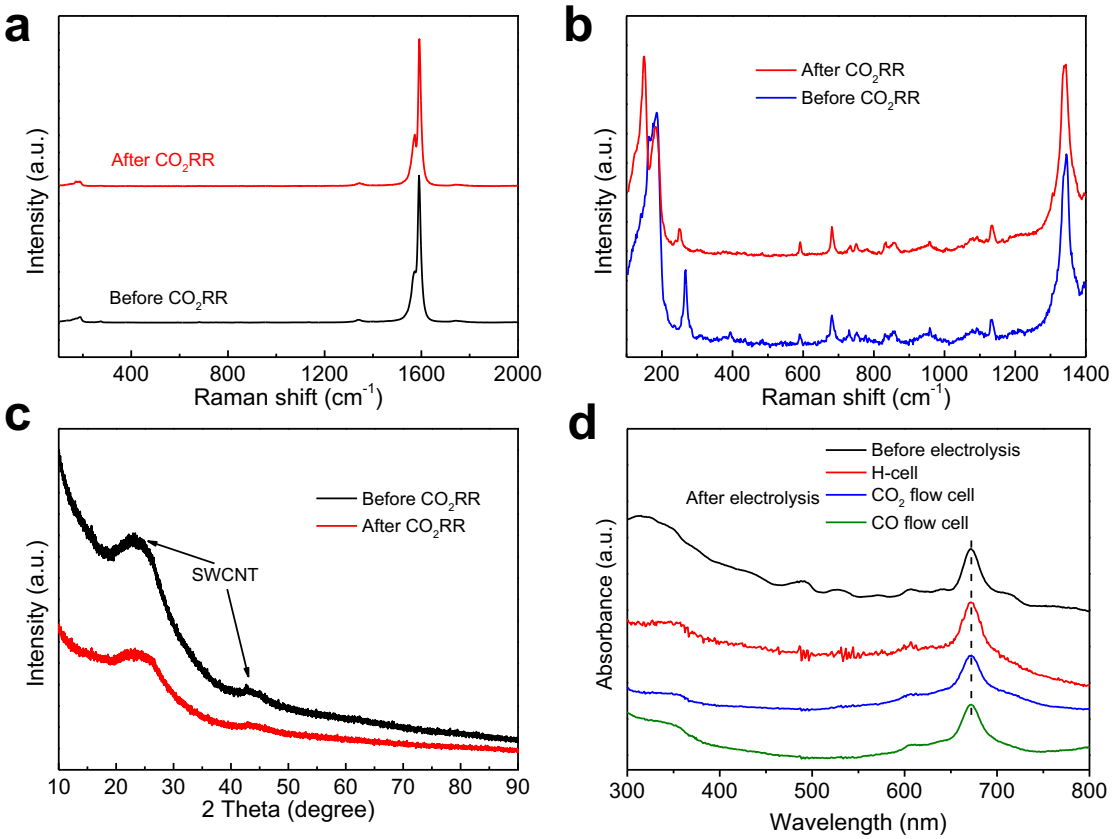

Figure A28: Characterization after the stability test of CoPc/SWCNT. (**a**), (**b**) Raman spectrum and (**c**) XRD patterns of CoPc/SWCNT before and after 10-hours CO_2 electrolysis in H-cell. (**d**) UV-vis spectrum of CoPc/SWCNT after the stability test. The UV-vis tested in ethanol solvent. Red curve: H-cell, blue curve: CO_2RR flow cell and green curve: CORR flow cell.

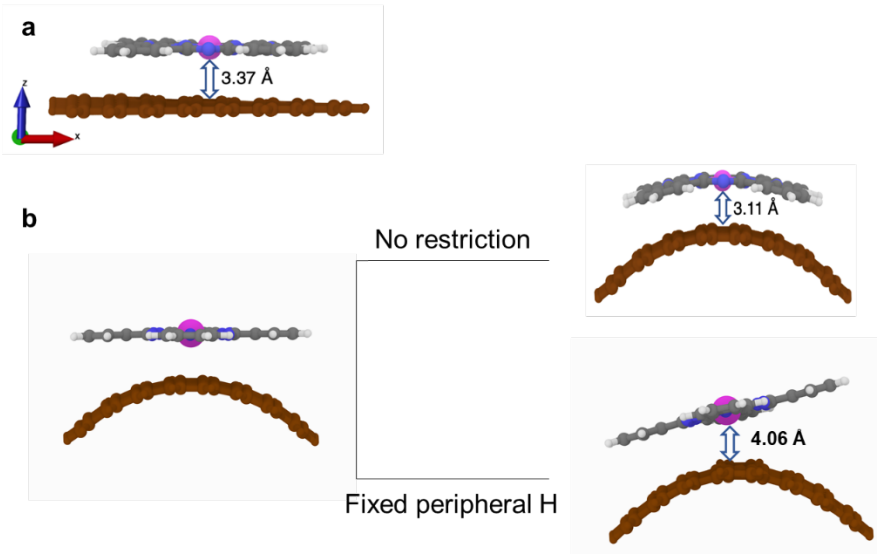

Figure A29: CoPc optimized on (**a**) flat and (**b**) curved $C_{116}H_{28}$ graphitic sheets with UFF+PQEq+UNB model. The brown atoms are the graphitic sheet. Pink, blue, grey, and white atoms are Co, N, C, and H, respectively. CoPc will adopt a curved structure on curved $C_{116}H_{28}$, while fixing the peripheral H to maintain the flat CoPc structure results in the longer Co-$C_{118}H_{28}$ distance.

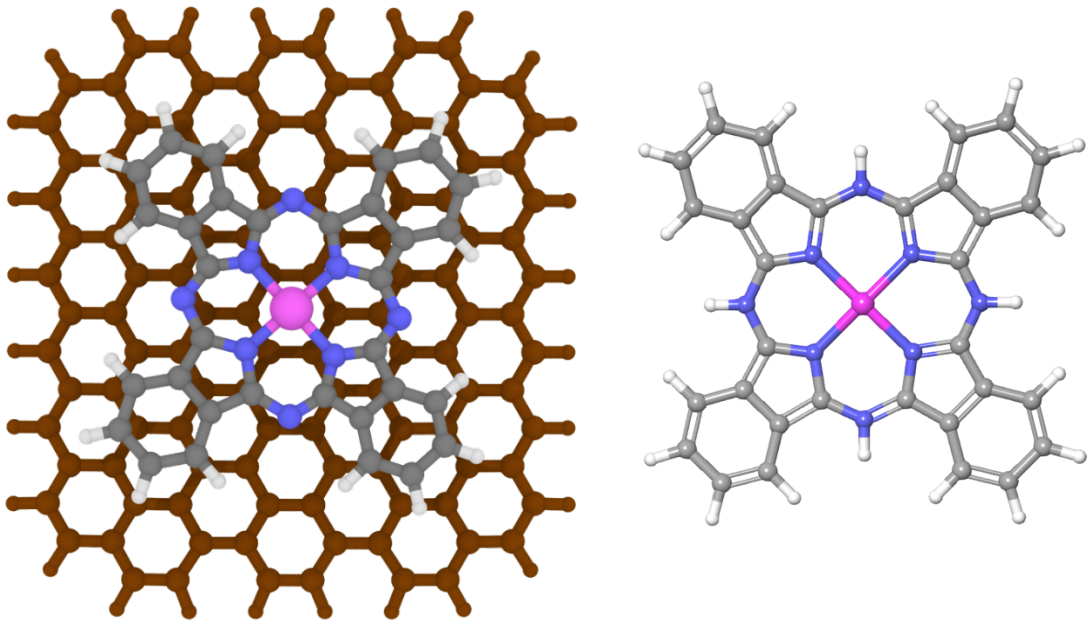

Figure A30: Top view of optimized CoPc on $C_{116}H_{28}$ graphitic sheet (left) and $CoPcH_4$ (right).

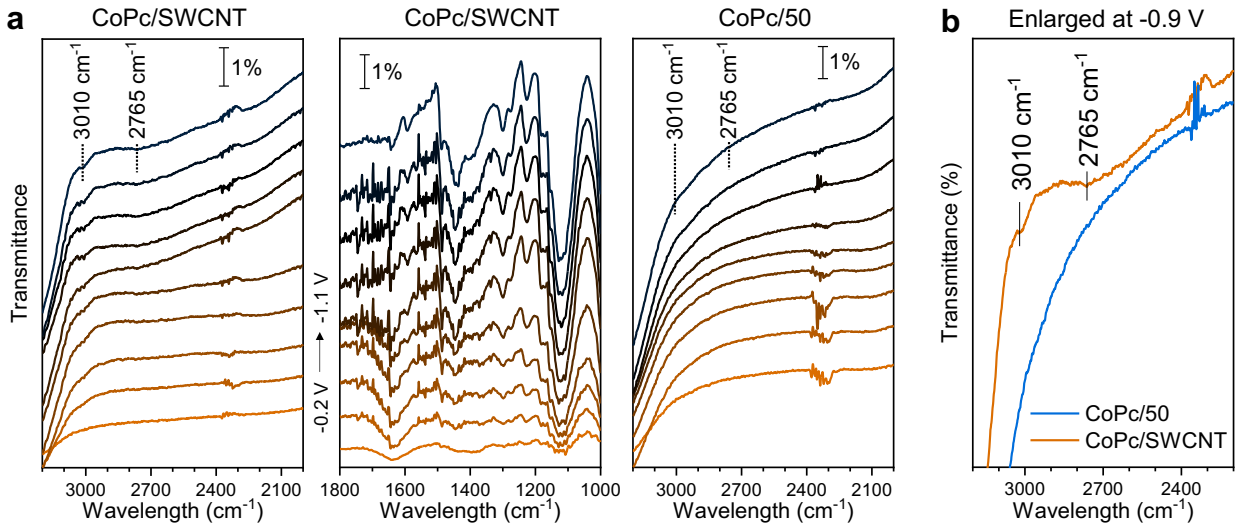

Figure A31: (**a**) In situ ATR-SEIRAS spectra recorded during CO_2RR on CoPc/SWCNT and CoPc/50 from -0.2 V to -1.1 V. (**b**) Comparison of signal at -0.9 V. Note that the 1000–1800 cm^{-1} window contains significant interference from electrolyte. All the potentials are non-iR compensated.

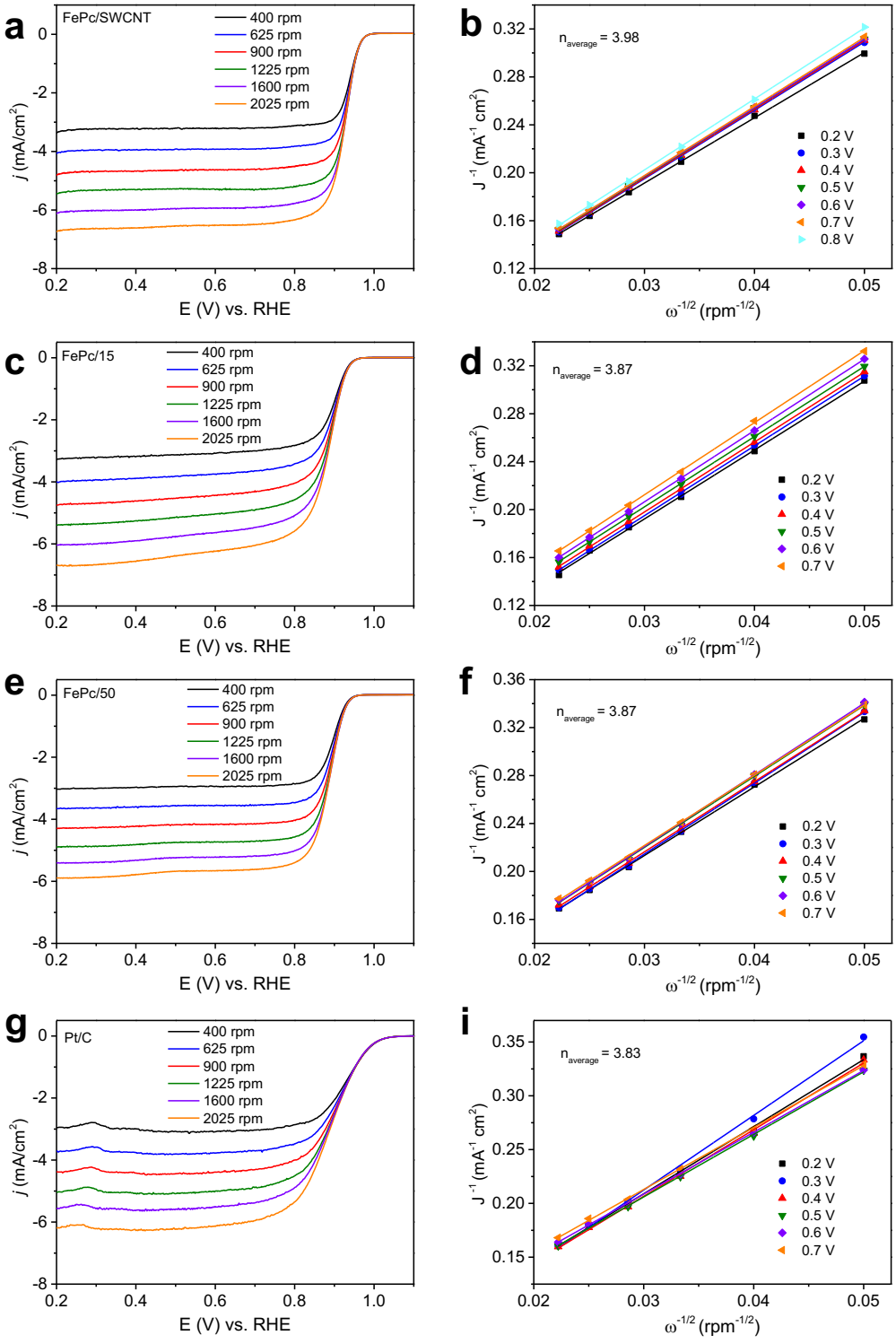

Figure A32: (**a**), (**c**), (**e**) and (**g**) LSV curves of FePc/SWCNT, FePc/15, FePc/50 and commercial Pt/C at different rotation speed. (**b**), (**d**), (**f**) and (**i**) corresponding Koutecky-Levich plots. The curves were collected in O_2-saturated 0.1 M KOH electrolyte at 10 mV/s.

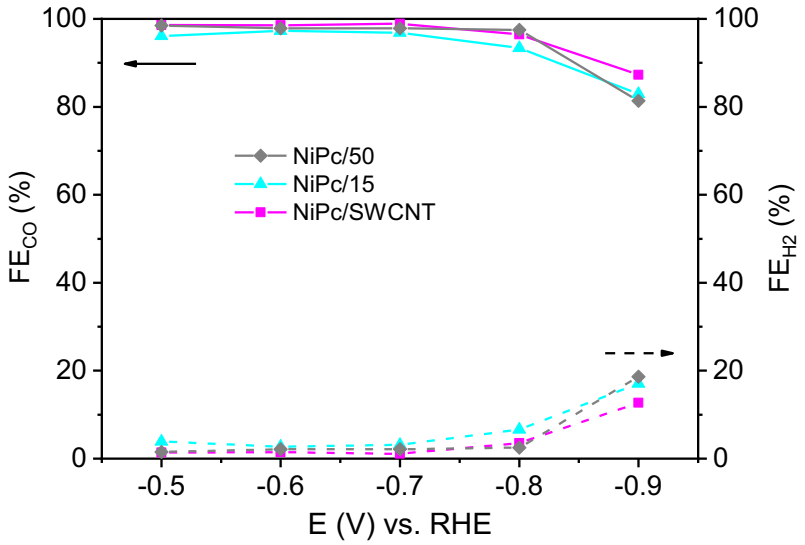

Figure A33: Selectivity of NiPc/SWCNT, NiPc/15 and NiPc/50 in CO_2-saturated 0.5 M $KHCO_3$ electrolyte using H-cell.

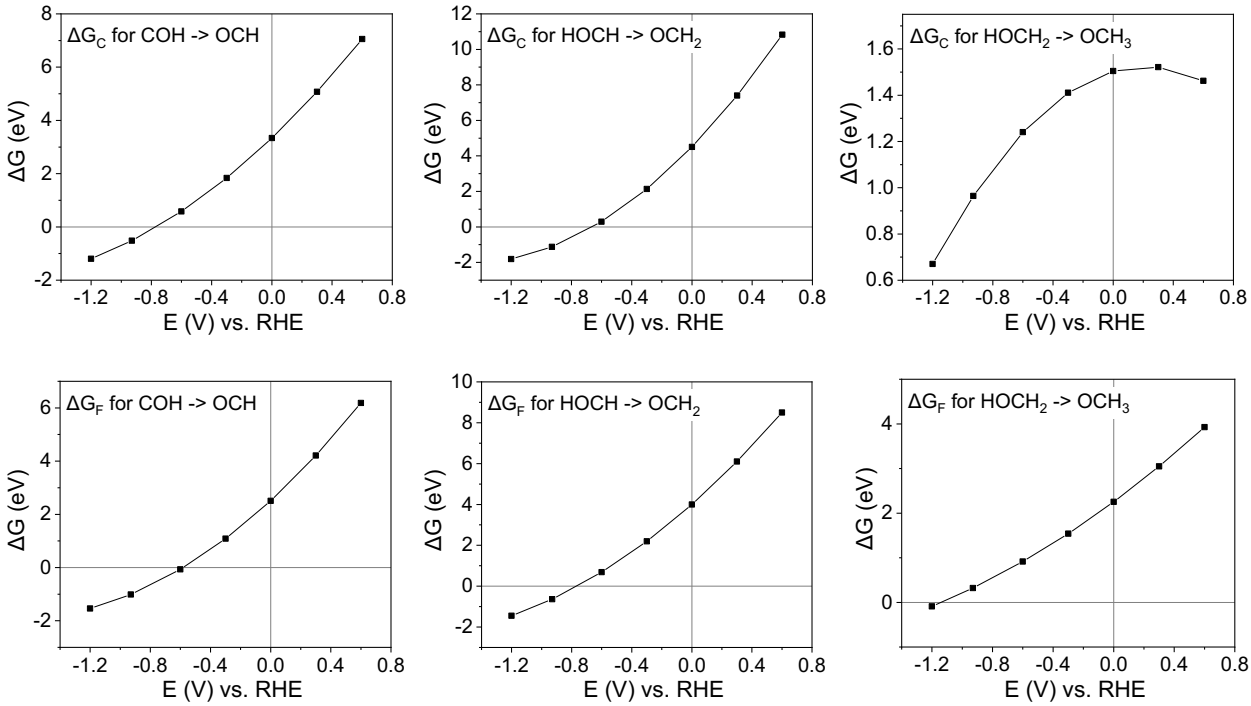

Figure A34: Relative stabilities of *COH vs. *OCH, *HOCH vs. *OCH_2, and *$HOCH_2$ vs. *OCH_3 at various potentials. Top row graphs are free energy changes for the curved CoPc and bottom row graphs are for the flat CoPc.

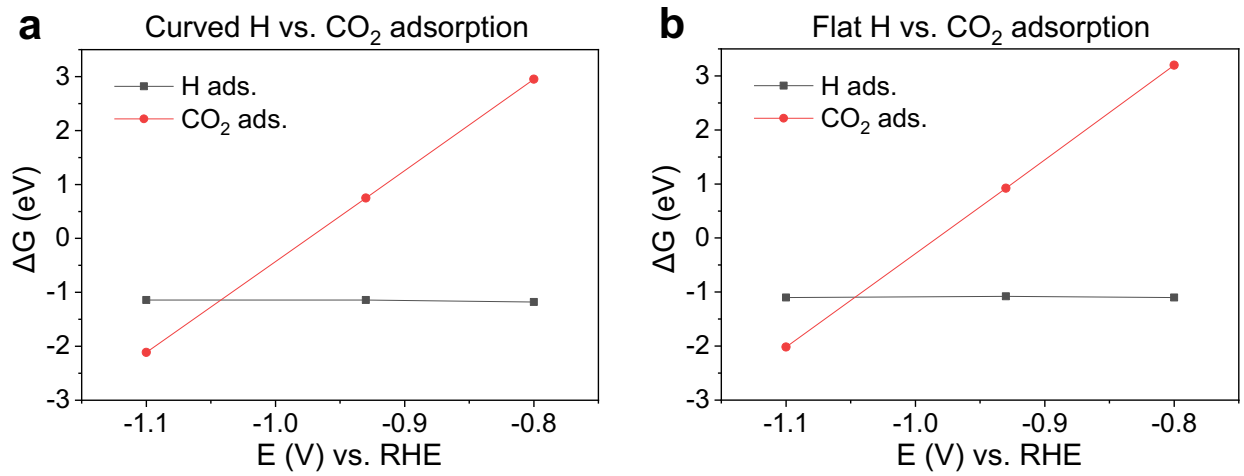

Figure A35: H vs. CO_2 adsorption free energies for the (**a**) curved and (**b**) flat CoPc at various potentials.

Table A1: Summarizing of Co K-edge EXAFS fitting results of CoPc/SWCNT, CoPc/50 and CoPc.

Sample	Path	EXAFS		D-W factor (σ^2), Å^2	Enot, eV	R-factor, %
		CN	R, Å			
CoPc	Co-N1	3.7 (3)	1.875 (1)	0.003 (1)	0.9	0.4
	Co-C1	8.3 (7)	2.844 (1)	0.006 (1)	-5.2	
	Co-N2	3.6 (7)	3.267 (2)	0.003 (2)	0.9	
CoPc/50	Co-N1	4.0 (1)	1.884 (4)	0.003 (1)	2.7	0.9
	Co-C1	7.5 (6)	2.844 (9)	0.004 (1)	-2.8	
	Co-N2	3.9 (6)	3.264 (9)	0.005 (3)	2.7	
	Co-C2 (In CNT)	2.2 (5)	3.382 (8)	0.012 (5)	-2.8	
CoPc/SWCNT	Co-N1	4.3 (2)	1.892 (4)	0.003 (1)	5.2	1.0
	Co-C1	8.4 (6)	2.959 (5)	0.003 (1)	8.4	
	Co-C2	2.2 (6)	3.187 (8)	0.006 (5)	8.4	
	Co-N2	4.1 (6)	3.248 (9)	0.003 (2)	5.2	

*Co K-edge EXAFS fitting results, in which CN is the average coordination number, R is the distance from absorber atom, and σ^2 the Debye–Waller factor. R-factor denotes a quality factor of the fitting, and ΔE_0 the energy shift from the absorption edge energy E_0. Multiple scattering paths of Co-N-C, Co-N-C-N, and Co-C-N are used to improve the fitting results.

Computational Details

All calculations were performed at pH = 7 with a reference oxidation potential of -4.66 eV ($\mu_{ref,SHE}$)[1]. In all tables, coefficients refer to the constants that result when free energy is fitted quadratically versus number of electrons. The top coefficient is the $(n\text{-}n_0)^2$ value, the middle coefficient is the $(n\text{-}n_0)^1$ value, and the bottom coefficient is the $(n\text{-}n_0)^0$ value. n(min;U) is the number of electrons at the minimized U, and G(n(min;U)) is the Grand

Canonical Potential (GCP) at n(min;U).

Table A2: Curved $CoPcH_4(CO)$ energies, ZPE and S contributions, and fitted coefficients.

Vibration contribution (eV)	14.877332	ZPE (kcal/mol)	292.172	S (cal/mol/K)	170.717	
NELECT	ΔNELECT	Free energy [Ha]	electrochemical potential [Ha]	U vs RHE	Free energy [eV]	coefficient
215.5	0.5	-444.80047	-0.1100081	-1.03	-12088.855	0.1420356
216	1	-444.84813	-0.1030838	-1.22	-12090.152	-2.9534591
216.5	1.5	-444.89587	-0.0956739	-1.42	-12091.451	-12087.341
217	2	-444.94101	-0.0882636	-1.62	-12092.679	

Table A3: Curved $CoPcH_4(CO)$ number of electrons and GCPs for given potentials.

U vs RHE	U vs SHE	n(min;U)	n(min;U)-n0	G(n(min;U))
0.6	0.1863	209.111189	-5.8888112	-11097.612
0.3	-0.1137	210.167263	-4.8327375	-11160.503
0	-0.4137	211.223336	-3.7766637	-11223.712
-0.3	-0.7137	212.27941	-2.72059	-11287.237
-0.6	-1.0137	213.335484	-1.6645162	-11351.08
-1	-1.4137	214.743582	-0.2564179	-11436.695
-1.2	-1.6137	215.447631	0.44763129	-11479.715
-1.4	-1.8137	216.15168	1.15168046	-11522.875

Table A4: Curved $CoPcH_4$ energies, ZPE and S contributions, and fitted coefficients.

Vibration contribution (eV)	15.591068	ZPE (kcal/mol)	290.736	S (cal/mol/K)	172.914

NELECT	ΔNELECT	Free energy [Ha]	electrochemical potential [Ha]	U vs RHE	Free energy [eV]	coefficient
215.5	0.5	-444.77673	-0.1025524	-1.24	-12087.495	0.259065
216	1	-444.82526	-0.0914783	-1.54	-12088.816	-3.0375908
216.5	1.5	-444.86939	-0.0841624	-1.74	-12090.017	-12086.04
217	2	-444.9084	-0.0760792	-1.96	-12091.078	

Table A5: Curved $CoPcH_4$ number of electrons and GCPs for given potentials.

U vs RHE	U vs SHE	n(min;U)	n(min;U)-n0	G(n(min;U))
0.6	0.1863	211.93376	-3.0662402	-11093.822
0.3	-0.1137	212.512766	-2.4872342	-11157.489
0	-0.4137	213.091772	-1.9082283	-11221.329
-0.3	-0.7137	213.670778	-1.3292224	-11285.344
-0.6	-1.0137	214.249784	-0.7502164	-11349.532
-1	-1.4137	215.021791	0.02179149	-11435.386
-1.2	-1.6137	215.407795	0.40779545	-11478.429
-1.4	-1.8137	215.793799	0.79379941	-11521.549

Table A6: Flat $CoPcH_4(CO)$ energies, ZPE and S contributions, and fitted coefficients.

Vibration contribution (eV)	15.94990	ZPE (kcal/mol)	292.727	S (cal/mol/K)	193.989	
NELECT	ΔNELECT	Free energy [Ha]	electrochemical potential [Ha]	U vs RHE	Free energy [eV]	coefficient
215.5	0.5	-444.82261	-0.1122098	-0.97	-12088.385	0.111084
216	1	-444.87248	-0.1019051	-1.25	-12089.742	-2.9218921
216.5	1.5	-444.9222	-0.0952519	-1.43	-12091.095	-12086.947
217	2	-444.96799	-0.0904633	-1.56	-12092.341	

Table A7: Flat $CoPcH_4(CO)$ number of electrons and GCPs for given potentials.

U vs RHE	U vs SHE	n(min;U)	n(min;U)-n0	G(n(min;U))
0.6	0.1863	207.32832	-7.6716798	-11098.83
0.3	-0.1137	208.678645	-6.3213552	-11161.231
0	-0.4137	210.028969	-4.9710306	-11224.037
-0.3	-0.7137	211.379294	-3.620706	-11287.249
-0.6	-1.0137	212.729619	-2.2703814	-11350.865
-1	-1.4137	214.530051	-0.4699486	-11436.317
-1.2	-1.6137	215.430268	0.43026779	-11479.313
-1.4	-1.8137	216.330484	1.33048418	-11522.489

Table A8: Flat $CoPcH_4$ energies, ZPE and S contributions, and fitted coefficients.

Vibration contribution (eV)	14.87454	ZPE (kcal/mol)	289.606	S (cal/mol/K)	179.107	
NELECT	ΔNELECT	Free energy [Ha]	electrochemical potential [Ha]	U vs RHE	Free energy [eV]	coefficient
215.5	0.5	-444.7982	-0.1047159	-1.18	-12088.796	0.1968552
216	1	-444.84797	-0.0941056	-1.47	-12090.15	-2.9928245
216.5	1.5	-444.89361	-0.0873548	-1.65	-12091.393	-12087.35
217	2	-444.93615	-0.0821337	-1.79	-12092.55	

Table A9: Flat $CoPcH_4$ number of electrons and GCPs for given potentials.

U vs RHE	U vs SHE	n(min;U)	n(min;U)-n0	G(n(min;U))
0.6	0.1863	210.851072	-4.1489276	-11096.084
0.3	-0.1137	211.613054	-3.386946	-11159.454
0	-0.4137	212.375036	-2.6249644	-11223.052

-0.3	-0.7137	213.137017	-1.8629829	-11286.879
-0.6	-1.0137	213.898999	-1.1010013	-11350.934
-1	-1.4137	214.914974	-0.0850258	-11436.697
-1.2	-1.6137	215.422962	0.42296191	-11479.731
-1.4	-1.8137	215.93095	0.93094963	-11522.866

Table A10: Energies for CO.

	Free energy [Ha]	ZPE (kcal/mol)	S (cal/mol/K)
CO	-21.745573	3.156	47.237

Table A11: Geometric values for flat and curved $CoPcH_4(CO)$ at varying electron count.

Flat	$n\text{-}n_0$	N-Co-N (degrees)	Co-C (Å)	C-O (Å)
	0.5	158.3	1.77	1.18
	1	151.2	1.75	1.18
	1.5	146.5	1.72	1.2
	2	145.8	1.72	1.2
Curved	0.5	154.5	1.76	1.18
	1	144.4	1.73	1.19
	1.5	140.1	1.72	1.2
	2	137.3	1.7	1.21

Method A1: Calculation of the ideal bending angle of CoPc molecule on SWCNT and

MWCNT.

The calculation is not based on a force field calculation. It is based on the following assumption: the interlayer distance between CoPc and SWCNT is 0.3 nm, the diameter of the CoPc molecule is ~1.34 nm, the CoPc is fully elastic and it can curve along the surface of CNT. Take a CNT with a diameter of 1 nm for example, ideally its bending angle is:

$$\theta = \frac{1.34}{(1 + 0.3 * 2) * \pi} * 360° = 96°$$

Method A2: Calculation of tandem overall Faradaic efficiency for reduction of CO_2 to MeOH.

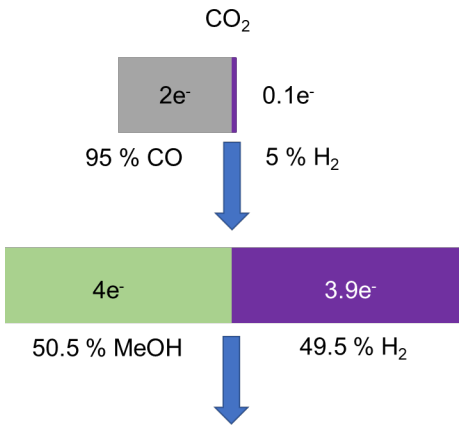

$$FE_{MeOH} = \frac{6e^-}{(0.1 + 2 + 3.9 + 4)e^-} = 60\%$$

Methane Formation: Methane formation often competes with methanol formation in CO_2RR. Following *CO formation, methane formation can occur through formation of *C, *CH, *CH_2, or *O:

*COH → *C (+ H_2O) → *CH → *CH_2 → *CH_3 → CH_4

*HOCH → *CH (+ H_2O) → *CH_2 → *CH_3 → CH_4

*$HOCH_2$ → *CH_2 (+ H_2O) → *CH_3 → CH_4

*OCH_3 → *O (+ CH_4)

The conversion of *COH to *C (reduction at O to form water) is +0.81 and +1.29 eV for curved and flat CoPc. The conversion of *HOCH to *CH (reduction at O to form water) is +0.63 and +0.71 eV for curved and flat CoPc. Conversion of *$HOCH_2$ to *CH_2 (reduction at O to form water) is -0.52 and -0.59 eV for curved and flat CoPc. Finally, the conversion of *OCH_3 to *O (reduction at C to form methane) is -0.03 and +0.31 eV for curved and flat CoPc.

These results indicate that for both curved and flat CoPc, *C formation is less favorable than *HOCH, *CH formation is less favorable than forming *$HOCH_2$, *CH_2 is less favorable than *MeOH, and *O (while exergonic) is less favorable than *MeOH, such that methanol formation will dominate over methane formation. This agrees with experiment in which no methane is detected for curved or flat CoPc.

Appendix B

Appendix for: Improving Iron Phthalocyanine Electrocatalytic Oxygen Reduction via Molecular Curvature

Reproduced with permission from:

Jianjun Su, Yun Song, Libei Huang, Yong Liu, Geng Li, Yinger Xin, Pei Xiong, Molly Meng-Jung Li, Haoran Wu, Minghui Zhu, Hao Ming Chen, Jianyu Zhang, Ben Zhong Tang, Marc Robert, Ruquan Ye, William A. Goddard III.

Manuscript submitted to Nature Chemical Engineering

Definitions:
ZPE-TS: the summation of the phonon-derived zero-point energy and entropy
NELECT: total number of electrons
ΔNELECT: difference in electrons relative to the 0-charge state
U v RHE: potential versus reversible hydrogen electrode in units of volts (V)
U v SHE: potential versus standard hydrogen electrode in units of volts (V)
n(min;U): equilibrium total number of electrons for a given potential
n(min;U)-n0: equilibrium difference in electrons relative to the 0-charge state for a given potential
G(n(min;U)): equilibrium Grand canonical free energy for a given potential in units of electronvolts (eV)

B1 Computational Methods

Intermediate adsorption energies were calculated via Equations B1-B3:

$$\Delta G_{*O} = G_{*O} + G_{H_2} - G_{*} - G_{H_2O} \qquad \text{(Equation B1)}$$

$$\Delta G_{*OH} = G_{*OH} + \frac{1}{2} * G_{H_2} - G_{*} - G_{H_2O} \qquad \text{(Equation B2)}$$

$$\Delta G_{*OOH} = G_{*OOH} + \frac{3}{2} * G_{H_2} - G_{*} - 2 * G_{H_2O} \qquad \text{(Equation B3)}$$

In Equations B1-B3, G's are Gibbs free energies, which can be rewritten as $H - TS$, where H is the enthalpy and S is the entropy. The oxygen reduction reaction free energy landscape can be computed via the intermediate adsorption energies:

$$\Delta G_{* \rightarrow *OOH} = \Delta G_{*OOH} - 4.92 + eU + pH * k_B T * \ln(10) \quad \text{(Equation B4)}$$

$$\Delta G_{*OOH \rightarrow *O} = \Delta G_{*O} - \Delta G_{*OOH} + eU + pH * k_B T * \ln(10) \quad \text{(Equation B5)}$$

$$\Delta G_{*O \rightarrow *OH} = \Delta G_{*OH} - \Delta G_{*O} + eU + pH * k_B T * \ln(10) \quad \text{(Equation B6)}$$

$$\Delta G_{*O \rightarrow OH^-} = -\Delta G_{*OH} + eU + pH * k_B T * \ln(10) \quad \text{(Equation B7)}$$

In Equations B4-B7, U is the applied potential in volts; U is multiplied by the unit electron (e) to yield units of eV. k_B is Boltzmann's constant.

Table B1: Electronic energies (Ha) at different charges for flat FePc.

NELECT	ΔNELECT	Free energy [Ha]
216	0	-397.77301
215.5	-0.5	-397.68651
214.5	-1.5	-397.48876

Table B2: Electronic energies (Ha) at different charges for flat FePc–OO.

NELECT	ΔNELECT	Free energy [Ha]
216	0	-429.79436
215.5	-0.5	-429.70118
215	-1	-429.59658

Table B3: Electronic energies (Ha) at different charges for flat FePc–OOH.

NELECT	ΔNELECT	Free energy [Ha]
217	0	-430.41398
216.5	-0.5	-430.33012
216	-1	-430.23883

Table B4: Electronic energies (Ha) at different charges for flat FePc–O.

NELECT	ΔNELECT	Free energy [Ha]
210	0	-413.76677
209.5	-0.5	-413.68527
209	-1	-413.5869

Table B5: Electronic energies (Ha) at different charges for flat FePc–OH.

NELECT	ΔNELECT	Free energy [Ha]
211	0	-414.3957
210.5	-0.5	-414.33438
210	-1	-414.24238

Table B6: Electronic energies (Ha) at different charges for flat FePc–OH_2.

NELECT	ΔNELECT	Free energy [Ha]
212	0	-415.06227
211	-1	-414.88236
210.5	-1.5	-414.78206

Table B7: Electronic energies (Ha) at different charges for curved FePc.

NELECT	ΔNELECT	Free energy [Ha]
216	0	-397.75527
215.5	-0.5	-397.66863
215	-1	-397.57351

Table B8: Electronic energies (Ha) at different charges for curved FePc–OO.

NELECT	ΔNELECT	Free energy [Ha]
216	0	-429.77196
215.5	-0.5	-429.68084
215	-1	-429.58381

Table B9: Electronic energies (Ha) at different charges for curved FePc–OOH.

NELECT	ΔNELECT	Free energy [Ha]
217	0	-430.39828

216.5	-0.5	-430.31449
216	-1	-430.22336

Table B10: Electronic energies (Ha) at different charges for curved FePc–O.

NELECT	ΔNELECT	Free energy [Ha]
210	0	-413.76092
209.5	-0.5	-413.67036
209	-1	-413.5724

Table B11: Electronic energies (Ha) at different charges for curved FePc–OH.

NELECT	ΔNELECT	Free energy [Ha]
211	0	-414.39857
210.5	-0.5	-414.31328
210	-1	-414.22101

Table B12: Electronic energies (Ha) at different charges for curved FePc–OH_2.

NELECT	ΔNELECT	Free energy [Ha]
212	0	-415.0442
211.5	-0.5	-414.95774
211	-1	-414.86348

Table B13: Grand canonical potential energy (eV) at different potentials (V) for flat FePc.

U vs RHE	U vs SHE	n(min;U)	n(min;U)-n0	G(n(min;U))
0	-0.7683	216.65968	0.65968038	-9983.5486
0.3	-0.4683	216.325337	0.32533671	-9918.6009
0.6	-0.1683	215.990993	-0.009007	-9853.7534
0.8	0.0317	215.768097	-0.2319027	-9810.5775
0.9	0.1317	215.656649	-0.3433506	-9789.0063
1	0.2317	215.545201	-0.4547985	-9767.4462

Table B14: Grand canonical potential energy (eV) at different potentials (V) for flat FePc–OO.

U vs RHE	U vs SHE	n(min;U)	n(min;U)-n0	G(n(min;U))
0	-0.7683	216.699105	0.69910546	-10854.95
0.3	-0.4683	216.457729	0.45772934	-10789.976

0.6	-0.1683	216.216353	0.21635322	-10725.075
0.8	0.0317	216.055436	0.05543581	-10681.848
0.9	0.1317	215.974977	-0.0250229	-10660.246
1	0.2317	215.894518	-0.1054816	-10638.653

Table B15: Grand canonical potential energy (eV) at different potentials (V) for flat FePc–OOH.

U vs RHE	U vs SHE	n(min;U)	n(min;U)-n0	G(n(min;U))
0	-0.7683	217.268282	0.26828155	-10867.328
0.3	-0.4683	217.009859	0.00985879	-10802.186
0.6	-0.1683	216.751436	-0.248564	-10737.122
0.8	0.0317	216.579154	-0.4208458	-10693.789
0.9	0.1317	216.493013	-0.5069867	-10672.136
1	0.2317	216.406872	-0.5931277	-10650.491

Table B16: Grand canonical potential energy (eV) at different potentials (V) for flat FePc–O.

U vs RHE	U vs SHE	n(min;U)	n(min;U)-n0	G(n(min;U))
0	-0.7683	210.273954	0.2739538	-10441.938
0.3	-0.4683	210.035593	0.03559252	-10378.892
0.6	-0.1683	209.797231	-0.2027688	-10315.917
0.8	0.0317	209.638324	-0.3616763	-10273.973
0.9	0.1317	209.55887	-0.44113	-10253.013
1	0.2317	209.479416	-0.5205838	-10232.061

Table B17: Grand canonical potential energy (eV) at different potentials (V) for flat FePc–OH.

U vs RHE	U vs SHE	n(min;U)	n(min;U)-n0	G(n(min;U))
0	-0.7683	210.596938	-0.4030622	-10455.06
0.3	-0.4683	210.472849	-0.5271512	-10391.9
0.6	-0.1683	210.34876	-0.6512401	-10328.776
0.8	0.0317	210.266034	-0.7339661	-10286.715
0.9	0.1317	210.224671	-0.775329	-10265.69
1	0.2317	210.183308	-0.816692	-10244.67

Table B18: Grand canonical potential energy (eV) at different potentials (V) for flat FePc–OH_2.

U vs RHE	U vs SHE	n(min;U)	n(min;U)-n0	G(n(min;U))
0	-0.7683	212.839064	0.83906374	-10469.047

0.3	-0.4683	212.438985	0.43898488	-10405.255
0.6	-0.1683	212.038906	0.03890602	-10341.583
0.8	0.0317	211.772187	-0.2278132	-10299.202
0.9	0.1317	211.638827	-0.3611728	-10278.032
1	0.2317	211.505468	-0.4945325	-10256.874

Table B19: Grand canonical potential energy (eV) at different potentials (V) for curved FePc.

U vs RHE	U vs SHE	n(min;U)	n(min;U)-n0	G(n(min;U))
0	-0.7683	216.779842	0.77984244	-9983.1224
0.3	-0.4683	216.413867	0.41386653	-9918.1434
0.6	-0.1683	216.047891	0.04789062	-9853.2741
0.8	0.0317	215.803907	-0.1960933	-9810.0889
0.9	0.1317	215.681915	-0.3180853	-9788.5147
1	0.2317	215.559923	-0.4400773	-9766.9526

Table B20: Grand canonical potential energy (eV) at different potentials (V) for curved FePc–OO.

U vs RHE	U vs SHE	n(min;U)	n(min;U)-n0	G(n(min;U))
0	-0.7683	217.514406	1.51440616	-10854.74
0.3	-0.4683	217.021617	1.02161666	-10789.559
0.6	-0.1683	216.528827	0.52882716	-10724.527
0.8	0.0317	216.200301	0.20030083	-10681.254
0.9	0.1317	216.036038	0.03603766	-10659.642
1	0.2317	215.871774	-0.1282255	-10638.046

Table B21: Grand canonical potential energy (eV) at different potentials (V) for curved FePc–OOH.

U vs RHE	U vs SHE	n(min;U)	n(min;U)-n0	G(n(min;U))
0	-0.7683	217.27528	0.27527952	-10866.906
0.3	-0.4683	217.012571	0.01257115	-10801.763
0.6	-0.1683	216.749863	-0.2501372	-10736.699
0.8	0.0317	216.574724	-0.4252761	-10693.366
0.9	0.1317	216.487154	-0.5128456	-10671.713
1	0.2317	216.399585	-0.600415	-10650.069

Table B22: Grand canonical potential energy (eV) at different potentials (V) for curved FePc–O.

U vs RHE	U vs SHE	n(min;U)	n(min;U)-n0	G(n(min;U))

0	-0.7683	211.17521	1.17520992	-10442.207
0.3	-0.4683	210.768245	0.76824502	-10378.916
0.6	-0.1683	210.36128	0.36128011	-10315.746
0.8	0.0317	210.08997	0.08997018	-10273.701
0.9	0.1317	209.954315	-0.0456848	-10252.699
1	0.2317	209.81866	-0.1813398	-10231.71

Table B23: Grand canonical potential energy (eV) at different potentials (V) for curved FePc–OH.

U vs RHE	U vs SHE	n(min;U)	n(min;U)-n0	G(n(min;U))
0	-0.7683	211.374219	0.37421935	-10454.998
0.3	-0.4683	211.100101	0.10010054	-10391.627
0.6	-0.1683	210.825982	-0.1740183	-10328.338
0.8	0.0317	210.643236	-0.3567642	-10286.191
0.9	0.1317	210.551863	-0.4481371	-10265.132
1	0.2317	210.46049	-0.53951	-10244.081

Table B24: Grand canonical potential energy (eV) at different potentials (V) for curved FePc–OH_2.

U vs RHE	U vs SHE	n(min;U)	n(min;U)-n0	G(n(min;U))
0	-0.7683	212.801974	0.80197361	-10468.586
0.3	-0.4683	212.420067	0.42006702	-10404.803
0.6	-0.1683	212.03816	0.03816042	-10341.134
0.8	0.0317	211.783556	-0.216444	-10298.752
0.9	0.1317	211.656254	-0.3437462	-10277.58
1	0.2317	211.528952	-0.4710484	-10256.421

Table B25: ωB97M-V/def2-TZVP Electronic energies (Ha) for different flat and curved intermediate FePc-C_{24} structures.

Intermediate	Spin	Flat	Curved
substrate	Singlet	-3852.8951	-3852.8198
	Triplet	-3852.9352	-3852.865
	Quintet	-3852.8514	-3852.8443
*OO	Singlet	-4003.2432	-4003.1742
	Triplet	-4003.2648	-4003.1949
	Quintet	-4003.2855	-4003.172
	Septet	-4003.2539	-4003.1885
*OOH	Doublet	-4003.9035	-4003.8361

	Quartet	-4003.9059	-4003.8392
	Sextet	-4003.8807	-4003.819
*O	Singlet	-3928.0629	-3927.9947
	Triplet	-3928.1063	-3928.0374
	Quintet	-3928.0377	-3928.0163
	Septet	-3928.0996	-3928.0367
*OH	Doublet	-3928.7508	-3928.6824
	Quartet	-3928.7579	-3928.6921
	sextet	-3928.7324	-3928.6713

Table B26: Intermediate zero-point energies plus entropies at 298 K (eV).

Intermediate	ZPE - TS
*O	0.0397
*OH	0.2978
*OOH	0.3728
*OO	0.0488

Table B27: ωB97M-V/def2-TZVP intermediate FePc-C_{24} binding energies (eV).

Intermediate	Flat	Curved
ΔG_{*O}	2.69	2.65
ΔG_{*OH}	0.87	0.75
ΔG_{*OOH}	4.22	4.13

Table B28: ωB97M-V/def2-TZVP intermediate FePc-C_{24} Mulliken charges.

Flat	intermediate	O1	O2	H Q	Total Q
	OOH	-0.4134	-0.3675	0.3681	-0.4128
	O	-0.4423	--	--	-0.4423
	OH	-0.7401	--	0.3392	-0.4009
Curved	OOH	-0.4161	-0.3631	0.3686	-0.4106
	O	-0.4447	--	--	-0.4447
	OH	-0.7489	--	0.3429	-0.406

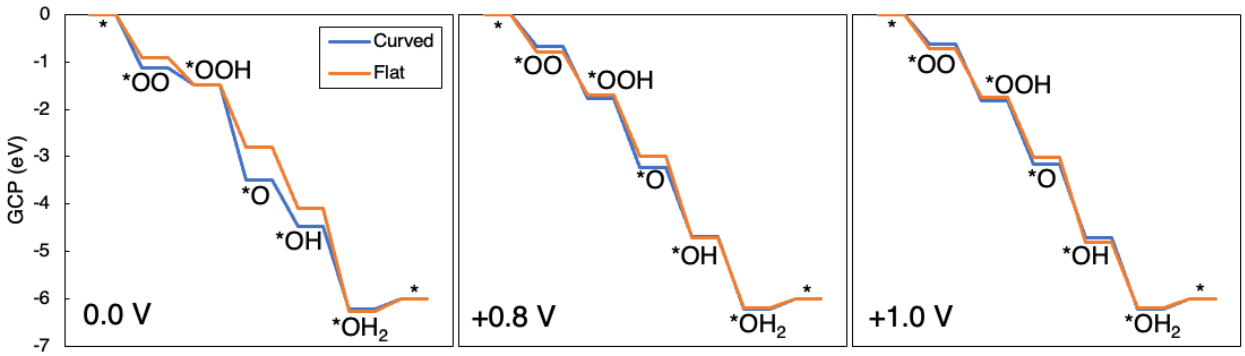

Figure B1: Grand canonical potential energies (eV) at 298 K and different potentials (vs. RHE) for the FePc-catalyzed oxygen reduction reaction according to the PBE-D3 level of theory.

B2 Kinetic Modelling

While the reaction kinetics cannot be ascertained from the thermodynamic picture that we illustrated in chapter 3, we can estimate the electrode kinetics via a simple model that assumes the rate-determining energy barrier is equal to the thermodynamic free energy difference of either $\Delta G_{O\rightarrow OH}$ or $\Delta G_{OH\rightarrow OH2}$ (whichever is larger).[1,2] Rigorous calculations have previously showed this approximation to work well for systems in which transfer of a solvated proton to *OH is exergonic.[3] The reaction's rate constant (k) can be written in the usual form (Equation B7).

$$k(U) = k_0 e^{-\Delta G(U)/kT} \qquad \text{(Equation B7)}$$

Here the rate constant is a function of the exponential of the free energy barrier, and the prefactor (k_0) contains information about the rate of proton recombination with a catalyst electron. If we approximate the current density (i) to be proportional to k times some

fraction which represents the portion of active catalyst sites on a catalyst area (N_{sites}/A, Equation B8), we can rewrite i to be a function of both ΔG and of N_{sites}/A (Equation B9).

$$i(U) = 2e\,{}^{N_{sites}}\!/_{A}\,k(U) \qquad \text{(Equation B8)}$$

$$i(U) = \tilde{\imath}e^{\,-\Delta G(U)/kT} \qquad \text{(Equation B9)}$$

For the sake of comparison, we adopt $k_0 = 200$ $s^{-1}site^{-1}$, which was previously derived for proton transfer on metal catalysts in the absence of a driving force; this yields $\tilde{\imath} = 96$ mA/cm^2. We can utilize ORR's known $U_0 = 1.23$ V to deduce a Butler-Volmer relation (Equation B10).

$$U = U_0 - \beta \log\left({}^{i}\!/_{i_0}\right) \qquad \text{(Equation B10)}$$

In which i_0 is the current density at 1.23 V, and β is the Tafel slope of $kT\ln(10/e)$, which at 300 K is ~0.06 V. The resulting potential vs. current density relation without any fitted values is plotted in Figure B2.

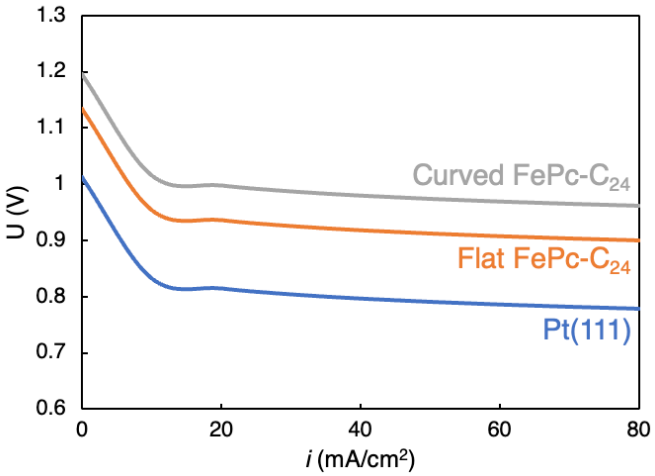

Figure B2: Computed potential vs. current density for the Pt(111), flat $FePcH_4$, and curved $FePcH_4$.

For the potential vs. current density plot, we used $\Delta G_{O\rightarrow OH} = 0.45$ eV for Pt(111), which was previously calculated by Nørskov.[1] For flat FePc-C_{24} we used $\Delta G_{OH\rightarrow H2O} = 0.33$ eV, and for curved FePc-C_{24} we used $\Delta G_{OH\rightarrow H2O} = 0.27$ eV. Based on these limiting free energy steps, the Butler-Volmer relation reveals that flat FePc-C_{24} performs marginally better than conventional Pt(111), and curved FePc-C_{24} outperforms both.

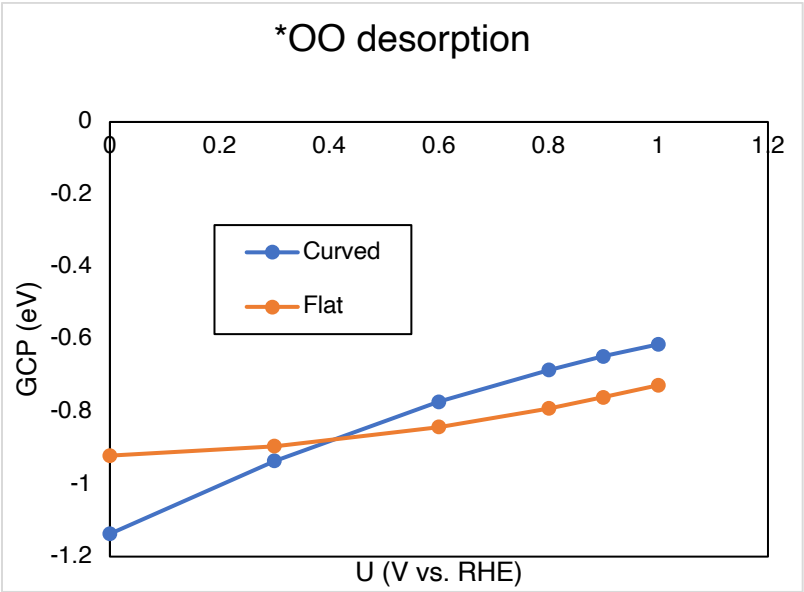

Figure B3: *OO desorption energy (eV) vs. applied potential (V vs. RHE) for curved and flat FePc-C_{24}.

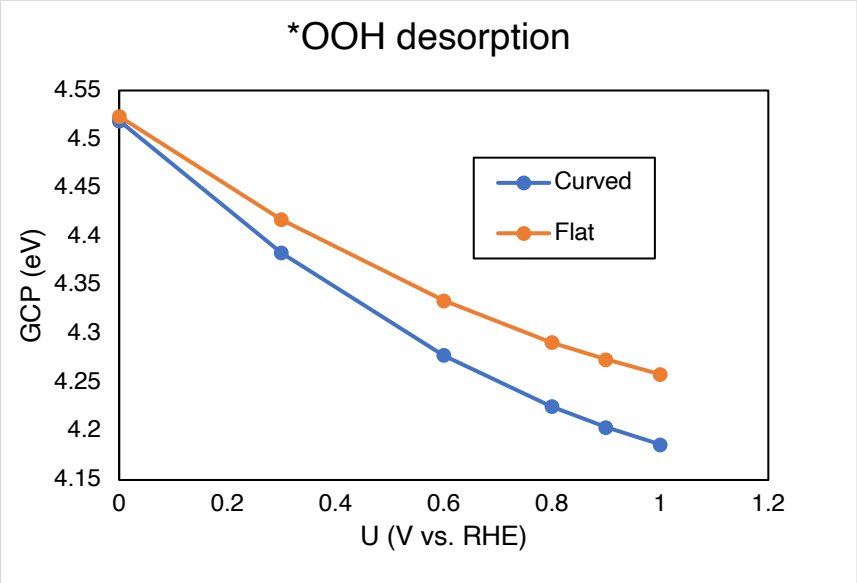

Figure B4: *OOH desorption energy (eV) vs. applied potential (V vs. RHE) for curved and flat FePc-C_{24}.

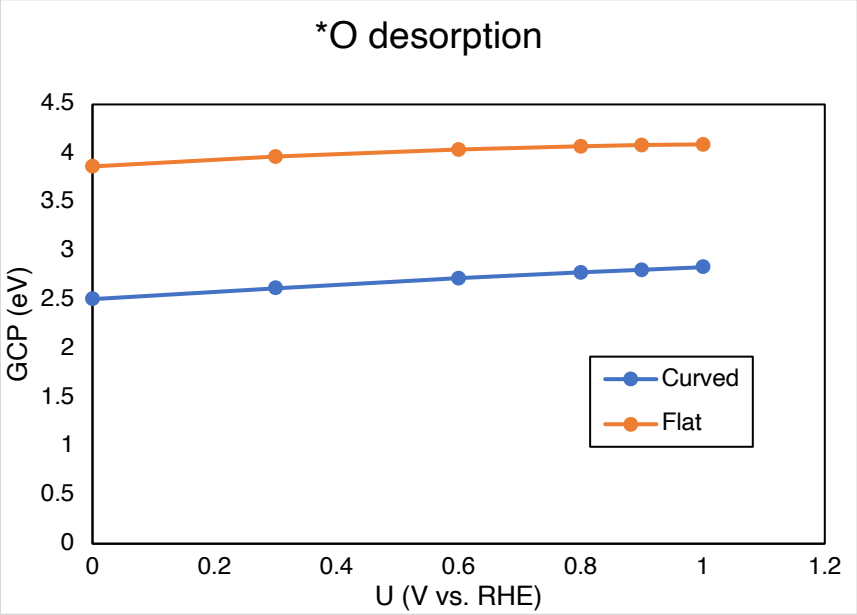

Figure B5: *O desorption energy (eV) vs. applied potential (V vs. RHE) for curved and flat FePc-C_{24}.

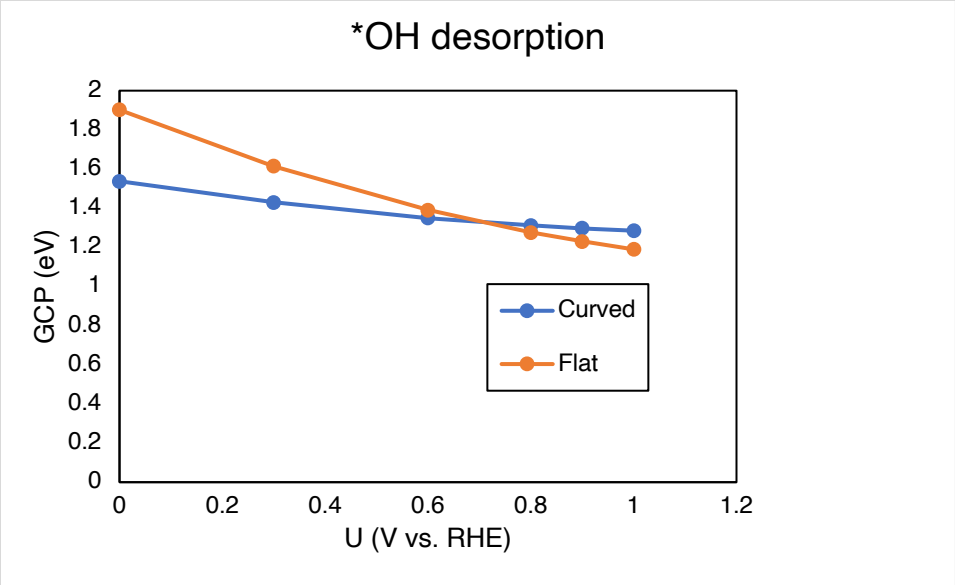

Figure B6: *OH desorption energy (eV) vs. applied potential (V vs. RHE) for curved and flat FePc-C_{24}.

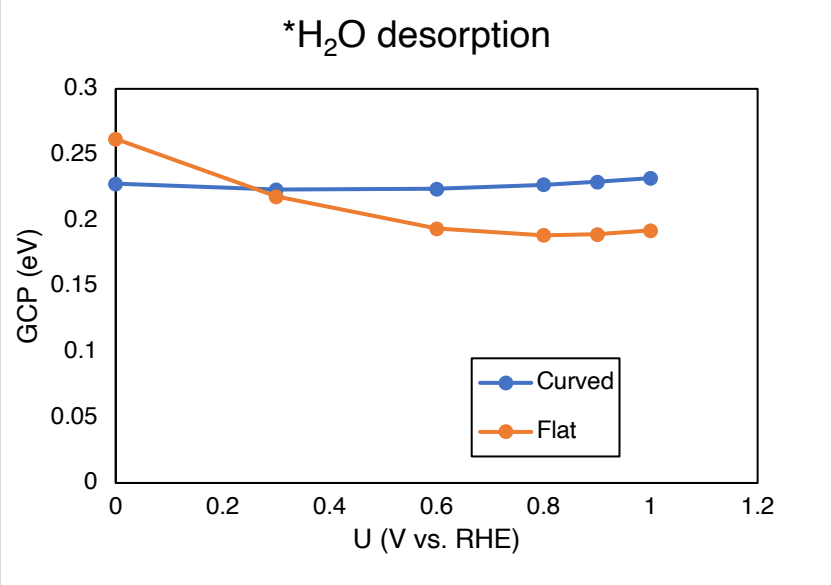

Figure B7: *H_2O desorption energy (eV) vs. applied potential (V vs. RHE) for curved and flat FePc-C_{24}.

References

(1) Nørskov, J. K.; Rossmeisl, J.; Logadottir, A.; Lindqvist, L.; Kitchin, J. R.; Bligaard, T.; Jónsson, H. Origin of the Overpotential for Oxygen Reduction at a

Fuel-Cell Cathode. *J. Phys. Chem. B* **2004**, *108* (46), 17886–17892. https://doi.org/10.1021/jp047349j.

(2) Nørskov, J. K.; Bligaard, T.; Logadottir, A.; Bahn, S.; Hansen, L. B.; Bollinger, M.; Bengaard, H.; Hammer, B.; Sljivancanin, Z.; Mavrikakis, M.; Xu, Y.; Dahl, S.; Jacobsen, C. J. H. Universality in Heterogeneous Catalysis. *J. Catal.* **2002**, *209* (2), 275–278. https://doi.org/10.1006/jcat.2002.3615.

(3) Desai, S. K.; Neurock, M. First-Principles Study of the Role of Solvent in the Dissociation of Water over a Pt-Ru Alloy. *Phys. Rev. B - Condens. Matter Mater. Phys.* **2003**, *68* (7). https://doi.org/10.1103/PhysRevB.68.075420.

Appendix C

Appendix for: Dual Atoms Catalysts for Rapid Electrochemical Reduction of CO to Ethylene

Reproduced with permission from:

Yuyin Li, Zhengtang Luo, William A. Goddard III.

Nano Energy, **2023***, 118, 108966*

Definitions:
Esolv: solution-phase electronic energy in units of Hartree (Ha)
H+ZPE-TS: the summation of the phonon-derived enthalpy, zero-point energy, and entropy in units of electronvolts (eV)
NELECT: total number of electrons
ΔNELECT: difference in electrons relative to the 0-charge state
U v RHE: potential versus reversible hydrogen electrode in units of volts (V)
U v SHE: potential versus standard hydrogen electrode in units of volts (V)
n(min;U): equilibrium total number of electrons for a given potential
n(min;U)-n0: equilibrium difference in electrons relative to the 0-charge state for a given potential
G(n(min;U)): equilibrium Grand canonical free energy for a given potential in units of electronvolts (eV)

Table C1: Solution-phase energies for substrate geometries.

Catalyst	Esolv (Ha)
Ti	-412.3982887
Cr	-469.7528824

Mn	-506.188073
Fe	-547.6228934
Co	-593.1045636
Ni	-638.9410382
Cu	-699.3127572
Mo	-432.5601964
Ru	-485.671338
Rh	-458.8883504
Pd	-487.6066601
Ag	-591.2652802
W	-433.075622
Re	-455.241182
Ir	-448.5823179
Pt	-473.5050857
Au	-364.8827851
Ga	-707.3224678
Sn	-435.2415494
Bi	-439.3203802

Table C2: Solution-phase energies and H+ZPE-TS contributions at 298.15 K for substrate–$(H)_2$ geometries.

Catalyst	Esolv (Ha)	H + ZPE - TS (eV)
Ti	-413.5522395	0.568682
Cr	-470.9217508	0.388298
Mn	-507.3446968	0.098846
Fe	-548.790509	0.17086
Co	-594.2578256	0.399651
Ni	-640.0153517	0.316406
Cu	-700.330329	0.210279
Mo	-433.7787798	0.379261
Ru	-486.8695818	0.495913
Rh	-460.0342033	0.248216
Pd	-488.6971171	0.148384
Ag	-592.2837187	0.318504
W	-434.3218958	0.403677
Re	-456.4739372	0.378383
Ir	-449.7350438	0.315668
Pt	-474.6173078	0.232095

Au	-365.8980379	0.205155
Ga	-708.4726897	0.380229
Sn	-436.4148447	0.316473
Bi	-440.3571307	0.271344

Table C3: Solution-phase energies and H+ZPE-TS contributions at 298.15 K for substrate–$(CO)_2$ geometries.

Catalyst	Esolv (Ha)	H + ZPE - TS (eV)
Ti	-455.9563045	0.321922
Cr	-513.332179	0.353279
Mn	-549.7761006	0.386976
Fe	-591.1881636	0.395264
Co	-636.6301333	0.304905
Ni	-682.439082	0.19084
Cu	-742.8100388	0.216471
Mo	-476.1929816	0.362999
Ru	-529.2556477	0.354754
Rh	-502.4023318	0.348362
Pd	-531.1045785	0.200246
Ag	-634.7612492	0.178078
W	-476.7203139	0.341398
Re	-498.8901572	0.379836
Ir	-492.1159773	0.380689
Pt	-517.0014827	0.180365
Au	-408.3777078	0.213909
Ga	-750.8358044	0.266401
Sn	--	--
Bi	-482.8031056	0.212686

Table C4: Solution-phase energies and H+ZPE-TS contributions at 298.15 K for substrate–OCCO geometries.

Catalyst	Esolv (Ha)	H + ZPE - TS (eV)
Ti	--	--
Cr	--	--
Mn	-549.7252294	0.360137
Fe	-591.1741727	0.395233
Co	-636.6456198	0.439288
Ni	-682.4156932	0.383261

Cu	--	--
Mo	-476.1358371	0.32969
Ru	-529.2402488	0.392584
Rh	-502.4086855	0.39027
Pd	-531.0801806	0.380652
Ag	--	--
W	-476.6652442	0.362977
Re	-498.8351569	0.387751
Ir	-492.1080367	0.40053
Pt	-516.9830308	0.400212
Au	-408.3762127	0.180667
Ga	-750.8360613	0.270818
Sn	-478.7320635	0.354455
Bi	--	--

Table C5: Solution-phase energies and H+ZPE-TS contributions at 298.15 K for the $FePc_{Ex}$ CO to C_2H_4 reaction.

Fe	Esolv (Ha)	H+ZPE-TS (eV)
2co	-591.18816	0.395264
occo	-591.17417	0.395233
hocco	-591.74248	0.681569
hoccoh	-592.32987	0.962499
hocc	-575.59715	0.565007
hocch	-576.24987	0.876428
cch	-559.53139	0.427172
cch2	-560.15838	0.76235
hcch2	-560.77698	1.045888
hcch	-560.16921	0.774616
substrate	-547.62289	0

Table C6: Solution-phase energies and H+ZPE-TS contributions at 298.15 K for the $RuPc_{Ex}$ CO to C_2H_4 reaction.

Ru	Esolv (Ha)	H+ZPE-TS (eV)
2co	-529.25565	0.354754
occo	-529.24025	0.392584
hocco	-529.81533	0.693909
hoccoh	-530.40565	0.992815
hocc	-513.6574	0.582506

hocch	-514.32407	0.885822
cch	-497.57889	0.479894
cch2	-498.23708	0.783925
hcch2	-498.84719	1.057445
hcch	-498.24195	0.79713
substrate	-485.67134	0

Table C7: Solution-phase energies and H+ZPE-TS contributions at 298.15 K for the $CoPc_{Ex}$ CO to C_2H_4 reaction.

Co	Esolv (Ha)	H+ZPE-TS (eV)
2co	-636.63013	0.304905
occo	-636.64562	0.439288
hocco	-637.2074	0.689628
hoccoh	-637.78896	0.983121
hocc	-621.06035	0.562711
hocch	-621.70867	0.881726
cch	-605.00121	0.453948
cch2	-605.61504	0.762186
hcch2	-606.24918	1.040108
hcch	-605.62804	0.771769
substrate	-593.10456	0

Table C8: Solution-phase energies and H+ZPE-TS contributions at 298.15 K for the $IrPc_{Ex}$ CO to C_2H_4 reaction.

Ir	Esolv (Ha)	H+ZPE-TS (eV)
2co	-492.11598	0.380689
occo	-492.10804	0.40053
hocco	-492.67673	0.698912
hoccoh	-493.25924	0.985586
hocc	-476.52242	0.570465
hocch	-477.17693	0.892336
cch	-460.44284	0.46816
cch2	-461.0635	0.78637
hcch2	-461.73072	1.071674
hcch	-461.09448	0.804806
substrate	-448.58232	0

Table C9: Solution-phase energies and H+ZPE-TS contributions at 298.15 K for the $IrCoPc_{Ex}$ CO to C_2H_4 reaction.

Ir-Co	Esolv (Ha)	H+ZPE-TS (eV)
2co	-564.3716	0.354626
occo	-564.37344	0.409744
hocco	-564.93096	0.686906
hoccoh	-565.51884	0.995673
hocc	-548.8136	0.57001
hocch	-549.4394	0.897104
cch	-532.70892	0.459831
cch2	-533.35243	0.783788
hcch2	-533.97936	1.056576
hcch	-533.35635	0.786978
substrate	-520.84387	0

Table C10: Solution-phase energies for the pristine $IrCoPc_{Ex}$ at charges of 0, -0.5, -1.0, and -1.5.

NELECT	ΔNELECT	Esolv (Ha)
220	0	-520.84387
220.5	0.5	-520.92269
221	1	-520.99644
221.5	1.5	-521.06687

Table C11: GCP energies and corresponding number of electrons at various applied potentials for the pristine $IrCoPc_{Ex}$.

U vs RHE (V)	U vs SHE (V)	n(min;U)	n(min;U)-n0	G(n(min;U)) (eV)
0	-0.4137	220.30318	0.30317999	-13238.728
-0.3	-0.7137	220.960118	0.96011832	-13304.918
-0.6	-1.0137	221.617057	1.61705665	-13371.304
-1	-1.4137	222.492974	2.49297443	-13460.126
-1.2	-1.6137	222.930933	2.93093332	-13504.669
-1.4	-1.8137	223.368892	3.36889221	-13549.299

Table C12: Solution-phase energies for 2 CO on $IrCoPc_{Ex}$ at charges of 0, -0.5, -1.0, and -1.5.

NELECT	ΔNELECT	Esolv (Ha)
240	0	-564.3716
240.5	0.5	-564.45039
241	1	-564.52454

241.5	1.5	-564.59517

Table C13: GCP energies and corresponding number of electrons at various applied potentials for 2 CO on $IrCoPc_{Ex}$.

U vs RHE (V)	U vs SHE (V)	n(min;U)	n(min;U)-n0	G(n(min;U)) (eV)
0	-0.4137	240.316083	0.31608317	-14337.898
-0.3	-0.7137	240.991981	0.99198094	-14410.095
-0.6	-1.0137	241.667879	1.66787872	-14482.494
-1	-1.4137	242.569076	2.56907575	-14579.341
-1.2	-1.6137	243.019674	3.01967427	-14627.9
-1.4	-1.8137	243.470273	3.47027278	-14676.549

Table C14: Solution-phase energies for OCCO on $IrCoPc_{Ex}$ at charges of 0, -0.5, -1.0, and -1.5.

NELECT	ΔNELECT	Esolv (Ha)
240	0	-564.37344
240.5	0.5	-564.45615
241	1	-564.53301
241.5	1.5	-564.6061

Table C15: GCP energies and corresponding number of electrons at various applied potentials for OCCO on $IrCoPc_{Ex}$.

U vs RHE (V)	U vs SHE (V)	n(min;U)	n(min;U)-n0	G(n(min;U)) (eV)
0	-0.4137	240.693767	0.69376706	-14337.999
-0.3	-0.7137	241.266582	1.2665822	-14410.293
-0.6	-1.0137	241.839397	1.83939735	-14482.759
-1	-1.4137	242.603151	2.60315088	-14579.647
-1.2	-1.6137	242.985028	2.98502765	-14628.206
-1.4	-1.8137	243.366904	3.36690441	-14676.841

Table C16: Solution-phase energies for HOCCO on $IrCoPc_{Ex}$ at charges of 0, -0.5, -1.0, and -1.5.

NELECT	ΔNELECT	Esolv (Ha)
241	0	-564.93096
241.5	0.5	-565.01061
242	1	-565.08614
242.5	1.5	-565.15843

Table C17: GCP energies and corresponding number of electrons at various applied potentials for HOCCO on $IrCoPc_{Ex}$.

U vs RHE (V)	U vs SHE (V)	n(min;U)	n(min;U)-n0	G(n(min;U)) (eV)
0	-0.4137	241.447111	0.44711131	-14348.558
-0.3	-0.7137	242.196392	1.19639151	-14421.105
-0.6	-1.0137	242.945672	1.9456717	-14493.876
-1	-1.4137	243.944712	2.94471196	-14591.254
-1.2	-1.6137	244.444232	3.44423209	-14640.093
-1.4	-1.8137	244.943752	3.94375222	-14689.032

Table C18: Solution-phase energies for HOCCOH on $IrCoPc_{Ex}$ at charges of 0, -0.5, -1.0, and -1.5.

NELECT	ΔNELECT	Esolv (Ha)
242	0	-565.51884
242.5	0.5	-565.5973
243	1	-565.67074
243.5	1.5	-565.74072

Table C19: GCP energies and corresponding number of electrons at various applied potentials for HOCCOH on $IrCoPc_{Ex}$.

U vs RHE (V)	U vs SHE (V)	n(min;U)	n(min;U)-n0	G(n(min;U)) (eV)
0	-0.4137	242.264882	0.26488215	-14359.977
-0.3	-0.7137	242.914812	0.91481209	-14432.754
-0.6	-1.0137	243.564742	1.56474204	-14505.726
-1	-1.4137	244.431315	2.4313153	-14603.325
-1.2	-1.6137	244.864602	2.86460193	-14652.255
-1.4	-1.8137	245.297889	3.29788856	-14701.271

Table C20: Solution-phase energies for HOCC on $IrCoPc_{Ex}$ at charges of 0, -0.5, -1.0, and -1.5.

NELECT	ΔNELECT	Esolv (Ha)
235	0	-548.8136
235.5	0.5	-548.89753
236	1	-548.97717
236.5	1.5	-549.05167

Table C21: GCP energies and corresponding number of electrons at various applied potentials for HOCC on $IrCoPc_{Ex}$.

U vs RHE (V)	U vs SHE (V)	n(min;U)	n(min;U)-n0	G(n(min;U)) (eV)
0	-0.4137	235.89438	0.89437984	-13935.74
-0.3	-0.7137	236.478675	1.4786754	-14006.596
-0.6	-1.0137	237.062971	2.06297096	-14077.627
-1	-1.4137	237.842032	2.84203171	-14172.608
-1.2	-1.6137	238.231562	3.23156208	-14220.216
-1.4	-1.8137	238.621092	3.62109245	-14267.901

Table C22: Solution-phase energies for HOCCH on $IrCoPc_{Ex}$ at charges of 0, -0.5, -1.0, and -1.5.

NELECT	ΔNELECT	Esolv (Ha)
236	0	-549.4394
236.5	0.5	-549.51859
237	1	-549.59257
237.5	1.5	-549.66289

Table C23: GCP energies and corresponding number of electrons at various applied potentials for HOCCH on $IrCoPc_{Ex}$.

U vs RHE (V)	U vs SHE (V)	n(min;U)	n(min;U)-n0	G(n(min;U)) (eV)
0	-0.4137	236.346503	0.34650292	-13948.022
-0.3	-0.7137	236.968115	0.96811481	-14019.02
-0.6	-1.0137	237.589727	1.5897267	-14090.203
-1	-1.4137	238.418543	2.41854256	-14185.405
-1.2	-1.6137	238.83295	2.83295049	-14233.13
-1.4	-1.8137	239.247358	3.24735841	-14280.938

Table C24: Solution-phase energies for CCH on $IrCoPc_{Ex}$ at charges of 0, -0.5, -1.0, and -1.5.

NELECT	ΔNELECT	Esolv (Ha)
229	0	-532.70892
229.5	0.5	-532.79295
230	1	-532.87243
230.5	1.5	-532.94883

Table C25: GCP energies and corresponding number of electrons at various applied potentials for CCH on $IrCoPc_{Ex}$.

U vs RHE (V)	U vs SHE (V)	n(min;U)	n(min;U)-n0	G(n(min;U)) (eV)

0	-0.4137	229.999026	0.99902551	-13523.102
-0.3	-0.7137	230.722669	1.72266853	-13592.21
-0.6	-1.0137	231.446312	2.44631156	-13661.536
-1	-1.4137	232.411169	3.41116893	-13754.307
-1.2	-1.6137	232.893598	3.89359761	-13800.838
-1.4	-1.8137	233.376026	4.37602629	-13847.464

Table C26: Solution-phase energies for HCCH on $IrCoPc_{Ex}$ at charges of 0, -0.5, -1.0, and -1.5.

NELECT	ΔNELECT	Esolv (Ha)
230	0	-533.35635
230.5	0.5	-533.435
231	1	-533.51005
231.5	1.5	-533.59249

Table C27: GCP energies and corresponding number of electrons at various applied potentials for HCCH on $IrCoPc_{Ex}$.

U vs RHE (V)	U vs SHE (V)	n(min;U)	n(min;U)-n0	G(n(min;U)) (eV)
0	-0.4137	230.336465	0.3364645	-13535.959
-0.3	-0.7137	231.10219	1.10218984	-13605.175
-0.6	-1.0137	231.867915	1.86791517	-13674.621
-1	-1.4137	232.888882	2.88888229	-13767.572
-1.2	-1.6137	233.399366	3.39936584	-13814.201
-1.4	-1.8137	233.909849	3.9098494	-13860.932

Table C28: Solution-phase energies for $HCCH_2$ on $IrCoPc_{Ex}$ at charges of 0, -0.5, -1.0, and -1.5.

NELECT	ΔNELECT	Esolv (Ha)
231	0	-533.97936
231.5	0.5	-534.05976
232	1	-534.13447
232.5	1.5	-534.21382

Table C29: GCP energies and corresponding number of electrons at various applied potentials for $HCCH_2$ on $IrCoPc_{Ex}$.

U vs RHE (V)	U vs SHE (V)	n(min;U)	n(min;U)-n0	G(n(min;U)) (eV)
0	-0.4137	231.458741	0.4587414	-13548.439

-0.3	-0.7137	231.943247	0.94324708	-13617.95
-0.6	-1.0137	232.427753	1.42775276	-13687.605
-1	-1.4137	233.07376	2.07376033	-13780.705
-1.2	-1.6137	233.396764	2.39676412	-13827.353
-1.4	-1.8137	233.719768	2.71976791	-13874.064

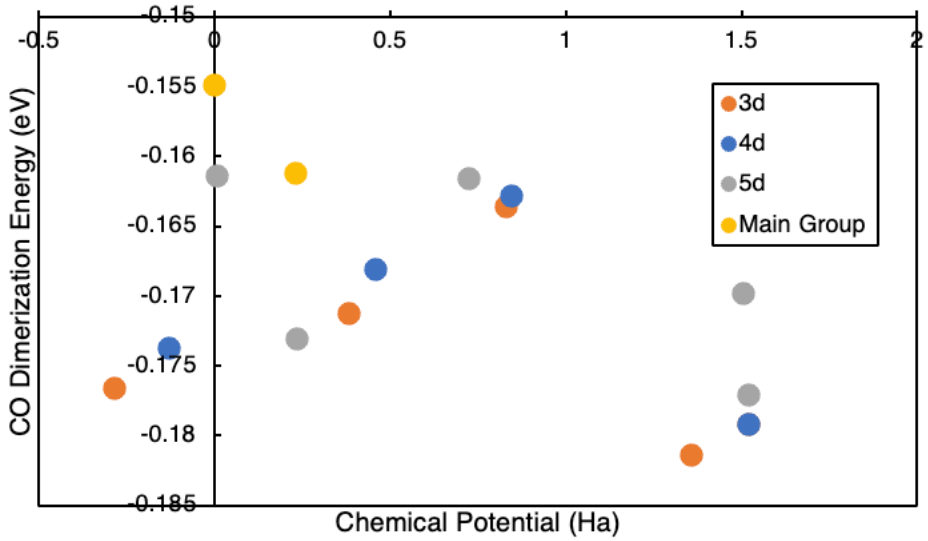

Figure C1: CO dimerization energy (eV) vs. chemical potential (Ha) of [X]Pc_{Ex}–OCCO.

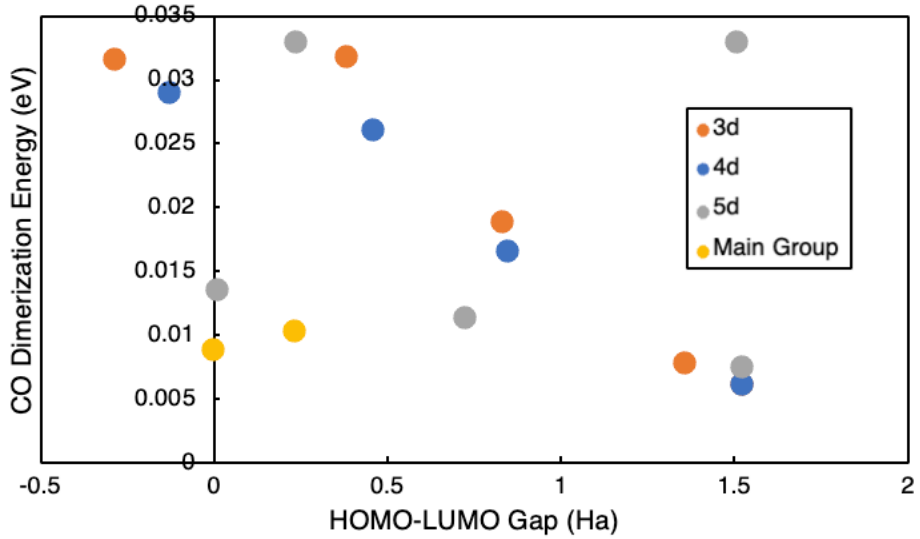

Figure C2: CO dimerization energy (eV) vs. HOMO–LUMO gap (Ha) of [X]Pc_{Ex}–OCCO.

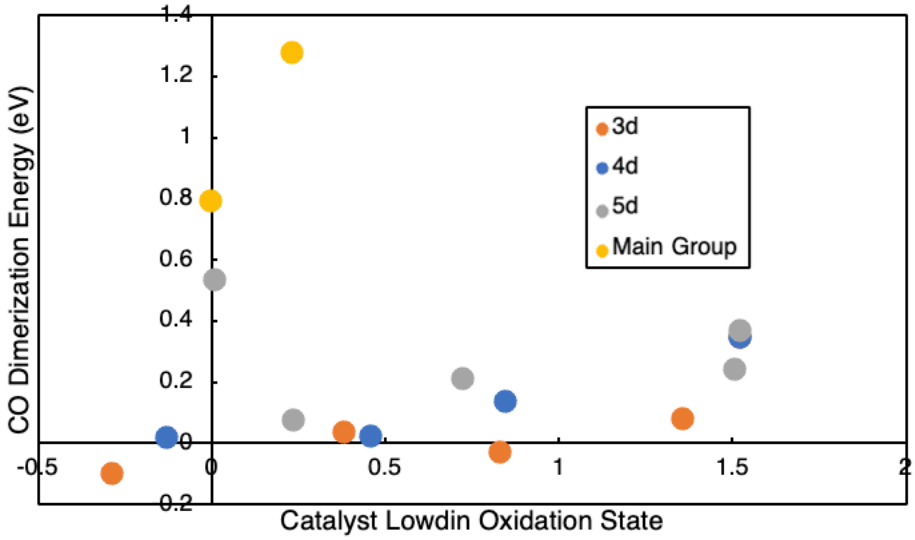

Figure C3: CO dimerization energy (eV) vs. catalyst (or [X]) Lowdin oxidation state of [X]Pc_{Ex}–OCCO.

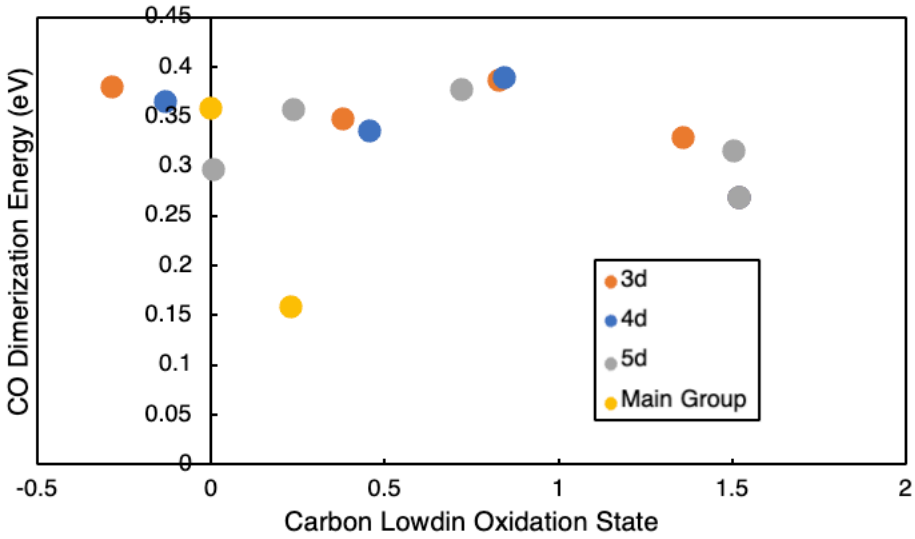

Figure C4: CO dimerization energy (eV) vs. carbon Lowdin oxidation state of [X]Pc_{Ex}–OCCO.

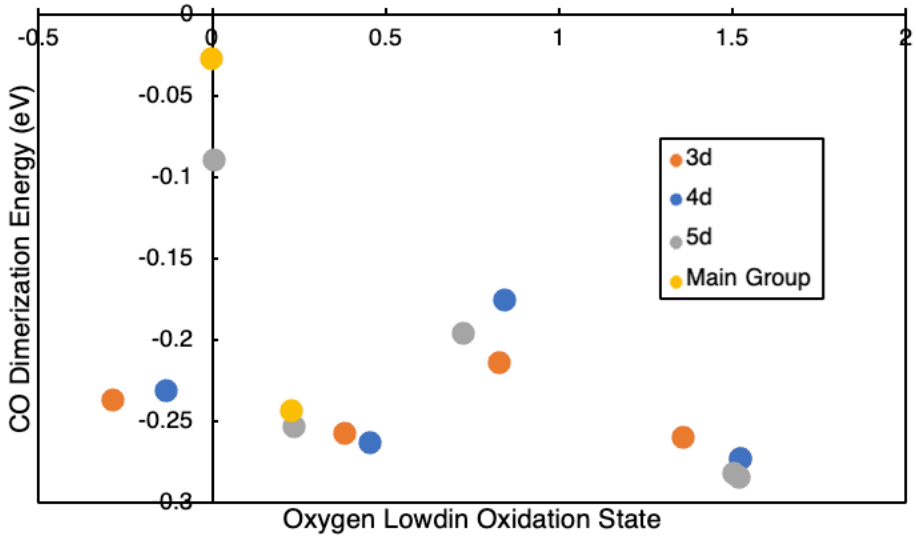

Figure C5: CO dimerization energy (eV) vs. oxygen Lowdin oxidation state of [X]Pc_{Ex}–OCCO.

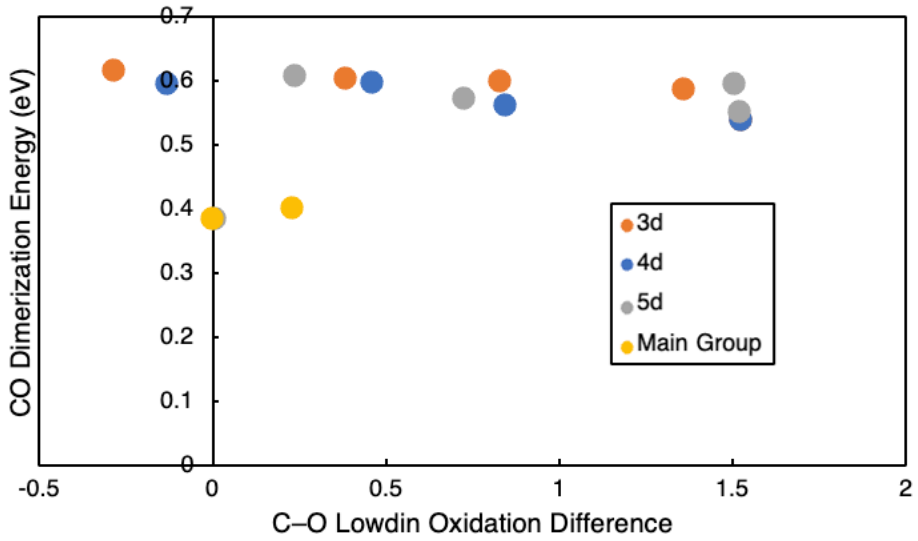

Figure C6: CO dimerization energy (eV) vs. the C–O Lowdin oxidation state difference of [X]Pc_{Ex}–OCCO.

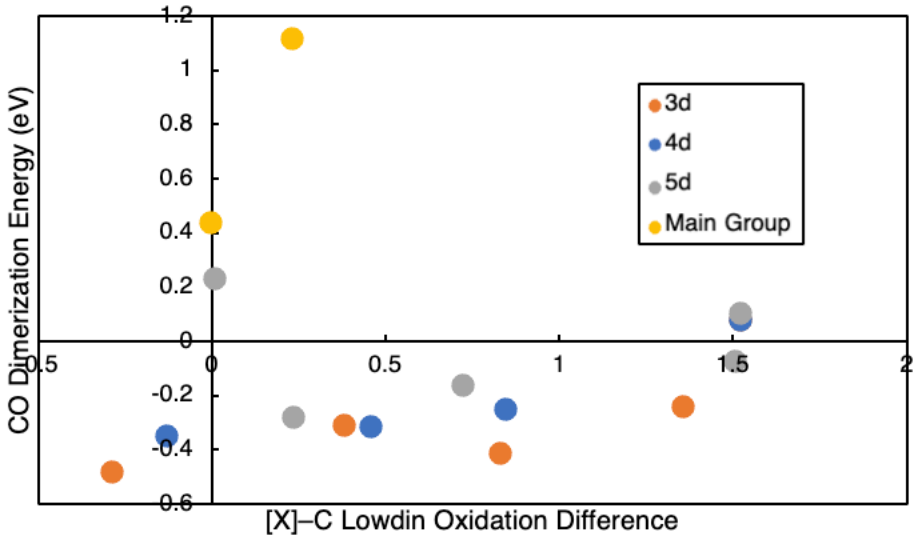

Figure C7: CO dimerization energy (eV) vs. the [X]–O Lowdin oxidation state difference of [X]Pc_{Ex}–OCCO.

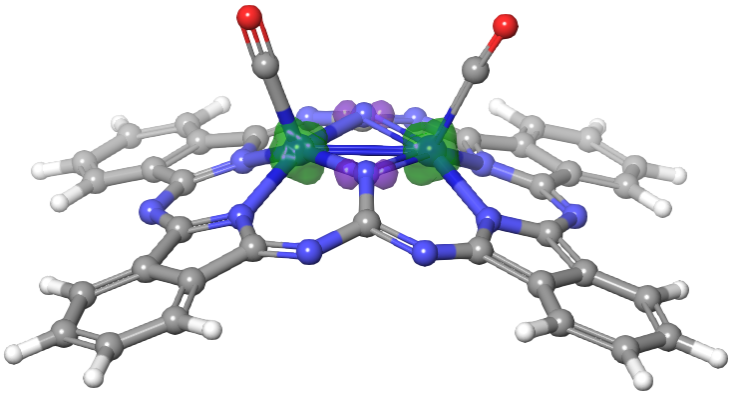

Figure C8: MN15 spin density of finite $CoPc_{Ex}$–$(CO)_2$. Overall spin treated as triplet.

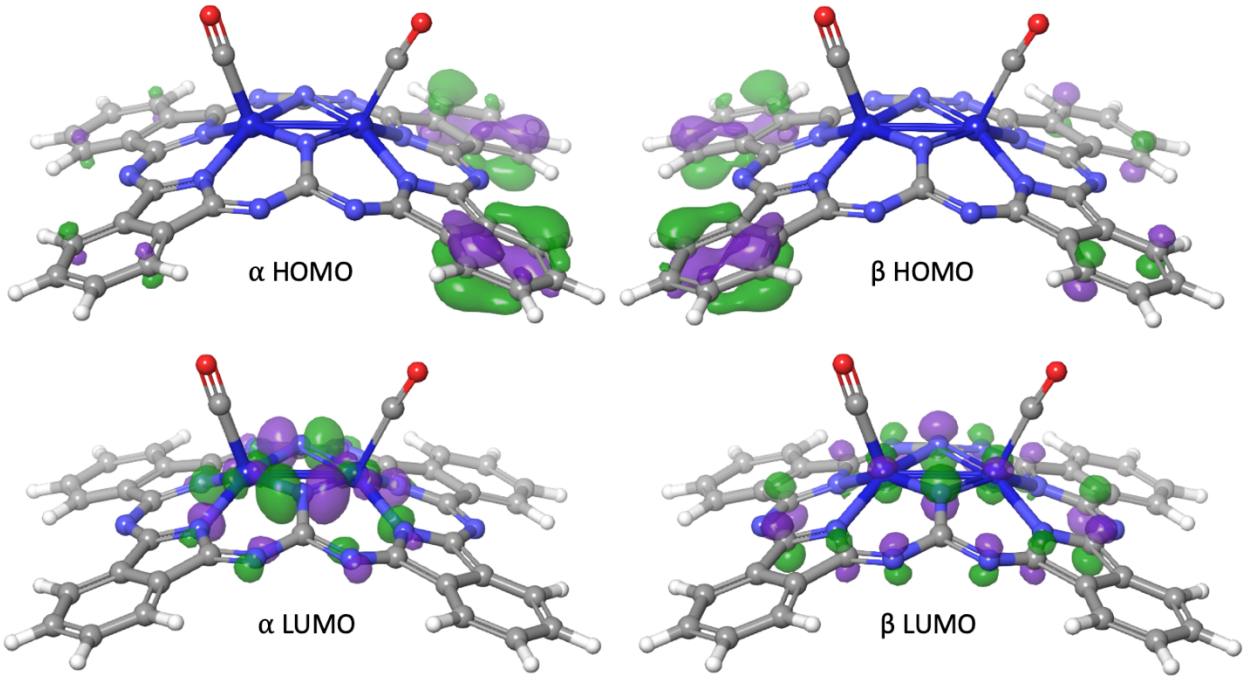

Figure C9: MN15 α and β HOMO and LUMO orbitals for finite $CoPc_{Ex}$–$(CO)_2$. Overall spin treated as triplet.

Appendix D

Appendix for: Partial Oxidation of Methane Enabled by Decatungstate Photocatalysis Coupled to Free Radical Chemistry

Reproduced with permission from:

Kaeleigh Olsen, Nichole S. Liebov, John T. Groves, William Goddard III, T. Brent Gunnoe.

ACS Catalysis, **2023**, 13, 9, 6382-6395

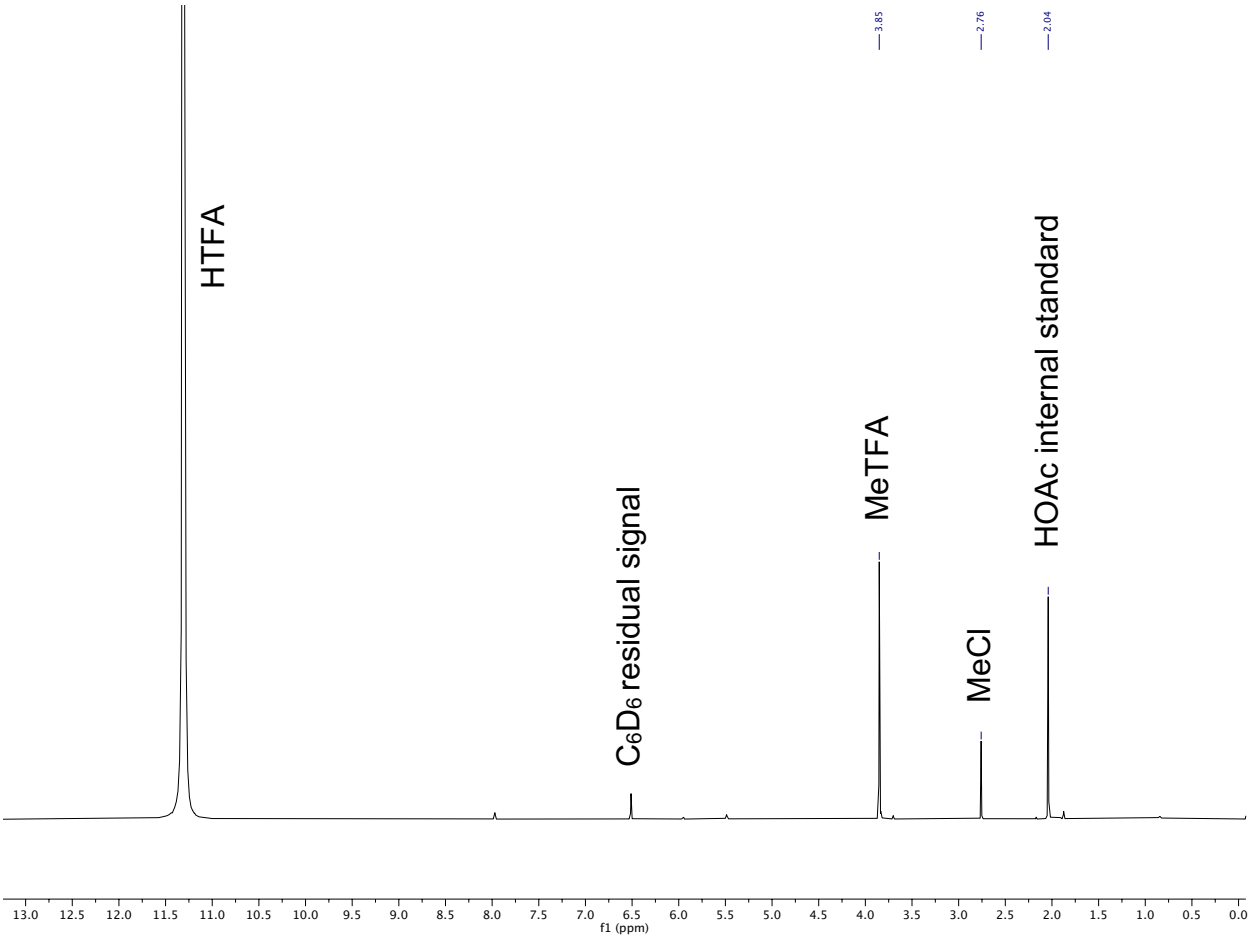

Figure D1: Labeled representative ^{1}H NMR spectrum for photochemical methane functionalization. Either HOAc (shown here) or CH_3NO_2 were used as internal standard, from which product yields were quantified. The small peak at 5.5 ppm may suggest that a small amount of MeCl was further chlorinated.

Figure D2: Photograph of a custom-built high pressure reaction vessel used for photolytic reactions.

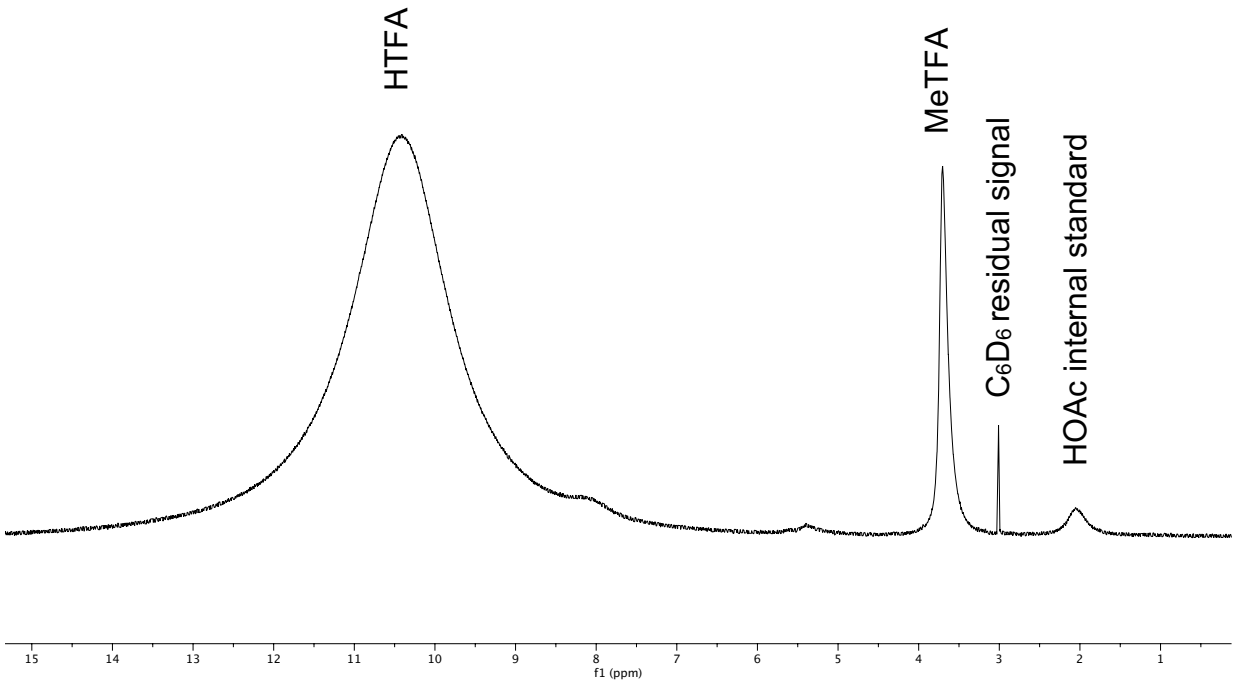

Figure D3: Labeled representative ^{1}H NMR spectrum for re-oxidation experiments with dioxygen in which signal broadening prevents the ability to detect or measure MeCl formation.

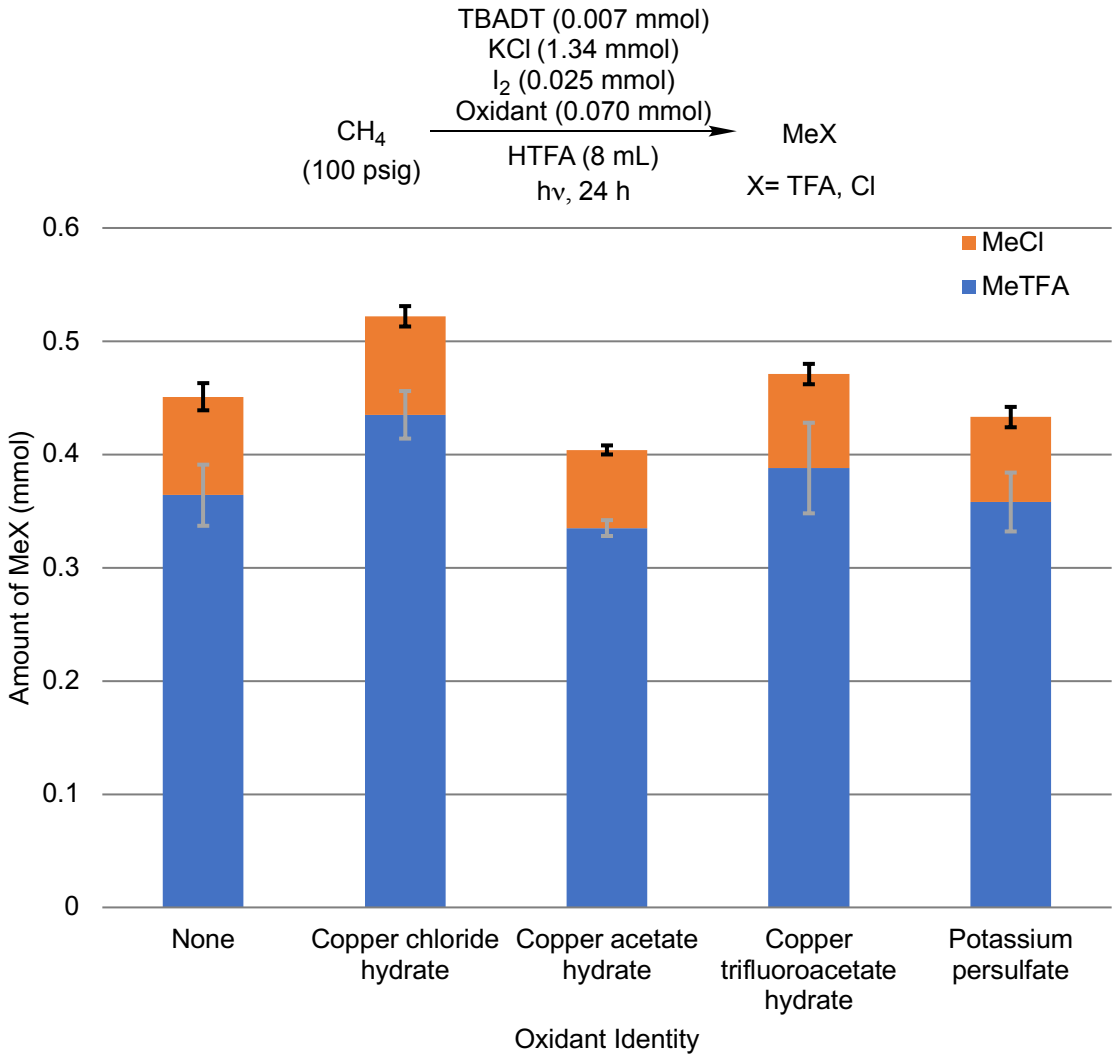

Figure D4: Comparison of the amount of MeX (X = TFA, Cl) produced as a method to screen substrates to serve as *in situ* oxidants for the re-oxidation of TBADT under standard aerobic reaction conditions. Each bar graph represents the average of at least three independent experiments with error bars depicting the standard deviations.

Screening of Peroxides as *In Situ* Co-oxidants

Anaerobic (*i.e.*, dinitrogen-purged), but otherwise standard, reaction conditions were used to probe the ability of alkyl peroxides to serve as *in situ* oxidants for the re-oxidation of TBADT. The addition of ten equivalents of either di-tert-butyl peroxide (DTBP) or tert-butyl hydroperoxide (tBuOOH) relative to TBADT led to a decrease in MeX (X = TFA, Cl) production (Table D1, Entries 3 and 4) compared to the reaction without alkyl peroxide addition (Table D1, Entry 1).

When the loading of tBuOOH was increased an additional ten-fold, both TBADT TOs and MeX yield increased (Table D1, Entry 5). The reaction with 100 equivalents of tBuOOH reflects the highest peroxide loading that can be used while maintaining an environment that falls safely within the pressure limitations of the reaction vessel. This threshold was determined by considering the reaction of each equivalent of added peroxide with one equivalent of HTFA to produce one equivalent of CO_2. Thus, in order to explore reactions with a higher excess of peroxide, the amount of methane was decreased to 15 psig (Table D1, Entry 6). The reaction with 15 psig methane and 100 equivalents of tBuOOH resulted in the same TOs, within standard deviation, but MeX yield was increased substantially.

When tBuOOH loading was increased to 1,000 equivalents, $> 100\%$ MeX yield was observed (Table D1, Entry 7). This $> 100\%$ yield alerted us to the likelihood that methyl

radical was being formed from a source other than methane under these conditions. The explanation for this additional methyl radical source was located in previous studies in which DTBP was shown to undergo photo-decomposition to form methyl radical.[1, 2] First, tert-butoxy radical is likely formed from photo-induced O–O bond cleavage of the peroxide. The unstable tert-butoxy radical then decomposes to form acetone and methyl radical. In our case, the data for the reactions with peroxide addition are in agreement with this route of photo-decomposition as a resonance in the ^{1}H NMR spectra at 2.25 ppm is present and was confirmed to be acetone.

When analogous conditions to Entry 6 were used, but with H_2O_2 as the peroxide, which is unable to generate methyl radicals, no improvement of MeX yield (within standard deviation) was observed (Table D1, Entry 8) relative to the high methane conversion aerobic reaction (Table D1, Entry 2).

Interestingly, all of the reactions with peroxides increased selectivity towards MeTFA. The reactions with peroxide addition, however, all suffered from large standard deviations.

Table D1: Screening of peroxides to serve as *in situ* oxidants for the re-oxidation of TBADT.[a]

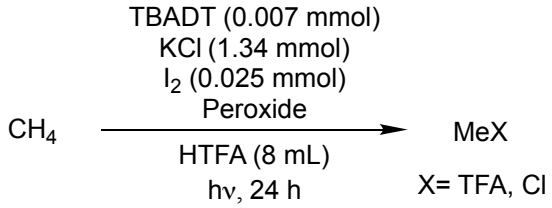

Entry	Peroxide identity	Equivalents of peroxide (relative to TBADT)	Methane pressure (psig)	TOs of MeX (X = TFA, Cl)[b]	% Yield of MeX (X = TFA, Cl)[c]	Molar ratio of MeTFA:MeCl
1	None	N/A	100	64 ± 4.3	1.9 ± 0.078	4.2:1
2	None	N/A	15	50 ± 0.82	8.9 ± 0.58	6.4:1
3	DTBP	10	100	20 ± 8.7	0.60 ± 0.24	35:1
4	tBuOOH	10	100	13 ± 6.2	0.39 ± 0.20	22:1
5	tBuOOH	100	100	160 ± 22	4.7 ± 0.53	280:1
6	tBuOOH	100	15	150 ± 23	39 ± 10	MeTFA exclusively
7	tBuOOH	1,000	15	660 ± 67	120 ± 12	69:1
8	H_2O_2	1,000	15	66 ± 25	13 ± 6.5	22:1

[a] Reaction conditions: 0.007 mmol TBADT, 1.34 mmol KCl, and 0.025 mmol I_2, 8 mL HTFA, N_2 purge, pressurized with CH_4, and 24 h of Hg lamp irradiation. Each entry line represents the average of at least three independent experiments reported with their standard deviations; [b] TOs are calculated with respect to TBADT; [c] Percent yields are calculated with respect to methane.

Reactions with Trifluoroacetic Anhydride

In our study of reaction tolerance to water, it was found that water should be considered as a potential detriment in reactions for which TBADT TOs exceed ~1,000. Experiments were performed in which trifluoroacetic anhydride (TFAA) was added at the start of the reaction in an effort to remove in situ formed water. When the solvent composition was changed from HTFA to a 3:1 mixture of HTFA to TFAA under otherwise identical standard aerobic reaction conditions, the production of MeX was hindered (Scheme D1A). When standard aerobic reaction conditions were used in a 3:1 solvent mixture of HTFA to TFAA and then charged with 7.0 mmol of water (1,000 equivalents relative to TBADT) before pressurization of methane, the production of MeX was hindered to a lesser extent (Scheme D1B). Due to the hinderance on MeX production, the addition of TFAA does not appear to be an effective strategy to remove *in situ* generated water.

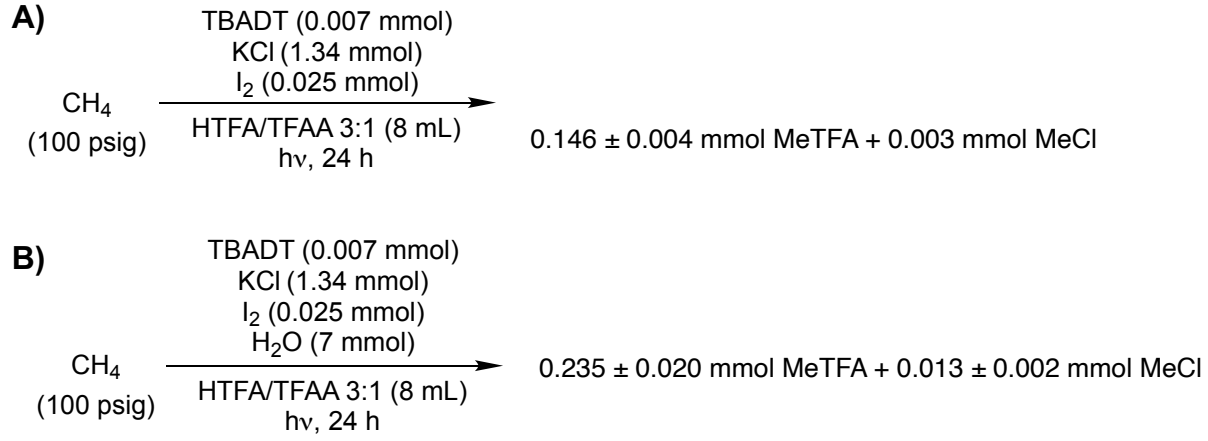

Scheme D1: Modification of standard aerobic reaction conditions to include a mixture of HTFA and TFAA as reaction solvent, without (A) and with (B) added water, led to decreased MeX (X = TFA, Cl) production. Each reaction scheme represents the average of at least three independent experiments reported with their standard deviations.

Background Reaction of Potassium Chloride and Iodine

Chlorine radicals are known to activate C–H bonds.[3] Thus, the reaction of KCl and I_2 in the absence of TBADT was investigated. As noted in the main text, preliminary screening of these reagents (1.34 mmol KCl, 0.050 mmol I_2) in 8 mL HTFA with 100 psig methane led to no MeX (X = TFA, Cl) formation within standard deviation (Table 1, Entry 4). However, when the loading of I_2 was halved but all other conditions remained identical, 0.52 ± 0.06 mmol of MeX (X = TFA, Cl) was produced in 2.1 ± 0.27% yield with a 3.9:1 ratio of MeTFA to MeCl after 24 h of subjection to a mercury arc lamp. After obtaining these results, we wanted to investigate in more detail the ability of this background reaction to perform methane functionalization.

A kinetic study was performed with 1.34 mmol of KCl and 0.025 mmol of I_2 in order to compare with the kinetic study using standard aerobic reaction conditions. The results from these 94 methane functionalization reactions, plotted as averages with standard deviations for each timepoint, are depicted in Figure D5. We observed experiments resulting in substantial MeX formation alongside experiments resulting in little to no MeX formation. Figure D6 and Table D2 contain the breakdown of each individual reaction, rather than the report of averages with standard deviations. The inconsistent results likely indicate that radical chain processes for MeX formation are

possible, but the success of such reactions is highly dependent on factors that we could not identify nor control.

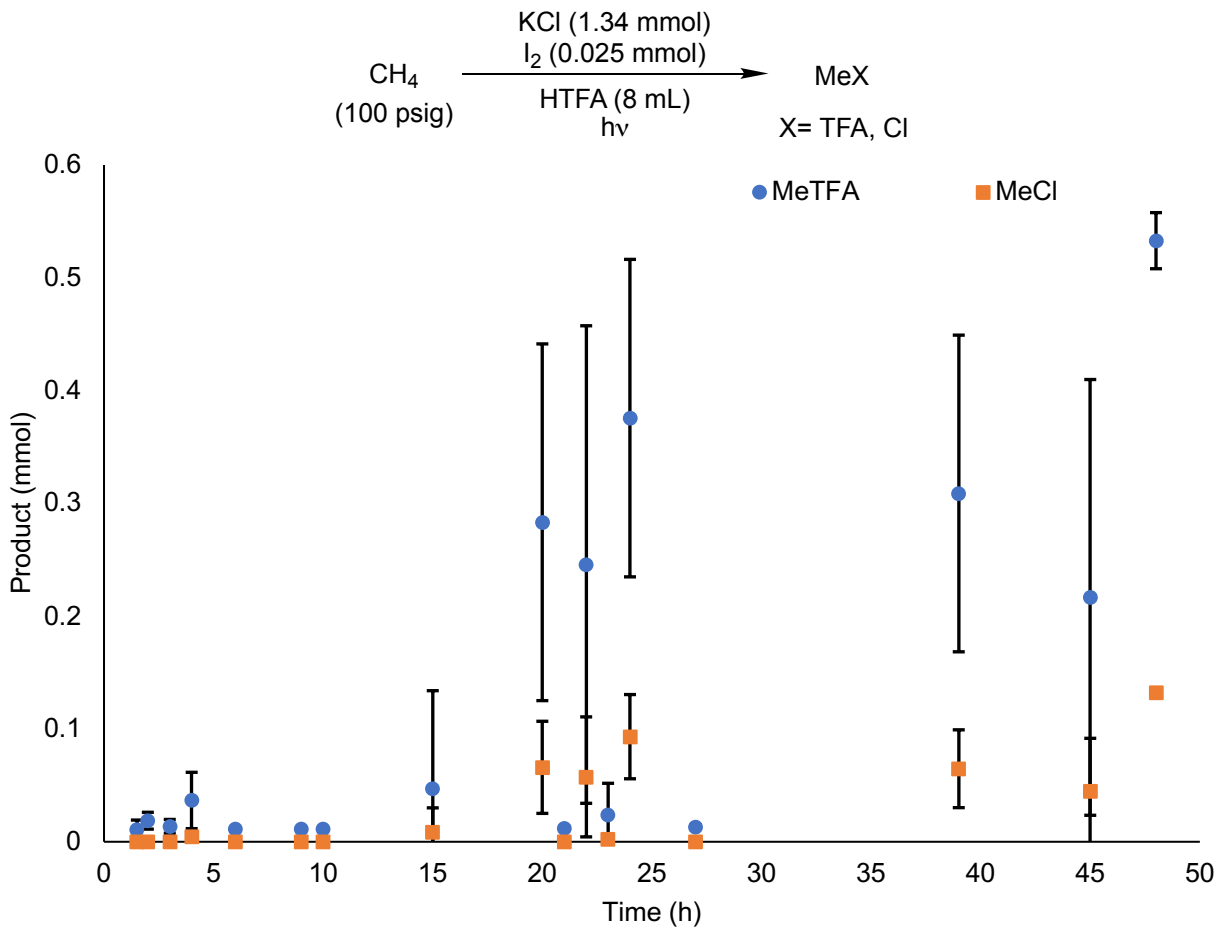

Figure D5: Photochemical methane functionalization under standard aerobic reaction conditions in the absence of TBADT as a function of time. Each data point represents the average of at least three independent experiments with error bars depicting the standard deviation of the three experiments.

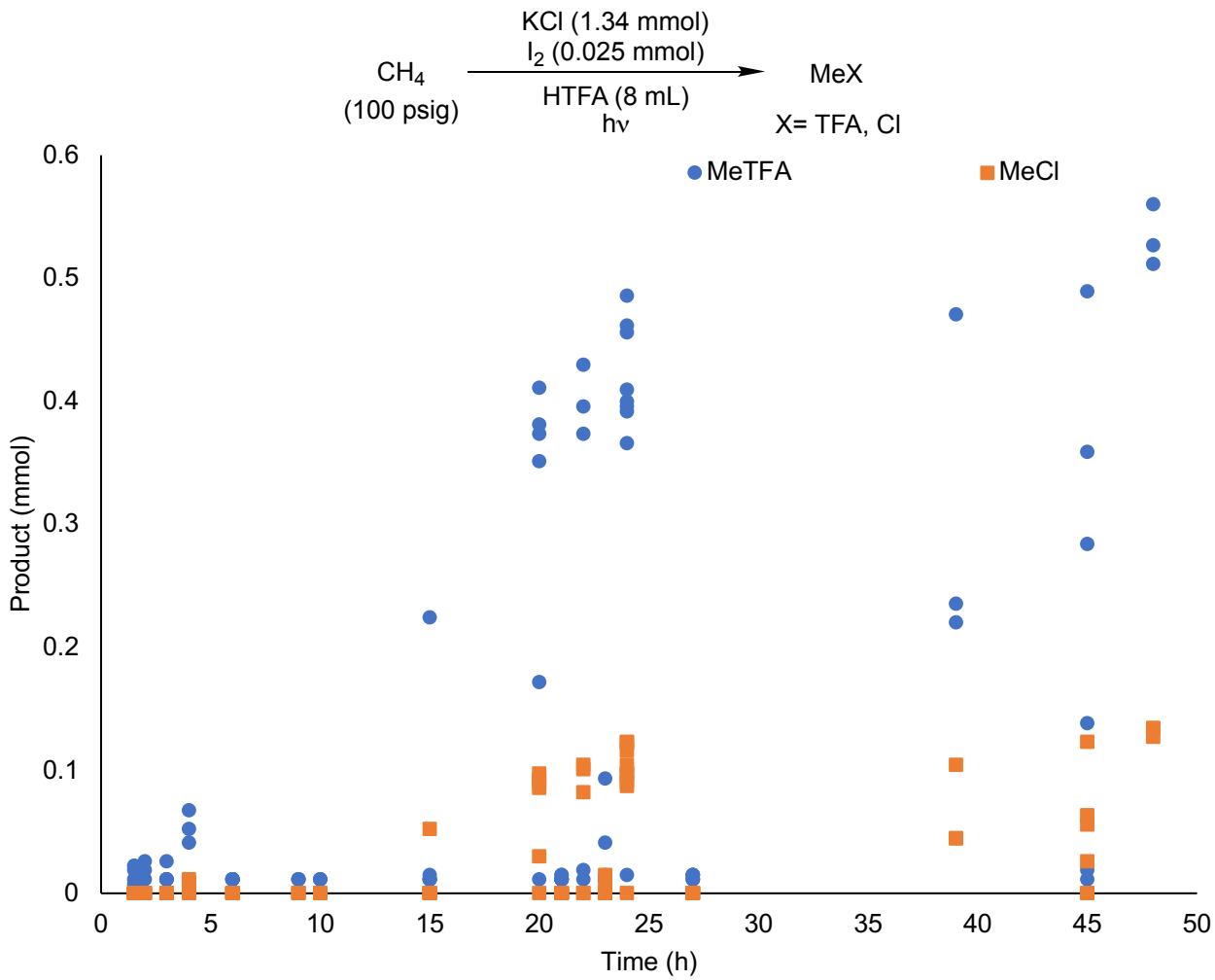

Figure D6: Depiction of the set of experiments in Figure D5 as a scatter plot in which each data point represents an independent experiment.

Table D2: Depiction of the set of experiments in Figure D5 as a table in which each line entry represents an independent experiment.

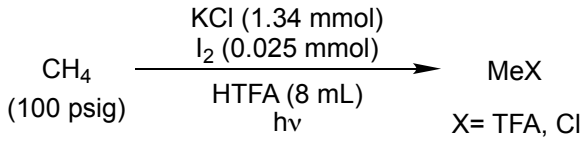

Reaction time (h)	Amount of MeTFA (mmol)	Amount of MeCl (mmol)
1.5	0.011	0
	0.019	0
	0.022	0
	0	0
	0.008	0
	0.004	0
2	0.011	0
	0.026	0
	0.019	0
3	0.011	0
	0.011	0
	0.011	0
	0.011	0
	0.011	0
	0.026	0
4	0.041	0.004
	0.011	0
	0.011	0
	0.067	0.011
	0.05	0.007
6	0.011	0
	0.01	0
	0.011	0
	0.011	0
	0.011	0
	0.011	0
9	0.011	0
	0.011	0
	0.011	0

10	0.011	0
	0.011	0
	0.011	0
15	0.011	0
	0.224	0.052
	0.015	0
	0.011	0
	0.011	0
	0.011	0
20	0.011	0
	0.172	0.030
	0.381	0.093
	0.351	0.086
	0.411	0.097
	0.374	0.090
21	0.011	0
	0.011	0
	0.011	0
	0.011	0
	0.011	0
	0.015	0
	0.011	0
	0.015	0
	0.011	0
22	0.396	0.101
	0.430	0.105
	0.374	0.082
	0.019	0
	0.011	0
23	0.011	0
	0.011	0
	0.011	0
	0.041	0.004
	0.093	0.015
	0.011	0
	0.011	0
	0.015	0

	0.011	0
24	0.462	0.122
	0.392	0.087
	0.409	0.091
	0.400	0.105
	0.456	0.116
	0.015	0
	0.366	0.097
	0.486	0.123
	0.396	0.097
27	0.011	0
	0.015	0
	0.015	0
	0.011	0
	0.015	0
	0.011	0
39	0.220	0.045
	0.471	0.105
	0.235	0.045
45	0.138	0.026
	0.489	0.123
	0.011	0
	0.284	0.056
	0.019	0
	0.359	0.063
48	0.527	0.134
	0.512	0.127
	0.560	0.134

Additional Calculations: Alternative Pathways

Our mechanism suggests a radical pool containing I•, Cl• and CH_3• species. It is plausible that these radicals react according to our proposed mechanism; however, it is

likely that the radicals also react in other undesired paths that could inhibit the desired methane oxidation chemistry. Consequently, we explored other mechanisms that could potentially occur through our radical species.

Given the presence of radical chlorine species, we sought out alternative paths in which Cl• could potentially react to give either the desired products or towards undesired byproducts. When Cl• is present in solution, one plausible reaction step is direct chlorination of methane to produce MeCl and H• according to the following reaction: $CH_4 + Cl^* \rightarrow MeCl + H•$. We evaluated direct chlorination and found the reaction to be uphill 21.5 kcal/mol with a transition state energy of 31.9 kcal/mol. Since this reaction step is substantially uphill with a large barrier to surmount, it is not likely to occur in solution.

Another feasible reaction is of Cl• with MeI to afford MeCl and leave I• according to: MeI+Cl•→MeCl+I•. Chlorination of MeI is downhill -12.7 kcal/mol with a transition state free energy of 32.6 kcal/mol. The C–Cl bond in MeCl is far stronger than the C–I bond in MeI, and I• makes a much better leaving group than Cl•, so this reaction is exergonic. However, the barrier is quite high, so we consider this step unlikely to occur. We predict that when chlorine and iodine are used simultaneously in catalysis, the two species compete for alkyl radical trapping. Once trapped, the alkyl halides cannot interconvert due to this large barrier (*i.e.,* MeI→MeCl or vise-versa).

Given the overwhelming presence of HTFA, we considered the possibility of HAT between a solvent HTFA and DT•• to form TFA•. DFT predicts that this HAT requires a barrier of 12.5 kcal/mol and is downhill -2.1 kcal/mol. This barrier is relatively large, such that we do not expect this reaction to occur. This agrees with previous experimental observations that claimed HTFA does not undergo HAT due to polarity mismatch with DT.

1. References

1. Brook, J. H. T., Reaction of Hydrocarbons with Tert.-butoxy Radicals. *Trans. Faraday Soc.* **1957,** *53*, 327-332.
2. Garnett McMillan, M. H. J. W., Reactions of Alkoxy Radicals v. Photolysis of Di-t-butyl peroxide. *Can. J. Chem.* **1958,** *36*, 1227-1232.
3. Gonzalez, M. I.; Gygi, D.; Qin, Y.; Zhu, Q.; Johnson, E. J.; Chen, Y.-S.; Nocera, D. G., Taming the Chlorine Radical: Enforcing Steric Control over Chlorine-Radical-Mediated C–H Activation. *J. Am. Chem. Soc.* **2022,** *144* (3), 1464-1472.

Appendix E

Appendix for: Manganese Catalyzed Partial Oxidation of Light Alkanes

Reproduced with permission from:

N Coutard, J Moon, N Liebov, RJ Nielsen, J Goldberg, M Li, X Jia, W Schinski, Z Wu, JT Groves, WA Goddard III, TB Gunnoe.

ACS Catalysis, **2022***,* 12, 9, 5356-5370

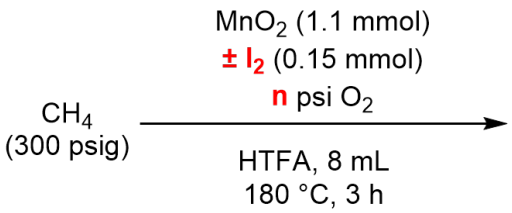

Conditions	MeTFA (mmol)
50 psig O_2	0.61 ± 0.06
I_2 + 50 psig O_2	0.54 ± 0.04
100 psig O_2	0.55 ± 0.11
I_2 + 100 psig O_2	0.57 ± 0.08

Figure E1: Effect of addition of O_2 on the activity of MnO_2 for methane oxidation to MeTFA, in the presence or absence of I_2. Deviations calculated from three experiments.

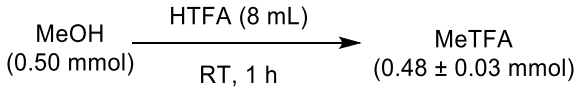

Figure E2: Solvolysis of MeOH to MeTFA in HTFA at 180°C. Deviation calculated from three experiments.

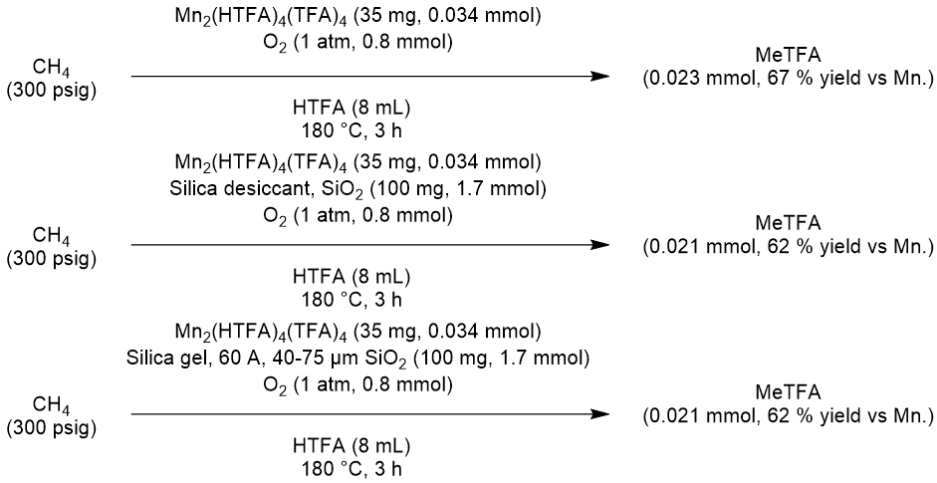

Figure E3: Effect of SiO_2 desiccant on the activity of $Mn_2(HTFA)_4(TFA)_4$ for methane oxidation to MeTFA.

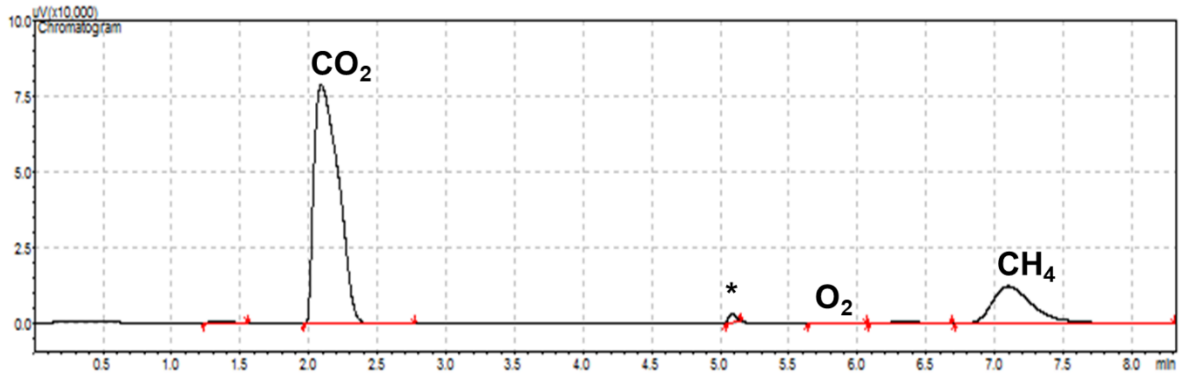

Figure E4: Typical GC-TCD spectrum for the headspace of the oxidation of methane with $Mn_2(HTFA)_4(TFA)_4$. No ethylene or ethane are observed. * The signal at 5.0 min is due to a brief change in column pressure from the position switching of a two-way valve and does not represent a change in gas composition, but rather in gas flow after a brief over-pressurization of the column.

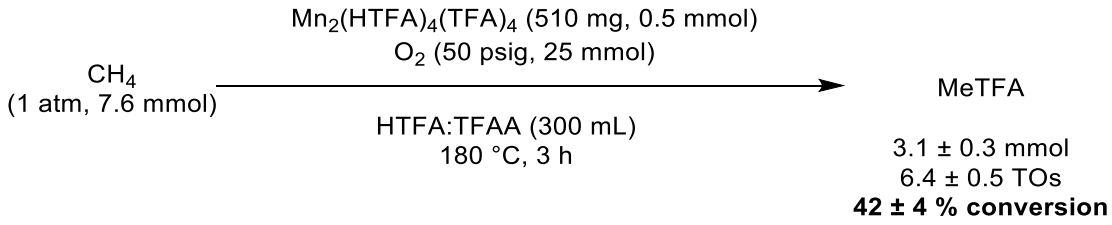

Figure E5: Scaled-up reaction in a 300 mL reactor, using $Mn_2(HTFA)_4(TFA)_4$ (510 mg, 0.5 mmol) for the conversion of methane to MeTFA in the presence of O_2. Conditions: CH_4 (1 atm), HTFA:TFAA 4:1 vol. ratio (300 mL), 180 °C, 3 h. Deviation is calculated based on three independent experiments.

Table E1: XAFS Refinement Mn–O first shell.

Parameter	Value	Error
S_0(Fixed)	0.93	
ΔE_0	3.9	1.0
CN_O	7.0	0.2
ΔR-O	2.178	0.008
σ^2 -O	0.007	0.007

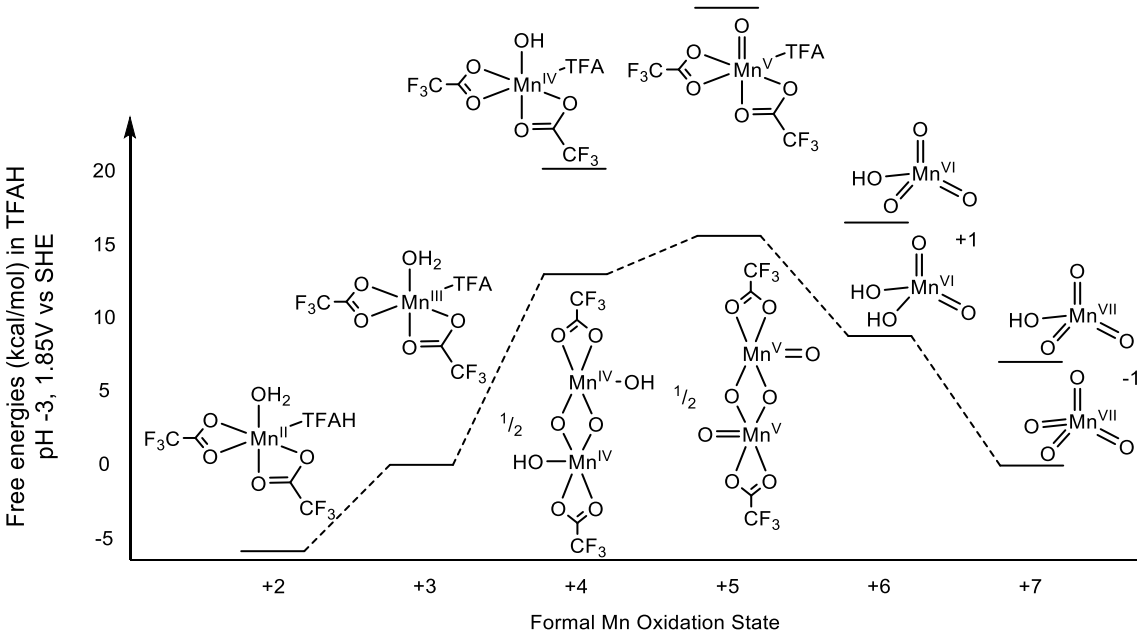

Figure E6: DFT free energies for the different oxidation states of Mn when exposed to the HTFA solvent and O_2. Even at conditions that theoretically favor higher oxidation states, the Mn(IV) monomer remains $>$ 25 kcal/mol above the Mn(II) monomer. Energies were calculated with the B3LYP-D3 functional.

Figure E7: DFT free energy barrier for the methyl radical to combine with a free TFA anion to generate a MeTFA radical anion.

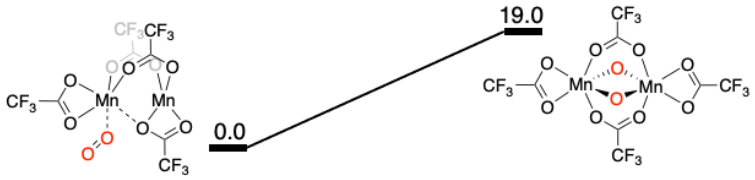

Figure E8: DFT free energies at 473 K for oxidation of $Mn_2(TFA)_4$ to $Mn_2(O)_2(TFA)_4$ via O_2. Energies are in kcal/mol.

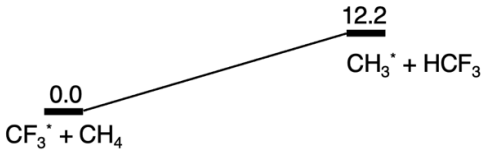

Figure E9: DFT free energies at 473 K for the reaction of the CF_3 radical with methane to generate fluoroform (HCF_3) and the methyl radical (radicals are denoted by *).

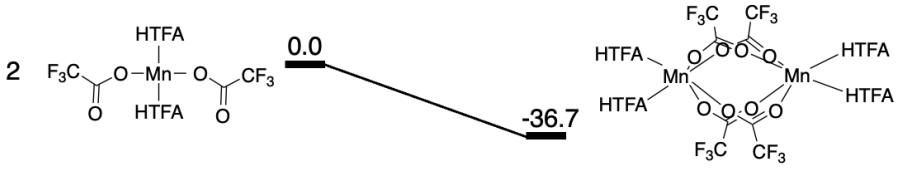

Figure E10: DFT free energy at 473 K for the dimerization of two Mn^{II}(TFA)2(HTFA)2 to $[Mn^{II}(TFA)_2(HTFA)_2]_2$.

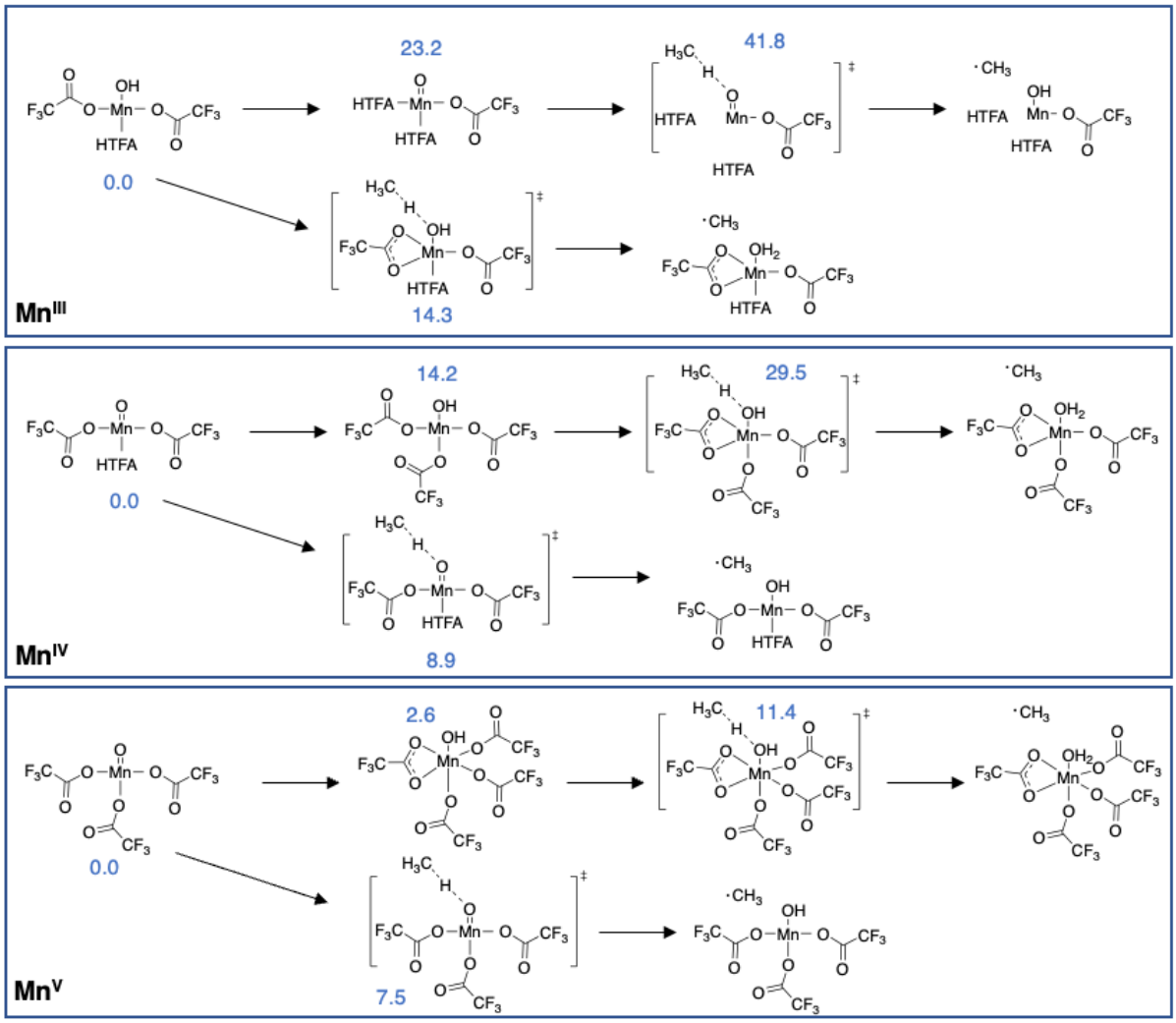

Figure E11: Relative DFT-calculated free energies at 473 K for Mn^{III} (top), Mn^{IV} (middle), and Mn^{V} (bottom) species. Values are reported in kcal/mol. The ground state Mn species for each oxidation state were normalized to 0.0 kcal/mol to illustrate the variation in HAT barrier with varying Mn oxidation. We note that the Mn^{IV} and Mn^{V} states are significantly higher in energy than the Mn^{III} due to the additional oxidation required.

Starting with Mn^{III}, we calculated the relative energies of $Mn^{III}(O)(TFA)(HTFA)_2$, $Mn^{III}(OH)(TFA)_2(HTFA)$, and $Mn^{III}(OO)(TFA)_2(HTFA)$ for which OO is a peroxo ligand. The peroxo ligand was calculated to be unstable; upon geometry optimization, the peroxo complex $Mn^{III}(OO)(TFA)_2(HTFA)$ dissociated O_2. Thus, only Mn^{III}–OH and Mn^{III}=O remained as likely candidates for the active Mn species to break methane C–H bonds. The conversion of the hydroxo complex $Mn^{III}(OH)(TFA)_2(HTFA)$ to the

oxo complex $Mn^{III}(O)(TFA)(HTFA)_2$ requires H atom transfer from the hydroxo ligand to a TFA ligand. Setting the $Mn^{III}(OH)(TFA)_2(HTFA)$ species to 0.0 kcal/mol, DFT predicts the $Mn^{III}(O)(TFA)(HTFA)_2$ complex to be 23.2 kcal/mol higher in free energy, indicating that Mn^{III} prefers bearing hydroxo/TFA ligand combination over an oxo/HTFA configuration. We calculated the HAT barriers from CH_4 to the hydroxo and oxo ligands of these two species. Relative to the $Mn^{III}(OH)(TFA)_2(HTFA)$ ground state, HAT from methane to generate the methyl radical and $Mn^{II}(OH_2)(TFA)_2(HTFA)$ requires a free energy barrier of 14.3 kcal/mol at 473 K. The HAT transition state from CH_4 to the oxo ligand $Mn^{III}(O)(TFA)(HTFA)_2$ lies 41.8 kcal/mol above the ground state, or 18.6 kcal/mol above the Mn^{III}=O species. We find that for Mn^{III} the hydroxo ligand provides a more facile route for methane HAT compared to the oxo.

In analogous calculations for Mn^{IV}, we find that the peroxo ligand is likely to undergo rapid dissociation from the Mn center to form molecular O_2, indicating that Mn^{IV}-OO would not be a stable intermediate. In contrast to Mn^{III}, DFT predicts Mn^{IV} to favor an oxo ligand over a hydroxo ligand. Specifically, DFT predicts $Mn^{IV}(O)(TFA)_2(HTFA)$ to be 14.2 kcal/mol lower than $Mn^{IV}(OH)(TFA)_3$. Moreover, DFT predicts that HAT from CH_4 to the oxo ligand of $Mn^{IV}(O)(TFA)_2(HTFA)$ requires a barrier of 8.9 kcal/mol, while HAT from CH_4 to the hydroxo ligand of $Mn^{IV}(OH)(TFA)_3$ requires a barrier of 29.5 kcal/mol (or 15.3 kcal/mol relative to the Mn^{III}-OH species).

Finally, an identical analysis was made for Mn^{V}. Again, the peroxo ligand was unstable, leaving Mn^{V}-OH and Mn^{V}=O as potential species. DFT predicts the $Mn^{V}(O)(TFA)_3$ species to be 2.6 kcal/mol more stable than $Mn^{V}(OH)(TFA)_4$. Homolytic breaking of the CH_4 C–H bond by $Mn^{V}(O)(TFA)_3$ would require a free energy barrier of 7.5 kcal/mol while the same reaction using $Mn^{V}(OH)(TFA)_4$ would require a barrier of 11.4 kcal/mol (or 8.8 kcal/mol relative to the Mn^{V}-OH state). While Mn^{IV} and Mn^{V} states provide lower free energy barriers for HAT from CH_4, they are highly unlikely to form under our reaction conditions and are intrinsically higher in energy than the Mn^{II} and Mn^{III} states, suggesting that the solution likely consists primarily of Mn^{II}, Mn^{III}. Hence, herein, we focus on the mechanism for partial oxidation of methane to MeTFA by a Mn^{III} active center. As we have calculated the Mn^{III}-OH species to be lower in free energy and to require a lower HAT barrier than the Mn^{III}=O species, we investigate the mechanism using $Mn^{III}(OH)(TFA)_2(HTFA)$ as the active catalyst.

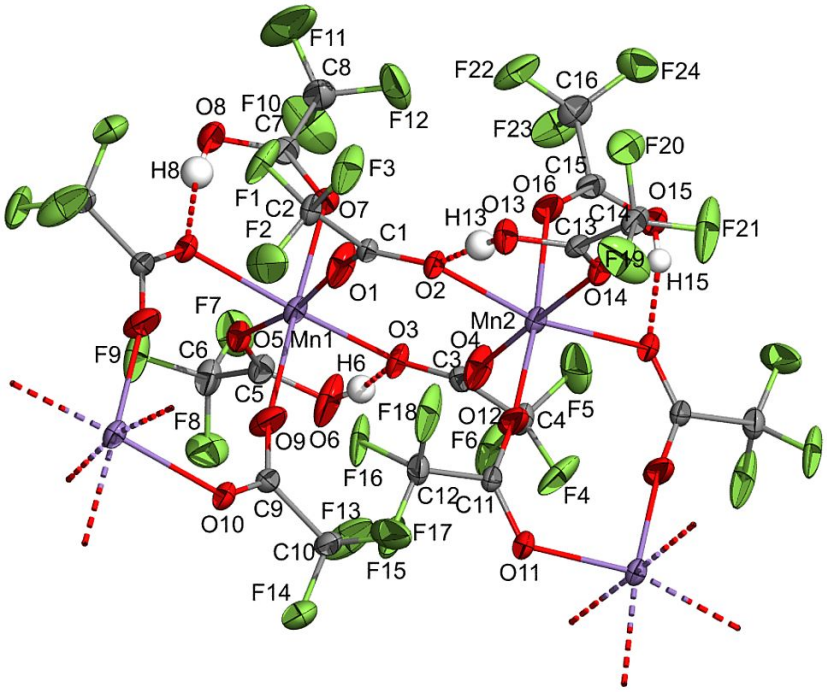

Figure E12: Solid state structure of $Mn_2(HTFA)_4(TFA)_4$. Thermal ellipsoids are shown at 50% probability. Only the major orientation of the disordered CF_3 groups is shown. While only 8 TFA or HTFA units are bound to one of the two Mn atoms in the crystal unit of formula $Mn_2(HTFA)_4(TFA)_4$, we have chosen to shown 10 TFA ligands along with two Mn atoms that do not belong to the crystal unit to help the reader understand the close coordinating environment of each Mn atom.

Table E2: Crystallographic data for $Mn_2(HTFA)_4(TFA)_4$

	$Mn_2(HTFA)_4(TFA)_4$
CCDC number	2131612
Formula	$C_{16}H_4F_{24}Mn_2O_{16}$
FW (g/mol)	1018.64
Temp (K)	100(2)
λ (Å)	0.71073
Size (mm)	0.090 x 0.188 x 0.213
Crystal habit	colorless plate
Crystal system	triclinic
Space group	P -1
a (Å)	10.3615(15)
b(Å)	13.550(2)
c (Å)	13.954(2)
α (°)	105.108(4)
β (°)	111.269(4)
γ (°)	107.177(4)
Volume ($Å^3$)	1588.5(4)
Z	2
Density (g/cm^3)	2.130
μ (mm^{-1})	1.005
F(000)	989
ϑ range (°)	1.72 to 26.45
Index ranges	$-12 \leq h \leq 12$

	$-16 \leq k \leq 16$ $-17 \leq l \leq 17$
Reflns collected	34969
Independent reflns	6519 [$R_{int} = 0.0965$]
Data / restraints /parameters	6519 / 53 / 581
GOF on F^2	1.009
R_1 ($I>2\sigma(I)$)	0.0490
wR_2 (all data)	0.1354

Appendix F

Appendix for: Phosphine Modulation for Enhanced CO_2 Capture: Quantum Mechanics Predictions of New Materials

Reproduced with permission from:

A Prokofjevs, WA Goddard III

J. Phys. Chem. Lett., **2022**, *13, 48, 11183-11190*

H: Enthalpy: U+ZPE+SCFE+nRT; U is total energy, ZPE is zero-point energy, SCFE is self-consistent field energy, R is ideal gas constant, T is temperature (298.15 K), n=1.

G: Corrected Gibbs free energy: H-T*(0.5*(Strans+Srot)+Svib+Selec); the 0.5 factor account for hindered librational modes in solvent.

Strans, Srot, Svib, Selec: Translational, rotational, vibrational, and electronic entropy, respectively

Table F1: Phosphine Energies. H and G are in Hartree. Entropies are in cal/mol/K.

Species	H	G	Strans	Srot	Svib

1	-648.947803	-648.97555	40.547	28.612	23.85
2	-782.818765	-782.85761	41.388	30.941	45.628
3	-915.50665	-915.54471	42.016	31.342	43.465
4	-3628.71483	-3628.7852	44.024	35.384	108.425
5	-2291.040279	-2291.0948	43.451	33.518	76.424
ref	-1649.895547	-1649.977	44.282	36.284	131.262
2.2.3	-1652.278539	-1652.354	44.005	35.974	118.981
2.2.3_P-H	-1652.27618	-1652.3502	44.005	35.886	115.81
2.2.1	-1544.423194	-1544.501	43.962	36.029	123.781

2.2.2	-1592.60481	-1592.6812	43.984	36.049	120.854
6	-447.78689	-447.80838	38.863	25.466	13.097
3.1	-1317.093193	-1317.1514	43.412	34.565	83.489

Table F2: CO_2-bound Phosphine Energies. H and G are in Hartree. Entropies are in cal/mol/K.

Species	H	G	Strans	Srot	Svib
1	-837.511419	-837.54687	41.404	30.322	38.785
2	-971.398625	-971.44322	42.056	31.84	56.95
3	-1104.080968	-1104.1251	42.568	32.336	55.404
4_3	-3817.267334	-3817.3442	44.318	35.91	121.64
4_4	-3817.266054	-3817.3425	44.318	35.946	120.858

5_2	-2479.589946	-2479.6515	43.804	34.249	90.57
5_3	-2479.59074	-2479.6525	43.804	34.426	90.953
ref	-1838.485019	-1838.5728	44.553	36.708	144.112
2.2.3	-1840.880421	-1840.9596	44.301	36.235	126.473
2.2.3_path2	-1840.9	-1840.9505	44.301	36.174	125.654
2.2.1	-1733.01331	-1733.0967	44.263	36.293	135.309
2.2.2	-1781.19944	-1781.2808	44.282	36.304	130.959
2.2.2_path2	-1781.1701	-1781.2534	44.282	36.774	135.171

6	-636.382386	-636.41059	40.238	28.211	25.162
6_Htransfer	-447.06216	-447.08471	38.822	25.398	15.388
3.1	-1505.670094	-1505.7337	43.769	35.102	94.545

Table F3: Phosphine Energies in different Solvents. H and G are in Hartree. Entropies are in cal/mol/K.

Species	H	G	Strans	Srot	Svib
2	-782.81877	-782.85761	41.388	30.941	45.628
2_wat	-782.82894	-782.8672	41.388	30.934	44.387
2_ace	-782.82233	-782.86078	41.388	30.935	44.81
2.1_far	-1104.7118	-1104.7669	42.725	33.666	77.851

2.2_far	-1426.6005	-1426.6713	43.644	35.513	109.395
co2	-188.56374	-188.576	37.27	13.054	0.662
wat_co2	-188.56179	-188.576	37.27	13.054	0.663
ace_co2	-188.56446	-188.576	37.27	13.054	0.663
formate	-189.27482	-189.28875	37.338	20.646	0.337

Table F4: Reaction Intermediate energies for CO_2 reduction to methanol. H and G are in Hartree. Entropies are in cal/mol/K.

Species	H	G	Strans	Srot	Svib	Selec
2.2	-1615.1928	-1615.2694	43.976	35.738	121.33	0
hoco	-1615.7049	-1615.7831	43.984	35.765	123.365	1.377

co	-1539.9031	-1539.9809	43.86	35.792	124.029	0
hco	-1540.4747	-1540.5511	43.867	35.64	119.728	1.377
coh	-1540.4092	-1540.4852	43.867	35.672	118.922	1.377
h2co	-1541.0854	-1541.159	43.875	35.682	115.041	0
hcoh	-1541.0402	-1541.1166	43.875	35.654	121.122	0
h3co	-1541.6508	-1541.7254	43.882	35.503	116.146	1.377
P-MeOH	-1426.6005	-1426.6713	43.644	35.513	109.395	0
methanol	-115.65783	-115.67143	36.324	18.996	0.993	0
H2_vac	-1.15472	-1.1621086	28.08	3.037	0	0

wat	-76.409372	-76.420412	34.608	11.875	0.006	0
CO	-113.3015	-113.3127	35.923	11.257	0	0

Table F5: Phosphine Features. Charges are Mulliken charges, angles are degrees, dipoles are debye.

Species	P charge	CO2 charge	O-C-O angle	Dipole magnitude	P charge w/o CO2	P charge change
1	0.828	-0.758	134.126	2.0357	0.577	0.251
2	0.54	-0.761	132.612	3.8949	0.317	0.223
3	1.17	-0.883	132.032	1.8647	0.661	0.509
4_3	-0.122	-0.476	138.458	1.1372	0.039	-0.161
4_4	-0.012	-0.589	136.387	1.1372	0.125	-0.137
5_2	-0.151	-0.371	140.31	0.3006	0.028	-0.179
5_3	-0.008	-0.455	140.861	0.3006	0.126	-0.134
ref	0.944	-0.852	130.75	4.5	0.57719	0.36681
2.2.3	1.04047	-1.02612	128.13	5.6077	0.52654	0.51393

2.2.1	1.08555	-0.84005	130.51	1.6154	0.71865	0.3669
2.2.2	1.05621	-0.90984	129.44	4.1871	0.61786	0.43835
6	0.487	-0.89318	121.2	6.1364	0.0911	0.3959
3.1	1.27282	-0.86706	131.9	0.9831	0.88741	0.38541

Table F6: Continued phosphine features. Charges are Mulliken charges, angles are degrees, dipoles are debye, HOMO-LUMO gap is kcal/mol. CH_3 denotes the charge of a -CH_3 group when bound to the central phosphine (for example, phosphine **1** has 1 CH_3 and **2** has 2).

Species	CH3 charge	Ligand charge	P-C dipole	Dipole w/ CO2	Dipole change	LUMO-HOMO Gap
1	0.043	-0.113	0.758	11.8255	9.7898	163.955813
2	0.045	0.176	0.437	9.6558	5.7609	155.057721
3		-0.287	1.126	13.8845	12.0198	139.928455
4_3	-0.03	0.628	-0.247	7.5379	6.4007	145.048937
4_4	0.012	0.589	-0.169	6.8758	5.7386	145.048937
5_2	0.093	0.429	-0.354	7.7115	7.4109	152.277852
5_3	0.05	0.413	-0.19	8.6527	8.3521	152.277852

Table F7: Modified **2,** and **2** in different solvent environments. H and G are in Hartree, entropies are cal/mol/K.

Species	H	G	Strans	Srot	Svib
2	-971.39863	-971.44322	42.056	31.84	56.95
2_wat	-971.40784	-971.45136	42.056	31.786	54.719
2_acetonitrile	-971.40555	-971.44997	42.056	31.846	56.585
2.1	-1293.2951	-1293.3554	43.168	34.14	88.332
2.2	-1615.1928	-1615.2694	43.976	35.738	121.33

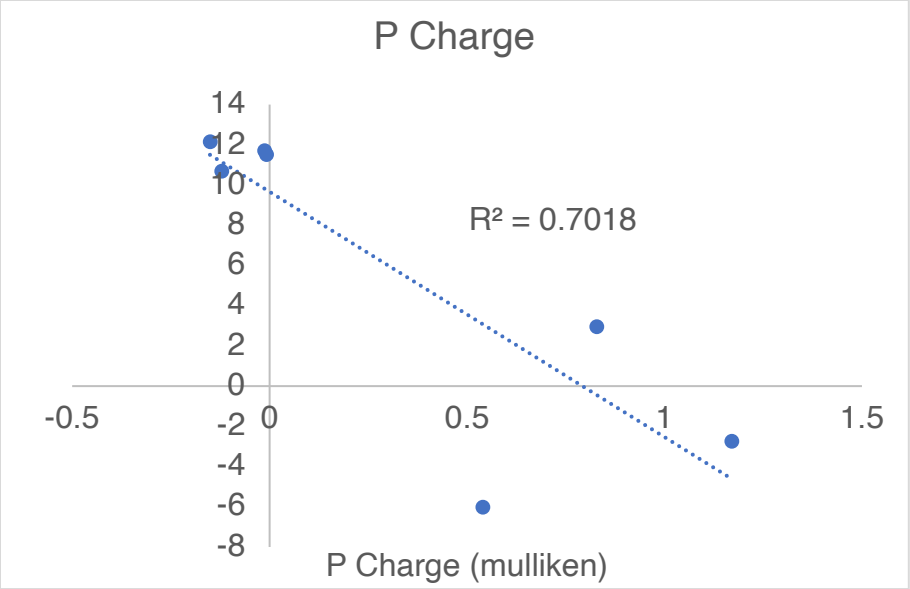

Figure F1: Phosphorus charge (Mulliken charge) in parent phosphine versus CO_2 binding free energy (kcal/mol, y axis).

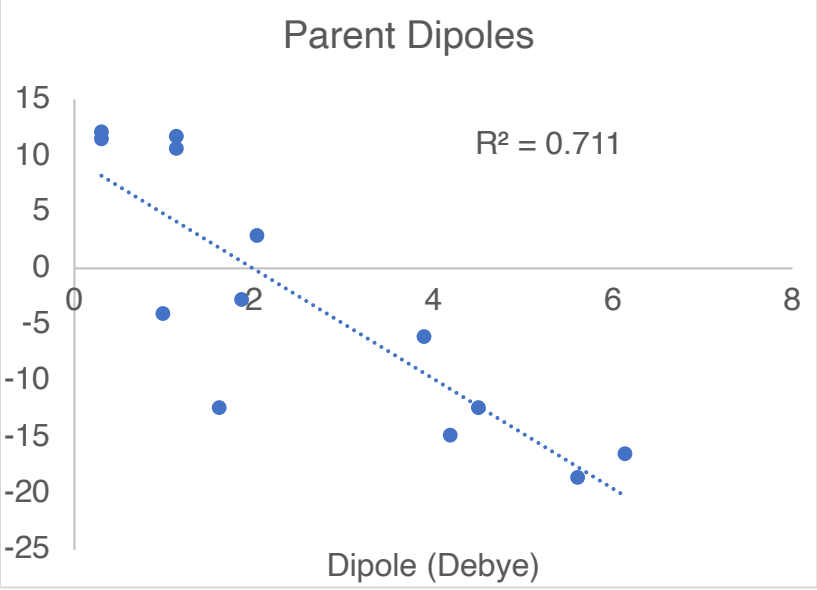

Figure F2: Dipole of parent phosphine (debye) versus CO_2 binding free energy (kcal/mol, y axis).

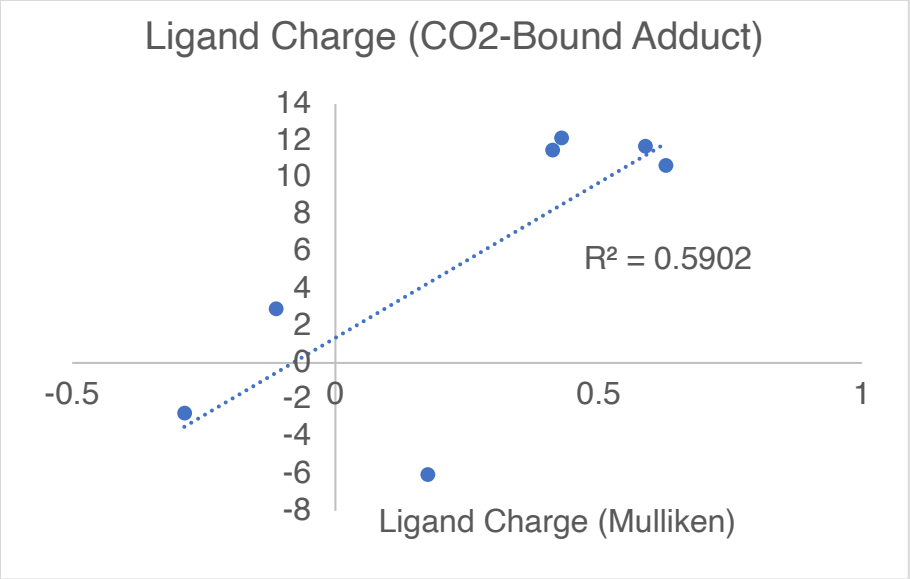

Figure F3: Ligand charge (Mulliken charge) in CO_2-bound adduct versus CO_2 binding free energy (kcal/mol, y axis). This is calculated by subtracting the P and CO_2 charges (and CH_3 charges if applicable) from the total charge.

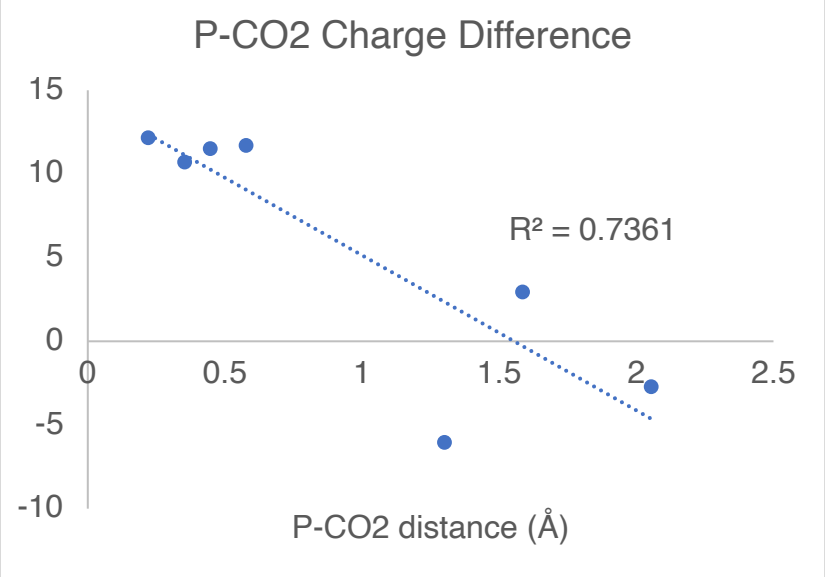

Figure F4: P-CO_2 charge difference (Mulliken charge) versus CO_2 binding free energy (kcal/mol, y axis). This is calculated as the P charge minus the CO_2 charge.

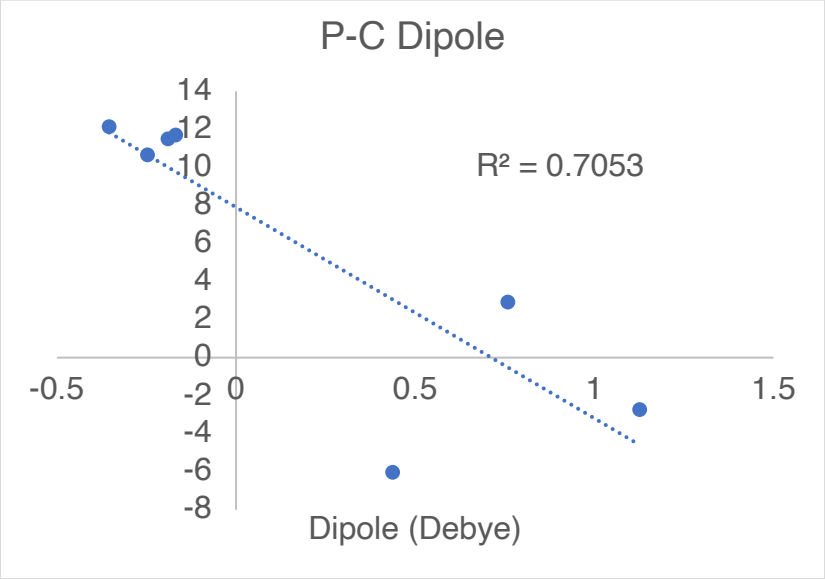

Figure F5: P-C charge difference (Mulliken charge) versus CO_2 binding free energy (kcal/mol, y axis). This is calculated as the P charge minus the C (in CO_2) charge.

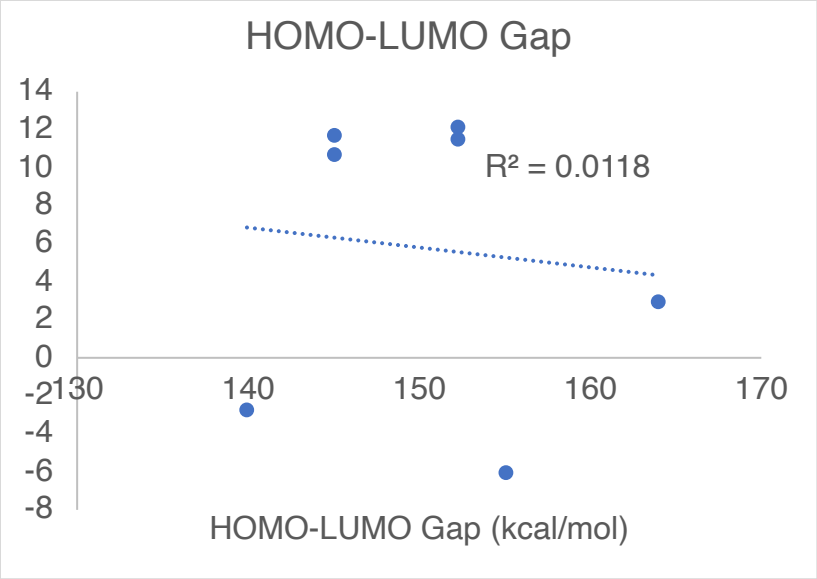

Figure F6: HOMO-LUMO gap (kcal/mol) of parent phosphine versus CO_2 binding free energy (kcal/mol, y axis). This is calculated as the LUMO energy minus the HOMO energy.

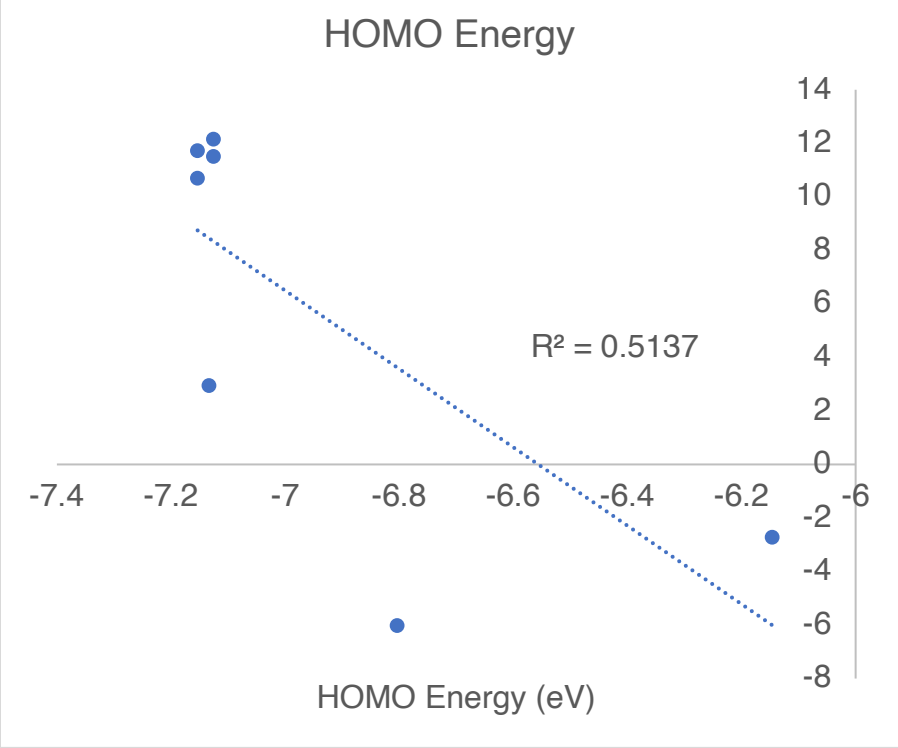

Figure F7: HOMO Energy (eV) of parent phosphine versus CO_2 binding free energy (kcal/mol, y axis).

Appendix G

Appendix for: Electrochemical Nitrate Reduction Catalyzed by 2D MBenes

Reproduced with permission from:

WA Goddard III

Definitions:

Esolv: solution-phase electronic energy in units of Hartree (Ha)

H+ZPE-TS: the summation of the phonon-derived enthalpy, zero-point energy, and entropy in units of electronvolts (eV)

NELECT: total number of electrons

ΔNELECT: difference in electrons relative to the 0-charge state

U v RHE: potential versus reversible hydrogen electrode in units of volts (V)

U v SHE: potential versus standard hydrogen electrode in units of volts (V)

n(min;U): equilibrium total number of electrons for a given potential

n(min;U)-n0: equilibrium difference in electrons relative to the 0-charge state for a given potential

G(n(min;U)): equilibrium Grand canonical free energy for a given potential in units of electronvolts (eV)

Table G1: Solution-phase energies (Hartree) for MBene pristine substrates, substrates with NO_3 adsorbed, and substrates with 2 H_2O adsorbed.

Element	Pristine Esolv	$*NO_3$ Esolv	$(*H_2O)_2$ Esolv
Tc	-1340.2578	-1398.4343	-1374.8769
Ti	-978.64908	-1036.8683	-1013.2642
Mn	-1729.1936	-1787.3701	-1763.794
Fe	-2060.8953	-2119.0681	-2095.5125
Cr	-1437.6749	-1495.8671	-1472.2919
V	-1196.711	-1254.9204	-1231.3262
Nb	-961.95162	-1020.1536	-996.56957
W	-1144.8297	-1203.0288	-1179.4585
Mo	-1140.7132	-1198.907	-1175.3301

Table G2: $*NO_3$ and $(*H_2O)_2$ entropies (eV) at 298.15 K.

Element	*NO_3 H+ZPE-TS	$(*H_2O)_2$ H+ZPE-TS
Tc	0.351132	1.254531
Ti	0.346193	1.215625
Mn	0.364658	1.27718
Fe	0.365103	1.240992
Cr	0.359729	1.267635
V	0.347262	1.22916
Nb	0.347293	1.238712
W	0.338886	1.238713
Mo	0.342285	1.228836

Table G3: Solution-phase energies (Ha) and entropies (eV) at 298.15 K of MnB intermediates.

Species	Esolv	H+ZPE-TS (eV)
Substrate	-1729.1936	0
NO3	-1787.3701	0.364658
HNO3	-1787.9406	0.574721

H2NO3	-1788.6227	0.913714
NO2	-1771.3275	0.253091
NO2H	-1771.9075	0.546941
NOH_O	-1771.8006	0.442516
NO_OH	--	--
NOH_OH	-1772.513	0.693756
NO2H2	-1772.513	0.73368
NOH2_OH	-1773.1206	1.062004
O_OH	-1762.0126	0.395143
(OH)2	-1762.6256	0.664694
OH_W	-1763.2119	0.959824
(H2O)2	-1763.794	1.27718

Table G4: Solution-phase energies (Ha) and entropies (eV) at 298.15 K of CrB intermediates.

Species	Energy (Ha)	Entropy (eV)
Substrate	-1437.6749	0
NO3	-1495.8671	0.359729
HNO3	-1496.4523	0.547344

H2NO3	-1497.0884	0.813218
NO2	-1479.8233	0.241225
NO2H	-1480.4122	0.554095
NOH_O	-1480.4405	0.483659
NO_OH	-1480.429	0.463563
NOH_OH	-1481.0702	0.829728
NO2H2	-1481.0653	0.828948
NOH2_OH	-1481.6551	1.073376
O_OH	-1470.5395	0.376464
(OH)2	-1471.1306	0.643121
OH_W	-1471.7074	0.934599
(H2O)2	-1472.2919	1.267635

Table G5: Solution-phase energies (Ha) and entropies (eV) at 298.15 K of VB intermediates.

Species	Energy (Ha)	Entropy (eV)
Substrate	-1196.711	0
NO3	-1254.9204	0.347262
HNO3	-1255.5153	0.580645

H2NO3	-1256.1945	0.85627
NO2	-1238.8841	0.230915
NO2H	-1239.4748	0.556672
NOH_O	-1239.5082	0.46371
NO_OH	-1239.4825	0.439654
NOH_OH	-1240.1312	0.828621
NO2H2	--	--
NOH2_OH	-1240.7188	1.087305
O_OH	-1229.6194	0.410069
(OH)2	-1230.1984	0.638344
OH_W	-1230.7577	0.917379
(H2O)2	-1231.3262	1.22916

Table G6: Solution-phase energies (Ha) and entropies (eV) at 298.15 K of reactant species.

Species	Energy (Ha)	Entropy (eV)
NO_3	-58.017908	0.48721263
NH_3	-11.776272	1.06103708
H_2O	-17.281288	0.65724608

H_2	-1.1653731	0.15606425

Table G7: Solution-phase energies (Ha) and entropies (eV) at 298.15 K of Ru-doped CrB intermediates.

Substrate	-1445.6871
NO3	-1503.859
HNO3	-1504.545
H2NO3	-1505.1396
NO2	-1487.8106
NO2H	-1488.4049
NOH_O	-1488.427
NO_OH	-1488.4259
NOH_OH	-1489.0507
NO2H2	-1489.0898
NOH2_OH	-1489.6965
O_OH	-1478.5219
(OH)2	-1479.1156
OH_W	-1479.6894
(H2O)2	-1480.2941

Table G8: Solution-phase energies (Ha) and entropies (eV) at 298.15 K of Mn-doped CrB intermediates.

Substrate	-1455.8887
NO3	-1514.0707
HNO3	-1514.7586
H2NO3	-1515.3496
NO2	-1498.0356
NO2H	--
NOH_O	-1498.6479
NO_OH	--
NOH_OH	-1499.3105
NO2H2	-1499.3073
NOH2_OH	-1499.9101
O_OH	-1488.7474
(OH)2	-1489.3354
OH_W	-1489.914
(H2O)2	-1490.4984

Table G9: Solution-phase energies (Ha) for Mn-doped CrB at different charges.

NELECT	ΔNELECT	Free energy [Ha]
289	0	-1455.8887
288.5	-0.5	-1455.8193
288	-1	-1455.7537
287.5	-1.5	-1455.6603

Table G10: Solution-phase energies (Ha) for *NO_3 on Mn-doped CrB at different charges.

NELECT	ΔNELECT	Esolv (Ha)
296	0	-1514.0707
295.5	-0.5	-1513.9951
295	-1	-1513.9153
294.5	-1.5	-1513.8301

Table G11: Solution-phase energies (Ha) for *HNO_3 on Mn-doped CrB at different charges.

NELECT	ΔNELECT	Esolv (Ha)
297	0	-1514.7586
296.5	-0.5	-1514.687

296	-1	-1514.6067
295.5	-1.5	-1514.523

Table G12: Solution-phase energies (Ha) for *H_2NO_3 on Mn-doped CrB at different charges.

NELECT	ΔNELECT	Esolv (Ha)
298	0	-1515.3496
297.5	-0.5	-1515.2765
297	-1	-1515.1989
296.5	-1.5	-1515.1143

Table G13: Solution-phase energies (Ha) for *NOH*O on Mn-doped CrB at different charges.

NELECT	ΔNELECT	Esolv (Ha)
291	0	-1498.6479
290.5	-0.5	-1498.5724
290	-1	-1498.4946
289.5	-1.5	-1498.4131

Table G14: Solution-phase energies (Ha) for *NOH*OH on Mn-doped CrB at different charges.

NELECT	ΔNELECT	Esolv (Ha)

292	0	-1499.3105
291.5	-0.5	-1499.2415
291	-1	-1499.1638
290.5	-1.5	-1499.0804

Table G15: Solution-phase energies (Ha) for *NOH_2*OH on Mn-doped CrB at different charges.

NELECT	ΔNELECT	Esolv (Ha)
293	0	-1499.9101
292.5	-0.5	-1499.8409
292	-1	-1499.767
291.5	-1.5	-1499.6809

Table G16: Solution-phase energies (Ha) for *O*OH on Mn-doped CrB at different charges.

NELECT	ΔNELECT	Esolv (Ha)
286	0	-1488.7474
285.5	-0.5	-1488.6698
285	-1	-1488.5865
284.5	-1.5	-1488.5023

Table G17: Solution-phase energies (Ha) for $(*OH)_2$ on Mn-doped CrB at different charges.

NELECT	ΔNELECT	Esolv (Ha)
287	0	-1489.3354
286.5	-0.5	-1489.2632
286	-1	-1489.1836
285.5	-1.5	-1489.1002

Table G18: Solution-phase energies (Ha) for *OH*H_2O on Mn-doped CrB at different charges.

NELECT	ΔNELECT	Esolv (Ha)
288	0	-1489.914
287.5	-0.5	-1489.8398
287	-1	-1489.7637
286.5	-1.5	-1489.6876

Table G19: Solution-phase energies (Ha) for $(*H_2O)_2$ on Mn-doped CrB at different charges.

NELECT	ΔNELECT	Esolv (Ha)
289	0	-1490.4984
288.5	-0.5	-1490.4356
288	-1	-1490.3689
287.5	-1.5	-1490.2863

Table G20: GCP energies and corresponding number of electrons at various applied potentials for the pristine Mn-doped CrB.

U vs RHE	U vs SHE	n(min;U)	n(min;U)-n0	G(n(min;U))
0.1	-0.6683	289.26411	0.26411011	-38463.153
0	-0.7683	289.02495	0.02494999	-38492.068
-0.1	-0.8683	288.78579	-0.2142101	-38520.958
-0.2	-0.9683	288.54663	-0.4533703	-38549.825
-0.6	-1.3683	287.589989	-1.4100107	-38665.052

Table G21: GCP energies and corresponding number of electrons at various applied potentials for $*NO_3$ on Mn-doped CrB.

U vs RHE	U vs SHE	n(min;U)	n(min;U)-n0	G(n(min;U))
0.1	-0.6683	295.953889	-0.0461105	-40018.079
0	-0.7683	296.143342	0.14334171	-40047.684
-0.1	-0.8683	296.332794	0.33279394	-40077.308
-0.2	-0.9683	296.522246	0.52224617	-40106.951

-0.6	-1.3683	297.280055	1.28005509	-40225.711

Table G22: GCP energies and corresponding number of electrons at various applied potentials for *HNO_3 on Mn-doped CrB.

U vs RHE	U vs SHE	n(min;U)	n(min;U)-n0	G(n(min;U))
0.1	-0.6683	296.693886	-0.3061143	-40032.658
0	-0.7683	296.845939	-0.1540607	-40062.335
-0.1	-0.8683	296.997993	-0.0020071	-40092.028
-0.2	-0.9683	297.150046	0.15004644	-40121.735
-0.6	-1.3683	297.758261	0.7582607	-40240.717

Table G23: GCP energies and corresponding number of electrons at various applied potentials for *H_2NO_3 on Mn-doped CrB.

U vs RHE	U vs SHE	n(min;U)	n(min;U)-n0	G(n(min;U))
0.1	-0.6683	297.681402	-0.3185982	-40044.472
0	-0.7683	297.840542	-0.1594576	-40074.248
-0.1	-0.8683	297.999683	-0.0003169	-40104.04

-0.2	-0.9683	298.158824	0.15882371	-40133.848
-0.6	-1.3683	298.795386	0.79538633	-40253.239

Table G24: GCP energies and corresponding number of electrons at various applied potentials for *NOH*O on Mn-doped CrB.

U vs RHE	U vs SHE	n(min;U)	n(min;U)-n0	G(n(min;U))
0.1	-0.6683	291.058838	0.05883774	-39618.236
0	-0.7683	291.364959	0.36495945	-39647.358
-0.1	-0.8683	291.671081	0.67108116	-39676.509
-0.2	-0.9683	291.977203	0.97720287	-39705.692
-0.6	-1.3683	293.20169	2.20168972	-39822.728

Table G25: GCP energies and corresponding number of electrons at various applied potentials for *NOH*OH on Mn-doped CrB.

U vs RHE	U vs SHE	n(min;U)	n(min;U)-n0	G(n(min;U))
0.1	-0.6683	291.07895	-0.9210497	-39630.682
0	-0.7683	291.052334	-0.9476664	-39659.789
-0.1	-0.8683	291.025717	-0.9742831	-39688.893

-0.2	-0.9683	290.9991	-1.0008998	-39717.994
-0.6	-1.3683	290.892634	-1.1073664	-39834.373

Table G26: GCP energies and corresponding number of electrons at various applied potentials for *NOH_2*OH on Mn-doped CrB.

U vs RHE	U vs SHE	n(min;U)	n(min;U)-n0	G(n(min;U))
0.1	-0.6683	292.085338	-0.9146623	-39642.777
0	-0.7683	292.058799	-0.9412011	-39671.985
-0.1	-0.8683	292.03226	-0.9677399	-39701.189
-0.2	-0.9683	292.005721	-0.9942788	-39730.391
-0.6	-1.3683	291.899566	-1.100434	-39847.172

Table G27: GCP energies and corresponding number of electrons at various applied potentials for *O*OH on Mn-doped CrB.

U vs RHE	U vs SHE	n(min;U)	n(min;U)-n0	G(n(min;U))
0.1	-0.6683	286.547389	0.54738885	-39368.959
0	-0.7683	286.82762	0.82761987	-39397.627

-0.1	-0.8683	287.107851	1.1078509	-39426.324
-0.2	-0.9683	287.388082	1.38808193	-39455.049
-0.6	-1.3683	288.509006	2.50900603	-39570.228

Table G28: GCP energies and corresponding number of electrons at various applied potentials for $(*OH)_2$ on Mn-doped CrB.

U vs RHE	U vs SHE	n(min;U)	n(min;U)-n0	G(n(min;U))
0.1	-0.6683	286.743754	-0.2562463	-39380.965
0	-0.7683	286.753872	-0.2461284	-39409.64
-0.1	-0.8683	286.76399	-0.2360104	-39438.316
-0.2	-0.9683	286.774108	-0.2258925	-39466.993
-0.6	-1.3683	286.814579	-0.1854207	-39581.71

Table G29: GCP energies and corresponding number of electrons at various applied potentials for $*OH*H_2O$ on Mn-doped CrB.

U vs RHE	U vs SHE	n(min;U)	n(min;U)-n0	G(n(min;U))
0.1	-0.6683	287.755559	-0.2444406	-39392.355
0	-0.7683	287.767347	-0.2326533	-39421.131

-0.1	-0.8683	287.779134	-0.2208661	-39449.908
-0.2	-0.9683	287.790921	-0.2090789	-39478.687
-0.6	-1.3683	287.83807	-0.16193	-39593.813

Table G30: GCP energies and corresponding number of electrons at various applied potentials for $(*H_2O)_2$ on Mn-doped CrB.

U vs RHE	U vs SHE	n(min;U)	n(min;U)-n0	G(n(min;U))
0.1	-0.6683	288.689145	-0.3108546	-39404.135
0	-0.7683	288.699764	-0.3002356	-39433.005
-0.1	-0.8683	288.710383	-0.2896166	-39461.875
-0.2	-0.9683	288.721002	-0.2789976	-39490.747
-0.6	-1.3683	288.763478	-0.2365217	-39606.244

Table G31: Energies (eV) for reducing $*NO_3$ to $*HNO_3$ for different MBenes.

Element	E($*NO_3$ → $*HNO_3$)
Tc	5.51145632
Ti	6.03699632
Mn	5.50214632

Fe	5.51002632
Cr	5.73991632
V	8.15995832
Nb	6.03609632
W	5.87579632
Mo	5.91557632

Table G32: Energies (eV) for reducing $(*OH)_2$ to $(*H_2O)_2$ for different doped MBenes.

Substrate	E($(*OH)_2$ --> $(*H_2O)_2$)
Tc	0.54148572
Ti	1.09902572
Mn	0.53381572
Fe	0.35609572
Cr	0.59155572
V	1.09817572
Nb	1.24924572
W	1.63542572
Mo	0.95743572

Ru	0.22018572

Appendix H

Appendix for: The Reaction Mechanism Underlying Pd(II) Catalyzed Oxidative Coupling of Ethylene and Benzene to Form Styrene: Identification of a Mono-Pd^{II} Bis-Cu^{II} Complex as the Active Catalyst

Reproduced with permission from:

MT Bennett, JF Ellena, DA Dickie, TB Gunnoe, WA Goddard III

Organometallics, **2022***, 41, 15, 1988-2000*

Section 1. Supplementary tables and figures for DFT calculations

Free energies (G) are provided in hartree and entropies (S) are provided in cal/mol/K. Strans, Srot, Svib, and Selec are the translational, rotational, vibrational, and electronic entropies, respectively.

Table H1. G's and S's for Structures in Scheme 4.

Species	G	Strans	Srot	Svib	Selec
A	-1505.8902	46.73	36.91	166.09	2.18
B	-1483.9034	46.94	36.98	162.46	1.38
C	-1751.6356	47.13	37.15	156.66	--
D	-1821.0448	46.94	37.77	155.57	1.38
E	-1978.2419	47.19	38.23	200.83	1.38
F	-1237.1853	45.62	35.21	89.62	1.38
G	-1394.3677	46.01	35.94	145.03	1.38
H	-1167.7291	45.93	35.32	88.25	--
I	-583.8706	43.86	30.48	35.70	--
J	-1324.9339	46.28	36.08	141.60	--
K	-1167.7548	45.93	34.74	100.74	--
L	-1237.2090	45.62	34.54	92.48	1.38

Table H2. G's and S's for Structures in Scheme 5.

Species	G	Strans	Srot	Svib	Selec
A	-1505.9169	46.73	36.91	166.09	2.18
A_benzene	-1738.0744	47.10	37.82	201.41	2.18
A_CMD	-1738.0409	45.36	36.76	143.81	2.18
B	-1829.2065	46.94	37.04	167.08	1.38

B_benzene	-1716.0801	47.29	37.97	198.38	1.38
B_CMD	-1716.0575	45.55	36.85	147.18	1.38
L	-1237.1856	45.62	34.54	92.48	1.38
L_benzene	-1469.4154	46.15	36.02	138.16	1.38
L_CMD	-1228.7536	46.15	36.05	131.37	1.38
C	-1983.8251	47.46	38.06	195.97	--
C_benzene	-1751.6101	47.13	37.15	156.66	--
C_CMD	-1694.0548	45.72	36.91	144.75	--

Table H3. G's and S's for Structures in Scheme 7.

Species	G	Strans	Srot	Svib	Selec
I0	-1505.9169	46.73	36.91	166.09	2.18
I1	-1738.0744	47.10	37.82	201.41	2.18
TS1	-1738.0409	45.36	36.76	143.81	2.18
I2	-1816.6377	47.22	38.08	221.70	2.18
TS2	-1587.5720	46.95	37.50	185.33	2.18
I3	-2436.4562	45.83	38.10	171.40	2.18
TS3	-2357.8653	45.72	37.84	141.73	2.18
I4	-2357.8824	45.72	37.92	152.55	2.18

Section 2. XYZ Coordinates

A

Cu1	1.6326206200	0.9597590124	0.0020158828
C2	0.0272661265	2.5793330066	-1.8464766044
O3	1.0873593340	2.5123010583	-1.1536228005
O4	-1.0044390934	1.8582675502	-1.6860290508
C5	-2.1735014542	-1.2529430070	1.8992018178
O6	-1.5405570138	-2.1384330224	1.2431129267
O7	-2.1157229121	-0.0027765195	1.7143194201
C8	-3.0977323617	-1.7518144087	2.9891443836
H9	-3.0930430044	-1.0532515367	3.8302274861
H10	-4.1169867887	-1.7898415383	2.5849630165
H11	-2.8079711637	-2.7518203760	3.3171378148
C12	-0.0224765558	3.6199793080	-2.9451201384
H13	0.9844252363	3.9176904997	-3.2447662871
H14	-0.5817089034	3.2325471777	-3.8014229086
H15	-0.5564588151	4.4990750737	-2.5627314198
Pd16	-0.0092323076	-1.9077120557	-0.0151810794
C17	-2.2829068804	-1.3323330758	-1.7871476760
O18	-2.6749872216	-0.3436401819	-1.1041328610
O19	-1.2152239216	-1.9974193159	-1.6016367287
C20	-0.0333984630	2.6184630250	1.8256890294
O21	1.0070610851	1.9106302841	1.6720399750
O22	-1.0899401453	2.5371828329	1.1273089767
C23	-0.0178537813	3.6638233920	2.9210336895

H24	-0.9792098676	3.6769796063	3.4420951776
H25	0.7981734860	3.4737055114	3.6214706807
H26	0.1312939055	4.6476287304	2.4591398439
C27	-3.1621713339	-1.7600306532	-2.9419047199
H28	-3.1564167350	-0.9660586055	-3.6974300140
H29	-2.8068863274	-2.6932631411	-3.3822508099
H30	-4.1923908437	-1.8741797584	-2.5901501981
Cu31	-1.6385119026	0.9629664336	0.0110797990
C32	2.2456579041	-1.3768094144	1.7913658231
O33	2.6246767179	-0.3520496097	1.1575711769
O34	1.1959860323	-2.0580862715	1.5640923474
C35	3.1159759246	-1.8337822466	2.9424532355
H36	3.0489331006	-1.0908986950	3.7455906227
H37	2.7948810633	-2.8081632268	3.3146881926
H38	4.1597117915	-1.8754195458	2.6158469333
C39	2.2056430050	-1.2554110482	-1.8867473177
O40	2.1870016426	-0.0090466341	-1.6743472906
O41	1.5230864737	-2.1340049212	-1.2726716090
C42	3.1487067932	-1.7689859483	-2.9540980035
H43	4.1067790503	-2.0098767944	-2.4767009710
H44	2.7517044279	-2.6765963322	-3.4138574373
H45	3.3243740655	-0.9974525549	-3.7070811154

B

Pd1	1.6620539936	0.9765893662	0.0098143228
C2	-0.0682468523	2.5612681999	-1.8589133756
O3	1.0593670849	2.4509586155	-1.2887499030
O4	-1.0961398692	1.8759320602	-1.6106696665
C5	-2.2307490888	-1.2469482747	1.8809456142
O6	-1.5837563373	-2.1615211402	1.2862966295
O7	-2.1475396834	-0.0102581975	1.6540646030
C8	-3.2057479569	-1.7022116041	2.9381227634
H9	-3.3402605216	-0.9198609510	3.6846577678
H10	-4.1708240391	-1.8822797821	2.4524950615
H11	-2.8721556919	-2.6308465821	3.3999481463
C12	-0.1787228091	3.6368534853	-2.9109697615
H13	0.7812540086	3.8027758496	-3.3986032742
H14	-0.9468437378	3.3738575163	-3.6374969572
H15	-0.4807950569	4.5648770214	-2.4143863985
Pd16	-0.0230315133	-1.9338786994	-0.0328267176
C17	-2.3384089829	-1.3066319878	-1.7872381779
O18	-2.6488960811	-0.3061430608	-1.0890524070
O19	-1.3057793759	-2.0305638362	-1.6375660435
C20	0.0065123425	2.6692301968	1.8049875438
O21	1.1419941306	2.1266858872	1.6304816544
O22	-1.0357888690	2.4335817838	1.1408785843

C23	-0.0787277155	3.7116307948	2.8922508356
H24	-1.0280517086	3.6185139763	3.4204641521
H25	0.7606203233	3.6258136488	3.5802672707
H26	-0.0498230437	4.6987553690	2.4206362218
C27	-3.2747563504	-1.6825292782	-2.9086699415
H28	-3.2685206330	-0.8785565872	-3.6495504841
H29	-2.9798457811	-2.6203697933	-3.3749491172
H30	-4.2900700225	-1.7569254148	-2.5137150642
Cu31	-1.5724672443	0.9068606300	0.0229703870
C32	2.2449451076	-1.3709459594	1.8792579087
O33	2.6115064244	-0.2958740061	1.3246474063
O34	1.2439559870	-2.0836519030	1.5829395767
C35	3.0990259621	-1.8400552292	3.0330052830
H36	2.9426692674	-1.1601171082	3.8750058170
H37	2.8344697264	-2.8540006302	3.3265117244
H38	4.1519323203	-1.7829632369	2.7523868236
C39	2.2951671467	-1.2602312700	-1.9138725349
O40	2.4027971616	-0.0342475061	-1.6210386724
O41	1.5380866371	-2.1129697053	-1.3705688596
C42	3.1934448947	-1.7685201219	-3.0163743883
H43	4.1046955892	-2.1648226383	-2.5577976905
H44	2.7036661228	-2.5750680891	-3.5606576205
H45	3.4693782722	-0.9558515713	-3.6868224885

C

Pd1	1.6368982636	0.9385252928	-0.0162029636
C2	-0.0661284877	2.6249145525	-1.8780076284
O3	1.0343046061	2.4330871919	-1.2884323135
O4	-1.1686096414	2.0564252356	-1.6314200866
C5	-2.2926136263	-1.2768964237	1.8999570964
O6	-1.5668456989	-2.1242034697	1.3077045695
O7	-2.3653080587	-0.0377893749	1.6579073506
C8	-3.1891406221	-1.8060967198	2.9928298955
H9	-3.4575489888	-1.0087331639	3.6842441451
H10	-4.1041785179	-2.1863624610	2.5283306208
H11	-2.7019988365	-2.6288366869	3.5149653453
C12	-0.0723658432	3.6642794853	-2.9721911045
H13	0.8839721025	3.6688873873	-3.4939108507
H14	-0.8938981082	3.4835022052	-3.6637947068
H15	-0.2178571831	4.6452912228	-2.5096755833
Pd16	-0.0004130689	-1.8852191492	0.0027221919
C17	-2.2741693507	-1.3542741083	-1.8592262243
O18	-2.6545154648	-0.3127660085	-1.2525184845
O19	-1.2359604150	-2.0342020356	-1.6210242723
C20	0.0653647340	2.6238865319	1.8785064052
O21	1.1676187194	2.0549902470	1.6313063614

O22	-1.0356433593	2.4322443945	1.2899809380
C23	0.0734088314	3.6642161391	2.9718788852
H24	-0.8857870297	3.6772380012	3.4881565785
H25	0.8895373908	3.4771748555	3.6683871338
H26	0.2301809618	4.6434371810	2.5090468805
C27	-3.1569806688	-1.8200931418	-2.9912915751
H28	-3.1049223635	-1.0845752184	-3.7982080336
H29	-2.8390908857	-2.7943853128	-3.3570425022
H30	-4.1923836311	-1.8597570139	-2.6481408756
Pd31	-1.6387150453	0.9395301419	0.0155492181
C32	2.2760767571	-1.3554366604	1.8588673124
O33	2.6549251803	-0.3145265339	1.2500594728
O34	1.2360023909	-2.0341322148	1.6255306443
C35	3.1642264394	-1.8234455113	2.9859097479
H36	3.1167677202	-1.0898904456	3.7946980263
H37	2.8476911117	-2.7982038023	3.3515769923
H38	4.1978140386	-1.8629669617	2.6373985918
C39	2.2896017156	-1.2797390673	-1.8977266090
O40	2.3597292185	-0.0395496350	-1.6600441419
O41	1.5666933195	-2.1263363766	-1.3010519762
C42	3.1862207156	-1.8109366450	-2.9895278246
H43	4.1054942241	-2.1812264999	-2.5252598029
H44	2.7034732432	-2.6411645497	-3.5037603398

H45	3.4467865951	-1.0169213935	-3.6877961533

D

Pd1	2.5538424169	9.2042018221	4.0712105625
Cu2	-0.5701325602	8.9917455704	4.6131183985
O3	2.4233856759	7.4286922800	5.0656345306
O4	2.3374990577	10.2164801897	5.8342328172
O5	0.2307045141	7.4935873437	5.5981311418
O6	0.0827881424	10.2699904514	5.9474532405
C8	1.2315553186	10.5807974780	6.3494044763
C10	1.3730266499	6.9719506659	5.6217274636
C12	1.3294139488	11.5042658043	7.5387599777
C14	1.5406957620	5.6937051067	6.4055955147
H15	0.4994290420	11.3238797226	8.2221020233
H16	2.4363164786	5.1597399243	6.0915715337
H17	0.6535945281	5.0708901680	6.2888851161
H18	1.2548471473	12.5330018275	7.1711886060
H19	2.2869571979	11.3850627720	8.0447943663
H20	1.6377534346	5.9551695231	7.4637390702
Pd17	-3.6861905407	8.8176078990	5.1826145276
O22	-3.5451382261	10.5870729482	4.1800695359
O23	2.8113730504	10.7262160359	2.6567316297
O24	-1.3630559852	10.4859227546	3.6137769842

O25	2.8625543818	8.6321176310	2.0793819004
C27	2.9173098561	9.8578075062	1.7266513311
C28	-2.4970361111	11.0260700230	3.6066627852
C30	3.0651378616	10.2542274671	0.2974635517
C31	-2.6562328819	12.3048384818	2.8219823834
H32	3.6309100915	9.4979121005	-0.2474668631
H33	-3.5453142826	12.8476875688	3.1385536463
H34	-1.7630948717	12.9193498887	2.9355242481
H35	2.0682418053	10.3281231453	-0.1494692116
H36	3.5504581537	11.2277212374	0.2242809863
H37	-2.7583559991	12.0436953729	1.7643772482
O32	-3.4921125643	7.7866873462	3.4280392419
O33	-1.2401202569	7.7145997086	3.2850664244
C34	-2.3960194257	7.4061736465	2.9037566460
C35	-2.5168892256	6.4650973442	1.7304888200
H38	-1.6987950516	6.6316542974	1.0300356095
H39	-2.4376653192	5.4426866493	2.1128821722
H40	-3.4822361265	6.5791246404	1.2394681352
O39	-3.9413124347	7.3087548835	6.6146576988
O40	-3.9784317835	9.4100211179	7.1682571037
C41	-4.0494353328	8.1884750238	7.5334187698
C42	-4.2638942368	7.8128183122	8.9598458456
H43	-3.7739459746	8.5356825405	9.6136455174

H44	-5.3376229572	7.8312460337	9.1721065245
H45	-3.8874214327	6.8066303403	9.1452317225

E

Pd1	2.4221743224	9.0383720618	3.9504326787
Cu2	-0.5501259294	8.9819133661	4.6563079555
O3	2.2645453395	7.2516743885	4.9613733437
O4	2.3246698204	10.1190445620	5.7477577996
O5	0.2187294112	7.6093807792	5.8306192524
O6	0.0905777623	10.3971018237	5.8584740912
C8	1.2753129947	10.6244916223	6.2388409183
C10	1.2914981506	6.9643698983	5.7332084907
C12	1.4507335132	11.6085912237	7.3703295118
C14	1.4652773743	5.7576582413	6.6190804894
H15	0.7023213952	11.4273533652	8.1424518313
H16	2.2732983162	5.1223589316	6.2598657819
H17	0.5263151068	5.2062042010	6.6742817149
H18	1.2882777034	12.6150901489	6.9738321031
H19	2.4551851343	11.5483278372	7.7853681673
H20	1.7106728274	6.1085031362	7.6260320378
Pd17	-3.5487338974	8.9741292433	5.3115417570
O22	-3.3459434170	10.7465363977	4.2824333937
O23	2.5612131117	10.7859776736	2.9639171554

O24	-1.2876581076	10.3518296949	3.4598732575
O25	4.8006277685	10.6199080421	2.8198606158
C27	3.7492707765	11.2293866393	2.6462613517
C28	-2.3546611572	11.0106838342	3.5263002473
C30	3.6982492792	12.5951109969	1.9849319383
C31	-2.4978760041	12.2043019872	2.6174837985
H32	4.6721800051	13.0775947329	2.0596057591
H33	-3.2903175137	12.8657918166	2.9641790237
H34	-1.5461212481	12.7316396527	2.5510679610
H35	3.4504449481	12.4615708542	0.9277074708
H36	2.9248019357	13.2181631372	2.4347362145
H37	-2.7540074346	11.8395003166	1.6179553678
O32	-3.4319143561	7.8686466443	3.5303971050
O33	-1.1999707783	7.5620561967	3.4639954957
C34	-2.3803400928	7.3448801268	3.0647163961
C35	-2.5451220058	6.3518347432	1.9393111952
H38	-1.8079172596	6.5483236851	1.1595295203
H39	-2.3526678266	5.3510461405	2.3366992074
H40	-3.5540418295	6.3879056571	1.5323259751
O39	-3.7342219926	7.2447412339	6.3210363880
O40	-5.9777170415	7.4098593159	6.3149333411
C41	-4.9412363491	6.7972503639	6.5539618792
C42	-4.9361498649	5.4014631396	7.1495404378

H43	-5.8732503931	5.2193532562	7.6749286268
H44	-4.8459582709	4.6794686777	6.3330173284
H45	-4.0853317777	5.2622077772	7.8168118465
C46	3.0912475312	7.8953567150	2.1803697301
C47	1.7308221765	8.0943658645	2.0859685031
H48	3.4902025969	6.9762045280	2.5961729674
H49	1.0184447148	7.3454093096	2.4134685424
H50	1.3290558136	8.9232451420	1.5136576777
H51	3.7966923258	8.5497051571	1.6825192886
C52	-2.9034966244	9.9340735890	7.1840732833
C53	-4.2592721310	10.1407727113	7.0471231057
H54	-2.5256254928	9.1089987949	7.7777100965
H55	-4.9830603420	9.4959249608	7.5311903343
H56	-4.6405684789	11.0582596624	6.6117151347
H57	-2.1767758328	10.6752354484	6.8708226363

F

Pd1	1.4021166730	0.9188862366	-0.0535034572
Cu2	0.0867080026	-1.9433482911	0.0791443612
C17	-2.2841018456	-2.0895308278	0.0526526216
O18	-1.6288609061	-2.0172983175	1.1429674983
O19	-1.6052325590	-2.0839428038	-1.0240834915
C27	-3.7755988562	-2.1723456809	0.0497373427

H28	-4.1832804303	-1.2625009446	0.4980856302
H29	-4.1545307008	-2.2888422456	-0.9644729512
H30	-4.0919182552	-3.0139031296	0.6709813477
C32	2.2722691674	-1.1528533820	1.8977465086
O33	2.5296695793	-0.0263622393	1.3674004719
O34	1.3569537147	-1.9450536646	1.5504120907
C35	3.1410115320	-1.5436744453	3.0666804209
H36	2.8153685277	-0.9727014402	3.9414353850
H37	3.0399475333	-2.6069927072	3.2767377117
H38	4.1811689583	-1.2839382845	2.8668829124
C39	2.2081815897	-1.2803562936	-1.8799882751
O40	2.3876047645	-0.0676724524	-1.5454535881
O41	1.4021328920	-2.0877754366	-1.3456499535
C42	3.0629483184	-1.8001343468	-3.0081220502
H43	3.8898530594	-2.3706234302	-2.5740917570
H44	2.4770667572	-2.4762824570	-3.6317312737
H45	3.4693207193	-0.9807630084	-3.5987707079
C41	-0.3537428983	2.6410043007	0.0030652100
O42	0.1786781701	2.1911938244	1.0725939509
O43	0.0817084339	2.1599445593	-1.0972590360
C44	-1.4283789313	3.6725077672	0.0254311139
H31	-1.7032565477	3.9161135038	1.0511574226
H46	-1.0753514394	4.5703356806	-0.4889485674

H47	-2.2989174293	3.3003587255	-0.5203310156

G

Cu1	1.1919234136	0.9199261792	-0.0643393517
Pd2	0.1014140644	-1.9361801930	0.2026962362
C17	-1.8086376339	-3.0028040441	-1.6868077615
O18	-1.7666309734	-4.0521028381	-1.0533315418
O19	-1.1846657375	-1.9008867686	-1.3545002619
C27	-2.6208735282	-2.8737659034	-2.9632223233
H28	-3.6509794093	-3.1758761750	-2.7602360552
H29	-2.6013188865	-1.8613513980	-3.3644634138
H30	-2.2128000483	-3.5680837407	-3.7023470657
C32	2.3216888599	-1.0322261612	1.9150231859
O33	2.4329954454	0.0098103535	1.2283080722
O34	1.4251702976	-1.9298555614	1.7698554363
C35	3.3137218388	-1.2512708076	3.0308261895
H36	3.0632003526	-0.5702441769	3.8496832140
H37	3.2828990938	-2.2777582692	3.3920474216
H38	4.3142675977	-0.9934336990	2.6810223503
C39	2.2296733456	-1.1880989695	-1.7942457846
O40	2.0320525848	0.0457804095	-1.5881960479
O41	1.6753287696	-2.1384807812	-1.1721614833
C42	3.2322039434	-1.5578751958	-2.8593378844

H43	4.2047549779	-1.6980283803	-2.3762138672
H44	2.9504161209	-2.4939139800	-3.3413465884
H45	3.3247000476	-0.7541348852	-3.5890100911
C41	0.9594145357	2.9304493952	1.4990074723
O42	0.2879964568	1.8270382340	1.4025269872
O43	1.8712242105	3.1942823907	0.6975980654
C44	0.5906467761	3.8651322745	2.6249038409
H31	-0.3486818974	3.5760326469	3.0949393660
H46	1.3894726654	3.8391569582	3.3720891116
H47	0.5285906578	4.8873678352	2.2470516201
C31	-1.4476425181	-0.9904379357	1.4570776334
C33	-1.4840742984	-2.3469734362	1.6949494693
H33	-2.1310696845	-0.5413727481	0.7454736574
H34	-2.1843190961	-2.9943019145	1.1806891803
H35	-0.9416081066	-2.7787986503	2.5290999818
H39	-0.8977527054	-0.3047791469	2.0924969449
C37	0.1210766753	2.3216945093	-1.7453223151
C38	-0.7541390517	1.3492947879	-1.4264571211
H40	0.8675387837	2.1815851849	-2.5193505530
H41	-0.7690554850	0.3902262225	-1.9328575640
H42	-1.5100206182	1.5175202834	-0.6671976739
H48	0.1005154917	3.2883770687	-1.2573859880

H

Pd1	1.3377916618	0.8814805429	-0.0471031041
Pd2	0.1142178481	-1.9564914780	0.0730248762
C17	-2.3454318556	-1.9160542890	0.0661881139
O18	-1.6746381886	-1.8913611989	1.1532181695
O19	-1.6714630109	-1.9669053766	-1.0170995400
C27	-3.8357681800	-1.8836837079	0.0725413296
H28	-4.1724001000	-0.9467335143	0.5257282930
H29	-4.2234243112	-1.9646400227	-0.9425705178
H30	-4.2149342766	-2.7049954228	0.6864310399
C32	2.3740931787	-1.1665577631	1.8843022267
O33	2.5138121079	-0.0161682375	1.3732729990
O34	1.5410486017	-2.0543585643	1.5407908092
C35	3.2892785755	-1.5000253898	3.0360390694
H36	2.9146631863	-0.9901699532	3.9285468865
H37	3.3036600447	-2.5733650972	3.2171779787
H38	4.2934053160	-1.1260912905	2.8324964747
C39	2.3101145978	-1.2806527742	-1.8725048291
O40	2.3919112175	-0.0669316185	-1.5241487296
O41	1.5533595828	-2.1647941824	-1.3753067569
C42	3.2301516026	-1.7327389669	-2.9795430315
H43	4.0858307464	-2.2440035609	-2.5282919851
H44	2.7141574552	-2.4425671337	-3.6266349640

H45	3.5890710515	-0.8778222942	-3.5501235490
C41	-0.4436806331	2.5765408066	-0.0083826586
O42	0.0882708957	2.1375961684	1.0656579221
O43	0.0044311499	2.0975647503	-1.1041543079
C44	-1.5290150791	3.5975483403	0.0060141976
H31	-1.8112180329	3.8398863272	1.0300458083
H46	-1.1812746673	4.4983902059	-0.5068582070
H47	-2.3932379584	3.2176565973	-0.5441903973

I

C8	2.5883962773	-2.7220164740	-0.8214612470
O9	1.4404544120	-2.1619049145	-0.9062472928
C10	3.8508194208	-1.9268390602	-0.7902331066
O11	2.5822315828	-3.9999489251	-0.7615679900
H5	4.7173030490	-2.5890593726	-0.7384964244
H6	3.9096823735	-1.3023965608	-1.6877281220
H7	3.8372551346	-1.2608141003	0.0791115806
C9	-1.4652989319	-5.2496613558	-0.8701876649
O10	-1.4612357742	-3.9711273907	-0.9358415475
C11	-2.7353227471	-6.0331948477	-0.8820052021
O12	-0.3166558144	-5.8076509573	-0.7939212836
H12	-2.5238342151	-7.1032549883	-0.8339412340
H13	-3.3527528604	-5.7354224784	-0.0278189895

H14	-3.2950904906	-5.8032200014	-1.7945758934
Pd15	0.5607852805	-3.9844964207	-0.8518488120

J

Pd1	1.2921787489	0.8798377533	-0.2209018913
Pd2	0.0938021040	-1.8599964907	0.2549786406
C17	-1.8415694791	-2.9727505388	-1.5750715492
O18	-1.7418089643	-4.0249777816	-0.9538994063
O19	-1.2417372189	-1.8523098116	-1.2578161883
C27	-2.7093790294	-2.8599651859	-2.8162725246
H28	-3.7301889744	-3.1524455829	-2.5592663435
H29	-2.7063371474	-1.8544226828	-3.2344358098
H30	-2.3408960237	-3.5696742703	-3.5610702464
C32	2.4231758155	-1.0033488104	1.8976016684
O33	2.6164874710	0.0077245860	1.1733091463
O34	1.4614544118	-1.8298319465	1.7932032373
C35	3.4088190913	-1.2570076486	3.0114917018
H36	3.1804668992	-0.5725529684	3.8340800796
H37	3.3358984528	-2.2829064476	3.3686169642
H38	4.4199003283	-1.0377849409	2.6665747453
C39	2.2455344048	-1.4001656953	-1.8689653216
O40	2.1994849310	-0.1322330717	-1.7667124882
O41	1.6220568879	-2.2268854614	-1.1543521918

C42	3.1567669123	-1.9558121106	-2.9355360494
H43	4.0731362028	-2.3072178363	-2.4519965318
H44	2.6831420117	-2.8106884842	-3.4192114818
H45	3.4138408751	-1.1885804600	-3.6641523052
C41	0.7469594415	3.0448481176	1.6201816593
O42	0.3807227911	1.8259197060	1.3105703415
O43	1.5334042254	3.7292801122	0.9759909344
C44	0.1014745131	3.5571350443	2.8957509589
H31	-0.7080426349	2.9123737308	3.2345024675
H46	0.8705204445	3.6065076241	3.6720573304
H47	-0.2659540806	4.5712912203	2.7292350126
C31	-1.4147208079	-0.9171985016	1.5438280419
C33	-1.4516313927	-2.2758893503	1.7774978420
H33	-2.1157387342	-0.4600343817	0.8546164222
H34	-2.1672341099	-2.9188831987	1.2796448595
H35	-0.8899246315	-2.7141397623	2.5952732773
H39	-0.8443852154	-0.2395726486	2.1686160973
C37	0.5179535362	2.2927498470	-1.7366262848
C38	-0.4363412326	1.3254215736	-1.5012042177
H40	1.2207278941	2.1928994148	-2.5568833610
H41	-0.5348104561	0.4467333079	-2.1281958049
H42	-1.2480959419	1.5134113669	-0.8075279518
H48	0.4874905927	3.2532419824	-1.2366384123

K

Pd1	1.4481110632	0.7022322569	-0.0101004023
Pd16	0.1272762514	-1.5999032881	0.2254185617
C32	-1.0762441843	0.4484955546	-1.5211166264
O33	-0.1246139483	1.2479180658	-1.2536648568
O34	-1.2317915138	-0.7341258727	-1.0827484893
C35	-2.1232034613	0.9639354942	-2.4766264140
H36	-1.6802776995	1.0259985844	-3.4747436435
H37	-2.9847759020	0.2992559423	-2.5022563799
H38	-2.4218193184	1.9716621901	-2.1828300089
C39	-0.5474933232	0.5285568629	2.1562181187
O40	0.3257750117	1.2910293224	1.6348222779
O41	-0.8345900454	-0.6600463233	1.8092651952
C42	-1.3517970375	1.1052010850	3.2943106215
H43	-2.2680069398	1.5360370251	2.8780335713
H44	-1.6317962833	0.3190410236	3.9953039877
H45	-0.7929992710	1.8945487971	3.7954611277
C17	2.6438405530	-1.3491659647	1.7435256456
O18	2.8254163723	-0.1843583061	1.2677367192
O19	1.6727828700	-2.1333861076	1.5048916927
C20	3.6955007944	-1.8388845632	2.7072775969
H21	3.6168413958	-1.2572217496	3.6301349746

H22	3.5559643192	-2.8952438233	2.9293759086
H23	4.6869080397	-1.6608647540	2.2868903641
C24	2.1243235431	-1.4178397332	-1.9436568980
O25	2.3815912465	-0.2156538818	-1.6198063028
O26	1.2832263268	-2.1973927316	-1.3957132990
C27	2.9226308103	-1.9917764254	-3.0874084651
H28	3.7831998346	-2.5234661983	-2.6691047274
H29	2.3190638113	-2.7063515232	-3.6470383454
H30	3.2865017041	-1.1961765017	-3.7362379076

L

Pd1	1.4492955659	0.7079322153	0.0170462470
Cu16	0.1737136361	-1.5204259287	0.2444761440
C32	-1.0420316958	0.4514194989	-1.4784229391
O33	-0.1062864876	1.2797063811	-1.2179680784
O34	-1.1398783806	-0.7242285548	-1.0276793545
C35	-2.1080198512	0.9400733643	-2.4263031397
H36	-1.6800486294	1.0029415638	-3.4308750918
H37	-2.9546002582	0.2558791762	-2.4361150464
H38	-2.4272518322	1.9432370514	-2.1395290486
C39	-0.5242101169	0.5360773647	2.1544498420
O40	0.3518759372	1.3193861281	1.6564637482
O41	-0.7819544573	-0.6358404160	1.7604582473

C42	-1.3379661066	1.0825520091	3.3001218999
H43	-2.2699181424	1.4865715815	2.8918866950
H44	-1.5911708192	0.2812408933	3.9946323194
H45	-0.8038259900	1.8840905577	3.8081765588
C17	2.6260235064	-1.3181515415	1.7544831215
O18	2.8384969774	-0.1509129208	1.2834852951
O19	1.6334482418	-2.0544797004	1.4944172272
C20	3.6599991505	-1.8350762750	2.7226991470
H21	3.5596240153	-1.2860154494	3.6634305252
H22	3.5136901772	-2.8977101197	2.9082301255
H23	4.6619830542	-1.6456331767	2.3345548753
C24	2.1161575908	-1.3878492359	-1.8937613061
O25	2.3870415102	-0.1769321895	-1.5960137239
O26	1.2838460391	-2.1299921129	-1.3004960182
C27	2.8840285983	-1.9836315260	-3.0465234797
H28	3.7243950035	-2.5536823514	-2.6383550031
H29	2.2466719302	-2.6726073793	-3.6014552951
H30	3.2736695405	-1.2035604553	-3.6986341894

A_benzene

Pd1	1.5575301046	1.0467815298	0.1569951085
C2	-3.7351874886	2.5956186556	-1.0768264981
O3	-4.0939244899	1.7261242335	-0.2444208930

O4	-2.4847729828	2.6984932826	-1.3881472951
C5	-2.0748294146	-1.3051122179	1.2972137367
O6	-1.6690926333	-2.4822089754	1.1140482960
O7	-1.3135169672	-0.3185913003	0.9786863127
C8	-3.4339423255	-1.0272192189	1.8853827452
H9	-3.3024683859	-0.5080363498	2.8391365204
H10	-3.9858644998	-0.3535854037	1.2195552408
H11	-3.9948925015	-1.9500982846	2.0387588048
C12	-4.7082911583	3.5189860224	-1.7585822220
H13	-5.6210109267	3.6094032420	-1.1639468826
H14	-4.2573048037	4.5019877650	-1.9215074348
H15	-4.9652158260	3.0963099529	-2.7375010756
Cu16	0.1333857165	-1.9816722228	0.1364526926
C17	-1.4969537677	-1.2086690027	-2.2779515647
O18	-1.8481100119	-0.0658006697	-1.8844223496
O19	-0.7505422816	-2.0388820512	-1.6655509461
C20	-0.1537941913	2.7032889692	1.8985961869
O21	1.0037485440	2.2016041493	1.6580877772
O22	-1.1725656374	2.5898394200	1.1802465466
C23	-0.2528447091	3.5115349246	3.1771899482
H24	-0.7306272169	2.8861157292	3.9428318851
H25	0.7341522017	3.8169264168	3.5337393265
H26	-0.8918191740	4.3839013196	3.0080223694

C27	-2.0280446249	-1.6658387678	-3.6278304542
H28	-2.1228260467	-0.8110504837	-4.3018130141
H29	-1.3875765122	-2.4351879889	-4.0631228603
H30	-3.0285494654	-2.0889606841	-3.4769648284
Cu31	-1.8705703880	1.1923269200	-0.2064950250
C32	2.0358436931	-1.1870617193	2.2204378470
O33	2.4183854362	-0.1485435504	1.5924260854
O34	1.1009798377	-1.9731081498	1.9015982984
C35	2.7889464418	-1.4829067704	3.5056291504
H36	2.3712876470	-0.8523486452	4.2999507053
H37	2.6731563621	-2.5319086082	3.7863806508
H38	3.8457002941	-1.2269566332	3.3918086064
C39	2.5711669386	-1.1892660923	-1.4447786819
O40	2.4481127653	0.0773231468	-1.2938609953
O41	1.9341681832	-2.0745843457	-0.8267319128
C42	3.6137385308	-1.6147657857	-2.4572534039
H43	4.5721868368	-1.7327665903	-1.9357589912
H44	3.3379221565	-2.5749798262	-2.8993151110
H45	3.7344118303	-0.8510964978	-3.2290501158
C46	2.8033229848	2.3480056726	-3.3426926410
C47	3.1484798634	3.0247342635	-2.1723632661
C48	2.1713755987	3.2674429763	-1.2015511706
C49	0.8432864648	2.8263425269	-1.4117335228

C50	0.5046731101	2.1538962711	-2.6074173938
C51	1.4851506811	1.9122937869	-3.5598666544
H52	3.5620145546	2.1622105806	-4.0998498657
H53	4.1695202283	3.3621581085	-2.0132731941
H54	2.4158899324	3.8359191278	-0.3081582065
H55	0.0480313189	3.1590636191	-0.7525421109
H56	-0.5225829296	1.8428549538	-2.7657313501
H57	1.2332620660	1.3935072343	-4.4813869031

A_CMD

Cu1	1.5662703186	0.8858640586	-0.3801203462
C5	-1.8790602100	-1.5240624950	2.3485463278
O6	-1.5083842603	-2.3731095769	1.4702456931
O7	-1.7613893594	-0.2730090893	2.2559725410
C8	-2.5394169830	-2.0750005611	3.5974640517
H9	-2.1401092183	-1.5584517809	4.4753348022
H10	-3.6141436382	-1.8630820461	3.5463142864
H11	-2.3856707170	-3.1521241706	3.6862878893
Cu16	-0.1313482997	-2.0378175496	0.0664427030
C17	-2.6558144946	-1.3118049057	-1.2574768349
O18	-2.9065770721	-0.3365033945	-0.4863565681
O19	-1.5394833905	-1.9012643353	-1.3770422886
C20	0.4263622684	2.5454492059	1.8692329919

O21	1.4171695186	2.0017321018	1.2968959224
O22	-0.7979553466	2.3175085465	1.6347359958
C23	0.7217087572	3.5962155708	2.9181530948
H24	-0.0660973858	3.6097195704	3.6748227840
H25	1.6971837254	3.4189312414	3.3762578263
H26	0.7397991976	4.5734237597	2.4201741520
C27	-3.7988116667	-1.7766968126	-2.1358395191
H28	-3.9808124081	-1.0104390449	-2.8988624152
H29	-3.5609262019	-2.7274240106	-2.6176442895
H30	-4.7093762175	-1.8692332622	-1.5359265935
Pd31	-1.6391315076	0.8984587779	0.5066582046
C32	2.3996159283	-1.3714621907	1.4343149518
O33	2.6837187593	-0.4287780314	0.6290587891
O34	1.2915075898	-1.9738468854	1.5041462332
C35	3.4989596092	-1.7729319486	2.3973754585
H36	3.6751422767	-0.9438611347	3.0919613144
H37	3.2229548069	-2.6719413636	2.9514270823
H38	4.4275693560	-1.9372740444	1.8416602584
C39	1.5895302341	-1.4608517527	-2.2332237950
O40	1.4946586502	-0.2009161674	-2.0708007276
O41	1.2193841912	-2.3383283771	-1.4031736362
C42	2.1972875753	-1.9244858580	-3.5410896012
H43	3.2751092929	-1.7218941457	-3.5157812251

H44	2.0258247446	-2.9914017344	-3.6966899285
H45	1.7733237598	-1.3429414059	-4.3663708657
C9	-3.3699842394	2.4965807177	-3.4143068530
C10	-3.7575461275	3.0612682549	-2.1923067290
C11	-2.9702725109	2.8572915378	-1.0600863361
C12	-1.7762710666	2.0979594282	-1.1285839611
C13	-1.4114551004	1.5277093241	-2.3743962331
C14	-2.1925569700	1.7401753623	-3.5070595036
H15	-3.9874224494	2.6448988825	-4.2981319948
H16	-4.6683986857	3.6534033099	-2.1284303773
H17	-3.2670061378	3.3006870096	-0.1115313187
H18	-0.4936430628	0.9532713610	-2.4572374841
H19	-1.8942809905	1.3156510435	-4.4635103039
H50	-0.7624268424	2.9705909161	-0.7380035355
C41	1.1454080968	3.7126864342	-1.2706820530
O42	1.5902377320	2.5653153489	-1.5393784500
O43	0.0261753694	3.9320439788	-0.6815011379
C44	1.9484609507	4.9205809138	-1.6915260705
H55	3.0099048693	4.7583488839	-1.4813028869
H46	1.8329626250	5.0586286231	-2.7724905546
H47	1.5914398933	5.8144945509	-1.1800553294

B_benzene

Pd1	1.6186000577	1.1191549019	0.1434365954
C2	-3.3396379707	2.6387388476	-1.3912668565
O3	-3.9620005800	2.1718687986	-0.4197231180
O4	-2.1149109865	2.2721198098	-1.6272548816
C5	-2.1771477761	-1.3745124325	1.6596750442
O6	-1.5800472194	-2.2705822444	0.9743165768
O7	-1.9607196557	-0.1363125613	1.5773458168
C8	-3.2386573295	-1.8595076963	2.6197145464
H9	-3.2321588533	-1.2371556419	3.5190317385
H10	-4.2166536059	-1.7400126346	2.1346773800
H11	-3.0922049308	-2.9118378006	2.8738768915
C12	-3.9470639350	3.6217858976	-2.3614073356
H13	-4.7723068621	4.1548487283	-1.8832877120
H14	-3.1955344374	4.3285941378	-2.7236804757
H15	-4.3387618841	3.0694044345	-3.2236549614
Pd16	0.0561616873	-1.8685805375	-0.0568248256
C17	-2.0200883738	-1.4681110761	-2.0257383621
O18	-2.5140187038	-0.5133410715	-1.3794906958
O19	-0.9243420862	-2.0741694655	-1.7632528543
C20	-0.1646987399	2.6518347882	1.8507774071
O21	1.0171541423	2.1688191926	1.6929362304
O22	-1.1124577076	2.5248207364	1.0465968057
C23	-0.3742383630	3.4726791338	3.1036580230

H24	-1.2711330703	3.1100604684	3.6146720522
H25	0.4906232438	3.4226795601	3.7671601173
H26	-0.5570487151	4.5134724812	2.8134695842
C27	-2.7823188100	-1.9674335753	-3.2361216697
H28	-2.9399936879	-1.1345824609	-3.9286537755
H29	-2.2511811095	-2.7788159066	-3.7357609857
H30	-3.7676957714	-2.3160290610	-2.9095997999
Cu31	-1.8943419771	0.9855303853	-0.1064298657
C32	2.0092615329	-1.2029321334	2.0729970179
O33	2.4649425532	-0.1615997581	1.5097835384
O34	1.0390799599	-1.9163167369	1.6873445557
C35	2.7076098460	-1.6180359449	3.3521313143
H36	2.4500339896	-0.8988493560	4.1377974152
H37	2.3987982374	-2.6192088360	3.6568971608
H38	3.7911009298	-1.5785816668	3.2088828510
C39	2.5391929833	-1.0392935067	-1.5980048540
O40	2.5491701336	0.2048129960	-1.3173364316
O41	1.7636885792	-1.9133329475	-1.1323392604
C42	3.5977643658	-1.4956429032	-2.5775930039
H43	4.4624828508	-1.8565647447	-2.0069479714
H44	3.2164125207	-2.3202519251	-3.1843100882
H45	3.9208795715	-0.6654655112	-3.2087761251
C46	3.1316975290	2.6989629668	-3.1255456147

C47	3.2679254553	3.3228912724	-1.8863112489
C48	2.1569313179	3.4313543491	-1.0392417521
C49	0.9074867377	2.9045793474	-1.4411803602
C50	0.7845101301	2.2807850421	-2.7021757995
C51	1.8906688359	2.1787967617	-3.5345267054
H52	3.9919098409	2.6198912923	-3.7868341935
H53	4.2279070298	3.7280899534	-1.5765138786
H54	2.2404729137	3.9659918854	-0.0969112769
H55	0.0084326759	3.1073137810	-0.8694574053
H56	-0.1880061627	1.9062168145	-3.0029814905
H57	1.8001242802	1.7020871458	-4.5076070024

B_CMD

Cu1	1.4866778001	0.8565772928	-0.3563419236
C5	-1.7848507652	-1.4167905893	2.3791945355
O6	-1.4183649839	-2.2860582978	1.5183380600
O7	-1.6813863412	-0.1676653130	2.2665573284
C8	-2.4287962036	-1.9578225745	3.6396463783
H9	-2.0904167044	-1.3735529288	4.5001987772
H10	-3.5155214308	-1.8336184287	3.5574871379
H11	-2.1982156521	-3.0154861965	3.7796524161
Pd16	-0.1151523027	-2.0385079793	0.0399118650
C17	-2.6456419761	-1.3517879945	-1.2215535915

O18	-2.8498290760	-0.3637642675	-0.4607604399
O19	-1.5719535560	-2.0270548963	-1.3199322827
C20	0.3780026759	2.5405244381	1.8898798704
O21	1.3402761619	1.9076790393	1.3635148732
O22	-0.8522121738	2.4077224881	1.6066455250
C23	0.7104339640	3.5792083304	2.9384500287
H24	-0.0777105572	3.6213609937	3.6939953255
H25	1.6767103044	3.3640023999	3.3991234650
H26	0.7636735052	4.5556753496	2.4422654702
C27	-3.7876981100	-1.7565830139	-2.1275357500
H28	-3.8650377460	-1.0152896181	-2.9313265515
H29	-3.6182626423	-2.7451643702	-2.5576169752
H30	-4.7260801923	-1.7377627069	-1.5658900020
Pd31	-1.6391513057	0.9583954569	0.4953774639
C32	2.3863126177	-1.4877615021	1.3798628223
O33	2.6126829271	-0.5125400301	0.6062872274
O34	1.3318026063	-2.1946962806	1.4013022903
C35	3.4715211095	-1.8404628236	2.3747894452
H36	3.5512959099	-1.0270731682	3.1059688570
H37	3.2411832034	-2.7763698397	2.8874125128
H38	4.4334121263	-1.9162691657	1.8570273000
C39	1.5938857533	-1.3920723591	-2.2659379446
O40	1.4991885919	-0.1368259235	-2.0983213112

O41	1.1827097346	-2.2813243115	-1.4638007891
C42	2.2727064198	-1.8598012129	-3.5345958032
H43	3.3428539521	-1.6332970592	-3.4573937952
H44	2.1324080833	-2.9323263140	-3.6814443163
H45	1.8775432332	-1.3002842219	-4.3884584106
C9	-3.4008780361	2.4603798023	-3.4498195130
C10	-3.7844703739	3.0560393485	-2.2408981150
C11	-2.9905596188	2.8859872932	-1.1084034391
C12	-1.7937831313	2.1304464567	-1.1656543845
C13	-1.4376949773	1.5223364186	-2.3964625870
C14	-2.2236307485	1.7016089297	-3.5302962750
H15	-4.0196454801	2.5905032311	-4.3357119163
H16	-4.6967878936	3.6471680039	-2.1902467523
H17	-3.2765215259	3.3623478319	-0.1727124287
H18	-0.5223350258	0.9412733683	-2.4641093354
H19	-1.9286799581	1.2549173468	-4.4776528933
H50	-0.7717919866	2.9509991173	-0.7777249164
C41	1.1611089765	3.7224596999	-1.2213678967
O42	1.6194034288	2.5687832555	-1.4505951550
O43	0.0207059705	3.9481685465	-0.6880919722
C44	1.9836863640	4.9209948945	-1.6360837161
H55	3.0500205415	4.6939710049	-1.5623851666
H46	1.7500997987	5.1543332496	-2.6827917130

H47	1.7276543136	5.7904947910	-1.0250915750

L_benzene

Pd1	1.4706922090	0.8174292186	-0.0771588545
Cu16	0.3302385578	-1.7335797364	0.5597177560
C32	-1.1102623101	-0.0343248005	-1.2941418460
O33	-0.2611850775	0.9118158934	-1.2147779677
O34	-1.0453987373	-1.1326896946	-0.6881124885
C35	-2.2761687351	0.2039488573	-2.2213032624
H36	-1.9240187270	0.1002644714	-3.2517775448
H37	-3.0636216437	-0.5244802552	-2.0359885589
H38	-2.6508981845	1.2208010424	-2.0979050232
C39	-0.2669361637	0.8226061457	2.2138381740
O40	0.4684441001	1.6170081760	1.5176779683
O41	-0.3891614350	-0.4044688259	2.0217053171
C42	-1.0406639290	1.4661165672	3.3386023785
H43	-2.0648630781	1.6369399874	2.9930256560
H44	-1.0821766246	0.7855074893	4.1896249326
H45	-0.6032384447	2.4214216896	3.6257987264
C17	0.7831962773	-3.6788157577	2.0067747527
O18	-0.2827902486	-3.7900378971	1.3617586974
O19	1.5007933125	-2.6187642228	1.8618094178
C20	1.2775186971	-4.7580248763	2.9303222863

H21	1.8422889101	-5.4866202561	2.3403018945
H22	1.9368672259	-4.3455718171	3.6937625326
H23	0.4339971506	-5.2737569083	3.3893524568
C24	2.2916292275	-1.3300134122	-1.7890518217
O25	2.4178355422	-0.0589039135	-1.6529994358
O26	1.6325421336	-2.0823329890	-1.0402768244
C27	3.0502321408	-1.9423292860	-2.9410332281
H28	3.9317818389	-2.4472959478	-2.5345799880
H29	2.4309648064	-2.6975037239	-3.4270885857
H30	3.3692005292	-1.1853233452	-3.6554871596
C31	5.2372247237	0.7123723905	-0.2946166526
C33	4.4633964031	1.7345904686	0.2151352796
C34	3.4112154310	1.4387589145	1.1134930462
C36	3.1597218817	0.0932950232	1.4763827053
C37	3.9682706549	-0.9384530908	0.9493003672
C38	4.9935202048	-0.6252223924	0.0807912148
H39	6.0449810108	0.9360517774	-0.9826213290
H40	4.6588813330	2.7654337192	-0.0553384837
H41	2.9099888775	2.2433718925	1.6384416179
H42	2.4506518085	-0.1523668156	2.2566425718
H46	3.7532282695	-1.9588011012	1.2356313813
H47	5.6229041297	-1.4130636609	-0.3186380584

L_CMD

Cu1	1.7167372995	0.7070838471	0.0242101167
Pd16	0.1525683862	-1.4728613896	0.0847492332
C39	-0.5387241611	0.4929998127	2.0315739750
O40	0.4851523579	1.1396641320	1.6693633504
O41	-0.9365723359	-0.6173366512	1.5385030481
C42	-1.4077555292	1.0801808085	3.1209717991
H43	-2.2112059817	1.6511979098	2.6403331749
H44	-1.8615833068	0.2856900085	3.7180841691
H45	-0.8281191115	1.7556188828	3.7534498738
C17	2.6513513734	-1.4089005570	1.7478254168
O18	2.9731644183	-0.2989775705	1.1989865614
O19	1.5937868012	-2.0539129043	1.5172888051
C20	3.6303157784	-1.9581903161	2.7644460723
H21	3.5457121775	-1.3692491115	3.6853293174
H22	3.4031501248	-3.0031933936	2.9840578152
H23	4.6552662643	-1.8569527650	2.3964801085
C24	2.2267497100	-1.5295166409	-1.9025715090
O25	2.4492602274	-0.3087748293	-1.6477875556
O26	1.3293349131	-2.2539635866	-1.3570742641
C27	3.1019337991	-2.2091766433	-2.9347899917
H28	3.9692081044	-2.6405437212	-2.4196821110
H29	2.5571597487	-3.0179175198	-3.4276640225

H30	3.4649995471	-1.4831159357	-3.6661580011
C9	-3.1002182654	-2.0601917095	-3.1817544418
C10	-3.4267119405	-2.1072525905	-1.8213016984
C11	-2.5348371796	-1.5939036008	-0.8792456465
C12	-1.3059553723	-1.0194344940	-1.2813439750
C13	-0.9957844426	-0.9925097924	-2.6630590297
C14	-1.8890071174	-1.4907172769	-3.6045146775
H15	-3.7920809343	-2.4635839684	-3.9182527598
H16	-4.3707332619	-2.5432925932	-1.5018229291
H17	-2.7920857913	-1.6132968236	0.1766234725
H18	-0.0674216194	-0.5341643012	-2.9913990568
H19	-1.6517499713	-1.4416219989	-4.6649666754
H50	-1.1980656737	0.2443466008	-0.8320168979
C41	-0.4925146493	2.3460910844	-1.0156212126
O42	0.7423926043	2.0696888966	-1.0746970502
O43	-1.4143199093	1.5273105169	-0.6873972248
C44	-0.9269855991	3.7454956139	-1.3938740339
H55	-0.0957141600	4.4482103881	-1.3046980336
H46	-1.2715922288	3.7316378679	-2.4358115471
H47	-1.7676143514	4.0576252622	-0.7677104805

C_benzene

Pd1	1.5543624973	1.3504760047	0.1395183628

C2	-2.9744889731	2.8420544201	-1.3324335797
O3	-4.0145187233	2.7672736322	-0.6926839280
O4	-1.8946323583	2.1290216471	-1.1223095112
C5	-1.9545126050	-1.9485889245	1.7584210031
O6	-1.2312554292	-2.5459252528	0.9028699245
O7	-2.1582373706	-0.7093860402	1.8291565646
C8	-2.6561932067	-2.8164463750	2.7734978451
H9	-2.6766575892	-2.3077515398	3.7378973557
H10	-3.6915779112	-2.9529542368	2.4464987773
H11	-2.1753192634	-3.7896746904	2.8548873743
C12	-2.8049789551	3.7991736172	-2.5024407186
H13	-3.6457385482	4.4906102916	-2.5428429067
H14	-1.8672974253	4.3525808550	-2.4159041745
H15	-2.7643919473	3.2240266685	-3.4317763252
Pd16	0.1683286821	-1.7432794309	-0.3693884721
C17	-2.3410764284	-1.3522009454	-1.9277902100
O18	-2.8486569569	-0.5571755488	-1.0939098248
O19	-1.1544934937	-1.8052634289	-1.9341469543
C20	-0.4396348931	2.7903355761	1.9409681883
O21	0.6670866460	2.7646902928	1.3108537148
O22	-1.4348762039	2.0486557468	1.7731471106
C23	-0.5404445846	3.8318589246	3.0310239846
H24	-0.1951761597	3.3773650789	3.9646649385

H25	0.0989003928	4.6853443529	2.8075097202
H26	-1.5770053764	4.1416355282	3.1579618932
C27	-3.2454718612	-1.8518692496	-3.0287701239
H28	-3.9991913815	-1.1026264095	-3.2668010187
H29	-2.6632698274	-2.1177768474	-3.9103022752
H30	-3.7530225729	-2.7516707433	-2.6678368055
Pd31	-1.9676845567	0.6951877255	0.3068469274
C32	1.9214520062	-1.0323001590	2.0081097872
O33	1.8828023073	0.2231326488	1.8642806548
O34	1.5203134904	-1.9108900288	1.1919294894
C35	2.4876548594	-1.5337364222	3.3160943784
H36	1.6723844618	-1.5708354496	4.0451509062
H37	2.8881747993	-2.5393950361	3.1945655194
H38	3.2493138017	-0.8502163982	3.6890616300
C39	2.7257504256	-0.7728291308	-1.6581768460
O40	2.9011234003	0.2417446595	-0.9184912982
O41	1.6747186318	-1.4580862644	-1.7570856667
C42	3.8987791388	-1.2043961169	-2.5023722849
H43	4.3161312570	-2.1203233473	-2.0740692994
H44	3.5503742273	-1.4401739445	-3.5092964173
H45	4.6656706111	-0.4330463370	-2.5287424967
C46	3.0974896208	2.2589554043	-3.3872357124
C47	3.3067605424	3.1183938191	-2.3144243932

C48	2.2564550561	3.3915352263	-1.4347534790
C49	0.9960686002	2.7785811063	-1.6317134883
C50	0.8060620641	1.8967356007	-2.7233421961
C51	1.8513918709	1.6440046400	-3.5923009249
H52	3.9092426350	2.0585859675	-4.0786143833
H53	4.2752117689	3.5808818679	-2.1632455442
H54	2.3831635224	4.1067639577	-0.6306607061
H55	0.1191243981	3.1173311266	-1.0973492554
H56	-0.1705995282	1.4492118550	-2.8515168237
H57	1.7126573367	0.9725167248	-4.4318705862

C_CMD

Pd1	1.6546528354	0.9293817718	-0.3518000432
C5	-1.8660723147	-1.5072428287	2.3202844339
O6	-1.5561899482	-2.3428167611	1.4045855658
O7	-1.6664348127	-0.2652274443	2.2787357266
C8	-2.5550053111	-2.0732109296	3.5432495689
H9	-2.1444384140	-1.6003429917	4.4403234117
H10	-3.6215917701	-1.8235168913	3.4929499982
H11	-2.4396449111	-3.1575104653	3.5975629430
Pd16	-0.2229804422	-1.9826199912	-0.0169396405
C17	-2.7469077305	-1.2839246155	-1.2239374747
O18	-2.9272592975	-0.3302771636	-0.4104618866

O19	-1.6683606821	-1.9368926979	-1.3934730182
C20	0.5706514699	2.5246128680	1.8577484848
O21	1.5992793720	2.0421508535	1.2796168750
O22	-0.6393551201	2.2639665400	1.6172405364
C23	0.8397558424	3.5534459236	2.9340136205
H24	0.0894035674	3.4749227438	3.7242997036
H25	1.8464725021	3.4362422137	3.3405367320
H26	0.7561261879	4.5477715017	2.4788056872
C27	-3.9260484140	-1.6647179015	-2.0904526263
H28	-4.0692392208	-0.8778601572	-2.8394538727
H29	-3.7559166663	-2.6206418836	-2.5886607779
H30	-4.8310439831	-1.7083349565	-1.4768807052
Pd31	-1.5869092441	0.8754747833	0.5261856939
C32	2.2230950985	-1.5011614379	1.4598324011
O33	2.5470356707	-0.5106040910	0.7408827033
O34	1.1527008823	-2.1771008178	1.3949608750
C35	3.2245947585	-1.9142105821	2.5176385978
H36	3.1557248016	-1.2065003851	3.3531299853
H37	3.0156441765	-2.9227401721	2.8807539388
H38	4.2381754104	-1.8518997367	2.1104899872
C39	1.7147499436	-1.3042908386	-2.2491311960
O40	1.8530487628	-0.0514154947	-2.0553315136
O41	1.1369901902	-2.1317822726	-1.4928955876

C42	2.3303085826	-1.8320027562	-3.5269314073
H43	3.4219399402	-1.7899103239	-3.4334151695
H44	2.0145515200	-2.8604613834	-3.7121864294
H45	2.0452627940	-1.1875434190	-4.3648605531
C9	-3.4634706002	2.2908887790	-3.3724595780
C10	-3.8409660417	2.8946010167	-2.1666060638
C11	-3.0129748928	2.7787469759	-1.0543387895
C12	-1.7886725479	2.0672578372	-1.1274806196
C13	-1.4353199190	1.4577838788	-2.3576064786
C14	-2.2581302137	1.5801757588	-3.4708398232
H15	-4.1107303508	2.3766586928	-4.2427669991
H16	-4.7751243869	3.4490926738	-2.1037768463
H17	-3.2932841124	3.2618168826	-0.1212571027
H18	-0.4978533147	0.9160952271	-2.4367127067
H19	-1.9723037717	1.1260259495	-4.4155743828
H50	-0.8160610312	2.8613836978	-0.7414728417
C41	1.0562752419	3.7312371297	-1.2808257080
O42	1.5533826936	2.5900286822	-1.5244270822
O43	-0.0279487485	3.9204277179	-0.6385788415
C44	1.7718737526	4.9403791555	-1.8372888391
H55	2.8480087582	4.7589582889	-1.8912029986
H46	1.4002016929	5.1265986499	-2.8532791217
H47	1.5558851734	5.8225315056	-1.2287413505

I2

Cu1	1.2123179038	1.3083582913	-1.0795194736
C2	-1.2940196437	-1.0206674170	2.7482911519
O3	-0.2244902526	-1.5510909433	2.3133336901
O4	-2.0739655769	-0.2744555192	2.0971363346
C5	-1.6737530707	-1.3372525931	4.1859545124
H6	-2.1073095680	-0.4547924462	4.6648964841
H7	-2.4383293440	-2.1237477252	4.1731573252
H8	-0.8110860467	-1.6973296142	4.7509442463
Cu9	0.2551822347	-1.8196932931	0.3757992190
C10	-2.7046330217	-1.9809142258	-0.5516702848
O11	-2.9823023579	-0.7382601992	-0.7085958233
O12	-1.6770267169	-2.4599924297	-0.0230958465
C13	-0.1031216394	2.3959147749	1.6902415275
O14	0.8126749600	1.7351028413	1.1336648367
O15	-1.3232121679	2.3575171266	1.3125556728
C16	0.2125358223	3.2866932480	2.8703199554
H17	0.3449956242	2.6521856969	3.7549848974
H18	1.1524549799	3.8206656675	2.7024328882
H19	-0.5976444296	3.9933205001	3.0597559107
C20	-3.7626040794	-2.9298358414	-1.0875023100
H21	-3.8537663484	-2.7908245168	-2.1708936605

H22	-3.4889128263	-3.9650973573	-0.8742625426
H23	-4.7344017199	-2.6956241928	-0.6403082523
Pd24	-1.9778809865	0.7896001500	0.1747443333
C25	3.0845941712	-0.8660673122	0.2592776671
O26	2.8991899701	-0.0508039182	-0.6747423638
O27	2.1937594688	-1.5745910154	0.8467726900
C28	4.5011485908	-1.0300997503	0.7941597268
H29	4.7852681572	-0.0984131113	1.2973322681
H30	4.5763010829	-1.8606959316	1.4991225938
H31	5.1877399764	-1.1819562445	-0.0448884881
C32	0.4989716113	-1.3441846029	-2.1915525971
O33	-0.0292873635	-0.3205741156	-1.6550248606
O34	0.7588079529	-2.3941692033	-1.5300193800
C35	0.8649082394	-1.2975091655	-3.6554976216
H36	1.8419943474	-0.8075377555	-3.7389680431
H37	0.9430671338	-2.3015737406	-4.0774060752
H38	0.1343977583	-0.6993936792	-4.2053510902
C39	-1.4463572113	3.0150989197	-3.9612585420
C40	-2.3481437440	1.9518611311	-3.8506537376
C41	-2.5952149676	1.3482891957	-2.6122118875
C42	-1.9196751476	1.8282937040	-1.4959852569
C43	-1.0540789912	2.9181205770	-1.5646302053
C44	-0.8060770191	3.4979516731	-2.8192855171

H45	-1.2531458010	3.4704503124	-4.9298338247
H46	-2.8613894606	1.5740601163	-4.7328427345
H47	-3.2709356924	0.5052208749	-2.5377716587
H48	-0.5887971009	3.3441384546	-0.6862169390
H49	-0.1100119669	4.3315530145	-2.8819492687
H50	2.3999421197	2.2412431352	1.1664740021
O51	2.5853254668	3.0652959620	-1.0384641209
O52	3.3212632930	2.6356185935	1.0496218058
C53	3.4757602112	3.0978647026	-0.1848971317
C54	4.8489359418	3.6443544865	-0.4537034344
H55	4.8191320893	4.3285118078	-1.3033166064
H56	5.2590917930	4.1401710077	0.4295492439
H59	5.5055716481	2.8029372320	-0.7063047158
C60	-4.2050757459	2.4118285828	0.1730726468
C61	-4.2591290975	1.4416548340	1.1186395668
H62	-3.6995459102	3.3550922948	0.3602952242
H63	-3.8216411346	1.5798589764	2.1023692847
H64	-4.7879425171	0.5089736245	0.9417573621
H65	-4.6878877548	2.2929664851	-0.7924550758

TS2

Cu1	1.5731571142	0.6764940472	0.6548482543
C2	-1.1524667141	-0.8302701664	2.4865262304

O3	-0.3014231664	-1.6811670906	2.0730725896
O4	-1.8058685295	-0.0194576879	1.7765651382
C5	-1.4102242921	-0.8190856225	3.9837328552
H6	-1.8053508266	0.1503969357	4.2967159884
H7	-2.1529311826	-1.5933937973	4.2140599874
H8	-0.4935898469	-1.0556437217	4.5304728027
Cu9	-0.0555178515	-2.1637097530	0.1262128053
C10	-2.9186501154	-2.0262659465	-0.7625117913
O11	-2.9304374832	-0.7963730141	-1.0658171112
O12	-1.9837236562	-2.6413587389	-0.1734602772
C13	-0.1861494101	2.8536766458	1.7266459290
O14	0.8650630163	2.1726246830	1.8607179158
O15	-1.0816787554	2.6864480044	0.8371085688
C16	-0.4346066889	3.9739560588	2.7265066012
H17	-0.9490149459	3.5491767386	3.5962129892
H18	0.5099290848	4.4028464366	3.0683462635
H19	-1.0737857546	4.7482792263	2.2982517176
C20	-4.1584752093	-2.8274150461	-1.1231987259
H21	-4.4777348463	-2.5806681439	-2.1407575201
H22	-3.9705144074	-3.8994607611	-1.0352309600
H23	-4.9698392712	-2.5469688702	-0.4401472923
Pd24	-1.7669877478	0.8620401087	-0.2215615848
C25	2.9230765185	-2.0596697555	0.4967798516

O26	3.0137796683	-0.8062281202	0.4136107461
O27	1.8429172996	-2.7372331527	0.4700638624
C28	4.2112606036	-2.8581863062	0.6159307173
H29	4.8683470204	-2.3840557460	1.3519751930
H30	4.0150675907	-3.8963015154	0.8936584525
H31	4.7249485299	-2.8378019278	-0.3532914319
C32	0.5674694983	-0.6873200759	-1.9853241607
O33	0.2687949916	0.1200202737	-1.0392491298
O34	0.3757681330	-1.9344972332	-1.8918421081
C35	1.1906123804	-0.1579674475	-3.2534338789
H36	1.4346150587	0.8997841640	-3.1528170602
H37	2.0878826692	-0.7368403210	-3.4880792316
H38	0.4848164817	-0.2869815934	-4.0782884925
C39	-0.8692026430	2.4827121609	-4.4229530970
C40	-1.8419317546	1.4825885775	-4.2987501272
C41	-2.4517973687	1.2467378043	-3.0678670560
C42	-2.0578910556	2.0006937626	-1.9498390121
C43	-1.1049376400	3.0245325023	-2.0733149706
C44	-0.5022378559	3.2493249299	-3.3109721230
H45	-0.4003788217	2.6658570676	-5.3871560217
H46	-2.1334057524	0.8910621248	-5.1638802426
H47	-3.2084077912	0.4778452750	-2.9654426564
H48	-0.8354690466	3.6186067287	-1.2085861108

H49	0.2478708213	4.0309005073	-3.4078870828
C60	-3.6412280502	2.5465354108	-0.8026677487
C61	-3.6049537193	1.6331431772	0.2988999368
H62	-3.3517215386	3.5753076616	-0.6120440114
H63	-3.3408339609	2.0019007531	1.2839529684
H64	-4.2319613911	0.7475333085	0.2647332645
H65	-4.4033859668	2.4096300571	-1.5640357131

I3

Cu1	1.5823179889	1.0918444230	-0.0597500762
C2	-0.4849879119	-0.3653139842	2.7882847338
O3	0.2921168618	-1.2668171348	2.3164907578
O4	-1.4134141086	0.2186160464	2.1748699540
C5	-0.2010178451	0.0555410413	4.2167655019
H6	0.5499377373	0.8523199581	4.1761877271
H7	-1.1035809735	0.4499773509	4.6856942975
H8	0.2109721158	-0.7731040053	4.7948834031
Cu9	0.1444071835	-1.8911756746	0.4818935307
C10	-2.7731266337	-2.0111310736	0.0449943775
O11	-2.9574064276	-0.8456485611	-0.4388330916
O12	-1.7620129288	-2.3960878793	0.6820332500
C13	-0.1148523196	2.9142136690	1.3198656922
O14	0.8934847810	2.1745864109	1.3887894785

O15	-1.1457040182	2.7022555866	0.5879789931
C16	-0.1657531745	4.1672373064	2.1671732029
H17	-0.7773246982	3.9584519351	3.0513798340
H18	0.8382359739	4.4527334891	2.4826112950
H19	-0.6443800687	4.9794052153	1.6162015621
C20	-3.8727700938	-3.0204028929	-0.2128744680
H21	-3.6291306439	-3.5583710021	-1.1358768751
H22	-3.9097526274	-3.7432459707	0.6035122728
H23	-4.8374254694	-2.5275466813	-0.3405704209
Pd24	-1.7675435752	0.7978276417	0.0252985702
C25	2.9000241502	-1.3809462215	-0.4370368049
O26	2.6398897083	-0.2555329270	-0.9552907220
O27	2.1133045222	-2.0528799070	0.2993589915
C28	4.2762245988	-1.9602292125	-0.6784293441
H29	4.9498101451	-1.5087449496	0.0582373801
H30	4.2799613545	-3.0430087169	-0.5461344435
H31	4.6318479149	-1.6852992984	-1.6733155790
C32	0.0173563145	-0.8186799731	-2.1586851349
O33	-0.2985172964	0.3296834084	-1.6703315915
O34	-0.0232512243	-1.9013877331	-1.5228649999
C35	0.5380138044	-0.8329707206	-3.5761996537
H36	1.6061084386	-0.5967291875	-3.5145929079
H37	0.4185525888	-1.8247313180	-4.0128186023

H38	0.0537845956	-0.0727889714	-4.1919690360
H50	-0.0402158009	1.6636524784	-2.4758943505
O51	1.5978746107	2.9731279587	-1.4450567750
O52	0.0397355047	2.5169352118	-3.0069705109
C53	0.9472291917	3.2995935637	-2.4319547328
C54	1.0831124672	4.6371968707	-3.1124742234
H55	1.8999869713	5.2018620012	-2.6649413404
H56	1.2584690271	4.4945289223	-4.1823470799
H59	0.1444606060	5.1901775546	-3.0054225379
C47	-3.6344469532	3.8701533848	-5.2295797483
C48	-3.0275357398	2.9487757569	-4.3773385445
C49	-3.8066530530	2.0485271254	-3.6343880389
C50	-5.2012662658	2.1030780324	-3.7473638171
C51	-5.8088585612	3.0252541300	-4.6002518410
C52	-5.0264885896	3.9108807866	-5.3437072999
H53	-3.0215464704	4.5573841235	-5.8064628104
H54	-1.9449152080	2.9226426814	-4.2760922634
C55	-3.1391301452	1.0696544703	-2.6842393233
H57	-5.8112396916	1.4110377510	-3.1714642863
H58	-6.8915458584	3.0503531363	-4.6860440306
H60	-5.4988572057	4.6288748802	-6.0080391550
H61	-3.8019529172	0.2364147721	-2.4456126667
H62	-2.2348663499	0.6606287377	-3.1414102641

C61	-2.7786174847	1.8452632433	-1.4349880068
H63	-2.0862763003	2.6651687225	-1.6249104958
H64	-3.6481875808	2.1806167168	-0.8556593387
C70	0.5045431551	-4.3459154594	1.5462419500
C71	0.4139891727	-4.6000470660	0.2368602509
H72	-0.3700628177	-4.3645980325	2.1888118257
H73	-0.5366089026	-4.8380377017	-0.2304557297
H74	1.2793229173	-4.5250578777	-0.4137678711
H75	1.4457215388	-4.0540967604	2.0011298655
C76	3.1721988862	0.5332195605	2.4437215227
C77	4.4542852115	0.1785810492	2.5453575973
H78	2.3813792998	-0.2069102094	2.3646214111
H79	4.7537011931	-0.8669275781	2.5656115975
H80	5.2535304605	0.9125051239	2.6164110872
H81	2.8619826587	1.5749387676	2.4238286456

TS3

Cu1	1.6297906767	1.1903492109	-0.5632714746
C2	-1.0975354508	-0.9397763685	2.7232219964
O3	-0.2663933041	-1.7893963836	2.2878553386
O4	-1.8138243130	-0.1513244330	2.0425355725
C5	-1.2099553547	-0.8363690640	4.2343634620
H6	-0.4160700171	-0.1684870215	4.5867302106

H7	-2.1740036145	-0.4149058697	4.5230681125
H8	-1.0575727407	-1.8129624504	4.6973375257
Cu9	0.0131436523	-2.1240152672	0.3873982706
C10	-2.8347164314	-2.2494266345	-0.5399342971
O11	-3.0010833066	-1.0424996259	-0.9079510271
O12	-1.8861388724	-2.7019092762	0.1560451502
C13	0.1045281427	2.2136640186	1.5846821004
O14	0.8561101312	1.2047902078	1.3849915975
O15	-0.9714423467	2.4198985504	0.9486223333
C16	0.5411702338	3.2277450290	2.6165760253
H17	0.6832177350	2.7227235555	3.5768544398
H18	1.5138843538	3.6233467165	2.3069647858
H19	-0.1877244345	4.0311874964	2.7240029931
C20	-3.8774361337	-3.2519726363	-1.0014011537
H21	-3.4604089178	-3.8157306670	-1.8426196384
H22	-4.0869877896	-3.9611996053	-0.1976653820
H23	-4.7925201869	-2.7541628489	-1.3245840693
Pd24	-1.8354290600	0.6103574536	-0.0413757446
C25	2.9324451050	-1.3660732347	0.2292294188
O26	2.8761940734	-0.3665664804	-0.5411852361
O27	1.9569205069	-2.0288433137	0.6977160732
C28	4.3072541592	-1.8159288121	0.6890156036
H29	5.0685271082	-1.5217830225	-0.0359907522

H30	4.5075284605	-1.3077163783	1.6380376065
H31	4.3309732754	-2.8932844544	0.8629231048
C32	0.2455202954	-0.9402939402	-2.0777390182
O33	-0.1036502412	0.1193722552	-1.4523946647
O34	0.2255306598	-2.1006552181	-1.5856494667
C35	0.8016842510	-0.7654149985	-3.4710560487
H36	1.8547175471	-0.4842304958	-3.3566899455
H37	0.7470038283	-1.6980618085	-4.0337426605
H38	0.2834408815	0.0401988272	-3.9946709713
H39	2.3283036324	1.0795733993	2.0874310709
O40	3.5437905273	2.8252874974	1.0915946179
O41	3.2865627195	0.9863040374	2.3755680495
C42	4.0164789125	1.9187353942	1.7647419295
C43	5.4984747511	1.7134066479	1.9642991322
H44	6.0370817478	2.6305606216	1.7258715626
H45	5.7140803356	1.3892925451	2.9850729951
H46	5.8264033775	0.9187580285	1.2853612619
H47	-2.2487109003	1.3677647248	-1.3290217707
C48	-3.7604644728	1.9627119358	-0.8634697972
C49	-3.6892902967	1.4786708830	0.4698292369
H50	-3.4715295764	2.1574697389	1.2879901642
H51	-4.2525360804	0.5851701598	0.7202368154
H52	-4.2591142784	1.3059546814	-1.5756922161

C54	-3.3013733451	5.9862374857	-2.2417168575
C55	-3.9240093699	5.0248251186	-3.0403740999
C56	-4.0552727062	3.7176674646	-2.5776534489
C57	-3.5790673835	3.3573288918	-1.3045563188
C58	-2.9479851722	4.3309175991	-0.5083511230
C59	-2.8117823171	5.6329966627	-0.9800121079
H60	-3.1918535541	7.0048864279	-2.6019899435
H61	-4.3029035116	5.2912923029	-4.0223661646
H62	-4.5353559497	2.9676481388	-3.2013933576
H63	-2.5270597270	4.0533098597	0.4504606730
H64	-2.3158115266	6.3764947758	-0.3631432374
C65	0.3568419907	-4.6525968672	1.3061064506
C66	0.5756168827	-4.7760773540	-0.0062294548
H67	1.1395135803	-4.3228352309	1.9817033512
H68	1.5454324537	-4.5555132150	-0.4408708420
H69	-0.2209511048	-5.0440568896	-0.6934810623
H70	-0.6278507128	-4.8133275304	1.7338586419
C73	2.2880116421	2.5465099699	-2.0391883048
C74	1.3030397143	3.1412394033	-1.2922722215
H75	3.3370415859	2.6937245997	-1.7956019053
H76	1.5616339254	3.7748190277	-0.4484009856
H77	0.2646891405	3.1436142885	-1.6136748405
H78	2.0642076544	2.0611954852	-2.9860382183

I4

Cu1	1.7336559866	1.0874820860	-0.5971596178
C2	-1.1787898591	-0.9522268033	2.6805784100
O3	-0.3027726120	-1.7655075074	2.2547870424
O4	-1.8703699486	-0.1519205317	1.9910300089
C5	-1.3793103818	-0.9255196066	4.1865558519
H6	-0.6093484887	-0.2793243714	4.6243920669
H7	-2.3606508879	-0.5195071065	4.4380187757
H8	-1.2556926968	-1.9260222802	4.6072641403
Cu9	0.0483166022	-2.0771254225	0.3632102771
C10	-2.7958930069	-2.0430951903	-0.6703100196
O11	-2.9273829824	-0.8103934206	-0.9929717817
O12	-1.8826368683	-2.5409820971	0.0333567712
C13	0.1222829237	2.2435049260	1.4813053571
O14	0.8792436716	1.2357719005	1.3402015383
O15	-0.9724148705	2.3964736082	0.8460658151
C16	0.5327853572	3.3347031337	2.4404307939
H17	0.5955125492	2.9121807032	3.4489343184
H18	1.5351044381	3.6748613590	2.1626373986
H19	-0.1750840728	4.1638878376	2.4349646413
C20	-3.8508722346	-2.9860158030	-1.2151123349
H21	-3.4241886637	-3.5222568934	-2.0701294102

H22	-4.1082020234	-3.7244173868	-0.4521011546
H23	-4.7405655659	-2.4452993588	-1.5412466922
Pd24	-1.8021824583	0.6940194965	-0.0672865555
C25	2.9933380257	-1.4448113906	0.3355975071
O26	2.9979448167	-0.4498842701	-0.4444131679
O27	1.9784139169	-2.0673778457	0.7774932768
C28	4.3375800474	-1.9323401596	0.8457867059
H29	5.1246602339	-1.7100050199	0.1218493734
H30	4.5481699312	-1.3837257210	1.7707580254
H31	4.3100469850	-2.9994737595	1.0751510156
C32	0.3442576548	-1.0301973142	-2.1434680387
O33	0.0437645155	0.0554630283	-1.5441686984
O34	0.3525518631	-2.1671816729	-1.5890757010
C35	0.7803477002	-0.9384809634	-3.5881186139
H36	1.8206390196	-0.5921589164	-3.5978892669
H37	0.7309151019	-1.9131586735	-4.0761753338
H38	0.1714769333	-0.2042220107	-4.1205444015
H39	2.3548909620	1.1558560632	2.0836205001
O40	3.6605205937	2.8923905069	1.1753075243
O41	3.2930214495	1.0462484546	2.4206698516
C42	4.0783206290	1.9674010934	1.8604279325
C43	5.5413628350	1.7244802505	2.1386007458
H44	6.1150387293	2.6304082001	1.9407825256

H45	5.6938563645	1.3866530721	3.1666834167
H46	5.8894792837	0.9290214690	1.4698362238
H47	-1.8903737931	1.4440262659	-1.3664108031
C48	-4.2960856249	2.0598426205	-0.4307489398
C49	-3.8914148310	1.5991612069	0.7953443795
H50	-3.4376736276	2.2488496105	1.5359775460
H51	-4.2183946299	0.6257571053	1.1435161076
H52	-4.8254165094	1.3570439507	-1.0725964245
C54	-3.7529762320	5.9286794532	-2.1544772155
C55	-4.5712568631	4.9805206023	-2.7742934195
C56	-4.7301698167	3.7200782444	-2.2018016494
C57	-4.0859275285	3.3903373092	-0.9927740862
C58	-3.2564386904	4.3543290741	-0.3813012618
C59	-3.0934878394	5.6080615802	-0.9610914845
H60	-3.6227885289	6.9108975481	-2.6007267857
H61	-5.0804537576	5.2220426245	-3.7030896756
H62	-5.3633253953	2.9801630154	-2.6860988348
H63	-2.7112464064	4.1023598474	0.5213392141
H64	-2.4458292246	6.3402192210	-0.4866808175
C65	0.1854158658	-4.6609279258	1.3109994219
C66	0.4793845801	-4.8023776138	0.0151654539
H67	0.9400789562	-4.3689523434	2.0347814152
H68	1.4842348319	-4.6318083143	-0.3591769983

H69	-0.2834236022	-5.0355894972	-0.7219555170
H70	-0.8301522697	-4.7731927508	1.6792968794
C73	2.5227983570	2.4204607762	-2.0427612400
C74	1.4910409431	3.0373264607	-1.3827530431
H75	3.5539730071	2.5641300185	-1.7289258843
H76	1.6915436272	3.6902840902	-0.5372639092
H77	0.4795333373	3.0355565178	-1.7814625352
H78	2.3645766392	1.9128281549	-2.9918715516

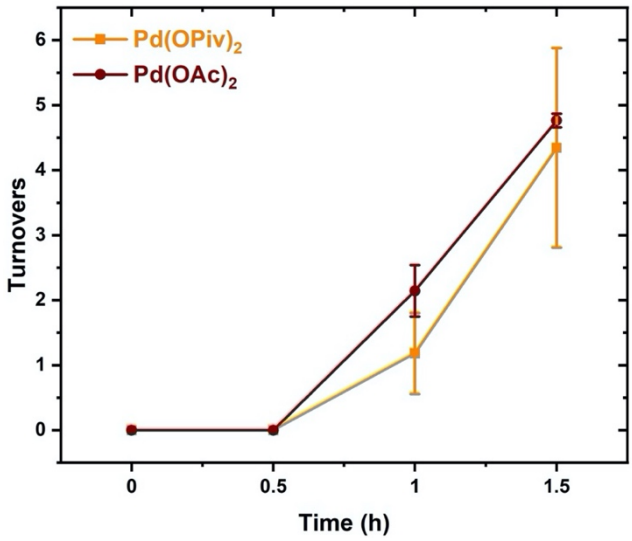

Figure H1. Turnovers of styrene as a function of time using $Pd(OAc)_2$ or $Pd(OPiv)_2$ as the catalyst precursor. Reaction conditions: 0.001 mol% $Pd(OAc)_2$ or $Pd(OPiv)_2$ (relative to benzene), 480 eq. of $Cu(OPiv)_2$ (relative to $Pd(OAc)_2$ or $Pd(OPiv)_2$), 960 eq. of HOPiv (relative to $Pd(OAc)_2$ or $Pd(OPiv)_2$),, 10 mL of benzene, 50 psig of ethylene, 120 °C. Turnovers of styrene were quantified by GC-FID analysis relative to the internal standard hexamethylbenzene. Each data point is the average of three independent experiments and error bars represent the standard deviation for the three experiments.

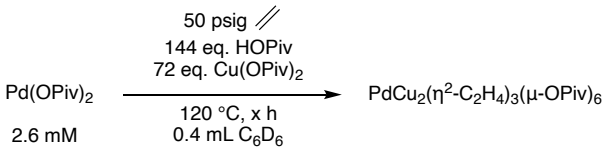

Scheme H1. Reaction conditions used to monitor transformation of $Pd(OPiv)_2$ to $PdCu_2(\eta^2\text{-}C_2H_4)_3(\mu\text{-}OPiv)_6$ under catalytic conditions by ^1H NMR spectroscopy.

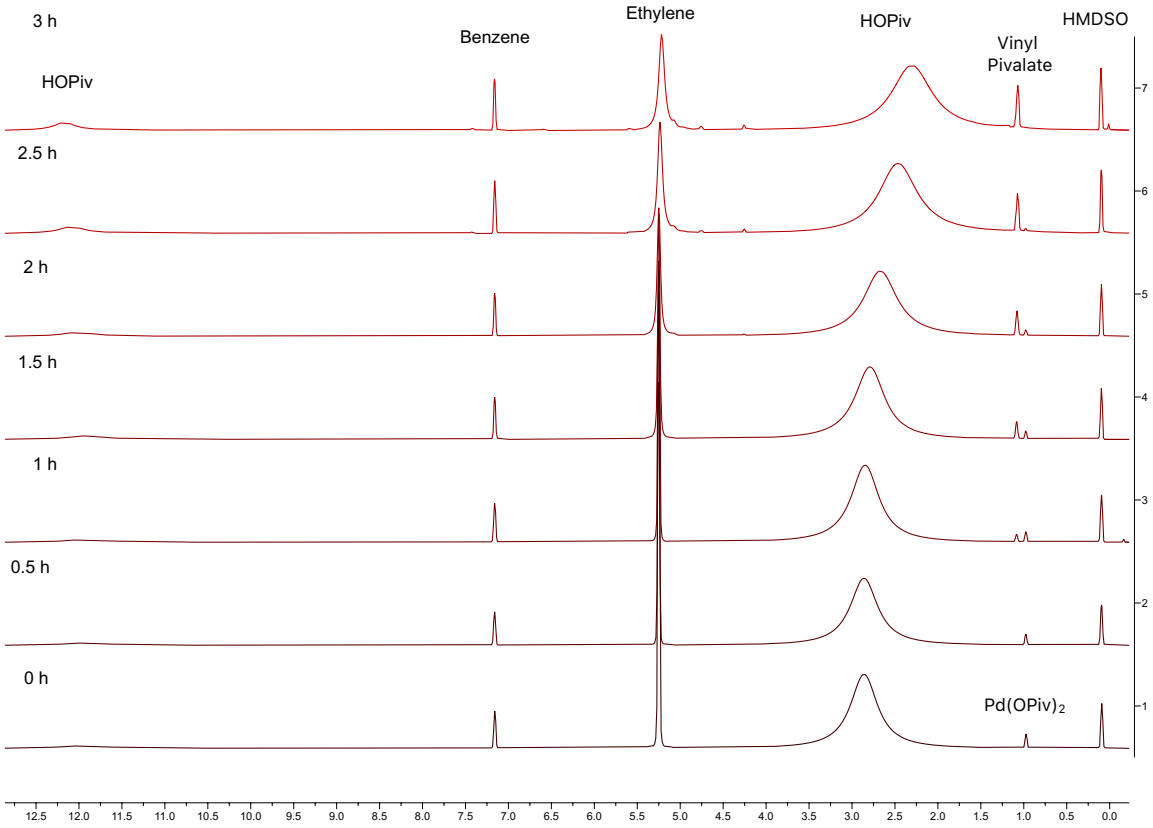

Figure H2. Transformation of $Pd(OPiv)_2$ into $PdCu_2(\eta^2\text{-}C_2H_4)_3(\mu\text{-}OPiv)_6$ in the presence of ethylene monitored by ^1H NMR. Reaction conditions: 2.6 mM $Pd(OPiv)_2$, 72 eq. (relative to $Pd(OAc)_2$) $Cu(OPiv)_2$, 144 eq. HOPiv, 5 eq. HMDSO, 0.4 mL C_6D_6, 50 psig ethylene, 120 °C (600 MHz).

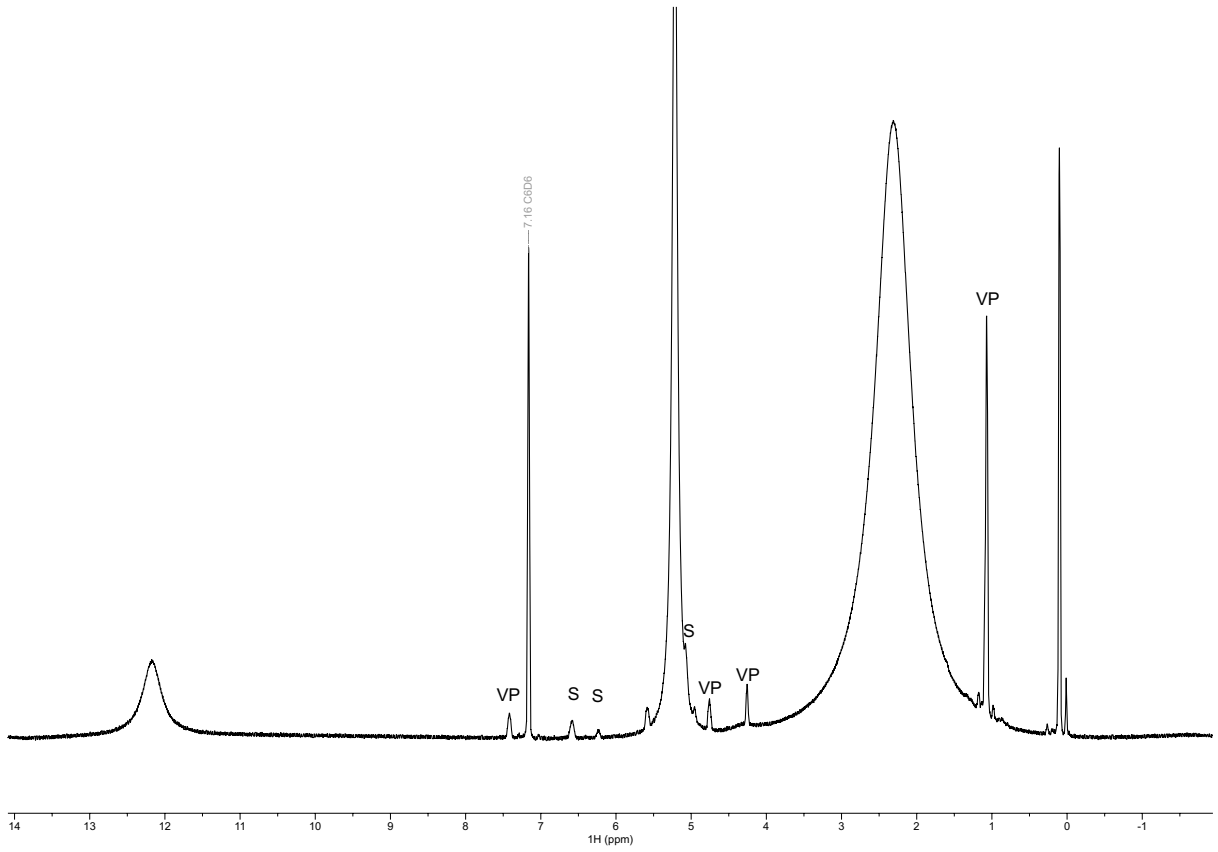

Figure H3. Observation of styrene-d_5 and vinyl pivalate by ^{1}H NMR spectroscopy. Vinyl pivalate peaks are labeled with "VP" and styrene-d_5 vinyl peaks are labeled with "S" (600 MHz, C_6D_6).

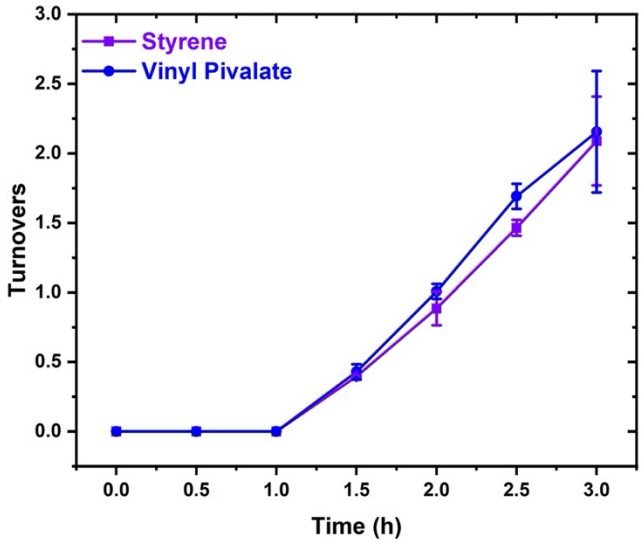

Figure H4. Turnovers of styrene-d_5 and vinyl pivalate as a function of time measured by ^{1}H NMR spectroscopy relative to internal standard HMDSO. Each data point is the average of three independent experiments and error bars represent the standard deviation for the three experiments.

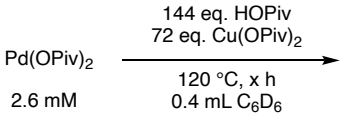

Scheme H2. Reaction conditions used to determine if $Pd(OPiv)_2$ is converted to a new species in the absence of ethylene by ^{1}H NMR spectroscopy.

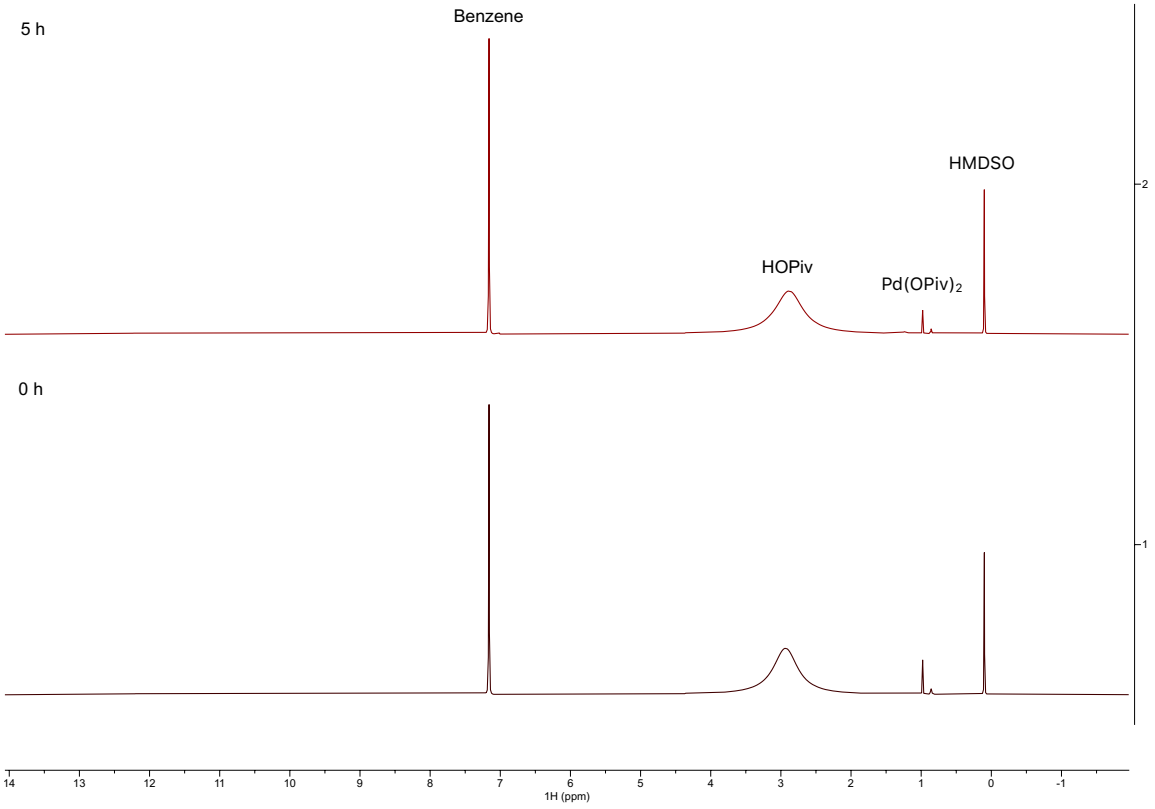

Figure H5. Transformation of $Pd(OPiv)_2$ in the absence of ethylene monitored by ^1H NMR. Reaction conditions: 2.6 mM $Pd(OPiv)_2$, 72 eq. (per Pd atom) $Cu(OPiv)_2$, 144 eq. HOPiv, 5 eq. HMDSO, 0.4 mL C_6D_6, 50 psig N_2, 120 °C (600 MHz).

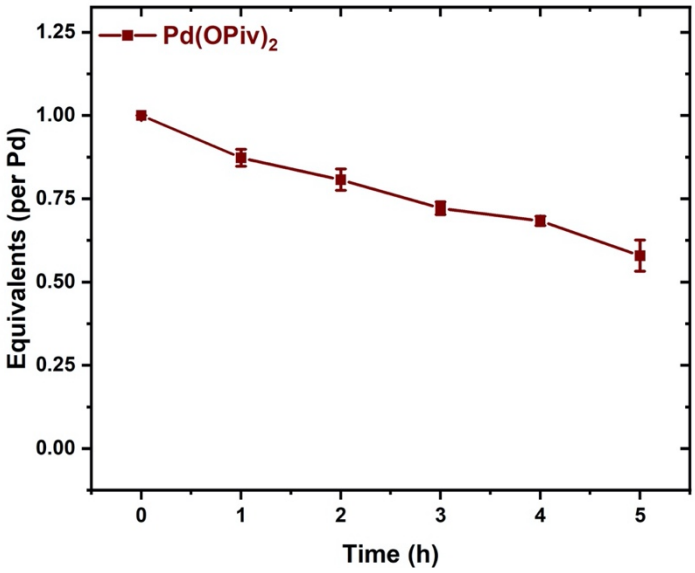

Figure H6. Concentration of $Pd(OPiv)_2$ as a function of time in the absence of ethylene as measured by ^1H NMR. Reaction conditions: 2.6 mM $Pd(OPiv)_2$, 72 eq. (per Pd atom) $Cu(OPiv)_2$, 144 eq. HOPiv, 5 eq. HMDSO, 0.4 mL C_6D_6, 50 psig N_2, 120 °C. Each data point is the average of three independent experiments and error bars represent the standard deviation for the three experiments.

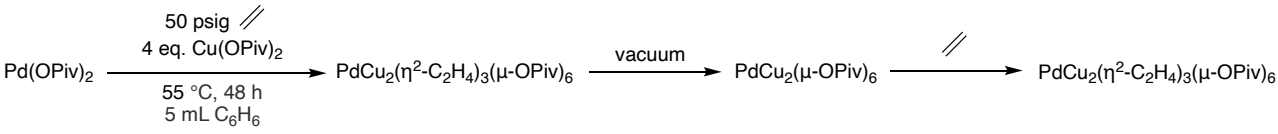

Scheme H3. Synthesis of $PdCu_2(\mu\text{-}OPiv)_6$ and $PdCu_2(\eta^2\text{-}C_2H_4)_3(\mu\text{-}OPiv)_6$.

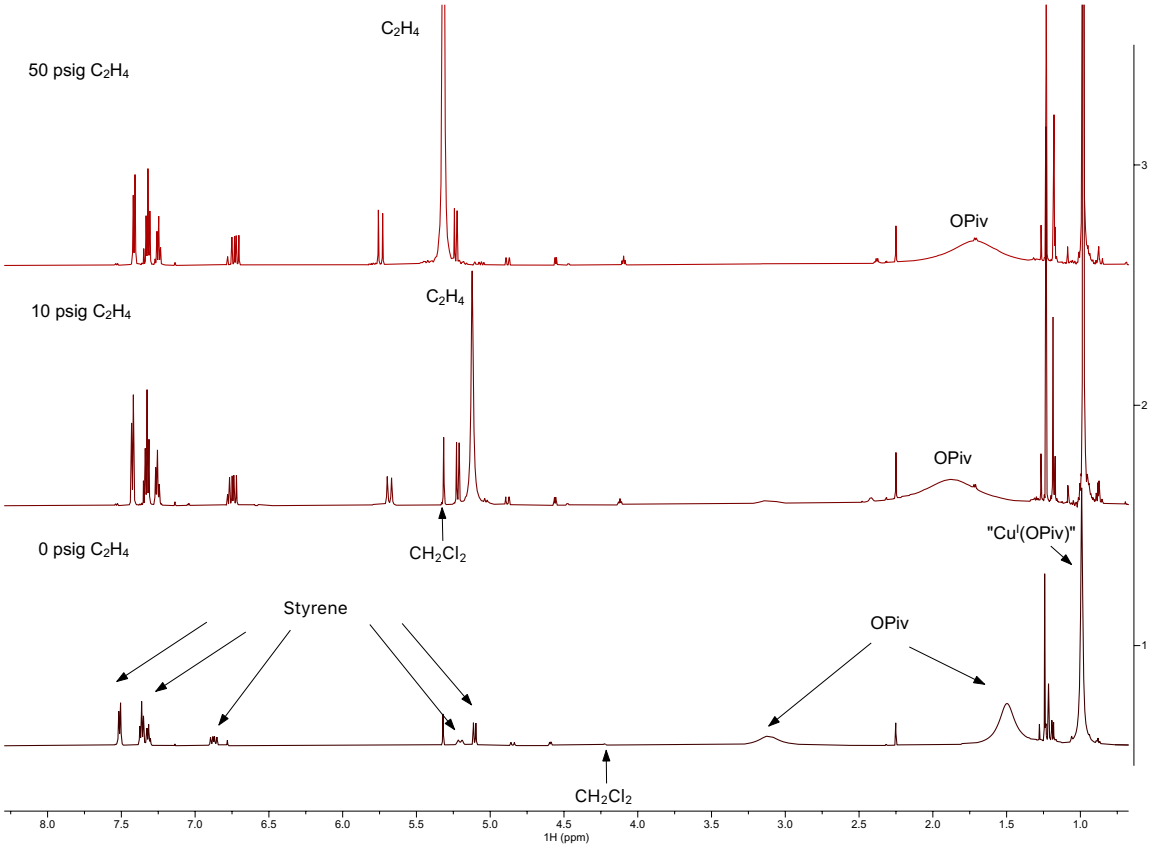

Figure H7. ^{1}H NMR spectrum of $PdCu_2(\eta^2\text{-}C_2H_4)_3(\mu\text{-}OPiv)_6$ in CD_2Cl_2 in the presence of no ethylene or 10 or 50 psig of ethylene. Changes in styrene chemical shift in the absence of ethylene are likely the result of coordination to Pd and/or Cu (600 MHz, CD_2Cl_2).

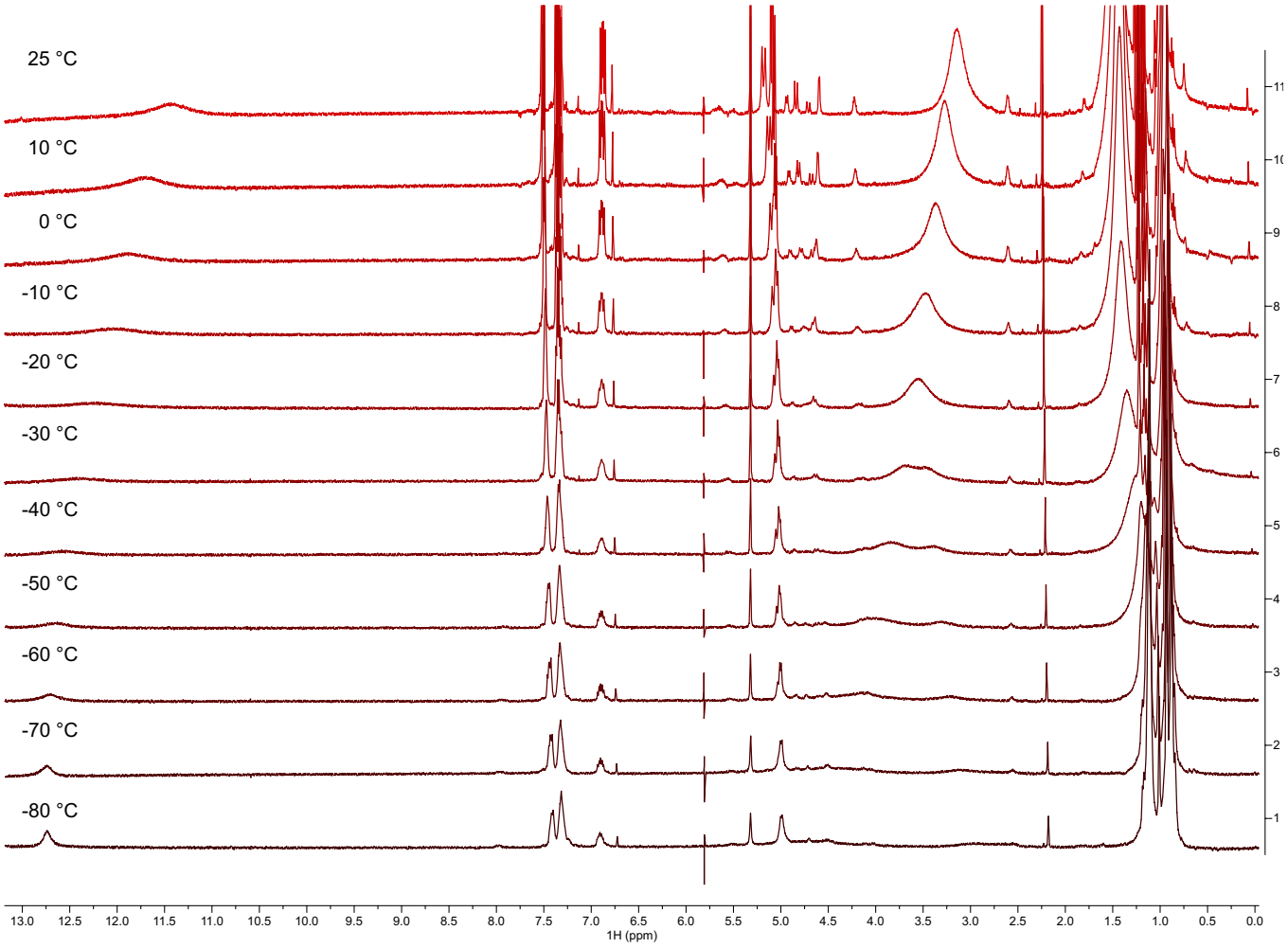

Figure H8. Variable temperature ^{1}H NMR spectra of $PdCu_2(\mu\text{-}OPiv)_6$ in the absence of ethylene (500 MHz, CD_2Cl_2).

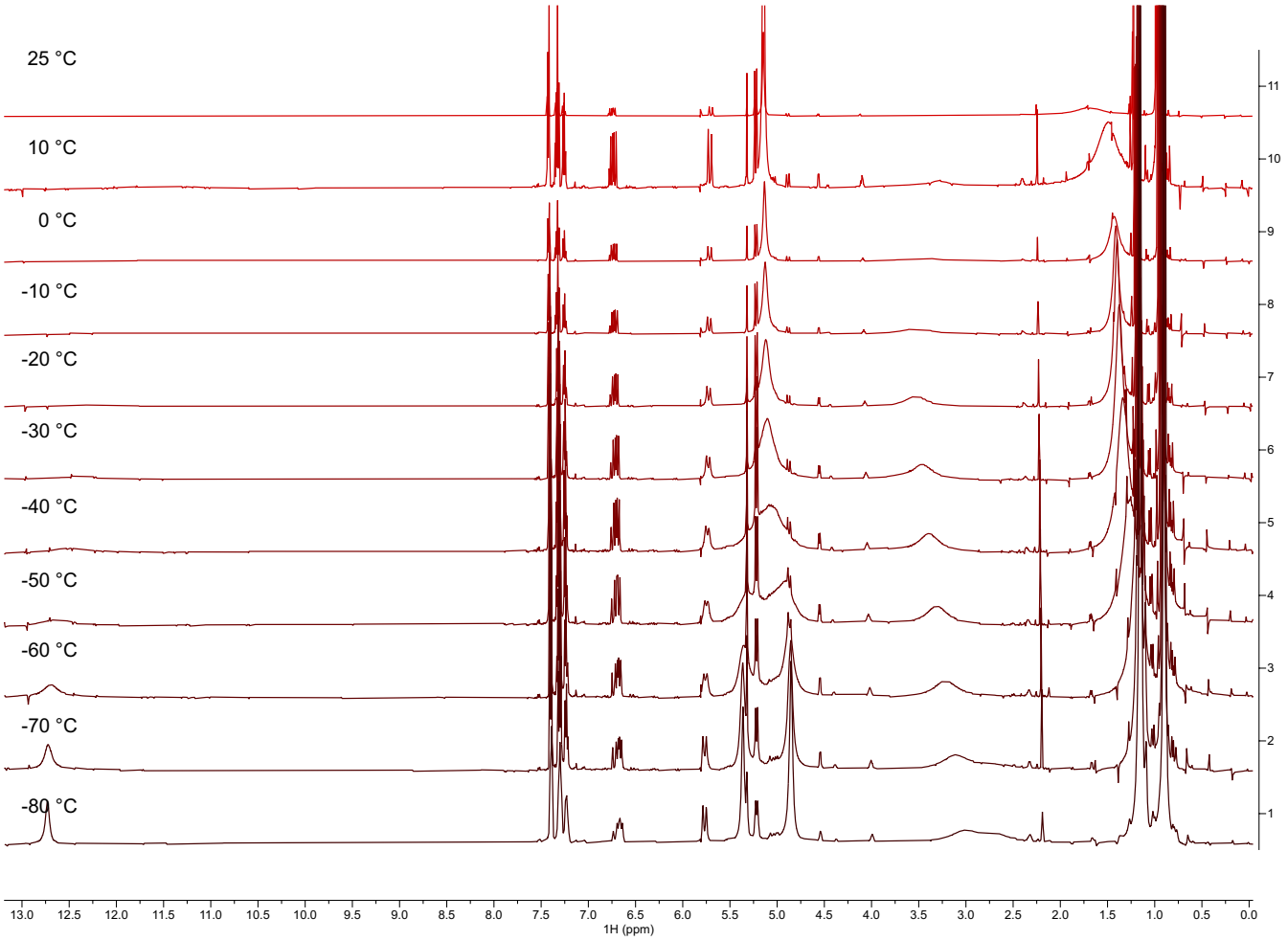

Figure H9. Variable temperature ^{1}H NMR spectra of $PdCu_2(\mu\text{-}OPiv)_6$ in the presence of 10 psig ethylene (500 MHz, CD_2Cl_2).

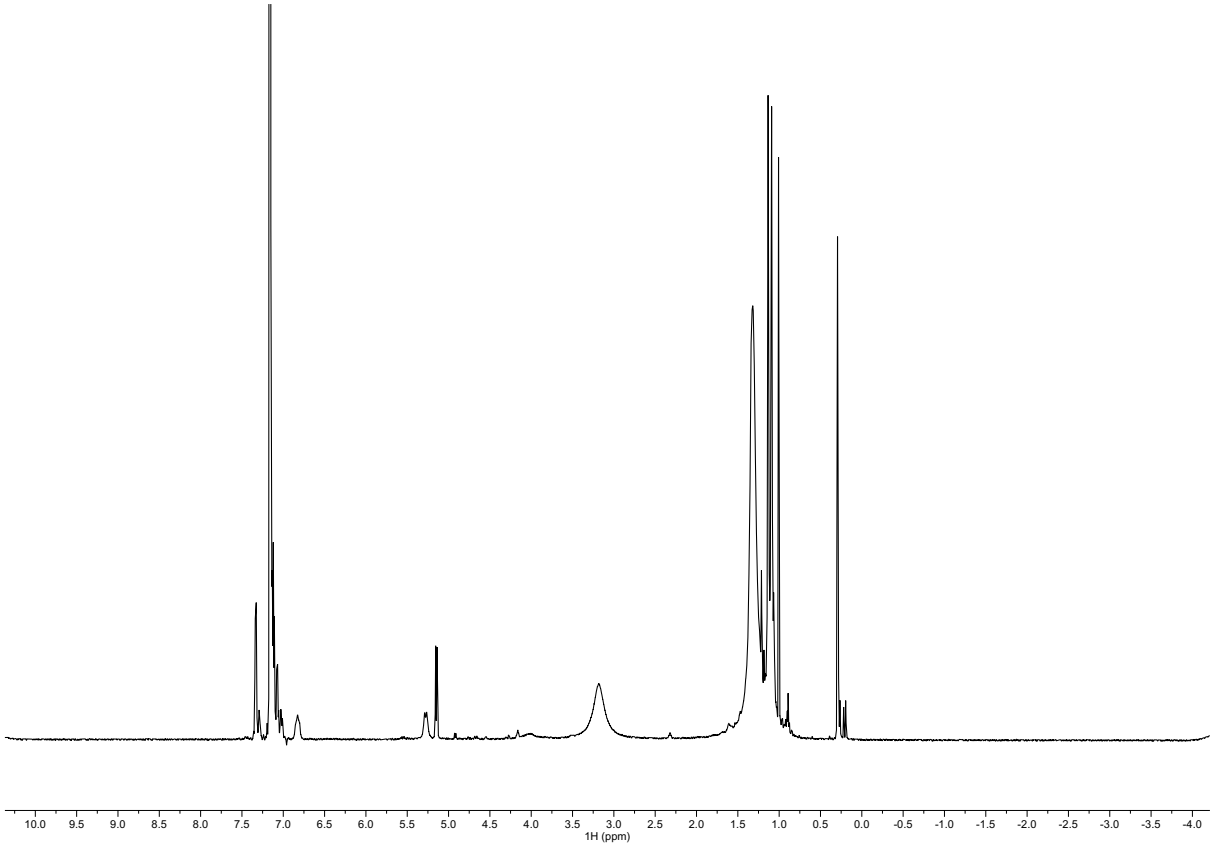

Figure H10. ^{1}H NMR spectrum of $PdCu_2(\mu\text{-}OPiv)_6$ (600 MHz, C_6D_6).

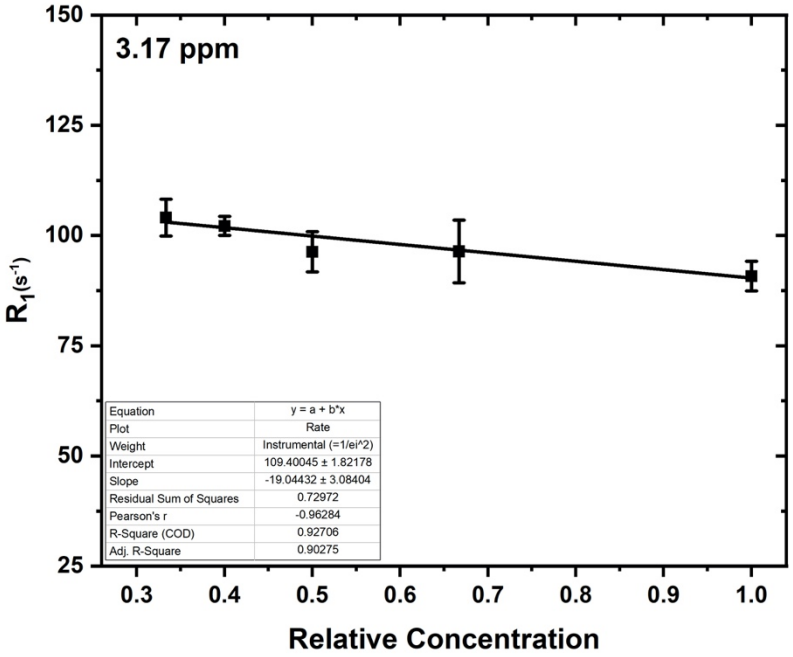

Figure H11. Spin-lattice relaxation rate at 25 °C for the peak observed at 3.18 ppm, which is attributed to $PdCu_2(\mu\text{-}OPiv)_6$ as a function of relative concentration in C_6D_6. Each data point is the average of three independent experiments and error bars represent the standard deviation for the three experiments.

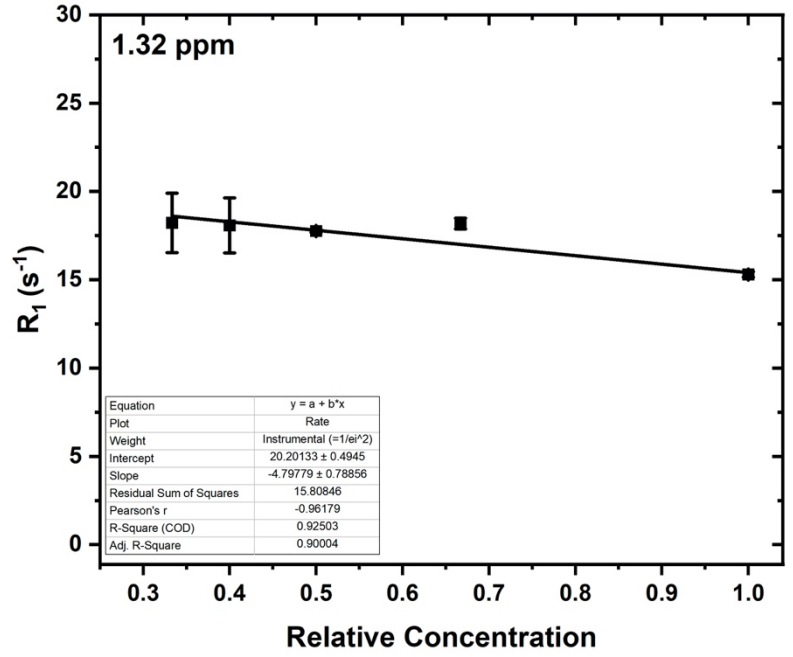

Figure H12. Spin-lattice relaxation rate at 25°C for the peak observed at 1.32 ppm due to exchange of OPiv between $PdCu_2(\mu\text{-}OPiv)_6$ and HOPiv as a function of relative concentration of $PdCu_2(\mu\text{-}OPiv)_6$ in C_6D_6. Each data point is the average of three independent experiments and error bars represent the standard deviation for the three experiments.

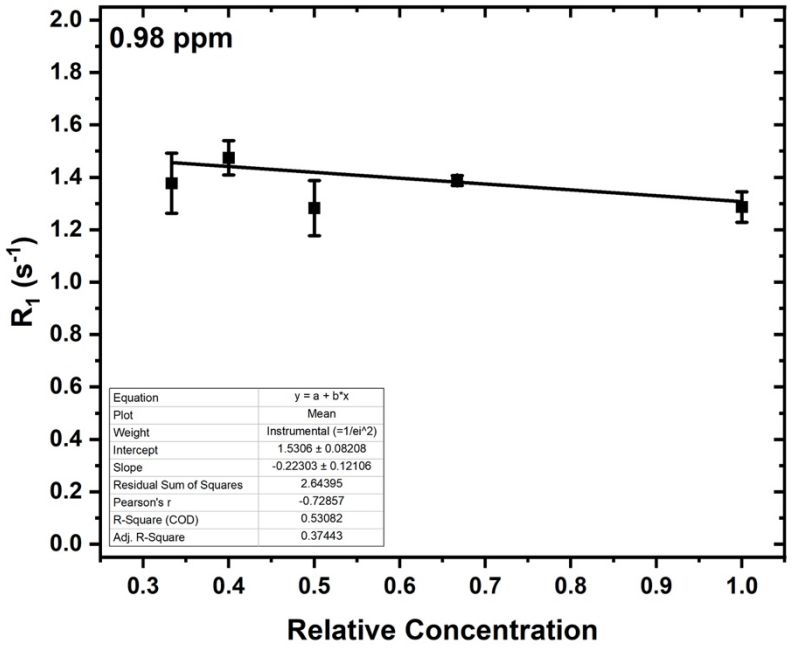

Figure H13. Spin-lattice relaxation rate at 25 °C for the peak observed at 0.98 ppm, assigned to $Pd(OPiv)_2$ in C_6D_6. Each data point is the average of three independent experiments and error bars represent the standard deviation for the three experiments.

Measurement of the spin-lattice relaxation rate of signals in a C_6D_6 solution containing $PdCu_2(OPiv)_6$, HOPiv, and $Pd(OPiv)_2$ revealed concentration independent relaxation rates of 109 s^{-1}, 20 s^{-1} and 1.5 s^{-1}, respectively (Table H4). Because chemical exchange

between HOPiv and $PdCu_2(OPiv)_6$ is occurring, the OPiv methyl relaxation rates cannot be quantitatively interpreted in terms of Cu – OPiv methyl distances. The concentration independence of the relaxation rates and substantially faster relaxation rate for $PdCu_2(OPiv)_6$ relative to $Pd(OPiv)_2$ is consistent with an intramolecular interaction between OPiv *tert*-butyl protons and Cu(II), and supports the existence of $PdCu_2(OPiv)_6$.

Table H4. Intramolecular spin-lattice relaxation rates observed in a solution of $PdCu_2(\mu\text{-}OPiv)_6$.

Chemical Shift (ppm)	R_1 (s^{-1})
3.18	109.4
1.32	20.2
0.98	1.5

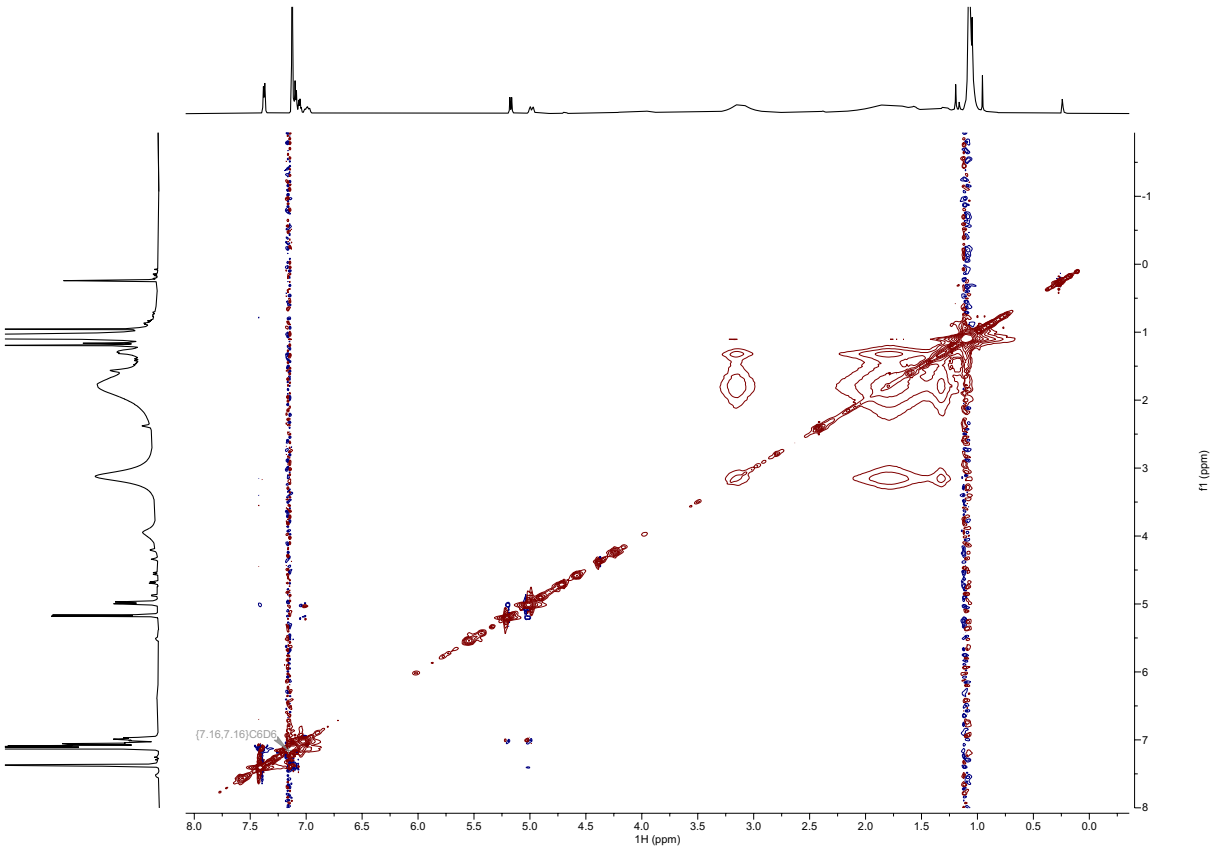

Figure H14. NOESY spectrum of $PdCu_2(\mu\text{-}OPiv)_6$ at 25 °C (C_6D_6 600 MHz). Mixing time = 0.03 s.

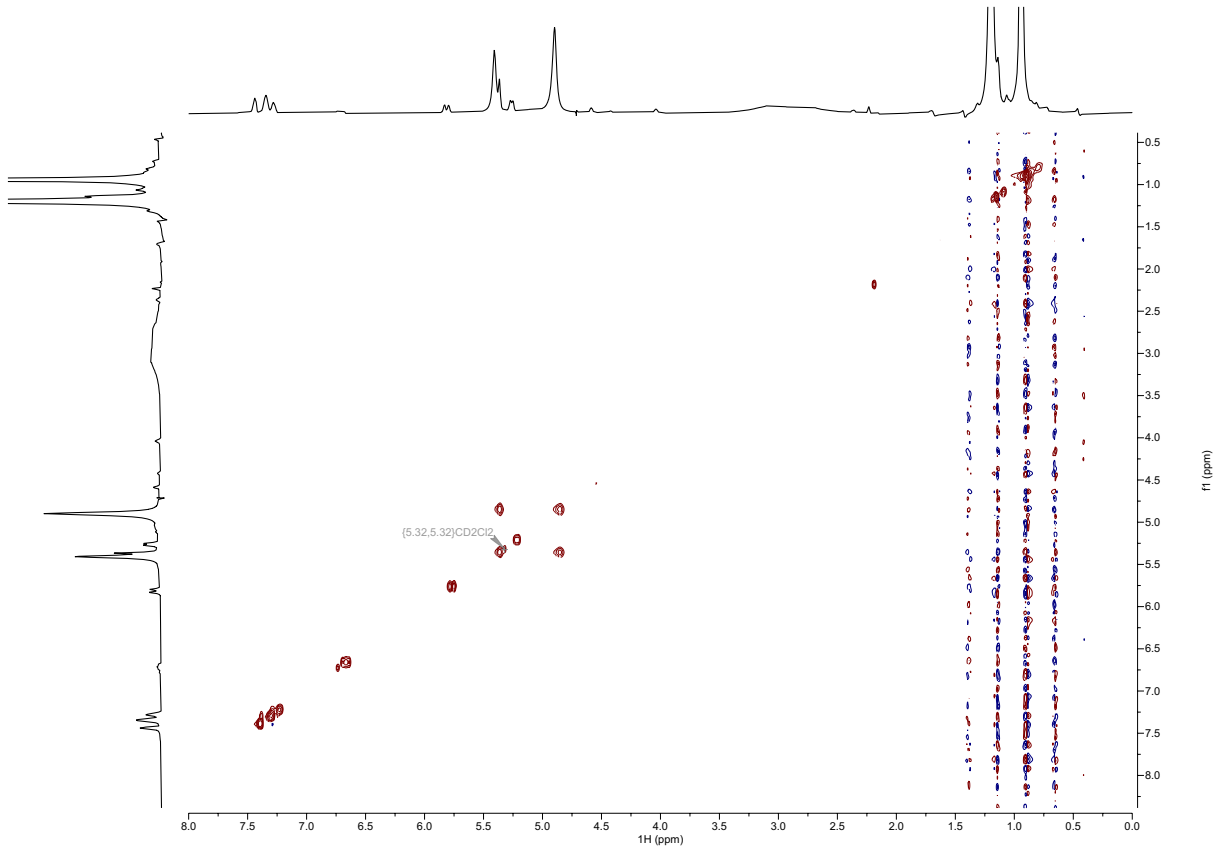

Figure H15. NOESY spectrum of $PdCu_2(\eta^2\text{-}C_2H_4)_3(\mu\text{-}OPiv)_6$ at -80 °C in the presence of 10 psig of ethylene (CD_2Cl_2, 500 MHz). Mixing time = 0.7 s.

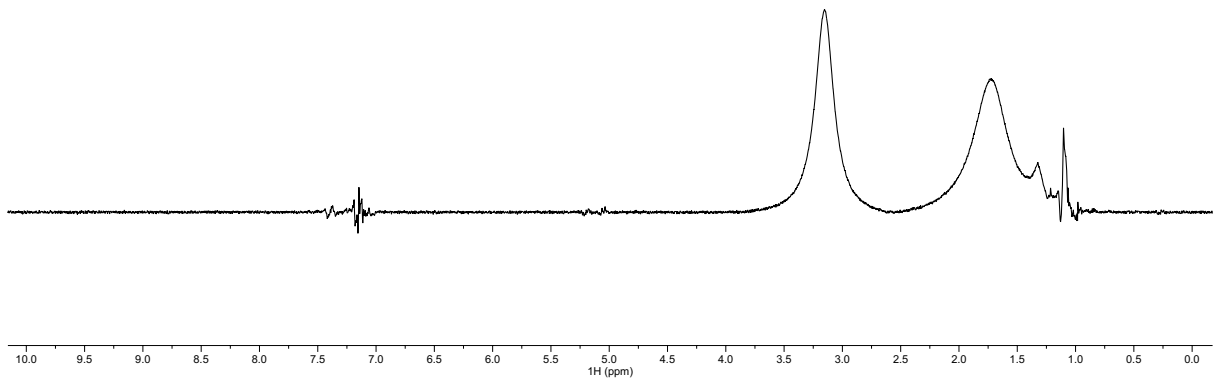

Figure H16. ^{1}H spin saturation transfer difference spectrum for a solution of $PdCu_2$ (μ-OPiv)$_6$ (C_6D_6, 600 MHz). The peak at 3.15 ppm was saturated with a 45 Hz magnetic field.

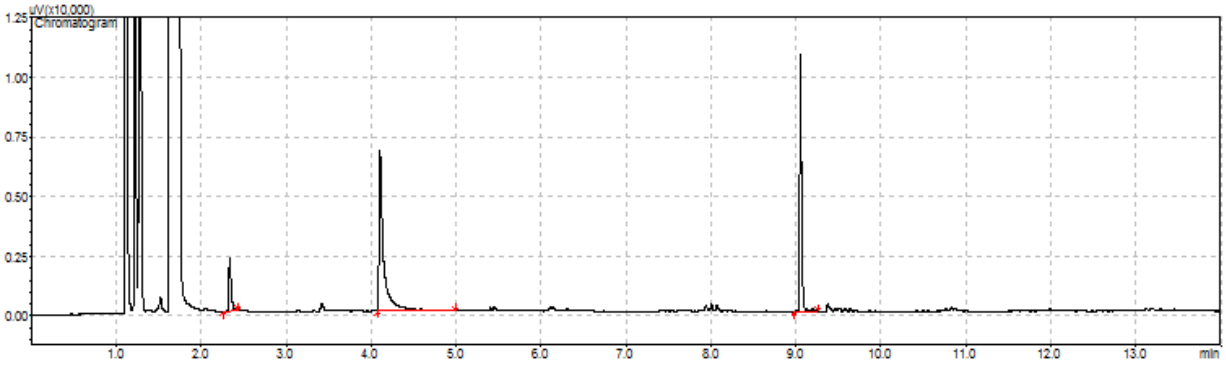

Figure H17. Representative GC-FID trace for the production of styrene using $Pd(OAc)_2$ as the catalyst precursor. 1-2 minutes: ethylene, dichloromethane, acetone and benzene; 2.3 minutes: vinyl pivalate; 4.1 minutes: styrene; 9.1 minutes: hexamethylbenzene.

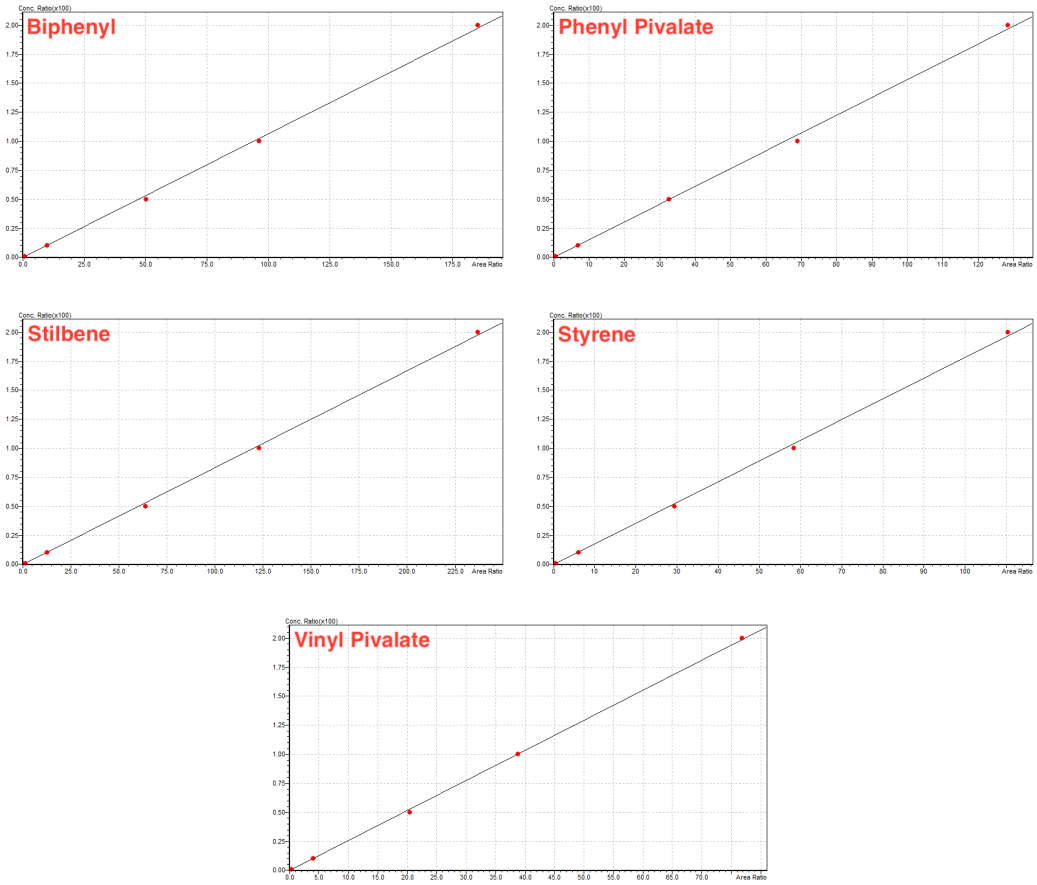

Figure H18. Regressions for GC-FID peak area of biphenyl, phenyl pivalate, *trans*-stilbene, styrene and vinyl pivalate relative to internal standard hexamethylbenzene as a function of concentration ratio.

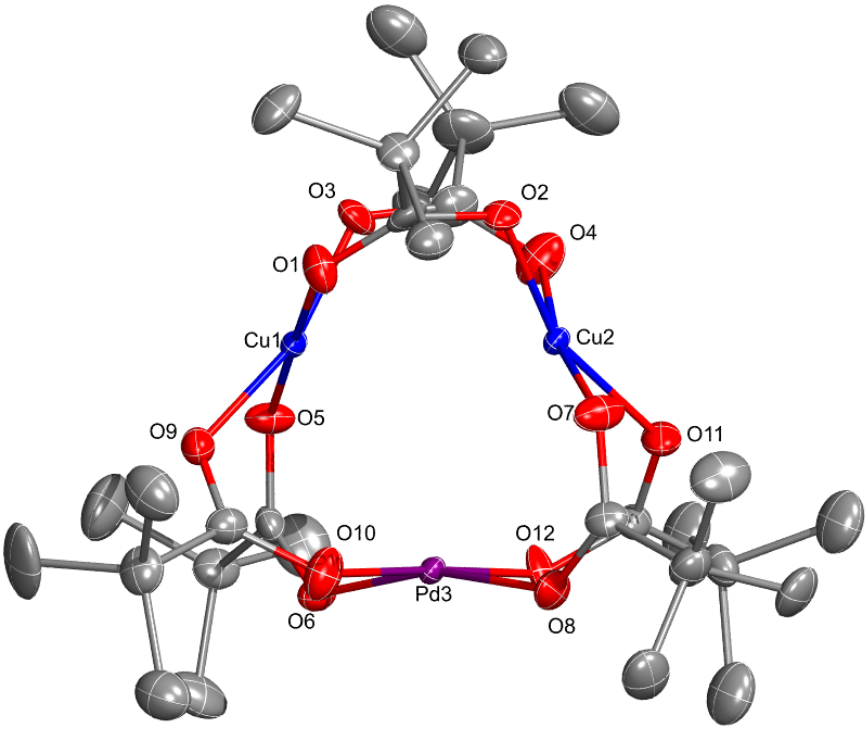

Figure H19. ORTEP of $PdCu_2(\mu\text{-}OPiv)_6$ (50% probability). H atoms are omitted for clarity and only the major positions for disordered atoms are shown.

X-Ray Crystallography Data and Structure Determination

A suiTable Hingle crystal of $PdCu_2(\mu\text{-}OPiv)_6$ was coated with Paratone oil and mounted on a MiTeGen Microloop. The X-ray intensity data were measured on a Bruker D8

Venture PhotonIII Kappa four-circled diffractometer system equipped with an Incoatec IμS 3.0 micro-focus sealed X-ray tube (Mo Kα, λ = 0.71073 Å) and a HELIOS double bounce multilayer mirror monochromator.

The total exposure time was 1.64 hours. The frames were integrated with the Bruker SAINT software package[1] using a narrow-frame algorithm. The integration of the data using an orthorhombic unit cell yielded a total of 43839 reflections to a maximum ϑ angle of 28.31° (0.75 Å resolution), of which 9617 were independent (average redundancy 4.558, completeness = 99.9%, R int = 8.32%, R sig = 7.41%) and 8306 (86.37%) were greater than 2σ(F 2). The final cell constants of a = 10.2449(10) Å, b = 16.7783(15) Å, c = 22.486(2) Å, volume = 3865.2(7) Å 3 , are based upon the refinement of the XYZ-centroids of 9996 reflections above 20 σ(I) with 4.369° ≤ 2ϑ ≤ 56.42°. Data were corrected for absorption effects using the Multi-Scan method (SADABS).[1] The ratio of minimum to maximum apparent transmission was 0.709. The

calculated minimum and maximum transmission coefficients (based on crystal size) are 0.7290 and 0.8950.

The structure was solved and refined using the Bruker SHELXTL Software Package[2] within APEX3[1] and OLEX2,[3] using the space group P $2_12_12_1$, with Z = 4 for the formula

unit, $C_{30}\,H_{54}\,Cu_{1.88}O_{12}Pd_{1.12}$. Non-hydrogen atoms were refined anisotropically. Hydrogen atoms were placed in geometrically calculated positions with $U_{iso} = 1.5U_{equiv}$ of the parent. Three t-butyl groups were each disordered over two positions. The relative occupancy of each pair of positions was freely refined, with constraints or restraints on the anisotropic displacement parameters of the disordered carbon atoms. Additionally, each metal site was found to be mixture of Cu and Pd. The relative occupancy of the metal atom at each site was freely refined, converging at a total of roughly two Cu and one Pd for the molecule as a whole. Constraints were used on the anisotropic displacement parameters of the metal atoms. The final anisotropic full-matrix least-squares refinement on F^2 with 458 variables converged at R1 = 6.71%, for the observed data and wR2 = 12.76% for all data. The goodness-of-fit was 1.156. The largest peak in the final difference electron density synthesis was 1.158 $e^-/Å^3$ and the largest hole was -1.187 $e^-/Å^3$ with an RMS deviation of 0.148 $e^-/Å^3$. On the basis of the final model, the calculated density was 1.452 g/cm^3 and F(000), 1744 e - .

Table H5. Crystallographic details for $PdCu_2(\mu\text{-}OPiv)_6$

CCDC number	2114500
Formula	$C_{30}H_{54}Cu_{1.88}O_{12}Pd_{1.12}$

FW (g/mol)	845.14
Temp (K)	100(2)
Size (mm)	0.071 x 0.132 x 0.212
Crystal habit	Blue-yellow plate
Crystal system	Orthorhombic
Space group	P $2_12_12_1$
A (Å)	10.2449(10)
B (Å)	16.7783(15)
C (Å)	22.486(2)
α (°)	90
β (°)	90
γ (°)	90
Volume ($Å^3$)	3865
Z	4
Density (g/cm^3)	1.452
μ (mm^{-1})	1.593
F(000)	1744
ϑ range (°)	2.18 to 28.31
Index ranges	$-13 \leq h \leq 11$ $-22 \leq k \leq 21$ $-30 \leq l \leq 30$
Data / restraints / parameters	9617 / 36 / 458

GOF on F^2	1.156
R1 ($I>2\sigma(I)$)	0.0671
WR_2 (all data)	0.1276

Table H6. Bond lengths (Å) for $PdCu_2(\mu\text{-}OPiv)_6$.

Cu1-O9	1.906(10)	Cu1-O5	1.955(10)
Cu1-O1	1.956(10)	Cu1-O3	1.980(10)
Cu1-Cu3	3.029(7)	Cu2-O7	1.932(8)
Cu2-O4	1.940(9)	Cu2-O2	1.952(8)
Cu2-O11	1.963(8)	Cu2-Cu3	2.977(12)
Cu3-O10	1.938(11)	Cu3-O6	1.972(11)
Cu3-O8	1.976(10)	Cu3-O12	1.996(11)
Pd1-O3	1.931(10)	Pd1-O1	1.943(10)
Pd1-O5	1.979(9)	Pd1-O9	1.998(9)
Pd1-Pd3	3.065(5)	Pd1-Pd2	3.127(6)
Pd2-O4	1.902(11)	Pd2-O11	1.930(11)
Pd2-O2	1.943(11)	Pd2-O7	1.956(10)
Pd2-Pd3	3.233(13)	Pd3-O6	1.939(9)
Pd3-O10	1.950(10)	Pd3-O8	1.963(9)
Pd3-O12	1.968(10)	O1-C1	1.263(14)

O2-C1	1.269(12)	O3-C6	1.271(14)
O4-C6	1.253(13)	O5-C11	1.269(11)
O6-C11	1.266(11)	O7-C16	1.271(11)
O8-C16	1.260(13)	O9-C21	1.266(11)
O10-C21	1.278(11)	O11-C26	1.253(12)
O12-C26	1.245(12)	C1-C2	1.534(14)
C2-C4	1.532(15)	C2-C5	1.543(14)
C2-C3	1.543(13)	C3-H3A	0.98
C3-H3B	0.98	C3-H3C	0.98
C4-H4A	0.98	C4-H4B	0.98
C4-H4C	0.98	C5-H5A	0.98
C5-H5B	0.98	C5-H5C	0.98
C6-C7	1.539(16)	C7-C8A	1.42(4)
C7-C10	1.42(3)	C7-C9A	1.49(3)
C7-C9	1.55(3)	C7-C8	1.57(3)
C7-C10A	1.65(4)	C11-C12	1.530(12)
C12-C15	1.513(15)	C12-C13	1.526(16)
C12-C14	1.527(14)	C13-H13A	0.98
C13-H13B	0.98	C13-H13C	0.98
C14-H14A	0.98	C14-H14B	0.98
C14-H14C	0.98	C15-H15A	0.98
C15-H15B	0.98	C15-H15C	0.98
C16-C17	1.504(14)	C17-C20	1.524(15)

C17-C18	1.526(16)	C17-C19	1.545(14)
C18-H18A	0.98	C18-H18B	0.98
C18-H18C	0.98	C19-H19A	0.98
C19-H19B	0.98	C19-H19C	0.98
C20-H20A	0.98	C20-H20B	0.98
C20-H20C	0.98	C21-C22	1.513(13)
C22-C23A	1.52(3)	C22-C23	1.53(3)
C22-C25	1.53(3)	C22-C24A	1.54(3)
C22-C25A	1.54(3)	C22-C24	1.54(2)
C26-C27	1.522(14)	C27-C30	1.45(3)
C27-C29A	1.47(3)	C27-C28A	1.52(3)
C27-C29	1.53(3)	C27-C28	1.56(3)
C27-C30A	1.61(3)	C8-H8A	0.98
C8-H8B	0.98	C8-H8C	0.98
C9-H9A	0.98	C9-H9B	0.98
C9-H9C	0.98	C10-H10A	0.98
C10-H10B	0.98	C10-H10C	0.98
C23-H23A	0.98	C23-H23B	0.98
C23-H23C	0.98	C24-H24A	0.98
C24-H24B	0.98	C24-H24C	0.98
C25-H25A	0.98	C25-H25B	0.98
C25-H25C	0.98	C28-H28A	0.98
C28-H28B	0.98	C28-H28C	0.98

C29-H29A	0.98	C29-H29B	0.98
C29-H29C	0.98	C30-H30A	0.98
C30-H30B	0.98	C30-H30C	0.98
C8A-H8AA	0.98	C8A-H8AB	0.98
C8A-H8AC	0.98	C9A-H9AA	0.98
C9A-H9AB	0.98	C9A-H9AC	0.98
C10A-H10D	0.98	C10A-H10E	0.98
C10A-H10F	0.98	C23A-H23D	0.98
C23A-H23E	0.98	C23A-H23F	0.98
C24A-H24D	0.98	C24A-H24E	0.98
C24A-H24F	0.98	C25A-H25D	0.98
C25A-H25E	0.98	C25A-H25F	0.98
C28A-H28D	0.98	C28A-H28E	0.98
C28A-H28F	0.98	C29A-H29D	0.98
C29A-H29E	0.98	C29A-H29F	0.98
C30A-H30D	0.98	C30A-H30E	0.98
C30A-H30F	0.98		

Table H7. Bond angles (°) for $PdCu_2(\mu\text{-}OPiv)_6$.

O9-Cu1-O5	93.7(4)	O9-Cu1-O1	87.0(4)
O5-Cu1-O1	179.2(5)	O9-Cu1-O3	165.3(5)
O5-Cu1-O3	85.6(4)	O1-Cu1-O3	93.8(5)

O9-Cu1-Cu3	75.4(4)	O5-Cu1-Cu3	77.2(3)
O1-Cu1-Cu3	102.6(3)	O3-Cu1-Cu3	118.6(3)
O7-Cu2-O4	170.2(4)	O7-Cu2-O2	86.8(3)
O4-Cu2-O2	93.9(4)	O7-Cu2-O11	90.4(4)
O4-Cu2-O11	85.6(4)	O2-Cu2-O11	160.0(4)
O7-Cu2-Cu3	78.5(3)	O4-Cu2-Cu3	109.2(4)
O2-Cu2-Cu3	121.8(3)	O11-Cu2-Cu3	76.8(3)
O10-Cu3-O6	92.5(5)	O10-Cu3-O8	88.0(4)
O6-Cu3-O8	156.9(4)	O10-Cu3-O12	169.6(5)
O6-Cu3-O12	85.2(4)	O8-Cu3-O12	90.2(5)
O10-Cu3-Cu2	111.1(4)	O6-Cu3-Cu2	124.8(4)
O8-Cu3-Cu2	76.0(3)	O12-Cu3-Cu2	78.3(3)
O10-Cu3-Cu1	77.6(3)	O6-Cu3-Cu1	75.4(3)
O8-Cu3-Cu1	127.0(4)	O12-Cu3-Cu1	111.5(4)
Cu2-Cu3-Cu1	63.16(19)	O3-Pd1-O1	95.8(4)
O3-Pd1-O5	86.3(4)	O1-Pd1-O5	172.0(4)
O3-Pd1-O9	157.6(4)	O1-Pd1-O9	84.9(4)
O5-Pd1-O9	90.2(4)	O3-Pd1-Pd3	124.9(3)
O1-Pd1-Pd3	106.8(3)	O5-Pd1-Pd3	78.0(3)
O9-Pd1-Pd3	75.6(3)	O3-Pd1-Pd2	74.9(3)
O1-Pd1-Pd2	77.0(3)	O5-Pd1-Pd2	111.0(3)
O9-Pd1-Pd2	126.6(3)	Pd3-Pd1-Pd2	62.9(3)
O4-Pd2-O11	87.6(5)	O4-Pd2-O2	95.4(5)

O11-Pd2-O2	168.7(5)	O4-Pd2-O7	178.2(6)
O11-Pd2-O7	90.7(5)	O2-Pd2-O7	86.3(4)
O4-Pd2-Pd1	74.3(4)	O11-Pd2-Pd1	118.1(4)
O2-Pd2-Pd1	73.2(3)	O7-Pd2-Pd1	106.6(3)
O4-Pd2-Pd3	105.3(4)	O11-Pd2-Pd3	72.3(3)
O2-Pd2-Pd3	117.1(4)	O7-Pd2-Pd3	74.2(3)
Pd1-Pd2-Pd3	57.60(14)	O6-Pd3-O10	93.1(4)
O6-Pd3-O8	164.8(3)	O10-Pd3-O8	88.0(4)
O6-Pd3-O12	86.9(3)	O10-Pd3-O12	177.5(4)
O8-Pd3-O12	91.4(4)	O6-Pd3-Pd1	74.4(3)
O10-Pd3-Pd1	76.0(3)	O8-Pd3-Pd1	120.5(3)
O12-Pd3-Pd1	106.4(3)	O6-Pd3-Pd2	121.2(3)
O10-Pd3-Pd2	107.6(3)	O8-Pd3-Pd2	72.6(3)
O12-Pd3-Pd2	74.6(3)	Pd1-Pd3-Pd2	59.5(2)
C1-O1-Pd1	125.0(7)	C1-O1-Cu1	129.1(7)
C1-O2-Pd2	127.4(7)	C1-O2-Cu2	122.8(7)
C6-O3-Pd1	125.7(7)	C6-O3-Cu1	129.6(7)
C6-O4-Pd2	128.1(8)	C6-O4-Cu2	125.0(7)
C11-O5-Cu1	124.3(6)	C11-O5-Pd1	123.6(6)
C11-O6-Pd3	130.1(6)	C11-O6-Cu3	126.4(6)
C16-O7-Cu2	124.6(7)	C16-O7-Pd2	127.0(7)
C16-O8-Pd3	132.0(6)	C16-O8-Cu3	128.0(6)
C21-O9-Cu1	127.8(6)	C21-O9-Pd1	124.2(6)

C21-O10-Cu3	124.0(7)	C21-O10-Pd3	126.1(7)
C26-O11-Pd2	130.0(7)	C26-O11-Cu2	125.7(7)
C26-O12-Pd3	125.3(7)	C26-O12-Cu3	122.6(7)
O1-C1-O2	125.5(10)	O1-C1-C2	117.8(9)
O2-C1-C2	116.6(10)	C4-C2-C1	110.2(9)
C4-C2-C5	110.9(8)	C1-C2-C5	110.7(9)
C4-C2-C3	110.1(9)	C1-C2-C3	104.6(7)
C5-C2-C3	110.2(9)	C2-C3-H3A	109.5
C2-C3-H3B	109.5	H3A-C3-H3B	109.5
C2-C3-H3C	109.5	H3A-C3-H3C	109.5
H3B-C3-H3C	109.5	C2-C4-H4A	109.5
C2-C4-H4B	109.5	H4A-C4-H4B	109.5
C2-C4-H4C	109.5	H4A-C4-H4C	109.5
H4B-C4-H4C	109.5	C2-C5-H5A	109.5
C2-C5-H5B	109.5	H5A-C5-H5B	109.5
C2-C5-H5C	109.5	H5A-C5-H5C	109.5
H5B-C5-H5C	109.5	O4-C6-O3	125.1(10)
O4-C6-C7	117.4(11)	O3-C6-C7	117.2(10)
C8A-C7-C9A	116.(2)	C8A-C7-C6	108.5(16)
C10-C7-C6	112.1(14)	C9A-C7-C6	107.5(16)
C10-C7-C9	113.9(16)	C6-C7-C9	109.0(13)
C10-C7-C8	112.8(17)	C6-C7-C8	103.6(12)
C9-C7-C8	104.8(16)	C8A-C7-C10A	107.(2)

C9A-C7-C10A	109.(2)	C6-C7-C10A	108.4(14)
O6-C11-O5	124.2(8)	O6-C11-C12	119.0(8)
O5-C11-C12	116.7(8)	C15-C12-C13	110.5(10)
C15-C12-C14	109.1(10)	C13-C12-C14	110.8(10)
C15-C12-C11	110.2(8)	C13-C12-C11	110.5(9)
C14-C12-C11	105.7(8)	C12-C13-H13A	109.5
C12-C13-H13B	109.5	H13A-C13-H13B	109.5
C12-C13-H13C	109.5	H13A-C13-H13C	109.5
H13B-C13-H13C	109.5	C12-C14-H14A	109.5
C12-C14-H14B	109.5	H14A-C14-H14B	109.5
C12-C14-H14C	109.5	H14A-C14-H14C	109.5
H14B-C14-H14C	109.5	C12-C15-H15A	109.5
C12-C15-H15B	109.5	H15A-C15-H15B	109.5
C12-C15-H15C	109.5	H15A-C15-H15C	109.5
H15B-C15-H15C	109.5	O8-C16-O7	122.8(9)
O8-C16-C17	117.4(8)	O7-C16-C17	119.6(10)
C16-C17-C20	110.5(10)	C16-C17-C18	110.6(8)
C20-C17-C18	111.8(10)	C16-C17-C19	104.5(8)
C20-C17-C19	110.3(9)	C18-C17-C19	108.9(10)
C17-C18-H18A	109.5	C17-C18-H18B	109.5
H18A-C18-H18B	109.5	C17-C18-H18C	109.5
H18A-C18-H18C	109.5	H18B-C18-H18C	109.5
C17-C19-H19A	109.5	C17-C19-H19B	109.5

H19A-C19-H19B	109.5	C17-C19-H19C	109.5
H19A-C19-H19C	109.5	H19B-C19-H19C	109.5
C17-C20-H20A	109.5	C17-C20-H20B	109.5
H20A-C20-H20B	109.5	C17-C20-H20C	109.5
H20A-C20-H20C	109.5	H20B-C20-H20C	109.5
O9-C21-O10	124.5(9)	O9-C21-C22	119.0(9)
O10-C21-C22	116.6(8)	C21-C22-C23A	109.7(12)
C21-C22-C23	105.4(12)	C21-C22-C25	109.8(12)
C23-C22-C25	109.3(17)	C21-C22-C24A	105.7(11)
C23A-C22-C24A	113.0(18)	C21-C22-C25A	109.3(12)
C23A-C22-C25A	109.6(18)	C24A-C22-C25A	109.5(19)
C21-C22-C24	113.0(11)	C23-C22-C24	111.2(15)
C25-C22-C24	108.1(16)	O12-C26-O11	127.1(10)
O12-C26-C27	115.5(9)	O11-C26-C27	117.4(9)
C30-C27-C26	108.8(12)	C29A-C27-C26	109.6(13)
C29A-C27-C28A	113.0(17)	C26-C27-C28A	111.5(12)
C30-C27-C29	113.8(17)	C26-C27-C29	107.6(12)
C30-C27-C28	113.9(17)	C26-C27-C28	109.6(12)
C29-C27-C28	103.0(16)	C29A-C27-C30A	108.1(17)
C26-C27-C30A	106.9(12)	C28A-C27-C30A	107.6(17)
C7-C8-H8A	109.5	C7-C8-H8B	109.5
H8A-C8-H8B	109.5	C7-C8-H8C	109.5
H8A-C8-H8C	109.5	H8B-C8-H8C	109.5

C7-C9-H9A	109.5	C7-C9-H9B	109.5
H9A-C9-H9B	109.5	C7-C9-H9C	109.5
H9A-C9-H9C	109.5	H9B-C9-H9C	109.5
C7-C10-H10A	109.5	C7-C10-H10B	109.5
H10A-C10-H10B	109.5	C7-C10-H10C	109.5
H10A-C10-H10C	109.5	H10B-C10-H10C	109.5
C22-C23-H23A	109.5	C22-C23-H23B	109.5
H23A-C23-H23B	109.5	C22-C23-H23C	109.5
H23A-C23-H23C	109.5	H23B-C23-H23C	109.5
C22-C24-H24A	109.5	C22-C24-H24B	109.5
H24A-C24-H24B	109.5	C22-C24-H24C	109.5
H24A-C24-H24C	109.5	H24B-C24-H24C	109.5
C22-C25-H25A	109.5	C22-C25-H25B	109.5
H25A-C25-H25B	109.5	C22-C25-H25C	109.5
H25A-C25-H25C	109.5	H25B-C25-H25C	109.5
C27-C28-H28A	109.5	C27-C28-H28B	109.5
H28A-C28-H28B	109.5	C27-C28-H28C	109.5
H28A-C28-H28C	109.5	H28B-C28-H28C	109.5
C27-C29-H29A	109.5	C27-C29-H29B	109.5
H29A-C29-H29B	109.5	C27-C29-H29C	109.5
H29A-C29-H29C	109.5	H29B-C29-H29C	109.5
C27-C30-H30A	109.5	C27-C30-H30B	109.5
H30A-C30-H30B	109.5	C27-C30-H30C	109.5

H30A-C30-H30C	109.5	H30B-C30-H30C	109.5
C7-C8A-H8AA	109.5	C7-C8A-H8AB	109.5
H8AA-C8A-H8AB	109.5	C7-C8A-H8AC	109.5
H8AA-C8A-H8AC	109.5	H8AB-C8A-H8AC	109.5
C7-C9A-H9AA	109.5	C7-C9A-H9AB	109.5
H9AA-C9A-H9AB	109.5	C7-C9A-H9AC	109.5
H9AA-C9A-H9AC	109.5	H9AB-C9A-H9AC	109.5
C7-C10A-H10D	109.5	C7-C10A-H10E	109.5
H10D-C10A-H10E	109.5	C7-C10A-H10F	109.5
H10D-C10A-H10F	109.5	H10E-C10A-H10F	109.5
C22-C23A-H23D	109.5	C22-C23A-H23E	109.5
H23D-C23A-H23E	109.5	C22-C23A-H23F	109.5
H23D-C23A-H23F	109.5	H23E-C23A-H23F	109.5
C22-C24A-H24D	109.5	C22-C24A-H24E	109.5
H24D-C24A-H24E	109.5	C22-C24A-H24F	109.5
H24D-C24A-H24F	109.5	H24E-C24A-H24F	109.5
C22-C25A-H25D	109.5	C22-C25A-H25E	109.5
H25D-C25A-H25E	109.5	C22-C25A-H25F	109.5
H25D-C25A-H25F	109.5	H25E-C25A-H25F	109.5
C27-C28A-H28D	109.5	C27-C28A-H28E	109.5
H28D-C28A-H28E	109.5	C27-C28A-H28F	109.5
H28D-C28A-H28F	109.5	H28E-C28A-H28F	109.5
C27-C29A-H29D	109.5	C27-C29A-H29E	109.5

H29D-C29A-H29E	109.5	C27-C29A-H29F	109.5
H29D-C29A-H29F	109.5	H29E-C29A-H29F	109.5
C27-C30A-H30D	109.5	C27-C30A-H30E	109.5
H30D-C30A-H30E	109.5	C27-C30A-H30F	109.5
H30D-C30A-H30F	109.5	H30E-C30A-H30F	

Additional Computations and Remarks

To evaluate all possible ground-state species that may play the role of active catalyst, we calculated the free energies of 12 different combinations of Pd and Cu (Scheme H4). The reference state here is 3 Pd_1 + 3 Cu_1 + 2 C_2H_4 species. Note that all Cu(II) have single unpaired spins.

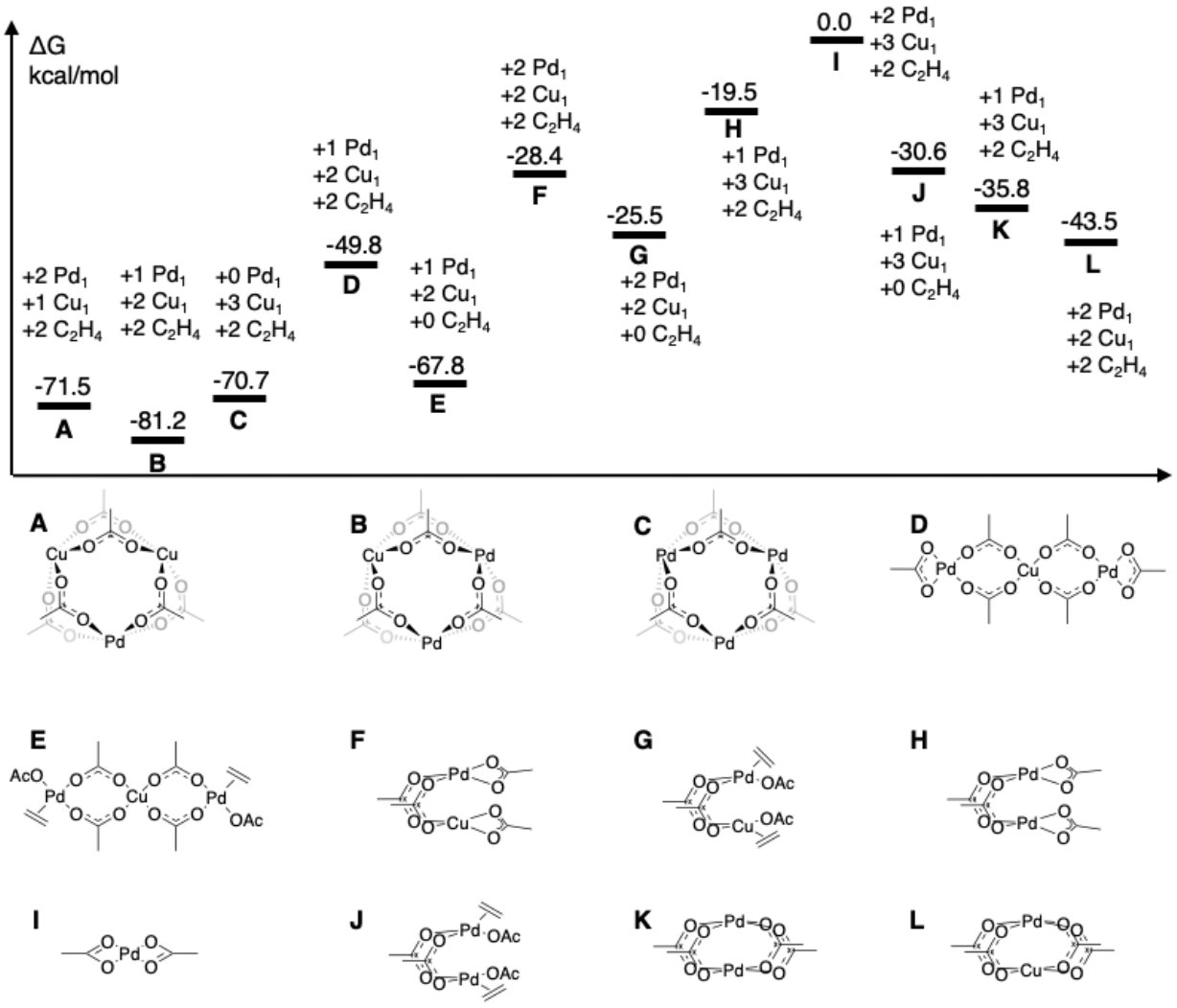

Scheme H4. DFT free energies at 423 K for different Pd, Cu, and mixed PdCu species.

In this study, there is still the question of the involved kinetics for formation of the active catalyst from the parent Pd and Cu species. While kinetics of speciation is difficult, especially with DFT, we outline a pathway below that explains how the active $PdCu_2$ catalyst is formed from Pd and Cu (Scheme H5). The pseudo-barrier ($p\Delta G^{\ddagger}$) to convert Pd_3 and Cu_3 to $PdCu_2$ is within the ballpark of the experimentally observed induction

period of ~1 hour. Given the variation in these free energies, we propose that the induction period is dominated by pure thermodynamic quantities as opposed to kinetic quantities (I.E. the induction period depends on intermediate state free energies rather than transition state barriers).

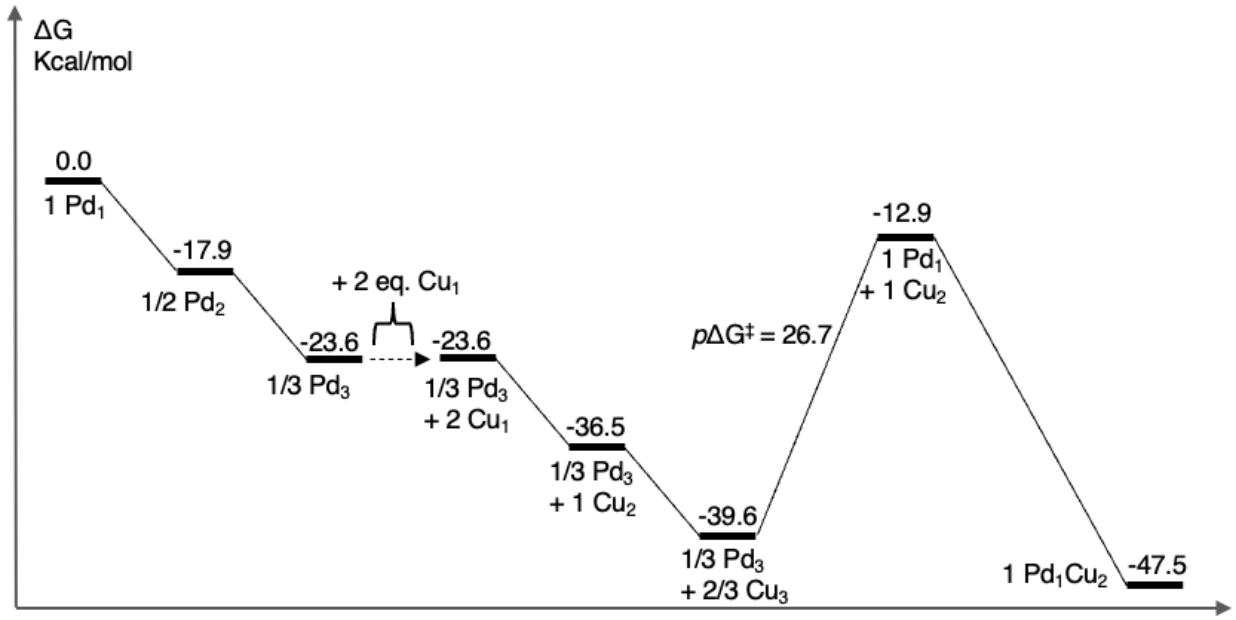

Scheme H5. DFT free energies for the pathway converting Pd and Cu to $PdCu_2$. $p\Delta G^{\ddagger}$ is the pseudo-barrier observed experimentally for the induction period of ~1 hour. Here the basis is 1 Pd_1 + 2 Cu_1 because we seek to find the pseudo-barrier for 1 equivalent of Pd_1Cu_2.

We state in the manuscript that despite the Pd_2Cu being lower in free energy, equilibrium is dominated by the $PdCu_2$ due to the excess Cu. Here we validate this statement. In experiment, Cu greatly outnumbers Pd, which drives equilibrium towards complexes rich

in Cu. Let's assume Pd_3 and Cu_3 can form either $PdCu_2$ or Pd_2Cu, with excess Cu taking the form Cu_3 (Reaction 1). Assuming a modest Pd:Cu ratio of 1:10 and an arbitrary basis of 10 Pd_3, we can solve for the reaction free energy (using values from Scheme 3 in the manuscript) as a function of $PdCu_2$, Pd_2Cu, and Cu_3. Let X, Y, and Z represent the number of $PdCu_2$, Pd_2Cu, and Cu_3 formed, respectively. From a simple mass balance, we can solve for $Y = 30 - X/2$ and $Z = (300 - 2X - Y)/3$. The reaction free energy as a function of X is shown in Figure H20.

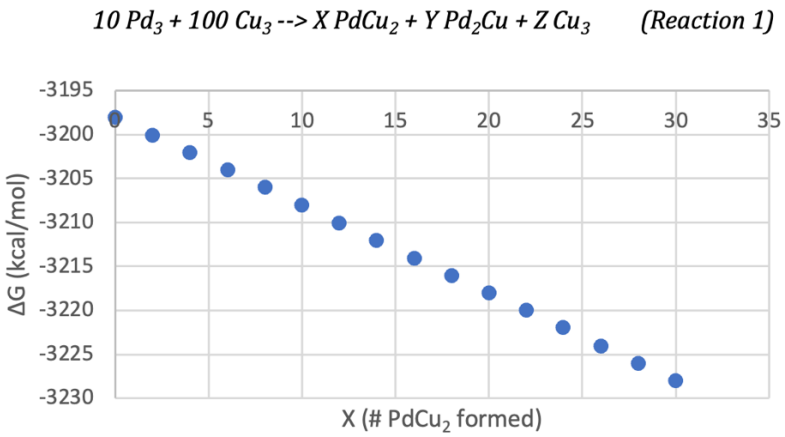

Figure H20. ΔG of reaction 1 as a function of X (# of $PdCu_2$ formed). According to the mass balance, Y = (30 - X)/2 and Z = (300 - 2X - Y)/3. Note that Y (# of Pd_2Cu formed) is proportional to -X, such that ΔG favors minimization of Pd_2Cu in order to maximize $PdCu_2$.

Unsurprisingly, the free energy is linear with X (# $PdCu_2$ formed), favoring formation of $PdCu_2$ over Pd_2Cu in excess Cu. Thus, we can expect that in experimental conditions, the equilibrium is dominated by $PdCu_2$, with tiny amounts of Pd_2Cu, PdCu.

It appears that the binding orientation of the OAc ligand also plays a role in stability of the mixed Pd/Cu complexes. For example, consider the two configurations of $Pd_2Cu(\mu\text{-}OAc)_6$ (**B** and **D**). When all 6 OAc ligands bridge the metal centers, the structure **B** is 9.8 kcal/mol above the baseline of complex **A**. However, when two OAc ligands become κ^2-bound to the Pd centers, the free energy increases significantly to 40.9 kcal/mol, resulting in 31.1 kcal/mol of destabilization for **D** relative to **B**. This result becomes obvious when one considers the significant strain induced by formation of κ^2 coordination to a metal center.

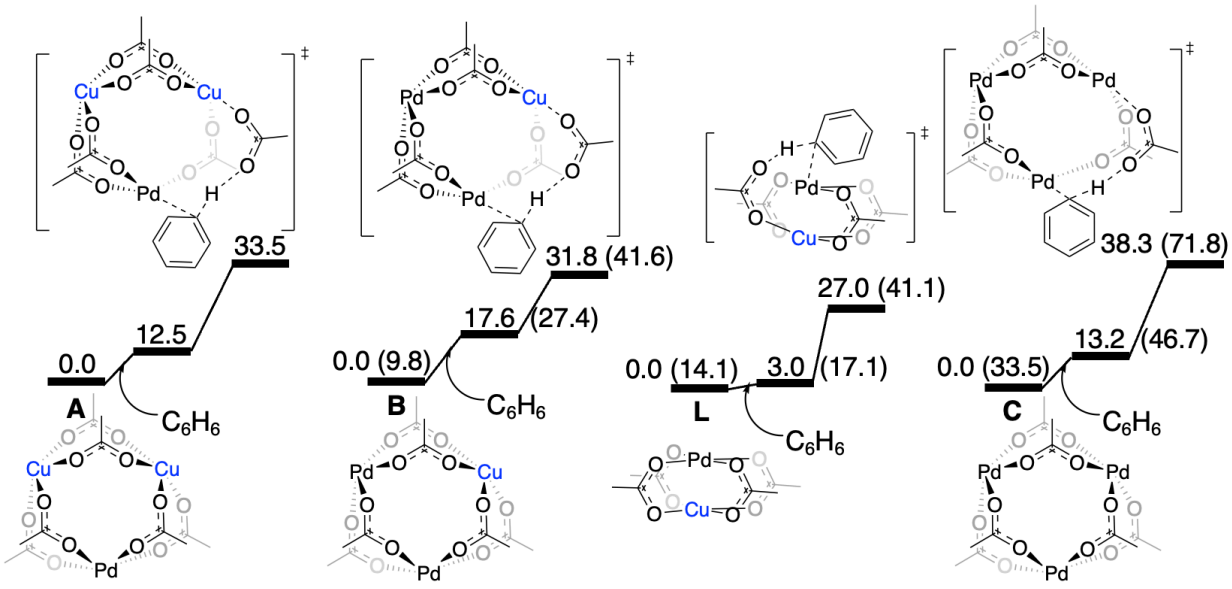

Scheme H6. DFT-free energies at 423 K for. Benzene coordination and Concerted Metalation Deprotonation for complexes **A**, **B**, **L**, and **C**. Values in parentheses are free energies relative to the ground state of **A**.

It is interesting to note that the lowest energy species, **A**, does not have the lowest CMD barrier; the lowest barrier (by 6.5 kcal/mol) instead belongs to **L**. Since the energy penalty for coordination of benzene to **L** is also substantially smaller, we presume some correlation between benzene coordination and the height of the overall CMD barrier. An interesting feature of **B** is that it can undergo two distinct CMD transition states. The 31.8 kcal/mol CMD transition state occurs when the OAc being protonated is bonded to the Cu(II) atom in the complex. Because there are two Pd atoms in this complex, the OAc being protonated can also be bonded to the other Pd, which results in a CMD barrier of 41.3 kcal/mol (see Supporting Information). This barrier, which involves only Pd centers, is significantly higher than its analog involving Pd and Cu, again showing that Cu(II) plays a key role in enabling facile C–H activation. Despite **B** having a slightly lower CMD barrier than **A**, complex **A** is 9.8 kcal/mol more stable than **B**. Thus, the majority of catalysis seems likely to occur from **A**.

References

1. Bruker (2012). *Saint; SADABS; APEX3*. Bruker AXS Inc., Madison, Wisconsin, USA.

2. Sheldrick, G. M. (2015). *Acta Cryst.* A**71**, 3-8.

3. Dolomanov, O. V.; Bourhis, L. J.; Gildea, R. J.; Howard, J. A. K.; Puschmann, H. *J. Appl. Cryst.* (2009). 42, 339-341.

Appendix I

Appendix for: Mechanistic Studies of Styrene Production from Benzene and Ethylene using $[(\eta^2\text{-}C_2H_4)_2Rh(\mu\text{-}OAc)]_2$ as Catalyst Precursor: Identification of a Multi-nuclear Bis-Rh^{I} Mono-Cu^{II} Complex as Catalyst

Reproduced with permission from:

W Zhu, N Coutard, JF Ellena, DA Dickie, TB Gunnoe, WA Goddard III

ACS Catalysis, **2021***, 11, 9, 5688 - 5702*

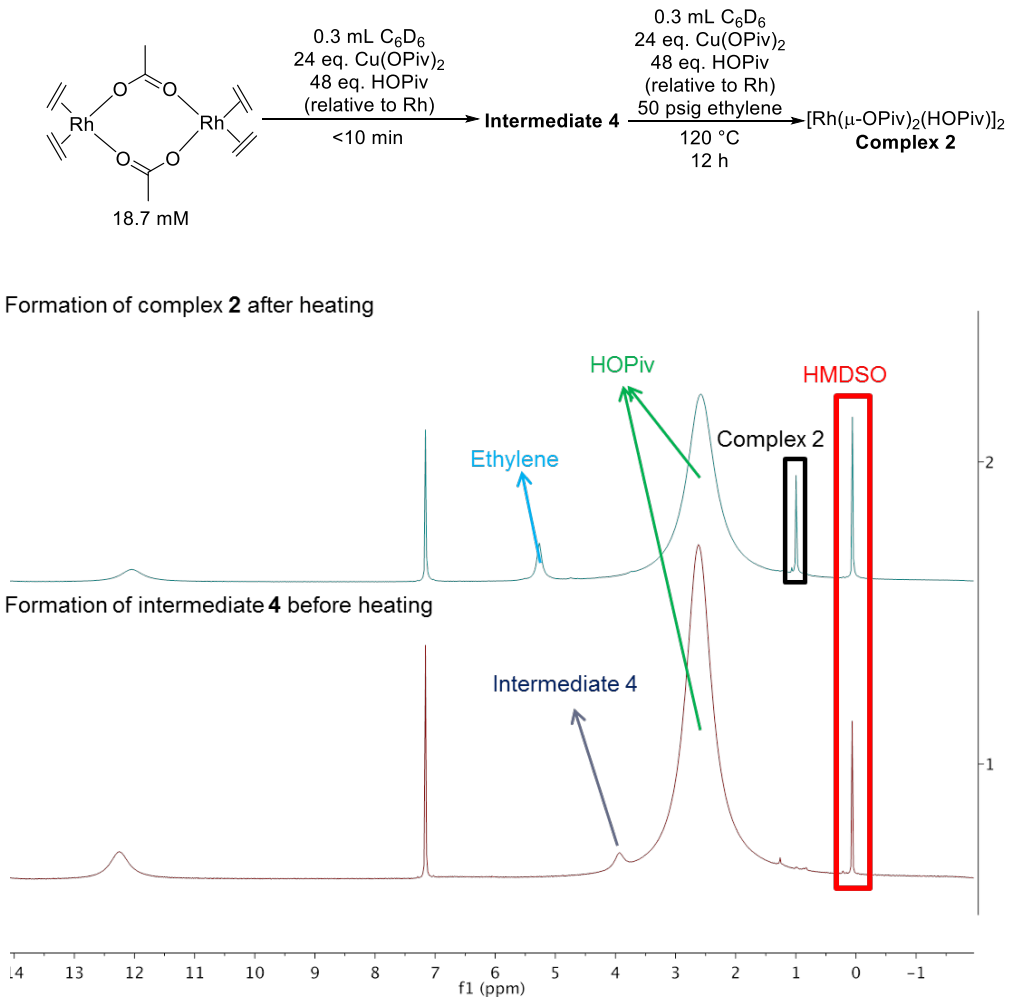

Figure I1. ^{1}H NMR spectra for conversion of $[(\eta^2\text{-}C_2H_4)_2Rh(\mu\text{-}OAc)]_2$ (**1**) to $[(\eta^2\text{-}C_2H_4)_2Rh^{I}(\mu\text{-}OPiv)_2]_2(\mu\text{-}Cu)$ (**4**) at room temperature and $[(HOPiv)Rh(\mu\text{-}OPiv)_2]_2$ (**2**) at 120 °C under 50 psig ethylene.

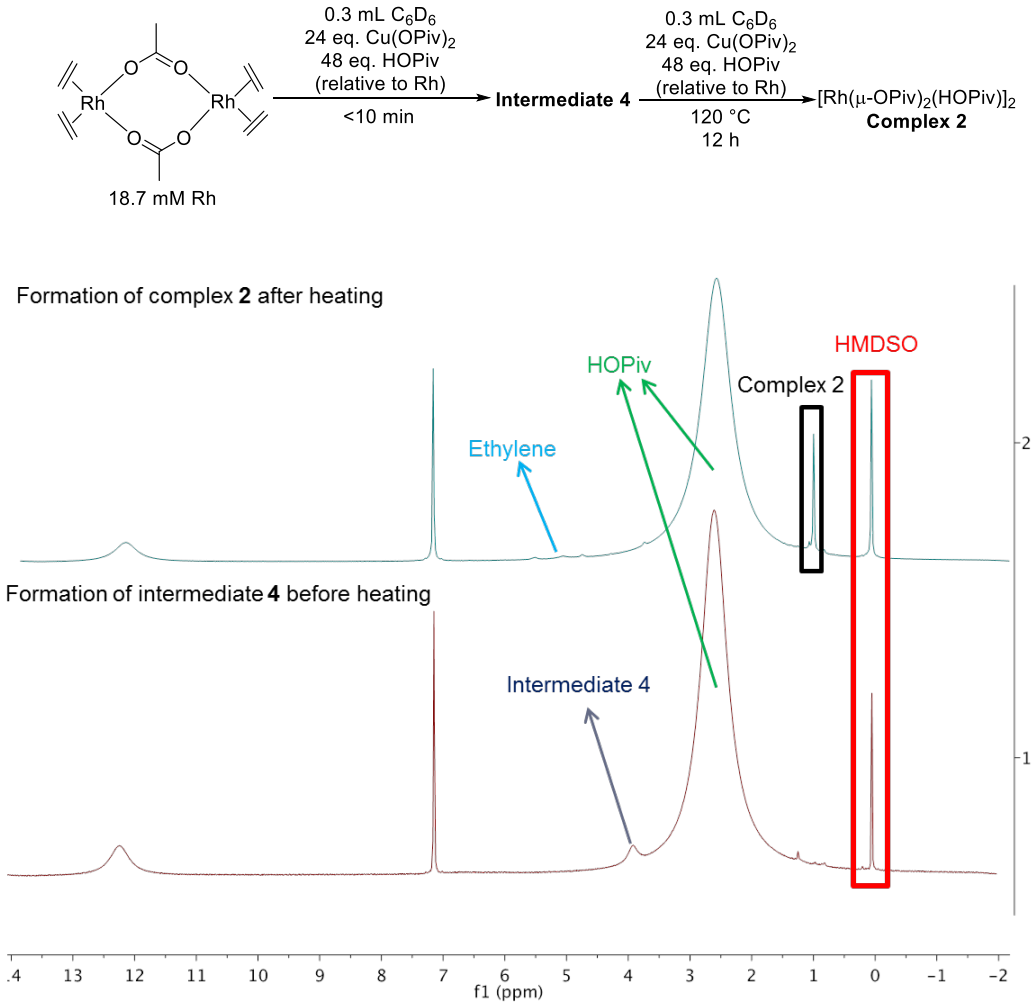

Figure I2. ^{1}H NMR spectra for conversion of $[(C_2H_4)_2Rh(\mu\text{-}OAc)]_2$ (**1**) to $[(\eta^2\text{-}C_2H_4)_2Rh^{I}(\mu\text{-}OPiv)_2]_2(\mu\text{-}Cu)$ (**4**) at room temperature and $[(HOPiv)Rh(\mu\text{-}OPiv)_2]_2$ (**2**) at 120 °C in the absence of ethylene.

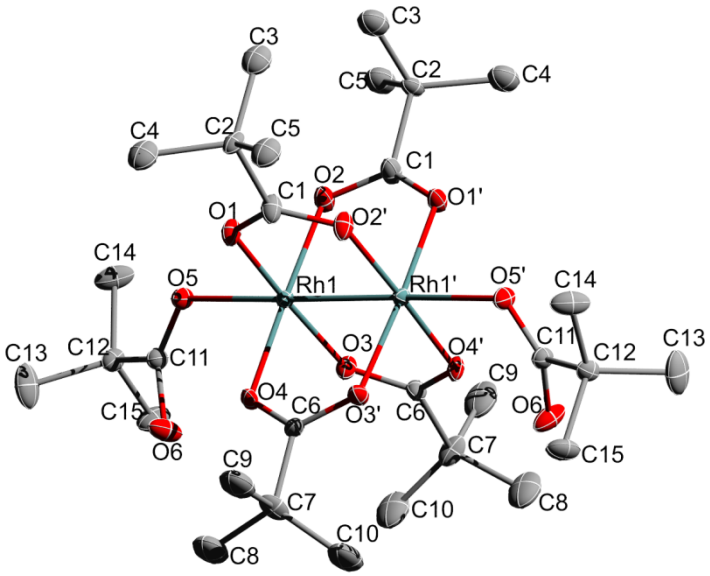

Figure I3. ORTEP of $[(HOPiv)Rh(\mu\text{-}OPiv)_2]_2$ (**2**) (50% probability). H atoms are omitted for clarity. Only the major position for the disordered atoms is shown. For the structure of complex **2**, only the major position for the disordered pivalate ligands is shown.

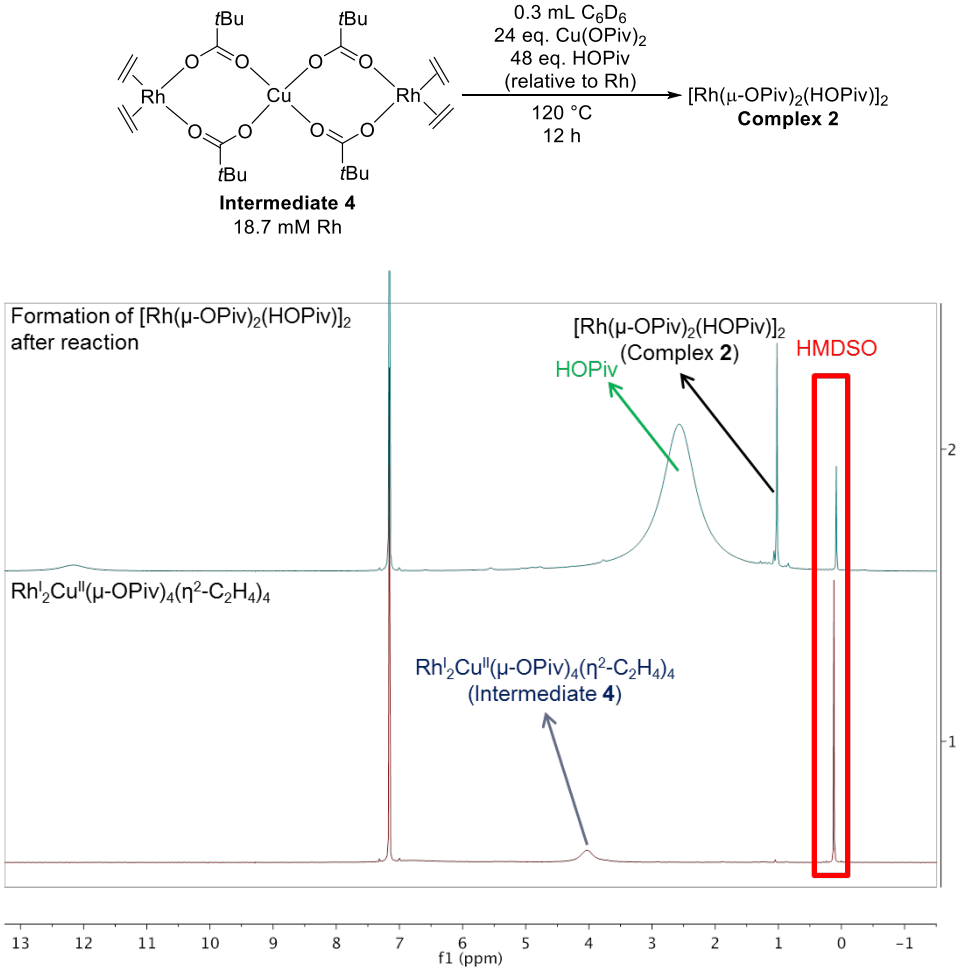

Figure I4. ^{1}H NMR spectra for conversion of $[(\eta^2\text{-}C_2H_4)_2Rh^{I}(\mu\text{-}OPiv)_2]_2(\mu\text{-}Cu)$ (**4**) to $[(HOPiv)Rh(\mu\text{-}OPiv)_2]_2$ (**2**) at 120 °C after 12 hours.

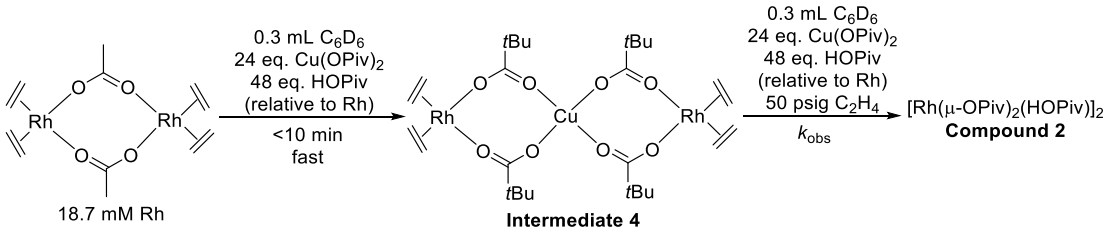
0.3 mL C6D6
24 eq. Cu(OPiv)2
48 eq. HOPiv
(relative to Rh)
<10 min
fast
0.3 mL C6D6
24 eq. Cu(OPiv)2
48 eq. HOPiv
(relative to Rh)
50 psig C2H4
kobs
[Rh(μ-OPiv)2(HOPiv)]2
Compound 2
18.7 mM Rh
Intermediate 4

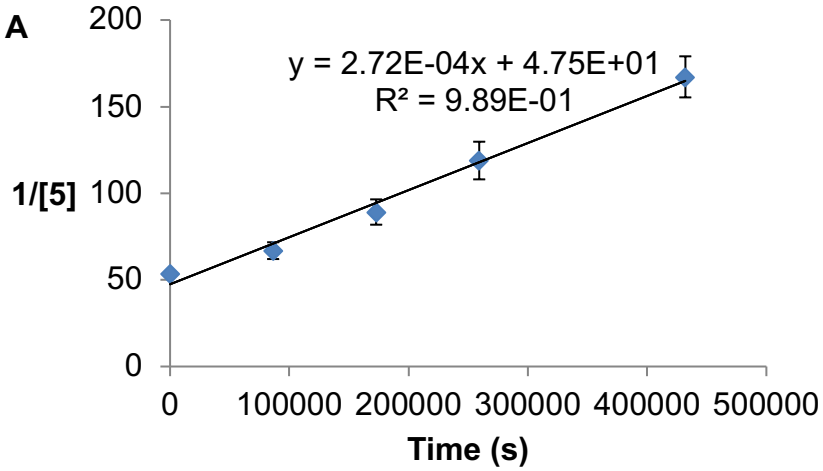
A
y = 2.72E-04x + 4.75E+01
R² = 9.89E-01
1/[5]
Time (s)

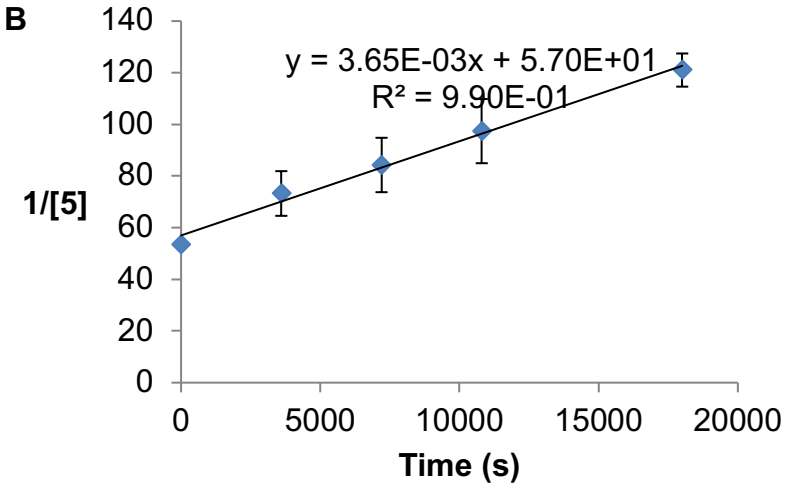
B
y = 3.65E-03x + 5.70E+01
R² = 9.90E-01
1/[5]
Time (s)

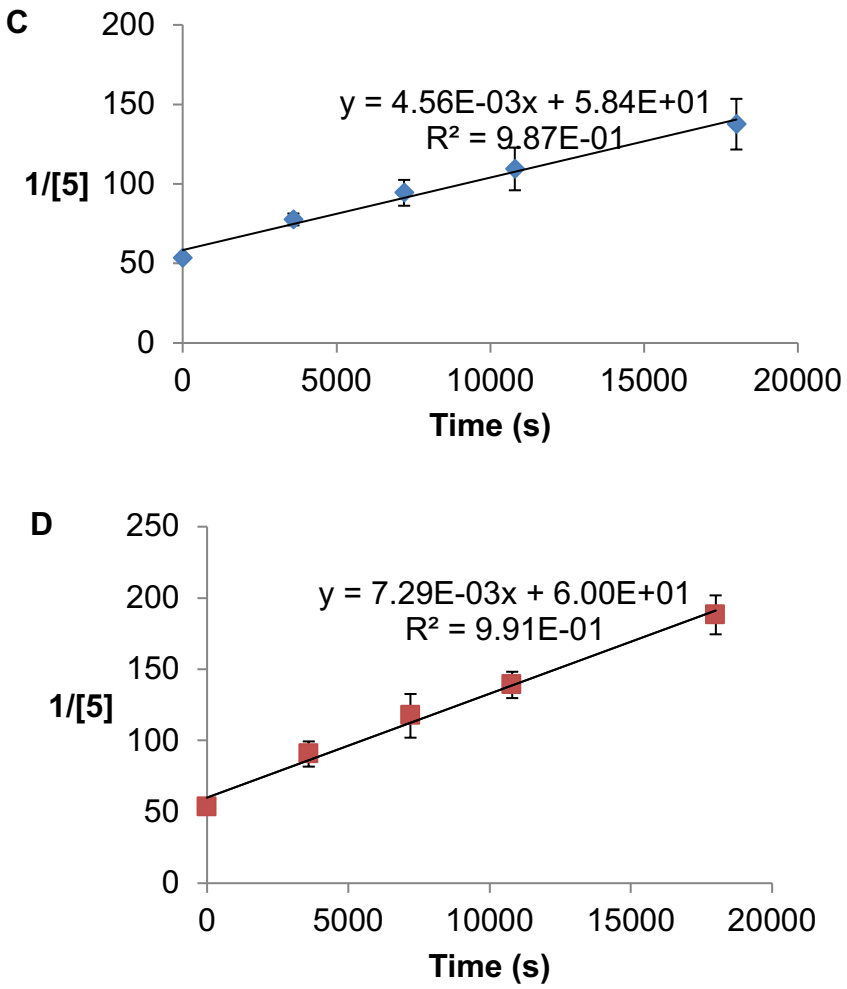

Figure I5. Kinetic plots for conversion of intermediate **5** to [(HOPiv)Rh(μ-OPiv)$_2$]$_2$ (**2**) at 21 (A), 45 (B), 50 (C), and 60 (D) °C under 50 psig ethylene. Decay of intermediate **5** is calculated based on the amount of formed [HOPiv)Rh(μ-OPiv)$_2$]$_2$ (**2**). Each data point is the average of three separate experiments. Error bars represent the standard deviations based on a minimum of three independent experiments.

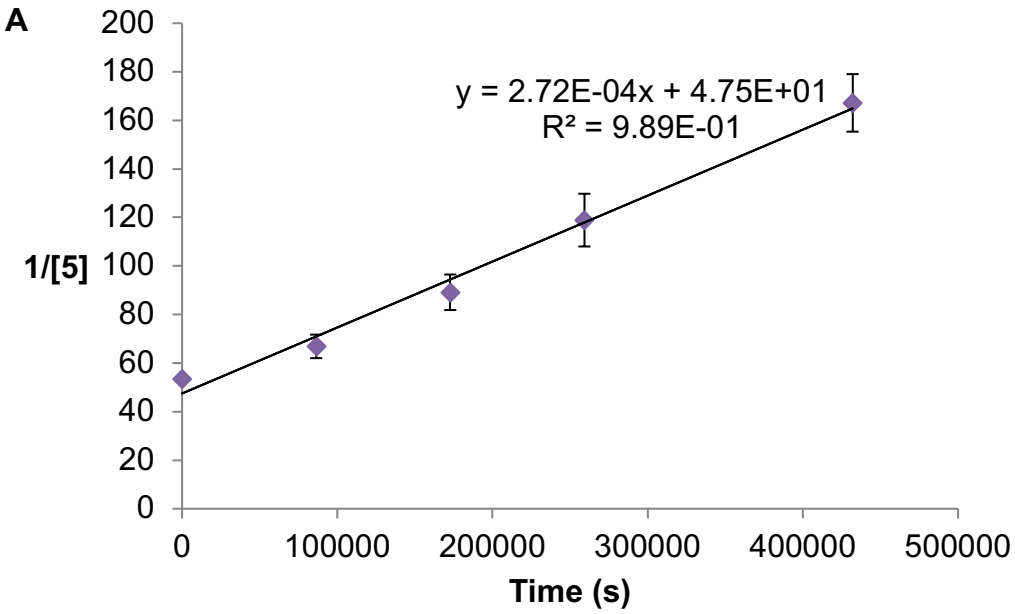
A
y = 2.72E-04x + 4.75E+01
R² = 9.89E-01
1/[5]
Time (s)
0
20
40
60
80
100
120
140
160
180
200
0
100000
200000
300000
400000
500000

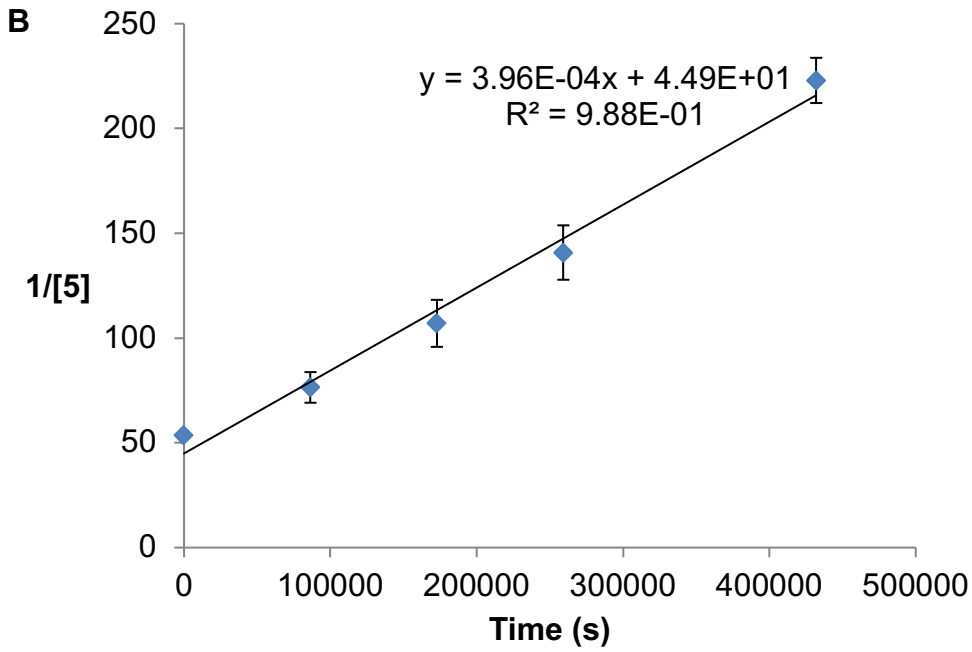
B
y = 3.96E-04x + 4.49E+01
R² = 9.88E-01
1/[5]
Time (s)
0
50
100
150
200
250
0
100000
200000
300000
400000
500000

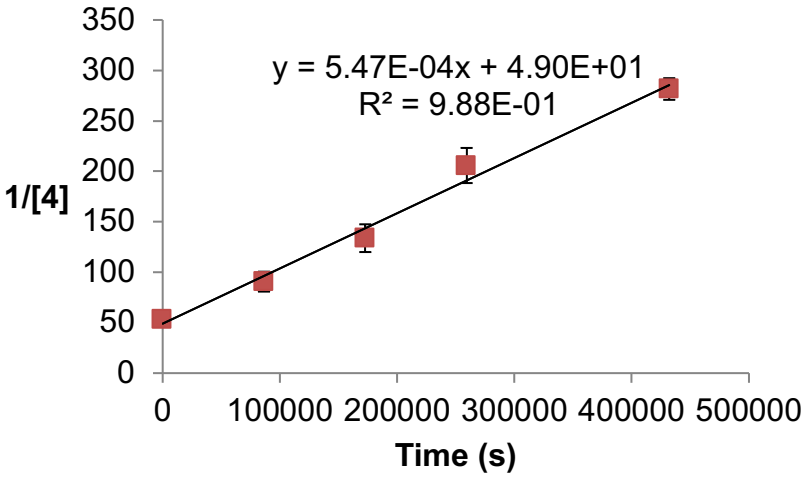
y = 5.47E-04x + 4.90E+01
R² = 9.88E-01
1/[4]
Time (s)
0
50
100
150
200
250
300
350
0
100000
200000
300000
400000
500000

C

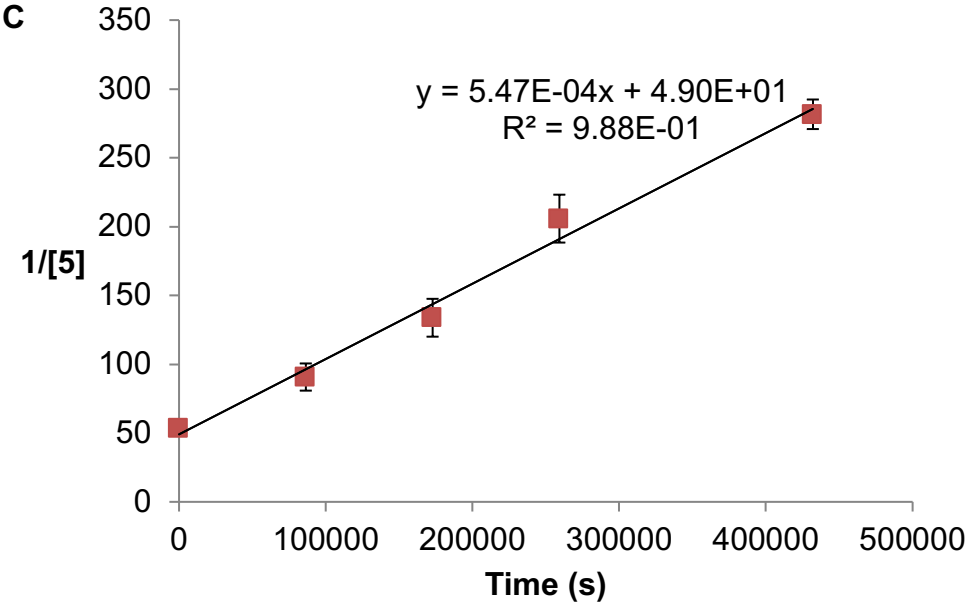
y = 5.47E-04x + 4.90E+01
R² = 9.88E-01
1/[5]
Time (s)
0
50
100
150
200
250
300
350
0
100000
200000
300000
400000
500000

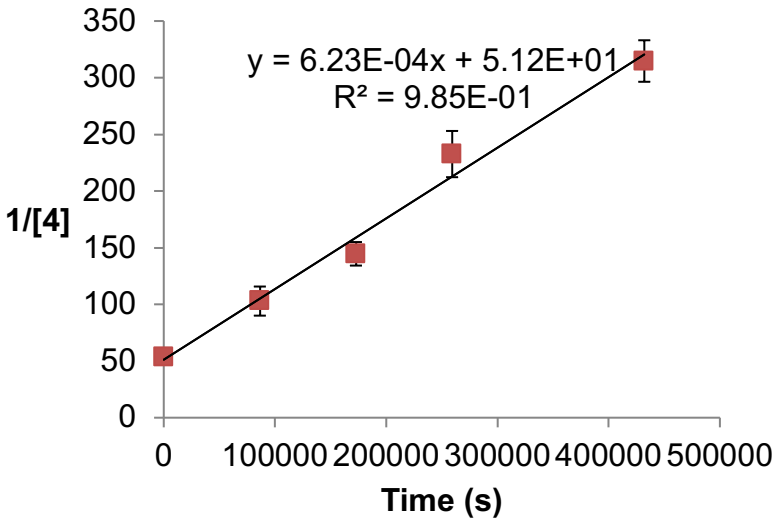

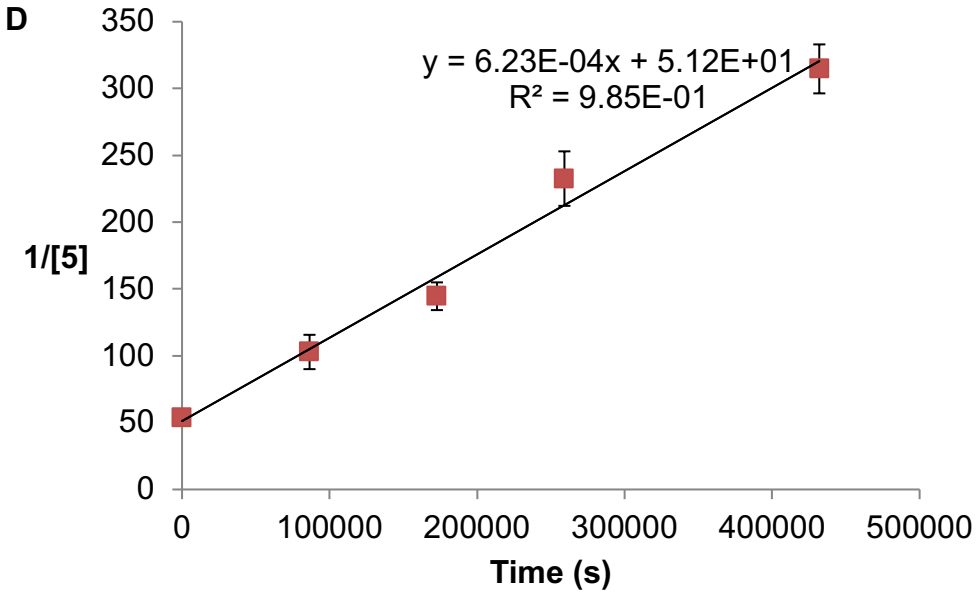

Figure I6. Kinetic plots for conversion of intermediate **5** to $[(HOPiv)Rh(\mu\text{-}OPiv)_2]_2$ (**2**) using 48 (A), 72 (B), 96 (C) or 120 (D) eq. of HOPiv (relative to Rh). Reaction conditions: 9.35 mM of $[(C_2H_4)_2Rh(\mu\text{-}OAc)]_2$ as starting material, 0.3 mL benzene-d_6, 24 eq. $Cu(OPiv)_2$ (relative to Rh), 50 psig ethylene, 21 °C. Decay of $[(\eta^2\text{-}C_2H_4)_2Rh^{I}(\mu\text{-}OPiv)_2]_2(\mu\text{-}Cu)$ (**4**) is calculated based on the amount of formed intermediate **5**. Each data point is the average of three separate experiments. Error bars represent the standard deviations based on a minimum of three independent experiments.

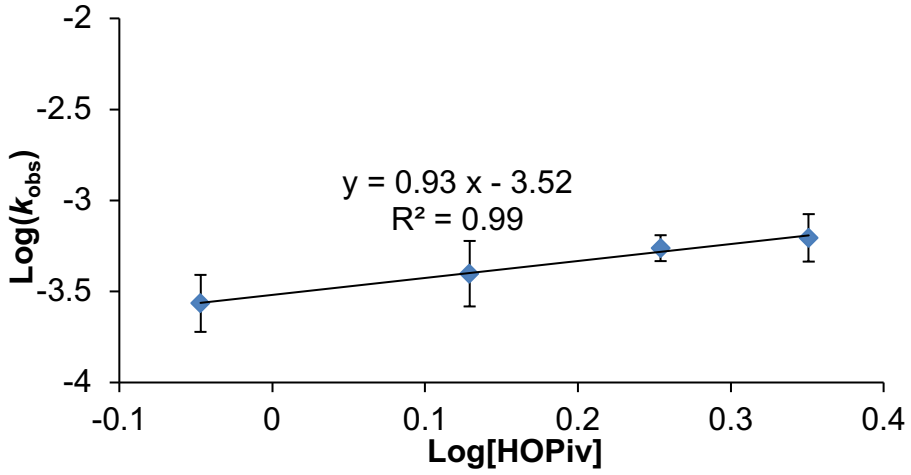

Figure I7. Log–log plot of observed rate constants (k_{obs}) for conversion of intermediate **5** to $[(HOPiv)Rh(\mu\text{-}OPiv)_2]_2$ (**2**) versus concentration of HOPiv. Reaction conditions: 9.35 mM of $[(C_2H_4)_2Rh(\boxtimes\text{-}OAc)]_2$ as starting material, 0.3 mL benzene-d_6, 24 eq. $Cu(OPiv)_2$ (relative to Rh), 48 (A), 72 (B), 96 (C) or 120 (D) eq. HOPiv (relative to Rh), 50 psig ethylene, 21 °C. Each data point is the average of three separate experiments. Error bars represent the standard deviations based on a minimum of three independent experiments.

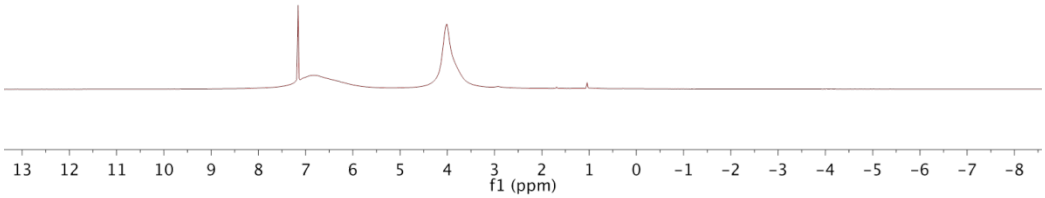

Figure I8. Paramagnetic ^{1}H NMR spectrum of $[(\eta^2\text{-}C_2H_4)_2Rh^{I}(\mu\text{-}OPiv)_2]_2(\mu\text{-}Cu)$ (**4**) (800 MHz, benzene-d_6).

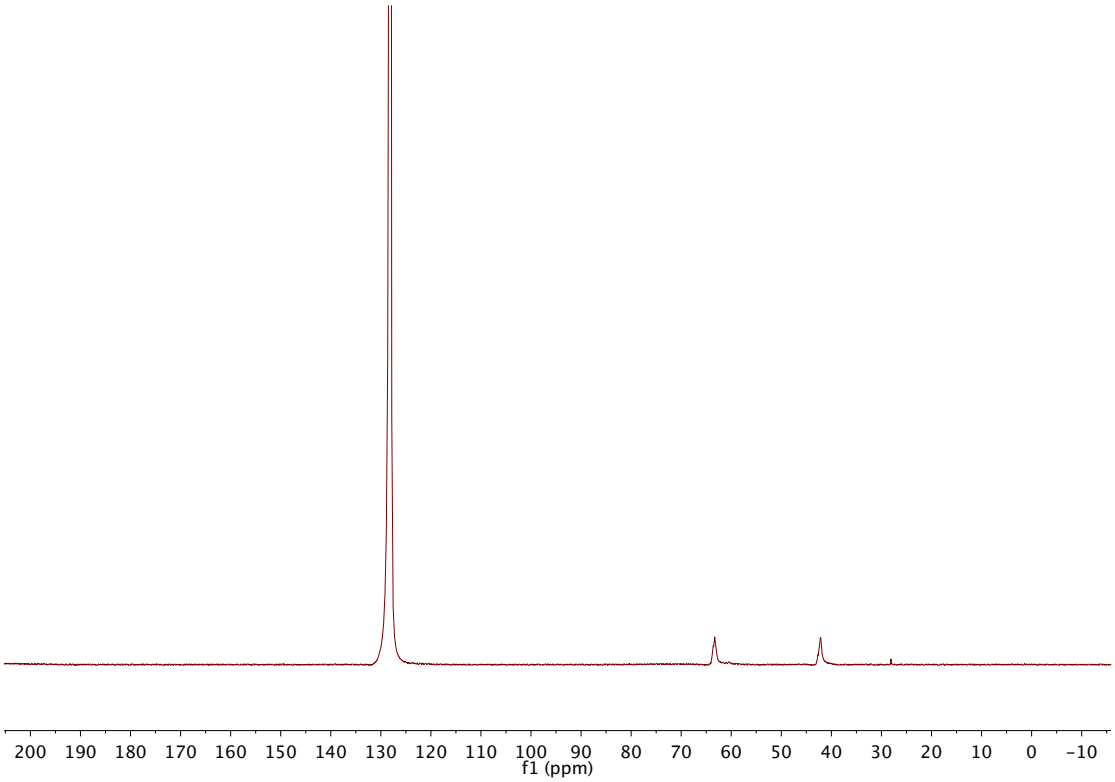

Figure I9. Paramagnetic ^{13}C NMR spectrum of $[(\eta^2\text{-}C_2H_4)_2Rh^{I}(\mu\text{-}OPiv)_2]_2(\mu\text{-}Cu)$ (**4**) (201 MHz,

benzene-d_6).

Dependence of R_1 on concentration for $[(\eta^2\text{-}C_2H_4)_2Rh^I(\mu\text{-}OPiv)_2]_2(\mu\text{-}Cu)$ (4)

In Figure I10, the spin-lattice relaxation rate of the ethylene protons (~4.0 ppm in the ^{1}H NMR spectrum) of a solution $[(\eta^2\text{-}C_2H_4)_2Rh^I(\mu\text{-}OPiv)_2]_2(\mu\text{-}Cu)$ (**4**) in benzene-d_6 is plotted as a function of relative concentration, obtained by dilution of an initial solution with further benzene-d_6. The intercept of this plot at 0 concentration (141 ± 7 s^{-1}) gives us the purely intramolecular spin lattice relaxation rate for these protons. Since the slope is small, meaning a weak dependence on concentration, we conclude that most or all of the spin lattice relaxation observed occurs from an intramolecular phenomenon, indicative that the paramagnetic center (Cu^{II}) and ethylene protons belong to the same molecule, supporting the persistence of **4** in solution.

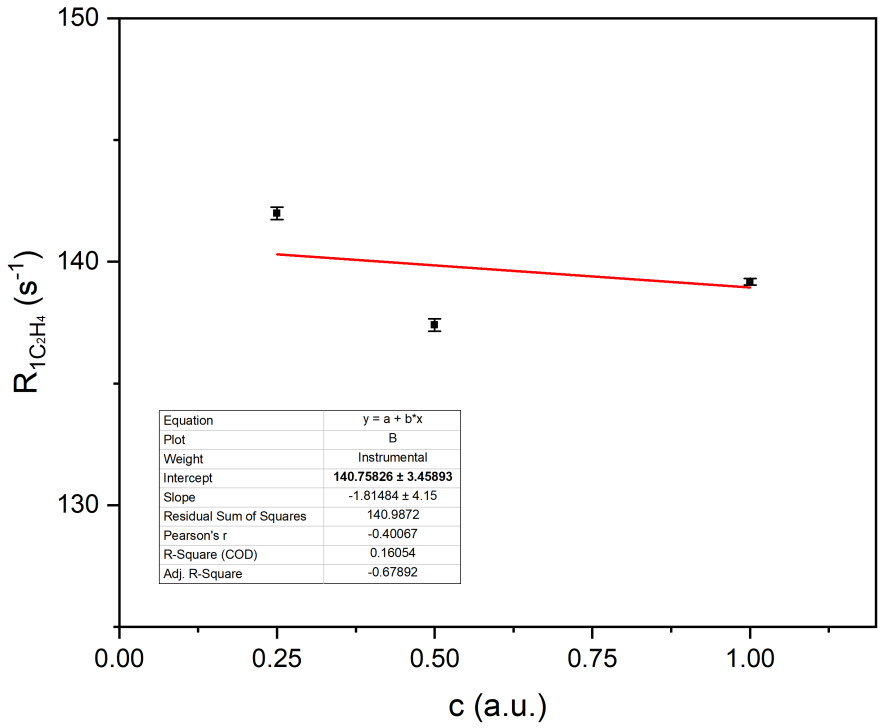

Figure I10. Plot of the spin-lattice relaxation rate (R1) of $[(\eta^2\text{-}C_2H_4)_2Rh^I(\mu\text{-}OPiv)_2]_2(\mu\text{-}Cu)$ (**4**) as a function of concentration.

Experimental determination of the average C_2H_4–Cu distance of $[(\eta^2\text{-}C_2H_4)_2Rh^I(\mu\text{-}OPiv)_2]_2(\mu\text{-}Cu)$ (4) using R_1

Although not essential to prove the existence of complex **4** in solution, equation (2) is a simplified Solomon-Bloembergen equation,[1] which allows us to estimate the distance between the unpaired electron on Cu and the ethylene protons of $[(\eta^2\text{-}C_2H_4)_2Rh^I(\mu\text{-}OPiv)_2]_2(\mu\text{-}Cu)$ (**4**) in dilute solution by measuring the ethylene proton spin-lattice relaxation rate (R_1). Although there are uncertainties that limit this method, we believe the assessment provides additional evidence for the existence of **4** in solution. We first needed to obtain the rotational correlation time of **4**. This was done by using the molecular

volume of **4** (828 $Å^3$) which was obtained from the crystal structure, then using the equation that relates the volume of a sphere to its radius. The radius of **4** is 5.83 Å from the solid-state X-ray structure. We used equation (1)[2] to obtain the rotational correlation time (τ_R) of **4** (1.22 x 10^{-10}s).

$$\tau_R = \frac{4\pi\eta r^3}{3k_B T} \quad (1)$$

η is the viscosity of benzene at 25 °C (0.604 cP), r = 5.83 Å (see above), k_B is Boltzmann's constant and T is the temperature.

R_1 of the ethylene protons was measured at three dilute concentrations. The dependence of R_1 on concentration was linear and the R_1 value at 0 concentration (141 s^{-1}) is due to intramolecular dipolar spin-lattice relaxation.[3] We then used equation (2) to calculate r, the average distance between the unpaired electron on Cu and the ethylene protons of **4** (6.05 Å).

$$r = 540\left(\left(\frac{3\tau_C}{1+\omega_I^2\tau_C^2} + \frac{7\tau_C}{1+\omega_S^2\tau_C^2}\right)/R_1\right)^{\frac{1}{6}} \quad (2)$$

where $\tau_C^{-1} = \tau_R^{-1} + \tau_{el}^{-1}$, τ_{el} is the electron spin-lattice relaxation time (1 x 10^{-9}s),[4, 5] ω_I is the proton Larmor frequency(3.77 x 10^9 rad/s), ω_S is the electron Larmor frequency (2.48 x 10^{12} rad/s) and the constant value (540) contains contributions from the electron spin quantum number, the proton magnetogyric ratio, the Bohr magneton, and the Lande g factor.

Average C_2H_4–Cu distance of complex 4 from the crystal structure and DFT

We compare the average distance between Cu and the ethylene protons

(C_2H_4-Cu) derived from spin-lattice relaxation in dilute solution with the average distance found in the original crystal structure and the structure predicted by DFT. Amongst the 16 ethylene protons, we find an average C_2H_4-Cu distance of 4.33 Å in the crystal structure. This average is composed of two separate averages consisting of short and long C_2H_4-Cu distances. The short and long C_2H_4-Cu averages are 3.58 and 5.08 Å, respectively. We concurrently evaluated the average C_2H_4-Cu distance using DFT. Similar to the crystal structure, we arrive at an average C_2H_4-Cu distance of 4.32 Å. The short and long C_2H_4-Cu averages predicted by DFT are 3.48 and 5.16 Å, respectively (Figure I11). The crystal structure and DFT structure are nearly identical based on the average C_2H_4-Cu distance. The DFT structure predicts the average ethylene C=C bond to be 1.39 Å and the average Rh–Cu distance to be 3.09 Å.

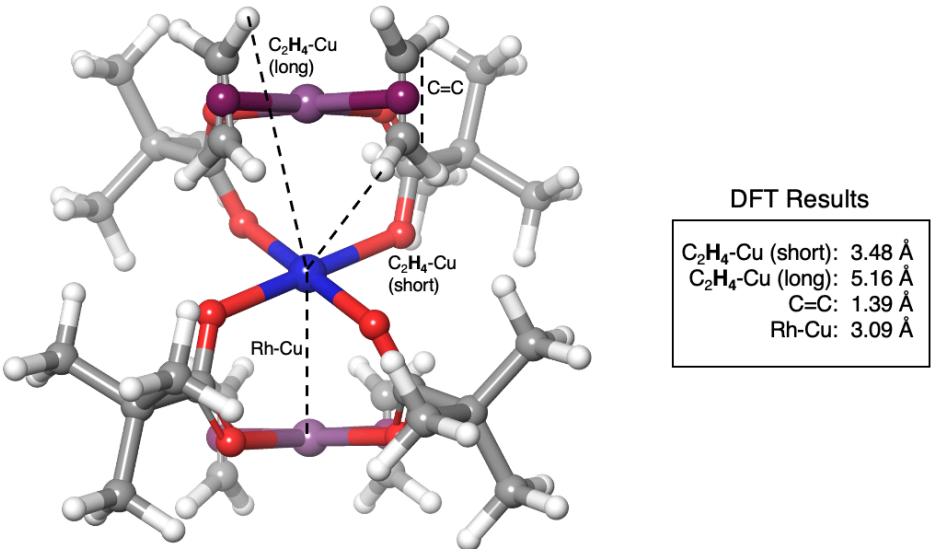

Figure I11. DFT average pair distances for the Rh-Cu-Rh trimer. The total C_2H_4-Cu average of 4.32 Å is composed of the long and short averages.

We also calculated Mulliken spin populations to determine if the unpaired spin on Cu(II) in complex **4** is delocalized. Spin populations reveal that with a net spin of +1.00, Cu(II) contains +0.64 unpaired spin density. The remaining +0.36 unpaired spin resides on the 4 oxygens bound to the Cu, such that each oxygen atom has a net unpaired spin of +0.09. This result indicates 36% spin delocalization in complex **4**.

Limitations to the Experimental determination of the average C_2H_4–Cu distance of $[(\eta^2\text{-}C_2H_4)_2Rh^I(\mu\text{-}OPiv)_2]_2(\mu\text{-}Cu)$ (4) using R_1

The limitations of this method, which likely prevent a highly accurate determination of the ethylene H and Cu distances include: 1) Uncertainty of the electron relaxation time. We have used previous estimates of electron relaxation time for Cu(II), but the 36% spin delocalization predicted by theory (see above) indicates that these previous estimates are likely not be reliable. 2) We have use the solid-state X-ray structure to measure complex **4**'s radius, but this value in solution is likely to be changed. 3) We have modeled solution structure using implicit solvent.

Computational Methods

All Density Functional Theory (DFT) calculations were performed using the Jaguar software version 10.9 by Schrodinger Inc.[6] Structure optimizations were

performed using the B3LYP[7] flavor of DFT including the Grimme-Becke-Johnson D3 correction for London dispersion.[8] Non-metal atoms were described by the triple-zeta 6-311G**++ basis set[9] while Rh and Cu were treated with the Los Alamos small-core (18 explicit electrons) effective core potential (LACV3P**++).[10, 11] Ultra-fine DFT grids were used for all calculations.

Vibrational frequency calculations at 423 K were performed at the B3LYP-D3 level and used to predict thermochemical properties including zero point energies, enthalpies as a function of temperature, and entropies as a function of temperature. These frequency calculations were also used to confirm local minima (no negative eigenvalues in Hessian) and transition states (1 negative eigenvalue in Hessian).

In such calculations there are 3 translational degrees of freedom (dof) and 3 rotational dof leading to large entropies, but in solvent these dof become hindered librational dof, reducing the entropy by 40 to 60 %. This becomes an issue for reactions that change the number of molecules. To account for this entropy loss, a correction is often applied to translational and rotational modes.[12] We assume in this paper a factor of 50%. This entropy correction is implemented via the following formula: $G = H - T*(0.5*(S_{tran}+S_{rot})+S_{vib}+S_{elec})$

All calculations included implicit solvent treatment. Solvent effects were implemented via the Poisson-Boltzmann finite element method (PBF).[13, 14] A

dielectric constant of 2.284 and a probe radius of 2.6 A were used to represent benzene.

DFT Structure Energies

Energies for the various structures at 423 K are listed in the following tables. The labels used here (1, 2, etc) for structures are defined in the manuscript. H is enthalpy, G is free energy, and S is total entropy.

Table I1. Energies at 423 K for the various structures from Scheme 5 in the manuscript. C_2H_4 is ethylene, HOAc is acetic acid, and C_6H_6 is benzene.

Structure	H (Hartree)	G (Hartree)	S (cal/mol/K)
2	-2298.798	-2298.925	376.559
4	-1643.7452	-1643.8312	255.328
1	-990.46403	-990.53251	203.193
5	-495.20742	-495.25016	126.812
6	-566.54466	-566.57988	104.518
7	-795.06909	-795.11385	132.804
$Cu(OAc)_2$	-653.21842	-653.25471	107.656
Cu(OAc)	-424.68808	-424.71598	82.798
C_2H_4	-78.560925	-78.580826	59.043

HOAc	-229.10325	-229.1287	75.502
C_6H_6	-232.20689	-232.23121	72.16

Table I2. Energies at 423 K for the various structures from Scheme 6 in the manuscript.

Structure	H (Hartree)	G (Hartree)	S (cal/mol/K)
4	-1643.7452	-1643.8312	255.328
4b	-1797.3616	-1797.4553	278.049
TS4.1	-1797.369	-1797.4436	221.214
4c	-1797.3817	-1797.4563	221.591
TS4.1'	-1797.361	-1797.4363	223.462
TS4.2	-1797.3653	-1797.4378	214.89
4d	-1797.3842	-1797.4606	226.759
4d'	-576.85585	-576.90543	147.095
TS4.3	-1797.3674	-1797.4426	223.313
4e	-1797.3828	-1797.459	226.098
TS4.4	-1797.38	-1797.4556	224.086
4f	-1566.3568	-1566.4268	207.757

Table I3. Energies at 423 K for the various structures from Scheme 7 in the manuscript.

Structure	H (Hartree)	G (Hartree)	S (cal/mol/K)
1	-990.46403	-990.53251	203.193
1b	-1144.0796	-1144.1506	210.596
TS1.1	-1144.0859	-1144.1418	166.05

1c	-1144.0942	-1144.1518	170.96
TS1.2	-1144.0745	-1144.1309	167.405
TS1.1'	-1144.0629	-1144.1205	170.74
1d	-1144.0935	-1144.1503	168.481
TS1.3	-1144.0825	-1144.1401	171.1
1e	-1144.0891	-1144.1458	168.142
TS1.4	-1144.0889	-1144.1435	162.032
1f	-913.06087	-913.11139	149.888

Table I4. Energies at 423 K for the various structures from Scheme 8 in the manuscript.

Structure	H (Hartree)	G (Hartree)	S (cal/mol/K)
5	-495.20742	-495.25016	126.812
5b	-648.83352	-648.8804	139.097
TS5.1	-648.81047	-648.85912	144.343
TS5.1'	-648.78023	-648.82745	140.094
5c	-648.8146	-648.86142	138.904
TS5.2	-648.80351	-648.8487	134.078
5d	-576.85585	-576.90543	147.095
TS5.3	-576.82864	-576.87603	140.589
5e	-576.8621	-576.912	148.038
TS5.4	-576.8561	-576.90483	144.592
5f	-345.82902	-345.86762	114.527

Table I5. Energies at 423 K for various structures from Scheme I1-I4 in this appendix.

Scheme	Structure	H	G	S
S1	$[Cu(OAc)_2]_2$	-1306.4713	-1306.5301	174.4
	$[Cu(OAc)_2]_3$	-1959.7393	-1959.8025	187.611
	$Cu(OAc)_2$	-653.21842	-653.25471	107.656
	Cu(OAc)	-424.68808	-424.71598	82.798

	$Cu(OAc)(HOAc)_2$	-882.96988	-883.01784	142.293
	$Cu(OAc)(HOAc)(C_2H_4)$	-732.42592	-732.47349	141.118
	$Cu(OAc)(C_2H_4)$	-581.86914	-581.91317	130.657
S2	Rh(II)Cu(II)Rh(II)	-1715.6454	-1715.7326	258.675
	Rh(III)Cu(II)Rh(1)	-1794.2502	-1794.3435	276.943
	Rh(III)Rh(I)	-1140.9777	-1141.0483	209.54
	Rh(II)Rh(II)	-1062.3641	-1062.4311	198.632
S3	TS: Premature C_2H_4 Insertion	-1797.3463	-1797.4174	210.938
S4	TS: External OAc Deprotonation	-2025.9667	-2026.0687	302.357

X-ray crystallography data and structure determination

A suiTable Iingle crystal of $[(HOPiv)Rh(\mu\text{-}OPiv)_2]_2$ (**2**) or $[(\eta^2\text{-}C_2H_4)_2Rh^I(\mu\text{-}OPiv)_2]_2(\mu\text{-}Cu)$ (**4**) was coated with Paratone oil and mounted on a MiTeGen MicroLoop. The X-ray intensity data were measured on a Bruker Kappa APEXII Duo system equipped with a fine-focus sealed tube (Mo K_α, λ = 0.71073 Å) and a graphite monochromator.

Complex **4** was identified as a two-component twin using CELL_NOW.[15] Starting with 1163 reflections, 963 reflections were fit to the first domain, 716 to

the second domain (112 exclusively), with 88 unindexed reflection remaining. The twin domain was oriented at a 179.6° rotation about the real axis -0.002 1.000 0.000. The twin law was -1.000 0.255 -0.007 / -0.003 1.000 0.000 / 0.005 1.000 -1.000. The frames of **2** or **4** were integrated with the Bruker SAINT software package[16] using a narrow-frame algorithm. Data were corrected for absorption effects using the Multi-Scan method SADABS (**2**) or TWINABS (**4**).[16]

The structures were solved and refined using the Bruker SHELXTL Software Package[17] within APEX3[15] and OLEX2.[18] Non-hydrogen atoms were refined anisotropically. The O-H hydrogen atoms in **2** were located in the diffraction map and refined isotropically. All other hydrogen atoms in both structures were placed in geometrically calculated positions with Uiso = $1.2\,U_{equiv}$ of the parent atom ($1.5\,U_{equiv}$ for methyl). Complex **4** was refined on HKLF5 data, with the BASF for the twin domains refining to 0.24640. In **2**, each ligand was disordered over multiple positions. The relative occupancies were freely refined, with the sum of each ligand set to one. Constraints and restraints were used on the bonds and anisotropic displacement parameters of the disordered atoms as needed.

Table I6. Crystallographic data for $[(HOPiv)Rh(\mu\text{-}OPiv)_2]_2$ (**2**) and $[(\eta^2\text{-}C_2H_4)_2Rh^{I}(\mu\text{-}OPiv)_2]_2(\mu\text{-}Cu)$ (**4**).

	2	**4**
CCDC number	2046179	2046180
Formula	$C_{30}H_{56}O_{12}Rh_2$	$C_{28}H_{52}CuO_8Rh_2$
FW (g/mol)	817.69	786.05
Temp (K)	100(2)	100(2)
Size (mm)	0.320 x 0.452 x 0.690	0.130 x 0.176 x 0.331
Crystal habit	green block	yellow rod
Crystal system	monoclinic	triclinic
Space group	C 2/c	P -1
a (Å)	19.0942(19)	9.3325(14)
b (Å)	16.8025(16)	9.9290(14)
c (Å)	11.7586(12)	10.2933(15)
α (°)	90	61.195(3)
β (°)	90.409(2)	86.071(3)
γ (°)	90	82.255(3)
Volume ($Å^3$)	3772.4(6)	828.2(2)
Z	4	1
Density (g/cm^3)	1.440	1.576
μ (mm^{-1})	0.928	1.663
F(000)	1695	403

ϑ range (°)	1.61 to 33.17	2.20 to 28.32
Index ranges	-29 ≤ h ≤ 29 -25 ≤ k ≤ 25 -18 ≤ l ≤ 14	-12 ≤ h ≤ 12 -11≤ k ≤ 13 0 ≤ l ≤ 113
Data / restraints /parameters	7212 / 156 / 376	4111 / 0 / 185
GOF on F^2	1.037	1.106
R_1 ($I>2\sigma(I)$)	0.0223	0.0367
wR_2 (all data)	0.0543	0.0945

Table I7. Bond lengths (Å) for $[(HOPiv)Rh(\mu\text{-}OPiv)_2]_2$ (**2**).

Rh1-O3'	2.026(16)	Rh1-O4	2.027(15)
Rh1-O1	2.0294(9)	Rh1-O2'	2.0321(9)
C12-C15	1.536(3)	Rh1-O5	2.2988(19)
O1-C1	1.2780(14)	O2-C1	1.2660(14)
C1-C2	1.562(3)	C2-C5	1.526(5)
C2-C4	1.550(5)	C2-C3	1.561(4)
C7-C9	1.558(9)	O3-C6	1.273(9)
O4-C6	1.274(9)	C6-C7	1.532(8)
C7-C10	1.488(8)	C7-C8	1.528(9)
C12-C13	1.545(4)	O5-C11	1.223(3)

O6-C11	1.334(3)	O6-H6	0.83(5)
C11-C12	1.520(3)	C12-C14	1.525(4)
C3-H3A	0.98	C3-H3B	0.98
C3-H3C	0.98	C4-H4A	0.98
C4-H4B	0.98	C4-H4C	0.98
C5-H5A	0.98	C5-H5B	0.98
C5-H5C	0.98	C8-H8A	0.98
C8-H8B	0.98	C8-H8C	0.98
C9-H9A	0.98	C9-H9B	0.98
C9-H9C	0.98	C10-H10A	0.98
C10-H10B	0.98	C10-H10C	0.98

Symmetry transformations used to generate equivalent atoms:

#1 -x+1, -y+1, -z+1

Table I8. Bond angles (°) for $[(HOPiv)Rh(\mu\text{-}OPiv)_2]_2$ (**2**).

O3'-Rh1-O4	88.4(8)	O3'-Rh1-O1	174.8(4)
O4-Rh1-O1	90.4(5)	O3'-Rh1-O2'	91.2(6)
O4-Rh1-O2'	177.8(3)	O1-Rh1-O2'	89.81(4)

O3'-Rh1-O5	88.4(4)	O4-Rh1-O5	95.0(3)
O1-Rh1-O5	96.68(6)	O2'-Rh1-O5	87.16(6)
C1-O1-Rh1	118.84(7)	C1-O2-Rh1'	119.45(8)
O2-C1-O1	125.06(11)	O2-C1-C2	117.44(13)
O1-C1-C2	116.62(13)	C5-C2-C4	108.9(3)
C5-C2-C3	110.1(2)	C4-C2-C3	112.1(2)
C5-C2-C1	107.5(2)	C4-C2-C1	108.7(2)
C3-C2-C1	109.4(2)	C2-C3-H3A	109.5
C2-C3-H3B	109.5	H3A-C3-H3B	109.5
C2-C3-H3C	109.5	H3A-C3-H3C	109.5
H3B-C3-H3C	109.5	C2-C4-H4A	109.5
C2-C4-H4B	109.5	H4A-C4-H4B	109.5
C2-C4-H4C	109.5	H4A-C4-H4C	109.5
H4B-C4-H4C	109.5	C2-C5-H5A	109.5
C2-C5-H5B	109.5	H5A-C5-H5B	109.5
C2-C5-H5C	109.5	H5A-C5-H5C	109.5
C6-O3-Rh1'	121.5(11)	C5A-C2A-C1	115.3(8)
C6-O4-Rh1	118.0(10)	O3-C6-O4	124.0(11)
O3-C6-C7	116.2(9)	O4-C6-C7	119.7(9)
C10-C7-C8	112.1(6)	C10-C7-C6	111.8(5)

C8-C7-C6	110.2(6)	C10-C7-C9	110.5(5)
C8-C7-C9	108.0(5)	C6-C7-C9	103.8(6)
C7-C8-H8A	109.5	C7-C8-H8B	109.5
H8A-C8-H8B	109.5	C7-C8-H8C	109.5
H8A-C8-H8C	109.5	H8B-C8-H8C	109.5
C7-C9-H9A	109.5	C7-C9-H9B	109.5
H9A-C9-H9B	109.5	C7-C9-H9C	109.5
H9A-C9-H9C	109.5	H9B-C9-H9C	109.5
C7-C10-H10A	109.5	C7-C10-H10B	109.5
H10A-C10-H10B	109.5	C7-C10-H10C	109.5
H10A-C10-H10C	109.5	H10B-C10-H10C	109.5
C11-O5-Rh1	122.42(16)	C11-O6-H6	111.(3)
O5-C11-O6	123.1(2)	O5-C11-C12	123.2(2)
O6-C11-C12	113.75(19)	C11-C12-C14	109.72(19)
C11-C12-C15	109.04(19)	C14-C12-C15	109.8(2)
C11-C12-C13	108.7(2)	C14-C12-C13	109.8(2)
C15-C12-C13	109.7(2)	C12-C13-H13A	109.5
C12-C13-H13B	109.5	H13A-C13-H13B	109.5
C12-C13-H13C	109.5	H13A-C13-H13C	109.5
H13B-C13-H13C	109.5	C12-C14-H14A	109.5

C12-C14-H14B	109.5	H14A-C14-H14B	109.5
C12-C14-H14C	109.5	H14A-C14-H14C	109.5
H14B-C14-H14C	109.5	C12-C15-H15A	109.5
C12-C15-H15B	109.5	H15A-C15-H15B	109.5
C12-C15-H15C	109.5	H15A-C15-H15C	109.5
H15B-C15-H15C	109.5		

Symmetry transformations used to generate equivalent atoms:

#1 -x+1, -y+1, -z+1

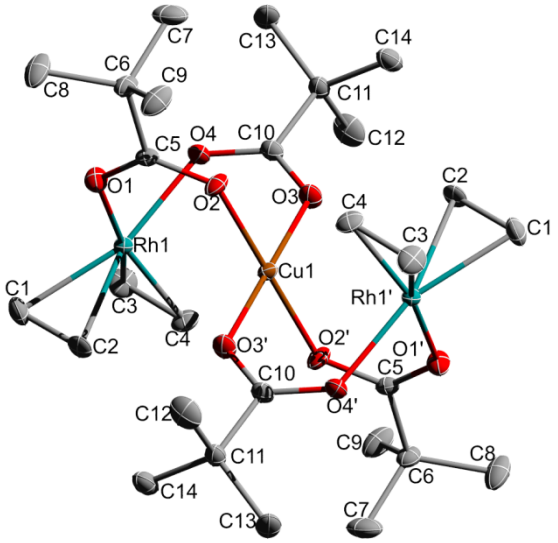

Figure I12. ORTEP of $[(\eta^2\text{-}C_2H_4)_2Rh^I(\mu\text{-}OPiv)_2]_2(\mu\text{-}Cu)$ (**4**) (50% probability). H atoms are omitted for clarity.

Table I9. Bond lengths (Å) for $[(\eta^2\text{-}C_2H_4)_2Rh^I(\mu\text{-}OPiv)_2]_2(\mu\text{-}Cu)$ (**4**).

Rh1-O4'	2.078(3)	Rh1-O1	2.079(3)
Rh1-C1	2.112(4)	Rh1-C3	2.112(4)
Rh1-C2	2.118(3)	Rh1-C4	2.122(4)
Rh1-Cu1	3.0095(5)	Cu1-O2'	1.948(3)
Cu1-O2	1.948(3)	Cu1-O3'	1.949(3)
Cu1-O3	1.949(3)	O1-C5	1.261(5)
O2-C5	1.262(4)	O3-C10	1.263(5)

O4-C10	1.264(5)	C1-C2	1.393(6)
C1-H1A	0.99	C1-H1B	0.99
C2-H2A	0.99	C2-H2B	0.99
C3-C4	1.402(6)	C3-H3A	0.99
C3-H3B	0.99	C4-H4A	0.99
C4-H4B	0.99	C5-C6	1.541(5)
C6-C9	1.523(5)	C6-C8	1.525(6)
C6-C7	1.546(5)	C7-H7A	0.98
C7-H7B	0.98	C7-H7C	0.98
C8-H8A	0.98	C8-H8B	0.98
C8-H8C	0.98	C9-H9A	0.98
C9-H9B	0.98	C9-H9C	0.98
C10-C11	1.532(5)	C11-C14	1.523(5)
C11-C13	1.539(5)	C11-C12	1.549(5)
C12-H12A	0.98	C12-H12B	0.98
C12-H12C	0.98	C13-H13A	0.98
C13-H13B	0.98	C13-H13C	0.98
C14-H14A	0.98	C14-H14B	0.98
C14-H14C	0.98		

Symmetry transformations used to generate equivalent atoms:

' -x+1, -y+1, -z+1

Table I9. Bond angles (°) for $[(\eta^2\text{-}C_2H_4)_2Rh^I(\mu\text{-}OPiv)_2]_2(\mu\text{-}Cu)$ (**4**).

O4'-Rh1-O1	87.78(11)	O4'-Rh1-C1	160.42(14)
O1-Rh1-C1	88.93(15)	O4'-Rh1-C3	87.99(14)
O1-Rh1-C3	159.70(14)	C1-Rh1-C3	88.43(18)
O4'-Rh1-C2	160.41(13)	O1-Rh1-C2	88.04(14)
C1-Rh1-C2	38.45(16)	C3-Rh1-C2	102.16(17)
O4'-Rh1-C4	88.44(13)	O1-Rh1-C4	160.80(13)
C1-Rh1-C4	100.63(17)	C3-Rh1-C4	38.66(16)
C2-Rh1-C4	89.24(16)	O4'-Rh1-Cu1	76.48(8)
O1-Rh1-Cu1	77.99(8)	C1-Rh1-Cu1	121.59(11)
C3-Rh1-Cu1	120.14(12)	C2-Rh1-Cu1	83.93(11)
C4-Rh1-Cu1	82.83(11)	O2'-Cu1-O2	180.0
O2'-Cu1-O3'	90.05(12)	O2-Cu1-O3'	89.95(12)
O2'-Cu1-O3	89.95(12)	O2-Cu1-O3	90.05(12)
O3'-Cu1-O3	180.0	O2'-Cu1-Rh1	101.06(8)
O2-Cu1-Rh1	78.94(8)	O3'-Cu1-Rh1	80.31(8)

O3-Cu1-Rh1	99.69(8)	O2'-Cu1-Rh1'	78.94(8)
O2-Cu1-Rh1'	101.06(8)	O3'-Cu1-Rh1'	99.69(8)
O3-Cu1-Rh1'	80.31(8)	Rh1-Cu1-Rh1'	180.0
C5-O1-Rh1	123.5(2)	C5-O2-Cu1	129.7(2)
C10-O3-Cu1	127.1(2)	C10-O4-Rh1'	126.2(2)
C2-C1-Rh1	71.0(2)	C2-C1-H1A	116.5
Rh1-C1-H1A	116.5	C2-C1-H1B	116.5
Rh1-C1-H1B	116.5	H1A-C1-H1B	113.5
C1-C2-Rh1	70.5(2)	C1-C2-H2A	116.6
Rh1-C2-H2A	116.6	C1-C2-H2B	116.6
Rh1-C2-H2B	116.6	H2A-C2-H2B	113.6
C4-C3-Rh1	71.1(2)	C4-C3-H3A	116.5
Rh1-C3-H3A	116.5	C4-C3-H3B	116.5
Rh1-C3-H3B	116.5	H3A-C3-H3B	113.5
C3-C4-Rh1	70.3(2)	C3-C4-H4A	116.6
Rh1-C4-H4A	116.6	C3-C4-H4B	116.6
Rh1-C4-H4B	116.6	H4A-C4-H4B	113.6
O1-C5-O2	125.9(3)	O1-C5-C6	117.7(3)
O2-C5-C6	116.3(3)	C9-C6-C8	110.6(3)
C9-C6-C5	109.6(3)	C8-C6-C5	112.0(3)

C9-C6-C7	109.3(4)	C8-C6-C7	110.2(4)
C5-C6-C7	105.0(3)	C6-C7-H7A	109.5
C6-C7-H7B	109.5	H7A-C7-H7B	109.5
C6-C7-H7C	109.5	H7A-C7-H7C	109.5
H7B-C7-H7C	109.5	C6-C8-H8A	109.5
C6-C8-H8B	109.5	H8A-C8-H8B	109.5
C6-C8-H8C	109.5	H8A-C8-H8C	109.5
H8B-C8-H8C	109.5	C6-C9-H9A	109.5
C6-C9-H9B	109.5	H9A-C9-H9B	109.5
C6-C9-H9C	109.5	H9A-C9-H9C	109.5
H9B-C9-H9C	109.5	O3-C10-O4	125.7(3)
O3-C10-C11	117.2(3)	O4-C10-C11	117.0(3)
C14-C11-C10	110.3(3)	C14-C11-C13	110.7(3)
C10-C11-C13	111.3(3)	C14-C11-C12	109.7(3)
C10-C11-C12	104.9(3)	C13-C11-C12	109.8(3)
C11-C12-H12A	109.5	C11-C12-H12B	109.5
H12A-C12-H12B	109.5	C11-C12-H12C	109.5
H12A-C12-H12C	109.5	H12B-C12-H12C	109.5
C11-C13-H13A	109.5	C11-C13-H13B	109.5
H13A-C13-H13B	109.5	C11-C13-H13C	109.5

H13A-C13-H13C	109.5	H13B-C13-H13C	109.5
C11-C14-H14A	109.5	C11-C14-H14B	109.5
H14A-C14-H14B	109.5	C11-C14-H14C	109.5
H14A-C14-H14C	109.5	H14B-C14-H14C	109.5

Symmetry transformations used to generate equivalent atoms:

' -x+1, -y+1, -z+1

Additional Calculations

Copper modeling

The modeling of Cu significantly impacts the energetic for Rh oxidation and reduction. For $Cu(OAc)_2$ we examined the monomeric, dimer, and trimeric forms (Scheme I1a). We found the trimeric $[Cu(OAc)_2]_3$ to be the most stable, the monomeric $Cu(OAc)_2$ to be the least stable, and the $[Cu(OAc)_2]_2$ dimer was moderately stable. Under catalytic conditions, Cu carboxylate oxidizes Rh to regenerate the active catalyst. This is observed to be a 1-electron oxidation, meaning $Cu(OAc)_2$ is reduced to some form of Cu(OAc). We examined different ligand configurations of Cu(OAc) with HOAc and C_2H_4 (Scheme I1b). We find $Cu(OAc)(HOAc)(C_2H_4)$ to be the most stable Cu(OAc) configuration. Based on these results, we predict Rh oxidation occurs by reduction of a trimeric

$[Cu(OAc)_2]_3$ to form the $[Cu(OAc)_2]_2$ dimer and liberate a Cu(OAc), which coordinates an HOAc and C_2H_4 to form $Cu(OAc)(HOAc)(C_2H_4)$.

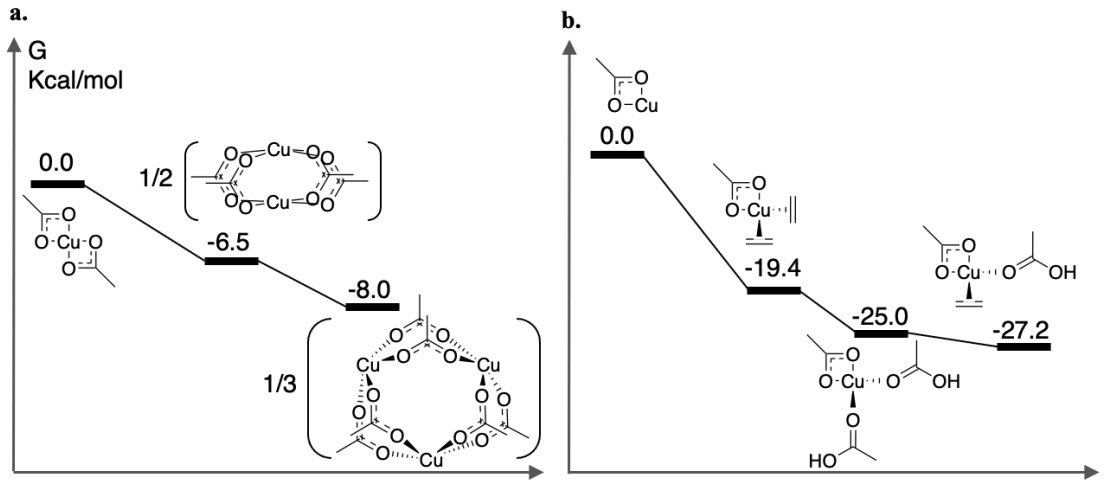

Scheme I1. B3LYP-D3 free energies at 423 K for (a) different configurations of $Cu(OAc)_2$ and (b) different ligand arrangements of Cu(OAc).

Rh oxidation by HOAc

In addition to Rh oxidation by Cu carboxylate, HOAc could also potentially oxidize Rh. (Scheme I2). **4** could be oxidized in a single step to a Rh(I)/Cu(II)/Rh(III) trimer or through multiple steps to form a Rh(II)/Cu(II)/Rh(II) trimer. **1** could be oxidized in a single step to a Rh(I)/Rh(III) dimer or to a Rh(II)/Rh(II) dimer through multiples steps. However, DFT predicts this 2-electron oxidation to be uphill in energy and therefore not feasible.

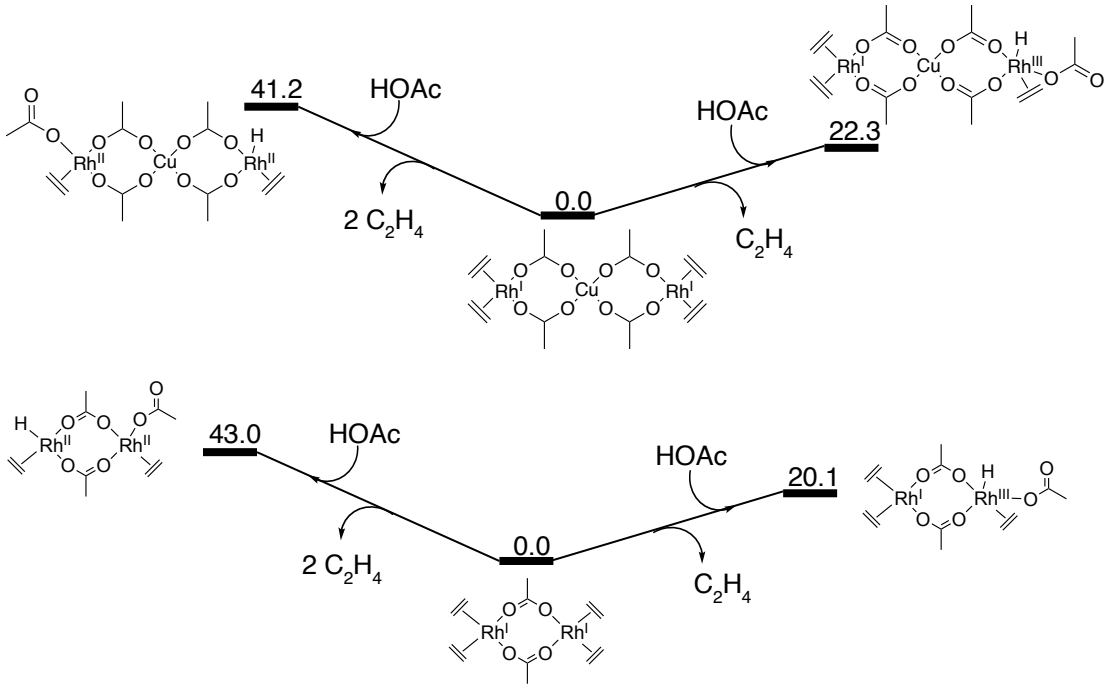

Scheme I2. B3LYP-D3 free energies at 423 K for oxidation of the Rh(I)/Cu(II)/Rh(I) trimer (top) and the Rh(I)/Rh(I) dimer (bottom) by HOAc.

Premature ethylene insertion of 4c

Following oxidative addition to yield the Rh-Ph bond, ethylene insertion into the Rh-Ph can occur. We calculate ethylene insertion following intermediate **4c**, finding a free energy barrier of 40.3 kcal/mol (s). This pathway is consequently not competitive.

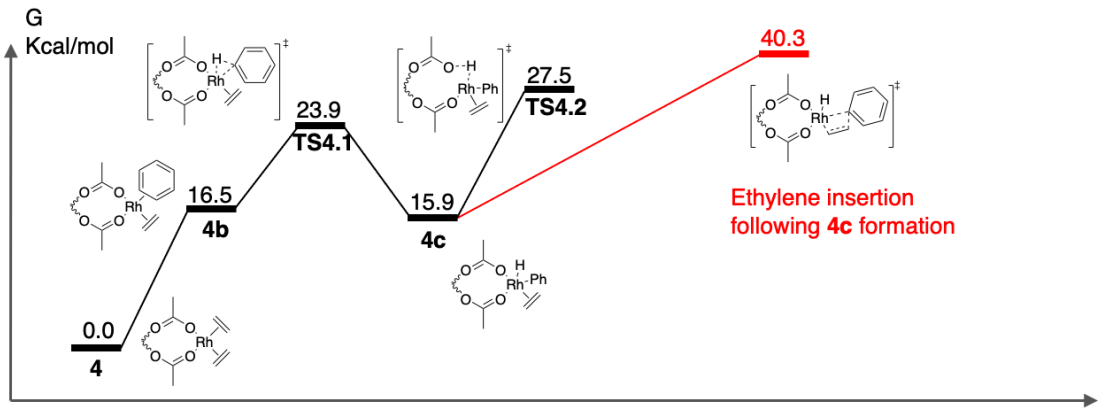

Scheme I3. B3LYP-D3 free energies at 423 K for premature ethylene insertion following the formation of intermediate **4c**.

Deprotonation of 4c by an external acetate

Previous studies have proposed the deprotonation of the transition metal by an external acetate ligand to yield HOAc. In our case this is highly unlikely due to excess HOAc and Cu, effectively suppressing any free acetate ligands in solution. We calculate the transition state for deprotonation of **4c** by an external acetate, finding a free energy barrier of 31.8 kcal/mol relative to the starting state **4** (Scheme I4). Thus, this pathway is not favorable due to the high barrier and lack of free acetates.

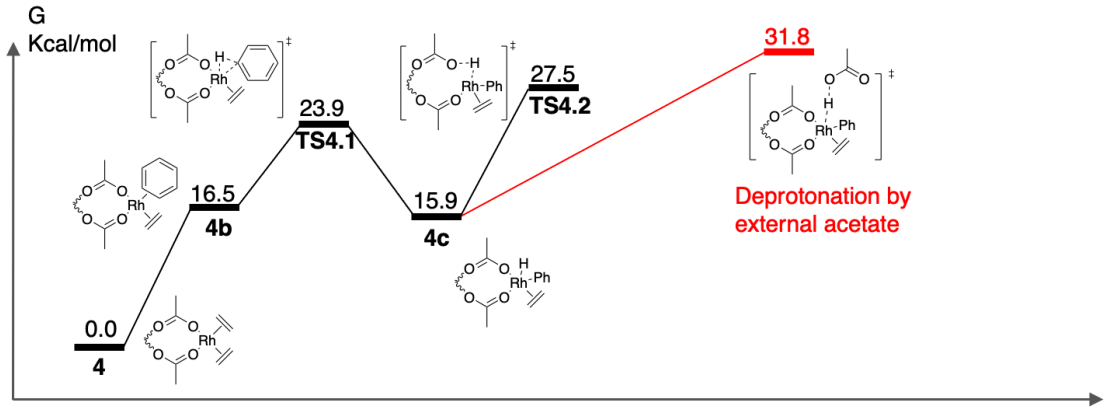

Scheme I4. B3LYP-D3 free energies at 423 K for deprotonation of intermediate **4c** by an external acetate.

DFT Structures

Scheme 5 Structures

$[(C_2H_4)_2Rh(\mu\text{-}OAc)]_2$ **1**

Rh1 -0.1670662842000 0.0123614243000 -0.7435728695000

Rh2 -0.0427973372000 0.3776538613000 2.5640254836000

O3 1.8497700268000 0.4824734391000 -0.2450034969000

C4 2.4770362330000 0.1704443223000 0.8098972024000

O5 1.9600800299000 -0.0054125906000 1.9478124575000

C6 3.9761769349000 0.0166163553000 0.6863756916000

H7 4.4272200904000 -0.2261347346000 1.6471900456000

H8 4.1953730062000 -0.7705828041000 -0.0394194988000

H9 4.4006078277000 0.9458172406000 0.2975374400000

O10 0.1047663928000 -1.9485313047000 0.0462043344000

C11 -0.1748409587000 -2.3735962643000 1.2022686399000

O12 -0.5354636948000 -1.6596931595000 2.1827939214000

C13 -0.0831742556000 -3.8684881571000 1.4150333433000

H14 -0.3228839226000 -4.1321664251000 2.4438132400000

H15 -0.7663382309000 -4.3768576974000 0.7297296188000

H16 0.9298042184000 -4.1994497907000 1.1724500784000

C17 -1.7600938129000 0.3477142676000 3.8673945627000

C18 -2.1385095653000 0.8526329568000 2.6256078064000

H19 -1.9034101606000 -0.7018557083000 4.1010311096000

H20 -2.6012327409000 0.2084248142000 1.8889393114000

H21 -2.3206607156000 1.9131631681000 2.4885989701000

H22 -1.6397035610000 1.0026745716000 4.7231536766000

X23 -1.0283733292000 -0.4820451926000 5.1864400580000

X24 -0.6131896850000 -0.0369930264000 4.3929974887000

C25 -0.5649648395000 2.1097044702000 -0.9892788147000

C26 0.0113412171000 1.6256977552000 -2.1614748065000

H27 -1.6254440359000 2.3324729880000 -0.9410700034000

H28 -0.5866354657000 1.4613959332000 -3.0509476463000

H29 1.0790342071000 1.7194823290000 -2.3284498056000

H30 0.0427339298000 2.6056871208000 -0.2433664347000

X31 0.8918582063000 0.6551213942000 -3.1657750527000

X32 0.4458410726000 0.2307995261000 -2.3777270409000

C33 -1.7073768416000 -0.8662598276000 -1.9558027233000

C34 -2.2725944991000 -0.4141198866000 -0.7629673775000

H35 -1.8613269574000 -0.3275752786000 -2.8845629784000

H36 -2.8791019764000 0.4848719944000 -0.7404458039000

H37 -2.4464560361000 -1.1054845684000 0.0543489436000

H38 -1.4168422692000 -1.9058650437000 -2.0662482153000

X39 -1.2457508015000 -1.4135889392000 -2.9595553417000

X40 -0.7964888223000 -0.8130891715000 -2.2980693607000

C41 0.7953440787000 1.9778941813000 3.7279563665000

C42 0.4514685574000 2.4677918050000 2.4677745824000

H43 0.1945774732000 2.2128747974000 4.5998053952000

H44 -0.4226838341000 3.0961363191000 2.3349350466000

H45 1.2071378492000 2.5635214492000 1.6955955896000

H46 1.8137506070000 1.6673269812000 3.9370424890000

X47 1.6015211733000 1.7127503857000 4.3100335750000

X48 1.0387020585000 1.1677262820000 3.6885970374000

X49 -0.2768118112000 1.8677011127000 -1.5753768106000

X50 -1.9899856703500 -0.6401898571000 -1.3593850504000

X51 -1.9493016891000 0.6001736122000 3.2465011845500

X52 0.6234063180500 2.2228429931500 3.0978654744500

$[(C_2H_4)Rh(\mu\text{-}OAc)]_2(C_2H_4)$ (C_6H_6) **1b**

Rh1 -0.4317567058000 9.0896701831000 4.7041434711000

C3 -0.1215229324000 7.7114660155000 6.3223500937000

C4 -0.0820395642000 10.7522087991000 6.0153223772000

C5 0.9563629488000 7.6162805386000 5.4442299991000

C6 1.0012651090000 10.6212053699000 5.1441462341000

Rh7 -3.8009485144000 8.9026513764000 4.8915906558000

O8 -3.3532423108000 10.7310057944000 3.9144719555000

O9 -3.2830516707000 7.9672602936000 3.0834694001000

O10 -1.1992024552000 10.4947497722000 3.3017055033000

O11 -1.1167431993000 7.4901619053000 3.4602234544000

C12 -3.6030166013000 6.9710823746000 5.7899765293000

C13 -2.1765553562000 7.4375532009000 2.7764545184000

C14 -2.3455534295000 11.0209455891000 3.2157259679000

C15 -4.9152653813000 7.1232304130000 5.3335052265000

C16 -2.1333857340000 6.6335787201000 1.4963974887000

C17 -2.5255290863000 12.0936661960000 2.1629355895000

H18 -1.1988241916000 6.8273847359000 0.9684153912000

H19 -3.3010033696000 12.7976555362000 2.4647851434000

H20 -1.5852308320000 12.6096845276000 1.9684672180000

H21 -2.1567680164000 5.5703652009000 1.7543148422000

H22 -2.9890690906000 6.8617392284000 0.8625488676000

H23 -2.8493743349000 11.6087536664000 1.2364374636000

H24 -0.9407081790000 7.0064258095000 6.2638044053000

H25 -0.0155667153000 8.2155599355000 7.2771578889000

H26 0.0094029878000 10.4594040392000 7.0559902138000

H27 -0.8712001199000 11.4627143335000 5.8039584711000

H28 1.9196495361000 8.0451227719000 5.6969796999000

H29 0.9746138041000 6.8531930838000 4.6739472423000

H30 1.0531854215000 11.2168754662000 4.2391438071000

H31 1.9477237445000 10.2198840273000 5.4892650709000

H32 -3.3720210563000 7.0226134773000 6.8486771328000

H33 -2.8747413847000 6.4306183843000 5.1964402527000

H34 -5.2188189561000 6.7096439337000 4.3777252677000

H35 -5.7235644463000 7.2982444843000 6.0373148561000

X36 0.4174200082000 7.6638732770500 5.8832900464000

X37 0.4596127724000 10.6867070845000 5.5797343056500

X38 -4.2591409913000 7.0471563938000 5.5617408779000

C39 -3.2156396432000 10.7740319908000 7.2914219931000

C40 -3.4041362755000 12.0584865123000 6.8371543997000

C41 -4.5617555127000 12.3911756764000 6.0993407393000

C42 -5.5085929273000 11.4338597119000 5.8163861037000

C43 -5.3242835105000 10.0991519400000 6.2550662741000

C44 -4.1735968954000 9.7639796560000 7.0072085892000

H45 -2.3452174446000 10.5202697695000 7.8832758308000

H46 -2.6687678114000 12.8253329369000 7.0534171600000

H47 -4.7021112506000 13.4112758239000 5.7591726997000

H48 -6.4002475928000 11.6890953250000 5.2562076726000

H49 -6.1629885581000 9.4188925388000 6.1987998302000

H50 -4.1484615464000 8.8535983572000 7.5918121093000

[(HOPiv)Rh(μ-OPiv)$_2$]$_2$ **2**

Rh1 0.2077201347000 0.0335649276000 -0.2569158428000

Rh2 -0.0317881265000 0.0168429255000 2.1625237867000

O3 1.8091697324000 1.3303742199000 0.0129880641000

C4 2.1543760483000 1.7023158127000 1.1641700663000

O5 1.5815350732000 1.3266028021000 2.2447236403000

C6 3.3370733842000 2.6676333678000 1.2576621869000

C7 3.6476703115000 3.0367841955000 2.7135221291000

C8 4.5552349974000 1.9736309281000 0.6133222247000

C9 2.9678093421000 3.9329556892000 0.4554899184000

O10 -1.0973952775000 1.6443449552000 -0.2848795156000

C11 -1.5673706972000 2.0921825876000 0.8051166427000

O12 -1.3131898255000 1.6346636584000 1.9583005067000

C13 -2.5103372883000 3.2938397113000 0.6944070410000

C14 -3.0557453671000 3.6918340656000 2.0717706408000

C15 -1.7036388284000 4.4582429841000 0.0830849317000

C16 -3.6688057082000 2.9076628580000 -0.2462242073000

O17 1.4769517213000 -1.5924295567000 -0.0509736887000

C18 1.7406697545000 -2.0429600604000 1.1052052251000

O19 1.2817325707000 -1.5871572773000 2.1941657652000

C20 2.7042633189000 -3.2316808662000 1.1666171055000

C21 2.8857827488000 -3.7160155271000 2.6107132294000

C22 2.1238430780000 -4.3618340056000 0.2934567117000

C23 4.0551516070000 -2.7623940464000 0.5881669914000

O24 -1.4144518372000 -1.2601521244000 -0.3333939988000

C25 -1.9852246928000 -1.6453053121000 0.7471671545000

O26 -1.6290916069000 -1.2895582253000 1.8974353110000

C27 -3.1706713276000 -2.5957220836000 0.5896470239000

C28 -3.7419640797000 -2.9746479596000 1.9619071623000

C29 -4.2446793496000 -1.8775501028000 -0.2544371377000

C30 -2.6760497289000 -3.8574268519000 -0.1482044658000

H31 -4.5878434355000 -3.6547508054000 1.8295718997000

H32 -2.9903126708000 -3.4690787179000 2.5796175142000

H33 -4.0853416741000 -2.0917712955000 2.5036735122000

H34 -5.1059103614000 -2.5374164490000 -0.3879653253000

H35 -4.5891569168000 -0.9666177903000 0.2422849047000

H36 -3.8631624168000 -1.6068282275000 -1.2399914783000

H37 -3.5085783790000 -4.5534102582000 -0.2805223059000

H38 -2.2730558942000 -3.6127950387000 -1.1319801883000

H39 -1.8963929971000 -4.3664185677000 0.4247310301000

H40 2.8051285067000 -5.2172023314000 0.2950788644000

H41 1.1575257068000 -4.6981900919000 0.6799292987000

H42 1.9832292935000 -4.0246721690000 -0.7341111497000

H43 3.5755567237000 -4.5647378801000 2.6280265260000

H44 3.2910557760000 -2.9250125683000 3.2441922122000

H45 1.9348301441000 -4.0309333529000 3.0445784644000

H46 4.7677288901000 -3.5919130725000 0.5932791506000

H47 3.9360562078000 -2.4056633416000 -0.4356727585000

H48 4.4767027164000 -1.9506511226000 1.1878091743000

H49 -2.3484480983000 5.3338415914000 -0.0327151094000

H50 -0.8673250622000 4.7371424229000 0.7303746705000

H51 -1.3037698028000 4.1826410071000 -0.8935928378000

H52 -3.7269216932000 4.5489760074000 1.9656968079000

H53 -3.6096599340000 2.8703399532000 2.5301168779000

H54 -2.2474792551000 3.9643774278000 2.7526463784000

H55 -4.3447585974000 3.7584468084000 -0.3687617245000

H56 -3.2909325715000 2.6132464887000 -1.2259268145000

H57 -4.2453979672000 2.0738596270000 0.1642791465000

H58 3.8045629186000 4.6363916226000 0.4738089821000

H59 2.7399880382000 3.6821152665000 -0.5809498316000

H60 2.0960765736000 4.4319330618000 0.8881791322000

H61 4.4936451131000 3.7283678681000 2.7406259716000

H62 2.7971963574000 3.5249099585000 3.1943028318000

H63 3.9127442154000 2.1565368843000 3.3031317143000

H64 5.4158481408000 2.6475571920000 0.6355573084000

H65 4.8229728838000 1.0641261754000 1.1584388568000

H66 4.3445885783000 1.7036530402000 -0.4219712683000

O67 -0.1969737179000 0.0427451011000 4.4850886497000

C68 0.4994602475000 0.6546036186000 5.2836547855000

O69 1.5027031503000 1.4447157977000 4.9271373723000

C70 0.2594763708000 0.5417106949000 6.7864181419000

C5 1.2158729395000 1.4268213630000 7.5967261899000

C72 -1.2043284165000 0.9535061072000 7.0489269209000

C73 0.4583754383000 -0.9425130297000 7.1629781307000

H74 0.9995633488000 1.3117541992000 8.6621533872000

H75 2.2577799391000 1.1495175882000 7.4260466398000

H76 1.1022342612000 2.4807851316000 7.3354295227000

H77 0.2518221638000 -1.0793240520000 8.2276160175000

H78 -0.2142708973000 -1.5808968117000 6.5885184322000

H79 1.4855881317000 -1.2644047965000 6.9712898295000

H80 -1.4332169517000 0.8325289256000 8.1109203734000

H81 -1.3735407556000 2.0000386880000 6.7811246055000

H82 -1.8903305899000 0.3355616378000 6.4682495352000

H17 1.6108036354000 1.4682692403000 3.9441211383000

O84 0.3469933135000 -0.0182019634000 -2.5908721032000

C85 -0.3807670938000 -0.6214321928000 -3.3694301307000

O86 -1.3949275241000 -1.3812595471000 -2.9841909868000

C87 -0.1599645418000 -0.5427685952000 -4.8774944633000

C88 -1.2195953116000 -1.3289725435000 -5.6607910180000

C89 -0.1988236886000 0.9485140429000 -5.2711211513000

C90 1.2461771354000 -1.1167174569000 -5.1562140349000

H91 -1.0192275460000 -1.2385270259000 -6.7317281359000

H92 -1.2061971292000 -2.3879851648000 -5.3966136249000

H93 -2.2239417548000 -0.9477668723000 -5.4657893621000

H94 1.4674839424000 -1.0375352596000 -6.2237381736000

H95 2.0055682243000 -0.5672367029000 -4.5979529912000

H96 1.3052845232000 -2.1715355364000 -4.8744117257000

H97 0.0101012881000 1.0502119562000 -6.3391334683000

H98 -1.1829910852000 1.3826765330000 -5.0748688113000

H99 0.5453869770000 1.5163124642000 -4.7111854310000

H100 -1.4787601319000 -1.3938809923000 -1.9963055614000

$[(\eta^2\text{-}C_2H_4)_2Rh^{I}(\mu\text{-}OAc)_2]_2(\mu\text{-}Cu)$ **4**

Rh1 2.4022802886000 9.0894057833000 4.2454355954000

Cu2 -0.6230520352000 9.0660703219000 4.6289195349000

O3 2.0829473287000 7.2598856013000 5.2627102109000

O4 2.0970669245000 10.1254602596000 6.0783008854000

O5 -0.0787690311000 7.5695001380000 5.8040176198000

O6 -0.1374247027000 10.3722437512000 6.0370218861000

C7 1.9514842818000 10.9388740445000 3.2289780931000

C8 1.0082964330000 10.5829836812000 6.5273058195000

C9 1.9522874960000 7.9941275854000 2.4401277290000

C10 1.0244432851000 6.9615661807000 5.8867024503000

C11 3.3144992029000 10.9026299452000 3.5101354085000

C12 1.0811410954000 11.4917744058000 7.7329968335000

C13 3.3239428153000 7.9404394344000 2.6676246795000

C14 1.0843559349000 5.7843014002000 6.8327447576000

H15 0.1860653241000 11.3849866269000 8.3455274359000

H16 1.9229144279000 5.1331734617000 6.5879235077000

H17 0.1437701507000 5.2326747670000 6.8095881842000

H18 1.1298414275000 12.5266736217000 7.3795016880000

H19 1.9776511308000 11.2855941236000 8.3167502457000

H20 1.2244580674000 6.1705440418000 7.8476305138000

Rh21 -3.6510902872000 8.9680075563000 4.9940611024000

O22 -3.3459448850000 10.8262976011000 4.0240497663000

O23 -3.3306718583000 7.9826018334000 3.1367891261000

O24 -1.1820888995000 10.5666809071000 3.4650994277000

O25 -1.0912510406000 7.7772347836000 3.2000725398000

C26 -3.1828160829000 7.0807649508000 5.9327173825000

C27 -2.2258460105000 7.5693459575000 2.6826108759000

C28 -3.2101684328000 9.9875603846000 6.8457388138000

C29 -2.2941443314000 11.1617159533000 3.4078683922000

C30 -4.5541666506000 7.1392821571000 5.7046720726000

C31 -2.2603619267000 6.7118770476000 1.4382035723000

C32 -4.5718569304000 10.0974305613000 6.5845335323000

C33 -2.3735176725000 12.3662944894000 2.4990840283000

H34 -1.3734226243000 6.8891073504000 0.8317614068000

H35 -3.2281402390000 12.9894489911000 2.7553527331000

H36 -1.4492216798000 12.9381583108000 2.5514289604000

H37 -2.2545936553000 5.6622278702000 1.7448730255000

H38 -3.1667511829000 6.8988650902000 0.8648382395000

H39 -2.4923827355000 12.0125526598000 1.4729548548000

H40 1.2488592786000 11.4556318914000 3.8708436180000

H41 1.5795093535000 10.7577775720000 2.2280623551000

H42 1.5369391065000 8.6409308597000 1.6759414161000

H43 1.2907460676000 7.2000900938000 2.7620657547000

H44 4.0393846118000 10.7007155613000 2.7282906939000

H45 3.7092839677000 11.3950668383000 4.3933431923000

H46 3.7655212470000 7.0872970064000 3.1741955641000

H47 4.0108281122000 8.5385240673000 2.0774563619000

H48 -2.7688338853000 7.2246568199000 6.9224738743000

H49 -2.5107454560000 6.5823759154000 5.2458590962000

H50 -2.5124146240000 10.7685899647000 6.5703235901000

H51 -2.8423271679000 9.3000178507000 7.5988601868000

H52 -4.9905433156000 6.6816955074000 4.8221902751000

H53 -5.2433988006000 7.3214426477000 6.5223580016000

H54 -5.2963512907000 9.5053851642000 7.1350690453000

H55 -4.9671669017000 10.9819150487000 6.0947071393000

$(\eta^2\text{-}C_2H_4)_2Rh^I(\kappa^2\text{-}OAc)$ **5**

Rh1 -0.0158701429000 0.2392801228000 0.1837707636000

C9 -2.1282890399000 0.5444560270000 0.4718784596000

C10 -1.9258608353000 -0.2809052778000 -0.6339150906000

H11 -2.3578985799000 0.1266851487000 1.4478461225000

H5 -1.9730644932000 -1.3619892250000 -0.5341054630000

H13 -2.0589929751000 0.0945791310000 -1.6425354480000

H14 -2.4214156700000 1.5809475169000 0.3354287267000

X15 -2.0270749376000 0.1317753746000 -0.0810183155000

C22 0.1997619329000 1.7907105351000 -1.2934838006000

C23 0.2717207986000 2.3502815247000 -0.0178312034000

H24 1.1005895663000 1.5492965414000 -1.8503450730000

H15 1.2342244916000 2.5338578003000 0.4518913813000

H26 -0.5554301112000 2.9197773240000 0.3914622935000

H27 -0.6927947457000 1.9179163033000 -1.8984880253000

X28 0.2357413657500 2.0704960299000 -0.6556575020000

O32 0.3891282052000 -1.6527680020000 1.1809583149000

C33 1.6298842359000 -1.3582964771000 1.2368208428000

O34 2.0258441793000 -0.2505780213000 0.7434967118000

C35 2.5984174059000 -2.3012925075000 1.8853126096000

H20 3.6219338911000 -1.9503114893000 1.7586911575000

H21 2.3646912325000 -2.3720409630000 2.9515967278000

H22 2.4824005471000 -3.2996481091000 1.4570635502000

$Rh^{II}(\kappa^2\text{-}OAc)_2$ **6**

Rh1 -0.0501942200000 -0.1358693697000 0.8266162137000

O3 0.2817058649000 1.4974267339000 -0.4836903838000

C4 0.2606727810000 2.3177335696000 0.4935384690000

O5 0.0597008077000 1.8175408914000 1.6488006924000

C6 0.4743267483000 3.7805547278000 0.2871968225000

H7 0.2919340198000 4.3296041986000 1.2098600418000

H8 1.5047533642000 3.9463308068000 -0.0407688002000

H9 -0.1862434396000 4.1385416638000 -0.5056565289000

O10 -0.1504484724000 -2.0877803266000 0.0036290170000

C11 -0.3250434135000 -2.5934228589000 1.1620051882000

O12 -0.3646293002000 -1.7739491124000 2.1379164325000

C13 -0.4568201076000 -4.0673345011000 1.3582857891000

H14 -0.8059761523000 -4.2900089186000 2.3656636197000

H15 -1.1419577976000 -4.4790428224000 0.6144702778000

H16 0.5212164909000 -4.5332651921000 1.2034250207000

$Rh^{III}(\kappa^2\text{-}OAc)_3$ **7**

C1 -2.1755648458000 -5.1461774448000 1.5174111546000

O2 -2.3713396792000 -5.0176178100000 0.2624200131000

O3 -1.9335145938000 -4.0705599560000 2.1593159356000

C4 -2.2210598077000 -6.4766804141000 2.1849226230000

H5 -2.1234475882000 -6.3636472905000 3.2636874758000

H6 -3.1616273018000 -6.9749318541000 1.9389384718000

H7 -1.4036777610000 -7.0935894723000 1.8011164452000

C8 -0.1826558426000 -1.4286755246000 0.7764781763000

O9 -0.0194533544000 -2.6550570674000 0.4616817755000

O10 -1.3914519458000 -1.0374544575000 0.8934177926000

C11 0.9731138088000 -0.5128874560000 0.9835489356000

H12 0.6290344651000 0.4597767834000 1.3320627564000

H13 1.6610295659000 -0.9544543386000 1.7082037261000

H14 1.5092641885000 -0.3998050017000 0.0371061943000

Rh15 -2.0923167389000 -2.9463202839000 0.4008669131000

C16 -3.9233106940000 -2.2672246134000 -1.1082245668000

O17 -2.6961128608000 -2.1807355412000 -1.4502350852000

O18 -4.1469997927000 -2.7181850548000 0.0639094431000

C19 -5.0211270321000 -1.8683698834000 -2.0318006736000

H20 -5.9881606771000 -1.9800416000000 -1.5437258443000

H21 -4.8724090386000 -0.8308522043000 -2.3414855681000

H22 -4.9782619425000 -2.4964889565000 -2.9259031438000

Scheme 6 structures

$[(\eta^2\text{-}C_2H_4)Rh^I(\mu\text{-}OPiv)_2]_2(\mu\text{-}Cu)(\eta^2\text{-}C_2H_4)(\eta^2\text{-}C_6H_6)$ **4b**

Rh1 2.4584831173000 9.0064804058000 4.3188301725000

Cu2 -0.5267339071000 9.2025277350000 4.4461211560000

O3 2.0246595570000 7.2106485459000 5.3651764888000

O4 2.1768068622000 10.1759514042000 6.0667267535000

O5 -0.1879448571000 7.5490391062000 5.5106734611000

O6 -0.0670831648000 10.2017029837000 6.1023934401000

C7 2.1261901327000 10.8346204584000 3.2120167639000

C8 1.0649421334000 10.4830693796000 6.5811250248000

C9 2.0307257566000 7.8680647727000 2.5290811653000

C10 0.8655973114000 6.9082151397000 5.7683249434000

C11 3.4760855728000 10.7434446184000 3.5352378389000

C12 1.0789332398000 11.2823896183000 7.8647697391000

C13 3.3756067912000 7.7182405115000 2.8487386797000

C14 0.7121910985000 5.6794022845000 6.6365148442000

H15 0.2607034395000 10.9641676972000 8.5117975514000

H16 1.6589293286000 5.1538171159000 6.7490126184000

H17 -0.0401008064000 5.0173230274000 6.2021314130000

H18 0.9187491549000 12.3362147882000 7.6178806598000

H19 2.0345190333000 11.1843160275000 8.3776457332000

H20 0.3453701696000 5.9883972659000 7.6191401811000

Rh21 -3.5744458700000 8.9649510045000 5.0413677325000

O22 -3.3339918732000 10.6049740104000 3.7160145235000

O23 -3.3045427870000 7.7826114349000 3.3369513523000

O24 -1.0994815803000 10.8560772115000 3.5674279398000

O25 -1.1022220861000 8.0846839358000 2.9337130894000

C26 -3.1654162567000 7.2562580692000 6.2772036065000

C27 -2.2435981075000 7.6084250805000 2.6745545857000

C28 -2.2960717334000 11.1589320298000 3.2730211173000

C29 -4.4884401365000 7.1856647720000 5.8413267951000

C30 -2.3390677464000 6.7233293857000 1.4525690482000

C31 -2.4735606364000 12.3108328043000 2.3122444976000

H32 -1.9555056206000 7.2628471831000 0.5841379556000

H33 -3.5250469683000 12.5733753303000 2.2131186642000

H34 -1.8999264771000 13.1690797829000 2.6683413483000

H35 -1.7053470158000 5.8456469974000 1.6031714790000

H36 -3.3672729469000 6.4104955910000 1.2765476949000

H37 -2.0691974483000 12.0261031658000 1.3378910278000

H38 1.4353076561000 11.4142334723000 3.8124839521000

H39 1.7750949176000 10.6301630031000 2.2077843152000

H40 1.7159569212000 8.5093885260000 1.7147663261000

H41 1.2891162420000 7.1398523113000 2.8327502894000

H42 4.2111136170000 10.4708557463000 2.7854237134000

H43 3.8667181352000 11.2491777571000 4.4125596098000

H44 3.7115689978000 6.8588218727000 3.4207260221000

H45 4.1436864444000 8.2377902786000 2.2861537981000

H46 -2.9346321650000 7.5563493815000 7.2952498038000

H47 -2.3727186480000 6.7128296508000 5.7824174985000

H48 -4.7493984301000 6.5925561345000 4.9712579825000

H49 -5.3168948373000 7.4134242738000 6.5042833879000

X50 2.8011378527500 10.7890325384000 3.3736273014000

X51 2.7031662739000 7.7931526421000 2.6889099225000

X52 -3.8269281966000 7.2209614206000 6.0592652008000

C53 -2.7565651715000 11.7227958378000 6.4189914689000

C54 -3.7383586622000 12.5935410226000 6.0051143612000

C55 -5.0953534272000 12.1994829052000 6.0006092198000

C56 -5.4524822951000 10.9490467854000 6.4496200429000

C57 -4.4562639718000 10.0383703231000 6.8967128057000

C58 -3.0960670133000 10.4164965112000 6.8539374332000

H59 -1.7126285544000 12.0006402568000 6.3993123050000

H60 -3.4731674470000 13.5909253324000 5.6714568655000

H61 -5.8550354718000 12.8909410231000 5.6540291995000

H62 -6.4944619450000 10.6517446243000 6.4868706753000

H63 -4.7660689141000 9.1896730311000 7.4917262888000

H64 -2.3247021576000 9.8171430005000 7.3166294363000

TS4.1

Rh1	2.3810747606	9.6226821080	3.9937022468
Cu2	-0.6270584470	9.5167403394	4.2012647964
O3	2.0447266973	9.0201512331	6.0192467153
O4	1.9243805455	11.6008932743	4.5716570435
O5	-0.1156488069	8.4556080705	5.7738845018
O6	-0.2162516387	11.2156787674	5.1385368278
C7	1.8079460461	10.2059469708	2.0017440224
C8	0.8238585117	11.9298160513	5.0997314978
C9	2.1646026307	7.5416798118	3.4271690718
C10	0.9452853028	8.5762847967	6.4541358530
C11	3.1724647622	10.4403006919	2.1605227387

C12	0.7368080973	13.2856801901	5.7606206756
C13	3.4970992545	7.7922366205	3.7324067868
C14	0.8651344640	8.1406715114	7.8975251498
H15	0.6670531962	13.1370176680	6.8416945969
H16	1.8185109936	8.2756997818	8.4055224093
H17	0.5644362323	7.0908618412	7.9394804396
H18	-0.1714146688	13.7974636066	5.4378093469
H19	1.6154643726	13.8879162257	5.5361251139
H20	0.0844934647	8.7240233473	8.3921882457
O21	-3.6366388128	10.6283940247	3.6325874987
O22	-3.1058497131	7.8423265837	2.8722328757
O23	-1.5383034069	10.6070016845	2.8162988193
O24	-0.8699847405	7.9277615992	3.0513087760
C25	-1.9387965771	7.5764453490	2.4712827805
C26	-2.7321266405	11.0228530316	2.8398712988
C27	-1.7956356120	6.7804254105	1.1957932905
C28	-3.0952770694	12.1109103298	1.8566223781
H29	-1.5637943581	7.4756972475	0.3828323435
H30	-2.7739504544	13.0723696212	2.2693825315
H31	-2.5647462133	11.9578449664	0.9163926641
H32	-0.9634726999	6.0807036815	1.2839132905
H33	-2.7185989716	6.2537646823	0.9572117841

H34	-4.1714750244	12.1417812399	1.6928544861
H35	1.0806089695	10.9990395213	2.1372550488
H36	1.4454759441	9.3580096711	1.4330305240
H37	1.8316814285	7.4484653552	2.4011670162
H38	1.4793978819	7.1229775707	4.1533313100
H39	3.9037557257	9.7817721126	1.7031825535
H40	3.5349181136	11.4300875568	2.4212171898
H41	3.8898921103	7.5754018837	4.7214146029
H42	4.2393311966	7.8911428234	2.9475990329
X43	2.6383999999#	10.9009500001#	3.4390500000#
X44	2.5943000000#	8.1144000000#	2.5217500000#
X45	2.8556636123#	10.3222815147#	2.1974555665#
X46	2.6584660414#	7.5284850813#	3.4905297092#
Rh47	-3.6310176896	8.8014337144	4.7159557209
C48	-2.4790438954	10.9281668767	8.9507924726
C49	-2.3607403872	11.5911459701	7.7313937059
C50	-2.8557996900	11.0219945768	6.5599673072
C51	-3.4313725621	9.7451577420	6.5813046062
C52	-3.6035570720	9.1098505700	7.8223694093
C53	-3.1153275498	9.6877028566	8.9922203323
H54	-2.0950511490	11.3777097681	9.8602089404
H55	-1.8757139521	12.5598422333	7.6813178857

H56	-2.7469490995	11.5557165810	5.6299045626
H57	-4.1136969642	8.1568684902	7.8897081049
H58	-3.2415963030	9.1692608471	9.9372808671
H59	-4.7973976101	9.4467063788	5.7052893218
C60	-4.3506493268	6.8679169907	5.4059555557
C61	-2.9855834478	6.9407829739	5.6456470547
H62	-4.7309693137	6.3927085343	4.5073108372
H63	-2.2717860149	6.5366069202	4.9386952852
H64	-2.5801755795	7.1289369862	6.6291910822
H65	-5.0692076396	6.9841474204	6.2096267807
X66	-2.9534332716#	6.8658886657#	6.0249908487#

4c

Rh1	2.0647758368000	9.3131386819000	4.5130919657000
Cu2	-0.5287510426000	9.8399674806000	3.1052134441000
O3	0.8590906872000	9.8717846875000	6.1903052799000
O4	2.1290170742950	11.3867856204626	4.2364983564370
O5	-1.0993033745000	9.3442446346000	5.2760340811000
O6	0.0837379948000	11.6773447886000	3.3441631666000
C7	2.6913733008000	8.9731123620000	2.4798071995000
C8	1.1907703728975	12.1023148927610	3.7812981293483
C9	1.3328395896000	7.2860068666000	4.6192253557000
C10	-0.4046558605000	9.8455230402000	6.2095527350000

C11	3.8191060100000	9.0433218998000	3.2959278699000
C12	1.4018081658349	13.6003103718914	3.7668452019887
C13	2.4037564774000	7.4237741499000	5.4987329215000
C14	-1.0973925768000	10.4540711074000	7.4080500841000
H15	0.7644478791369	14.0486624758188	4.5347806813324
H16	-0.4036792767000	11.0629631443000	7.9855872751000
H17	-1.4824779165000	9.6581416989000	8.0513550639000
H18	1.0968739726595	14.0084326654386	2.8012933875828
H19	2.4400467079587	13.8536149493637	3.9751687112894
H20	-1.9443251949000	11.0543237283000	7.0705053924000
O21	-3.3922736961000	11.3801683393000	4.6451441505000
O22	-3.4413972769000	8.8377892060000	2.7513428214000
O23	-3.2956311159000	11.4813504510000	2.4042212584000
O24	-1.3363671306000	8.3170485264000	2.1820934842000
C25	-2.5669265615000	8.0995821618000	2.1553556001000
C26	-3.2283457499000	12.0212853567000	3.6096048963000
C27	-3.0928523977000	6.9175286729000	1.3836385151000
C28	-2.8846026082000	13.4759224059000	3.5985181594000
H29	-2.2910873855000	6.4074582496000	0.8522186465000
H30	-1.8058550226000	13.5357771260000	3.4238635657000
H31	-3.3930713480000	13.9924297310000	2.7835245972000
H32	-3.5731711083000	6.2264321726000	2.0821376487000

H33	-3.8612551710000	7.2520885134000	0.6824465108000
H34	-3.1247034859000	13.9291492447000	4.5582005197000
H35	2.3542067625000	9.8435265249000	1.9276814866000
H36	2.3348291629000	8.0241284067000	2.0964017009000
H37	1.4543467115000	6.7650610317000	3.6761023521000
H38	0.3078331632000	7.3891230124000	4.9536812102000
H39	4.3672260855000	8.1449006622000	3.5599887109000
H40	4.3726808729000	9.9721370627000	3.3927670860000
H41	2.2354109263000	7.6306907317000	6.5510184293000
H42	3.3763990226000	7.0078685611000	5.2582287902000
X44	2.5943000000000	8.1144000000000	2.5217500000000
X45	2.8770410000000	10.2574380000000	2.5011240000000
X46	2.0974430000000	7.6045910000000	3.6964660000000
Rh47	-3.3450565823000	9.0932030405000	4.9242687132000
H48	-3.3969996560000	10.4918574274000	2.4707726475000
X67	3.2552396554000	9.0082171309000	2.8878675347000
X68	1.8682980335000	7.3548905082500	5.0589791386000
C48	-3.3826578610687	9.1793857851495	9.9232465334431
C49	-3.9416296218452	10.1764770562219	9.1229635918432
C50	-3.8818787306899	10.0869373015975	7.7319181504953
C51	-3.2500640000000	8.9994590000000	7.1050020000000
C52	-2.7042110342392	7.9992770047287	7.9198384234945

C53	-2.7679319101191	8.0874111250842	9.3130451965129
H54	-3.4321118049714	9.2486574601281	11.0048564100562
H55	-4.4338350898294	11.0288662218556	9.5823693507815
H56	-4.3354672042969	10.8691645095747	7.1353046628192
H57	-2.2243288938711	7.1309467086601	7.4825217807433
H58	-2.3383803167013	7.2954892504920	9.9195741036958
C60	-4.3316910000000	7.0016750000000	4.8331110000000
C61	-2.9995000000000	6.7508720000000	5.1248480000000
H62	-4.6750690000000	7.0327230000000	3.8051360000000
H63	-2.2892610000000	6.5701710000000	4.3251790000000
H64	-2.7006830000000	6.4285050000000	6.1149700000000
H65	-5.1039950000000	6.8576480000000	5.5781740000000
X66	-3.6655950000000	6.8762730000000	4.9789790000000

TS4.2

Rh1	2.0373898481	9.7065887541	4.0627034479
Cu2	-0.6216495041	10.0818820789	3.5231868902
O3	1.4137774153	9.0530038915	5.9760902607
O4	1.8699354029	11.6889312591	4.7160363399
O5	-0.7093118465	8.8775323377	5.3486321882
O6	-0.3198617475	11.8427755765	4.2699777499
C7	1.9599752585	10.5095751803	2.0165616930
C8	0.7623153754	12.3009990111	4.7420078247

C9	1.6562116558	7.6627409229	3.3080620518
C10	0.2001446860	8.7482869954	6.2085299860
C11	3.2857602808	10.4166847569	2.4088848655
C12	0.7187949980	13.6544007775	5.3957624334
C13	2.9165237122	7.7015246400	3.8711911061
C14	-0.1514268035	8.1862417592	7.5600733150
H15	0.4724302702	13.5120886101	6.4527591273
H16	0.6570464066	8.3376998004	8.2742648163
H17	-0.3402689885	7.1128609452	7.4479940737
H18	-0.0602676637	14.2685488658	4.9438962694
H19	1.6902449359	14.1437090174	5.3326636493
H20	-1.0770845941	8.6471562085	7.9077439799
O21	-2.6473017850	10.2565817310	3.8483128034
O22	-2.2961454595	7.3352895271	3.2605275149
O23	-4.8305318769	10.1353139612	3.5655343412
O24	-0.8672031360	8.7200634131	2.2037968411
C25	-1.5947260297	7.6609301981	2.2937757979
C26	-3.7263125500	10.6843057951	3.3182945657
C27	-1.5251979811	6.7342855867	1.0996951609
C28	-3.6500855675	11.8417692571	2.3664570735
H29	-1.3701099595	7.2946099386	0.1826812459
H30	-3.3317589906	11.4616170878	1.3915403537

H31	-4.6212504908	12.3207863831	2.2549337318
H32	-0.6742599709	6.0661137674	1.2356607246
H33	-2.4264794231	6.1294060545	1.0343819132
H34	-2.9017439747	12.5534375033	2.7128715172
H35	1.4357188939	11.4563193218	2.0881965246
H36	1.5053120781	9.7813922896	1.3566934499
H37	1.5192024533	7.6887469485	2.2353040885
H38	0.7936722571	7.3318473783	3.8716978832
H39	3.9166060979	9.6161655876	2.0400934429
H40	3.8076807240	11.2801620801	2.8089895633
H41	3.0746056207	7.4102222691	4.9040168072
H42	3.8047887074	7.7441419863	3.2514538526
X43	2.6383999998#	10.9009500002#	3.4390499999#
X44	2.5943000001#	8.1144000001#	2.5217500000#
X45	2.8770408244#	10.2574380178#	2.5011237168#
X46	2.0974428772#	7.6045906335#	3.6964658939#
Rh47	-3.0105720308	8.4393012563	5.1280464808
C48	-3.9503682743	11.2700648995	8.9404328805
C49	-2.9849319420	11.5816043723	7.9834212712
C50	-2.7738784310	10.7402165958	6.8922132677
C51	-3.5128482074	9.5516232684	6.7236269107
C52	-4.4843894485	9.2621327416	7.6949425308

C53	-4.7013977491	10.1057047351	8.7853106642
H54	-4.1177080572	11.9245896070	9.7881991304
H55	-2.3942403862	12.4870611479	8.0837125441
H56	-2.0245894603	11.0161224490	6.1610458144
H57	-5.0930377825	8.3690937337	7.6177352442
H58	-5.4632847928	9.8495852122	9.5144053474
H59	-4.4378539674	9.1046361526	4.4115978957
C60	-4.6110548849	7.0600682047	5.2693757291
C61	-3.5128968437	6.6250022028	6.0496393335
H62	-4.7710969508	6.6226210795	4.2918764189
H63	-2.8516406862	5.8595202553	5.6571054129
H64	-3.5494172648	6.6866957829	7.1308227127
H65	-5.5094497417	7.4432505018	5.7369353307
X66	-3.4463413410#	6.6898271182#	5.7518292191#

TS4.1'

Rh1	-0.5117062237	11.0218986886	9.2498158700
Cu2	-1.3544405124	11.2075806344	6.4420409193
O3	-1.7999108564	9.3251659401	9.3619215697
O4	-2.2127578899	12.3088664966	9.3843567353
O5	-2.2988959853	9.1684065050	7.2047513955
O6	-2.6393628225	12.4910376655	7.1862648661

C7	0.6088847845	12.7254875579	8.5606059839
C8	-2.8855721408	12.7314632158	8.4020141852
C9	0.9786403799	9.6968434111	8.4475792111
C10	-2.3982135127	8.7655683092	8.4010741885
C11	0.6403967286	12.6950569765	9.9539598755
C12	-4.0861494004	13.6052079833	8.6953794548
C13	1.0639776164	9.6696906716	9.8377287861
C14	-3.2402279657	7.5553506233	8.7324727446
H15	-4.9528610528	13.2285370150	8.1477361983
H16	-3.4214379374	7.5035265827	9.8043605237
H17	-2.7025489057	6.6559304686	8.4219804991
H18	-3.8853272788	14.6166052972	8.3321770041
H19	-4.2997679092	13.6402959431	9.7620246617
H20	-4.1835207483	7.5916046014	8.1900725636
O21	-2.9129429336	10.8361520209	4.7193797395
O22	-1.0438390982	8.4491280763	4.5314476256
O23	-5.0597902891	11.0780271821	4.1796374519
O24	0.0235997136	10.2180992828	5.4590710963
C25	-0.0178563351	9.1523639703	4.7953930055
C26	-3.8704253682	11.5438933426	4.3223004753
C27	1.3050831783	8.6349397089	4.2629819666
C28	-3.6307019107	12.9943252195	4.0435558744

H29	1.8340315336	9.4419673971	3.7525249441
H30	-2.7426761252	13.1050020799	3.4200189097
H31	-4.4939957021	13.4633656795	3.5762135599
H32	1.9229493936	8.3227044986	5.1096310287
H33	1.1630752264	7.7919392213	3.5888719926
H34	-3.4182517766	13.4608993834	5.0099571635
H35	-0.1022207183	13.3510935336	8.0334394387
H36	1.4726052967	12.4305201593	7.9764139019
H37	1.7038622170	10.2308110965	7.8458887744
H38	0.4119860272	8.9515670453	7.9026375372
H39	1.5344777113	12.3825650679	10.4820495109
H40	-0.0576582415	13.2904076494	10.5336717863
H41	0.5648717570	8.8923042101	10.4073230773
H42	1.8716668701	10.1779632444	10.3536077184
X43	2.6383999998#	10.9009500002#	3.4390499999#
X44	2.5943000001#	8.1144000001#	2.5217500000#
X45	2.5825683226#	10.4512856260#	2.1173739141#
X46	2.6635270613#	7.6605020685#	3.4769305490#
Rh47	-3.0961782104	8.7165681613	5.1359229832
C48	-7.3893126587	8.8429294387	7.4709016904
C49	-6.3672990272	9.7518037009	7.7528350581
C50	-5.2337959594	9.7935119090	6.9504721653

C51	-5.0757449229	8.9289615963	5.8394488073
C52	-6.1371788585	8.0412624956	5.5672864719
C53	-7.2758555736	7.9950924762	6.3698362350
H54	-8.2729112715	8.8047366550	8.0986809407
H55	-6.4555691432	10.4252884319	8.5986385360
H56	-4.4531651044	10.5141971821	7.1689915920
H57	-6.0857933196	7.3804055053	4.7095981894
H58	-8.0747269841	7.2996907632	6.1339518861
H59	-5.0567414375	9.9715341315	4.7611653704
C60	-3.3493914278	6.7728926168	4.1944189807
C61	-3.1359168703	6.5628576508	5.5480555091
H62	-2.5218868311	6.7213426065	3.4957970258
H63	-2.1424480883	6.3326928525	5.9138930846
H64	-3.9632372849	6.3241297523	6.2033448146
H65	-4.3431309030	6.7046088586	3.7668464785
X66	-3.4074037590#	6.8390054744#	5.8798962600#
X67	0.6099777664#	12.6311081989#	9.1971362772#
X68	0.8557633633#	9.6303641676#	9.1046284193#
X69	-3.1565336914#	6.5833954627#	4.9389526294#

4d

Rh1	2.1339590711	9.3090184226	4.3122841625
Cu2	-0.5160577983	9.8521879708	3.1307105207

O3	1.0419732925	10.0151534139	6.0082810248
O4	2.2890261226	11.3511003625	3.7363631501
O5	-0.9784368558	9.4130964843	5.3068970520
O6	0.0921134586	11.7042313410	3.4181196003
C7	2.5918833494	8.8332145386	2.2617449297
C8	1.2808513661	12.1009074292	3.5754408137
C9	1.3860275490	7.3059122792	4.6076725228
C10	-0.2168122555	10.0212506714	6.1255242753
C11	3.7816202509	8.9111750134	2.9830606116
C12	1.5188411250	13.5944783760	3.5941672911
C13	2.5149633175	7.4882997259	5.4024259114
C14	-0.7925161562	10.8092478007	7.2748975695
H15	1.2366745991	13.9752734196	4.5808064465
H16	-0.0953634034	11.5936515079	7.5673660816
H17	-0.9504608679	10.1454480419	8.1274155452
H18	0.8917239219	14.0873330273	2.8498649307
H19	2.5692904024	13.8247649490	3.4220795260
H20	-1.7600211672	11.2246176773	6.9995630491
O21	-3.3405615817	11.1810597679	5.0447368044
O22	-3.3896734952	8.8636106884	2.7952421817
O23	-3.2993943447	11.4826564387	2.8178644716
O24	-1.3227043813	8.4370752860	2.0519447079

C25	-2.5622035235	8.2464554983	2.0343692901
C26	-3.1986073745	11.9085021849	4.0555631364
C27	-3.1256005212	7.2114737749	1.0927145231
C28	-2.8417736598	13.3524646447	4.1826184810
H29	-2.3631625243	6.8520270563	0.4038861348
H30	-1.7635524027	13.4112682591	3.9995517609
H31	-3.3502405653	13.9505840165	3.4257641494
H32	-3.5078049663	6.3704573387	1.6801035541
H33	-3.9704581145	7.6319437001	0.5434143022
H34	-3.0636841840	13.7131966101	5.1847637979
H35	2.2363117115	9.6835501853	1.6900865351
H36	2.1763056068	7.8775577843	1.9639835823
H37	1.4395233139	6.7187353642	3.6974878744
H38	0.3891462587	7.4469091870	5.0060214948
H39	4.3221859485	8.0114589158	3.2580305740
H40	4.3679803712	9.8247199111	2.9825807967
H41	2.4183656183	7.7703103091	6.4463588433
H42	3.4661304086	7.0439146992	5.1294374513
X44	2.5942999997#	8.1143999987#	2.5217500003#
X45	2.8770410004#	10.2574379986#	2.5011240003#
X46	2.0974429994#	7.6045909989#	3.6964660003#
Rh47	-3.2216238569	8.9679146368	5.1540857461

H48	-3.3839748189	10.4819070021	2.7782329171
X67	3.2552396553#	9.0082171294#	2.8878675351#
X68	1.8682980328#	7.3548905072#	5.0589791389#
C48	-4.2055292348	9.3045157769	9.8617176219
C49	-4.8768349464	10.0686791259	8.9076669913
C50	-4.5614053344	9.9434173408	7.5531088374
C51	-3.5706085018	9.0496571540	7.1269465350
C52	-2.9062727343	8.2836253046	8.0913003627
C53	-3.2178087189	8.4129070905	9.4468512835
H54	-4.4485280022	9.4042698802	10.9140906087
H55	-5.6462600841	10.7700550768	9.2151335104
H56	-5.0808920639	10.5660513019	6.8331082914
H57	-2.1185025136	7.5963279288	7.8071706358
H58	-2.6822533718	7.8145540138	10.1775783290
C60	-4.0290557111	6.9401642363	5.1433881549
C61	-2.6439958962	6.8677908393	5.1083113364
H62	-4.6087092708	6.8958675954	4.2267190802
H63	-2.1050692048	6.7476113722	4.1755917018
H64	-2.0797241007	6.6188711679	5.9973331120
H65	-4.5678412358	6.7517876230	6.0649350040
X66	-3.6655950010#	6.8762730008#	4.9789789999#

TS4.3

Rh1	2.1750900746	9.5123749142	4.0517863486
Cu2	-0.6127680815	10.0161434872	3.3724784062
O3	1.3997251088	8.9069340967	5.9389303777
O4	1.9370440631	11.5592787083	4.6140956026
O5	-0.7723540997	9.0111969064	5.4427430623
O6	-0.2021541115	11.8391564596	3.9818696559
C7	2.3160053151	10.2050004510	2.0193409250
C8	0.8754125684	12.2386067894	4.5041833124
C9	1.6959807923	7.5374999546	3.3585274761
C10	0.1774119521	8.7779293777	6.2396681746
C11	3.5905521726	10.1970341646	2.5832700730
C12	0.8860624129	13.6413313540	5.0720761019
C13	2.9728950189	7.5122493425	3.9155918787
C14	-0.1234720515	8.2981573331	7.6448989880
H15	0.3532658297	13.6290926588	6.0277741789
H16	0.7632295086	8.3613550831	8.2727957273
H17	-0.4448758846	7.2541289997	7.6041137746
H18	0.3531343512	14.3201953846	4.4049590670
H19	1.9033791261	13.9907917566	5.2411601461
H20	-0.9358563337	8.8827655245	8.0771852283

O21	-3.0550623069	10.3076970069	3.7949425815
O22	-2.5924774916	7.4078751570	3.3191598903
O23	-4.4993974075	11.9084299855	4.4343390262
O24	-1.0412321580	8.5582095495	2.1481119002
C25	-1.8579988138	7.6133040324	2.3083587400
C26	-3.5525911084	11.4240189601	3.6491864468
C27	-1.9439398074	6.5859277949	1.1941463825
C28	-3.0953985962	12.3442385339	2.5683660593
H29	-1.6549400666	7.0261684573	0.2403079572
H30	-3.0460790618	11.7959861357	1.6272417848
H31	-3.7404913318	13.2156670923	2.4784364100
H32	-1.2463608626	5.7736541793	1.4215398907
H33	-2.9464494776	6.1623734834	1.1333239566
H34	-2.0756533935	12.6456662509	2.8275264075
H35	1.7324820558	11.1175297710	1.9817212449
H36	2.0071102562	9.4414035828	1.3157011594
H37	1.5432537161	7.5211794384	2.2866542895
H38	0.8244328282	7.2495154854	3.9348408206
H39	4.3089605871	9.4292084440	2.3175128527
H40	4.0126389618	11.1053685332	3.0014670858
H41	3.1217193691	7.2003966964	4.9442629683
H42	3.8522051776	7.4622472302	3.2824299228

X43	2.6384000003#	10.9009500000#	3.4390500012#
X44	2.5943000005#	8.1144000001#	2.5217500007#
X45	2.8770408251#	10.2574380179#	2.5011237181#
X46	2.0974428773#	7.6045906334#	3.6964658945#
Rh47	-3.0776516771	8.5657059198	5.1405087616
H59	-4.6737767566	11.2916387537	5.1764211883
C2	-2.8375485176	6.5180403651	5.9084117868
H3	-3.4329085391	5.9069191559	5.2409701303
C4	-3.4169514599	7.2364106875	6.9286450597
H5	-2.8375994062	7.6279091140	7.7526636489
H6	-4.4864069398	7.1869365244	7.0984997054
H7	-1.7688055205	6.3452062382	5.8704257151
C55	-4.6879757450	11.9085286387	8.2596074714
C56	-3.3280617617	11.7912629968	7.9670786207
C57	-2.8666184807	10.7707050307	7.1356036768
C58	-3.7555207256	9.8391077658	6.5767326483
C59	-5.1197250019	9.9622818356	6.8860036178
C60	-5.5837103787	10.9919944183	7.7143577365
H14	-5.0444699513	12.7059335071	8.9018788865
H62	-2.6220840960	12.5055831199	8.3788861765
H63	-1.8154233048	10.7238467546	6.8815422772
H64	-5.8372730980	9.2527740064	6.4854763840

H65	-6.6446225280	11.0707676133	7.9288231051
X	-3.2856520008#	7.2160449999#	6.5682499989#

4e

Rh1	2.0923837488	9.3169682522	4.4222116542
Cu2	-0.5244306853	9.7877506442	3.1696315787
O3	0.9551232232	9.8028557051	6.1699650614
O4	2.1746242523	11.3994702983	4.0150686878
O5	-1.0482745524	9.3471572178	5.3105802941
O6	0.0367511626	11.6727206915	3.3660396600
C7	2.6071794709	9.0389429266	2.3390338530
C8	1.1704806862	12.1078043067	3.7109787244
C9	1.3778543263	7.2823954084	4.5123083516
C10	-0.3073316203	9.7957742859	6.2373676082
C11	3.7791839818	9.0895574882	3.0912437574
C12	1.3427403412	13.6110665542	3.7655413134
C13	2.4905030267	7.3944527444	5.3419150926
C14	-0.9444305558	10.3613068428	7.4854039437
H15	0.7900712553	13.9920803066	4.6294100542
H16	-0.1985283850	10.8309718093	8.1240357950
H17	-1.4406317948	9.5606096993	8.0393386732
H18	0.9168635198	14.0665227478	2.8698061076
H19	2.3914115729	13.8847242398	3.8689273754

H20	-1.7126175880	11.0813842544	7.1968088501
O21	-3.4272228889	11.3244893502	4.7693141890
O22	-3.3941342941	8.9030256561	2.8333065096
O23	-3.2575405730	11.4960641103	2.5358032459
O24	-1.3419444695	8.2783496490	2.1969019470
C25	-2.5822266161	8.1158416358	2.2180502487
C26	-3.2319462777	11.9951831255	3.7524747115
C27	-3.1882623369	6.9503807984	1.4783220501
C28	-2.9117049173	13.4542966543	3.8078526007
H29	-2.4211082994	6.3495290489	0.9934986914
H30	-1.8343385356	13.5380799793	3.6361834217
H31	-3.4262694677	13.9955415139	3.0129098433
H32	-3.7535108451	6.3342393000	2.1821329308
H33	-3.8985551895	7.3255491337	0.7371058629
H34	-3.1625031178	13.8629215156	4.7843440149
H35	2.2378870407	9.9230465996	1.8317049370
H36	2.2312582949	8.0989576825	1.9524473423
H37	1.4522375465	6.7911598715	3.5487782390
H38	0.3715740969	7.3624060140	4.9046937458
H39	4.3396581177	8.1828541331	3.2936915090
H40	4.3367578057	10.0166703604	3.1793409604
H41	2.3726449615	7.5672828637	6.4069996817

H42	3.4516490211	6.9928692990	5.0390288971
X44	2.5943000000#	8.1144000000#	2.5217500000#
X45	2.8770410000#	10.2574380000#	2.5011240000#
X46	2.0974430000#	7.6045910000#	3.6964660000#
Rh47	-3.3478466429	9.1218215753	5.0905089206
H48	-3.3381500268	10.4964184936	2.5699845898
H49	-3.8920734085	6.4957386343	4.7426707390
C50	-7.4944543319	6.8662320293	8.2793016049
C51	-7.3581037633	7.1041628098	6.9095915042
C52	-6.1021418584	7.3397159057	6.3600569536
C53	-4.9555726887	7.3334952316	7.1675197535
C54	-5.1051739338	7.1082677084	8.5412489876
C55	-6.3634507109	6.8709275889	9.0936558673
H56	-8.4749598402	6.6854517804	8.7058108662
H57	-8.2349647002	7.1137718181	6.2707766760
H58	-6.0127971092	7.5447405363	5.2981302577
H59	-4.2293143501	7.1126916873	9.1828797761
H60	-6.4579033376	6.6930540683	10.1596094114
C61	-3.5877290864	7.5432738353	6.6157080063
H62	-2.8187923146	7.6275070921	7.3780502878
H63	-3.5739982312	9.3622238461	6.5959771413
C64	-3.1819853212	7.0416211830	5.3574388849

H65	-2.1409293106	6.7770216118	5.2031903256
X66	-3.4310660286#	7.3657532165#	6.0458595796#
X67	3.2552396554#	9.0082171309#	2.8878675347#
X68	1.8682980335#	7.3548905082#	5.0589791386#

TS4.4

Rh1	2.0647758368000	9.3131386819000	4.5130919657000
Cu2	-0.5287510426000	9.8399674806000	3.1052134441000
O3	0.8590906872000	9.8717846875000	6.1903052799000
O4	2.1290170742950	11.3867856204626	4.2364983564370
O5	-1.0993033745000	9.3442446346000	5.2760340811000
O6	0.0837379948000	11.6773447886000	3.3441631666000
C7	2.6913733008000	8.9731123620000	2.4798071995000
C8	1.1907703728975	12.1023148927610	3.7812981293483
C9	1.3328395896000	7.2860068666000	4.6192253557000
C10	-0.4046558605000	9.8455230402000	6.2095527350000
C11	3.8191060100000	9.0433218998000	3.2959278699000
C12	1.4018081658349	13.6003103718914	3.7668452019887
C13	2.4037564774000	7.4237741499000	5.4987329215000
C14	-1.0973925768000	10.4540711074000	7.4080500841000
H15	0.7644478791369	14.0486624758188	4.5347806813324
H16	-0.4036792767000	11.0629631443000	7.9855872751000
H17	-1.4824779165000	9.6581416989000	8.0513550639000

H18	1.0968739726595	14.0084326654386	2.8012933875828
H19	2.4400467079587	13.8536149493637	3.9751687112894
H20	-1.9443251949000	11.0543237283000	7.0705053924000
O21	-3.3922736961000	11.3801683393000	4.6451441505000
O22	-3.4413972769000	8.8377892060000	2.7513428214000
O23	-3.2956311159000	11.4813504510000	2.4042212584000
O24	-1.3363671306000	8.3170485264000	2.1820934842000
C25	-2.5669265615000	8.0995821618000	2.1553556001000
C26	-3.2283457499000	12.0212853567000	3.6096048963000
C27	-3.0928523977000	6.9175286729000	1.3836385151000
C28	-2.8846026082000	13.4759224059000	3.5985181594000
H29	-2.2910873855000	6.4074582496000	0.8522186465000
H30	-1.8058550226000	13.5357771260000	3.4238635657000
H31	-3.3930713480000	13.9924297310000	2.7835245972000
H32	-3.5731711083000	6.2264321726000	2.0821376487000
H33	-3.8612551710000	7.2520885134000	0.6824465108000
H34	-3.1247034859000	13.9291492447000	4.5582005197000
H35	2.3542067625000	9.8435265249000	1.9276814866000
H36	2.3348291629000	8.0241284067000	2.0964017009000
H37	1.4543467115000	6.7650610317000	3.6761023521000
H38	0.3078331632000	7.3891230124000	4.9536812102000
H39	4.3672260855000	8.1449006622000	3.5599887109000

H40	4.3726808729000	9.9721370627000	3.3927670860000
H41	2.2354109263000	7.6306907317000	6.5510184293000
H42	3.3763990226000	7.0078685611000	5.2582287902000
X44	2.5943000000000	8.1144000000000	2.5217500000000
X45	2.8770410000000	10.2574380000000	2.5011240000000
X46	2.0974430000000	7.6045910000000	3.6964660000000
Rh47	-3.3450565823000	9.0932030405000	4.9242687132000
H48	-3.3969996560000	10.4918574274000	2.4707726475000
H49	-4.1002640437000	6.3993009555000	5.0079482374000
C50	-7.3562445508000	6.7217300536000	8.4608883703000
C51	-7.3093210859000	7.5990226313000	7.3773672018000
C52	-6.0840151905000	7.9375658751000	6.8067669772000
C53	-4.8920259815000	7.4043789964000	7.3055177542000
C54	-4.9467158346000	6.5286318735000	8.3941195800000
C55	-6.1712986136000	6.1883470127000	8.9679454505000
H56	-8.3080483181000	6.4602100117000	8.9100722528000
H57	-8.2248760542000	8.0252586110000	6.9807859521000
H58	-6.0503088342000	8.6306461774000	5.9706353479000
H59	-4.0284865109000	6.1091989814000	8.7939988464000
H60	-6.1988068047000	5.5088216855000	9.8130994857000
C61	-3.5640044826000	7.7256347068000	6.6626830852000
H62	-2.7350940070000	7.6051154324000	7.3635266658000

H63	-3.5579446361000	9.4027865560000	6.4887888937000
C64	-3.2981275747000	7.0058717262000	5.4290360739000
H65	-2.3166370439000	6.5499250226000	5.3073860505000
X66	-3.4310660286500	7.3657532165000	6.0458595795500
X67	3.2552396554000	9.0082171309000	2.8878675347000
X68	1.8682980335000	7.3548905082500	5.0589791386000

4f

Rh1	2.0432947677	9.3050678188	4.4872837005
Cu2	-0.4712288285	9.8647407297	3.1150180703
O3	0.8145794890	9.6919901669	6.1916097947
O4	2.1749511746	11.4050332653	4.1852246372
O5	-1.1645682540	9.3939968067	5.2196403111
O6	0.1097928420	11.7219798865	3.3512568186
C7	2.6760862729	9.1015717716	2.4371800152
C8	1.2201134222	12.1356466723	3.7895411982
C9	1.3019084830	7.2803961034	4.4611419426
C10	-0.4473903213	9.6740513813	6.2308229705
C11	3.8026534828	9.1271646298	3.2569070957
C12	1.4189564306	13.6338332409	3.8575021947
C13	2.3907686429	7.3457524503	5.3267396087
C14	-1.1080217183	10.0060739743	7.5470579939
H15	0.8191992205	14.0263078390	4.6840871868

H16	-0.3623878559	10.2664096676	8.2961973056
H17	-1.6928119213	9.1488376721	7.8887456063
H18	1.0627067820	14.0983949420	2.9363812376
H19	2.4645193243	13.8842164671	4.0293644293
H20	-1.8046430216	10.8341840006	7.4014623555
O21	-3.3685794349	11.3526016495	4.5538622546
O22	-3.3046910645	8.7287028383	2.6242544521
O23	-3.2018096002	11.3335115877	2.3118897245
O24	-1.1580121202	8.3181590000	2.1325165782
C25	-2.3773606409	8.0298337510	2.0809160123
C26	-3.1909887921	11.9361607446	3.4780642807
C27	-2.7976655797	6.7769662650	1.3510833357
C28	-2.8954524470	13.3982952623	3.4147332565
H29	-1.9550209378	6.3211323995	0.8336136206
H30	-1.8098816209	13.4821491188	3.3004409450
H31	-3.3694818817	13.8562166311	2.5460408518
H32	-3.2090512781	6.0658530485	2.0743520073
H33	-3.5954885101	7.0149875127	0.6441837829
H34	-3.2037749275	13.8885966219	4.3358401396
H35	2.3327169292	10.0022948171	1.9405057074
H36	2.3242051504	8.1768050435	1.9951366895
H37	1.3969707183	6.8320093488	3.4790570683

H38	0.2845540966	7.3587376626	4.8250078891
H39	4.3567537780	8.2178150860	3.4641605042
H40	4.3493056741	10.0520790031	3.4127377294
H41	2.2436613710	7.4734534861	6.3947802632
H42	3.3552616008	6.9427791488	5.0360196793
X44	2.5943000000#	8.1144000000#	2.5217500000#
X45	2.8770410000#	10.2574380000#	2.5011240000#
X46	2.0974430000#	7.6045910000#	3.6964660000#
Rh47	-3.4099077018	9.1856415321	4.9456070941
H48	-3.2648572283	10.3320329756	2.4072615620
X67	3.2552396554#	9.0082171309#	2.8878675347#
X68	1.8682980335#	7.3548905082#	5.0589791386#
C60	-4.4856925096	7.3283481510	5.1986174853
C61	-3.1315881875	7.1010331259	5.4300741876
H62	-4.9198920796	7.1184681551	4.2255939126
H63	-2.4921074294	6.6932095831	4.6545633552
H64	-2.7512692219	7.0060183581	6.4406777993
H65	-5.1825877108	7.4102837229	6.0258271401
X66	-3.6655950000#	6.8762730000#	4.9789790000#
H57	-3.7111413930	9.4743174565	6.4185134534

Scheme 7 Structures

1b

Rh1	-0.4317567058	9.0896701831	4.7041434711
C3	-0.1215229324	7.7114660155	6.3223500937
C4	-0.0820395642	10.7522087991	6.0153223772
C5	0.9563629488	7.6162805386	5.4442299991
C6	1.0012651090	10.6212053699	5.1441462341
Rh7	-3.8009485144	8.9026513764	4.8915906558
O8	-3.3532423108	10.7310057944	3.9144719555
O9	-3.2830516707	7.9672602936	3.0834694001
O10	-1.1992024552	10.4947497722	3.3017055033
O11	-1.1167431993	7.4901619053	3.4602234544
C12	-3.6030166013	6.9710823746	5.7899765293
C13	-2.1765553562	7.4375532009	2.7764545184
C14	-2.3455534295	11.0209455891	3.2157259679
C15	-4.9152653813	7.1232304130	5.3335052265
C16	-2.1333857340	6.6335787201	1.4963974887
C17	-2.5255290863	12.0936661960	2.1629355895
H18	-1.1988241916	6.8273847359	0.9684153912
H19	-3.3010033696	12.7976555362	2.4647851434
H20	-1.5852308320	12.6096845276	1.9684672180
H21	-2.1567680164	5.5703652009	1.7543148422
H22	-2.9890690906	6.8617392284	0.8625488676
H23	-2.8493743349	11.6087536664	1.2364374636

H24	-0.9407081790	7.0064258095	6.2638044053
H25	-0.0155667153	8.2155599355	7.2771578889
H26	0.0094029878	10.4594040392	7.0559902138
H27	-0.8712001199	11.4627143335	5.8039584711
H28	1.9196495361	8.0451227719	5.6969796999
H29	0.9746138041	6.8531930838	4.6739472423
H30	1.0531854215	11.2168754662	4.2391438071
H31	1.9477237445	10.2198840273	5.4892650709
H32	-3.3720210563	7.0226134773	6.8486771328
H33	-2.8747413847	6.4306183843	5.1964402527
H34	-5.2188189561	6.7096439337	4.3777252677
H35	-5.7235644463	7.2982444843	6.0373148561
X36	-0.0390639581#	7.4856943008#	5.7251781396#
X37	0.1848845976#	10.4074529351#	5.8642810549#
X38	-3.8753000000#	7.1838000000#	5.8009500000#
C39	-3.2156396432	10.7740319908	7.2914219931
C40	-3.4041362755	12.0584865123	6.8371543997
C41	-4.5617555127	12.3911756764	6.0993407393
C42	-5.5085929273	11.4338597119	5.8163861037
C43	-5.3242835105	10.0991519400	6.2550662741
C44	-4.1735968954	9.7639796560	7.0072085892
H45	-2.3452174446	10.5202697695	7.8832758308

H46	-2.6687678114	12.8253329369	7.0534171600
H47	-4.7021112506	13.4112758239	5.7591726997
H48	-6.4002475928	11.6890953250	5.2562076726
H49	-6.1629885581	9.4188925388	6.1987998302
H50	-4.1484615464	8.8535983572	7.5918121093

TS1.1

Rh1	-0.3469371945	8.9938635532	4.4851860952
C3	-0.0496477928	7.4659733430	5.9827469364
C4	-0.1371244243	10.5210332754	5.9962929191
C5	1.0679480579	7.4992939824	5.1465193679
C6	0.9873635133	10.5453686233	5.1780345507
Rh7	-3.6206986982	8.9329143397	5.0135594481
O8	-3.2885129208	10.7408905917	3.9585330630
O9	-3.2622002302	7.9181874161	3.1475226623
O10	-1.1847179510	10.4815236148	3.2237602683
O11	-1.0648161799	7.4810922002	3.1896376336
C12	-3.5301201368	6.9469413852	5.8705607215
C13	-2.2203720590	7.3876048354	2.6826979393
C14	-2.3186466642	11.0288839212	3.2071699798
C15	-4.8602637013	7.2379035940	5.5712855455
C16	-2.3397019465	6.5580568001	1.4208128142
C17	-2.5420877520	12.1321699862	2.1962291844

H18	-1.6153263354	6.9181212958	0.6807157892
H19	-3.0830555312	12.9595795118	2.6540892276
H20	-1.5949122630	12.4799255080	1.7833016888
H21	-2.0760976464	5.5257148389	1.6508973851
H22	-3.3459519827	6.6085785790	1.0069328122
H23	-3.1580261519	11.7347546450	1.3965288236
H24	-0.8317246846	6.7378486731	5.8154378609
H25	-0.0171986714	7.8805322433	6.9887781686
H26	-0.1013936544	10.1076087154	6.9978960980
H27	-0.9549886612	11.2086338884	5.8244853771
H28	2.0110256796	7.9338463648	5.4720900163
H29	1.1463844221	6.8153392827	4.3051674647
H30	1.0404714791	11.2481628452	4.3526474025
H31	1.9410863851	10.1463082072	5.5116905711
H32	-3.1515217686	6.9668344627	6.8835925906
H33	-2.9325151596	6.3637806749	5.1748035968
H34	-5.3034637044	6.9124270466	4.6445751283
H35	-5.5591893214	7.4979874750	6.3457460499
X36	0.4174200082#	7.6638732771#	5.8832900464#
X37	0.4596127724#	10.6867070845#	5.5797343056#
X38	-4.2591409913#	7.0471563938#	5.5617408779#
C39	-3.0982574338	11.9173208492	8.1387763082

C40	-3.2074942060	11.2118744954	9.3394354374
C41	-3.6045782716	9.8759549086	9.3074216359
C42	-3.8586882099	9.2434185865	8.0886035159
C43	-3.6747426314	9.9210479504	6.8657612875
C44	-3.3496261363	11.2901458966	6.9232380297
H45	-2.8183796202	12.9683412911	8.1440949430
H46	-3.0066385682	11.7034639876	10.2844492331
H47	-3.7304912577	9.3158514007	10.2358544089
H48	-4.1969307850	8.2087173404	8.1168508030
H49	-4.8927265527	9.6742513862	5.7803464902
H50	-3.2762543738	11.8609806714	6.0051816544

1c

Rh1	-0.6129778625	8.9885933354	4.7706575955
C3	-0.5690070117	7.3922483557	6.2510173069
C4	-0.8619355558	10.4754634802	6.3512864720
C5	0.6990480549	7.5458328742	5.7097334588
C6	0.4167295585	10.5886070065	5.8250703120
Rh7	-3.6786704988	8.9010462670	4.8021061478
O8	-3.2969970794	10.7762035766	3.9022820868
O9	-3.1556839747	7.9358821693	2.8383409930
O10	-1.1378614983	10.4732640809	3.3705499623
O11	-1.0012912614	7.5126467750	3.3251506349

C12	-3.8117156879	6.8336907940	5.5522640360
C13	-2.0373415852	7.4289249812	2.5833001869
C14	-2.2493673027	11.0662766400	3.2601388419
C15	-5.0990883380	7.2523031681	5.2815841920
C16	-1.8692868963	6.6232456180	1.3135591933
C17	-2.3435055689	12.2062322798	2.2747572975
H18	-1.0605832802	7.0526562000	0.7171699184
H19	-2.9988234408	12.9853999750	2.6656345752
H20	-1.3571850973	12.6087072476	2.0476611413
H21	-1.5765863687	5.6021957490	1.5720814278
H22	-2.7925756262	6.6086873207	0.7365802571
H23	-2.7911551670	11.8243695822	1.3520264182
H24	-1.2184800343	6.6162689510	5.8704983764
H25	-0.8055566696	7.7619369250	7.2425748101
H26	-1.0375764612	10.0014531689	7.3091163589
H27	-1.6664282443	11.1199771164	6.0196799062
H28	1.4900894519	8.0423485765	6.2601424493
H29	1.0230309737	6.9158889562	4.8874638747
H30	0.6342163772	11.3198819998	5.0535962957
H31	1.2782216630	10.2126446321	6.3661780102
H32	-3.4450469937	6.7966225912	6.5693814326
H33	-3.2706380845	6.2350862461	4.8291397090

H34	-5.5794392904	6.9855434819	4.3468245256
H35	-5.7554003619	7.5856029572	6.0765280346
X36	0.4174200082#	7.6638732770#	5.8832900464#
X37	0.4596127724#	10.6867070845#	5.5797343056#
X38	-4.2591409913#	7.0471563938#	5.5617408779#
C39	-4.8847804870	11.8609110486	7.6809500651
C40	-4.5973430520	11.2935669797	8.9232036821
C41	-4.0854081492	9.9991128640	8.9722876565
C42	-3.8631736441	9.2824704613	7.7929643170
C43	-4.1321769687	9.8422423064	6.5351712212
C44	-4.6570109000	11.1449914883	6.5055086952
H45	-5.2871475150	12.8680774168	7.6238714250
H46	-4.7724613322	11.8513012909	9.8371266526
H47	-3.8566032314	9.5395655545	9.9293443778
H48	-3.4533603882	8.2832555361	7.8791181299
H49	-5.1015761485	9.2088453670	4.3698874070
H50	-4.8690547358	11.6145154180	5.5531073785

TS1.2

Rh1	-0.9784252629	10.6315538512	3.3004137076
C7	-1.0737752426	12.6310799530	4.1168270244
C9	0.8902965660	11.0690121711	2.3614611092
C11	-0.7547819904	11.7496546770	5.1423223590

C13	1.0957549142	10.1003702149	3.3440685919
O21	-3.0508285580	10.3407096386	3.8157892110
O22	-2.1478780007	7.4594045955	3.0987357669
O23	-5.0862875886	9.5327440175	3.5117032329
O24	-1.1645554427	9.0851466020	1.8835423360
C25	-1.6486014041	7.9153715585	2.0485009190
C26	-4.2026107949	10.3914461067	3.2613026875
C27	-1.5620448305	6.9953002020	0.8486906713
C28	-4.4796254941	11.5065850168	2.3024329763
H29	-1.4284611045	7.5591736325	-0.0760452104
H30	-3.8132901294	11.3897393322	1.4290092895
H31	-5.5226689983	11.4910749470	1.9782608112
H32	-0.6982985139	6.3367495916	0.9794255053
H33	-2.4516114081	6.3740572549	0.7982318121
H34	-4.2501225051	12.4649223868	2.7889163654
H35	-2.1007888476	12.9449534576	3.9648197149
H36	-0.3254539026	13.2830421799	3.6823056451
H37	1.2012149603	12.0954693046	2.5183902199
H38	0.7625093968	10.7742737636	1.3285136024
H39	0.2562736823	11.6924156253	5.5267161401
H40	-1.5223896285	11.3669213886	5.8055441392
H41	1.1259334779	9.0464488498	3.0833438343

H42	1.5635328930	10.3578749689	4.2874612082
X44	0.5608621907#	12.2126559719#	3.2444564800#
X45	-0.3866764112#	11.4475189637#	5.0304340049#
X46	0.5837926996#	11.3441204343#	2.1805719779#
Rh47	-2.8028884822	8.4412942816	4.9960696779
C48	-3.7395593451	10.9241721176	9.0174759857
C49	-4.7364554912	10.8123501633	8.0417377630
C50	-4.5234545527	10.0424041806	6.8970318743
C51	-3.3051003385	9.3643616668	6.6965987696
C52	-2.3235048852	9.4688663844	7.7038156123
C53	-2.5309379476	10.2458776259	8.8438375778
H54	-3.9052867368	11.5251960365	9.9048950727
H55	-5.6844705991	11.3281366879	8.1703429655
H56	-5.3142455106	9.9789629550	6.1506871138
H57	-1.3719490999	8.9486377517	7.5991948637
H58	-1.7492846981	10.3150453555	9.5984388910
H59	-4.3853599440	8.6548355606	4.3303504306
C60	-3.8250433847	6.6267660794	5.5284043728
C61	-2.5013418061	6.5609513296	5.9625737615
H62	-4.1116788032	6.1489996438	4.5977818005
H63	-1.7611354907	6.0271444723	5.3745681442
H64	-2.2682867173	6.7062552602	7.0111171453

H65	-4.6336437394	6.8311644061	6.2217519763
X66	-3.4463413410#	6.6898271181#	5.7518292190#

TS1.1'

Rh1	-1.3925915759	11.4789302729	6.0229290682
C7	-2.3789871012	13.2470001936	6.7960193512
C9	0.4490305904	12.1867207264	6.8540951493
C11	-2.8666934811	12.1217640968	7.4548175301
C13	-0.0051959899	11.0995072266	7.6058959907
O21	-3.0601619742	11.0152230020	4.6710998774
O22	-1.3955149298	8.4913019435	4.3920413167
O23	-5.1202064674	11.1546975529	3.9044233618
O24	-0.1211851895	10.3036515473	4.8329974240
C25	-0.3351775133	9.1532701067	4.3256148776
C26	-3.9658382236	11.6575742338	4.0457501079
C27	0.8387731355	8.5209975451	3.6057814059
C28	-3.6798905667	12.9909145409	3.4273447883
H29	1.5355799354	9.2812503691	3.2539352571
H30	-3.7806210552	12.8904129254	2.3432335778
H31	-4.4222961262	13.7207591078	3.7563508721
H32	1.3654990622	7.8679398939	4.3092737535
H33	0.4856538789	7.9064682654	2.7773786664
H34	-2.6737896298	13.3259733244	3.6673519102

H35	-2.9364148796	13.6952722450	5.9807415847
H36	-1.6818010126	13.9196062874	7.2829628323
H37	0.3797032489	13.1966080480	7.2422878011
H38	1.1800310265	12.0384633688	6.0667138691
H39	-2.5692034729	11.8897956879	8.4712804125
H40	-3.7982080985	11.6684232222	7.1363502173
H41	0.3771455669	10.1020395226	7.4169364042
H42	-0.4413781932	11.2475896985	8.5878571683
X44	-1.1841958763#	13.0627030664#	7.3225030005#
X45	-3.0745101570#	12.4488349240#	6.9417652587#
X46	-0.1057876543#	12.6144728079#	6.5994159990#
Rh47	-3.4450683467	8.8985917938	4.9550435986
C48	-7.9056263442	8.5294998251	6.9300482301
C49	-7.7475435891	8.1484094510	5.5984392845
C50	-6.5459963195	8.3992970761	4.9365659602
C51	-5.4584472090	9.0364076635	5.5710075141
C52	-5.6662279532	9.4377127988	6.9098229298
C53	-6.8563043958	9.1788222730	7.5844045107
H54	-8.8359443820	8.3301485930	7.4513929755
H55	-8.5604308381	7.6566767124	5.0727845691
H56	-6.4553135626	8.1104542337	3.8944403655
H57	-4.8653947994	9.9337169874	7.4464189402

H58	-6.9674897640	9.4810523453	8.6215795115
H59	-5.1071193072	10.0964178205	4.5695338382
C60	-3.7234867774	6.8512810543	4.4200688224
C61	-3.4724379866	6.9372838068	5.7945628537
H62	-2.9185067077	6.6121095211	3.7332346330
H63	-2.4714967959	6.7661390315	6.1786161175
H64	-4.2757644334	6.8136545651	6.5128589065
H65	-4.7244848533	6.6476900833	4.0575288180
X66	-3.4355194990#	6.6442066478#	4.9924763564#
X	-0.1162853042#	11.7072082566#	7.2099966538#

1d

Rh1	-0.7188189814	9.9647360755	3.8516186538
C7	-1.1563044396	11.8366465135	4.8268490220
C9	0.4631061927	11.0167594937	2.3887191919
C11	-0.2598564411	11.1214687447	5.6164245457
C13	1.3108580788	10.2204738996	3.1661155655
O21	-4.0203141433	10.5360548152	3.7405163328
O22	-2.8990409439	7.8199865178	2.7276571246
O23	-4.5405323690	9.6072753557	1.7607014423
O24	-0.7669285847	8.3984639492	2.3705056474
C25	-1.7932961597	7.7237502491	2.0968111256
C26	-4.5332075264	10.6023857567	2.6223936175

C27	-1.7117197234	6.7210274087	0.9719871737
C28	-5.1929763686	11.8519410425	2.1250720744
H29	-0.8184537926	6.8807707829	0.3700697209
H30	-4.5383631517	12.3190161635	1.3824574743
H31	-6.1354185543	11.6137897886	1.6281537013
H32	-1.6798375200	5.7156352676	1.4037977082
H33	-2.6081253524	6.7799089124	0.3513172652
H34	-5.3549390211	12.5453154372	2.9478622723
H35	-2.2169602517	11.8198561964	5.0480169162
H36	-0.8198804373	12.6755419896	4.2272587808
H37	0.4422451925	12.0934953650	2.5211769303
H38	0.1134864259	10.6625116384	1.4244098660
H39	0.7899897436	11.3937819514	5.6491299379
H40	-0.6212857626	10.5548264619	6.4660179918
H41	1.6129988629	9.2388905667	2.8157329478
H42	1.9555467745	10.6642389460	3.9168831144
X44	0.5608621907#	12.2126559719#	3.2444564800#
X45	-0.3866764112#	11.4475189637#	5.0304340049#
X46	0.5837926996#	11.3441204343#	2.1805719779#
Rh47	-3.0242353221	8.8555046837	4.7811299821
C48	-3.9388480452	11.0495159459	9.0270940910
C49	-4.6436846428	11.3519914164	7.8633787126

C50	-4.3345176855	10.7144020973	6.6603613170
C51	-3.3138154575	9.7458524656	6.5687333342
C52	-2.6310453064	9.4496691493	7.7643732889
C53	-2.9291637804	10.0905283581	8.9676988640
H54	-4.1736330738	11.5481365906	9.9614464578
H55	-5.4382428683	12.0923641526	7.8864963642
H56	-4.8940079833	10.9930281387	5.7766699714
H57	-1.8419236636	8.7073488591	7.7842977309
H58	-2.3690389588	9.8335760398	9.8621116252
H59	-4.0022859612	8.8348377015	2.1054994083
C60	-2.6900428599	6.9702167935	5.6965999284
C61	-1.4328054466	7.5285207343	5.4563365646
H62	-3.0950265412	6.2298514763	5.0122879186
H63	-0.8473622577	7.1957162474	4.6073839909
H64	-0.8479415633	7.9604412320	6.2578113822
H65	-3.1151980523	6.9678432836	6.6941437965
X66	-3.4463413410#	6.6898271181#	5.7518292190#

TS1.3

Rh1	-0.4930867698	9.4195456027	4.1443084635
C7	-0.3007824723	11.2439509892	5.2443128120
C9	1.0978115011	10.0743303342	2.8327867641
C11	0.1268362821	10.1737669334	6.0367208460

C13	1.5841176493	9.0166804085	3.6026734355
O21	-3.6117499584	10.4864919674	3.2515920515
O22	-3.0211479196	7.6812053567	3.0659136668
O23	-3.6211558909	12.4406539470	4.3763073724
O24	-0.8529366967	7.9949069437	2.6019589299
C25	-1.9865204843	7.4750621212	2.3782713288
C26	-3.6718545344	11.7155113360	3.2694083174
C27	-2.0793942832	6.5256271329	1.2065048890
C28	-3.7830850595	12.5376667199	2.0240059873
H29	-1.8861427435	7.0753301475	0.2818307661
H30	-3.9606459770	11.8886911729	1.1702685015
H31	-4.5713340074	13.2868052831	2.1226360174
H32	-1.3045848153	5.7599929714	1.2998424581
H33	-3.0640970219	6.0623409055	1.1647824295
H34	-2.8405501339	13.0756985454	1.8816173976
H35	-1.2901572969	11.6617076837	5.3532067161
H36	0.4224672135	11.9192128227	4.7982946383
H37	1.4024137037	11.0946297061	3.0404653004
H38	0.7102606243	9.8966289073	1.8347916999
H39	1.1829633000	10.0090327594	6.2206665150
H40	-0.5300226387	9.7349198738	6.7819472247
H41	1.5714020023	8.0052906054	3.2116740161

H42	2.2755299151	9.1946130548	4.4194546279
X44	-0.0295973610#	8.5932244802#	1.9552233203#
X45	-0.1711377772#	11.7421048249#	4.7624923726#
X46	1.2243541586#	9.4255721060#	3.3417257520#
Rh47	-3.1043091316	8.9800075386	4.7610038292
H59	-3.5775557470	11.8531743645	5.1669412922
C2	-2.5142405772	7.2070142945	5.9410133705
H3	-3.1535841442	6.4098178940	5.5767388701
C4	-3.0237480591	8.2156599378	6.7900100690
H5	-2.3379658633	8.6727492957	7.4905982509
H6	-4.0076646542	8.0449170836	7.2079752163
H7	-1.4446582594	7.0530033254	5.8428098778
C55	-5.2220453860	11.8775405151	8.2696946600
C56	-3.8317697625	11.9082523752	8.2231922991
C57	-3.1293494307	11.0741934032	7.3444994938
C58	-3.7982379587	10.1959869070	6.4722556074
C59	-5.2123964554	10.1922087019	6.5299856996
C60	-5.9120543020	11.0094067552	7.4206218015
H14	-5.7607312469	12.5276465983	8.9500958881
H62	-3.2819882048	12.5905557431	8.8643658023
H63	-2.0486888444	11.1185145142	7.3507099149
H64	-5.7763985594	9.5541666400	5.8561723064

H65	-6.9976062647	10.9813726650	7.4355179264
X	-3.2081879894#	7.1743973157#	6.6442487454#

1e

Rh1	-0.6727082648	9.9064796350	4.1676164249
C7	-0.9691308319	11.8110074438	5.0899237474
C9	0.5848070535	10.8118427210	2.6438740190
C11	0.0326186285	11.1240782446	5.7820014099
C13	1.3557287415	9.8984777776	3.3636006588
O21	-4.3136645592	10.7775212711	4.3876935016
O22	-3.1343048698	8.1759263333	3.1890722568
O23	-5.0153756535	9.9114778900	2.4337147732
O24	-0.9539318149	8.3128931915	2.7277986638
C25	-2.1041258202	7.8852837958	2.4824597542
C26	-4.9773763815	10.8608442793	3.3650584160
C27	-2.3206317769	6.9656020004	1.3079815738
C28	-5.8293019417	12.0492854243	3.0292266757
H29	-1.4468771854	6.9574925970	0.6580781354
H30	-5.4331354466	12.5353048998	2.1330874934
H31	-6.8482321011	11.7257761051	2.8030371195
H32	-2.5011630110	5.9539559154	1.6843696632
H33	-3.2082690238	7.2699771589	0.7487983745
H34	-5.8308284566	12.7524572315	3.8593181007

H35	-1.9954400886	11.8196149586	5.4373642589
H36	-0.7098105374	12.6222979616	4.4174127912
H37	0.7079118637	11.8797026171	2.7966384928
H38	0.1373074990	10.5287006521	1.6966990114
H39	1.0725589142	11.4105167938	5.6588557341
H40	-0.1703203605	10.5970273703	6.7076172469
H41	1.4934222539	8.8876156961	2.9947409467
H42	2.0897968624	10.2344908708	4.0870284596
X44	0.5608621907#	12.2126559719#	3.2444564801#
X45	-0.7080804403#	11.4790576291#	5.2216367839#
X46	0.8869821358#	10.6186166966#	2.7774173787#
Rh47	-3.0044456009	8.9937971734	5.1361773699
C48	-5.3143867469	10.5956614445	7.5585504117
C49	-4.0035646576	10.9852817783	7.4072340553
C50	-2.9744582132	10.0166159369	7.2898163886
C51	-3.2832239921	8.6376700966	7.3648373633
C52	-4.6486558655	8.2646522885	7.5228878960
C53	-5.6370600757	9.2214492483	7.6181095248
H54	-6.0999909955	11.3382201941	7.6414456065
H55	-3.7446474587	12.0374780080	7.3770084119
H56	-1.9462030013	10.3357247024	7.3717571358
H57	-4.8977772647	7.2106577490	7.5899522760

H58	-6.6703461199	8.9179520283	7.7499701230
H59	-4.3915926528	9.1747993914	2.6709001024
C60	-2.1721142261	7.5929732188	7.3462519491
C61	-1.9345888888	7.3881001711	5.8484819148
H62	-2.4736691281	6.6882918245	7.8848990740
H63	-2.4190055468	6.4874349051	5.4563979336
H64	-0.8810194545	7.3831848451	5.5595801225
H65	-1.2858241082	7.9925257846	7.8470297409
X	-2.7438221452#	7.9354791313#	7.0769327177#

TS1.4

Rh1	-0.7590750895	9.8898414961	4.0095758927
C7	-1.3160927978	11.7753748492	4.8560516794
C9	0.6977287478	10.8865038407	2.7276072434
C11	-0.5529958625	11.0722731891	5.7910318013
C13	1.3774620513	10.0630422367	3.6235761763
O21	-4.2328586293	10.4546396028	3.6860613742
O22	-2.9007953914	7.9647426944	2.5610820544
O23	-4.5467087232	9.7274579086	1.5698838759
O24	-0.6823931329	8.2826630946	2.5534824855
C25	-1.7271766050	7.7706301190	2.0795964899
C26	-4.6986226236	10.6078201746	2.5535258484
C27	-1.6152619480	6.8658405577	0.8832273634

C28	-5.4810585572	11.8247141390	2.1674439659
H29	-0.5792881675	6.7841326160	0.5627895245
H30	-4.9067403859	12.3951910340	1.4328230204
H31	-6.4163154369	11.5240227326	1.6920593142
H32	-2.0018667133	5.8796355307	1.1431254751
H33	-2.2210651967	7.2532578799	0.0670013293
H34	-5.6882473529	12.4427732178	3.0408919652
H35	-2.3999175668	11.7739907963	4.9105113433
H36	-0.8848394934	12.6035396779	4.3018846062
H37	0.6935353783	11.9647745837	2.8567594187
H38	0.4765095254	10.5424103095	1.7224755092
H39	0.4818907671	11.3441181067	5.9777888848
H40	-1.0339328924	10.5414266117	6.6048954195
H41	1.6828229432	9.0628059444	3.3311185461
H42	1.9146086967	10.4813457362	4.4689752641
X44	0.5608621907#	12.2126559719#	3.2444564800#
X45	-0.7080804404#	11.4790576291#	5.2216367839#
X46	0.8869821357#	10.6186166966#	2.7774173787#
Rh47	-3.0843288428	8.8042090339	4.6172033402
H59	-3.9706114994	8.9687816769	1.8738136196
H49	-2.5136167571	6.2279957934	5.2613959833
C50	-6.0514937134	6.8020126112	8.9116506861

C51	-5.9373699832	6.3675885165	7.5881467596
C52	-4.8398028191	6.7417793937	6.8194516825
C53	-3.8339614279	7.5607485188	7.3559169671
C54	-3.9619678228	7.9954481728	8.6829029764
C55	-5.0582861002	7.6168750471	9.4561561556
H56	-6.9093065989	6.5100906305	9.5095714047
H57	-6.7085940351	5.7379828094	7.1540652605
H58	-4.7696712836	6.4032244652	5.7917219642
H43	-3.1937683470	8.6322690632	9.1159681032
H60	-5.1367943153	7.9620607366	10.4824980796
C61	-2.6314516320	7.9811126639	6.5704814404
H62	-1.9283332740	8.5585295172	7.1660846512
H63	-3.2020923053	9.5003522291	6.0641319075
C64	-2.0519145571	7.1677678559	5.5545467351
H65	-0.9797069868	7.2193173528	5.3986835703
X66	-2.4278299913#	7.6024378231#	6.3213597125#

1f

Rh1	-0.7216242612	9.9316605558	3.8365998264
C9	-1.4621891039	7.6777658379	5.6491307862
C13	-2.7075228356	7.0484167735	5.7039519601
O21	-4.1128389241	10.5646801016	3.8434132286
O22	-2.9382773093	7.8253477592	2.6916213838

O23	-4.4955853390	9.7247973841	1.7923603313
O24	-0.7670238248	8.3069772766	2.4202328543
C25	-1.8062254554	7.6602828077	2.1258644952
C26	-4.5866314801	10.6631453743	2.7085958670
C27	-1.7096766278	6.6073542443	1.0481547407
C28	-5.3116628482	11.8930150719	2.2559237869
H29	-0.7482442944	6.6536693074	0.5391555450
H30	-4.6886885363	12.4153970173	1.5235296103
H31	-6.2430319356	11.6185199387	1.7567195245
H32	-1.8317503774	5.6220413770	1.5078200001
H33	-2.5259662497	6.7341750493	0.3334439531
H34	-5.5069117266	12.5486699484	3.1015762516
H37	-1.0474611763	8.1564629375	6.5275391823
H38	-0.7296744977	7.3681441134	4.9110974663
H41	-2.9611331904	6.2704439552	4.9885965415
H42	-3.0841481286	9.6373983209	6.1189405157
X44	0.5608621907#	12.2126559719#	3.2444564800#
X46	-2.2017113242#	7.2760660822#	5.7662110593#
Rh47	-3.0247039893	8.9086010544	4.7545518323
H59	-3.9457025289	8.9475633981	2.1120328160
C7	-1.1487541133	11.8352843252	4.7458518331
C29	0.5012124534	10.9205840616	2.3558631953

C11	-0.3170955480	11.1078831311	5.5964638516
C30	1.3306517691	10.1622699877	3.1867586182
H35	-2.2203479694	11.8587020297	4.9104951090
H36	-0.7542121035	12.6546986394	4.1542491695
H39	0.4741711384	12.0021807639	2.4379687367
H40	0.1719032939	10.5207022150	1.4021976997
H43	0.7378254476	11.3482925461	5.6811212945
H44	-0.7367511094	10.5675284381	6.4379691844
H45	1.6417207677	9.1663533547	2.8885154891
H46	1.9547181831	10.6401284240	3.9342301103
X45	-0.7080800000#	11.4790580000#	5.2216370000#
X39	0.8869820000#	10.6186170000#	2.7774170000#
H47	-3.2808876697	7.0393457176	6.6265504624

Scheme 8 Structures

5b

Rh1	-0.0519851853	0.1975598115	0.2166274076
C22	0.2926185840	1.7612291580	-1.1950400888
C23	0.2300734559	2.3031737451	0.0952480427
H24	1.2499623018	1.5409814506	-1.6583867129
H15	1.1391868586	2.5019935429	0.6553010366
H26	-0.6359017790	2.8748265344	0.4142725542
H27	-0.5263709965	1.9084816581	-1.8925161049

X28	0.2357413658#	2.0704960299#	-0.6556575020#
O32	0.4866898063	-1.7237434002	1.1995859970
C33	1.6985470103	-1.3519474768	1.1752101444
O34	1.9821656380	-0.2157111495	0.6579426968
C35	2.7792580516	-2.2168275407	1.7515106262
H20	3.7626384059	-1.7871614976	1.5629327158
H21	2.6205855824	-2.3121035642	2.8297270627
H22	2.7148595194	-3.2186939416	1.3196320627
C16	-2.1162023772	-0.1572474085	-0.6600093769
C17	-2.2715847291	0.4795056537	0.5980103672
C18	-2.5645873555	-0.3106351123	1.7470934796
C19	-2.6598503687	-1.6785039410	1.6410325433
C20	-2.5045805284	-2.3139738273	0.3843087638
C21	-2.2562406537	-1.5723711916	-0.7469209242
H23	-2.1393622882	0.4234877368	-1.5735313634
H25	-2.4189734350	1.5511624143	0.6528036232
H28	-2.7113751240	0.1807178742	2.7020330769
H29	-2.8594950839	-2.2793680961	2.5210244440
H30	-2.5872302033	-3.3930079784	0.3189827544
H31	-2.1649957502	-2.0536639279	-1.7137585843

TS5.1

Rh1 -3.2665174098735 8.6486494812802 5.0288381628814

C2 -2.8025491792229 9.5526205997829 2.6952127462521

O3 -3.3835308989599 10.2456001783524 3.6022869945633

O4 -2.4526472153706 8.3609232793021 2.9598668117780

C5 -2.5348686289747 10.1688810182822 1.3558950091008

H6 -3.4285756899150 10.6871089339557 1.0021436433764

H7 -1.7414077668806 10.9149480095862 1.4636098594418

C9 -3.3383839623327 11.3731196139088 9.0232615340018

C10 -3.2280752743291 11.9099706007659 7.7408956676901

C11 -3.3082162084968 11.0857270116476 6.6187008309440

C12 -3.4646907003854 9.6988360247878 6.7665624397398

C13 -3.6147751887906 9.1719809743200 8.0567300885647

C14 -3.5410631955687 10.0029180904641 9.1750408465548

H15 -3.2785988138037 12.0177474838630 9.8934604079317

H16 -3.0848258256816 12.9775496945289 7.6077102497799

H17 -3.2389771677461 11.5219459024853 5.6294432028513

H18 -3.7920316773229 8.1138222533881 8.2086505604499

H19 -3.6474621784657 9.5737839359692 10.1661833820723

H29 -4.6024619819208 8.8543065895180 5.7428147782868

C30 -3.6129222050211 6.6222674797682 5.7738423751398

C31 -2.3079157275230 6.9924401054595 6.0615959068825

H32 -3.8480157101222 6.0528028487396 4.8795797408001

H33 -1.4980552861251 6.7302335040472 5.3859195173880

H34 -2.0079045093352 7.2741641450542 7.0628005732216

H35 -4.3698479202033 6.5974154348588 6.5495474282471

X -2.9604189662720 6.8073537926138 5.9177191410111

H30 -2.2211138130323 9.4107528743344 0.6392537240987

5c (2-olefin variant)

Rh1	-0.4422230347	1.8655555442	1.4991053708
C8	0.5013260940	6.5715027452	1.8356828917
C9	-0.2633625328	6.0919977857	0.7714325535
C10	-0.6387328763	4.7468844546	0.7249071855
C11	-0.2362255766	3.8458403417	1.7254620094
C12	0.5076643905	4.3536210592	2.8048286631
C13	0.8837084030	5.6977960697	2.8547672376
H14	0.7859603706	7.6180003159	1.8769034439
H15	-0.5766368301	6.7672943495	-0.0195466634
H16	-1.2463348710	4.3982760418	-0.1045153623
H17	0.8022657260	3.6954654254	3.6171503706
H18	1.4666579365	6.0642182165	3.6949630838
C23	-0.4927115170	-0.1949370642	0.4614535437
C24	-0.0278815526	-0.3960188679	1.7336809447
H25	-1.5219591537	-0.4051158530	0.1930574644
H26	-0.6718922227	-0.7755216286	2.5195661349
H27	1.0378326193	-0.4263038732	1.9474124783

H28	0.1906767617	-0.0594985995	-0.3736790503
X29	-0.1009084412#	0.0544147331#	0.9333886367#
C31	-1.9810164910	1.8837915001	2.9594954459
C32	-2.5451717290	2.0367796950	1.6720403528
H33	-2.0327501547	0.9278508767	3.4730916030
H34	-3.0406997654	1.2003935835	1.1857303177
H35	-2.8851221120	3.0154415533	1.3442583884
H36	-1.8870275326	2.7444560332	3.6154248354
X37	-2.6068471678#	1.2368394136#	2.4585888672#

TS5.2

Rh1 -1.5271798362000 1.8870821536000 2.0572070167000

C2 2.7639684210000 1.7017110521000 2.1600473010000

C3 3.1146859271000 2.6243845640000 1.1747275791000

C4 2.1138003928000 3.3246114511000 0.5023472301000

C5 0.7685162887000 3.1045327931000 0.8098929071000

C6 0.4192043624000 2.1613861561000 1.7824701860000

C7 1.4214651222000 1.4664185960000 2.4647713447000

O8 -1.8472872311000 3.9250908105000 2.2235455114000

C9 -1.6117502981000 4.4224565626000 3.3973690270000

C10 -1.7026591891000 5.9309596339000 3.4848735268000

H11 -1.8448801373000 6.2457744250000 4.5173861142000

C12 -1.3036058365000 -0.2064546858000 1.4184480129000

C13 -1.5953140194000 -0.1897461059000 2.7697851571000

O16 -1.3117312079000 3.7417145988000 4.3906887447000

H17 -0.7632154074000 6.3518215226000 3.1144898391000

H18 -2.5087852964000 6.3057322355000 2.8536896730000

H19 -0.8298434844000 -0.3648229435000 3.5160990488000

C18 4.5963869569887 2.8779736945219 0.8402808555284

H20 2.3737127331258 4.0510022594917 -0.2534318175260

H21 0.0074119920989 3.6797985105292 0.3037411472038

H23 1.1722895362000 0.7525563004000 3.2402765611000

H24 3.5349744932000 1.1600423831000 2.6987462958000

H25 -1.2273382406000 2.0914368766000 3.5531169826000

H30 -2.0901318845000 -0.3423462784000 0.6796077311000

H31 -0.2916271889000 -0.3733828521000 1.0686717754000

H32 -2.6161964456000 -0.3110216566000 3.1233920584000

X -1.4494599279500 -0.1981003958500 2.0941165850000

H28 4.6683255886884 3.6262440655819 0.0509670490718

H29 5.1137019968762 3.2378685811213 1.7296406365539

H33 5.0573595402404 1.9495518246605 0.5031798186665

TS5.1'

Rh1 -1.6545656514000 2.0654850658000 1.9415832864000

C9 2.5460985722000 0.2181637560000 2.8631609174000

C10 2.4229548158000 1.0691412342000 1.7632879161000

C11 1.3429136521000 1.9473403748000 1.6801300203000

C12 0.3466814679000 1.9786372614000 2.6786297218000

C13 0.5175767899000 1.1383228461000 3.7988707061000

C14 1.5955857334000 0.2578210692000 3.8848197232000

H15 3.3896804139000 -0.4610366994000 2.9324477593000

H16 3.1739127941000 1.0551407278000 0.9795062955000

H10 1.2718392819000 2.6234610242000 0.8336209470000

H18 -0.1991025546000 1.1814401865000 4.6133144073000

H19 1.7026113311000 -0.3878669395000 4.7508500308000

H29 -0.1434173986000 3.3175536752000 2.9949187465000

C41 -1.5599259191000 4.7378556260000 3.0476522543000

O42 -2.3390224789000 3.9324270983000 2.4647728970000

O43 -0.3539608966000 4.4502772811000 3.3518270595000

C44 -2.0643310277000 6.1107265353000 3.3892697435000

H45 -3.1399628697000 6.1779124472000 3.2380207807000

H46 -1.8046644771000 6.3487013416000 4.4223071131000

H47 -1.5586617470000 6.8365646202000 2.7460471899000

C30 -3.2661911824000 1.9808471074000 0.4773409235000

C31 -3.7339183285000 1.4623437071000 1.6785460542000

H32 -3.4858558681000 3.0043449080000 0.1921849406000

H24 -4.3265790250000 2.0720749289000 2.3522828826000

H34 -3.8064477295000 0.3886189973000 1.8315690859000

H35 -2.9628357961000 1.3234819370000 -0.3334622911000

X36 -3.5000547554500 1.7215954072500 1.0779434888500

5d

Rh1 -1.0546770834351 0.4205711569621 2.5224753422208

H2 0.3008874184698 2.2092253997774 1.3681971444169

C14 1.3918845046070 0.3823979656545 1.4453445963544

H15 1.9680821380948 -0.2806310506208 2.0743226202590

C17 0.8823904007163 1.5111816174050 1.9583684180737

H18 1.0497546834563 1.7493870216696 3.0021107542830

X19 0.7888724890685 0.6711033453026 1.9290897123405

C23 -2.2799513442826 1.5602618064836 0.5797631940853

C24 -1.8626859808301 0.4040903570030 0.0452742508814

H25 -3.2445930914389 1.6436518946611 1.0604108529206

H26 -2.4802747595689 -0.4846067463280 0.0765817634155

H27 -0.9035694088503 0.3320401625172 -0.4549880249374

H28 -1.6749230954640 2.4542458620022 0.5308623339139

X29 -1.9941239395349 0.9436833269737 0.4913857755644

X30 -1.6101112124889 0.8277869486158 1.0000302267432

C31 -2.8695980062514 -1.3096408186767 2.8160386901189

C32 -3.2459954198026 -0.1172261451233 3.3036928538371

H33 -3.0498364003106 -1.6037938028729 1.7937888727127

H34 -3.7547680855172 0.6180283469204 2.6902252790843

H35 -3.0554885240674 0.1257907467180 4.3388537031040

H36 -2.3642799356467 -2.0245690177787 3.4574735791138

X37 -2.6112765697242 -0.6405167655506 3.0006141589879

X38 -2.2998077302126 -0.4856542965429 2.5588841515965

H29 1.2461258094993 0.0990440677268 0.4097392893863

C26 0.9293416845941 -0.9789084608471 6.6450950953399

C27 0.6502268714219 0.3809645631548 6.4313344971080

C28 0.0742856984358 0.7976938366497 5.2200329498744

C29 -0.2225406613781 -0.1454499138574 4.2224920008727

C30 0.0565331449467 -1.5052932668537 4.4361663547794

C33 0.6325153247803 -1.9220522113541 5.6475541463382

H32 1.3818112397902 -1.3062983365140 7.5967149794393

H37 0.8834758308568 1.1218496534722 7.2151322447591

H38 -0.1449759041728 1.8659984736396 5.0521245691009

H39 -0.1766740779238 -2.2461133641228 3.6524870722113

H40 0.8517769273889 -2.9903568483441 5.8154625271117

TS5.3

Rh1 -0.7055489072000 1.9577753733000 1.6556172925000

C2 1.1441074565000 2.8127825660000 1.0425523666000

H3 1.9437792889000 2.1329707364000 1.3247667094000

C4 0.8313650887000 3.8677811103000 1.9456082930000

H5 0.6627392072000 4.8439876577000 1.5084799414000

H6 1.3129496587515 3.9064794821211 2.9115165380765

H7 1.1003076298000 3.0300214929000 -0.0238161383000

C8 -3.3497949941000 5.7610747855000 2.8161600956000

C9 -2.9367762351000 5.5260366325000 1.5030021293000

C10 -1.8777801480000 4.6576286889000 1.2486078118000

C11 -1.2385549431000 3.9623387200000 2.2916536526000

C12 -1.6424803311000 4.2381965970000 3.6053999360000

C13 -2.6882180607000 5.1233150031000 3.8663829507000

H14 -4.1671731887000 6.4446934961000 3.0186598378000

H15 -3.4321210681000 6.0293250098000 0.6783799362000

H16 -1.5498402515000 4.5093009463000 0.2232702337000

H17 -1.1508542389000 3.7430188688000 4.4362174106000

H18 -2.9911984129000 5.3095150574000 4.8922006882000

C23 -0.4048764553753 0.1293426292056 0.3526981157385

C24 0.2074085635318 -0.1247806411069 1.5714646031019

H25 -1.3694273872996 -0.3089388966815 0.1177924014557

H26 -0.2714914520544 -0.7487215740997 2.3174595418148

H27 1.2816981431191 -0.0338752780018 1.6851099888975

H28 0.1805686174890 0.4410233903268 -0.5068329054108

X29 -0.0987339459217 0.0022809940494 0.9620813594202

C31 -2.3803220214025 1.1339494229790 3.0866937489750

C32 -2.9758173974186 1.3681514951295 1.8707460840069

H33 -2.1014498635576 0.1286947888132 3.3826674722255

H34 -3.1672006892010 0.5572752586946 1.1771645098379

H35 -3.5186423899464 2.2857768549509 1.6808093240765

H36 -2.4449220539533 1.8570475347521 3.8907915547479

X37 -2.6780697094105 1.2510504590542 2.4787199164910

5e

Rh1 -3.0322901822065 8.6598527442865 4.8743489248049

H2 -4.2197892250295 6.5381285674028 6.0404216369775

C3 -7.9101203121752 8.6733281054245 8.2991069901385

C4 -7.5329094833718 8.8199611409170 6.9636334293260

C5 -6.1901574684989 8.7364466541275 6.6046288206527

C6 -5.2040910965103 8.5026120505920 7.5690050613641

C7 -5.5902474519240 8.3619060529025 8.9045968269261

C8 -6.9345352015937 8.4452136825337 9.2681374939248

H9 -8.9550176757741 8.7404776224794 8.5816516991122

H10 -8.2842798605153 9.0037973267229 6.2027395697851

H11 -5.8946158611045 8.8534749709903 5.5654285130165

H12 -4.8368303688056 8.1836236237064 9.6655898561637

H13 -7.2180714382405 8.3334703483397 10.3094076683552

C14 -3.7537860815007 8.3721419348145 7.1683188037102

H15 -3.0888583771350 8.4763449234511 8.0287758839551

H16 -3.5266298607001 9.2944536807067 6.6259384642866

C17 -3.3960300396615 7.2064578184953 6.2915215699389

H18 -2.5059047821088 6.6554050048849 6.5939211855387

X19 -3.5749080605811 7.7892998766549 6.7299201868246

C23 -1.9701194458813 7.2450373280988 3.6140344177643

C24 -3.1834579730798 7.5839545168728 3.0126835308355

H25 -1.0410470006728 7.6962388309361 3.2791518261310

H26 -3.2125320898437 8.2808492760446 2.1795309680409

H27 -4.0354308757905 6.9129320318658 3.0730545626422

H28 -1.8600463102308 6.3030407554042 4.1404769841566

X29 -2.5767887094805 7.4144959224858 3.3133589742999

X30 -2.8011524485927 7.9411930310600 4.1982907719654

C31 -3.4430693794141 10.6427907049506 3.8607426637391

C32 -2.0836739626912 10.4285366118619 3.8034544743792

H33 -4.0808612584470 10.4403473813483 3.0068742560590

H34 -1.6139497363376 10.0576127067770 2.8977128375586

H35 -1.4101544904600 10.8850133456203 4.5221525786970

H36 -3.8743247218894 11.2845084197916 4.6235711144457

X37 -2.7633716710527 10.5356636584062 3.8320985690591

X38 -3.0668993954326 9.7342759078590 4.3582531310630

TS5.4

Rh1	-1.1388112077	0.4484087067	2.0890389424
H2	0.9721384396	0.6455741508	0.4582525233

C3	3.5824591137	-2.5515924156	3.4488562093
C4	2.6943955999	-2.6049570204	2.3722376467
C5	1.8458664502	-1.5343513970	2.1075743389
C6	1.8744559859	-0.3813733580	2.9055328785
C7	2.7624289977	-0.3432227223	3.9879429998
C8	3.6101135720	-1.4171141271	4.2578772077
H9	4.2388952045	-3.3893449295	3.6575423814
H10	2.6563543697	-3.4886087341	1.7437463316
H11	1.1374976158	-1.5986974245	1.2892682608
H12	2.7922324086	0.5362071491	4.6241370729
H13	4.2909784247	-1.3658464109	5.1010693349
C14	1.0019378752	0.7997922827	2.6369543971
H15	1.1319602958	1.5964051400	3.3666237294
H16	-0.3716833418	0.3026742646	3.4417972888
C17	0.6270778631	1.2104096472	1.3210606339
H18	0.4830984548	2.2721325653	1.1336203719
X19	0.8458716948#	1.0570021884#	2.0886629523#
C31	-2.8242033271	-0.5425775540	1.0623144919
C32	-3.2265561729	0.7403777963	1.3961004901
H33	-2.4883303698	-0.7906544117	0.0600017817
H34	-3.2153962098	1.5471581173	0.6692971733
H35	-3.8179279674	0.9294489493	2.2881103530

H36	-3.0888218182	-1.3937137151	1.6840362140
X37	-3.0255816536#	0.0730434129#	1.1365478106#

5f

Rh1 -1.0546770834351 0.4205711569621 2.5224753422208

H2 0.3008874184698 2.2092253997774 1.3681971444169

C14 1.3918845046070 0.3823979656545 1.4453445963544

H15 1.9680821380948 -0.2806310506208 2.0743226202590

H16 -0.3587984862754 -0.0133487176495 3.8912800555721

C17 0.8823904007163 1.5111816174050 1.9583684180737

H18 1.0497546834563 1.7493870216696 3.0021107542830

X19 0.7888724890685 0.6711033453026 1.9290897123405

C23 -2.2799513442826 1.5602618064836 0.5797631940853

C24 -1.8626859808301 0.4040903570030 0.0452742508814

H25 -3.2445930914389 1.6436518946611 1.0604108529206

H26 -2.4802747595689 -0.4846067463280 0.0765817634155

H27 -0.9035694088503 0.3320401625172 -0.4549880249374

H28 -1.6749230954640 2.4542458620022 0.5308623339139

X29 -1.9941239395349 0.9436833269737 0.4913857755644

X30 -1.6101112124889 0.8277869486158 1.0000302267432

C31 -2.8695980062514 -1.3096408186767 2.8160386901189

C32 -3.2459954198026 -0.1172261451233 3.3036928538371

H33 -3.0498364003106 -1.6037938028729 1.7937888727127

H34 -3.7547680855172 0.6180283469204 2.6902252790843

H35 -3.0554885240674 0.1257907467180 4.3388537031040

H36 -2.3642799356467 -2.0245690177787 3.4574735791138

X37 -2.6112765697242 -0.6405167655506 3.0006141589879

X38 -2.2998077302126 -0.4856542965429 2.5588841515965

H29 1.2461258094993 0.0990440677268 0.4097392893863

Additional Structures

$[Cu^{II}(\mu\text{-}OAc)_2]_3$

Cu1 1.7001041201000 0.9749080867000 -0.0270682404000

C2 0.0148657465000 2.5834155618000 -1.8453255785000

O3 1.0958587124000 2.4970675478000 -1.1872886530000

O4 -1.0231687139000 1.8793150367000 -1.6586403441000

C5 -2.2210138567000 -1.3212284027000 1.8746320854000

O6 -1.6018982501000 -2.2000913425000 1.2018518605000

O7 -2.1566597143000 -0.0670707743000 1.6951555506000

C8 -3.1335200970000 -1.8089368121000 2.9824909596000

H9 -3.0687895991000 -1.1347841787000 3.8412448870000

H10 -4.1664552254000 -1.7860660157000 2.6138215754000

H11 -2.8802878305000 -2.8296534720000 3.2750406277000

C12 -0.0520298176000 3.6276692034000 -2.9404034563000

H13 0.9474211437000 3.9639840925000 -3.2216938914000

H14 -0.5786604537000 3.2206769476000 -3.8080717972000

H15 -0.6298659816000 4.4820176745000 -2.5681924041000

Cu16 -0.0107473109000 -1.9584497118000 -0.0019311117000

C17 -2.2945957407000 -1.2603681438000 -1.8242964303000

O18 -2.7367018480000 -0.2931434432000 -1.1310365354000

O19 -1.1904791451000 -1.8550728759000 -1.6459376975000

C20 -0.0139403919000 2.5896904114000 1.8380639438000

O21 1.0315817432000 1.8986633163000 1.6470924789000

O22 -1.0927135630000 2.5006297919000 1.1758258346000

C23 0.0304926884000 3.6302124418000 2.9376428430000

H24 -0.9459604009000 3.7183034506000 3.4194964405000

H25 0.8023143501000 3.3797563443000 3.6686717956000

H26 0.2799709199000 4.5975446330000 2.4846287103000

C27 -3.1624721599000 -1.7136550082000 -2.9801944632000

H28 -3.0904612328000 -0.9668464598000 -3.7795234938000

H29 -2.8324309233000 -2.6824575710000 -3.3587326309000

H30 -4.2080428855000 -1.7618957065000 -2.6630702199000

Cu31 -1.7045457930000 0.9776178337000 0.0223858570000

C32 2.2751363052000 -1.2777947068000 1.8210625357000

O33 2.7151611782000 -0.3039893001000 1.1365337192000

O34 1.1696858895000 -1.8707096460000 1.6421790219000

C35 3.1485425753000 -1.7458785034000 2.9674645329000

H36 3.0892426618000 -1.0048146752000 3.7729458051000

H37 2.8147763225000 -2.7153743551000 3.3410265106000

H38 4.1908899373000 -1.7990498132000 2.6405288052000

C39 2.2202033847000 -1.3291066212000 -1.8694461336000

O40 2.1725558033000 -0.0736471337000 -1.6919431025000

O41 1.5830937664000 -2.1988439095000 -1.2017217893000

C42 3.1403964909000 -1.8351714478000 -2.9625090429000

H43 4.1528243235000 -1.9157669507000 -2.5464393675000

H44 2.8219470593000 -2.8197299665000 -3.3115019466000

H45 3.1695135524000 -1.1225951820000 -3.7913717684000

$[Cu^{II}(\mu\text{-}OAc)_2]_2$

Cu1 1.4492955659000 0.7079322153000 0.0170462470000

Cu16 0.1737136361000 -1.5204259287000 0.2444761440000

C32 -1.0420316958000 0.4514194989000 -1.4784229391000

O33 -0.1062864876000 1.2797063811000 -1.2179680784000

O34 -1.1398783806000 -0.7242285548000 -1.0276793545000

C35 -2.1080198512000 0.9400733643000 -2.4263031397000

H36 -1.6800486294000 1.0029415638000 -3.4308750918000

H37 -2.9546002582000 0.2558791762000 -2.4361150464000

H38 -2.4272518322000 1.9432370514000 -2.1395290486000

C39 -0.5242101169000 0.5360773647000 2.1544498420000

O40 0.3518759372000 1.3193861281000 1.6564637482000

O41 -0.7819544573000 -0.6358404160000 1.7604582473000

C42 -1.3379661066000 1.0825520091000 3.3001218999000

H43 -2.2699181424000 1.4865715815000 2.8918866950000

H44 -1.5911708192000 0.2812408933000 3.9946323194000

H45 -0.8038259900000 1.8840905577000 3.8081765588000

C17 2.6260235064000 -1.3181515415000 1.7544831215000

O18 2.8384969774000 -0.1509129208000 1.2834852951000

O19 1.6334482418000 -2.0544797004000 1.4944172272000

C20 3.6599991505000 -1.8350762750000 2.7226991470000

H21 3.5596240153000 -1.2860154494000 3.6634305252000

H22 3.5136901772000 -2.8977101197000 2.9082301255000

H23 4.6619830542000 -1.6456331767000 2.3345548753000

C24 2.1161575908000 -1.3878492359000 -1.8937613061000

O25 2.3870415102000 -0.1769321895000 -1.5960137239000

O26 1.2838460391000 -2.1299921129000 -1.3004960182000

C27 2.8840285983000 -1.9836315260000 -3.0465234797000

H28 3.7243950035000 -2.5536823514000 -2.6383550031000

H29 2.2466719302000 -2.6726073793000 -3.6014552951000

H30 3.2736695405000 -1.2035604553000 -3.6986341894000

Cu(OAc)(HOAc)(η^2-C_2H_4)

C1 -1.2930207909000 -4.2269949930000 -3.0021980958000

O2 -1.1921039639000 -5.5069149500000 -2.7926055193000

C3 -2.2244157510000 -3.8560115736000 -4.1195009798000

O4 -0.6883037161000 -3.3624115352000 -2.3527030971000

H5 -2.2214989637000 -2.7798278209000 -4.2765006186000

H6 -1.9231901625000 -4.3736811041000 -5.0333949728000

H7 -3.2336018813000 -4.1962234074000 -3.8716041403000

C8 -0.0700816133000 -5.8309325265000 0.3924213085000

O9 0.1237427636000 -4.5871493656000 0.5637417033000

C10 -0.3303252376000 -6.6676133203000 1.6267578797000

O11 -0.0836837862000 -6.4045604723000 -0.7309844978000

H12 -0.0047637094000 -7.6954570564000 1.4676336458000

H13 0.1569747731000 -6.2378440368000 2.5014020647000

H14 -1.4100175957000 -6.6806073905000 1.8077483552000

Cu15 0.7217207698000 -3.3802559041000 -0.8849047457000

H16 -0.6401479104000 -5.7706839132000 -1.9503454861000

C17 2.1566685552000 -2.0172772350000 -1.5523542748000

C18 2.5393152333000 -2.5190589917000 -0.3336856265000

H19 2.5443466399000 -2.4301746905000 -2.4796312660000

H20 3.2374576594000 -3.3481786925000 -0.2578746143000

H21 2.3252351893000 -1.9905123864000 0.5913064670000

H22 1.6270827005000 -1.0720592121000 -1.6342313606000

X23 2.3479918942500 -2.2681681133500 -0.9430199506500

X24 1.6700102992000 -3.1025739138000 -1.0013159852000

$Cu(OAc)_2$

Cu1	0.9114831144	2.2610617653	1.1129480789
C2	-1.1406208290	3.4121655465	1.2570453536
O3	-0.0270416689	4.0312105114	1.2046906747
O4	-1.0905133727	2.1404784781	1.2311078169
C5	-2.4346391264	4.1531236993	1.3464603229
H6	-3.2764259691	3.4631724775	1.3509072694
H7	-2.4388289525	4.7545548876	2.2595527231
H8	-2.5139439917	4.8404064423	0.5003529605
C18	2.9571115878	1.1023184568	0.9416983410
O19	2.9099030962	2.3761560291	0.9678000455
O20	1.8454494109	0.4863997363	1.0167201425
C21	4.2586585395	0.3775250978	0.8310273449
H22	4.0992754346	-0.6979796176	0.7800631807
H23	4.7883487535	0.7237941087	-0.0599505427
H24	4.8785880579	0.6234186395	1.6976226439

Cu(OAc)

C1	-0.0388561666	-0.0727142122	-0.0280071665
O2	-0.0652925359	1.1973619901	-0.0289641869
C3	-1.3437766334	-0.8343746981	-0.0095887169

O4	1.0647114811	-0.7000781654	-0.0431096261
H5	-1.1728157371	-1.9091153530	-0.0013485742
H6	-1.9180341029	-0.5428206216	0.8728822328
H7	-1.9319553950	-0.5594499655	-0.8884188455
Cu8	2.0611066502	1.1730264497	-0.0603911484

Cu(OAc)(HOAc)2

C8	-1.0918645074	-3.7666564868	-3.0651495534
O9	-1.5860636949	-4.9158724657	-2.7438486427
C10	-1.6704649191	-3.1536977517	-4.3085095585
O11	-0.2068090258	-3.1991675829	-2.3978713357
H5	-1.1683913618	-2.2200767663	-4.5538640750
H6	-1.5802476070	-3.8578217168	-5.1384434995
H7	-2.7362419552	-2.9690246685	-4.1517964580
C9	-0.2566796112	-6.0822304566	0.3180909266
O10	0.5014100527	-5.0999155580	0.5969661082
C11	-0.3862553281	-7.1641520613	1.3687141215
O12	-0.9032250742	-6.2288697568	-0.7490676072
H12	-1.4343782538	-7.2489997633	1.6658449366
H13	-0.0938217353	-8.1226016629	0.9335763377
H14	0.2283577997	-6.9476405581	2.2407139899
Cu15	1.0189894823	-3.6084668384	-0.4648979092
H16	-1.1892297952	-5.3471993795	-1.8736025059

C17	2.0986282050	-1.1116579180	-1.7208801893
O18	1.2296665266	-1.0632628200	-2.7046432063
C19	3.0925689970	0.0068146921	-1.7180711951
O20	2.1058841395	-2.0044754661	-0.8669173573
H21	3.7587622088	-0.0819939279	-0.8631845165
H22	3.6688941855	-0.0206497171	-2.6470226226
H23	2.5647554675	0.9635817919	-1.6906841366
H24	0.6068015347	-1.8523955121	-2.6604056232

$Cu(OAc)(HOAc)(C_2H_4)$

C1	-1.2930207909	-4.2269949930	-3.0021980958
O2	-1.1921039639	-5.5069149500	-2.7926055193
C3	-2.2244157510	-3.8560115736	-4.1195009798
O4	-0.6883037161	-3.3624115352	-2.3527030971
H5	-2.2214989637	-2.7798278209	-4.2765006186
H6	-1.9231901625	-4.3736811041	-5.0333949728
H7	-3.2336018813	-4.1962234074	-3.8716041403
C8	-0.0700816133	-5.8309325265	0.3924213085
O9	0.1237427636	-4.5871493656	0.5637417033
C10	-0.3303252376	-6.6676133203	1.6267578797
O11	-0.0836837862	-6.4045604723	-0.7309844978
H12	-0.0047637094	-7.6954570564	1.4676336458
H13	0.1569747731	-6.2378440368	2.5014020647

H14	-1.4100175957	-6.6806073905	1.8077483552
Cu15	0.7217207698	-3.3802559041	-0.8849047457
H16	-0.6401479104	-5.7706839132	-1.9503454861
C17	2.1566685552	-2.0172772350	-1.5523542748
C18	2.5393152333	-2.5190589917	-0.3336856265
H19	2.5443466399	-2.4301746905	-2.4796312660
H20	3.2374576594	-3.3481786925	-0.2578746143
H21	2.3252351893	-1.9905123864	0.5913064670
H22	1.6270827005	-1.0720592121	-1.6342313606
X23	2.3408592770#	-2.3688048844#	-1.1087559829#
X24	1.6700102992#	-3.1025739138#	-1.0013159852#

Cu(OAc)(C_2H_4)

C1	0.3983993014	-5.8101691841	0.4560660363
O2	-0.0643191103	-4.8090347564	1.0488348551
C3	0.4098861308	-7.1603512057	1.1454422226
O4	0.8727755597	-5.7381232320	-0.7316906996
H5	0.8353253878	-7.9334712970	0.5070944188
H6	0.9886109331	-7.0869901705	2.0695434018
H7	-0.6115245403	-7.4320889703	1.4231352026
Cu8	0.5904345359	-3.7445515504	-1.0733358838
C9	-1.3546134881	-3.9216595581	-2.0154560703
C10	-1.0159907304	-2.6066565552	-2.0795828189

H11	-1.1632402057	-4.5995408031	-2.8419183071
H12	-0.5519683393	-2.1838397242	-2.9648561161
H13	-1.3363240922	-1.9049556491	-1.3156183044
H14	-1.9447189254	-4.3126720619	-1.1925948853
X15	-0.8909886349#	-3.0838337865#	-2.5633758190#
X16	-0.2832955649#	-3.4623718193#	-1.8652217805#
C17	2.5254341222	-3.0820930262	-0.3601794979
C18	1.8871260221	-1.9742567054	-0.8219886857
H19	2.4665122300	-3.3735515492	0.6836423182
H20	1.3085355205	-1.3395581378	-0.1577847778
H21	2.0574707549	-1.5989777787	-1.8258908250
H22	3.2213481891	-3.6384043528	-0.9809533570
X23	2.3408590000#	-2.3688050000#	-1.1087560000#
X24	1.6700100000#	-3.1025740000#	-1.0013160000#

Rh(II)Cu(II)Rh(II)

Rh1	1.8235533455	9.8820023157	4.0847015907
Cu2	-0.5663164359	7.9251948854	4.6438070300
O3	2.2711580917	7.7012716374	4.7143029690
O4	1.1356584021	10.4459440023	6.0218275416
O5	0.5089168372	6.3823751259	5.1496198909
O6	-0.3654113096	8.8062252781	6.3733364225
C8	0.2685580533	9.8534870093	6.7172749992

C9	2.0482014977	9.2609517685	2.0099205112
C10	1.7641322219	6.6226885107	5.1049545653
C12	-0.0811762858	10.4148841505	8.0710627128
C13	3.2996681126	9.5894817259	2.5066335060
C14	2.6678136210	5.5080700670	5.5785478642
H15	0.0400723837	9.6351648367	8.8263001971
H16	3.6862220306	5.6609154118	5.2240925204
H17	2.2841579393	4.5423468176	5.2466197983
H18	-1.1361283713	10.6995762354	8.0508903784
H19	0.5422553632	11.2740073688	8.3120566178
H20	2.6681298330	5.5085482686	6.6730485150
Rh21	-3.3763003090	9.0073979754	5.3871059016
O22	-5.2260938460	10.5916968642	5.7828099229
O23	-3.7072115431	7.6150228118	3.8627671184
O24	-3.3067409702	10.4722988799	6.8474487704
O25	-1.6259305757	6.9262608357	3.3306874350
C26	-3.2317663644	7.4073288352	6.8720485038
C27	-2.8798898216	6.9469413387	3.1735861073
C28	-4.4360844228	11.0580443453	6.6316209055
C29	-4.5703640862	7.7031214643	6.7100194520
C30	-3.4419332096	6.0814707735	2.0724689749
C31	-4.7596562758	12.3018542083	7.4131917542

H32	-2.9399461742	6.3262083586	1.1340876856
H33	-5.7360033534	12.1911905785	7.8901228035
H34	-3.9967031411	12.5070869637	8.1629864313
H35	-3.2191838108	5.0358298826	2.2997770825
H36	-4.5167623089	6.2193753175	1.9723741886
H37	-4.8262936225	13.1435396259	6.7185542132
H40	1.5024163519	9.9524090290	1.3782349279
H41	1.7144023665	8.2292062734	1.9853157696
H44	3.9571656077	8.8157456505	2.8909499658
H45	3.7609145818	10.5409340772	2.2658591111
H46	-2.6516353930	7.8320122862	7.6825288689
H47	-2.7811245760	6.5666629131	6.3528896363
H48	1.7593811687	11.3629513664	3.6674960424
H49	-5.0834783504	8.3590337674	7.4031339127
X51	2.5841728011#	8.3838904319#	2.4084324805#
X52	-3.6260456412#	6.9915058172#	6.2665450057#
O53	-2.7311427317	10.4605729507	3.9916576618
O54	-0.6649896628	9.6562975507	3.6833595136
C55	-1.5800889429	10.5282444984	3.4963362743
C56	-1.2400806134	11.7080202342	2.6270070828
H57	-2.1143073663	12.3386230085	2.4783404063
H58	-0.4429403244	12.2809757314	3.1067302927

H59	-0.8594203164	11.3546696725	1.6665882462
H60	-5.1980885354	7.1187427548	6.0469517360

Rh(III)Cu(II)Rh(I)

Rh1	2.2275755219	9.4695189635	4.4086412277
Cu2	-0.4946787757	8.5315598993	3.8691772001
O3	2.3243870838	7.4775517670	5.0874192859
O4	1.2559763264	10.0366454932	6.2206874454
O5	0.2040109955	6.8795909413	4.6609474090
O6	-0.8010347093	9.3250235015	5.7127403085
C7	1.5461491444	11.3866533091	3.6245131404
C8	0.0401739600	9.8628249622	6.5041078694
C9	2.3599450561	8.6760453218	2.4005404560
C10	1.3606440755	6.6613211920	5.1240772767
C11	2.7996865597	11.5508849381	4.1931070999
C12	-0.4478190623	10.3110910302	7.8548038957
C13	3.6483357131	8.8988332681	2.8790715063
C14	1.5907744499	5.3170121921	5.7692250026
H15	-0.7383798708	9.4312710848	8.4355232365
H16	2.6433139509	5.1694788723	6.0043634577
H17	1.2327037396	4.5284172060	5.1047463524
H18	-1.3475788364	10.9124116237	7.7252515760
H19	0.3315363906	10.8540549474	8.3856933748

H20	1.0015156266	5.2649362815	6.6887662755
Rh21	-3.2248488966	9.0360987237	5.4126634832
O22	-5.6954025893	10.4758113577	6.8533332254
O23	-3.2349739041	7.5010583684	3.9146434852
O24	-3.4370436767	10.4347006162	6.8620471357
O25	-1.4524906958	7.4221695808	2.5362733484
C26	-2.9220027850	7.4817610070	6.9187056774
C27	-2.6170739063	7.0817905739	2.8937925263
C28	-4.6023231624	10.8816250385	7.2410190344
C29	-4.2721461689	7.4974053566	6.6359787674
C30	-3.3232245414	6.0525427133	2.0409644373
C31	-4.5030103002	12.0177097826	8.2476651676
H32	-3.1066661964	6.2296511155	0.9868422872
H33	-5.2659847031	11.8908732315	9.0172766983
H34	-3.5138829642	12.0790832434	8.7007110992
H35	-2.9328347976	5.0637892257	2.3012318319
H36	-4.3968047631	6.0703684456	2.2217788958
H37	-4.7090160895	12.9557055017	7.7238013686
H38	0.6469755526	11.6088122331	4.1838309073
H39	1.4114072582	11.3423496790	2.5509658235
H40	1.9034078066	9.3462938066	1.6813264079
H41	1.9210757274	7.6838869425	2.4385126482

H42	3.6866947445	11.6485944022	3.5770334567
H43	2.8997919964	11.8969299316	5.2177501993
H44	4.2245813059	8.0867562596	3.3112860358
H45	4.2277506177	9.7468921114	2.5301606536
H46	-2.5396661389	7.9963890144	7.7918742694
H47	-2.2535924855	6.7779332691	6.4350617065
H48	-4.7108683862	9.0745766220	5.1543179016
H49	-4.9735634952	8.0211442499	7.2733419021
X50	2.4069459912#	11.2246795476#	3.5524968176#
X51	2.5841728012#	8.3838904319#	2.4084324805#
X52	-3.6260456411#	6.9915058172#	6.2665450057#
O53	-3.0692847754	10.6008894423	4.0192443295
O54	-1.1127584741	10.1447907994	2.9818844313
C55	-2.1604639932	10.8325939991	3.1777061118
C56	-2.3226547404	12.0557090252	2.3052218403
H57	-3.2279234115	12.6018891235	2.5634596707
H58	-1.4480788283	12.6993370179	2.4242420871
H59	-2.3612780655	11.7423218588	1.2589898940
H60	-4.6948689498	6.8037541260	5.9190664192

Rh(III)Rh(I)

Rh1	-0.5052927297	9.0519787598	4.5969607240
C3	-0.2216794231	7.5433141704	6.1511206568

C4	-0.6556008597	10.5958305771	6.1244572990
C5	0.9446510699	7.6651888720	5.4116213582
C6	0.5781707355	10.7074393182	5.4971170309
Rh7	-3.5407124806	8.9535668636	4.9217337611
O8	-5.9281015429	10.2186750079	6.6998350512
O9	-3.3229948001	7.8687209030	3.1356658780
O10	-3.6835071579	9.9984989310	6.6544322659
O11	-1.1069693241	7.4955279118	3.2969371676
C12	-3.5394585090	7.0749982644	6.0518826135
C13	-2.2352876960	7.3527775330	2.7411063307
C14	-4.8040369435	10.4419823850	7.1475369310
C15	-4.8491801963	7.3234906551	5.6956661175
C16	-2.2908364141	6.4669225927	1.5201335125
C17	-4.6003988856	11.3211106477	8.3712802586
H18	-1.5098164757	6.7649973892	0.8177779833
H19	-5.4805724889	11.2775187956	9.0128637561
H20	-3.7063423145	11.0326821600	8.9246430194
H21	-2.0841170798	5.4365779607	1.8240910403
H22	-3.2694636429	6.5161213383	1.0454125547
H23	-4.4735036833	12.3536210797	8.0313875547
H24	-0.9109664640	6.7407232176	5.9299453617
H25	-0.3079679839	7.9747883089	7.1419389236

H26	-0.7502080138	10.1539677187	7.1085831827
H27	-1.5010253145	11.2063345431	5.8328501338
H28	1.8050842830	8.2006376756	5.7961352601
H29	1.1452465848	6.9861094783	4.5886354360
H30	0.7243782452	11.4116948764	4.6847746601
H31	1.4845655426	10.3677983437	5.9871025039
H32	-3.1730636844	7.3327559382	7.0390081495
H33	-2.9472323396	6.3712159811	5.4790175603
H34	-5.0083357367	9.1990693091	4.6448005795
H35	-5.5436362011	7.7920517146	6.3813089804
X36	0.4174200082#	7.6638732771#	5.8832900464#
X37	0.4596127724#	10.6867070845#	5.5797343056#
X38	-4.2591409913#	7.0471563938#	5.5617408779#
O38	-3.3062425146	10.7632817669	3.8745804686
O39	-1.1909682963	10.4610859194	3.1917888310
C40	-2.3123983401	11.0469967956	3.1502022871
C41	-2.4874211856	12.1645814922	2.1516029056
H42	-3.1338886930	12.9378395939	2.5677472986
H43	-1.5236922623	12.5799083436	1.8596741919
H44	-2.9807703588	11.7579727818	1.2633398923
H45	-5.2835678801	6.8415313209	4.8268735107

Rh(II)Rh(II)

Rh1	-0.2807690738	8.9856176439	4.5422717436
C3	0.3495901226	7.4983060545	6.0196672454
C5	1.2654990082	7.5182917249	4.9815819561
Rh7	-3.7099040269	8.9543903302	5.0922559030
O8	-5.7441199988	10.1615726502	5.7302724984
O9	-3.6575964548	7.9579677106	3.2600378347
O10	-3.8873596594	9.9985451744	6.8898498505
O11	-1.5066265093	7.3921693991	3.5173815828
C12	-3.5180791425	7.0882795199	6.2172557913
C13	-2.5895220660	7.3906401660	2.8711243660
C14	-5.0684147603	10.4868999809	6.7319840788
C15	-4.8495241276	7.2441296719	5.8843646671
C16	-2.6454466640	6.6392690913	1.5629172053
C17	-5.5836107349	11.4583025530	7.7575052799
H18	-1.7984641017	6.9344450856	0.9404446594
H19	-6.6723288306	11.4204929634	7.7982607495
H20	-5.1534830006	11.2510152344	8.7379373921
H21	-2.5438562944	5.5699927651	1.7693296401
H22	-3.5834107193	6.8217438689	1.0411693810
H23	-5.2850022782	12.4671054094	7.4556913246
H24	-0.4450733255	6.7592265507	6.0251237730
H25	0.5579230637	7.9816188339	6.9670334785

H28	2.2091698047	8.0453692201	5.0853936380
H29	1.2023491190	6.7997384926	4.1709771854
H32	-3.1577103022	7.3666918841	7.2020142175
H33	-2.8689479360	6.4560914165	5.6213957124
H34	0.2135801309	9.9896184947	5.5992470037
H35	-5.5586506449	7.6517189345	6.5942549644
X36	0.4174200082#	7.6638732770#	5.8832900464#
X38	-4.2591409913#	7.0471563938#	5.5617408779#
O31	-3.2731388387	10.7676072414	4.1252550895
O32	-1.1347391698	10.5528705309	3.4475365213
C33	-2.2592457028	11.1367267968	3.4734280567
C34	-2.4092292907	12.3779522853	2.6253654024
H36	-3.1506313487	13.0459694992	3.0627443371
H37	-1.4509915119	12.8834520936	2.5095903035
H38	-2.7650916260	12.0759817400	1.6353987699
H39	-5.2725775221	6.7560728469	5.0139363793

TS: Premature C_2H_4 Insertion

Rh1	2.2922741187	9.4770310146	3.7912845595
Cu2	-0.5923303090	9.8184247435	3.6706030475
O3	1.7210137432	8.6131137976	5.6543344075
O4	2.0963823340	11.3893905190	4.6421278002
O5	-0.5034758084	8.6549341620	5.3880432141

O6	-0.1460343937	11.4252558336	4.7000667407
C7	1.9261226157	10.4234996197	1.8812948906
C8	0.9872268912	11.9031499646	4.9760923832
C9	1.9191797300	7.5205028814	2.8984722529
C10	0.5438545752	8.3717144578	6.0422691835
C11	3.2991681504	10.3942446325	2.1103099631
C12	1.0214026271	13.1751815757	5.7864076125
C13	3.2290027212	7.5711285009	3.3476899684
C14	0.4191261972	7.6910044177	7.3858917142
H15	0.9772480590	12.9071794811	6.8466155527
H16	0.9657447600	8.2707138756	8.1327440867
H17	0.8892808184	6.7057615085	7.3304364529
H18	0.1530298928	13.7916369234	5.5555430771
H19	1.9473779791	13.7205163470	5.6081605862
H20	-0.6168871508	7.5822080670	7.6905417747
O21	-3.4064045957	10.4730286852	4.1385677134
O22	-2.8749645787	7.5743123895	3.3452571316
O23	-1.8425894090	10.9083850798	2.5819465832
O24	-0.9030114462	8.2926358634	2.5250076115
C25	-1.9513765535	7.5753711464	2.4959589662
C26	-2.9803610613	11.0802283040	3.1273223736
C27	-2.0746604573	6.6462818540	1.3084946291

C28	-3.8803225232	12.1350088557	2.5203386660
H29	-2.2021173311	7.2480935164	0.4047716360
H30	-3.8397563136	13.0238451117	3.1561710996
H31	-3.5532161650	12.4031461805	1.5168316951
H32	-1.1519694267	6.0738288266	1.1937988968
H33	-2.9244094037	5.9758659340	1.4250727771
H34	-4.9109499507	11.7800071474	2.5091057443
H35	1.3506207762	11.3181415007	2.0971812331
H36	1.4490844343	9.7329653335	1.1958774901
H37	1.6777900238	7.6171372625	1.8475153876
H38	1.1298156246	7.0894115330	3.4998175327
H39	3.9299764152	9.6835903965	1.5866249827
H40	3.8083648323	11.2655954794	2.5101673137
H41	3.4933283350	7.1851512465	4.3277590955
H42	4.0545647273	7.7010128611	2.6568415921
X43	2.6383999998#	10.9009500003#	3.4390499999#
X44	2.5943000001#	8.1144000002#	2.5217500000#
X45	2.7922575448#	10.0919381090#	2.0484747992#
X46	2.4395227059#	7.4687465692#	3.6438921038#
Rh47	-3.0851198346	8.5879461245	5.2496535194
C48	-3.7990787322	11.9895689497	8.6426011992
C49	-2.5151180043	11.5674281713	8.2964978773

C50	-2.3346993308	10.4615951914	7.4693539897
C51	-3.4364225242	9.7493025446	6.9759006799
C52	-4.7223682005	10.1912951412	7.3127749042
C53	-4.9010467094	11.2989466572	8.1397904196
H54	-3.9390844207	12.8488135464	9.2890915027
H55	-1.6475882537	12.1076602113	8.6617726801
H56	-1.3326477814	10.1677452497	7.1853722977
H57	-5.5922961403	9.6693475568	6.9298195596
H58	-5.9069082514	11.6241847983	8.3862054251
H59	-4.5772984421	8.4320712706	5.0711683815
C60	-3.3428041934	7.7183368996	7.2384506990
C61	-3.0133827338	6.7373172679	6.2606474117
H62	-4.3562946986	7.7167547328	7.6145596329
H63	-3.7830369852	6.0853447272	5.8635514901
H64	-2.0014492921	6.3524626587	6.1965915356
H65	-2.6124908186	7.9380894608	8.0038737521
X66	-3.3125013660#	7.2712294752#	6.9662537869#

TS: External OAc Deprotonation

Rh1	2.4178624187	9.6475826676	3.4566895442
Cu2	-0.4965392496	9.2094380371	4.2716205220
O3	2.5813016451	8.1402146324	4.9660863131
O4	2.2146399065	11.1068346384	4.9909391521

O5	0.4061554738	7.5689390478	5.1239534405
O6	0.2637709817	10.3350975279	5.8132218835
C7	1.5291295932	11.0761352761	2.1763967722
C8	1.2737384821	11.0939109229	5.8463687774
C9	1.9282900630	8.1055150145	2.0863792929
C10	1.6241596586	7.4597999896	5.4522391958
C11	2.9039105022	11.2557212177	2.1705365401
C12	1.3499498907	12.0767315958	6.9997885098
C13	3.3046502144	8.2515771994	2.1363167569
C14	1.9493718631	6.4261626748	6.5134540541
H15	1.1190711854	11.5664349986	7.9396965060
H16	1.6049940810	6.8018146704	7.4845457922
H17	3.0228776255	6.2320901710	6.5647265668
H18	0.5956306303	12.8558426898	6.8439260647
H19	2.3351693305	12.5432448127	7.0575736227
H20	1.4061208766	5.5001089857	6.3043941574
O21	-6.4540725429	8.3601909283	4.7564287620
O22	-2.7500652853	7.0978310181	4.0762238009
O23	-6.6471990251	6.4059218248	5.9083173765
O24	-1.1978082464	8.0985972341	2.7626745096
C25	-2.1318297532	7.2430596648	2.9885637235
C26	-7.1039383322	7.3133679994	5.1794837697

C27	-2.4995368052	6.3842170675	1.7865083552
C28	-8.5488631229	7.2962899929	4.6948277366
H29	-3.0637261396	7.0085710093	1.0727312783
H30	-8.5766161971	7.3240787155	3.5914285800
H31	-9.0639193644	6.3997445146	5.0568611424
H32	-1.5927897025	6.0247124813	1.2757515327
H33	-3.1227045920	5.5396486560	2.0996991235
H34	-9.0685570660	8.1978255719	5.0603380738
H35	0.8808960667	11.6412261553	2.8404187353
H36	1.0175275058	10.6076907477	1.3387570021
H37	1.3493242988	8.4822385006	1.2469044423
H38	1.4055222645	7.3757848377	2.6972635019
H39	3.5066399026	10.9425143677	1.3194829860
H40	3.3743285319	11.9809692658	2.8329905452
H41	3.9089994203	7.6293412980	2.7947039462
H42	3.8462005681	8.7389940241	1.3285252690
X43	2.6383999998#	10.9009500003#	3.4390499999#
X44	2.5943000001#	8.1144000002#	2.5217500000#
X45	2.7922575448#	10.0919381090#	2.0484747992#
X46	2.4395227059#	7.4687465692#	3.6438921038#
Rh47	-3.4792578868	8.9774152992	5.2805366000
C48	-4.4650098059	13.0201106772	7.5693898231

C49	-3.1511388610	12.6564370313	7.2440213518
C50	-2.8865541760	11.4374909954	6.6073402586
C51	-3.9298477346	10.5537582639	6.2733863914
C52	-5.2422414096	10.9232065918	6.6091874276
C53	-5.5092430887	12.1447225199	7.2467785982
H54	-4.6716708285	13.9674620850	8.0656672568
H55	-2.3252944761	13.3236071909	7.4873232018
H56	-1.8590634159	11.1783876529	6.3609686660
H57	-6.0686637919	10.2637665425	6.3556762605
H58	-6.5369804462	12.4115113094	7.4907652938
H59	-5.1218565747	8.4187614737	5.1486880452
C60	-3.9299639421	7.6939896154	6.9114394759
C61	-2.5927257111	8.0635272660	6.9253445427
H62	-4.2504762390	6.7467423450	6.4892187486
H63	-1.8258761172	7.4203794223	6.4987914613
H64	-2.2251376181	8.8382302353	7.5952289633
H65	-4.6485092100	8.1645018879	7.5795879945
X66	-3.3125013660#	7.2712294752#	6.9662537869#
O67	-3.5291686035	10.2070299232	3.4852342156
O68	-1.3580454844	10.8583237403	3.4788417012
C69	-2.5799580026	10.9496316955	3.1154003069
C70	-2.8869803439	12.0964137908	2.1683836242

H71	-2.7152223211	13.0425083742	2.6970158970
H72	-2.2059052005	12.0649191229	1.3108555085
H73	-3.9256713519	12.0554136652	1.8313383672

References

1. Krugh, T. R. Spin-Label-Induced Nuclear Magnetic Resonance Relaxation Studies of Enzymes. In *Spin Labeling, Theory and Applications*. Academic Press, New York; 1976; p. 339–372.

2. Cavanagh, J.; Fairbrother, W. J.; Palmer III, A. G.; Rance, M.; Skelton, N. J. Protein Nmr Spectroscopy: Principles and Practice, 2nd Edition, Academic Press, New York; 2007; p. 21.

3. Jacob, J.; Baker, B.; Bryant, R. G.; Cafiso, D. S. Distance Estimates from Paramagnetic Enhancements of Nuclear Relaxation in Linear and Flexible Model Peptides. *Biophys. J.* **1999,** *77*, 1086-1092.

4. Satterlee, J. D. Fundamental Concepts of Nmr in Paramagnetic Systems. Part Ii: Relaxation Effects. *Concepts in Magnetic Resonance* **1990,** *2*, 119-129.

5. Banci, L.; Bertini, I.; Luchinat, C. Nuclear and Electron Relaxation: The Magnetic Nucleus – Unpaired Electron Coupling in Solution; 1991; p. 130.

6. Bochevarov, A. D.; Harder, E.; Hughes, T. F.; Greenwood, J. R.; Braden, D. A.; Philipp, D. M.; Rinaldo, D.; Halls, M. D.; Zhang, J.; Friesner, R. A. Jaguar: A High-Performance Quantum Chemistry Software Program with Strengths in Life and Materials Sciences. *Int. J. Quantum Chem* **2013,** *113*, 2110-2142.

7. Becke, A. D. Density-Functional Thermochemistry. Iii. The Role of Exact Exchange. *The Journal of Chemical Physics* **1993,** *98*, 5648-5652.

8. Grimme, S.; Antony, J.; Ehrlich, S.; Krieg, H. A Consistent and Accurate Ab Initio Parametrization of Density Functional Dispersion Correction (Dft-D) for the 94 Elements H-Pu. *The Journal of Chemical Physics* **2010,** *132*, 154104.

9. Hehre, W. J.; Ditchfield, R.; Pople, J. A. Self—Consistent Molecular Orbital Methods. Xii. Further Extensions of Gaussian—Type Basis Sets for Use in Molecular Orbital Studies of Organic Molecules. *The Journal of Chemical Physics* **1972,** *56*, 2257-2261.

10. Kahn, L. R.; Goddard, W. A. Ab Initio Effective Potentials for Use in Molecular Calculations. *The Journal of Chemical Physics* **1972,** *56*, 2685-2701.

11. Roy, L. E.; Hay, P. J.; Martin, R. L. Revised Basis Sets for the Lanl Effective Core Potentials. *J Chem Theory Comput* **2008,** *4*, 1029-1031.

12. Wertz, D. H. Relationship between the Gas-Phase Entropies of Molecules and Their Entropies of Solvation in Water and 1-Octanol. *J. Am. Chem. Soc.* **1980,** *102*, 5316-5322.

13. Friedrichs, M.; Zhou, R.; Edinger, S. R.; Friesner, R. A. Poisson−Boltzmann Analytical Gradients for Molecular Modeling Calculations. *The Journal of Physical Chemistry B* **1999,** *103*, 3057-3061.

14. Tannor, D. J.; Marten, B.; Murphy, R.; Friesner, R. A.; Sitkoff, D.; Nicholls, A.; Honig, B.; Ringnalda, M.; Goddard, W. A. Accurate First Principles Calculation of Molecular Charge Distributions and Solvation Energies from Ab Initio Quantum Mechanics and Continuum Dielectric Theory. *J. Am. Chem. Soc.* **1994,** *116*, 11875-11882.

15. Sheldrick, G. M. (2008). *Cell_ now*, version 2008/4.

Georg-August-Universität Göttingen, Göttingen, Germany

16. Bruker (2012). *Saint; SADABS; TWINABS; APEX3*. Burker AXS Inc., Madison, Wisconsin, USA.

17. Sheldrick, G. M., SHELXT–Integrated space-group and crystal-structure determination. *Acta Crystallogr., Sect. A: Found. Crystallogr.* **2015,** *71*, 3-8;

18. Dolomanov, O. V.; Bourhis, L. J.; Gildea, R. J.; Howard, J. A.; Puschmann, H., OLEX2: a complete structure solution, refinement and analysis program. *J. Appl. Crystallogr.* **2009,** *42*, 339-341.